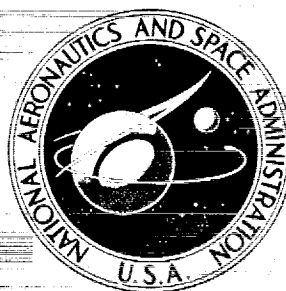


**NASA TECHNICAL
MEMORANDUM**



NASA TM X-2272

NASA TM X-2272

**CASE FILE
COPY**

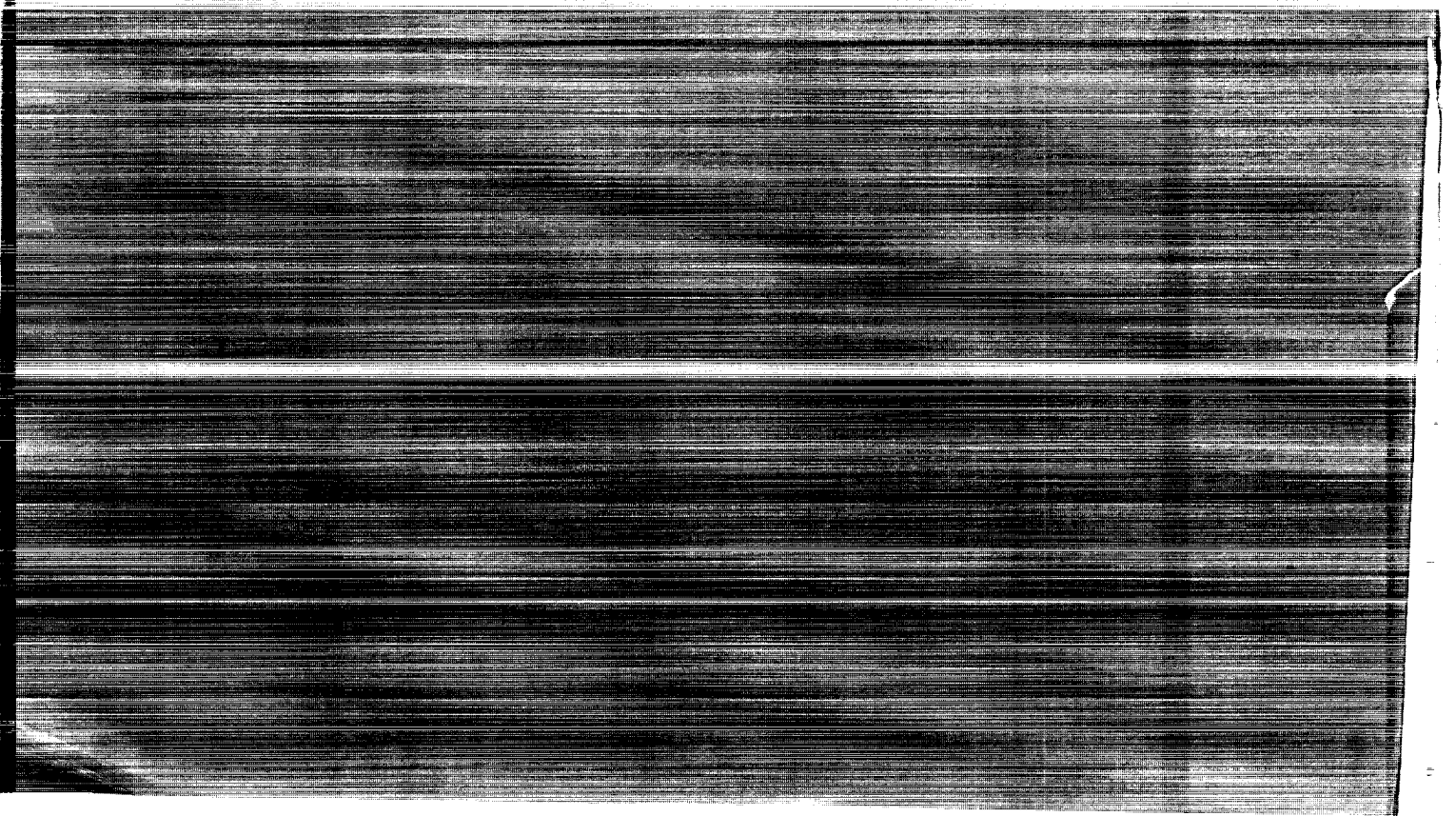
**NASA SPACE SHUTTLE
TECHNOLOGY CONFERENCE**

**Volume I - Aerothermodynamics, Configurations,
and Flight Mechanics**

**Held at
Langley Research Center
Hampton, Virginia
March 2-4, 1971**

NATIONAL AERONAUTICS AND SPACE ADMINISTRATION • WASHINGTON, D. C. • APRIL 1971

[The top half of the page contains extremely faint, illegible text, likely bleed-through from the reverse side of the document. The text is organized into several paragraphs and possibly a table, but the characters are too light to transcribe accurately.]



1. Report No. NASA TM X-2272		2. Government Accession No.		3. Recipient's Catalog No.	
4. Title and Subtitle NASA SPACE SHUTTLE TECHNOLOGY CONFERENCE Volume I - Aerothermodynamics, Configurations, and Flight Mechanics				5. Report Date April 1971	
				6. Performing Organization Code	
7. Author(s)				8. Performing Organization Report No. L-7737	
9. Performing Organization Name and Address				10. Work Unit No.	
				11. Contract or Grant No.	
				13. Type of Report and Period Covered Technical Memorandum	
12. Sponsoring Agency Name and Address National Aeronautics and Space Administration Washington, D.C. 20546				14. Sponsoring Agency Code	
15. Supplementary Notes Held at the NASA Langley Research Center, March 2-4, 1971.					
16. Abstract The conference encompassed three technology efforts, each published as a separate NASA Technical Memorandum. Volume I - Aerothermodynamics, Configurations, and Flight Mechanics (includes aerodynamics; atmospheric operations; and aerodynamic heating). NASA TM X-2272, 1971. Volume II - Structures and Materials (includes structural design technology; thermal protection systems; and materials technology). NASA TM X-2273, 1971. Volume III - Dynamics and Aeroelasticity (includes dynamic loads and response; aeroelasticity; and flight dynamics and environment). NASA TM X-2274, 1971.					
17. Key Words (Suggested by Author(s)) Space shuttle Aerothermodynamics Dynamics Aeroelasticity Structural design Thermal protection				18. Distribution Statement Unclassified - Unlimited	
19. Security Classif. (of this report) Unclassified		20. Security Classif. (of this page) Unclassified		21. No. of Pages 760	
				22. Price* \$9.00	

* For sale by the National Technical Information Service, Springfield, Virginia 22151

FOREWORD

A significant factor in the development of new technology is the timely exchange of information to highlight areas of progress and to establish areas in need of greater emphasis - in short, to provide both program management and technical contributors an opportunity to review their work and plans in the context of the requirements and constraints of the total program.

During the past two years, the Langley Research Center has made a concerted effort to support the NASA objectives for development of a low-cost space transportation system - the space shuttle. The Langley effort covers a broad base of technology including electronics and life support systems, but its primary focus has been in the areas of Aerothermodynamics, Configurations, and Flight Mechanics; Structures and Materials; and Dynamics and Aeroelasticity.

Thus it was in the context of the need for a technology status review and our own active involvement in the aforementioned areas of technology that the Langley Research Center was pleased to host the Shuttle Technology Conference which culminated in this document. As the reader will recognize, the development and presentation of this information was largely achieved by very busy people doing an additional job. Nevertheless, I believe the results of the conference reflect a highly motivated and cooperative effort on the part of industry and NASA centers to provide the best information available for technical review and assessment. This effort is deeply appreciated by those of us involved in the implementation of the conference. Thus, to the authors, session chairmen, and numerous individuals involved in the logistic support of this conference, I offer my thanks both for your effort and for your cooperation. A job well done!

George W. Brooks
General Chairman

CONTENTS

VOLUME I.- AEROTHERMODYNAMICS, CONFIGURATIONS, AND

FLIGHT MECHANICS

Chairman - A. Henderson, LaRC

GLOSSARY	ix
--------------------	----

OPENING REMARKS

1. CURRENT SHUTTLE STATUS	1
by C. J. Donlan, Acting Director, Space Shuttle Program, OMSF	
2. INTRODUCTORY REMARKS	17
by A. O. Tischler, Director of Shuttle Technologies Office, OART	

HEAT TRANSFER

Chairman - J. C. Dunavant, LaRC

Co-Chairman - J. G. Marvin, ARC

3. FLOW FIELDS AND AERODYNAMIC HEATING OF SPACE SHUTTLE ORBITERS	21
by J. G. Marvin, W. K. Lockman, G. G. Mateer, H. L. Seegmiller, C. C. Pappas, C. DeRose, and G. E. Kaattari (ARC)	
4. AN ANALYSIS OF PREDICTED SPACE SHUTTLE TEMPERATURES AND THEIR IMPACT ON THERMAL PROTECTION SYSTEMS	75
by R. V. Masek (MDAC) and J. A. Forney (MSFC)	
5. BOUNDARY-LAYER TRANSITION AND HEATING CRITERIA APPLICABLE TO SPACE SHUTTLE CONFIGURATIONS FROM FLIGHT AND GROUND TESTS	97
by Charles B. Johnson (LaRC)	
6. A NUMERICAL PROCEDURE TO CALCULATE THE INVISCID FLOW FIELD ABOUT A SPACE SHUTTLE ORBITER TRAVELING AT A SUPERSONIC/HYPERSONIC VELOCITY	157
by B. Grossman, F. Marconi, Jr., and G. Moretti (GAC)	
7. SHOCK INTERFERENCE HEATING AND DENSITY-RATIO EFFECTS:	
PART I - FLOW FIELD VISUALIZATION, THERMOCOUPLE MEASUREMENTS, AND ANALYSIS	
by H. Lee Seegmiller (ARC)	

PART II - HYPERSONIC DENSITY-RATIO EFFECTS	217
by James L. Hunt and Theodore R. Creel, Jr. (LaRC)	
8. SHOCK INTERFERENCE HEATING ON THE SPACE SHUTTLE BOOSTER DURING ASCENT	245
by O. Brevig and C. Young (GD/C)	
9. LEE-SIDE HEATING INVESTIGATIONS:	
PART I - EXPERIMENTAL LEE-SIDE HEATING STUDIES ON A DELTA-WING ORBITER	267
by Jerry N. Hefner and Allen H. Whitehead, Jr. (LaRC)	
PART II - LEE-SIDE HEATING INVESTIGATIONS OF SIMPLE BODY-LIKE CONFIGURATIONS	289
by George Maise (GAC)	
AERODYNAMICS	
Chairman - B. Z. Henry, LaRC	
Co-Chairman - T. Sieron, AFFDL	
10. STATIC AND DYNAMIC AERODYNAMICS OF SPACE SHUTTLE VEHICLES	311
by Victor L. Peterson, Elliott D. Katzen, John A. Axelson, Jack J. Brownson, Donald L. Ciffone, Joseph W. Cleary, Peter F. Intrieri, Gerald N. Malcolm, and Jack A. Mellenthin (ARC)	
11. CONTROL AND HANDLING QUALITIES OF SPACE SHUTTLE ORBITERS	375
by Richard W. Powell, James J. Adams, and Lawrence W. Brown (LaRC)	
12. PLUME IMPINGEMENT DURING SEPARATION OF A TWO-STAGE SPACE SHUTTLE VEHICLE	393
by Ivy Fossler (MSC) and Robert Prozan (IMSC)	
13. CONSIDERATION OF REYNOLDS NUMBER SIMULATION FOR SUBSONIC SHUTTLE TESTS	423
by Thomas B. Sellers (MDAC)	
14. CORRELATION OF SPACE SHUTTLE APPLICABLE EXPERIMENTAL HYPERSONIC AERODYNAMIC CHARACTERISTICS WITH THEORY	455
by Richard K. Hamilton (MDAC)	
15. THE DELTA BODY - A POTENTIAL SPACE SHUTTLE ORBITER	493
by Grover L. Alexander (IMSC - Sunnyvale)	

OPERATIONAL FLIGHT MECHANICS

Chairman - P. F. Holloway, LaRC

Co-Chairman - C. R. Huss, MSC

16. SPACE SHUTTLE SEPARATION SYSTEM	539
by Frank Jarlett (GD/C)	
17. FLIGHT DYNAMICS OF A STRAIGHT-WING SPACE SHUTTLE BOOSTER DURING ENTRY	581
by L. G. Kimbrel and J. T. Patha (Boeing)	
18. BOOSTER WING GEOMETRY TRADE STUDIES	611
by H. G. Struck (MSFC) and J. E. Butsko (GD/C)	
19. ORBITER ENTRY TRAJECTORY CONTROL:	
PART I - HIGH-SPEED ENTRY PHASE	643
by J. McNamara (GAC)	
PART II - TERMINAL PHASE ENTRY	675
by L. Weiss (GAC)	
20. MINIMUM SHUTTLE THERMAL PROTECTION SYSTEM WEIGHT THROUGH TRAJECTORY SHAPING	691
by Henry W. Kipp and David O. Swain (MDAC)	

GLOSSARY

AC	aerodynamic center
ACLS	air cushion landing system
ACPS	attitude control propulsion system
ADV	advanced
AEM	acoustical emission monitoring
AFFDL	Air Force Flight Dynamics Laboratory
AFML	Air Force Materials Laboratory
APU	auxiliary power unit
ARC	Ames Research Center
ASCEP	Advanced Structural Concepts Experimental Program
ASOP	Automated Structural Optimization Program
AS-REC	as received
ATT	attitude
ATTACH	attachment
BBN	Bolt, Beranek, and Newman
BL	boundary layer
BPR	bypass ratio
BS	body station
BST	booster
CDC	Control Data Corporation
CER	cost estimating relationship
CONT	control
CONV	conventional
CPU	central processing unit
C.R.	cross range

CRIT	critical
CRT	cathode ray tube
CTI	cryogenic insulation
CW	cold worked
DB	dead band
DIA	diameter
DISP	dispersion; displacement
DSM	dispersion-strengthened metals
DW	double wall
EB	electron beam
ECS	environmental control system
ELONG	elongation
EMR	electromagnetic radiation
FLT	flight
FPL	fluctuating pressure level
FSW	flyback system weight
GAC; GAEC	Grumman Aerospace Corporation
GDC; GD/C	General Dynamics/Convair
GDLSWT	General Dynamics low speed wind tunnel
GE	General Electric Co.
GEN	generator; generated
GE-RES	General Electric Reentry and Environmental Systems Division
HABP	hypersonic arbitrary-body program
HASP	hypersonic aerospace structures program
h. c.	honeycomb
HCF	hardened compacted fibers

HDWE	hardware
HMG	high-modulus graphite
HS	heat sink
HSG	high-strength graphite
HT	high temperature
HX	heat exchanger
HYP	hypersonic
IMU	inertial measurement unit
INSUL	insulation
INT	internal
i. s.	isogrid
IU	instrument unit
L	longitudinal
LaRC; LRC	Langley Research Center
LCR	low cross range
LE	leading edge
LeRC	Lewis Research Center
L. LOAD	limit load
LMSC	Lockheed Missiles and Space Company
LW	left wing
MAC	mean aerodynamic chord
MARL	Mobile Acoustic Research Laboratory
MDAC	McDonnell-Douglas Astronautics Corporation
MDC	McDonnell Douglas Corporation
MEAS	measured
MGMT	management
MIN	minimum

MMC	Martin Marietta Corporation
MRP	moment reference point
MSC	Manned Spacecraft Center
MSFC	Marshall Space Flight Center
MTF	Mississippi Test Facility
NAR; NR	North American Rockwell
NDE	nondestructive evaluation
NDI	nondestructive inspection
NDT	nondestructive testing
NPSH	nominal positive suction head
OA FPL	overall fluctuating pressure level
OA PWL	overall acoustic power level
OART	Office Advanced Research and Technology
OA SPL	overall sound pressure level
OMSF	Office Manned Space Flight
ORB	orbiter
POS	positive
ppm	parts per million
PS	post support
PSD	power spectral density
PWR	power
R _{CR}	cruise range
RCS	reaction control system
RDT&E	Research, Development, Tests, and Engineering
REI	reusable external insulation
REQ'D	required
RT	room temperature

RW	right wing
SAT	Saturn
SBC	single body canard
s/c	skin corrugation
SEP	separated
SF	safety factor
SL	sea level
SLA	spacecraft lunar module adapter
SPL	sound pressure level
SR&T	space research and technology
s.s.	simple support
SSV	space shuttle vehicle
STR	strengthened
SUB	subsonic
SW	single wall
T	transverse
T'COUPLES	thermocouples
TECH	technology
TPS	thermal protection system
TURB	turbulent
TWT	transonic wind tunnel
UB	underbody
u.i.s.	unidirectional
ULT	ultimate
VMSC	Vought Missiles and Space Corporation
WL	water line
WT	wind tunnel

CURRENT SHUTTLE STATUS

By C. J. Donlan, Acting Director, Space Shuttle Program, OMSF
NASA Headquarters, Washington, D.C.

Space Shuttle Program objectives are to provide future capabilities to support a wide range of scientific, defense, and commercial uses at substantially lower costs than current space operations.

SPACE SHUTTLE COST TRENDS (Figure 1)

The dotted band in figure 1 defines the locus of costs for current transportation systems ranging in size from the Scout to the Saturn V. For a particular payload capability, the points on the curve show the transportation cost per pound for the lowest cost transportation system available for that payload.

The line identified as Fixed Cost/Flight is that projected for the Space Shuttle. For the maximum payload envisioned, approximately 65 000 pounds ($\approx 29\,500$ kg), it is seen that a reduction in cost of a factor of 10 is possible. Of equal importance is that the payload weight carried by the shuttle can also be reduced by a factor of 10 and still allow the shuttle to place the lower size payload in orbit cheaper than any other available system. It is this flexibility in operation that makes the shuttle an attractive transportation system.

Study results also support the thesis that an equally important reduction in manufacturing cost-per-pound of payload can be achieved by designing the payload to make use of features supplied by the shuttle, such as a more benign environment at launch and the ability to maintain or retrieve the payload in orbit. Lower transportation costs and lower cost of the payloads transported are both essential to a continued effective space program.

SPACE SHUTTLE COST TRENDS

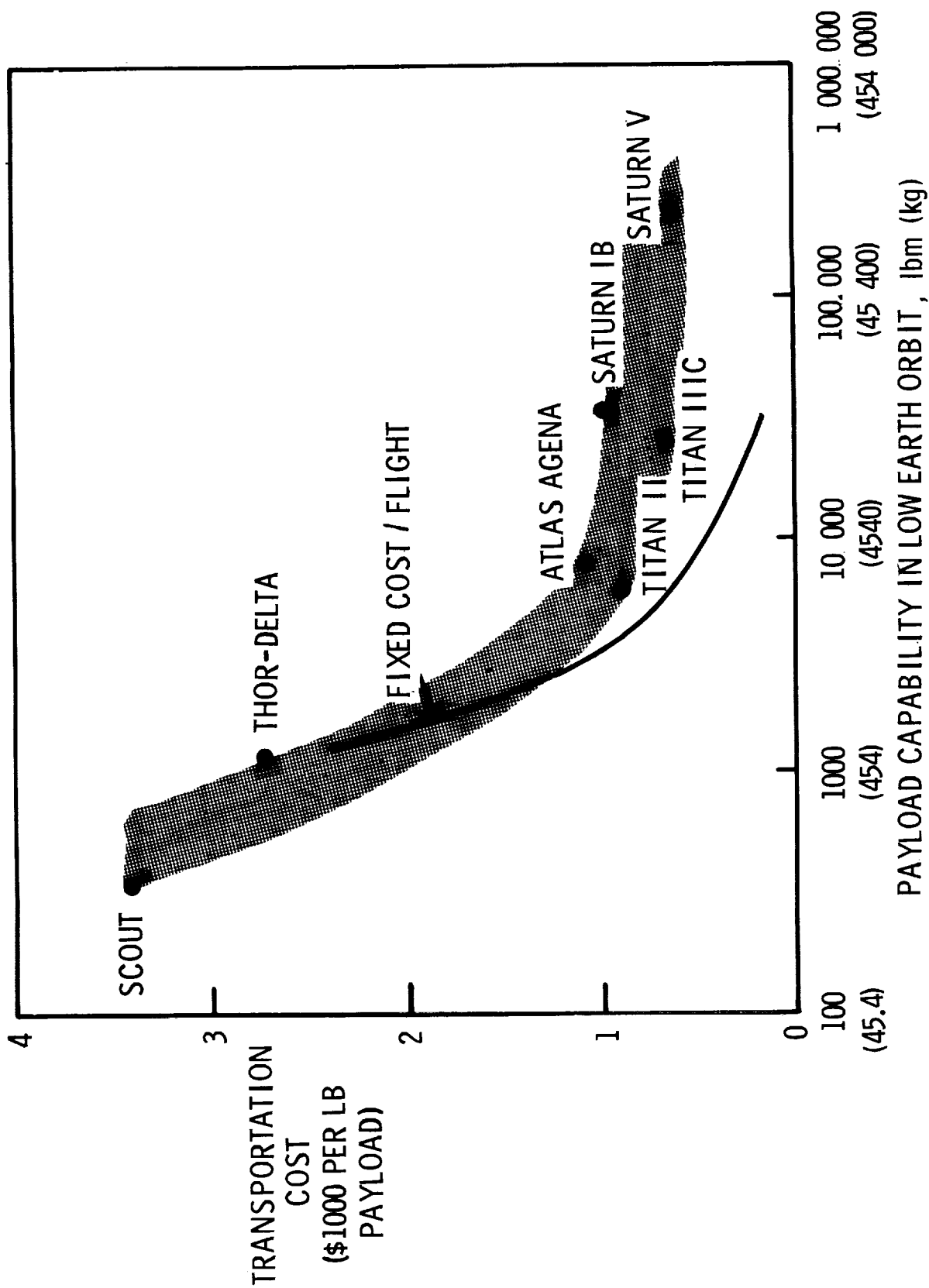


Figure 1

TECHNOLOGY CONTRIBUTIONS

(Figure 2)

For the past 12 to 18 months, the technology has been primarily plans oriented and directed toward problem assessment. There has been much progress made relative to mobilization of personnel and resources within NASA and in industry to address the technology problems of shuttle. These programs are now well under way and are proceeding in an effective manner.

As of this time, in support of the Phase B effort, much progress has been made in the area of assessing performance requirements, engine size, and vehicle configuration. Such information has provided a basis for narrowing the range of the Phase B configuration studies and settling on more precise performance specifications.

TECHNOLOGY CONTRIBUTIONS

- PROBLEM ASSESSMENT
- MOBILIZATION OF PEOPLE AND RESOURCES
- BROAD TECHNOLOGY PROGRAM PLANNED AND UNDERTAKEN
- DIRECT SUPPORT OF PHASE B IN SETTING
 - PERFORMANCE REQUIREMENTS
 - ENGINE SIZE
 - VEHICLE CONFIGURATION

SPACE SHUTTLE CONFIGURATION EVOLUTION

(Figure 3)

This figure shows the steps in the evolution of the low cross-range orbiter and the high cross-range orbiter and the associated boosters during the course of the Phase B studies. The straight-wing designs of both the orbiter and the booster have been dropped from the program because of deficiencies determined from aerothermal analyses and wind-tunnel studies. The high cross-range orbiter has evolved into a delta-type configuration with a single vertical tail. Both boosters have evolved into a canard-type configuration for similar reasons.

SPACE SHUTTLE CONFIGURATION EVOLUTION

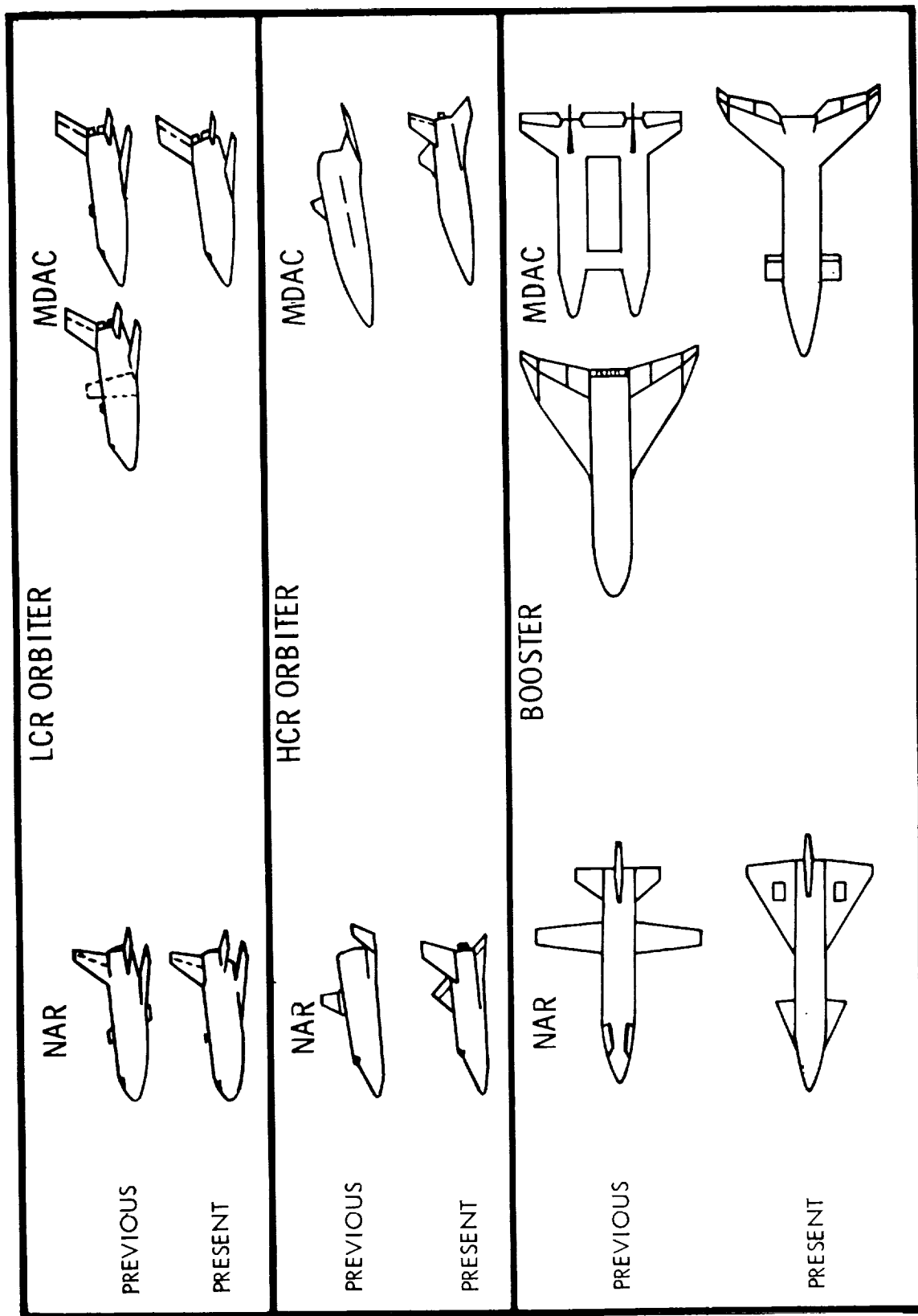


Figure 3

SPACE SHUTTLE PERFORMANCE SPECIFICATIONS

(Figure 4)

This figure is a summary of the current Level I requirements for the reusable shuttle.

The cargo bay is baselined as 15 feet (4.6 m) in diameter by 60 feet (18.3 m) in length. The 60-foot dimension is perhaps the firmest dimension inasmuch as it provides space for rockets such as the Agena and Centaur stages.

It is anticipated that most missions will operate with the airbreathers in; however, as experience with the shuttle is acquired, it is feasible to consider operation with the airbreathers out, in which case, another 20 000 pounds (9075 kg) of payload can be carried in the east or south circular orbits. The design of the structural landing load is based upon a return payload weight of 40 000 pounds (18 150 kg).

The 1100 nautical mile cross range allows a return to the initial launch site in a single revolution in the event of an abort to orbit.

The life support system and fuel requirements for the shuttle while in orbit are based on 7 days of self-sustaining orbital flight. The systems will be qualified for 30 days in orbit, but the expendables for orbital flight in the excess of 7 days will be charged against payloads.

SPACE SHUTTLE PERFORMANCE SPECIFICATIONS

- TWO-STAGE, FULLY REUSABLE SHUTTLE
- CARGO BAY - 15 ft DIAMETER \times 60 ft LENGTH (4.6 m \times 18.3 m)

MISSION	PAYLOAD	
	AIRBREATHERS OUT, lbm (kg)	AIRBREATHERS IN, lbm (kg)
100 n.mi. DUE EAST CIRCULAR ORBIT	65 000 (29 484)	\approx 45 000 (20 412)
100 n.mi. SOUTH POLAR CIRCULAR ORBIT	40 000 (18 144)	\approx 20 000 (9072)
270 n.mi. AT 55° INCLINATION	\approx 45 000 (20 412)	25 000 (11 340)
DOWN PAYLOAD	40 000 (18 144)	25 000 (11 340)

- 1100 n.mi. ORBITER NOMINAL CROSSRANGE
- MISSION DURATION - 7 DAYS SELF SUSTAINING FROM LIFT-OFF TO LANDING
- 30 DAYS EXPENDABLES CHARGED AGAINST PAYLOADS
- MAIN ENGINE BASELINED AT 550 000 lbf (2 446 400 N) SEA LEVEL THRUST (BOOSTER AND ORBITER)
- AIR BREATHING ENGINES USE JET FUEL
- ACCELERATION NOT TO EXCEED 3 g

Figure 4

SPACE SHUTTLE CURRENT STATUS

(Figure 5)

Level I Program requirements have been summarized on the preceding figure.

The President's budget contains \$100 million for the space shuttle with a positive recommendation to proceed with the development of the engine for which the RFP* was released on March 1, 1971. We are indicating an August 1971 release for the vehicle RFP should the current Phase B studies and complementary Phase A activity provide the confidence to move out into Phase C.

The schedule assumes also that the necessary approvals to proceed in this manner will be obtained in the same time period.

*RFP Request for proposal.

SPACE SHUTTLE CURRENT STATUS

- LEVEL I PROGRAM REQUIREMENTS REDEFINED
- PHASE B STUDIES NOW IN 8TH MONTH, WILL BE COMPLETED IN MAY (6 WEEK EXTENSION FOR MAIN ENGINE STUDIES)
- PRESIDENT'S FY 1972 BUDGET CONTAINS \$100M FOR SPACE SHUTTLE AN INCREASE OF \$20M OVER FY 1971
- PROGRAM PLANNING:
 - MAIN ENGINES - RFP - MARCH 1971
START PHASE C - AUGUST 1971
 - VEHICLE - RFP - AUGUST 1971
START PHASE C - MARCH 1972

Figure 5

SPACE SHUTTLE PLANNING SCHEDULE

(Figure 6)

Current planning anticipates first horizontal flight tests of an orbiter in mid-1976 with the first manned orbital flight of the shuttle system planned in the second quarter of calendar year 1978.

Because shuttle development is planned to start in 12 to 16 months, the technology program must be harnessed to provide definitive answers to the design and development teams in the next year and a half.

SPACE SHUTTLE PLANNING SCHEDULE

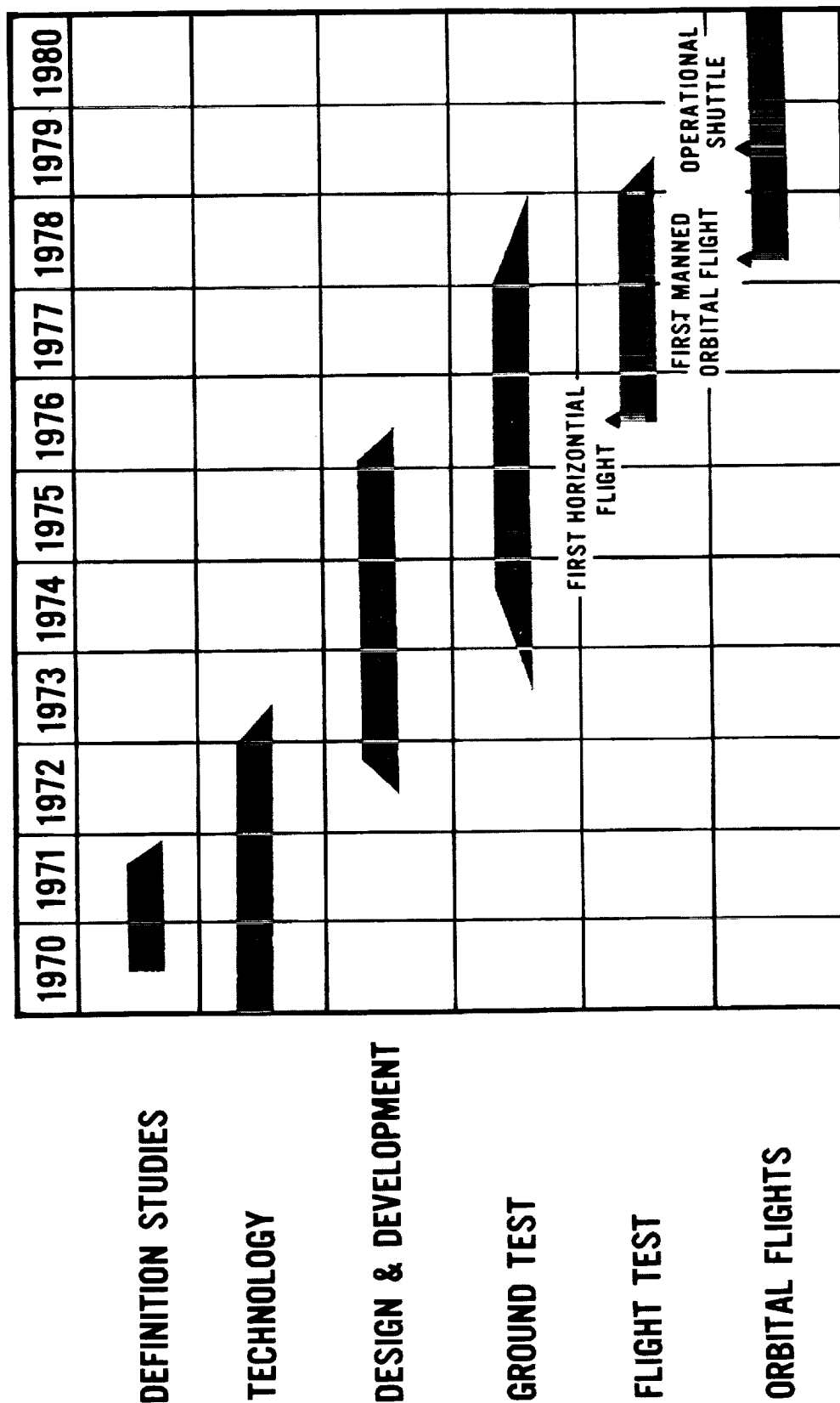


Figure 6

TECHNOLOGY CHALLENGE

(Figure 7)

The greatest technology challenge from the point of view of the Shuttle Program Office is to generate the design data relative to advanced materials properties, aerodynamic heating, and flight loads in enough depth to allow Phase C activities to proceed with confidence and to provide hard data to support or challenge solutions relative to the thermal protection and advanced structural concepts being proposed.

The technology teams and researchers need to assure that their programs are relevant and that the results of the programs are made highly visible for assimilation into the shuttle design and development process.

TECHNOLOGY CHALLENGE

- GENERATE DESIGN DATA RELATIVE TO ADVANCED MATERIALS
PROPERTIES, AERODYNAMIC HEATING AND FLIGHT LOADS
- DEMONSTRATE APPLICATION OF THERMAL PROTECTION
AND ADVANCED STRUCTURAL CONCEPTS

Figure 7

INTRODUCTORY REMARKS

By A. O. Tischler
Director of Shuttle Technologies Office, OART
NASA Headquarters, Washington, D.C.

PAPER 2

This conference is on the technology work being done for the reusable space launch vehicle commonly known as the shuttle. It covers three areas of work. These are the related fields of aerodynamics and configuration refinement, structures and materials, including thermal protection systems, and aeroelasticity and dynamics. Since this audience of experts knows as well as I what is involved in these activities, any remarks here will be confined to three points.

First let me thank Edgar Cortright and his staff at the Langley Research Center for hosting this three-day conference. This is the first of a series of four such conferences to be held this spring. They will cover all technology working group activities.

May I thank Dr. George Brooks and Eugene Love, Chairman and Vice-Chairman, for making all the necessary detail arrangements. I should also like to extend my thanks to the working group chairmen, who were responsible for lining up the presentations for this conference. Their success will soon be judged by you all.

Second, I should like to review some history of this program. It will interest those of you who were not here then that approximately two years ago a conference was held in this same hall to consider both the shuttle and the space station as new space projects. We have come a long way since that time.

Roughly 20 months ago Dr. George Mueller, then head of the Office of Manned Space Flight, persuaded Bruce Lundin, then head of the Office of Advanced Research and Technology, to conduct a technology program to prepare the base

for developing a shuttle. Thus, he succeeded in getting OART to spend its money to do what OMSF would otherwise be required to fund. Despite the obvious disparity in annual incomes, this procedure, I felt, was a socially acceptable form of pick-pocketing since I had for a long time felt that OART needed to focus its meager technology efforts on supporting real space mission prospects. Although there must always be some part of every research establishment that searches for breakthroughs into new arenas of endeavor, it was observable to me that when spread to cover all technologies of interest, OART efforts were thin enough to be virtually transparent. Better, I insisted, to put enough weight behind one spearhead to punch through the barrier. In addition, OART centers, particularly the Langley Research Center, and Headquarters personnel had for some time been examining technological problems pertinent to a flyable reentry vehicle.

Bruce therefore accepted George's proposition to participate, Dutch treat, but retaliated by assigning me to manage the job; thus, he cleverly designed everyone's punishment to fit his own particular crime.

Thus we began this crusade to flesh out fancy with fact. And progress is being made. That progress, I believe, is attributable to the drive and dedication of the people who make up this program. For the first time, perhaps, all NASA Centers are participating actively in one total effort. Some parochial boundaries are beginning to disappear. We would like you to participate also in generating, getting, and using the results of this total effort, and that is the principal purpose of this conference.

Let me return to the present to make my third point. The papers presented in this conference cover only part of the total effort encompassed by the technology program. They do, however, uncover many of the problems that stand in

the way of complete technological readiness for building the shuttle. But this review will reveal more experimental results than previous reviews have, and that trend will continue in future conferences. I want to encourage this audience to engage the presentors, personally, by telephone or by mail, to gain a fuller understanding of these problems and results. If you agree, you can support each other's conviction. If you disagree one of you, or perhaps both of you, has the opportunity to enhance his engineering acumen. In this game, there is no substitute for knowing what we are doing. Since there is so much to learn and confirm, I say now let's get on with it.

FLOW FIELDS AND AERODYNAMIC HEATING

OF SPACE SHUTTLE ORBITERS

By J. G. Marvin, W. K. Lockman, G. G. Mateer,
H. L. Seegmiller, C. C. Pappas, C. DeRose,
and G. E. Kaattari

NASA Ames Research Center
Moffett Field, California

INTRODUCTION

Ames Research Center has devoted considerable effort toward defining the flow fields and heating environment that space shuttle orbiters will encounter. The purpose of this work is to provide a broad base of data which can be relied on to evaluate prediction techniques with the ultimate objective of providing a means for extrapolating ground-based facility data to flight conditions. A review of earlier work was presented at the first technology symposium (see Ref. 1). The highlights of our technology effort during the past six months are given in this paper. Photographs of streamline oil-flow patterns, pressure-distribution data, and heating data on the windward surface of low and high cross-range orbiters are presented and comparisons with theory are shown. All the data were obtained in the Ames 3.5-foot hypersonic wind tunnel.

ORBITER CONFIGURATIONS

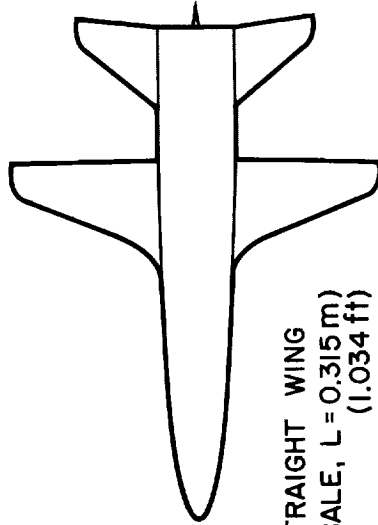
(Slide 1)

The configurations tested are shown on Slide 1. They are the Manned Space Flight Center (MSC) straight-wing orbiter, and the North American Rockwell (NAR) straight-wing and delta-wing orbiters. The scaled model size and length are shown for reference. The two delta-wing models were geometrically similar, but the 129 model had a slightly larger wing area. These configurations represent typical concepts for space shuttle vehicles, and the flow field and heating problems on these shapes are typical of those on other proposed configurations.

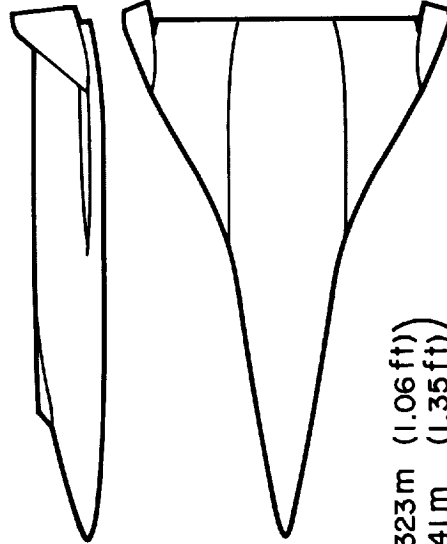
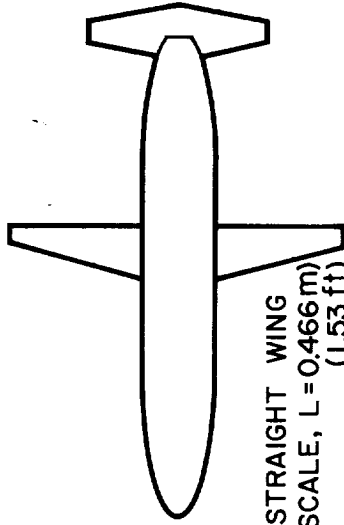
ORBITER CONFIGURATIONS



NAR STRAIGHT WING
(0.006 SCALE, L = 0.315 m)
(1.034 ft)



MSC STRAIGHT WING
(0.01 SCALE, L = 0.466 m)
(1.53 ft)



NAR DELTA WING
(134 - 0.006 SCALE, L = 0.323 m (1.06 ft))
(129 - 0.008 SCALE, L = 0.41 m (1.35 ft))

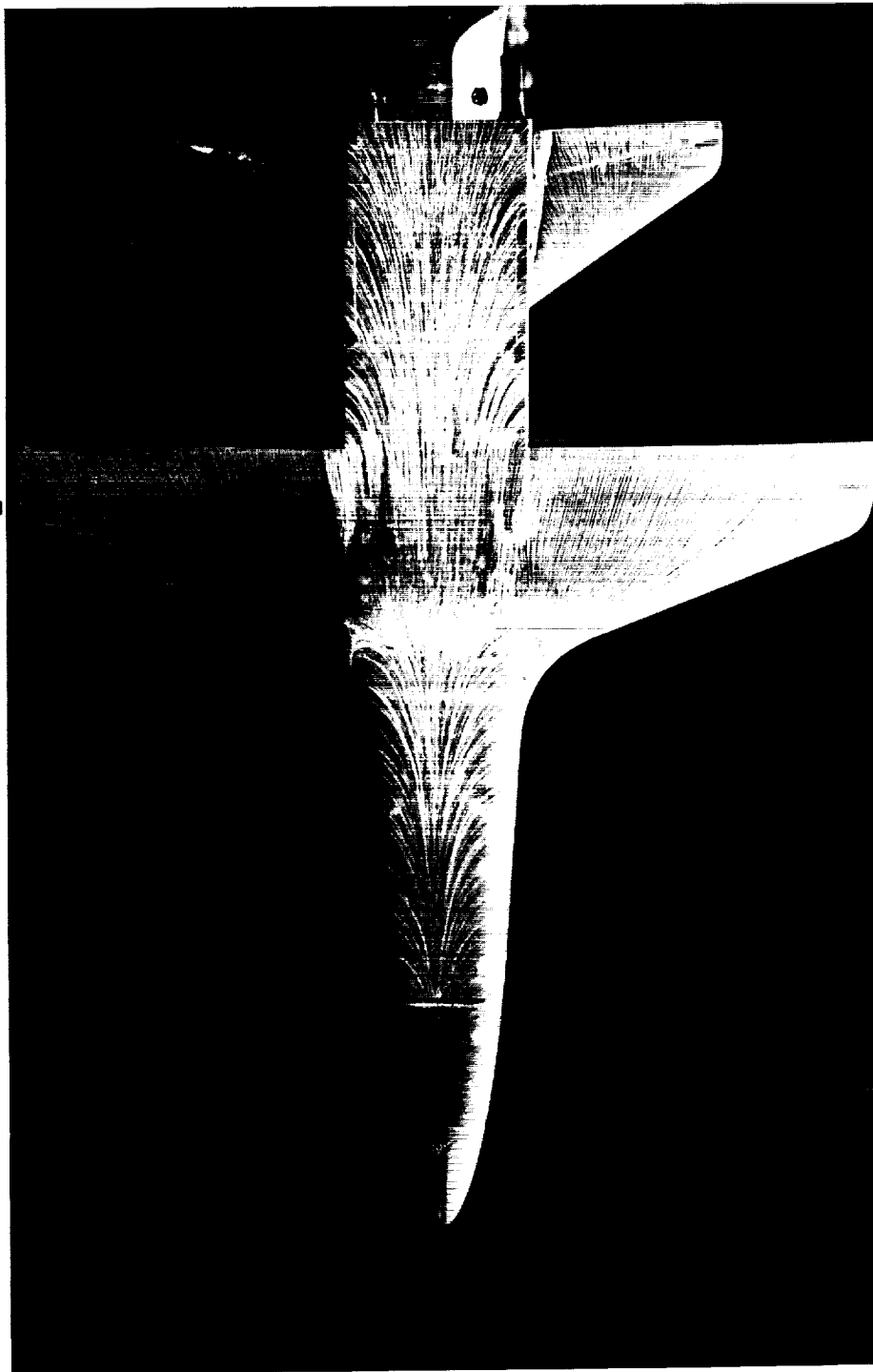
WINDWARD SURFACE OIL-FLOW PHOTOGRAPH

(Slide 2)

Slide 2 is a photograph of an oil-flow pattern representing the surface streamline directions on the lower surface of the NAR straight-wing orbiter at $\alpha = 60^\circ$ and $M_\infty = 7.4$. Uniform patterns which show significant cross flow are formed on the fuselage ahead and downstream of the wing location. The influence of the wing on the fuselage pattern appears as an oil buildup and a rapid out-turning of the oil near the beginning of the wing fileet. This effect is related to the increase in surface fuselage pressure caused by the presence of the wing. On the wing itself, a stagnation region appears with a reversed flow region near the fileet and a stagnation line emanating from this region is easily recognized. This photograph is helpful in interpreting the pressure and heating distributions presented in the following slides.

WINDWARD SURFACE OIL-FLOW PHOTOGRAPH
NAR STRAIGHT-WING ORBITER

$M_\infty = 7.4$ $\alpha = 60^\circ$ $Re_{\omega_L} = 1.4 \times 10^6$



Slide 2

CENTERLINE PRESSURES AND HEATING RATES

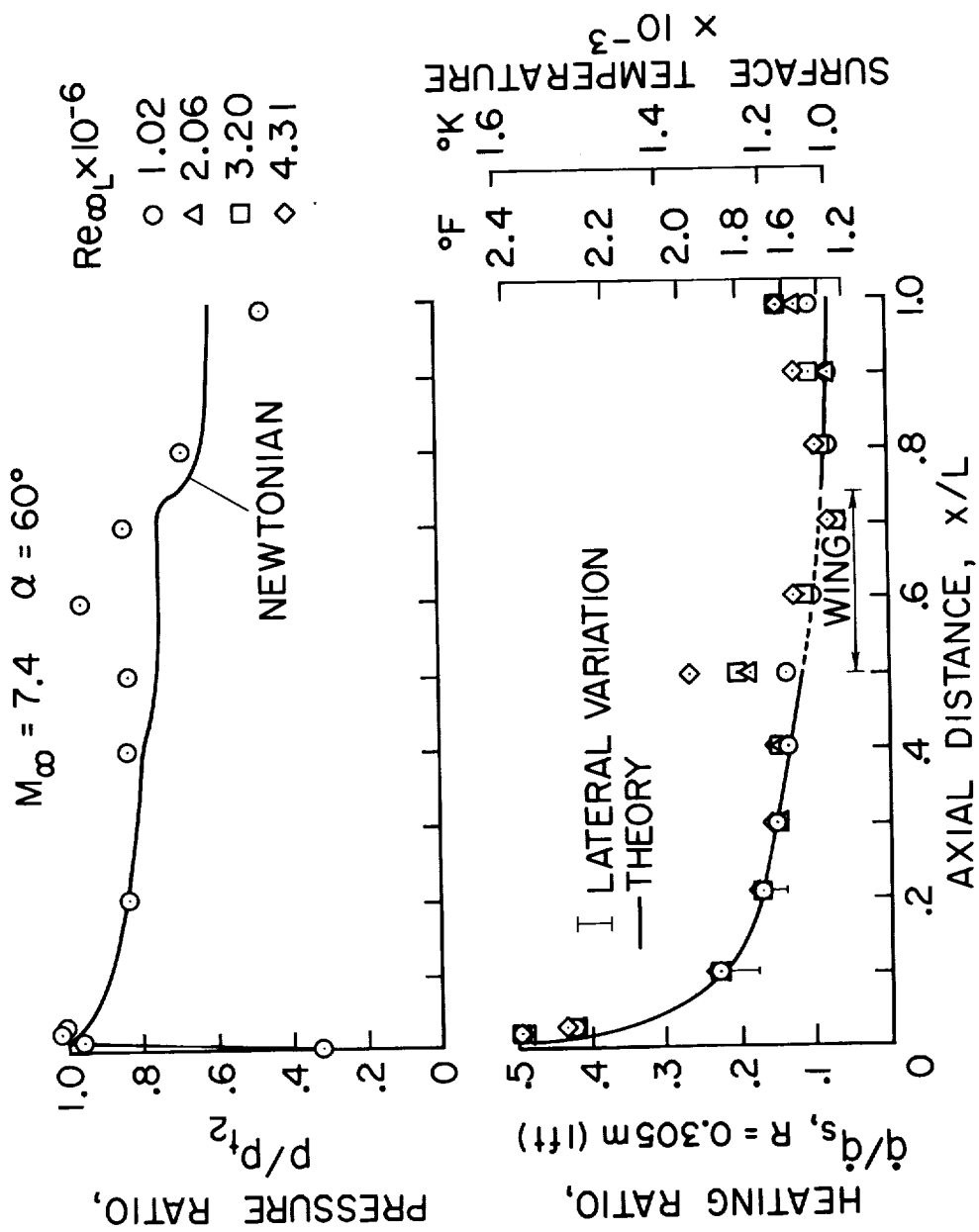
(Slide 3)

Normalized pressures and heating rates are plotted versus the axial distance along the fuselage. The pressures, normalized by free-stream stagnation pressure, decrease with distance from the stagnation region, rise sharply in the wing region, and then decrease. No significant differences in pressure distribution occurred with changes in Reynolds number. Over most of the fuselage the measured pressures are somewhat higher than the Newtonian prediction. A notable difference in this trend occurs at the most rearward station where the measured pressure may indicate the expansion of the flow around the model base.

Heating rates obtained with a thermocouple model are normalized by a theoretical scaled-sphere heating rate. Radiation equilibrium surface temperatures corresponding to the peak heating rate along a typical low cross-range trajectory are shown.* The lowest Reynolds number corresponds to the value for a full-scale vehicle near peak heating. At the beginning of the wing region, the data indicate a trend of increased heating with increased Reynolds number, indicating the complex nature of the flow in this region. The data toward the rear of the fuselage also depend on Reynolds number, indicating that transition to turbulent flow may be taking place. The laminar theory line represents the calculated heating rates using cross-flow theory from Ref. 2. Along the fuselage centerline, this theory reduces to swept-cylinder theory, modified to account for differences in centerline velocity gradient by applying the velocity gradient correlation equation from Ref. 3. Beyond $x/L = .1$, the theory and data agree reasonably well, except in the regions where Reynolds number effects occurred.

* For the straight-wing orbiters, $q_s, R = .305$ m = 567 kW/m^2 ($50 \text{ Btu/ft}^2\text{sec}$) and $\epsilon = .8$.

CENTERLINE PRESSURES AND HEATING RATES NAR STRAIGHT-WING ORBITER



Slide 3

WINDWARD SURFACE OIL-FLOW PHOTOGRAPH

(Slide 4)

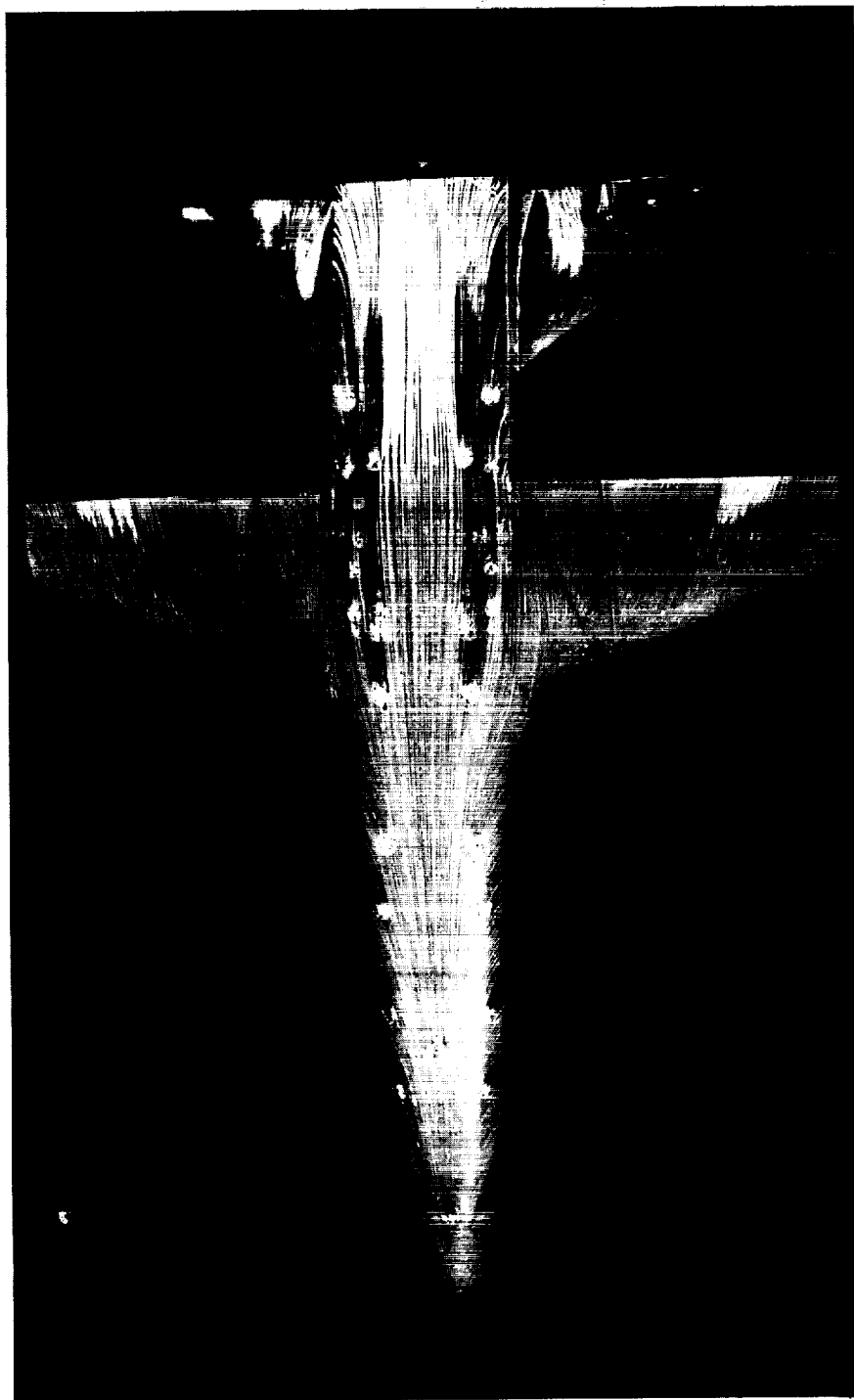
Slide 4 is a photograph of an oil-flow pattern representing the surface streamline directions on the lower surface of the NAR low cross-range orbiter at $\alpha = 30^\circ$ and $M_\infty = 7.4$. The streamline patterns on the fuselage ahead of the wing are uniform and show less cross flow than at $\alpha = 60^\circ$. In the region of the wing the cross flow is diminished considerably, whereas downstream of the wing evidence of cross flow reappears. On the wing, the patterns indicate the body- and wing-shock interaction region, which is discussed by H. Lee Seegmiller (paper no. 7-I of volume I of this compilation).

WINDWARD SURFACE OIL-FLOW PHOTOGRAPH
NAR STRAIGHT-WING ORBITER

$$M_{\infty} = 7.4$$

$$\alpha = 30^{\circ}$$

$$Re_{\infty L} = 1.4 \times 10^6$$



Slide 4

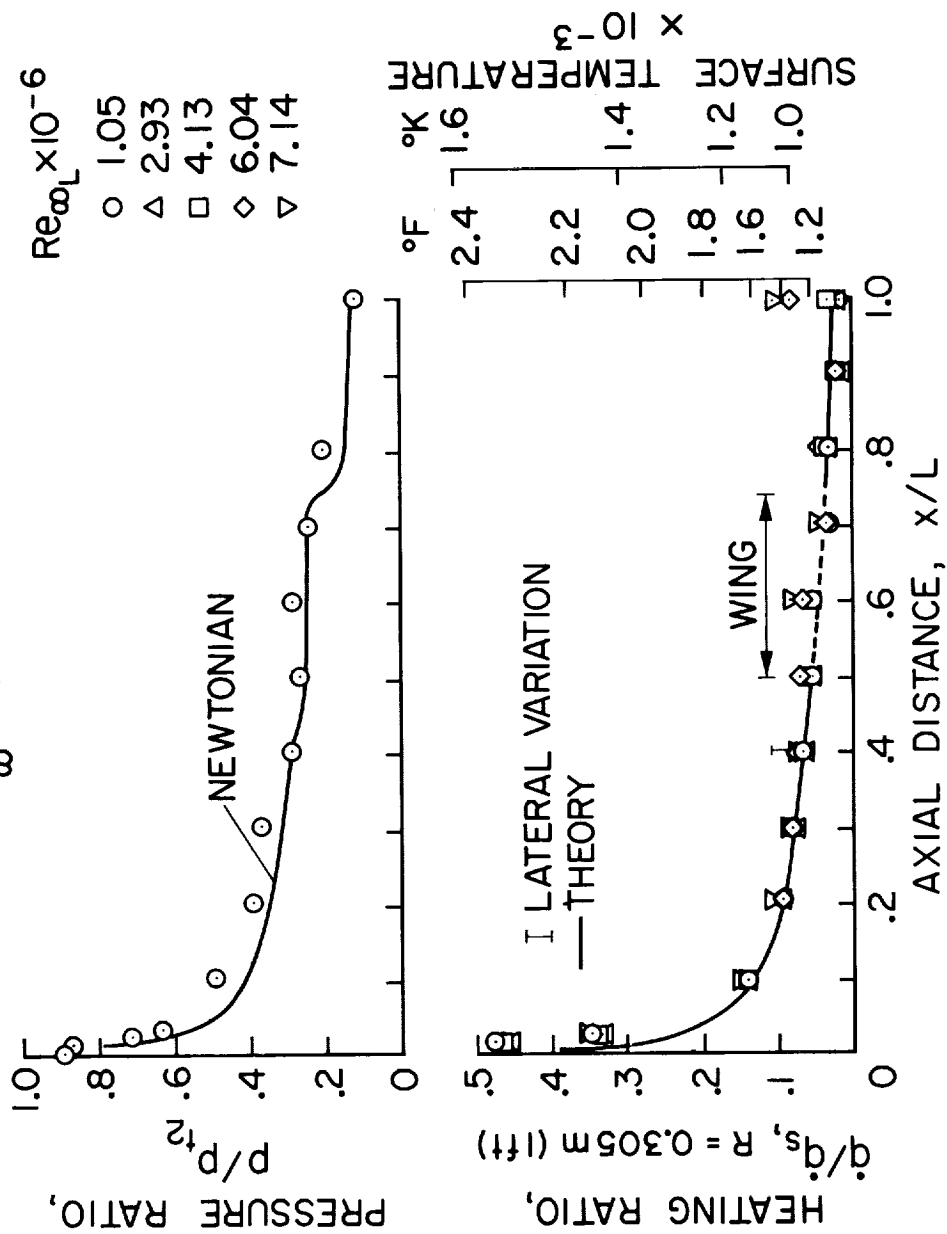
CENTERLINE PRESSURES AND HEATING RATES

(Slide 5)

Normalized centerline pressure and heating-rate distributions for $\alpha = 30^\circ$ and $M_\infty = 7.4$ are given on Slide 5. The pressures decrease with distance from the stagnation region, except for the slight increase in the wing region. The pressures agree reasonably well with Newtonian theory. The heating rates for a range of Reynolds number also show a uniform decrease with distance from the stagnation region. As at $\alpha = 60^\circ$, an exception in this trend occurs near the beginning of the wing region where increases in Reynolds number result in increases in heating rate, but the effect is less severe than at $\alpha = 60^\circ$. Also, increased heating with increased Reynolds number occurs at the most rearward location, probably because transition to turbulent flow is taking place, but there was insufficient data to obtain quantitative transition locations. Except in the stagnation and wing regions, the heating rates agree very well with the laminar cross-flow theory described previously.

CENTERLINE PRESSURES AND HEATING RATES NAR STRAIGHT-WING ORBITER

$M_\infty = 7.4$ $\alpha = 30^\circ$



Slide 5

FLIGHT AND WIND-TUNNEL LAMINAR HEAT-TRANSFER PARAMETER FROM THEORY

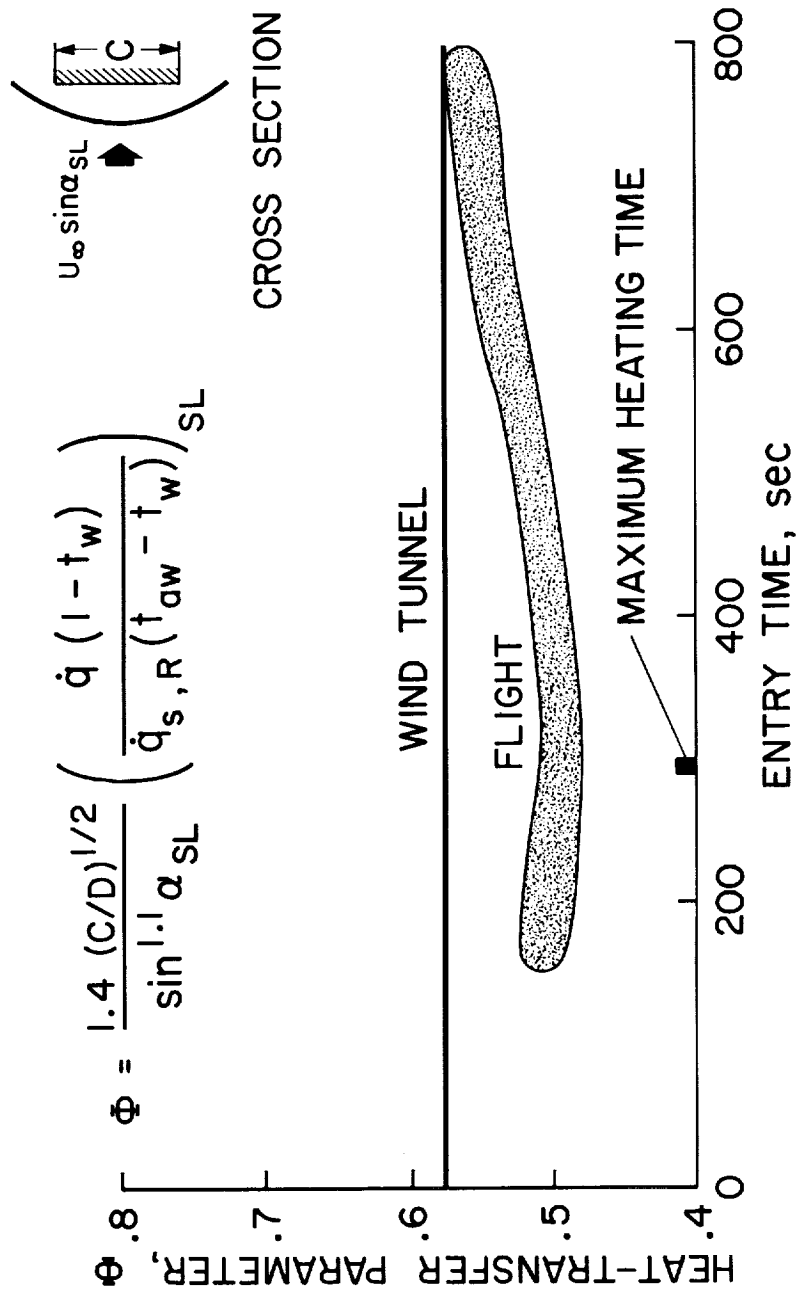
(Slide 6)

Extrapolation of the laminar cross-flow theory to flight altitudes and velocities provides an interesting comparison. In Slide 6, a heat-transfer parameter, which is proportional to the ratio of heat-transfer coefficients $h/h_{O,R}$, is plotted versus entry time for a typical low cross-range trajectory. The nominal angle of attack is 60° and α_{SL} varies between 70° and 50° as a result of body curvature changes between $x/L = .1$ and 1.0 .

The solid line labeled wind tunnel is the magnitude of the parameter for ideal gas conditions at reasonably high Mach number. The magnitude is equivalent to the ratio of the body cross-flow velocity gradient to the corresponding gradient on a cylinder of the same radius. The influence of transport properties and angle of attack is accounted for in the constant of proportionality $\frac{1.4}{\sin^{1.1} \alpha_{SL}}$. The shaded region labeled flight shows the deviation from cold tunnel conditions, wherein account has been taken for real-gas effects on velocity gradient and transport properties. The largest deviation results from changes in the velocity gradient ratio calculated using the inviscid flow computer program described in Ref. 4. The limits on the shaded region itself account for transport property changes evaluated from the real-gas boundary layer solutions of Ref. 5. The maximum deviation is only about 20%, which corresponds to a 5% deviation in radiation equilibrium surface temperatures. Based on this theory, direct extrapolation of wind-tunnel heat-transfer coefficients would yield good results.

FLIGHT AND WIND-TUNNEL LAMINAR HEAT-TRANSFER PARAMETER FROM THEORY

LOW CROSS-RANGE TRAJECTORY



Slide 6

WING PRESSURES AND HEATING RATES

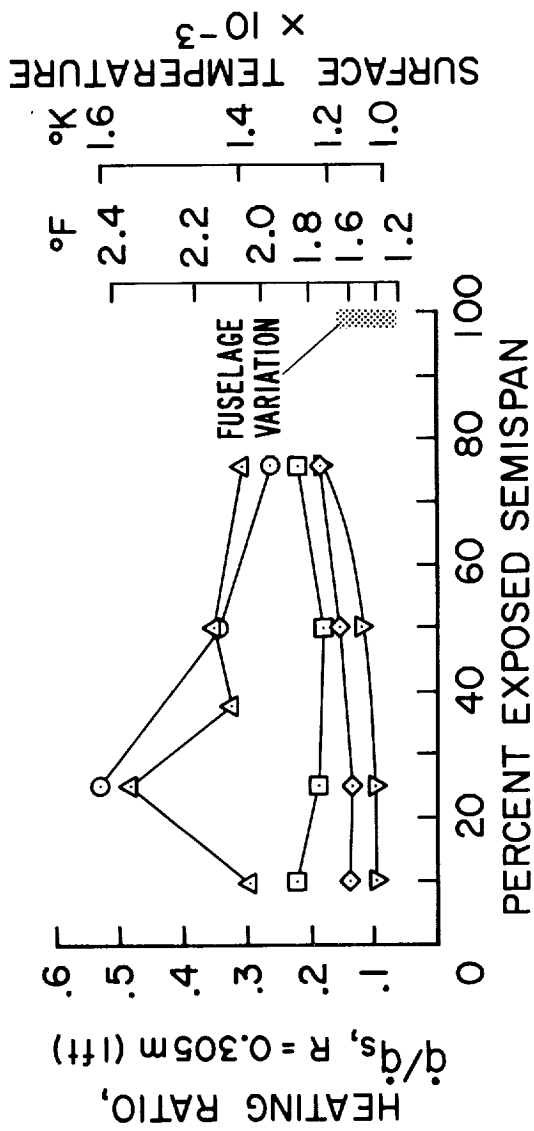
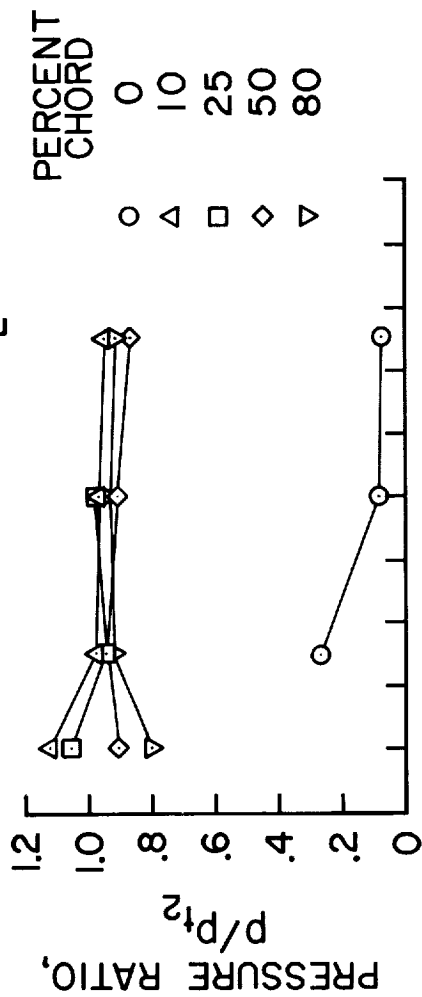
(Slide 7)

Wing pressures and heating rates are plotted versus percent of exposed semispan. At a given span location the pressures increase rapidly from the leading edge to the 10% chord location and decrease thereafter. This trend is expected since the stagnation line lies somewhat downstream of the 10% chord location, and pressure should be highest along this line. Inboard of the 20% semispan location some of the pressures exceed the normal shock value. Except for the wing leading edge, the pressures have essentially the same magnitude as on the fuselage centerline at $x/L = .6$, where the pressures showed an abrupt increase.

The heating distributions are similar to the pressure distributions. The heating is highest along the 10% chord location, except at the 25% semispan location where the leading edge heating is highest. (The actual magnitudes of these heating rates may be affected by conduction errors.) The wing heating is always as high or higher than the fuselage heating. The maximum indicated equilibrium surface temperatures are about 1600°K (2400°F). However, it should be noted that real-gas effects were not simulated in these tests.

WING PRESSURES AND HEATING RATES NAR STRAIGHT-WING ORBITER

$M_\infty = 7.4$ $\alpha = 60^\circ$ $Re_{\omega L} = 1.02 \times 10^6$



Slide 7

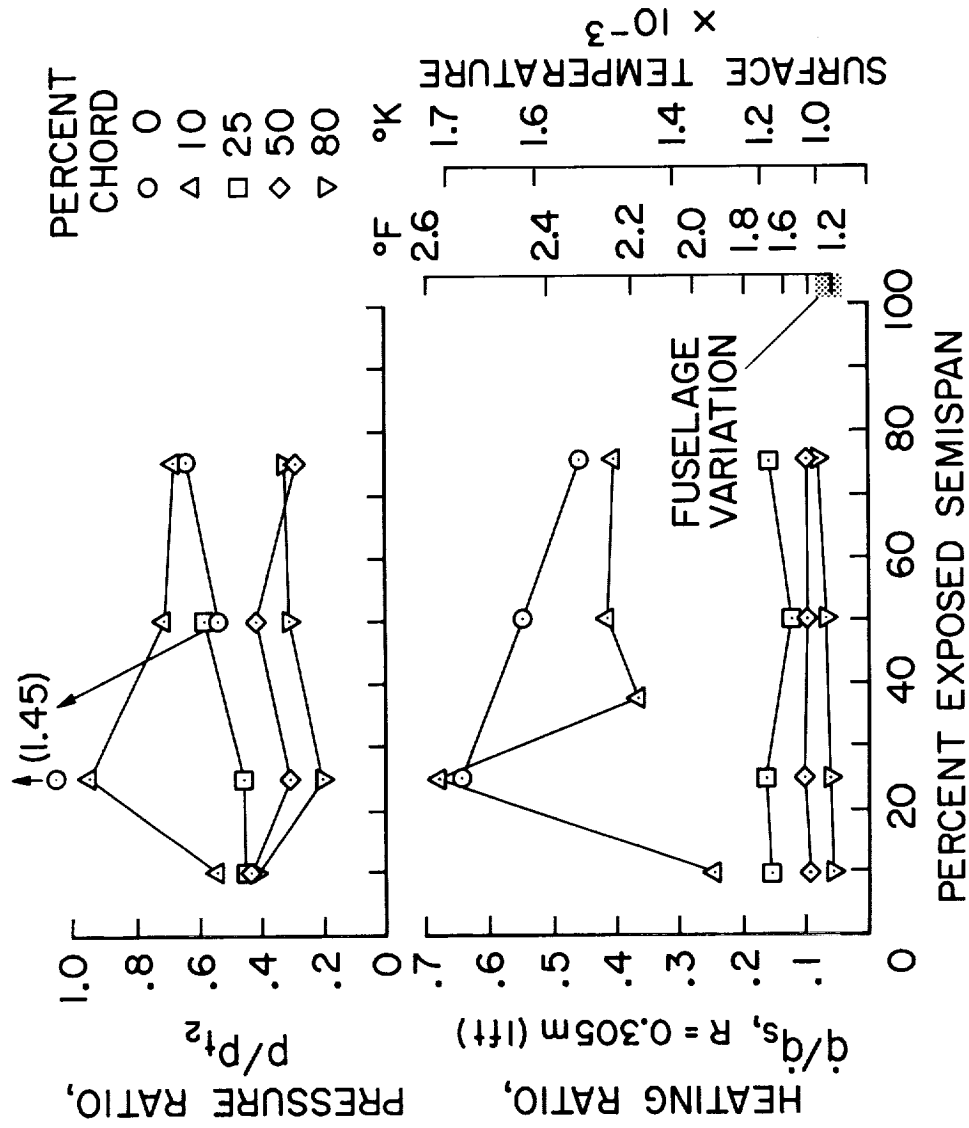
WING PRESSURES AND HEATING RATES

(Slide 8)

Wing pressures and heating rates at $\alpha = 30^\circ$ and $M_\infty = 7.4$ are shown. Both the pressure and heating distributions reflect the complex nature of the flow over the wing at this angle of attack. For example, the leading edge pressure at the 25% semispan location is 1.45 times the normal shock pressure, indicating a complex shock system. The heating at this location, however, is not the highest measured value. The highest heating appears at the 10% chord location. (Conduction errors may be affecting the very high rates.) Although the flow over the wing is complex, the highest temperatures are confined to the region between 0% and 25% chord, where temperatures reach 1700°K (2600°F). The temperatures at greater chord distances are essentially the same as those on the fuselage centerline.

WING PRESSURES AND HEATING RATES NAR STRAIGHT-WING ORBITER

$M_\infty = 7.4$ $\alpha = 30^\circ$ $Re_{\omega_L} = 1.05 \times 10^6$



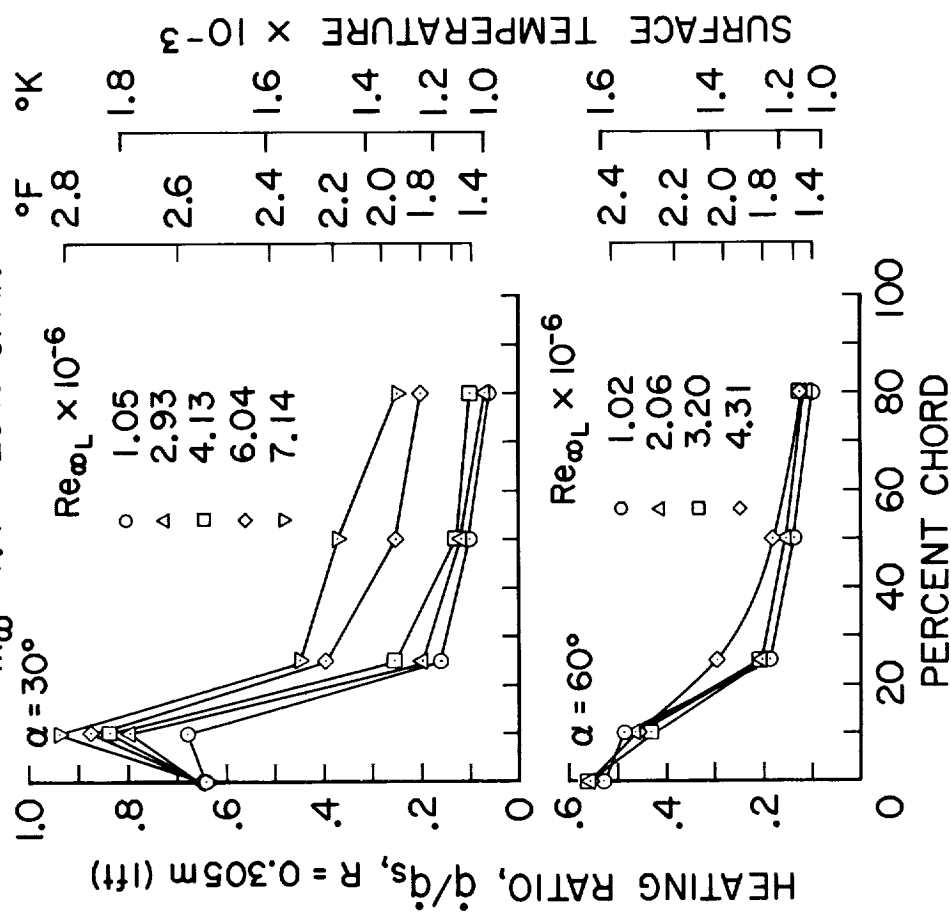
Slide 8

EFFECT OF REYNOLDS NUMBER ON WING HEATING RATES

(Slide 9)

Changing the free-stream Reynolds number affected the heating at all span locations. An example of this effect (for the 25% semispan location) is shown for two angles of attack. At both angles of attack, the heating rate increased with increasing Reynolds number. The greatest changes in heating occurred at $\alpha = 30^\circ$, where the wing and body shock interaction was most severe. Although the Reynolds numbers are higher than those usually associated with the peak heating point along typical trajectories, inclusion of this parameter in any theoretical studies is clearly necessary.

EFFECT OF REYNOLDS NUMBER ON WING HEATING RATES NAR STRAIGHT-WING ORBITER $M_\infty = 7.4$ 25% SPAN



SURFACE OIL-FLOW PHOTOGRAPH

(Slide 10)

Tests were performed on the MSC straight-wing orbiter to obtain boundary layer transition and turbulent heating data. These tests were performed on the fuselage without the wing because of structural limitations. A photograph of the oil-flow patterns taken at two Reynolds numbers is shown on Slide 10. The highest Reynolds number resulted in boundary layer transition on the fuselage centerline about 20% of the axial distance from the leading edge. Although the thickness of the oil on the model surface for the two tests was not controlled precisely, an examination of the streamline patterns indicates less streamline turning for the turbulent test. Since the patterns are representative of surface streamlines, the observed differences in turning are consistent with previous studies which show cross flow to have a small influence on shear and heating in turbulent boundary layers.

SURFACE OIL-FLOW PHOTOGRAPH
MSC STRAIGHT-WING ORBITER FUSELAGE

TURBULENT, $Re_{\omega_L} = 9.6 \times 10^6$

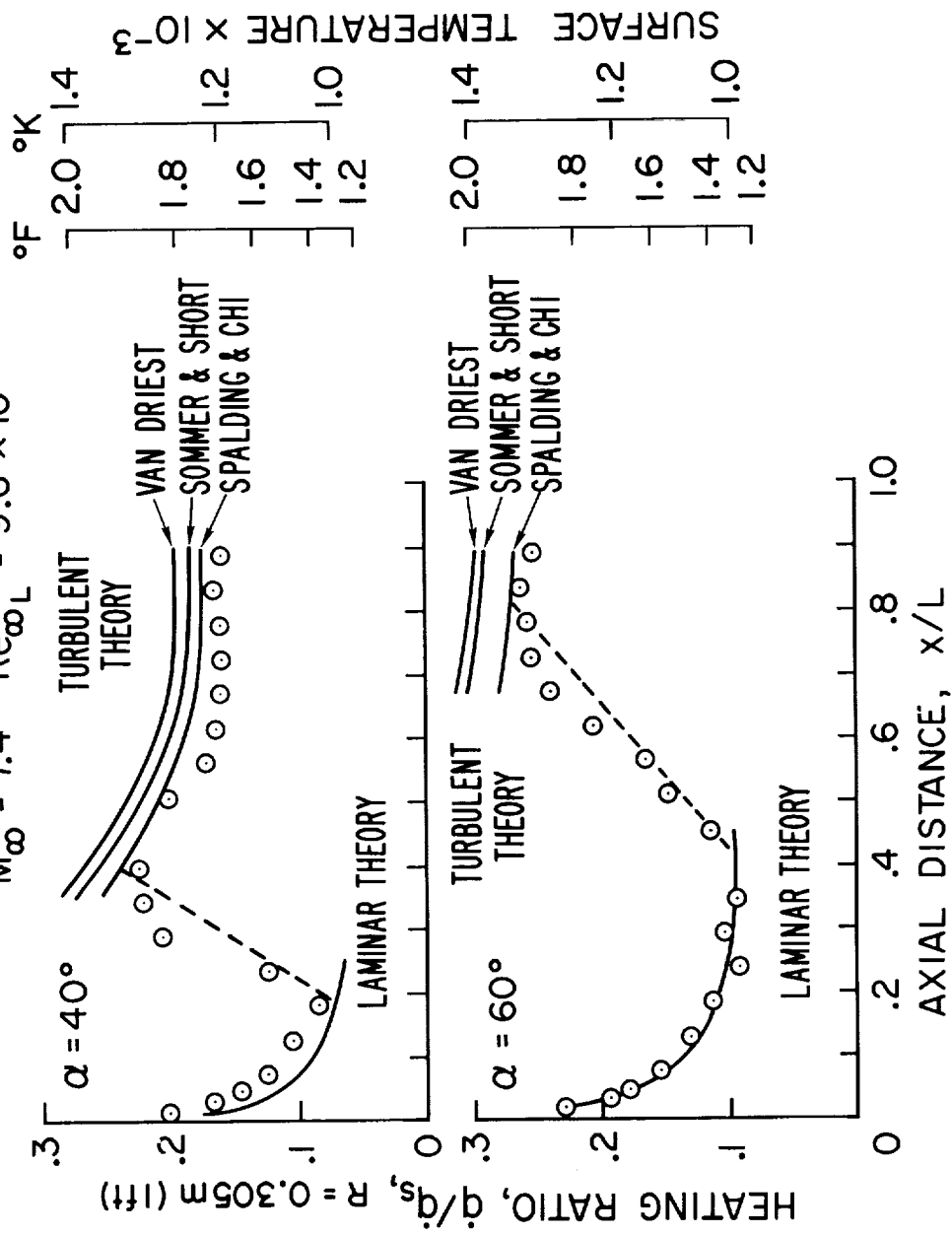
LAMINAR, $Re_{\omega_L} = 2 \times 10^6$

Slide 10

Turbulent heating data at $\alpha = 40^\circ$ and $\alpha = 60^\circ$ are shown. These data are typical of data obtained at other test conditions, but these tests resulted in the largest extent of turbulent flow over the model. The data show typical laminar heating from the stagnation point, a region of transitional heating, and finally turbulent heating. The extent of the transition length is about equivalent to the laminar length. The data are compared with a laminar theory and three turbulent theories connected with a linear curve in the transition region where the transition length is assumed equal to the laminar length. The laminar theory predicts the heating rates reasonably well beyond $x/L = .1$, as shown previously. The turbulent heating was calculated by strip theory which accounted for flow divergence, although the corrections for divergence were small. The boundary layer edge conditions were taken to be those for a swept cylinder (i.e., equivalent to Newtonian values). The origin of turbulent heating was assumed located at the beginning of transition and the Reynolds analogy factor was 1.0, a value experimentally verified by data on plates and cones tested in the same facility (see Ref. 6). The heating is predicted better by the Spalding and Chi theory. At $\alpha = 60^\circ$, the extent of turbulent flow is limited, but the conclusions regarding the comparisons of theory and data appear to be consistent with those at $\alpha = 40^\circ$. It should be noted that turbulent theory based on boundary layer edge conditions obtained by isentropic expansion from normal shock pressure to the local Newtonian pressure underpredicted the data.

CENTERLINE TURBULENT HEATING RATES MSC STRAIGHT-WING ORBITER FUSELAGE

$$M_\infty = 7.4 \quad Re_{\infty L} = 9.6 \times 10^6$$



Slide 11

WINDWARD SURFACE OIL-FLOW PHOTOGRAPH

(Slide 12)

This slide shows a photograph of the oil-flow patterns on a delta-wing orbiter for $\alpha = 50^\circ$ and $\alpha = 30^\circ$.^{*} Contrasting features of the two patterns point out interesting features of the flow at high and intermediate angles of attack. (The elevons at the rear of the delta wing are undeflected at $\alpha = 30^\circ$ and deflected away from the flow at $\alpha = 50^\circ$, but these differences are incidental to the comparisons made here.) At the highest angle of attack the uniform patterns over the fuselage ahead of the wing and on the wing itself show significant cross flow. A parting line forms downstream of the leading edge of the wing where the streamlines ahead of the line flow forward over the blunt leading edge and aft of the line flow back and outward. The streamlines over the delta wing appear to run almost parallel to the wing leading edge. At the lower angle of attack, there is less cross flow over the fuselage. The parting line where the streamlines flow forward over the blunt leading edge of the wing moves closer to the leading edge, and the streamlines aft of this line appear to flow straight back over the delta wing.

^{*}The configuration is the NAR 129 delta wing which has a slightly larger wing area than the 134 model used in the heating and pressure tests.

WINDWARD SURFACE OIL-FLOW PHOTOGRAPH

NAR DELTA-WING ORBITER

$M_\infty = 7.4$ $Re_{\omega_L} = 2.7 \times 10^6$



Slide 12

WINDWARD CENTERLINE PRESSURES

(Slide 13)

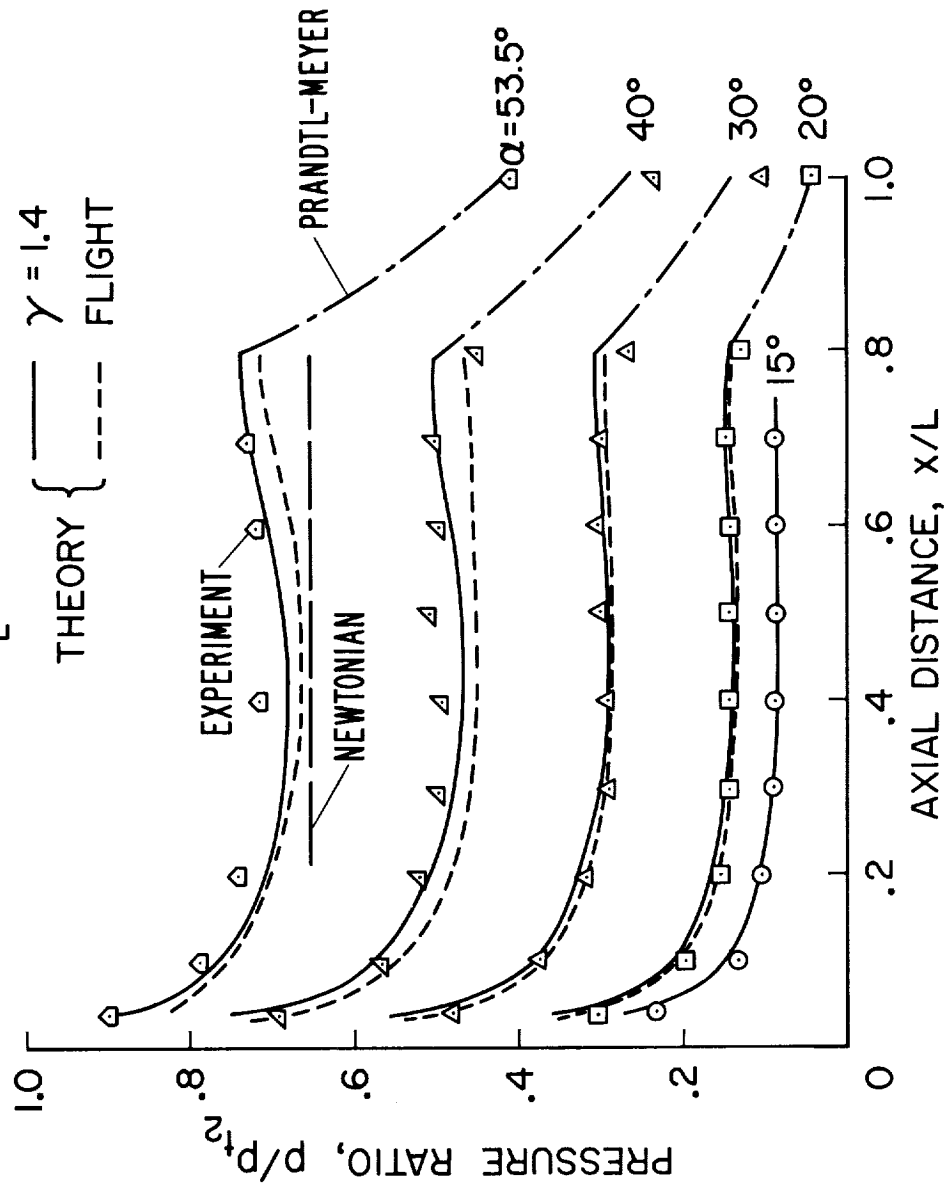
Windward centerline pressures on the delta wing for various angles of attack are plotted versus axial distance. At each angle of attack the pressures decrease with distance from the stagnation region, remain constant over the flat portion of the body, and then decrease rapidly beyond the 80% station where boat-tailing of the body surface occurs. The solid line represents a prediction of the pressures for wind tunnel conditions using an equivalent-elliptic-cone method. The angle β between the body and shock is obtained from a continuity relationship similar to that given in Ref. 7. The pressures are then obtained from a general correlation of pressure coefficient and β with angle of attack as a parameter. Good agreement is obtained at all angles of attack. Over the boattailed section, a Prandtl-Meyer expansion predicts the decrease in pressure. Also shown at the highest angle of attack is a Newtonian prediction of the pressure over the flat portion of the body surface. For this and all other angles of attack, Newtonian theory underpredicts the pressures by about 15% to 20%. As shown by the dashed line, an extrapolation of the equivalent-elliptic-cone prediction to typical flight conditions shows that the pressure ratio decreases slightly. The extrapolation agrees more closely with Newtonian theory because at flight speeds and altitudes the body and shock curvatures come into closer alignment.

WINDWARD CENTERLINE PRESSURES

NAR DELTA-WING ORBITER

$$M_\infty = 7.4 \quad \text{Re}_\infty = 1.1 \times 10^6 - 3.3 \times 10^6$$
$$\gamma = 1.4$$

FLIGHT



Slide 13

WINDWARD CENTERLINE HEATING RATES

(Slide 14)

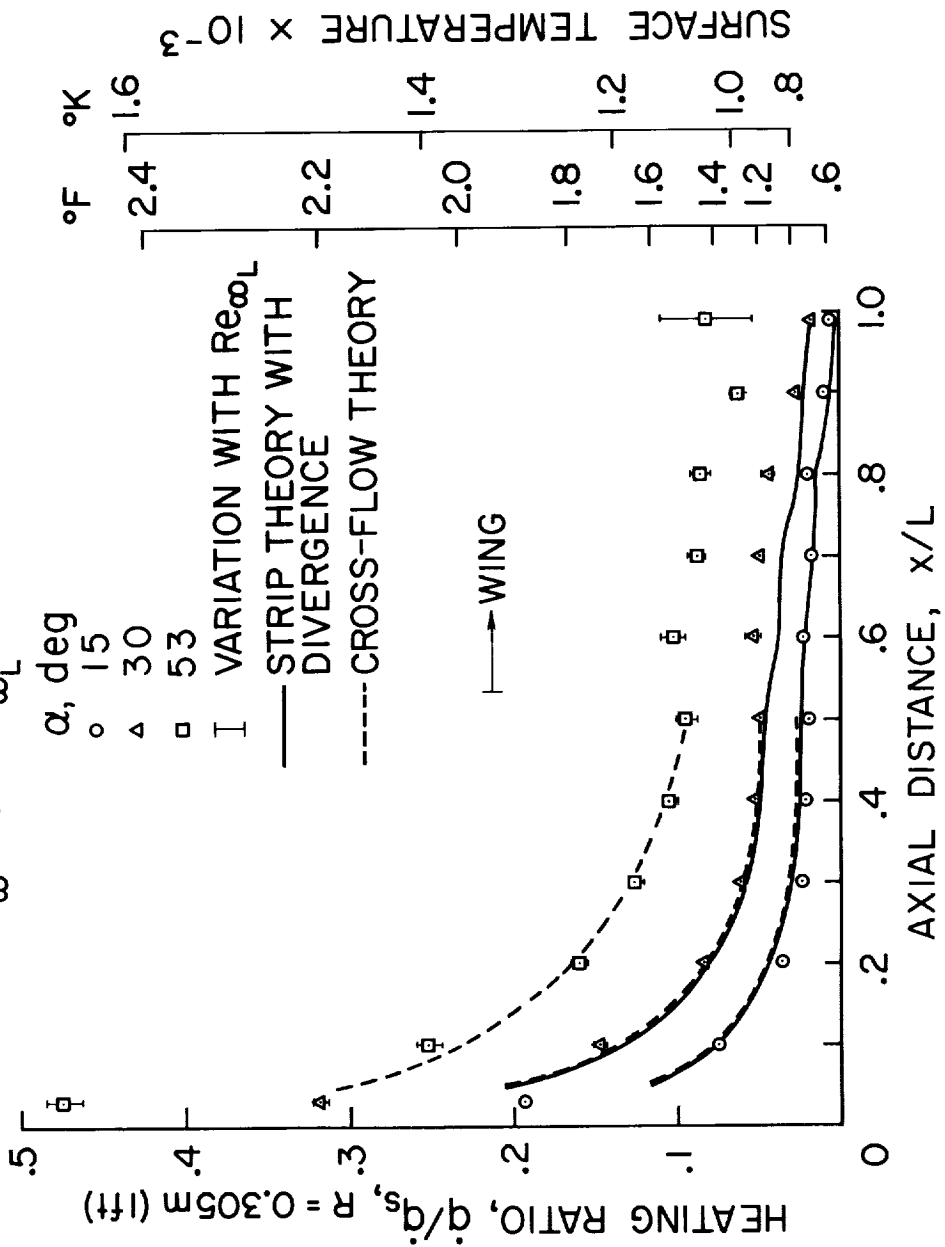
Centerline heating rates for various angles of attack are shown. The data, obtained using a thermocouple model, are shown for Reynolds numbers between 1×10^6 and 4×10^6 . The data are believed to be laminar, except at $\alpha = 53^\circ$, where the last station showed a consistent increase in heating with increase in Reynolds number which is usual when transition to turbulent flow occurs. Data at higher Reynolds number are shown later. The corresponding radiation equilibrium surface temperatures for the maximum heating rate along a typical lifting trajectory with the body at $\alpha = 30^\circ$ are shown for comparison.* At $\alpha = 30^\circ$ the laminar heating rates on the delta-wing orbiter fuselage are lower than those on the straight-wing orbiter fuselage at $\alpha = 60^\circ$. However, surface area and insulation requirements are greater for this configuration and the possibility of turbulent heating near peak heating is more probable. The solid lines are laminar heating predictions using strip theory accounting for flow divergence (e.g., see Ref. 8). The expression for divergence used here was Eq. (14) of Ref. 8, and the cross-flow velocity gradient was taken from the correlation equation given in Ref. 3. The agreement between theory and prediction is good, except at $\alpha = 30^\circ$ in the wing region, probably because of the expression used to describe the divergence. It is believed that strip theory accounting for divergence will provide better agreement when inviscid flow calculations are used to obtain the streamline divergence. The dashed curve is the laminar cross-flow theory discussed previously, and it agrees very well with the data ahead of the wing location. Application of this theory over the wing region was not attempted.

* For the delta-wing orbiter, $q_{s,R=305\text{ m}} = 681 \text{ kW/m}^2 (60 \text{ Btu/ft}^2\text{sec})$ and $\epsilon = .8$.

WINDWARD CENTERLINE HEATING RATES

NAR DELTA-WING ORBITER

$$M_\infty = 7.4 \quad Re_{\omega_L} = 1 \times 10^6 - 4 \times 10^6$$



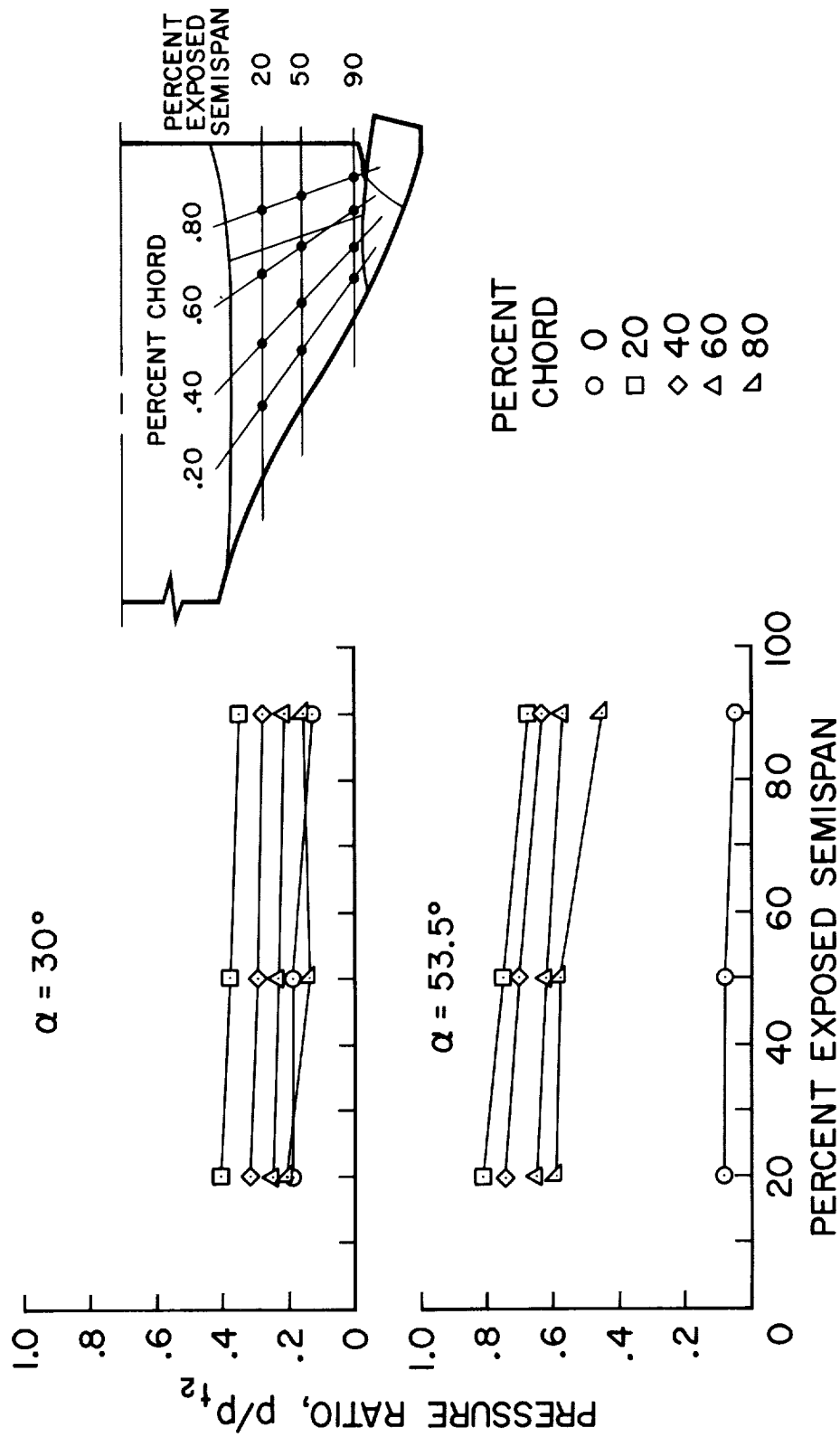
WINDWARD WING PRESSURE

(Slide 15)

The wing pressure distributions on the delta-wing orbiter are given for two angles of attack. The pressure ratios are shown as a function of percent exposed semispan for various chord locations. For a given chord location the pressures decrease slightly with increasing span. At a given span location the pressures are highest at the 20% chord location and decrease both forward and aft of this location as would be expected from an inspection of the streamline patterns shown previously.

WINDWARD WING PRESSURE NAR DELTA-WING ORBITER

$M_\infty = 7.4$ $Re_{\omega_L} = 1.0 \times 10^6 - 4.0 \times 10^6$



Slide 15

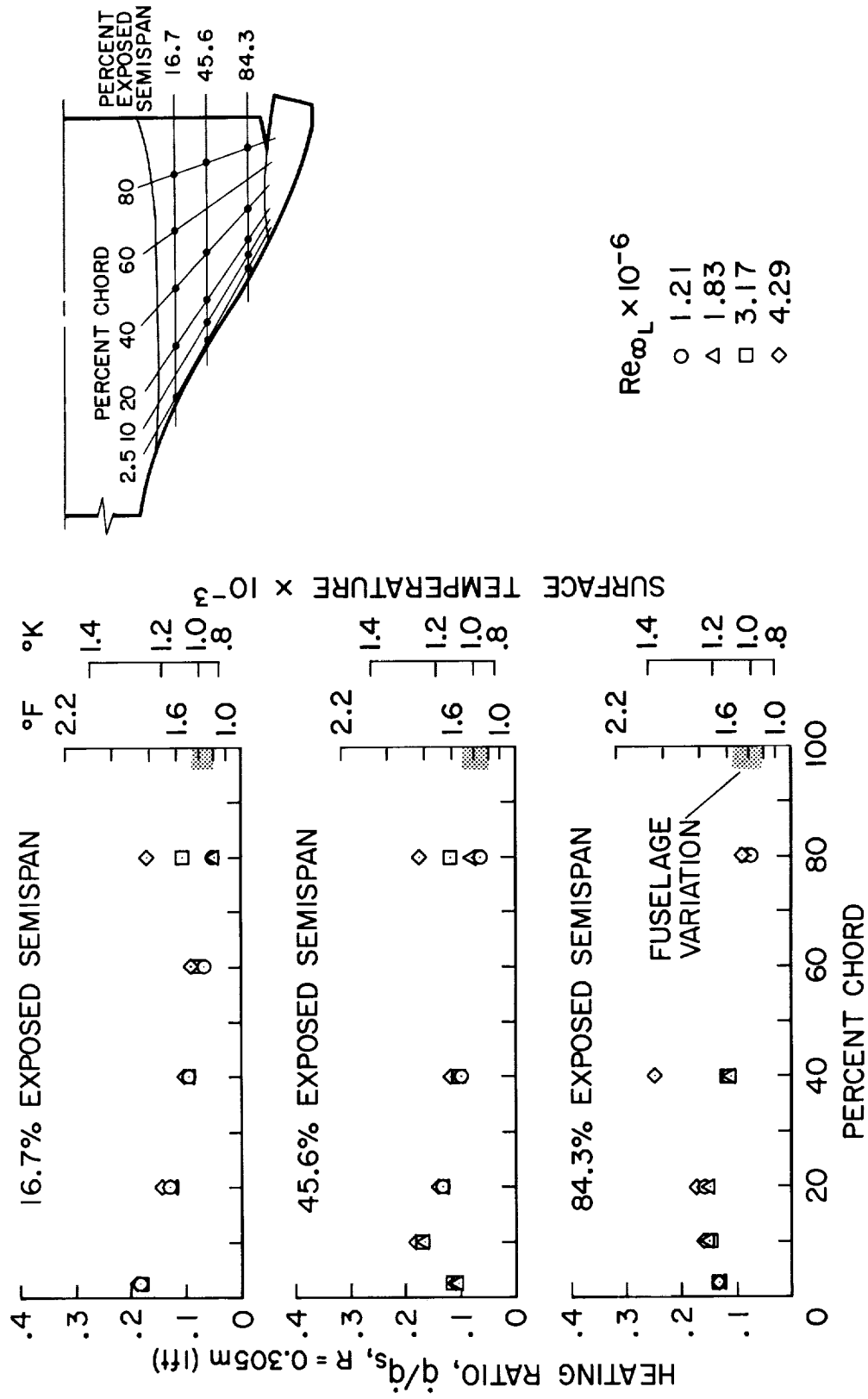
WINDWARD WING HEATING RATES

(Slide 16)

Windward wing heating rates on the delta wing at $\alpha = 53^\circ$ for three span locations are shown. The heating is highest over the leading-edge region of the wing. Beyond the 30% chord location the heating levels and corresponding equilibrium surface temperatures are nearly the same as those on the fuselage centerline. At this angle of attack, the heating rate at the rearward chord location increased with increasing Reynolds number, indicating the possibility of transition to turbulent flow. This same effect was noted previously for the centerline heating at $\alpha = 53^\circ$. This suggests that transition was taking place uniformly across the orbiter's lower surface. However, the data were not sufficient to obtain a quantitative definition of the transition location. Also, at the 84.3% span location the heating at the 40% chord location shows a marked increase at the highest Reynolds number. The exact cause for this increase is not known at this time, but it may be related to irregular heating patterns which are discussed subsequently.

WINDWARD WING HEATING RATES NAR DELTA-WING ORBITER

$M_\infty = 7.4$ $\alpha = 53^\circ$



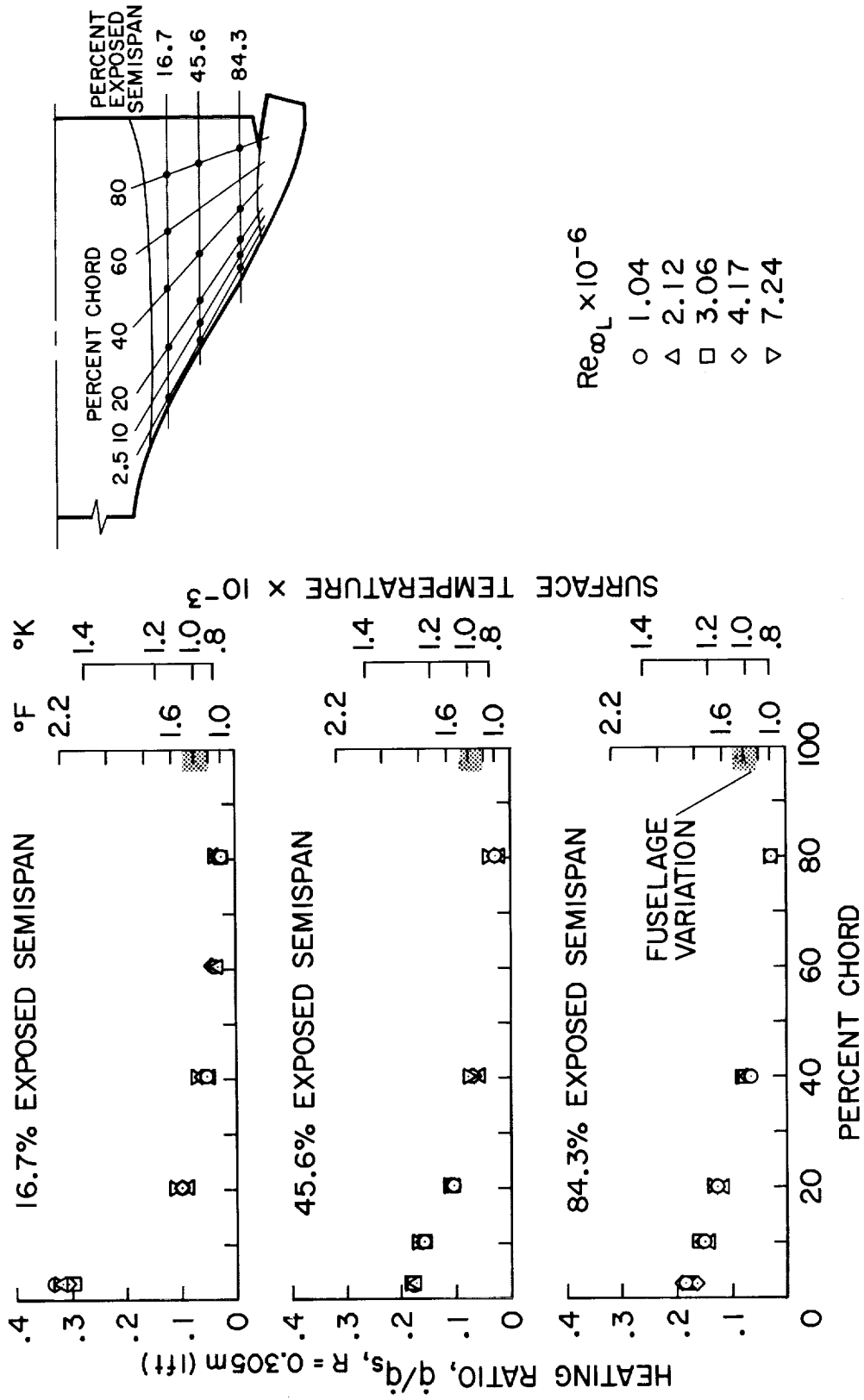
WINDWARD WING HEATING RATES

(Slide 17)

Windward wing heating rates on the delta wing at $\alpha = 30^\circ$ for three span locations are shown. The heating rates are highest over the leading edge of the wing. Beyond the 30% chord location the heating rates and corresponding temperatures are at about the same magnitude as the fuselage centerline rates. The effect of Reynolds number variation on the heating ratios is negligible, indicating that the flow was probably laminar. However, it will be shown later that at the highest Reynolds number, 7.24×10^6 , transition from laminar to turbulent flow occurred on the fuselage centerline. Therefore, at this angle of attack, transition does not occur uniformly across the orbiter's lower surface, but begins first on the fuselage centerline.

WINDWARD WING HEATING RATES NAR DELTA-WING ORBITER

$M_\infty = 7.4$ $\alpha = 30^\circ$



PHOTOGRAPH SHOWING IRREGULAR HEATING PATTERNS

AT HIGH REYNOLDS NUMBER

(Slide 18)

Phase-change paint heating tests were performed on the NAR delta wing. The model (NAR 129) had a somewhat larger delta wing than the thermocouple model (NAR 134), but otherwise the two models are geometrically similar. At reasonably high Reynolds numbers, but not high enough to cause transition to turbulent heating, irregular heating patterns were observed for angles of attack to 30° . A photograph illustrating such a pattern is shown in this slide. The darkened streaks indicate high heating regions, indicated by the insert showing the heating ratios across the wing. These irregular patterns appear to be vortices, streaking back from the wing leading edge, and they set up rather severe lateral gradients in heating. Furthermore, these vortices could be precursors to boundary layer transition and further studies of them will be undertaken.

IRREGULAR HEATING PATTERNS AT HIGH REYNOLDS NUMBER

$M_\infty = 7.4$	$\alpha = 10^\circ$	$Re_{\infty L} = 4.9 \times 10^6$	$x/L = 0.93$
------------------	---------------------	-----------------------------------	--------------



Slide 18

IRREGULAR SPANWISE HEATING RATES

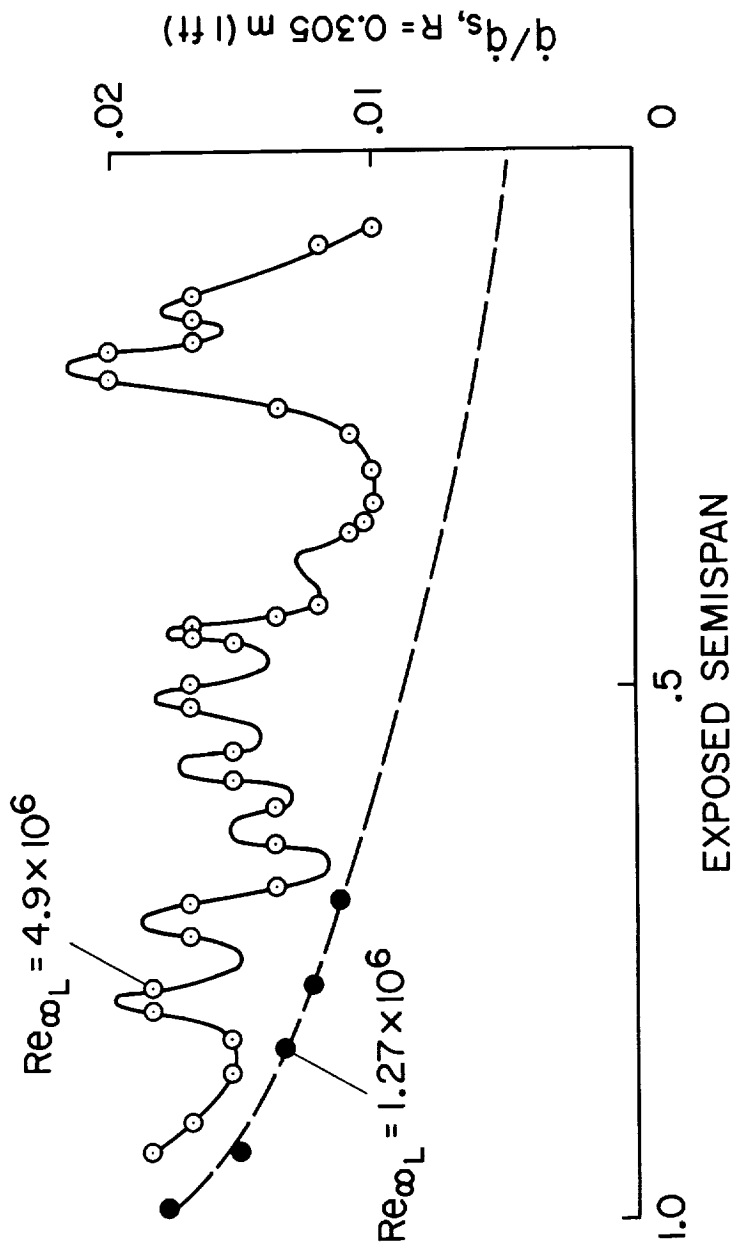
(Slide 19)

The insert shown in the previous slide is reproduced here to allow a quantitative assessment of the effects of the vortical streaks. The irregular heating data at the higher Reynolds number can be compared with the uniform heating data at the lower Reynolds number to assess the relative effects of the vortices. Factor-of-two differences in heating ratio were achieved, and these differences could prove to be a formidable problem in the design of the heat shield.

IRREGULAR SPANWISE HEATING RATES

NAR DELTA-WING ORBITER

$M_\infty = 7.4$ $\alpha = 10^\circ$ $x/L = 0.93$



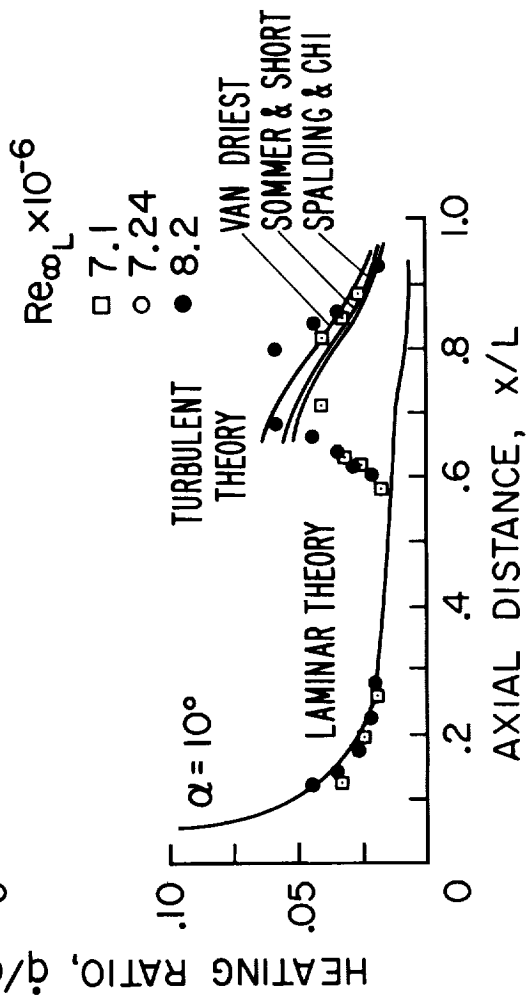
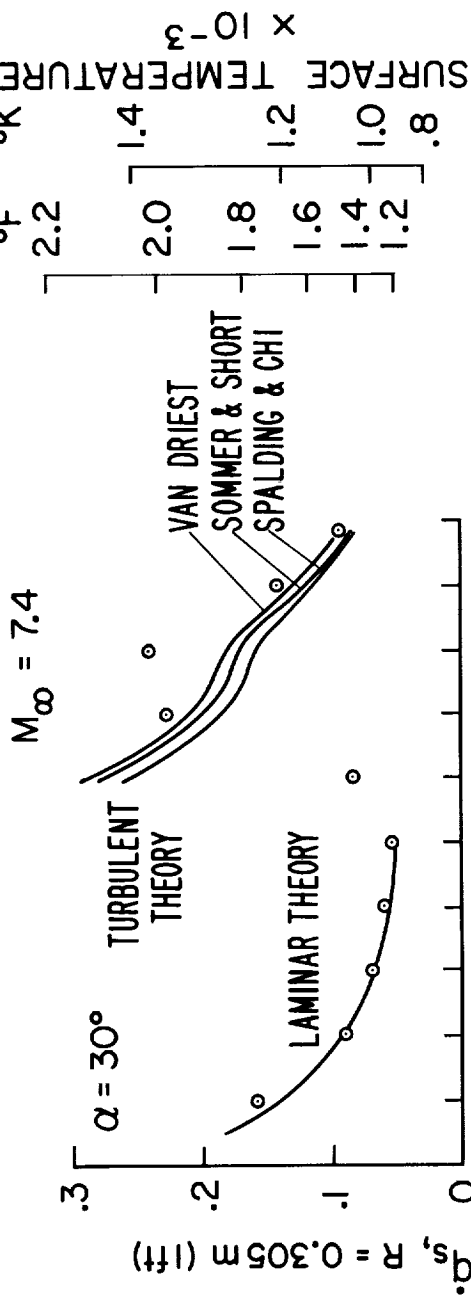
Slide 19

WINDWARD CENTERLINE TURBULENT HEATING RATES

(Slide 20)

Turbulent heating rate data on the centerline of the NAR delta-wing orbiter are shown for two angles of attack. The data at $\alpha = 30^\circ$ were taken on the thermocouple model (NAR 134), while those at $\alpha = 10^\circ$ were taken on a styrcast model (NAR 129) using the phase-change paint technique. The heating rates are laminar over the first half of the models. Transition to turbulent flow occurs in a region which covers less than half the laminar flow extent. Turbulent heating was achieved over the remaining 20 to 30% of the body length. Corresponding radiation equilibrium temperatures at $\alpha = 30^\circ$ indicate a maximum temperature near 1400° K (2000° F) at the end of transition. The laminar rates compare favorably with strip theory, accounting for divergence as shown previously. The data are also compared with three turbulent theories using strip theory, accounting for divergence, but, as mentioned previously, corrections are small for turbulent theory. The origin of the turbulent flow was assumed to be at the beginning of transition (i.e., where the heating rates begin to depart from laminar theory) and the Reynolds analogy factor was 1.0. All three theories predict the measured decrease in turbulent heating rates. However, more turbulent heating data over a larger extent of the delta-wing orbiter will be required before a definitive choice of turbulent theory can be made.

WINDWARD CENTERLINE TURBULENT HEATING RATES NAR DELTA-WING ORBITER



Slide 20

WINDWARD SURFACE CENTERLINE TRANSITION LOCATIONS

(Slide 21)

In previous slides, boundary layer transition from laminar to turbulent flow was indicated in the heating distribution data. A table of the locations of the beginning of transition obtained from various heating data is given in this slide. The nominal body angle of attack, the angle of attack of the body surface at the transition location, and the tunnel test conditions are all given along with the values of x/L at transition. These data represent only those tests where a quantitative determination of boundary layer transition location could be made. The data shown here are for smooth models, but the "dusty" test environment in the Ames 3.5-foot hypersonic wind tunnel caused by sediment in the pebble heater did create a certain amount of model pitting during the tests. The data indicating possible boundary layer tripping were those where pitting may have been excessive. Some tests with controlled roughness will be discussed subsequently.

WINDWARD SURFACE CENTERLINE TRANSITION LOCATIONS

$$M_{\infty} = 7.4 \quad T_w / T_t = 0.4$$

α	α_w	P_t		T_t		$(x/L)_t$
		kN/m ²	psia	°K	°R	
60	56	2758	400	750	1350	0.71
60	56	4619	670	772	1390	.66
60	56	6412	930	783	1410	.60
60	60	8136	1180	772	1390	.52
60	61.2	9928	1440	778	1400	.43
40	36	6412	930	761	1370	.57 (TRIPPED?)
40	36	8274	1200	761	1370	.83
40	41.5	9928	1440	789	1420	.4 (TRIPPED?)
40	36	11170	1620	767	1380	.75
15	15	9928	1440	839	1510	.56
15	15	10273	1490	772	1390	.55
20	20	10273	1490	783	1410	.52
30	30	10273	1490	783	1410	.54
10*	10	10756	1560	772	1390	.53
20*	20	10825	1570	833	1500	.42
30*	30	8343	1210	827	1490	.29 (TRIPPED?)

MSC
FUSELAGE
WITHOUT WING
(SMOOTH MODEL)

NAR 134
DELTA WING

* PHASE-CHANGE PAINT DATA AND LARGER DELTA WING (NAR 129)

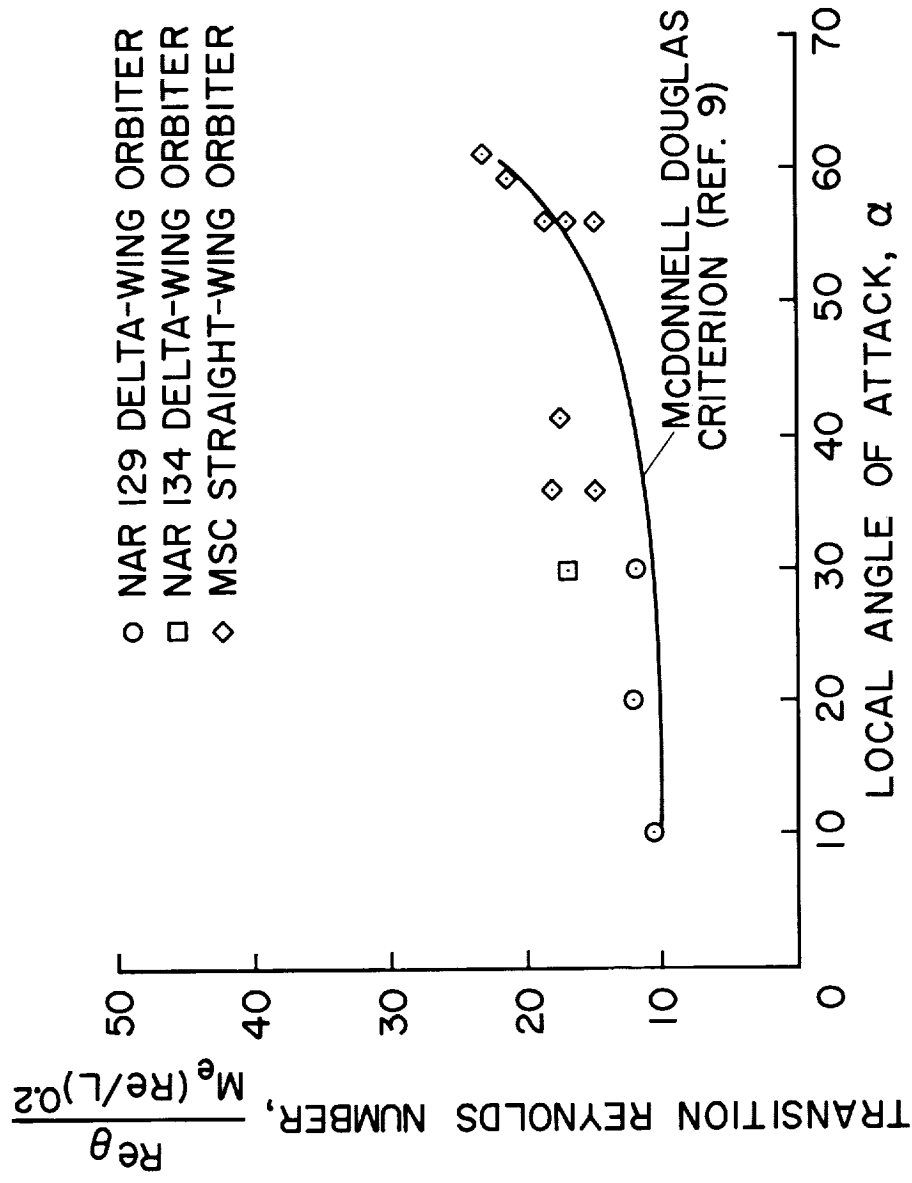
MEASURED TRANSITION REYNOLDS NUMBERS COMPARED

WITH CRITERION BASED ON ANGLE OF ATTACK

(Slide 22)

The transition data from the previous table have been compared with various boundary layer transition criteria. A comparison with the criterion based on angle of attack presented by R. V. Masek from McDonnell Douglas in Ref. 9 is shown in this slide. The local momentum-thickness transition Reynolds number, normalized by local Mach number and unit Reynolds number, is plotted versus local body angle of attack. The local boundary layer edge conditions of pressure, velocity, and temperature were evaluated as if the flow were over a swept cylinder. The local momentum thickness was calculated with account taken for flow divergence as suggested by Masek. For local angles of attack below 56° , the data lie above the correlation line. For local angles of attack above 56° , the data scatter about the correlation line. The comparison suggests that the criterion based on angle of attack would predict shorter lengths to transition than those measured during these tests. Also, the effect of local unit Reynolds number was not completely correlated by normalization with $(Re/L)^{0.2}$.

MEASURED TRANSITION REYNOLDS NUMBERS COMPARED WITH CRITERION BASED ON ANGLE OF ATTACK



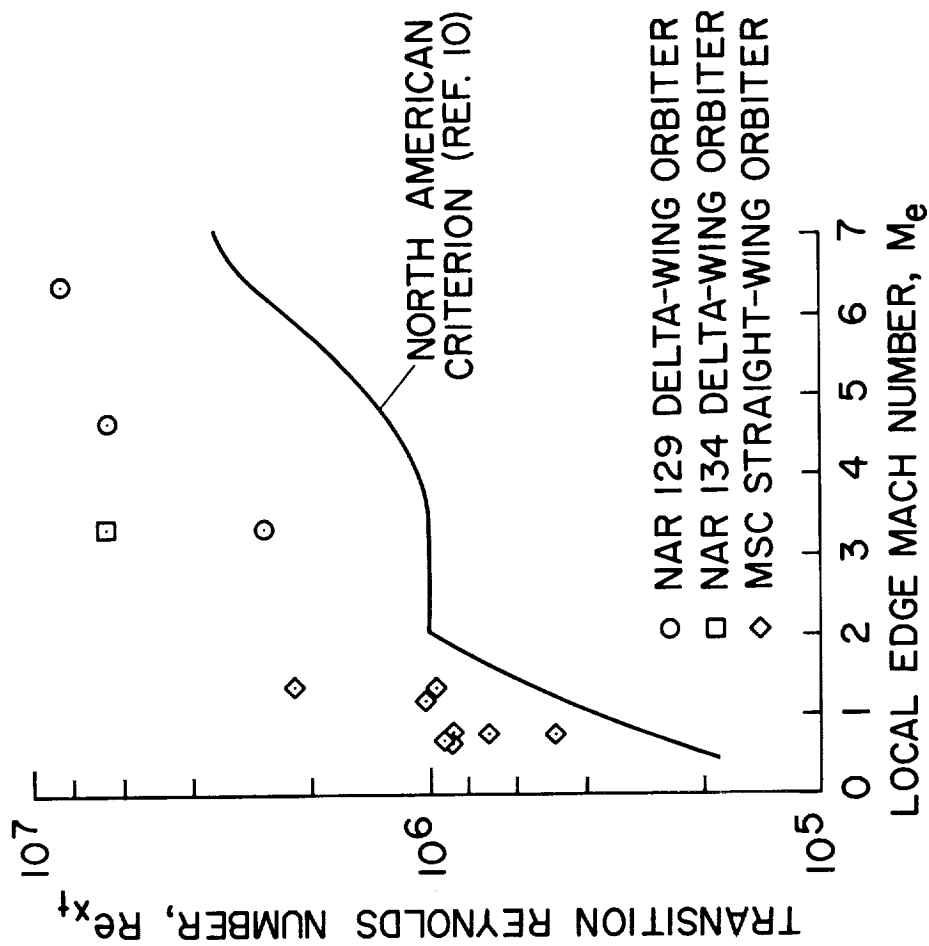
Slide 22

MEASURED TRANSITION REYNOLDS NUMBERS COMPARED
WITH CRITERION BASED ON LOCAL MACH NUMBER

(Slide 23)

A comparison of the transition data from the previous table with a criterion based on local Mach number, given by Jack D. Moote from North American Rockwell in Ref. 10, is shown in this slide. The local boundary layer edge conditions of pressure, velocity, and temperature were evaluated in two ways to be consistent with the assumptions used by Moote. For angles of attack of 30° and below, local conditions were evaluated as if the flow were over a swept cylinder (at this Mach number equivalent cone conditions are only slightly different from swept-cylinder conditions). Above these angles, the conditions were evaluated assuming the flow had expanded isentropically from normal shock pressure to a local pressure obtained from Newtonian theory. All the data lie above the correlation line, indicating that this criterion would predict shorter lengths to transition than those measured during the tests. A comparison of these results with those shown on the previous slide using a criterion based on angle of attack can be misleading. Although the criterion based on local Mach number appears more conservative relative to the present data, in application to flight conditions the criterion based on angle of attack becomes more conservative because that correlation depends on the local unit Reynolds number which can be several orders of magnitude different from that in the wind-tunnel tests. Before any conclusions can be reached regarding appropriate transition criteria, more transition data on bodies at angle of attack will be required. Moreover, more refined calculations of local boundary layer edge properties will be required before more meaningful correlations are attempted.

MEASURED TRANSITION REYNOLDS NUMBERS COMPARED WITH CRITERION BASED ON LOCAL MACH NUMBER



Slide 23

EFFECT OF SIMULATED PANEL JOINTS ON
BOUNDARY LAYER TRANSITION

(Slide 24)

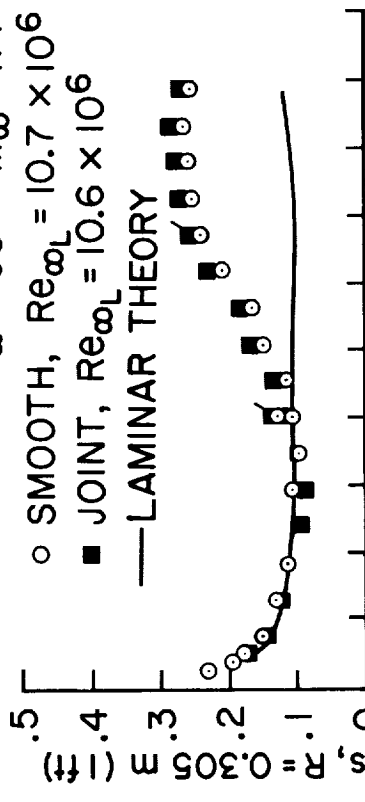
Practical designs of heat-shield structures may introduce a certain degree of surface roughness. As shown previously, pitting roughness sometimes resulted in early boundary layer transition. Some tests have been performed to determine the effects of simulated heat-shield panels on boundary layer transition. The results are preliminary and more tests are planned, but the results are informative. The fuselage of the MSC straight-wing orbiter was tested with simulated panel joints and the heating distributions were compared with those obtained on a smooth model. The scaled panel dimensions are shown on the slide. At $\alpha = 60^\circ$ the simulated panel joints had little effect on boundary layer transition. At $\alpha = 40^\circ$ the simulated joints had a significant effect on the location of transition. The exact reason for the dramatic differences at the two angles of attack is not known, but changes in cross flow, local Mach number, and boundary layer thickness all probably have affected the results. Results similar to those at $\alpha = 40^\circ$ were also obtained during some of the "smooth" model tests where pitting roughness was not removed between tests. The implication of these tests is that roughness introduced by heat-shield design may be an important parameter.

EFFECT OF SIMULATED PANEL JOINTS ON BOUNDARY LAYER TRANSITION

MSC STRAIGHT-WING FUSELAGE

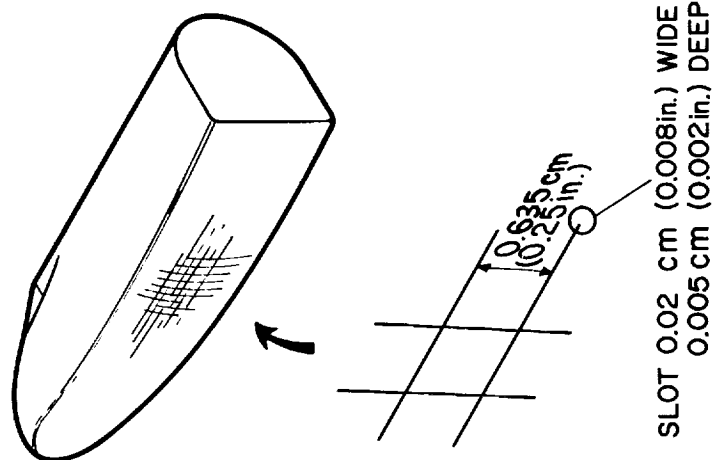
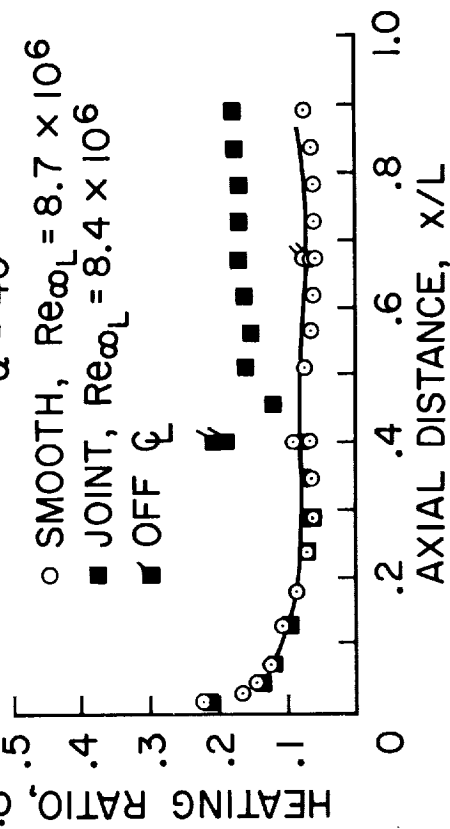
$$\alpha = 60^\circ \quad M_\infty = 7.4$$

- SMOOTH, $Re_{\omega_L} = 10.7 \times 10^6$
- JOINT, $Re_{\omega_L} = 10.6 \times 10^6$
- LAMINAR THEORY



$$\alpha = 40^\circ$$

- SMOOTH, $Re_{\omega_L} = 8.7 \times 10^6$
- JOINT, $Re_{\omega_L} = 8.4 \times 10^6$
- OFF ζ



CONCLUSIONS

Straight Wing

1. Fuselage laminar heating rates were predicted by cross-flow theory. Laminar wind-tunnel heat-transfer coefficients were shown to extrapolate to flight conditions with reasonable accuracy.
2. Wing heating rates were highest ahead of the 25% chord location. Heating rates on the remainder of the wing were near fuselage heating levels; however, heating increased with increased Reynolds number.

3. Turbulent heating rates were predicted with strip theory accounting for flow divergence. Spalding and

Chi theory with Reynolds analogy factor of 1.0 agreed with measured heating rates.

4. For Reynolds numbers to 10×10^6 , transition lengths were equal to laminar flow lengths. Transition

Reynolds numbers were generally higher than proposed criteria. Roughness effects need further investigation.

Delta Wing

1. Centerline pressures were predicted by an equivalent-elliptic-cone method. Heating to an angle of attack of 30° was predicted reasonably well by strip theory accounting for flow divergence. Better agreement is expected when inviscid flow calculations are used to describe streamline divergence.
2. Wing heating rates were highest ahead of the 25% chord location. Heating rates on the remainder of the wing were near the fuselage centerline heating levels. For Reynolds numbers less than those for transition, vortices caused irregular heating patterns.

3. Centerline turbulent heating rates were predicted with strip theory accounting for flow divergence. More

data are required to resolve the choice of strip theory.

4. Heating patterns in the transition region changed with angle of attack. For Reynolds numbers near 8×10^6 , centerline transition lengths were less than half the laminar flow lengths. Transition Reynolds numbers were generally higher than proposed criteria. Roughness effects need further investigation.

REFERENCES

1. Katzen, E. D.; Marvin, J. G.; Seegmiller, H. L.; Axelson, J. A.; Brownson, J. J.; Cleary, J. W.; Lockman, W. K.; and Kaattari, G. E.: Static Aerodynamics, Flow Fields and Aerodynamic Heating of Space Shuttle Orbiters. Space Transportation System Technology Symposium, NASA TM X-52876, Vol. I, 1970, pp. 142-193.
2. Beckwith, Ivan E.; and Cohen, Nathaniel B.: Application of Similar Solutions to Calculation of Laminar Heat Transfer on Bodies With Yaw and Large Pressure Gradient in High-Speed Flow. NASA TN D-625, 1961.
3. Bertram, Mitchel H.; and Henderson, Arthur, Jr.: Recent Hypersonic Studies of Wings and Bodies. ARS J., vol. 31, no. 8, Aug. 1961, pp. 1129-1139.
4. Inouye, Mamoru; Marvin, Joseph G.; and Sinclair, A. Richard: Comparison of Experimental and Theoretical Shock Shapes and Pressure Distributions on Flat-Faced Cylinders at Mach 10.5. NASA TN D-4397, 1968.
5. Cohen, Nathaniel B.: Boundary-Layer Similar Solutions and Correlation Equations for Laminar Heat-Transfer Distribution in Equilibrium Air at Velocities up to 41 100 Feet Per Second. NASA TR R-118, 1961.
6. Hopkins, Edward J.; Rubesin, Morris W.; Inouye, Mamoru; Keener, Earl R.; Mateer, George C.; and Polek, Thomas E.: Summary and Correlation of Skin-Friction and Heat-Transfer Data for a Hypersonic Turbulent Boundary Layer on Simple Shapes. NASA TN D-5089, 1969.
7. Kaattari, George E.: Predicted Shock Envelopes About Two Types of Vehicles at Large Angles of Attack. NASA TN D-860, 1961.
8. Vaglio-Laurin, Roberto: Laminar Heat Transfer on Three-Dimensional Blunt Nosed Bodies in Hypersonic Flow. ARS J., vol. 29, no. 2, Feb. 1959, pp. 123-129.

9. Masek, R. V.: Boundary Layer Transition on Lifting Entry Vehicle Configurations at High Angle-of-Attack. Space Transportation System Technology Symposium, NASA TM X-52876, Vol. I, 1970, pp. 445-462.
10. Moote, Jack D.: A Minimum Heating Flight Mode for High Lateral Range Space Shuttle Entries Including the Effects of Transition. Space Transportation System Technology Symposium, NASA TM X-52876, Vol. I, 1970, pp. 531-546.

AN ANALYSIS OF PREDICTED SPACE SHUTTLE TEMPERATURES
AND THEIR IMPACT ON THERMAL PROTECTION SYSTEMS

By R. V. Masek
McDonnell Douglas Corporation
St. Louis, Missouri

and J. Alan Forney
NASA George C. Marshall Space Flight Center
Marshall Space Flight Center, Alabama

SUMMARY

The aeroheating methodologies used by the prime Phase B Space Shuttle contractors are analyzed to determine which of the methodology assumptions accounts for the discrepancies in predicted temperatures. The corresponding effect of methodology assumption on thermal protection system (TPS) unit weight is determined for two TPS concepts, a metallic heat shield and a surface insulation concept. The low and high crossrange missions are considered. Flow field assumptions included conical flow and normal shock expansion to Newtonian pressure. Two boundary layer transition criteria were considered, one currently utilized by McDonnell Douglas and the other a transition Reynolds number vs. Mach number relation utilized by North American Rockwell. Temperature time histories were computed at five lower centerline locations for various combinations of flow field method, transition criteria, turbulent heating method and trajectory.

For the low crossrange mission peak temperature was found to be most sensitive to flow field assumption and for the high crossrange mission transition criteria were found to be most influential. The conical flow assumption produced temperatures 166°C - 222°C higher than the normal shock assumption. The effect of transition criteria was about 111°C . For the low crossrange mission the TPS unit weight corresponding to NAR aeroheating methodology was 32.1 N/m^2 lighter than for the MDAC aeroheating methodology.

METHODOLOGY COMPARISON

METHODOLOGY ITEM	MDAC	NAR
HIGH CROSSRANGE MISSION: FLOW FIELD TRANSITION CRITERIA TURBULENT HEATING TRAJECTORY DISPERSION DESIGN FACTOR	OBLIQUE SHOCK $(Re_{\theta}/M_L)(X/Re_x)^2$ AS $f(\delta)$ $\rho\mu$ YES (- 762 METERS) 1.1	OBLIQUE SHOCK Re_x AS $f(M_L)$ SPALDING - CHI NO 1.15
LOW CROSSRANGE MISSION: FLOW FIELD (ALL REMAINING METHODOLOGY ITEMS UNCHANGED FOR LCR MISSION)	OBLIQUE SHOCK	NORMAL SHOCK

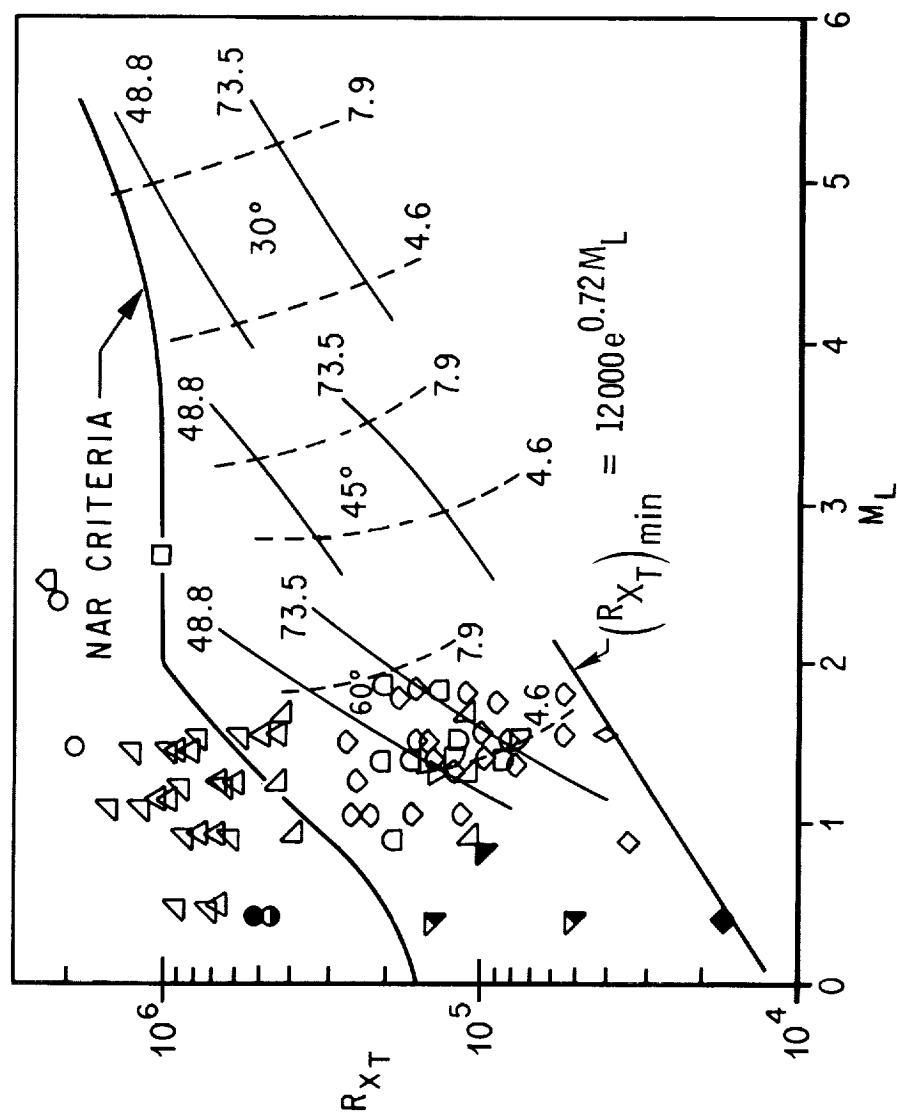
Slide 1

Methodology Comparison

(Slide 1)

The essential features of the McDonnell Douglas (MDAC) and North American Rockwell (NAR) aeroheating methodology are listed. For the high crossrange mission, the vehicle angle-of-attack is in the vicinity of 20° - 30° whereas for the low crossrange mission angles-of-attack of 50° - 60° are generally used. The MDAC transition parameter varies from a value of about 10 at low surface deflection angles ($\delta = 0 - 20^\circ$) to about 20 for $\delta = 60^\circ$. The 762 m trajectory dispersion used by MDAC is to account for guidance errors. The MDAC design factor is applied to both laminar and turbulent heating rate. The NAR design factor is used for turbulent heating only. The change by NAR in flow field method to normal shock for the low crossrange mission will be seen to have a large effect on their predicted temperatures. The methodologies listed represent the state of assumptions as of approximately October 1970. Some changes have been made by each company since that time.

TRANSITION CRITERIA COMPARISON



TRANSFORMATION OF
MDAC CRITERIA INTO
 R_{X_T} VS M_L PLANE

ALTITUDE, km

VELOCITY, km/sec

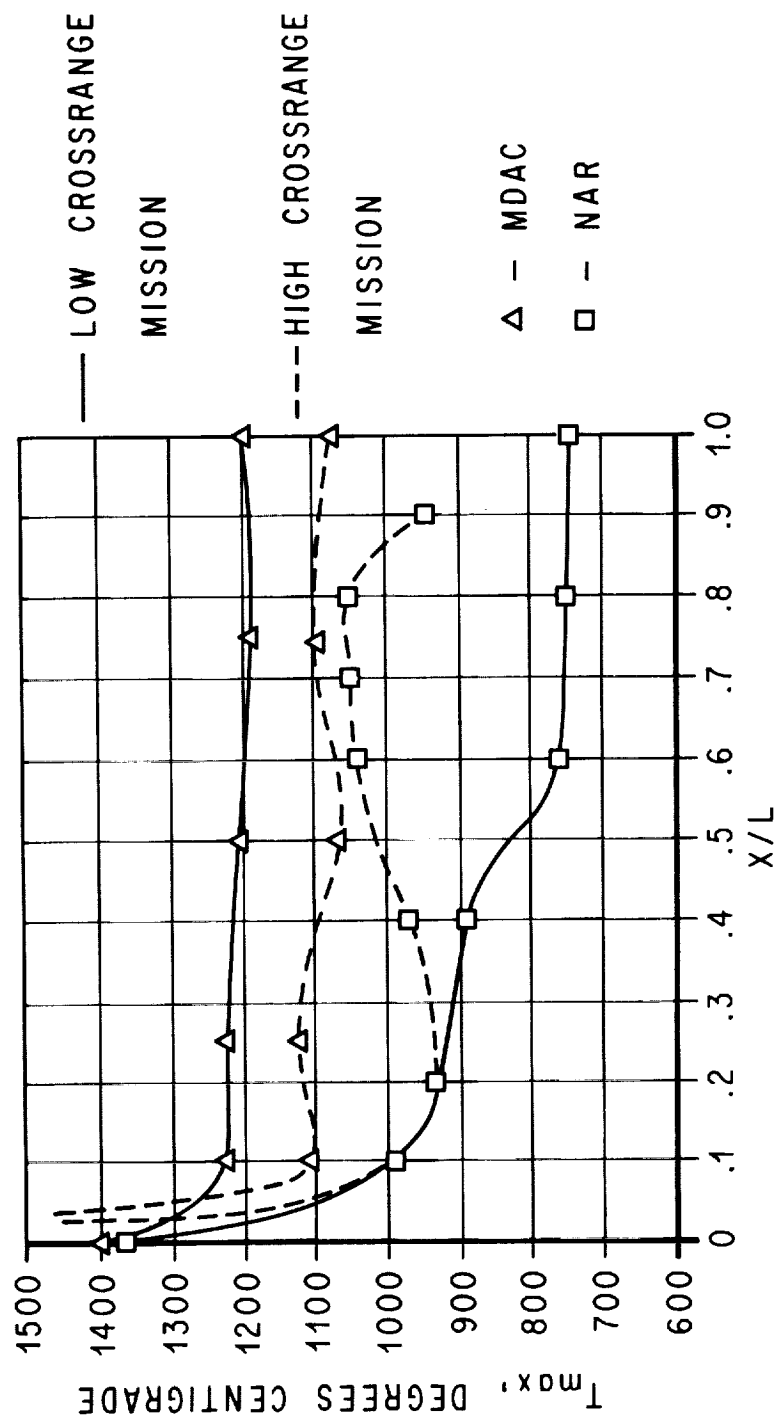
$\alpha =$

Transition Criteria Comparison

(Slide 2)

In order to compare transition criteria, it is necessary to transform the MDAC parameter into the $R_{X_{TP}}$ vs. M_L form. The result is the series of altitude-velocity curves shown at various angles-of-attack. $R_{X_{TP}}$ represents Reynolds number based on boundary layer run length at transition onset and M_L is the local Mach number. These data were compiled by Jerry N. Hefner of NASA Langley Research Center, and the value of $(R_{X_{TP}})_{\min}$ was suggested as the lower boundary for transition. Note that the MDAC criterion is more conservative than the NAR criteria in that it would predict transition earlier in flight along a typical re-entry trajectory. Different methods of computing inviscid flow field properties can give large differences in local Mach number and Reynolds number and this fact must be remembered when comparing transition criteria.

PREDICTED TEMPERATURES



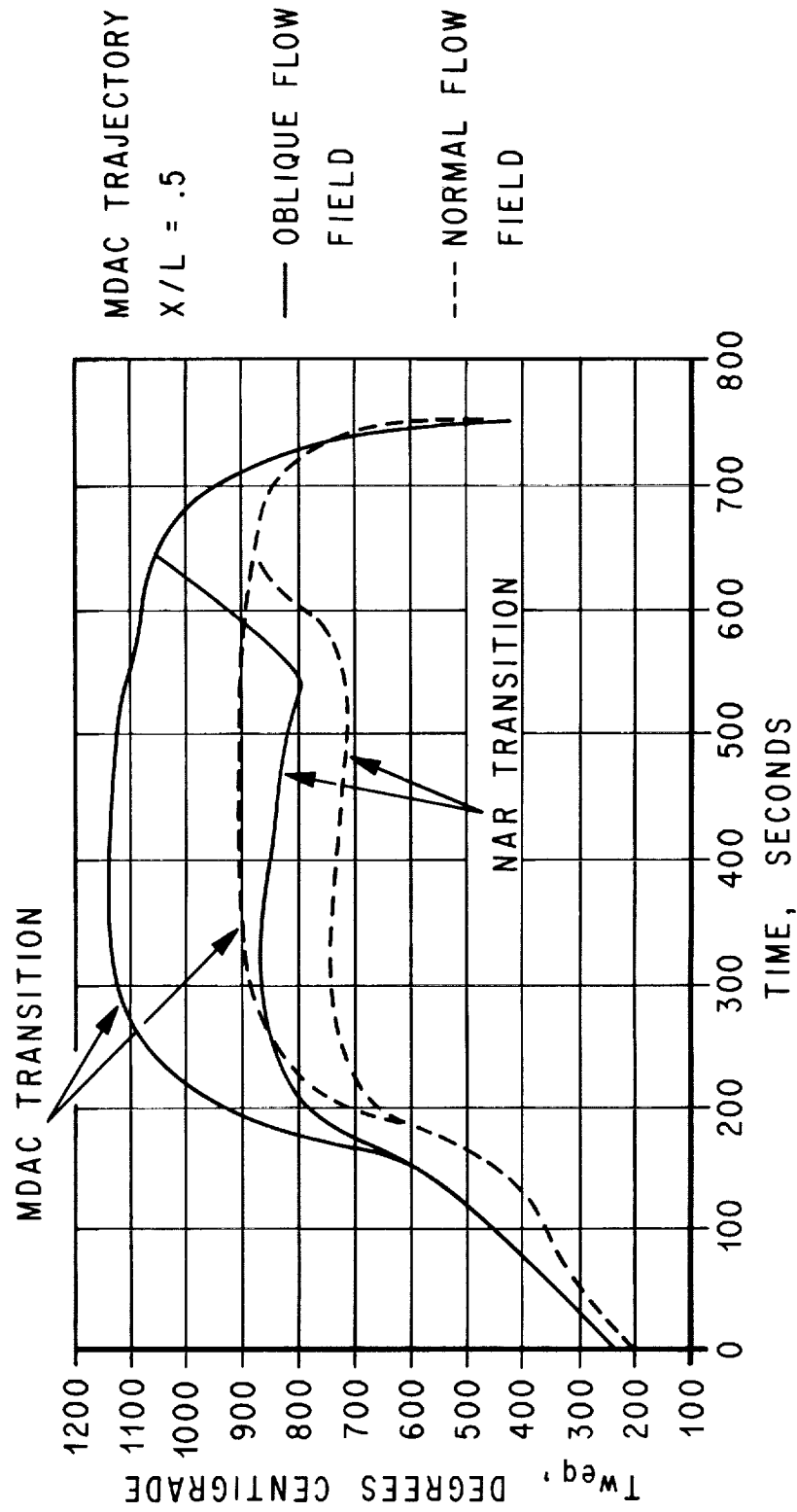
Slide 3

Predicted Temperatures

(Slide 3)

Peak lower surface centerline temperatures predicted by MDAC and NAR are shown as a function of X/L (L is vehicle length, X is axial distance originating at the nose). The low crossrange mission is performed by a straight wing orbiter and the high crossrange mission by a delta wing orbiter. These temperatures were used as checkpoints to insure that each Shuttle contractor's aeroheating methodology was being properly duplicated for the calculations of the study. Note that for the low crossrange mission there is an 444°C difference between the predictions of MDAC and NAR for the aft 50 percent of the vehicle. For the high crossrange mission the differences in predicted temperature are smaller, being on the order of 166°C at forward orbiter locations.

TYPICAL LOW CROSSRANGE TEMPERATURE HISTORIES



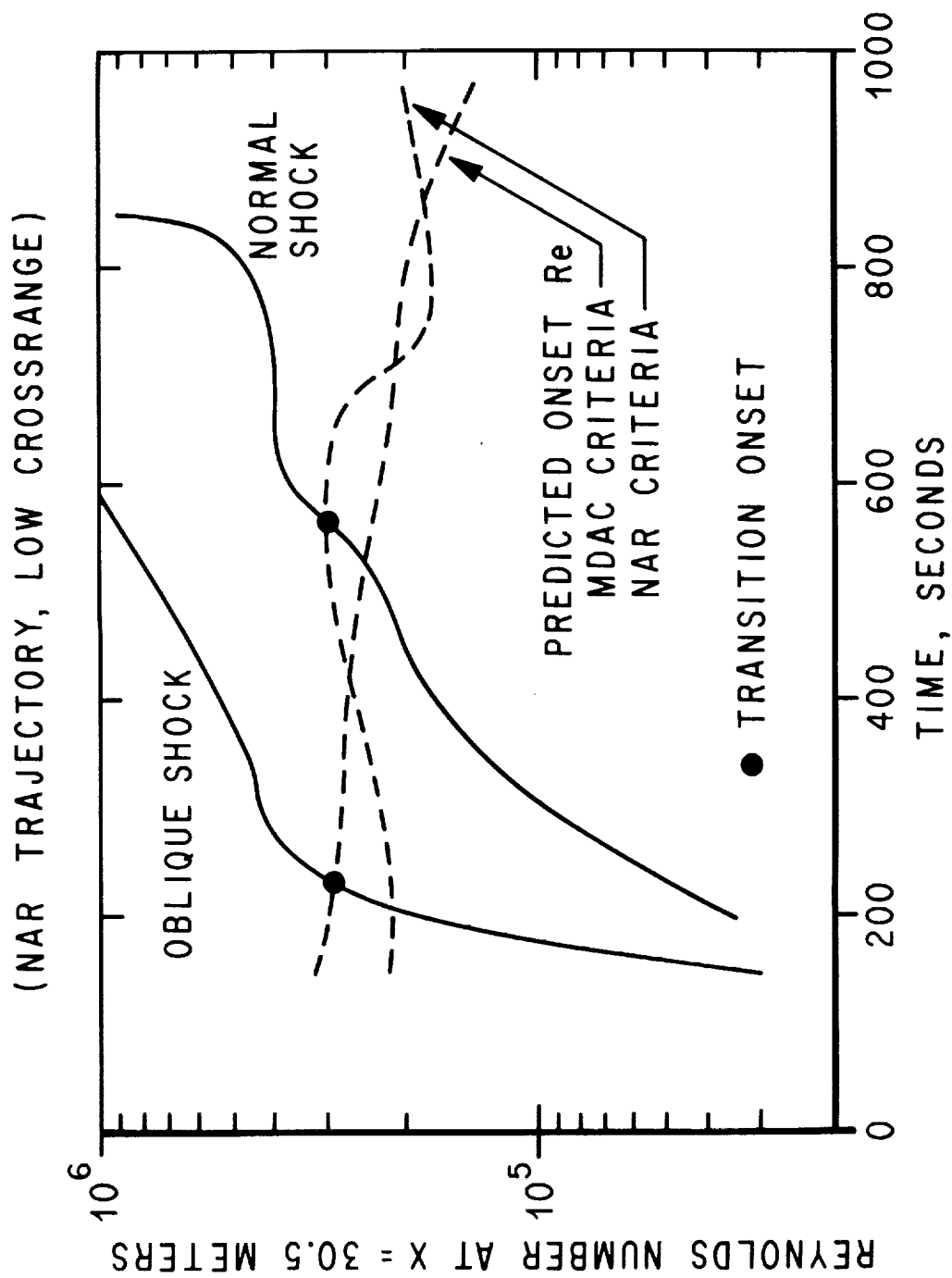
Slide 4

Typical Low Crossrange Temperature Histories

(Slide 4)

After matching the predicted temperatures shown on the previous slide with each contractor's aeroheating methodology, a systematic variation of the flow field method, transition criteria, turbulent heating method, etc. was undertaken. This slide shows some of the resulting equilibrium wall temperature histories. Using the MDAC transition criteria, the normal shock flow field gives 233°C lower temperatures than does the oblique flow field. For the NAR transition criteria, this flow field difference gives a 183°C difference in peak temperature. Using the oblique shock flow field, the NAR transition criteria give 78°C lower temperature than that given by MDAC transition criteria. For the normal shock flow field, this transition criteria difference gives a 39°C peak temperature difference.

REYNOLDS NUMBER VARIATION DURING ENTRY



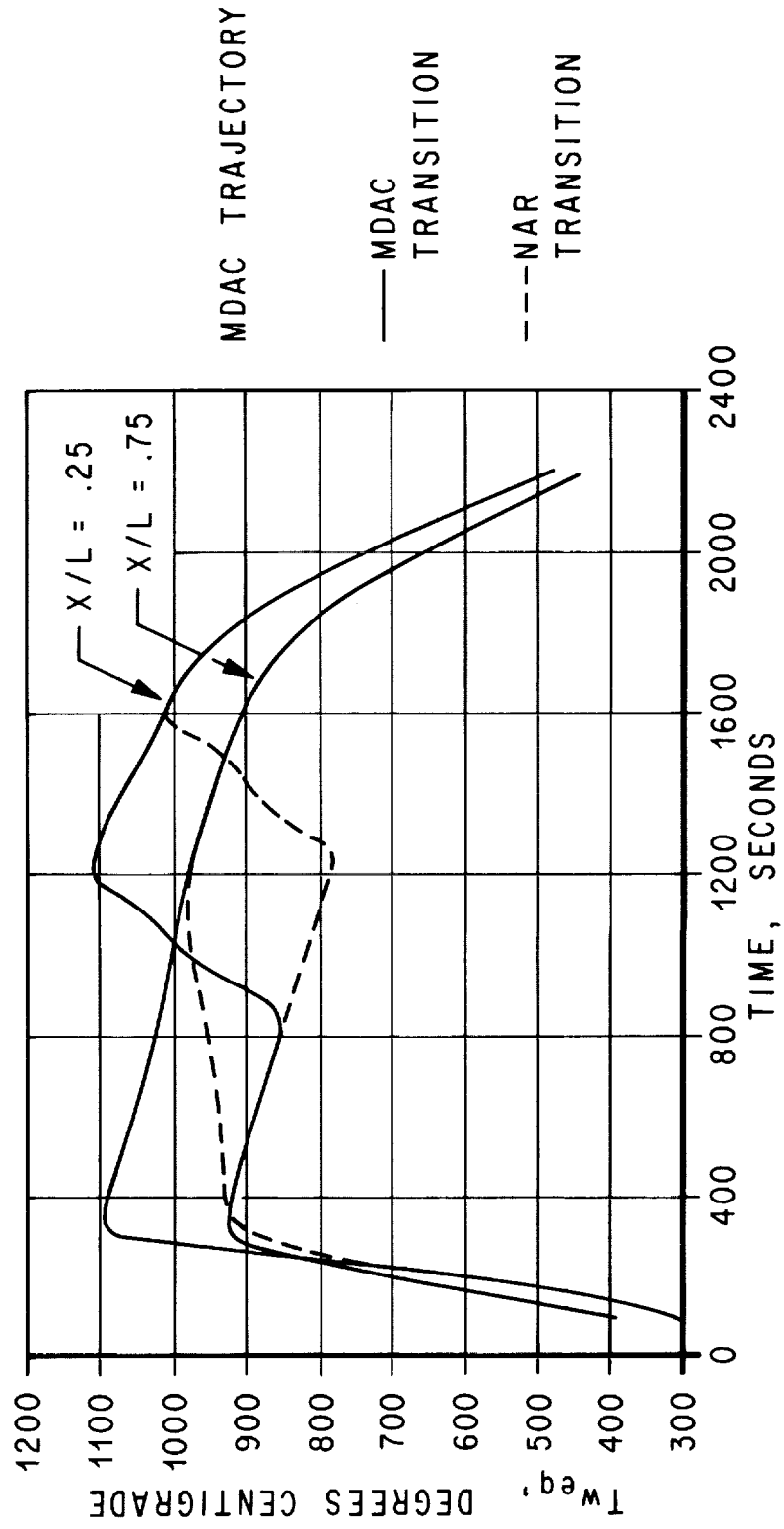
Slide 5

Reynolds Number Variation During Re-Entry

(Slide 5)

Reynolds number at the $X = 30.5$ m location is shown as a function of re-entry time for two flow field assumptions, oblique shock and normal shock. Recall that oblique shock is used by MDAC and normal shock is used by NAR. Other flow field quantities such as Mach number and momentum thickness were computed and used to construct the dashed curves. The dashed curves represent the variation during re-entry of Reynolds number required for transition onset for the MDAC and the NAR transition criteria. NAR would predict transition onset at the time when the normal shock Reynolds number curve crosses the predicted onset Reynolds number curve for their transition criteria. Note that the onset Reynolds number is quite similar for the two transition criteria. However the NAR normal shock flow field method gives much lower Reynolds numbers at the same trajectory conditions and hence transition onset occurs substantially later in flight.

TYPICAL HIGH CROSSRANGE TEMPERATURE HISTORIES



Slide 6

Typical High Crossrange Temperature Histories

(Slide 6)

The effect of transition criteria on lower centerline temperature histories for the $X/L = .25, .75$ locations is shown. Transition occurs later in flight according to the NAR criteria and corresponds to a reduction in peak temperature of $\sim 111^{\circ}\text{C}$ for these two body locations. At other locations the effect was found to be smaller.

EFFECT OF METHODOLOGY ASSUMPTIONS ON PEAK TEMPERATURE

METHODOLOGY ITEM	LOW CROSSRANGE	HIGH CROSSRANGE
TRANSITION CRITERIA	~ 83° C	~ 111° C
FLOW FIELD METHOD	~ 194° C	NONE
TURBULENT HEATING METHOD	—	* ~ 56° C
TRAJECTORY	~ 111° C	~ 111° C
TOTAL	NAR ~ 388° C COOLER	NAR ~ 166° C COOLER

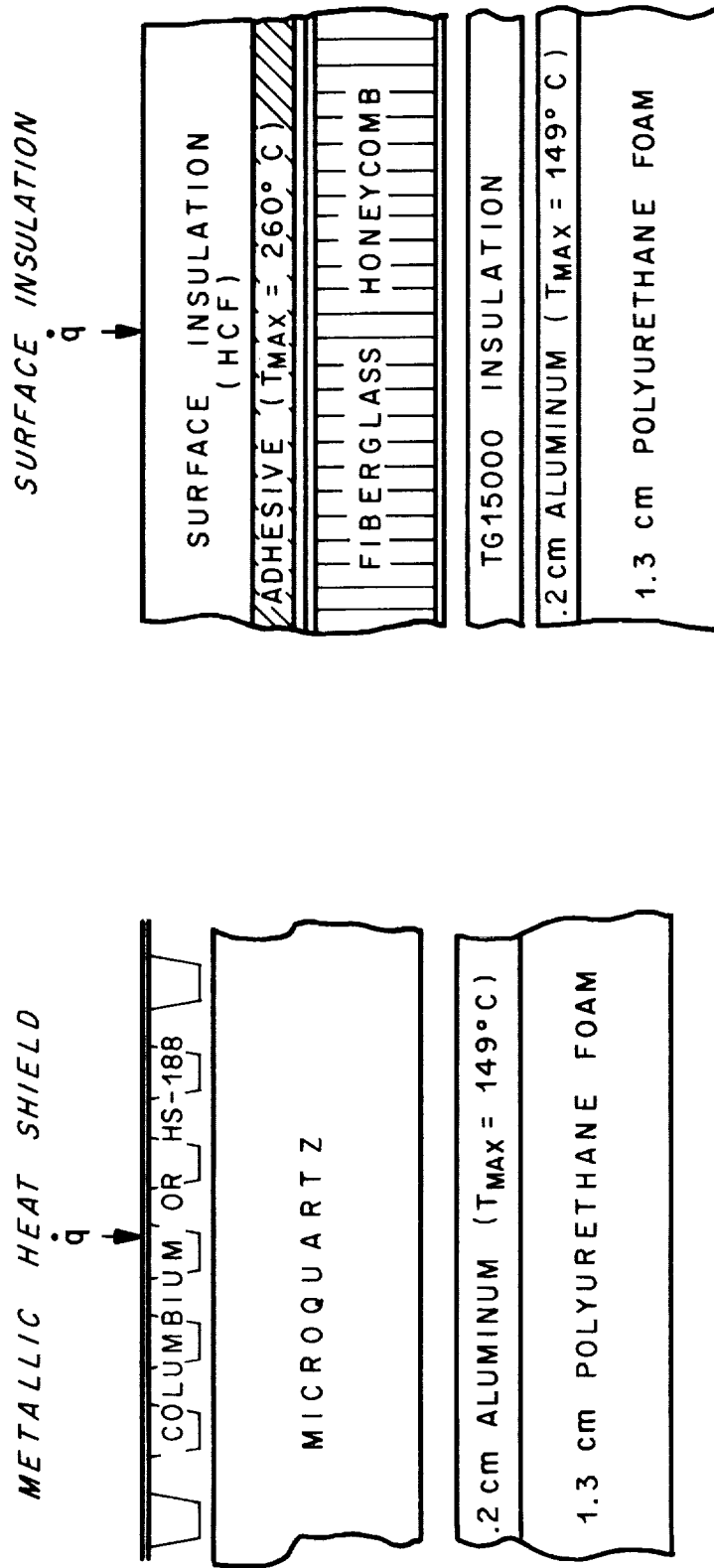
Slide 7

Effect of Methodology Assumptions on Peak Temperature

(Slide 7)

In determining the contribution of a particular methodology assumption to the discrepancies in the Shuttle contractor temperature predictions, it was found that the answer depended on vehicle location as well as the remaining methodology assumptions required to calculate a temperature history. For example the question of how much cooler the NAR transition criteria are than the MDAC criteria depends on the flow field assumption used to evaluate the transition criteria effect. As a result the temperature effects shown are essentially averages for a number of body locations and combinations of methodology assumptions. The low crossrange results shown are applicable to the aft 50 percent of the straight wing orbiter and the high crossrange results are applicable to no particular point but represent typical maximum values at several points. Positive numbers indicate NAR is cooler; the asterisk indicates NAR is hotter.

REPRESENTATIVE TPS ARRANGEMENTS



NOTE: EMITTANCE OF ALL INTERNAL SURFACES
ASSUMED TO BE 0.8

Slide 8

Representative TPS Arrangements

(Slide 8)

Two thermal analysis models were developed to define the temperature distribution through the thermal protection system and the resultant unit weight. One-dimensional heat flow was assumed and no accounting was made for local heat shorts and attachments. These models are shown schematically in the figure. The one on the left consists of a metallic heat shield which may be columbium or cobalt superalloy depending on the peak temperature. The maximum use temperature of the cobalt superalloy was assumed to be 1094°C and columbium was used at temperatures above 1094°C . The insulation was assumed to be 56.02 kg/m^3 Microquartz and this was sized to limit the aluminum structure to 149°C . The metallic heat shield was sized for the critical combination of flight temperature and pressure. The second concept consisted of a surface insulation layer of HCF having a density of 240.08 kg/m^3 , supported by a honeycomb substructure. In this arrangement, the HCF was sized to limit the bond between it and the honeycomb to 260°C , and the aluminum structure was also constrained to a peak temperature of 149°C . Ground cooling was assumed after a 1200 second subsonic cruise and taxi.

COMPARISON OF LOWER FUSELAGE TPS REQUIREMENTS

TRAJECTORY: MDAC — LOW CROSSRANGE

FLOW FIELD / TRANSITION CRITERION	AVERAGE UNIT WEIGHT (N / m ²)	
	METALLIC	HCF
OBLIQUE / MDAC	143	129
OBLIQUE / NAR	127	124
BLUNT BODY / MDAC	117	122
BLUNT BODY / NAR	111	118

Slide 9

Comparison of Lower Fuselage TPS Requirements - Low Crossrange

(Slide 9)

Temperature histories derived for the MDAC trajectory for the combinations of flow field and transition criteria were used to define the TPS average unit weight over the lower fuselage. Both thermal analyses models were utilized to show the effect of TPS concept on unit weight sensitivity. The table shows that the variation from maximum to minimum is 32.08 N/m^2 for the metallic heat shield and 11.5 N/m^2 for the surface insulation concept. The major reason for the differing sensitivities is due to a change in heat shield materials from columbium to the lighter HS-188 for the metallic concept. As shown in the table there appears to be a turnaround in the relative weights for the two concepts as flow field assumptions are changed, and based on the analysis assumptions made in this study the metallic system is slightly lighter for the blunt body flow field assumptions. In addition to flow field sensitivity, the trajectory utilized in the analysis affects the unit weight of the TPS. The NAR trajectory has slightly cooler peak temperatures than the MDAC trajectory but a longer heat pulse. The net result has not been completely assessed but calculations at one vehicle station ($X/L = 0.5$) for the surface insulation concept indicate that the longer trajectory time increases the weight of the surface insulation by approximately 9.6 N/m^2 .

REPRESENTATIVE TPS REQUIREMENTS

HIGH CROSSRANGE MISSION

($X/L = .5$)

FLOW FIELD / TRANSITION CRITERION	UNIT WEIGHT (N/m^2)	
	MDAC TRAJECTORY	NAR TRAJECTORY
OBLIQUE / MDAC	164	154
OBLIQUE / NAR	152	141

Slide 10

Comparison of Lower Fuselage TPS Requirements - High Crossrange

(Slide 10)

A single vehicle station was evaluated for the high crossrange missions. Since both contractors utilize the same flow field assumptions, only the transition criterion was varied. The analysis was conducted for the metallic heat shield concept. The peak temperatures at this location are lower than 1094°C and the analysis assumed HS-188 cobalt superalloy as heat shield material. The results shown in the table indicate the transition criterion results in an increment of approximately 9.6 N/m^2 and the trajectory in an increment of about 12.0 N/m^2 so the total difference is approximately 21.6 N/m^2 . It should be noted that the unit weight numbers depend on a number of assumptions. Therefore, the absolute values of unit weight may differ when computed by different analysts. However, the increments presented herein should be changed only slightly if differing assumptions are used.

CONCLUSIONS

NAR AEROHEATING METHODOLOGY IS 278°C - 388°C COOLER THAN MDAC FOR THE LOW CROSSRANGE MISSION AND ~ 56°C COOLER FOR THE HIGH CROSSRANGE MISSION.

FOR BOTH THE LOW AND HIGH CROSSRANGE MISSION THE NAR TRAJECTORIES ARE ~ 111°C COOLER THAN THE MDAC TRAJECTORIES.

THE NAR TRANSITION CRITERIA IS 83°C - 111°C COOLER THAN THE MDAC TRANSITION CRITERIA FOR BOTH LOW AND HIGH CROSSRANGE TRAJECTORIES.

FOR THE LOW CROSSRANGE TRAJECTORY THE NORMAL SHOCK FLOW FIELD METHOD OF NAR IS ~ 194°C COOLER THAN THE MDAC OBLIQUE SHOCK METHOD.

THE NAR AEROHEATING METHODOLOGY RESULTS IN LOWER UNIT TPS WEIGHTS FOR THE LOW CROSSRANGE MISSION; 32.1 N/m² FOR THE METALLIC HEAT SHIELD AND 11.5 N/m² FOR THE SURFACE INSULATION CONCEPT.

TRANSITION CRITERIA DIFFERENCES ACCOUNT FOR A 9.6 N/m² INCREMENT IN UNIT TPS WEIGHT.

BOUNDARY-LAYER TRANSITION AND HEATING CRITERIA APPLICABLE TO
SPACE SHUTTLE CONFIGURATIONS FROM FLIGHT AND GROUND TESTS

By Charles B. Johnson
NASA Langley Research Center
Hampton, Virginia

INTRODUCTION

As was pointed out by Masek and Forney (paper no. 4 of volume I of this compilation), two significant problems in shuttle technology are (1) the boundary-layer transition criterion and (2) the method used to determine boundary-layer edge conditions. In addition, the method by which the two problems are solved has a large effect on the skin temperature of the shuttle. The present paper examines the same two problems by first presenting the results of two new sets of transition data applicable to space shuttle configurations. One set is from Langley Mach 8 ground tests and the other set is from a flight test with a cone reentering at angles of attack. Second, these new data are used in three transition correlations and are compared with three existing transition criteria. Finally, the three transition criteria are applied to a space shuttle trajectory for which the local flow properties on the shuttle are calculated by a real-gas variable-entropy solution.

SYMBOLS

A.S.	acoustic sensor
E.S.	electrostatic sensor
h	heat-transfer coefficient
h_0	stagnation-point heat-transfer coefficient
M_e	local Mach number at edge of boundary layer
M_∞	free-stream Mach number
$p_{t,1}$	total pressure in settling chamber of test facility
$p_{t,3}$	pitot pressure
Re_x	local Reynolds number based on wetted length
Re, x_t	local Reynolds number based on distance to onset of transition
Re, δ_T^*	local Reynolds number based on transformed displacement thickness
Re, θ	local Reynolds number based on momentum thickness
R_∞/m	unit Reynolds number
r_n	nose radius
V_∞	free-stream velocity
x	surface distance
y	distance normal to wall
α	angle of attack, deg

α_c	cone center-line angle of attack, deg
α_{LOCAL}	local angle of attack, deg
ψ	angle relative to windward meridian, deg

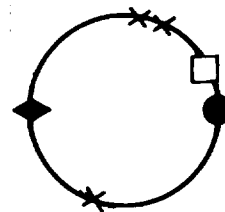
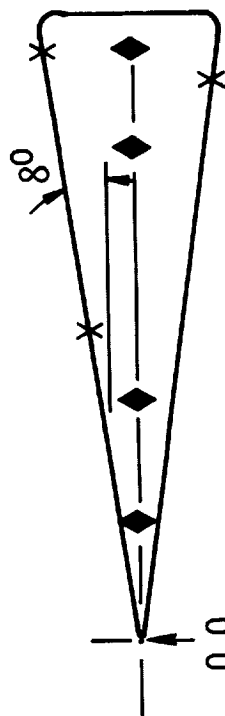
INSTRUMENTATION ON FLIGHT CONFIGURATION

(Figure 1)

The cone which was used to obtain flight angle-of-attack boundary-layer transition data is shown in figure 1. The 8° half-angle beryllium cone, which had a 2.54-mm-radius graphite nose, reentered the earth's atmosphere at approximately 6.9 km/sec at an angle of attack up to 75° . The onboard instrumentation used to detect transition consisted of three acoustic sensors and eight electrostatic sensors. The first effort to determine transition was made with the three acoustic sensors which gave transition data but which did not give a longitudinal location for the onset of transition because there was only one sensor in a ray. The second analysis for transition was made with the eight electrostatic sensors which were located four in one ray and three in another ray. This arrangement made possible a more precise determination of the location of transition. Some of the preliminary data obtained with these sensors are given in appendix A.

INSTRUMENTATION ON FLIGHT CONFIGURATION

- X ACOUSTIC SENSOR
(IN THREE RAYS)
- THREE } ELECTROSTATIC SENSORS
◆ FOUR } (IN THREE RAYS)
□ SINGLE }



ANGLE-OF-ATTACK FLIGHT REENTRY $V_{\infty} \approx 6.86$ km/sec
LOCAL ANGLE OF ATTACK UP TO 75°

STATUS: ● TRANSITION DATA FROM THREE ACOUSTIC SENSORS
(17 DATA POINTS, α UP TO 31°)

● TRANSITION DATA FROM EIGHT ELECTROSTATIC SENSORS
(APPROXIMATELY 51 DATA POINTS, LAMINAR AND
TURBULENT)

Figure 1

CONE CENTER-LINE ANGLE OF ATTACK DURING REENTRY

(Figure 2)

Figure 2 shows the center-line angle of attack of the cone during reentry. At an altitude of approximately 80 km, the cone has maximum local angle of attack of approximately 75° . As the cone penetrates the earth's atmosphere, the oscillation of the center-line angle of attack is damped. Even though the cone experienced large local angles of attack, no boundary-layer transition is detected above an altitude of approximately 46 km. Both the electrostatic and acoustic sensors show that the first indication of transition is at an altitude of approximately 46 km.

Two flight tests of this particular configuration were made by TRW, Inc., for the Department of Defense. One of these heavily instrumented flights entered at the design 0° angle of attack, and the other flight (fig. 2) reentered at high angles of attack due to some anomaly above the earth's atmosphere. The results of the anomalous angle-of-attack flight, which were of no use to the Department of Defense, were not reduced until Langley Research Center funds were made available.

The vehicle has a rolling motion in addition to the pitching motion shown in the figure. As a result of these motions, the various rays of instrumentation are at some instant on the windward meridian. Because both electrostatic and acoustic sensors have an almost instantaneous response time, the condition of the boundary layer could be determined at the instant that the sensor was on the windward meridian. In addition, some transition data were obtained when the sensor was off the windward meridian. The motion of the vehicle caused a rapid change in the local angle of attack which coupled with the rapid change in free-stream conditions resulted in a large variation of flow properties at the edge of the boundary layer. This body motion further caused a particular sensor, for the three instances when it was on the windward meridian, to indicate a turbulent, then laminar, and then turbulent boundary layer for high, then low, and then high local angles of attack, respectively.

CONE CENTER-LINE ANGLE OF ATTACK DURING REENTRY

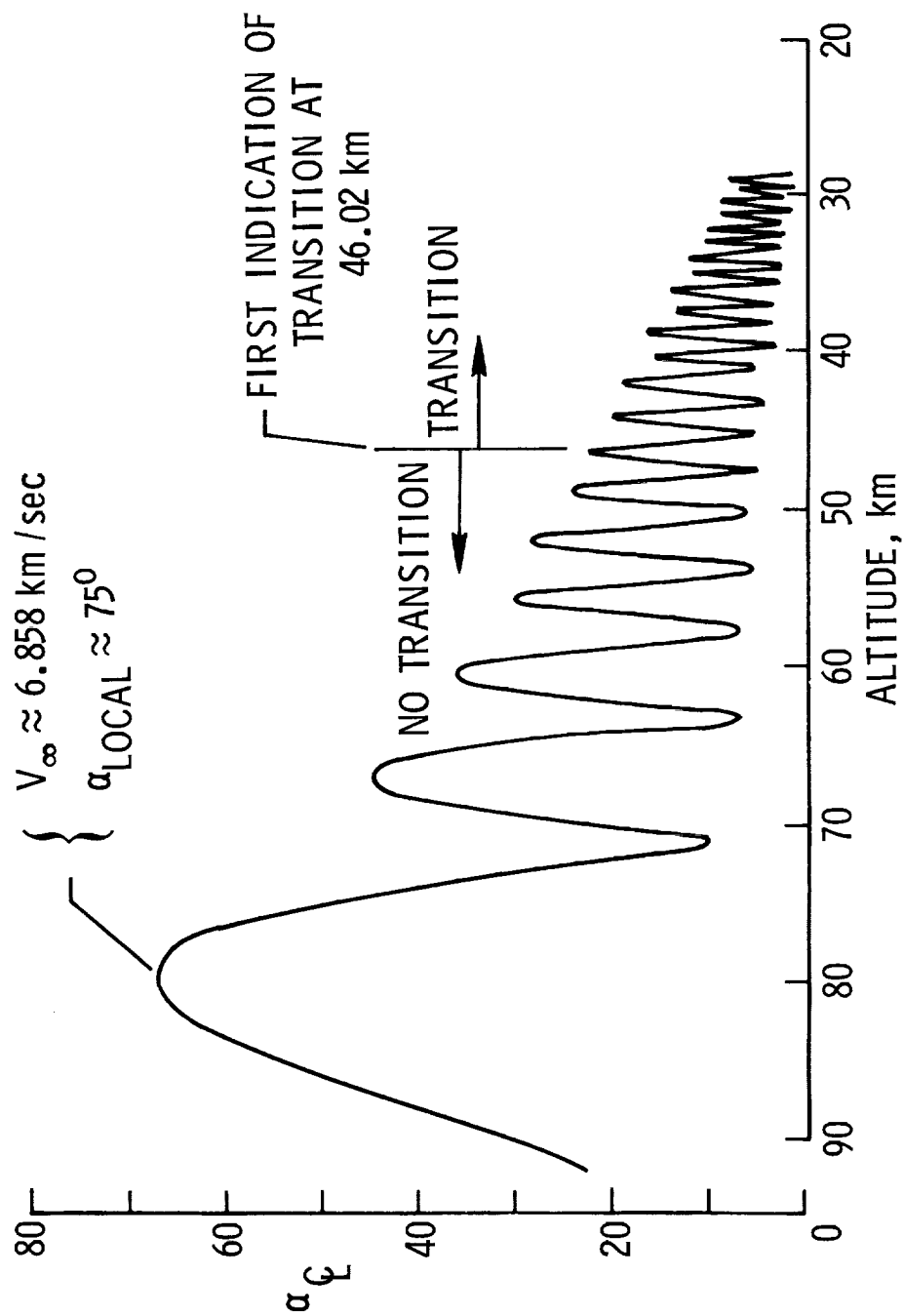


Figure 2

DELTA-WING AND STRAIGHT-BODY MODELS FOR GROUND TEST TRANSITION STUDIES

(Figure 3)

Figure 3 shows the two models made of high-temperature epoxy plastic which were used in ground tests of boundary-layer transition at the Langley Research Center. Both models are approximately 23 cm long and have an initial sweep angle of 75° ; however, one model is a delta wing and the other is a straight body. The models were tested at Mach 8 at angles of attack of 0° , 20° , 40° , and 60° over a range of Reynolds numbers per meter from 1.378×10^6 to 19.0×10^6 . The test surface was the flat-bottom surface. The models had a stainless-steel nose piece of 6.35-mm radius and the swept and straight leading edges were also 6.35 mm in radius.

DELTA-WING AND STRAIGHT-BODY MODELS FOR GROUND TEST TRANSITION STUDIES

$$M_{\infty} = 8$$

$$0^{\circ} \leq \alpha \leq 60^{\circ}$$

$$1.378 \times 10^6 \leq R_{\infty} / m \leq 19 \times 10^6$$

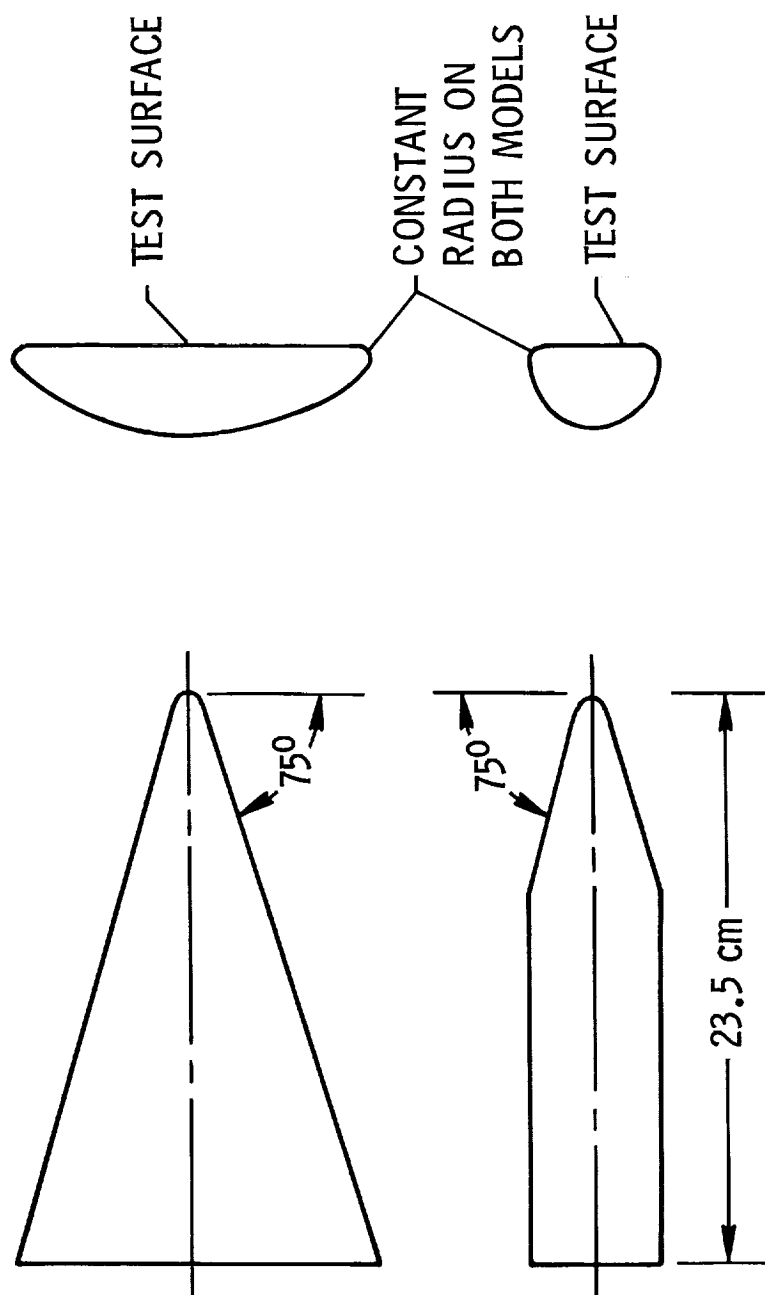


Figure 3

PHASE-CHANGE-PAINT HEAT-TRANSFER PATTERNS

(Figure 4(a))

In figure 4(a) is shown a phase-change-paint heat-transfer pattern on the delta-wing model at 20° angle of attack and a free-stream unit Reynolds number per meter of 13.95×10^6 . The plot of the heat-transfer distribution, h/h_0 as a function of the surface distance, shows the characteristic distribution at boundary-layer transition, that is, a decrease in laminar heating up to the start of transition and thereafter a rapid increase in heating. From the complex phase-change pattern it would appear that the front of transition indicated by the high-number contours is quite curved. This curved front of transition indicates that a two-dimensional strip theory would be applicable for analysis of the heating because the distance along the center line from the tip to the start of transition is approximately the same as the distance off the center line from the swept leading edge to the point of the start of transition.

PHASE - CHANGE - PAINT HEAT - TRANSFER PATTERNS DELTA WING

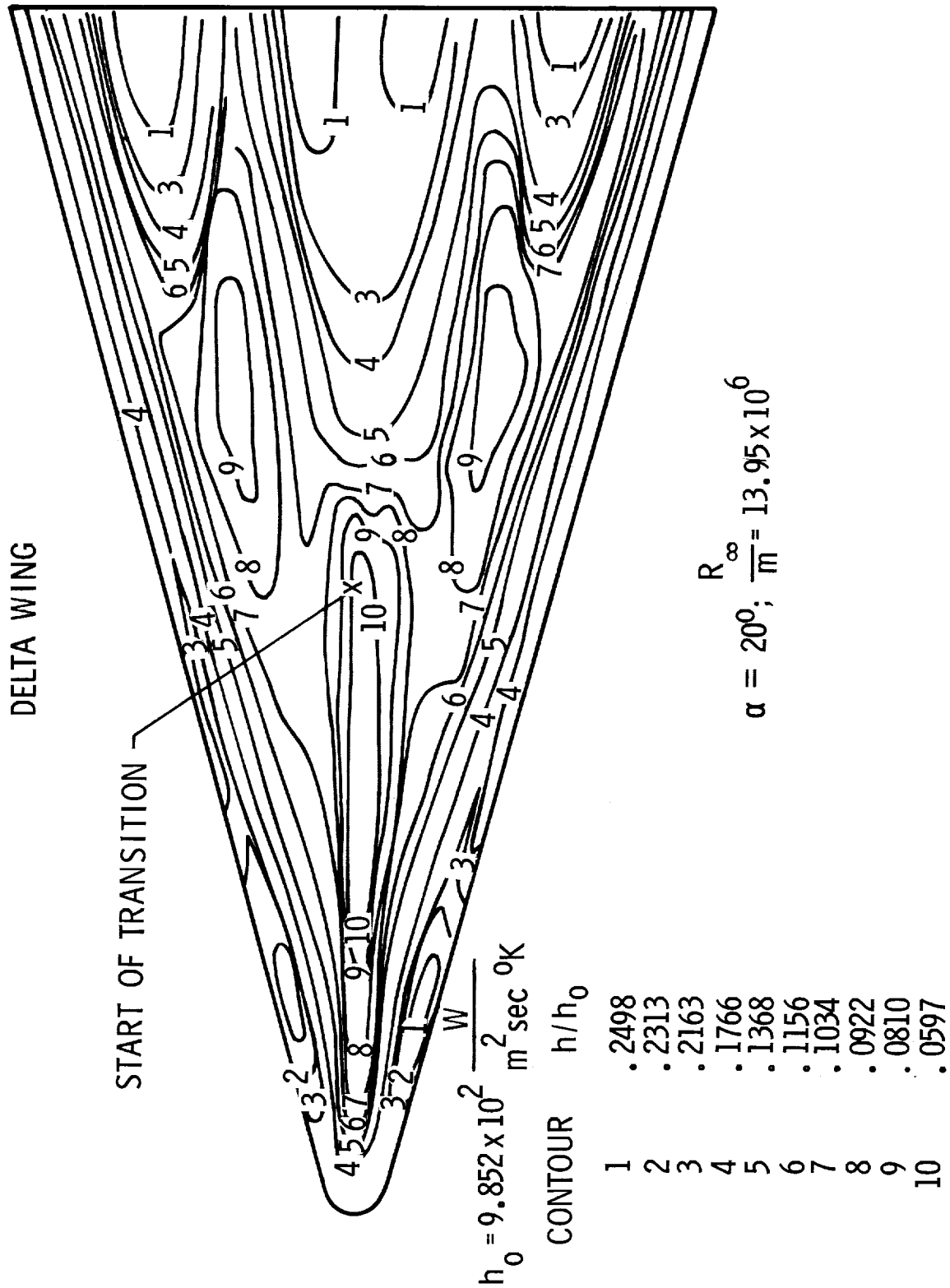


Figure 4(a)

VARIATION OF h/h_0 WITH x/L

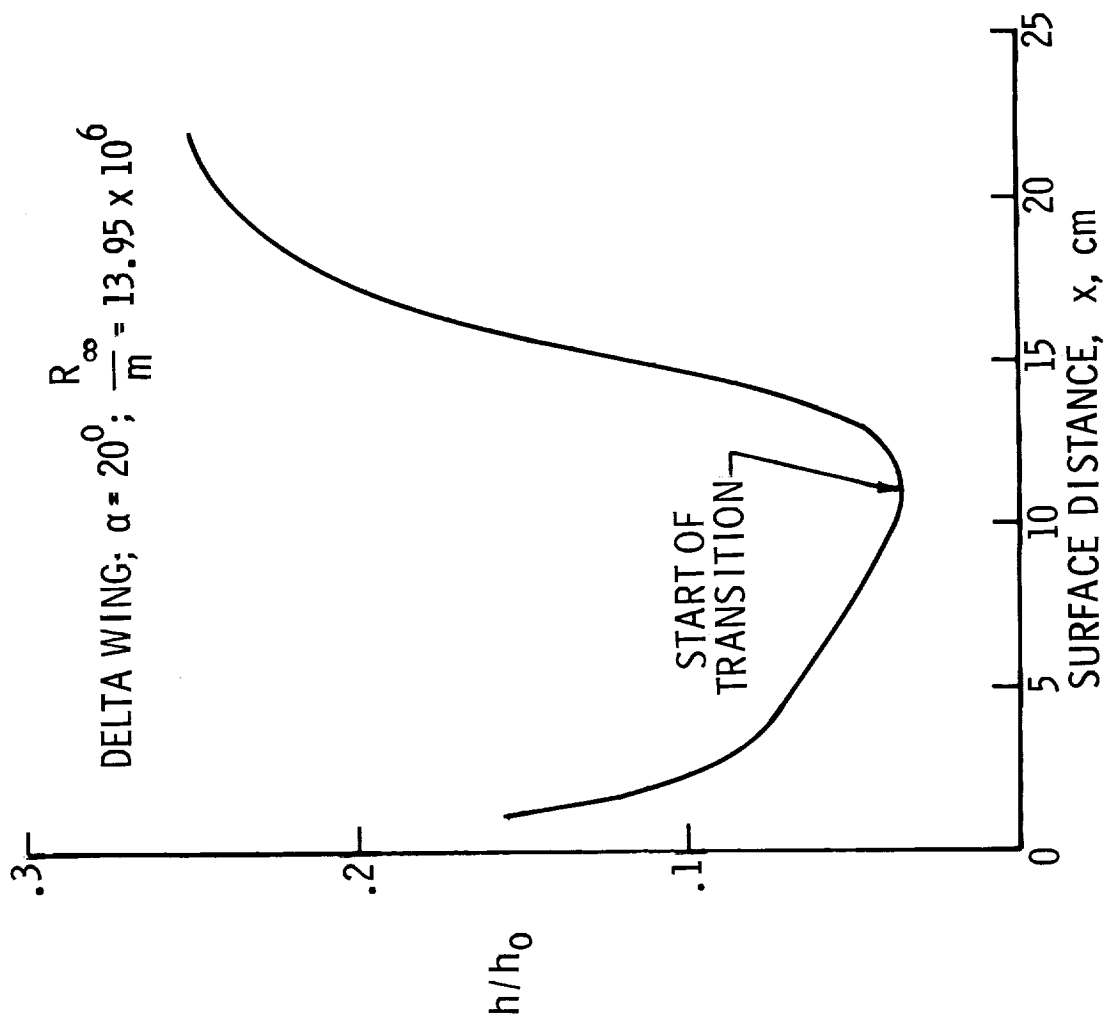


Figure 4(a) - Concluded

(Figure 4(b))

In figure 4(b) is shown the heating pattern for the straight-body model at $\alpha = 20^\circ$ and $R_\infty/m = 13.95 \times 10^6$, the same conditions as those for the delta-wing model in figure 4(a). The heating pattern on the straight body is simpler than the pattern on the delta wing downstream of the point where the leading edge becomes parallel to the center line. This change in pattern indicates that swept-cylinder analysis may be appropriate for the straight body at angle of attack.

PHASE-CHANGE-PAINT HEAT-TRANSFER PATTERNS STRAIGHT BODY

$$h_0 = 9.885 \times 10^2 \frac{W}{m^2 \text{ sec}^0 K}$$

$$\alpha = 20^0; \frac{R_{\infty}}{m} = 13.95 \times 10^6$$

CONTOUR	h/h ₀
1	.2421
2	.1976
3	.1644
4	.1398
5	.1236
6	.1101
7	.0962
8	.0671

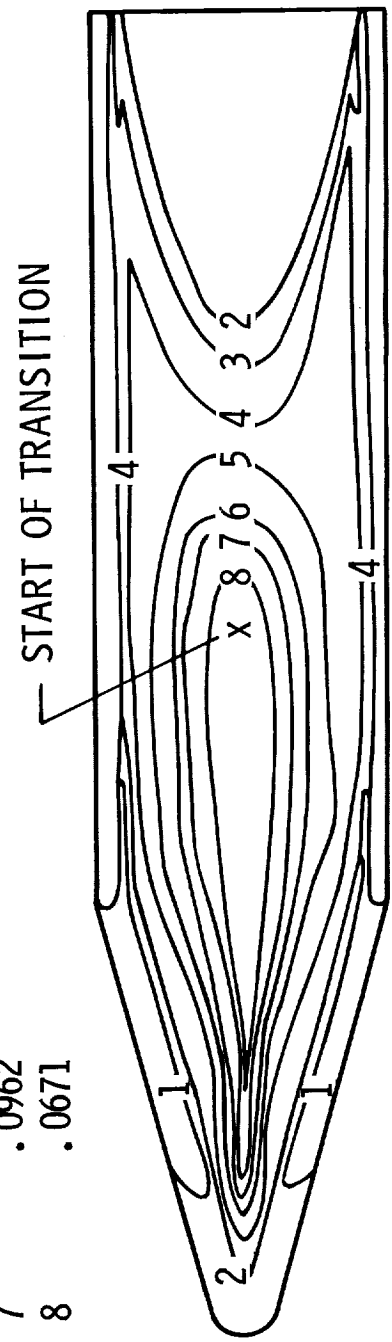


Figure 4(b)

PHASE-CHANGE-PAINT HEAT-TRANSFER PATTERNS

(Figure 4(c))

In figure 4(c) the angle of attack on the delta-wing model is increased to 40° at the same unit Reynolds number as in figures 4(a) and 4(b). The heat-transfer pattern has considerably simplified, which is believed due to increase in flow divergence at the higher angle of attack. In addition, the increase in angle of attack has moved the start of boundary-layer transition upstream from the position found at 20° angle of attack.

PHASE-CHANGE-PAINT HEAT-TRANSFER PATTERNS DELTA WING

$$h_0 = 9.919 \times 10^2 \frac{W}{m^2 \sec ^\circ K} \quad \alpha = 40^\circ; \quad \frac{R_\infty}{m} = 13.95 \times 10^6$$

CONTOUR	h/h_0
1	.5870
2	.3389
3	.2219
4	.2013
5	.1445

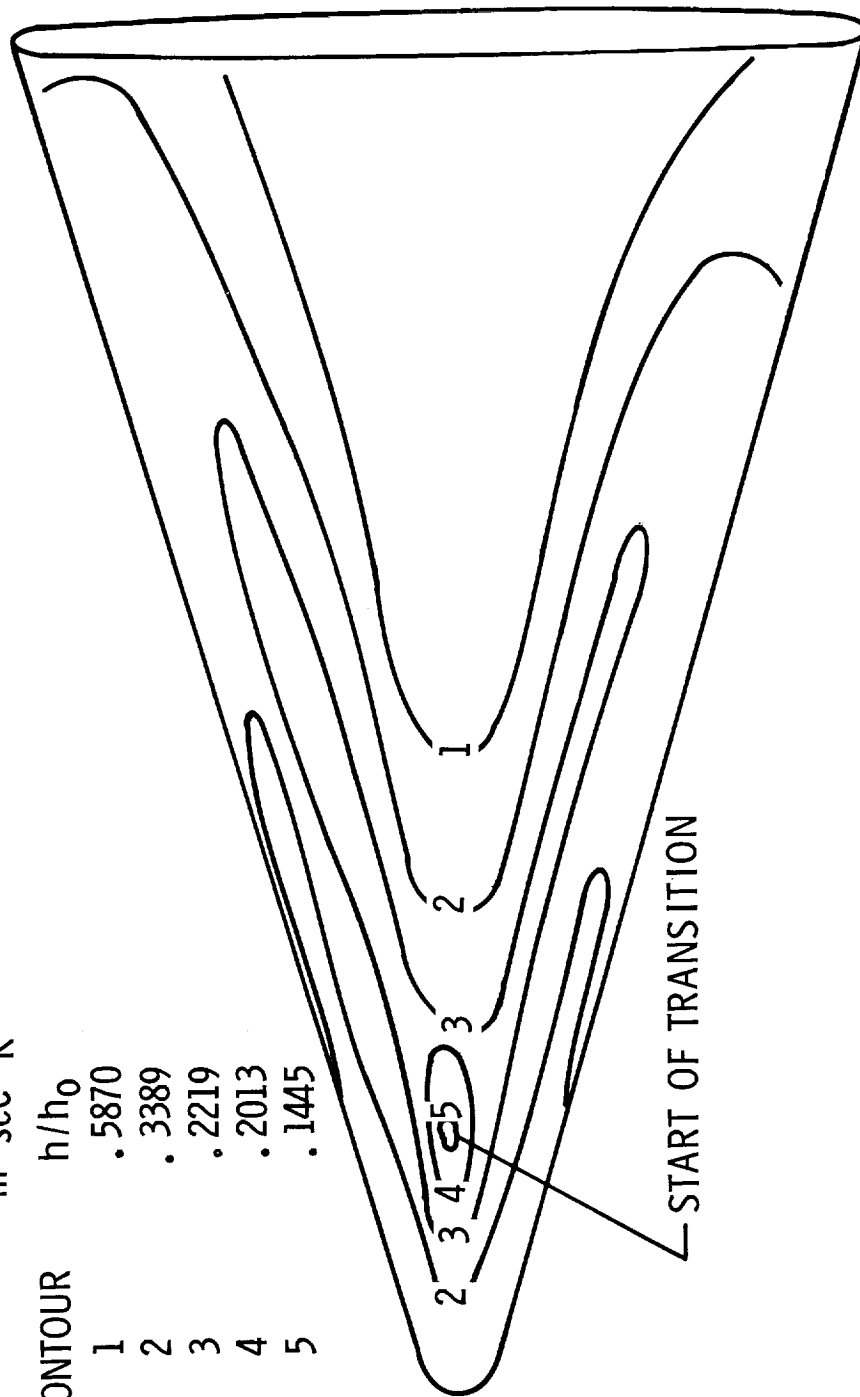


Figure 4(c)

PHASE-CHANGE-PAINT HEAT-TRANSFER PATTERNS

(Figure 4(d))

In figure 4(d) the angle of attack is increased to 40° on the straight-body model at the same unit Reynolds number as for $\alpha = 20^\circ$. The pattern at $\alpha = 40^\circ$ is somewhat similar to the pattern at $\alpha = 20^\circ$; however, as would be expected, the pattern at $\alpha = 40^\circ$ indicates more flow divergence. As was noted for the pattern at $\alpha = 20^\circ$, a swept-cylinder analysis would be appropriate for this pattern. Also of interest, this pattern shows both the minimum heating at the start of boundary-layer transition and the peak heating at the start of fully turbulent flow.

PHASE-CHANGE-PAINT HEAT-TRANSFER PATTERNS STRAIGHT BODY

$$\alpha = 40^{\circ}; \quad \frac{R_{\infty}}{m} = 13.95 \times 10^6$$

	$h_0 = 9.923 \times 10^2$	$\frac{W}{m^2 \text{ sec}^{\circ}K}$
CONTOUR	h/h_0	
1	.4942	
2	.4280	
3	.2853	
4	.2097	
5	.1883	

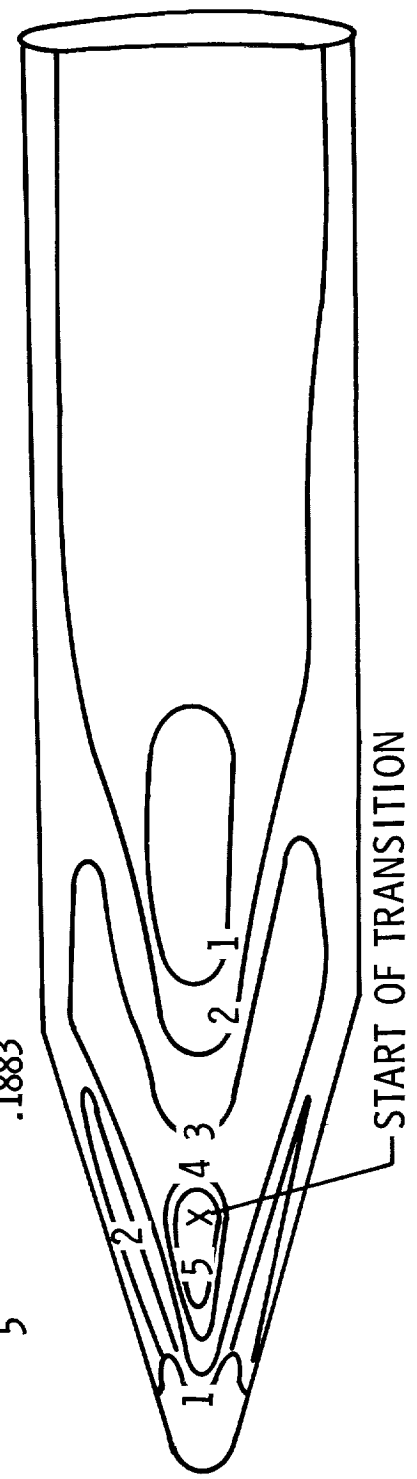


Figure 4(d)

PHASE-CHANGE-PAINT HEAT-TRANSFER PATTERNS

(Figure 4(e))

In figure 4(e) is shown the heating pattern for the delta wing at $\alpha = 60^\circ$ and $R_\infty/m = 3.94 \times 10^6$, a unit Reynolds number lower than that for the four previous patterns (figs. 4(a) to (d)). The pattern is considerably simplified at this higher angle of attack due to the increase in flow divergence. The minimum point of heating is believed to be the onset of boundary-layer transition; however, further testing and analysis are required to verify that this is transition.

PHASE-CHANGE-PAINT HEAT-TRANSFER PATTERNS DELTA WING

$$h_0 = 5.133 \times 10^2 \frac{W}{m^2 \text{ sec}^0 K}$$

$$\alpha = 60^0; \quad \frac{R_\infty}{m} = 3.94 \times 10^6$$

CONTOUR	h/h_0
1	.5226
2	.2698
3	.2164
4	.1857
5	.1695
6	.1552
7	.1445
8	.1368
9	.1327

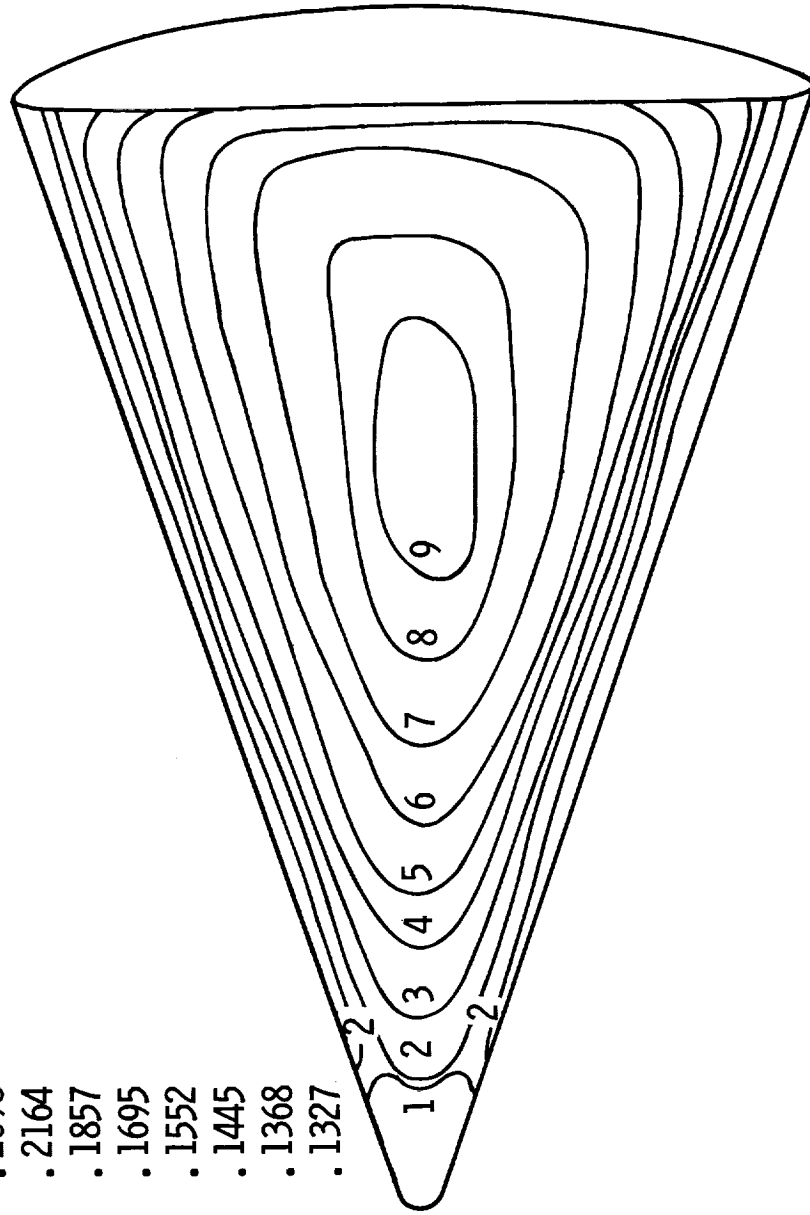


Figure 4(e)

VARIABLE-ENTROPY EFFECT AND SCHLIEREN PHOTOGRAPHS OF FLOW-FIELD SURVEY

(Figure 5)

The correct local flow properties are necessary in order to properly evaluate the boundary-layer transition and heat-transfer results shown in figure 4. Two methods were used to determine the edge properties of the Langley ground tests: (1) a theoretical variable-entropy solution using a conical flow-field assumption and (2) a flow-field survey to determine the entropy at the edge of the boundary layer. The variable-entropy solution shown in figure 5(a) was made for an ideal gas and shows that oblique-shock theory is applicable about 10 nose radii downstream from the stagnation point. Also shown in figure 5(b) are two schlieren photographs of the flow-field survey rake mounted on the delta-wing and straight-body configurations at $\alpha = 40^\circ$. The flow-field survey was made from the body to the shock which required that the rake be mounted on the surface and also offset. The rake consisted of six tubes, three tubes each in two vertical planes.

VARIABLE-ENTROPY EFFECT

$\alpha = 40^\circ$; $r_\eta = 6.35\text{mm}$; $M_\infty = 8.0$

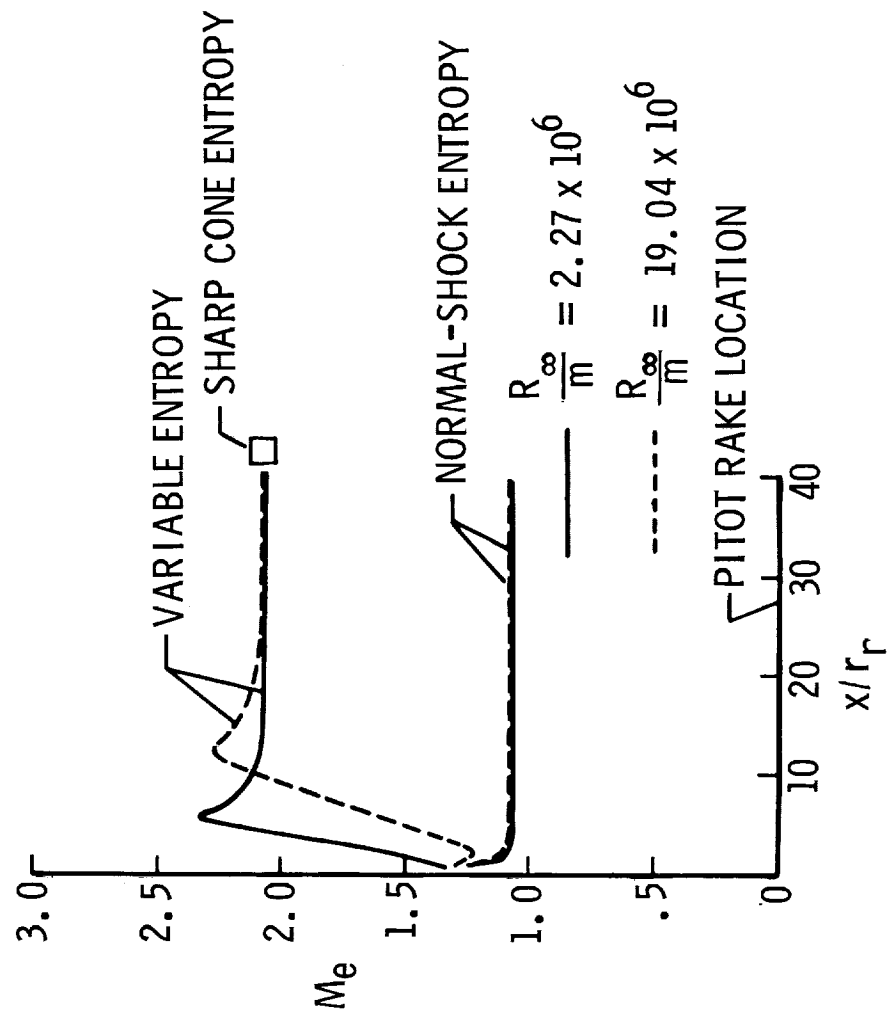
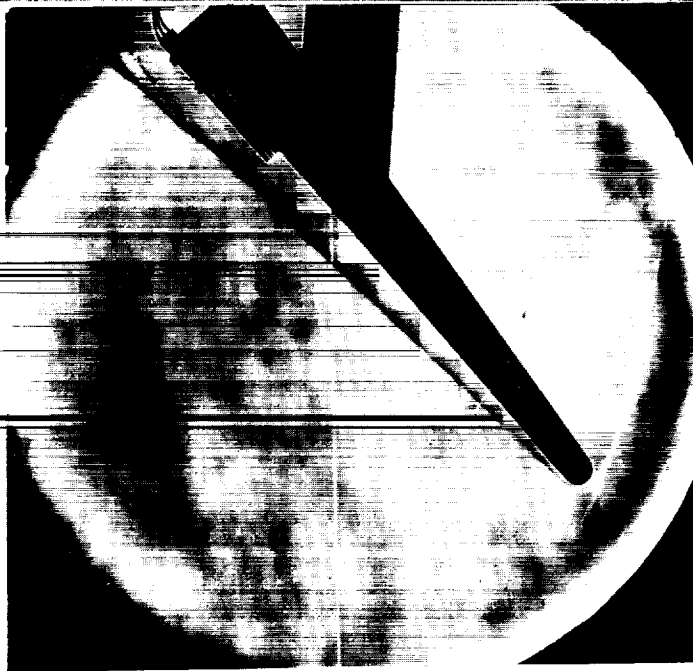


Figure 5(a)

SCHLIEREN PHOTOGRAPHS OF FLOW-FIELD SURVEY

$\alpha=40^\circ$; $M_\infty=8.0$



DELTA WING;

$$\frac{R_\infty}{m} = 2.27 \times 10^6$$



STRAIGHT BODY;

$$\frac{R_\infty}{m} = 19.04 \times 10^6$$

Figure 5(b)

PITOT PRESSURES FROM FLOW-FIELD SURVEY

(Figure 6)

Some preliminary results from flow-field surveys on the delta-wing and straight-body models are shown in figures 6(a) and 6(b). The results are presented in terms of the ratio of the measured pitot pressure to pressure in the stagnation chamber of the test facility. The results show that the entropy at the edge of the boundary layer is at an oblique-shock value. The local Mach number at the edge of the boundary layer calculated from the measured pitot and the local static pressures agrees with the value determined from sharp-cone and variable-entropy solutions. Results of additional flow-field surveys on a straight-wing orbiter and a delta-wing orbiter are presented in appendix B.

PITOT PRESSURE RATIO FROM A FLOW-FIELD SURVEY

$$\alpha = 40^\circ; \quad \frac{R_\infty}{m} = 2.27 \times 10^6; \quad M_\infty = 7.84$$

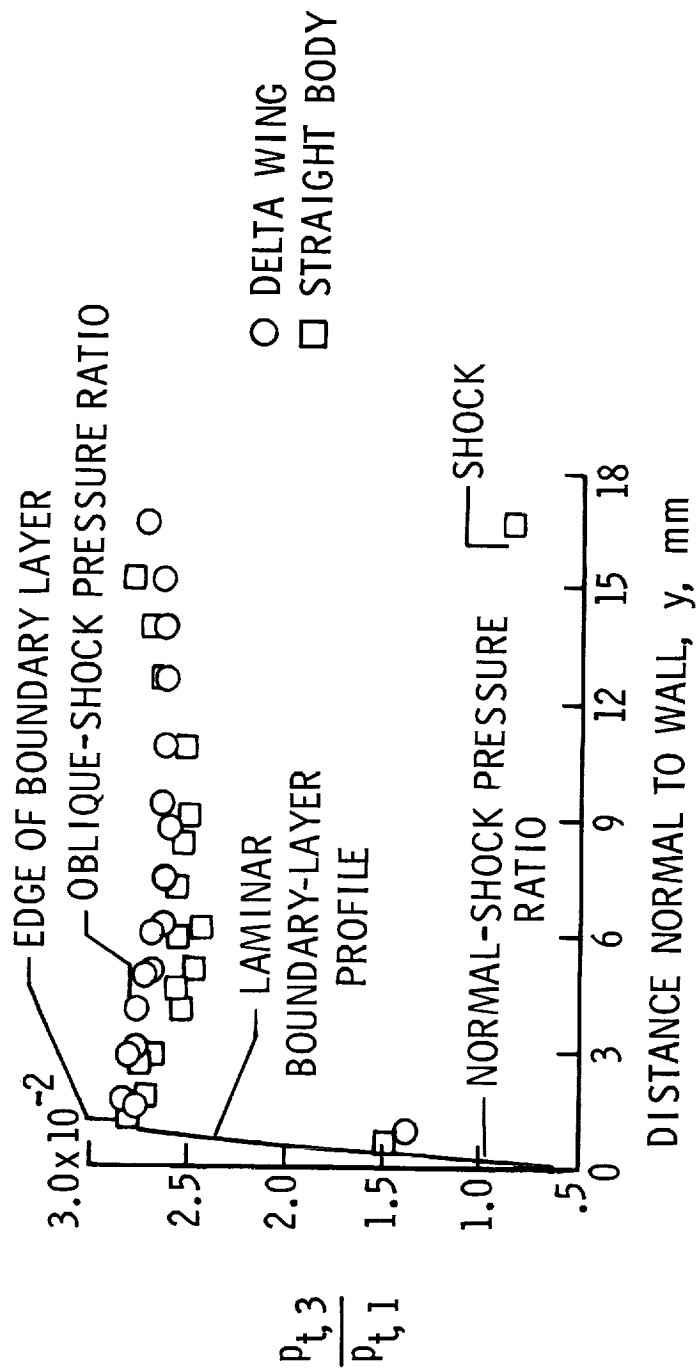


Figure 6(a)

PITOT PRESSURE RATIO FROM A FLOW-FIELD SURVEY

$$\alpha = 40^\circ; \quad \frac{R_\infty}{m} = 19.04 \times 10^6; \quad M_\infty = 7.99$$

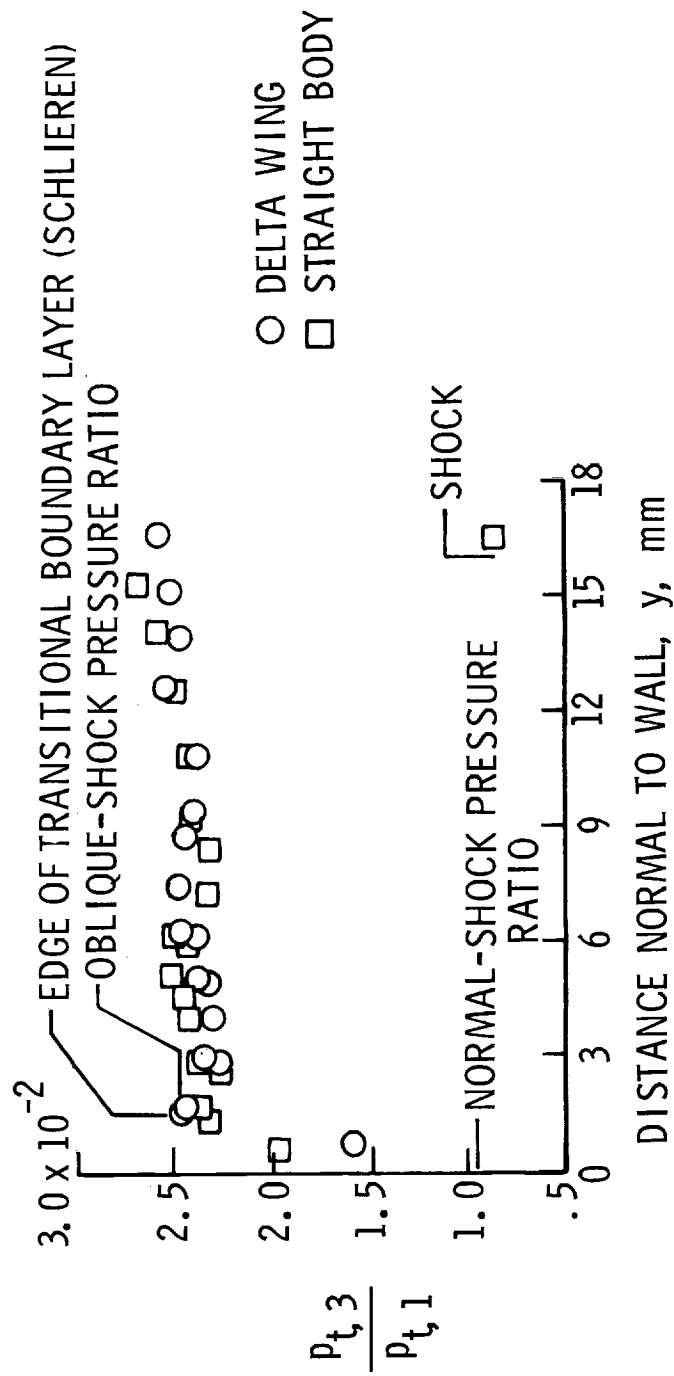


Figure 6(b)

TRANSITION CORRELATIONS

(Figure 7(a))

Figure 7(a) shows new boundary-layer transition data obtained from the Langley Mach 8 ground tests on the delta-wing and straight-body configurations and from the flight of a cone which reentered the earth's atmosphere at angles of attack. In addition, the transition results from two other flights are shown. The boundary-layer edge conditions for the ground test data and the flight angle-of-attack cone data were calculated by using oblique-shock entropy. In general, the new ground test data and cone angle-of-attack flight data fall below the McDonnell Douglas transition criterion; this indicates that with respect to these data the transition criterion is optimistic. The cone flight values labeled A.S. and E.S. refer to data obtained from the acoustic and electrostatic sensors, respectively, with the flagged symbols for the A.S. indicating data off the windward meridian.

McDONNELL DOUGLAS TRANSITION CORRELATION NEW FLIGHT AND GROUND TEST DATA

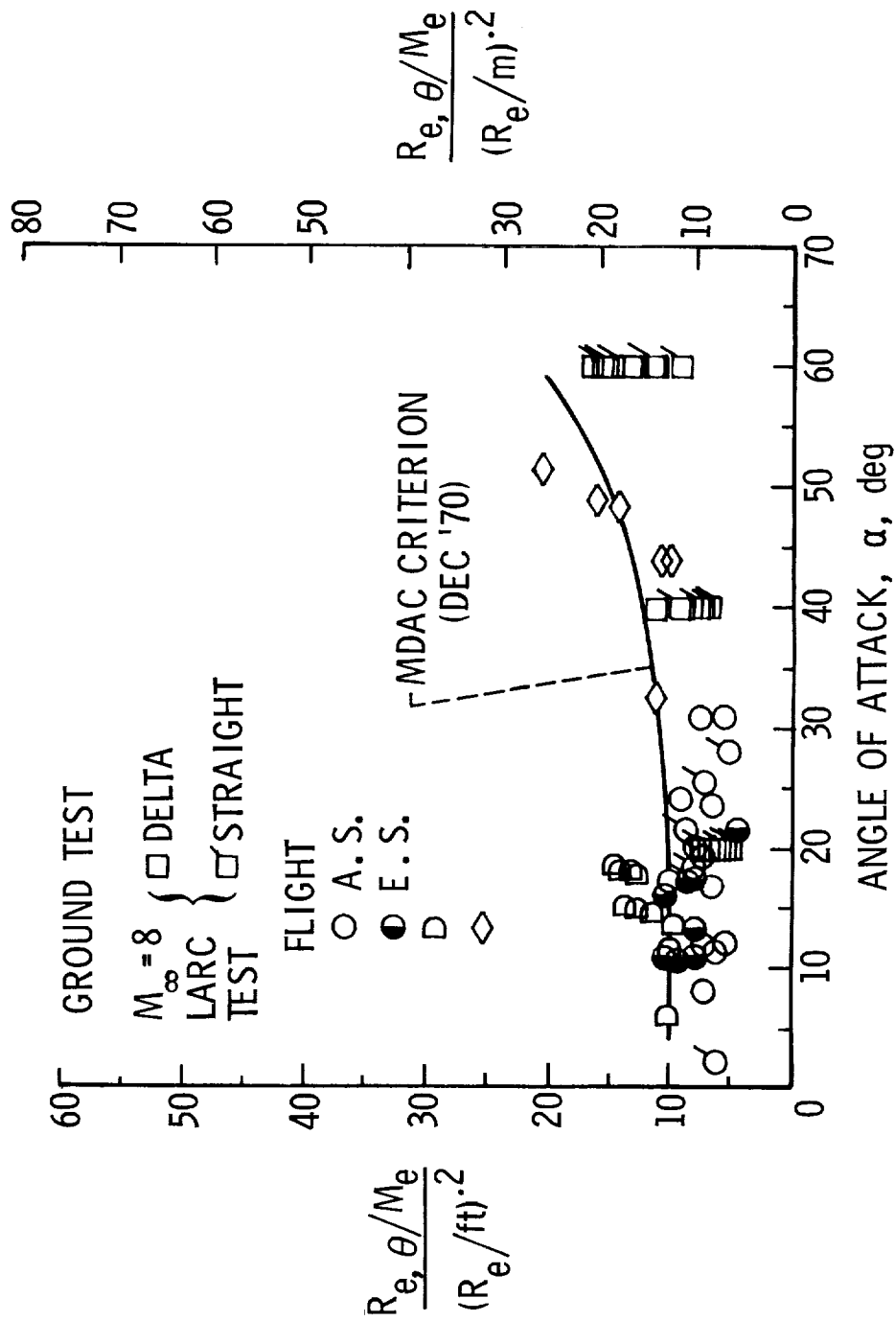


Figure 7(a)

TRANSITION CORRELATIONS

(Figure 7(b))

Figure 7(b) shows the new boundary-layer transition data presented in figure 7(a) and data from reference 1. The boundary-layer edge conditions for Hefner's data (ref. 1) have been calculated by using oblique-shock entropy. In general, most of the data fall below the McDonnell Douglas transition criterion; this indicates that the boundary-layer transition criterion is somewhat optimistic. The local Reynolds number based on momentum thickness Re_{θ} used in this correlation includes the effect of flow divergence and is calculated by a McDonnell Douglas method.

McDONNELL DOUGLAS TRANSITION CORRELATION

ADDITIONAL DATA

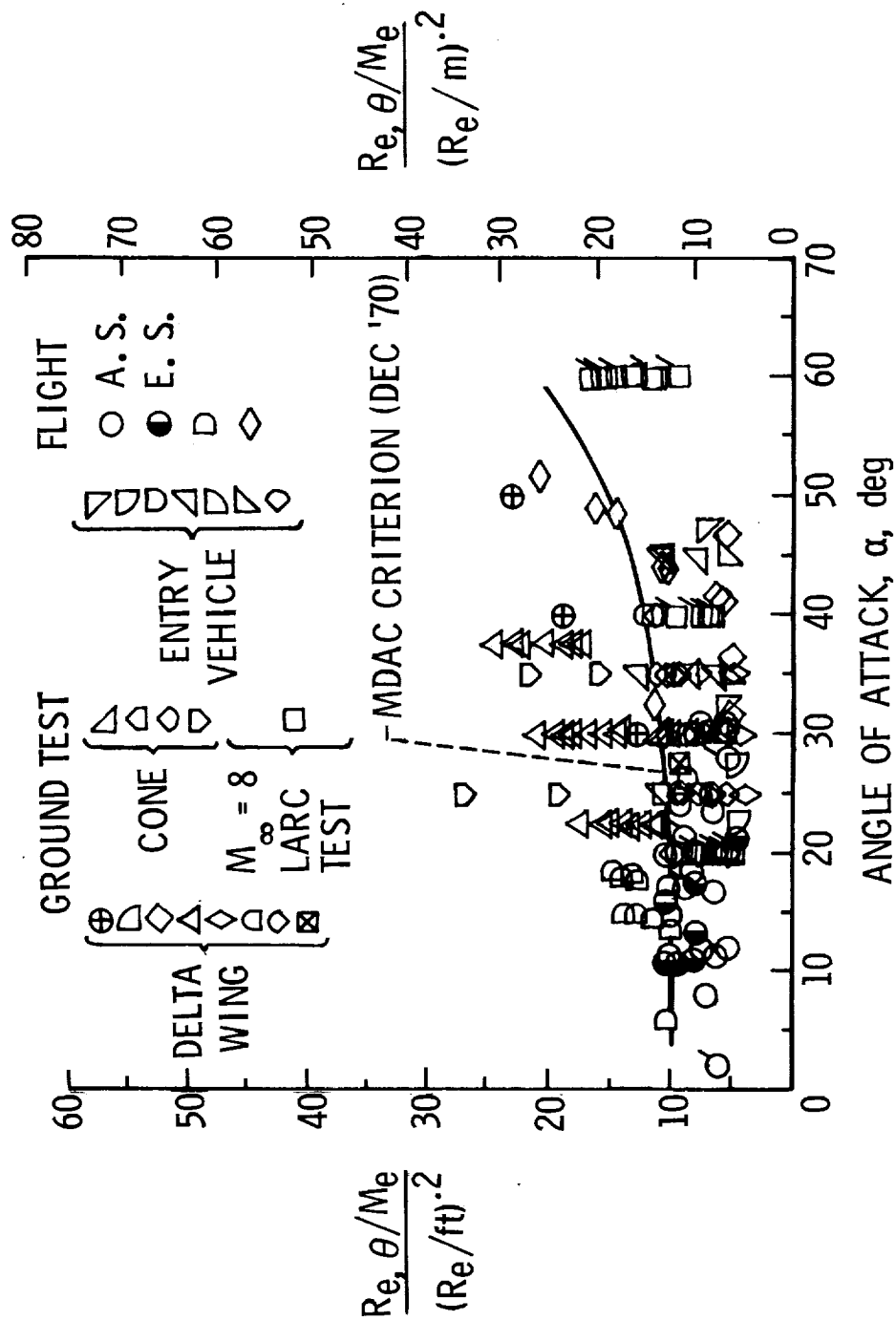


Figure 7(b)

TRANSITION CORRELATION

(Figure 8(a))

Figure 8(a) shows the new boundary-layer transition data obtained from Langley Mach 8 ground tests on the delta-wing and straight-body configurations and from the cone angle-of-attack flight. The edge conditions for the Langley ground test data are calculated by using normal-shock entropy (because the transition criterion is based on normal shock entropy), but the cone angle-of-attack and other flight data are calculated by using oblique-shock entropy. In general, the Langley Mach 8 ground test data are below the North American Rockwell transition criterion; this indicates that the criterion may be somewhat high for Mach numbers less than 3.0. However, above a Mach number of 5 the North American Rockwell criterion falls within the scatter of the cone angle-of-attack flight data. Also shown is the lower bound transition criterion of Hefner (ref. 1).

NORTH AMERICAN ROCKWELL TRANSITION CORRELATION NEW FLIGHT AND GROUND TEST DATA

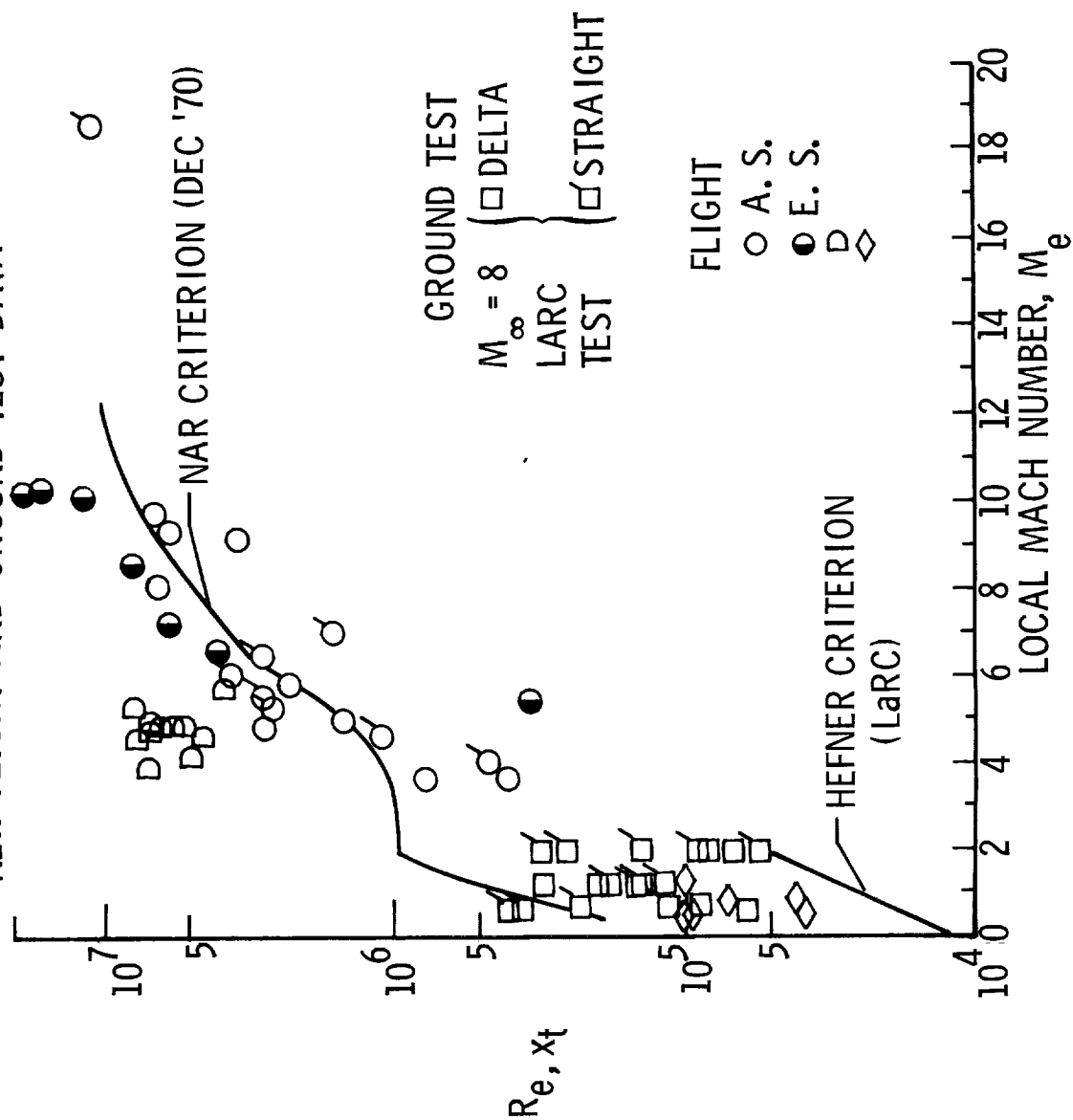


Figure 8(a)

TRANSITION CORRELATION

(Figure 8(b))

Figure 8(b) shows the new boundary-layer transition data presented in figure 8(a) and data from reference 1. The boundary-layer conditions are the same as those used in reference 1 (i.e., normal shock for blunt-nose configurations and oblique shock for sharp-nose configurations). The scatter of the data below a Mach number of 4.0 is large; however, most of the data fall below the criterion and this indicates that up to a Mach number of 4.0 the North American Rockwell transition criterion is optimistic. Also shown is the lower bound transition criterion of Hefner (ref. 1).

NORTH AMERICAN ROCKWELL TRANSITION CORRELATION ADDITIONAL DATA

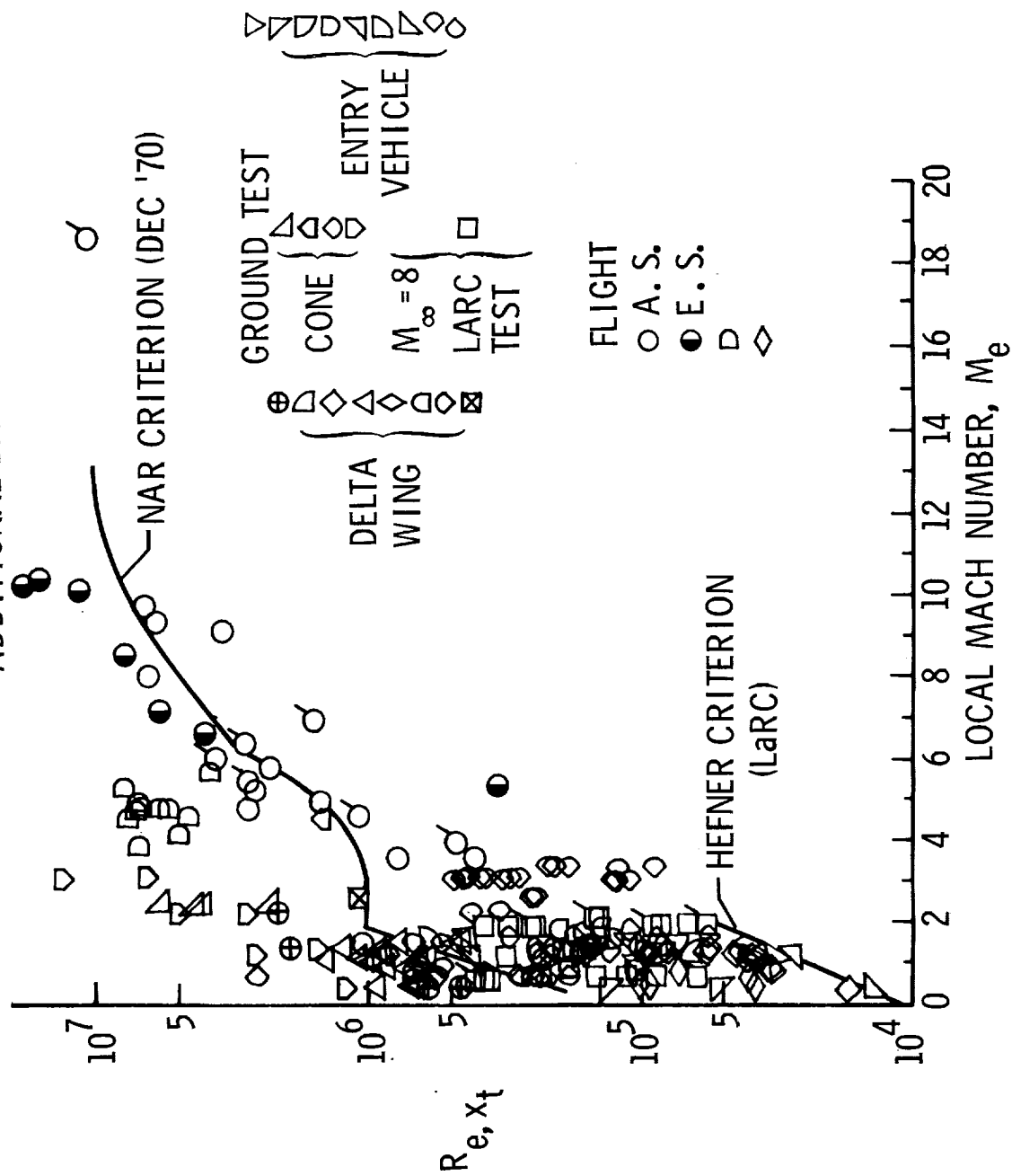


Figure 8(b)

TRANSITION CORRELATION

(Figure 9(a))

Figure 9(a) shows the new boundary-layer transition data from (1) the Langley Mach 8 ground tests, (2) the cone angle-of-attack flight, (3) two other flights, and (4) some blunt-cone flight data. The solid line represents the best linear fit to 78 flight data points at $\alpha = 0^\circ$ and was established independently of any other data presented in figure 9. The new data are presented in terms of a correlating parameter established by Beckwith and Stainback of the Langley Research Center from a statistical analysis (ref. 2). In general, the cone angle-of-attack flight data scatter around the linear fit to the 78 flight data points from $M_e = 5$ to 12. Below a Mach number of 5 the data drop sharply from the $\alpha = 0^\circ$ linear fit. The angle-of-attack blunt-body extension of the correlation is shown by the dashed line. The edge conditions are calculated by using oblique-shock entropy. The method of determining R_e, δ_T^* is presented in reference 2 by Bertram and Beckwith.

LANGLEY TRANSITION CORRELATION NEW FLIGHT AND GROUND TEST DATA

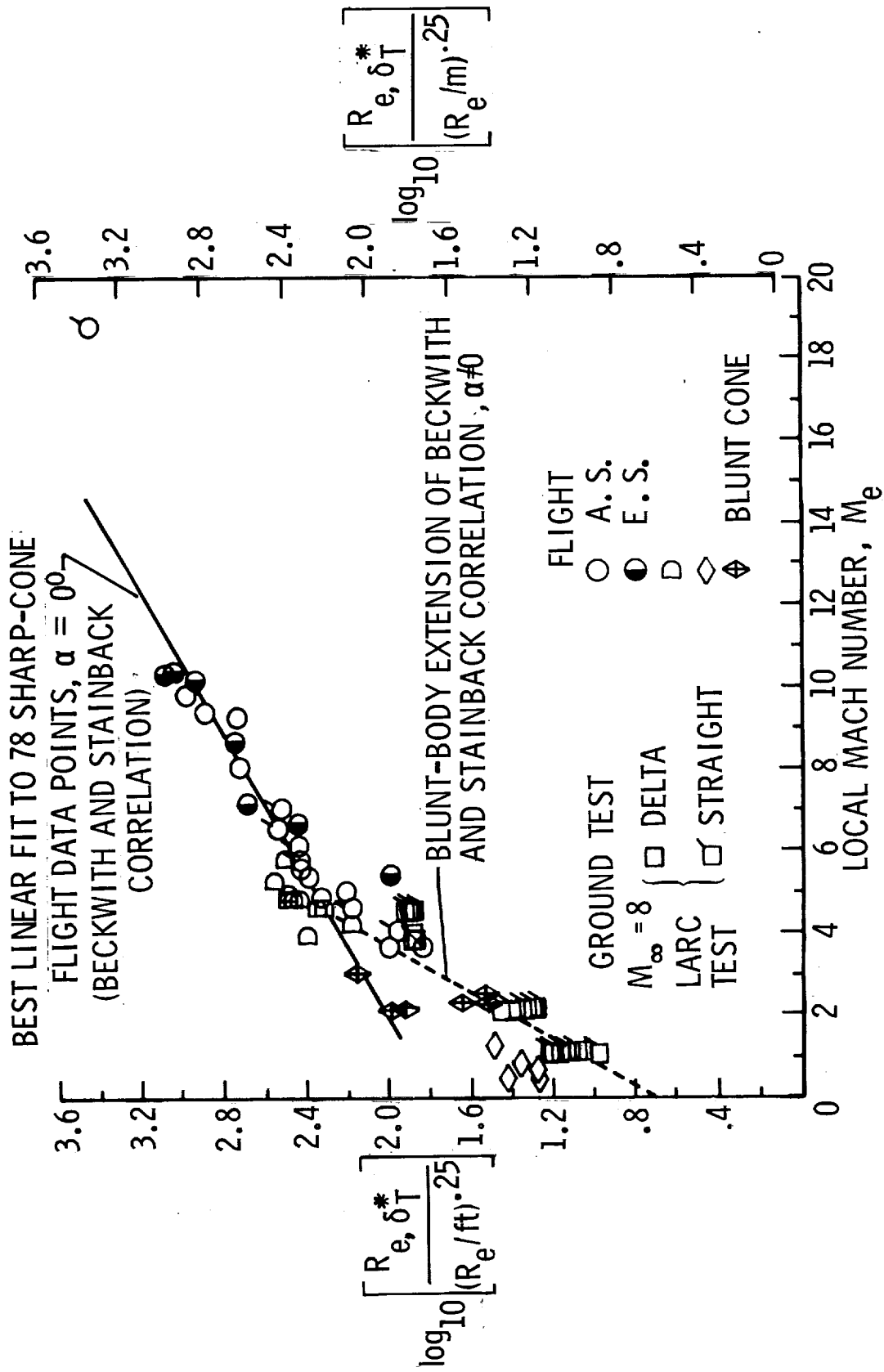


Figure 9(a)

TRANSITION CORRELATION

(Figure 9(b))

Figure 9(b) shows the new boundary-layer transition data presented in figure 9(a) and data from reference 1. The boundary-layer edge conditions for the data of reference 1 have been calculated by using oblique-shock entropy. The blunt-body extension shown in figure 9(a) is a linear fit to all data herein below a Mach number of about 5.0.

LANGLEY TRANSITION CORRELATION ADDITIONAL DATA

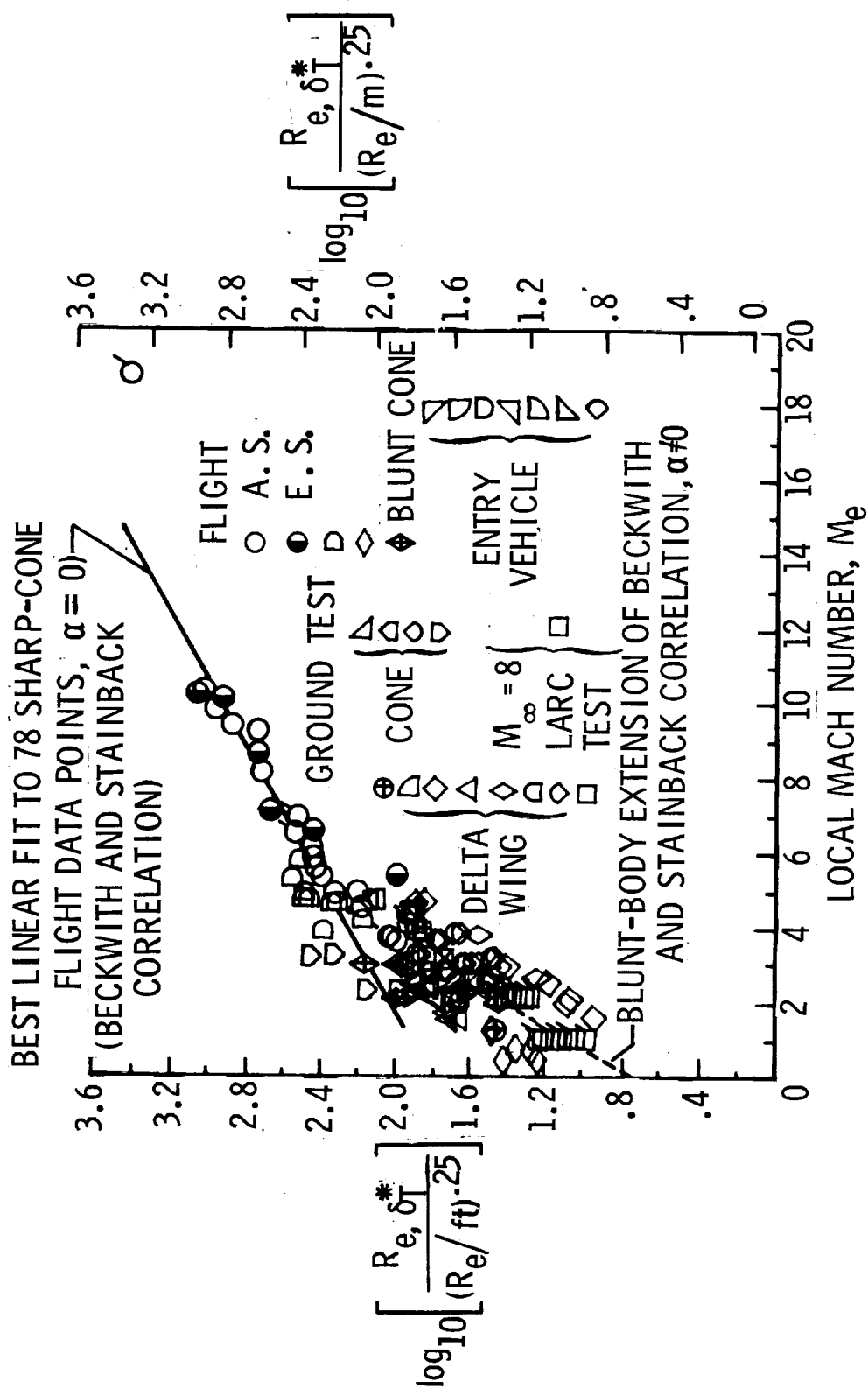


Figure 9(b)

APPLICATION OF TRANSITION CRITERION TO FLIGHT CALCULATIONS

(Figure 10)

The variation of the McDonnell Douglas boundary-layer transition parameter, calculated with variable entropy and real gas, for several points along a hypothetical space shuttle trajectory at 40° and 60° angles of attack is shown in figure 10. The calculation was made along the plane of symmetry, with a conical flow-field assumption, for a configuration that is geometrically similar to the models used in the Langley delta-wing and straight-body ground tests. For the flight-trajectory calculations, a full-scale configuration was used having a 1.524-m (5.0 ft) nose radius. When the McDonnell Douglas transition criterion is applied to the $\alpha = 40^\circ$ trajectory (altitude, 76.81 km), transition first occurs at about 12 nose radii from the stagnation point and moves forward to 3 nose radii at an altitude of 64.77 km. For the $\alpha = 60^\circ$ trajectory (altitude, 81.69 km), transition starts at about 24 nose radii from the stagnation point.

APPLICATION OF TRANSITION CRITERION TO FLIGHT CALCULATIONS

REAL-GAS SPACE SHUTTLE TRAJECTORY; VARIABLE ENTROPY

$\alpha = 40^\circ; 4.0 \leq M_e \leq 3.6$

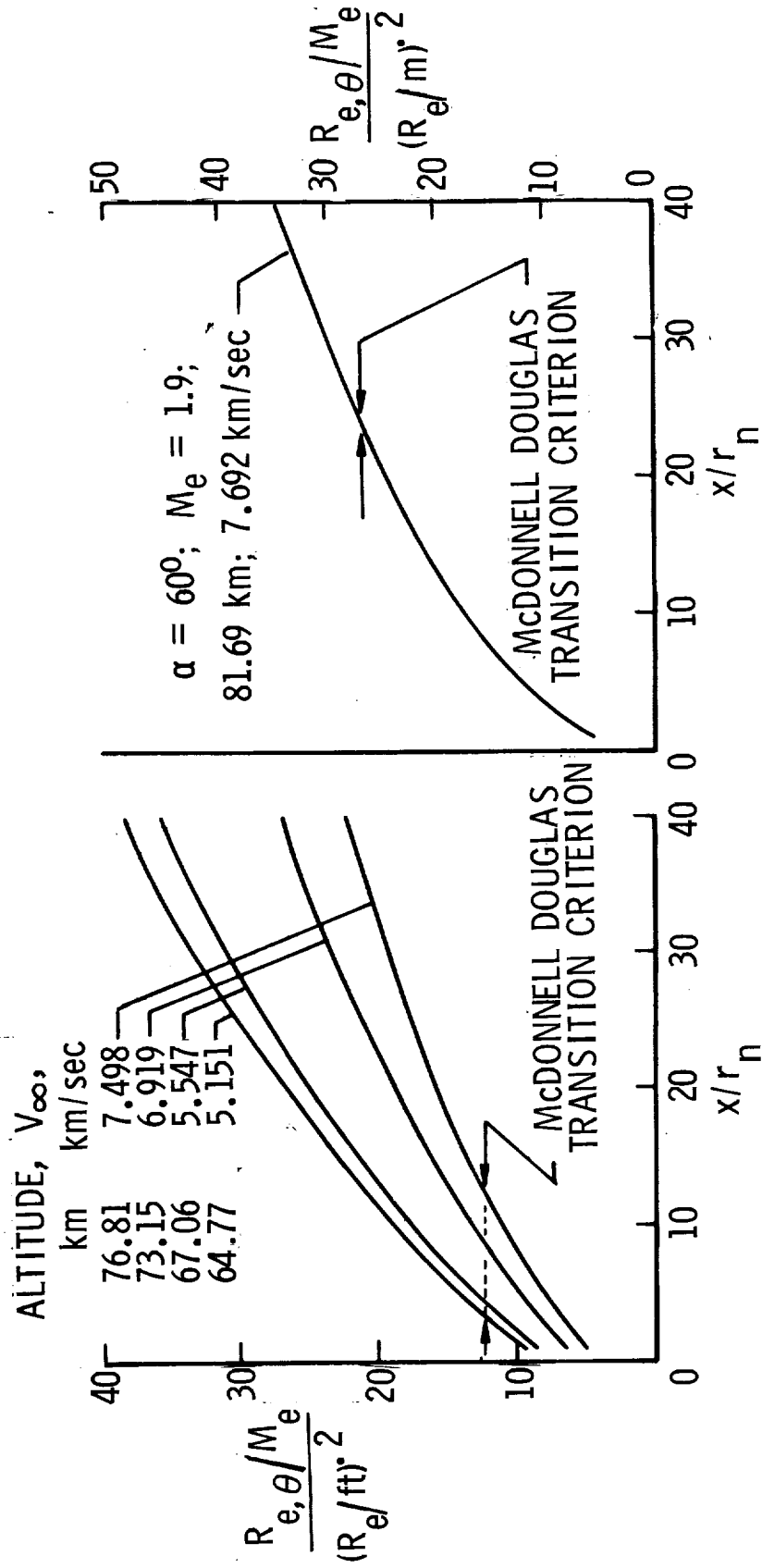


Figure 10

APPLICATION OF TRANSITION CRITERION TO FLIGHT CALCULATIONS

(Figure 11)

The variation of the North American Rockwell boundary-layer transition parameter, calculated with variable entropy and real gas and with normal-shock entropy and real gas, for the same points as in figure 10 along a hypothetical space shuttle trajectory at 40° and 60° angles of attack is shown in figure 11. The calculation assumptions and the configuration geometry were the same as those used for the McDonnell Douglas transition parameter. A comparison of $Re_{e,x}$ calculated by using the two entropies indicates that the level of $Re_{e,x}$ obtained with variable entropy is about a factor of 5 higher than that obtained with normal-shock entropy. When the North American Rockwell transition criterion is applied to $Re_{e,x}$ calculated with variable entropy, transition first occurs at about 30 nose radii from the stagnation point at an altitude of 76.81 km. At an altitude of 64.77 km, transition moves forward to approximately 7 nose radii. For $Re_{e,x}$ at $\alpha = 40^\circ$ calculated with normal-shock entropy, transition first occurs at an altitude of 67.06 km at about 25 nose radii from the stagnation point. At $\alpha = 60^\circ$ and an altitude of 81.69 km, the North American Rockwell transition criterion indicates no transition for either method of determining boundary-layer edge conditions. Thus, the boundary-layer edge conditions calculated with variable entropy give a more conservative prediction of the onset of transition than the edge conditions calculated with normal-shock entropy. Hefner's lower bound criterion (ref. 1) indicates onset of transition close to the vehicle nose.

APPLICATION OF TRANSITION CRITERION TO FLIGHT CALCULATIONS REAL-GAS SPACE SHUTTLE TRAJECTORY

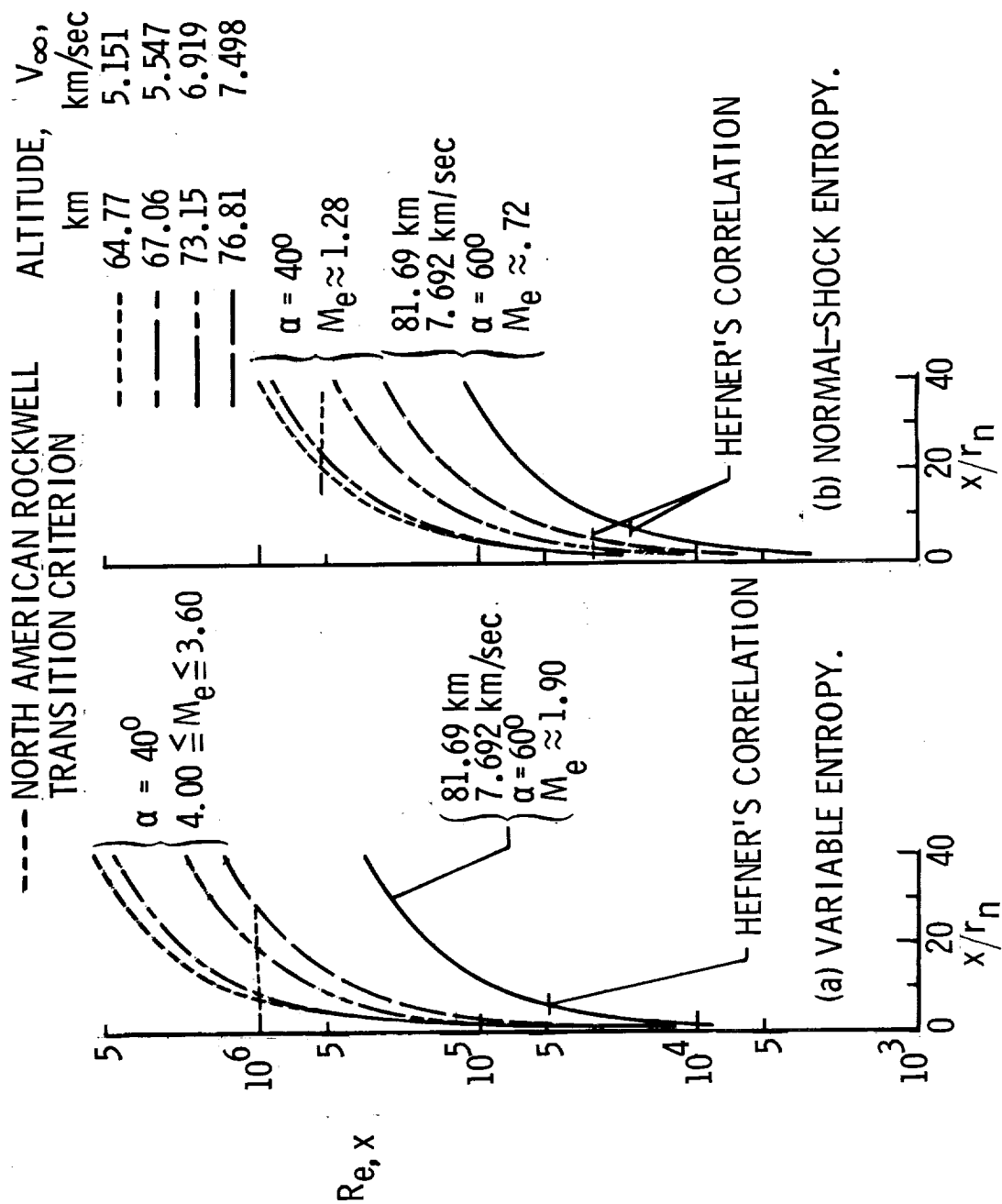


Figure 11

APPLICATION OF TRANSITION CRITERION TO FLIGHT CALCULATIONS

(Figure 12)

The variation of the Beckwith-Stainback boundary-layer transition parameter, calculated with variable entropy and real-gas, for the same point as in figures 10 and 11 along a hypothetical space shuttle trajectory at 40° and 60° angles of attack is shown in figure 12. The calculation assumptions and the configuration geometry were the same as those used for the MDAC and NAR transition parameters. When the blunt-body extension transition criterion is applied to the flight calculation, transition occurs between 4 and 6 nose radii from the stagnation point for all altitudes.

As pointed out by Masek and Forney (paper no. 4 of volume I), the present transition criteria treat the unit Reynolds number differently. As a result, the skin temperature of the shuttle can be appreciably affected. The sensitivity of the three transition correlation parameters to a unit Reynolds number effect can be seen by examining the values of the transition parameters for the high and low altitudes and 40° angle of attack in figures 10, 11, and 12. At the end of the body, the variations of the transition parameters for the Beckwith and Stainback and McDonnell Douglas correlations are 23 and 73 percent, respectively, whereas the variation of the transition parameter for the North American Rockwell correlation is 300 percent.

APPLICATION OF TRANSITION CRITERION TO FLIGHT CALCULATIONS

REAL-GAS SPACE SHUTTLE TRAJECTORY
(VARIABLE ENTROPY)

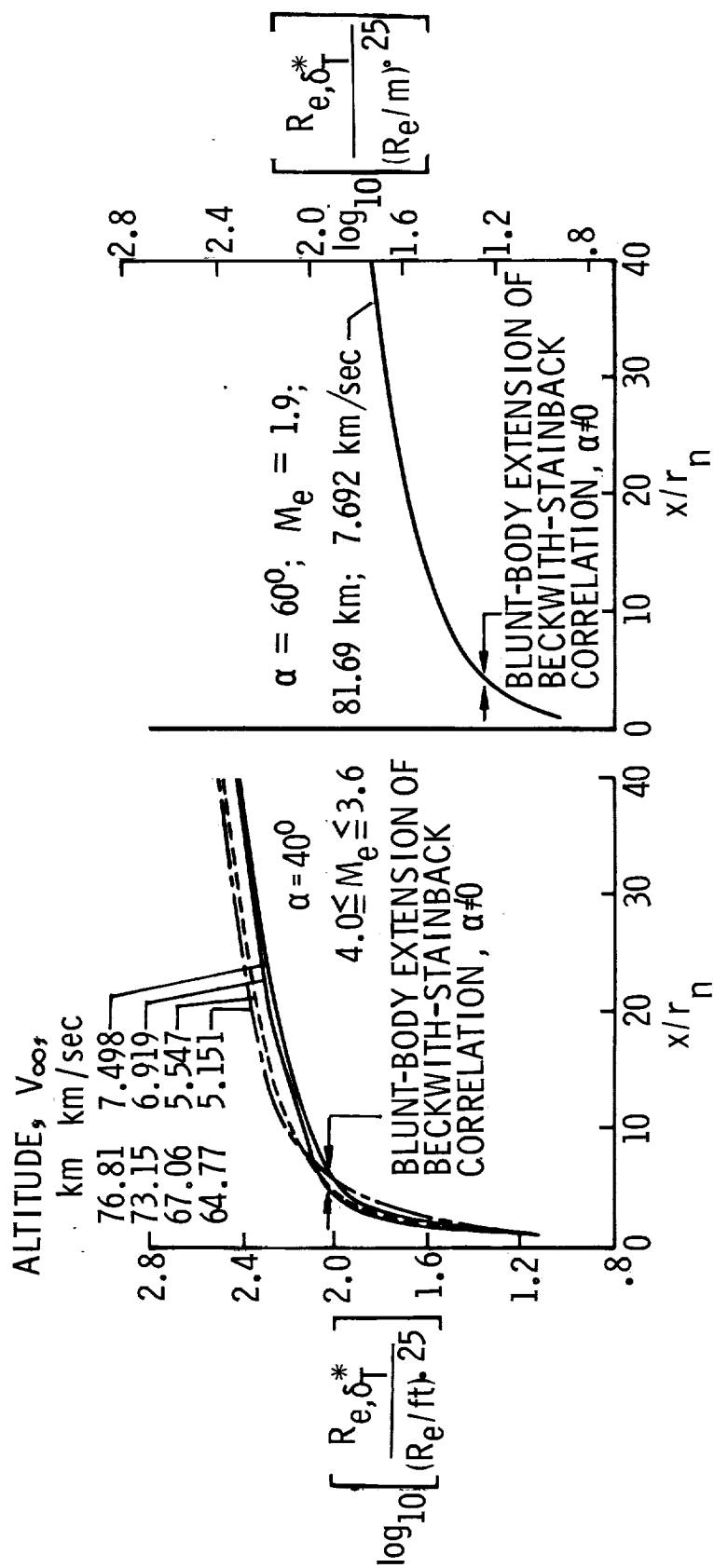


Figure 12

CONCLUDING REMARKS

It appears from calculations of boundary-layer edge conditions using variable entropy and from a flow-field survey that oblique-shock entropy should be used for shuttle configurations, both for flight and wind-tunnel applications.

It is recognized that as new boundary-layer transition data applicable to shuttle technology become available and that as the method of determining edge conditions is fixed, the transition criteria presented in this paper will possibly change. However, on the basis of transition criteria and methodology of December 1970, it appears that the McDonnell Douglas and North American Rockwell criteria are both optimistic when compared with the new data.

The three transition parameters for a hypothetical real-gas shuttle trajectory show a large variation with a change in altitude due to the unit Reynolds number effects. Furthermore, when transition criteria established from the same three transition parameters are applied to a hypothetical shuttle trajectory calculated for the same vehicle and using the same assumptions for determining the boundary-layer edge conditions, the departure of the criteria from the data is reflected in the distance to the onset of transition. For instance, at an altitude of 77 km and 40° angle of attack, the McDonnell Douglas criterion gives a distance to the onset of transition that is less than one-half the distance found for the North American Rockwell criterion, and the Beckwith-Stainback correlation gives a distance to the onset of transition that is approximately one-fourth the North American Rockwell distance.

APPENDIX A

PRELIMINARY ANGLE-OF-ATTACK CONE FLIGHT TRANSITION DATA

Some preliminary boundary-layer transition data from a cone angle-of-attack flight are presented in table I. The cone had an 8° half-angle and a 2.54-mm nose radius. Data from the acoustic sensors both on and off the windward meridian are included in the table. Data presented herein from the electrostatic sensors are evaluated only when the sensor is on the windward meridian. Future data from the electrostatic sensors will include data off the windward meridian. The reason some electrostatic-sensor data are missing from a given ray is that, at the instant the sensor is on the windward meridian, the sensor gives no reading because either (1) the reading was outside the range of the amplifier or (2) the sensor was in the process of a calibration sweep.

The Systems Group of TRW Inc. under NASA Contract NAS 1-10078 has completed the analysis of the acoustic and electrostatic sensors and has obtained transition data.

TABLE I.- PRELIMINARY ANGLE-OF-ATTACK CONE FLIGHT TRANSITION DATA

x, m	ψ , deg	Azimuth angle, deg	Boundary layer (a)	M_∞	α_t' , deg	M_e	$R_{e,x}$	$R_{e,\theta}$	α_{LOCAL}' , deg
Acoustic sensors									
2.2354	0	101	T	20.83	22.78	3.67	4.0900 x 10 ⁵	171.9	30.78
	0	101	T	21.28	15.35	4.999	1.5050 x 10 ⁶	366.0	23.35
	0	101	TR	21.42	3.29	9.829	6.5900 x 10 ⁶	935.0	11.29
	0	101	TR	21.52	6.13	8.146	6.3300 x 10 ⁶	869.3	14.13
	0	101	L	21.08	4.03	9.291	3.4900 x 10 ⁶	668.9	12.03
	-13.0	101	T	20.82	20.7	4.07	4.7200 x 10 ⁵	190.0	28.2
	117.9	101	T	21.47	12.3	18.8	1.1200 x 10 ⁷	1920.0	2.2
	-35.5	101	T	21.5	13.9	6.11	3.6600 x 10 ⁶	618.0	19.3
4.2166	0	110	T	21.29	15.97	4.864	2.7700 x 10 ⁶	492.1	23.97
	0	110	TR	20.83	22.76	3.674	7.8000 x 10 ⁵	236.4	30.76
	0	110	TR	21.09	3.84	9.427	5.9400 x 10 ⁶	875.0	11.84
	62.7	110	T	20.78	19.25	7.04	1.6000 x 10 ⁶	450.0	16.83
	-27.25	110	T	20.81	19.49	4.61	1.0900 x 10 ⁶	305.0	25.32
	43.7	290	T	20.98	16.84	5.86	2.2700 x 10 ⁶	485.0	20.17
	58.6	290	T	21.01	19.72	6.52	2.8200 x 10 ⁶	577.0	18.28
	-34.6	290	T	21.17	17.18	5.33	2.6200 x 10 ⁶	500.0	22.13
	-43.9	290	T	21.16	18.43	5.59	2.8000 x 10 ⁶	532.0	21.29
Electrostatic sensors									
0.8315	0	0	L	20.40	11.63	5.92	0.2095 x 10 ⁶	148	19.63
1.2064	0	0	L	20.40	11.63	5.93	.3070 x 10 ⁶	178	19.63
2.2354	0	0	L	20.40	11.63	5.93	.5747 x 10 ⁶	244	19.63
2.2354	0	0	L	20.57	27.0	3.13	1.0910 x 10 ⁵	84.8	35.0
0.8315	0	0	L	21.76	3.9	9.42	2.6970 x 10 ⁶	601	11.9
1.2064	0	0	L	21.76	3.9	9.44	3.9530 x 10 ⁶	724	11.9
2.2354	0	0	L	21.76	3.9	9.45	7.4000 x 10 ⁶	991	11.9
0.8315	0	0	L	22.00	2.9	10.15	4.1610 x 10 ⁶	763	10.9
1.2064	0	0	L	22.00	2.9	10.16	6.0990 x 10 ⁶	919	10.9
2.2354	0	0	T	22.00	2.9	10.18	11.4200 x 10 ⁶	1247	10.9
0.8315	0	0	L	22.20	9.63	6.66	2.6630 x 10 ⁶	541	17.63
1.2064	0	0	T	22.20	9.63	6.66	3.9020 x 10 ⁶	656	17.63
0.8315	0	180	L	23.70	13.81	5.31	1.3290 x 10 ⁴	35.6	21.81
3.5308	0	180	L	23.70	13.81	5.36	5.8870 x 10 ⁴	74.9	21.81
4.2166	0	180	L	23.70	13.81	5.37	7.0450 x 10 ⁴	81.8	21.81

^aBoundary-layer type:
L laminar
T turbulent
TR transition

TABLE I.- PRELIMINARY ANGLE-OF-ATTACK CONE FLIGHT TRANSITION DATA - Concluded

x, m	ψ , deg	Azimuth angle, deg	Boundary layer (a)	M_∞	α_c , deg	M_e	$R_{e,x}$	$R_{e,\theta}$	α_{LOCAL} , deg
Electrostatic sensors									
0.8315	0	180	L	22.6	6.82	7.66	1.3220×10^5	127	14.82
1.7020	0	180	L	22.6	6.82	7.70	2.7760×10^5	182.0	14.82
3.5308	0	180	L	22.6	6.82	7.73	5.8460×10^5	263	14.82
4.2166	0	180	L	22.6	6.82	7.74	6.9970×10^5	288	14.82
0.8315	0	180	L	22.61	6.78	7.68	2.2110×10^5	162	14.78
1.7020	0	180	L	22.61	6.78	7.73	9.7440×10^5	338	14.78
3.5308	0	180	L	22.61	6.78	7.74	11.6650×10^5	372	14.78
4.2166	0	180	L	22.64	6.05	8.10	8.9140×10^5	333	14.05
0.8315	0	180	L	22.64	6.05	8.13	1.8630×10^6	478	14.05
1.7020	0	180	L	22.64	6.05	8.14	3.9074×10^6	685	14.05
3.5308	0	180	L	22.64	6.05	8.15	4.6740×10^6	753	14.05
4.2166	0	180	L	22.64	4.16	9.22	1.6980×10^6	475	12.16
0.8315	0	180	L	22.64	4.16	9.24	3.5480×10^6	683	12.16
1.7020	0	180	L	22.64	4.16	9.26	7.4440×10^6	983	12.16
3.5308	0	180	L	22.64	4.16	9.26	8.9080×10^6	1073	12.16
4.2166	0	180	L	21.65	8.98	6.87	1.3550×10^6	390	16.98
0.8315	0	180	L	22.62	2.57	10.38	3.6410×10^6	714	10.57
1.7020	0	180	L	22.62	2.57	10.40	7.6080×10^6	1027	10.57
3.5308	0	180	T	22.62	2.57	10.42	15.9530×10^6	1481	10.57
4.2166	0	180	T	22.62	2.57	10.43	19.0890×10^6	1617	10.57
0.8315	0	180	L	22.10	5.25	8.64	3.7050×10^6	689	13.25
1.7020	0	180	T	22.10	5.25	8.66	7.7290×10^6	990	13.25
3.5308	0	180	T	22.10	5.25	8.67	16.1940×10^6	1423	13.25
4.2166	0	180	T	22.10	5.25	8.67	19.3700×10^6	1570	13.25
4.2166	0	150	L	20.41	12.88	5.59	1.0460×10^6	319	20.88
	0	150	L	20.90	4.08	9.26	5.7050×10^6	859	12.08
	0	150	T	21.43	7.99	7.28	5.8690×10^6	819	15.99
	0	150	T	21.88	2.74	10.30	18.7650×10^6	1595	10.74

^aBoundary-layer type:
L laminar
T turbulent
TR transition

APPENDIX B

MEASURED BOUNDARY-LAYER EDGE PROPERTIES ON STRAIGHT-WING

AND DELTA-WING CONFIGURATIONS

By George C. Ashby, Jr.
NASA Langley Research Center
Hampton, Virginia

Pitot pressure surveys and surface pressure measurements have been obtained at four stations along the center line of the North American Rockwell straight-wing orbiter (130B) at Mach 20.3 in helium and angles of attack from 20° to 58° . Similar measurements were made on a Martin Marietta delta-wing orbiter at Mach 6.8 in air and an angle of attack of 20° .

APPENDIX B - Continued
BOUNDARY-LAYER EDGE MACH NUMBER STUDY

(Figure 13)

Figure 13 shows a model, its shock system, the single-tube traverse probe, the survey stations, and the orifice locations. A calculated boundary-layer thickness was used as a guide in locating the boundary-layer edge. The calculated boundary-layer edge was in good agreement with the apparent boundary-layer edge obtained from the profiles.

BOUNDARY-LAYER EDGE MACH NUMBER STUDY

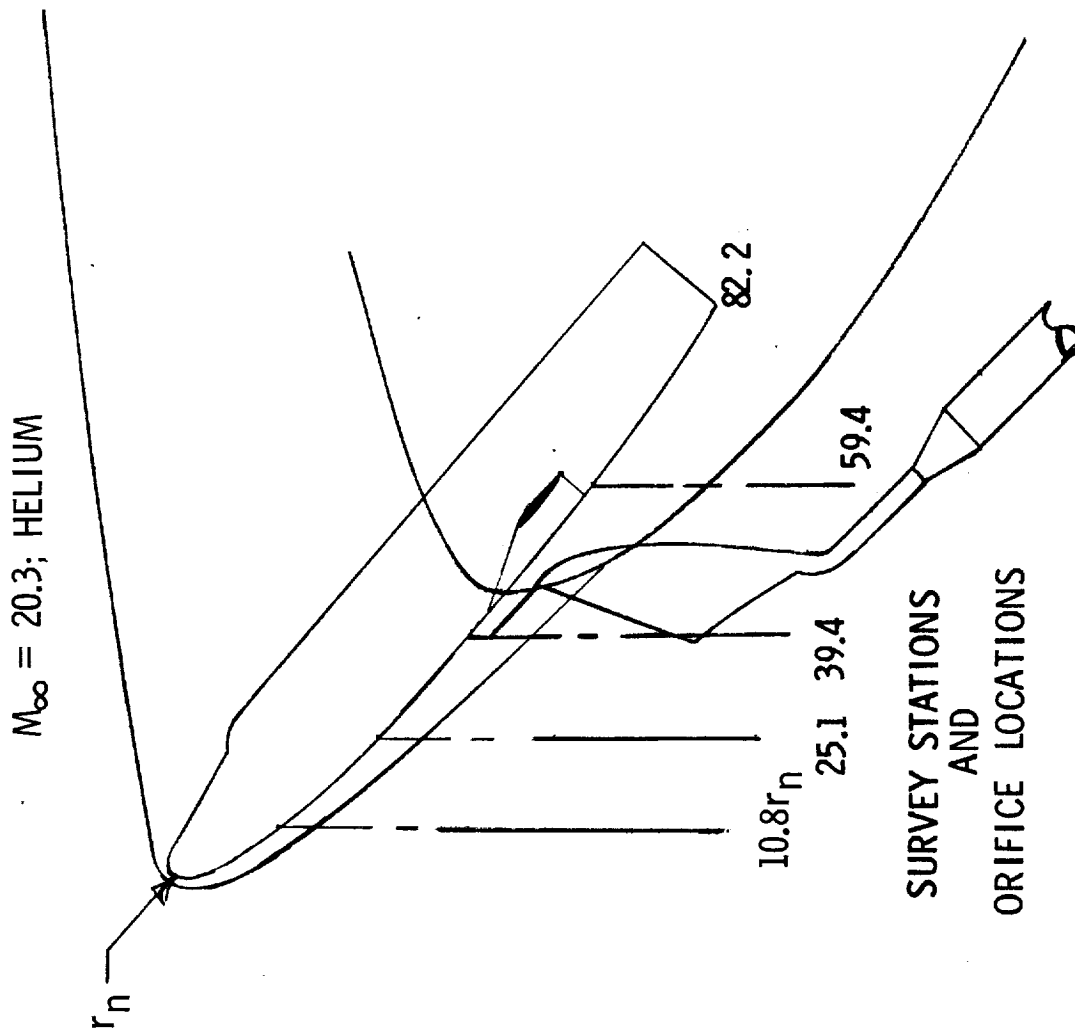


Figure 13

APPENDIX B - Continued

BOUNDARY-LAYER EDGE MACH NUMBER

North American Rockwell Straight-Wing Orbiter

(Figure 14)

The boundary-layer edge Mach numbers determined from the measured pressures are compared with those estimated by various methods in figure 14. The data show that for orifice locations rearward of the most forward survey station (approximately 11 nose radii), the Mach number at the edge of the boundary layer agrees closely with the tangent-cone estimate up to shock detachment. Beyond shock detachment, the boundary-layer edge Mach number on the forward portion of the configuration agrees with the estimate assuming Newtonian surface pressure and normal-shock entropy. As the flow moves rearward on the body, the high entropy is progressively absorbed in the boundary layer and the Mach number approaches oblique-shock values. A lower bound of oblique-shock entropy obtained by assuming that the shock is parallel to the body surface is shown for comparison.

BOUNDARY-LAYER EDGE MACH NUMBER NORTH AMERICAN ROCKWELL STRAIGHT-WING ORBITER

$M_{\infty} = 20.3$; HELIUM

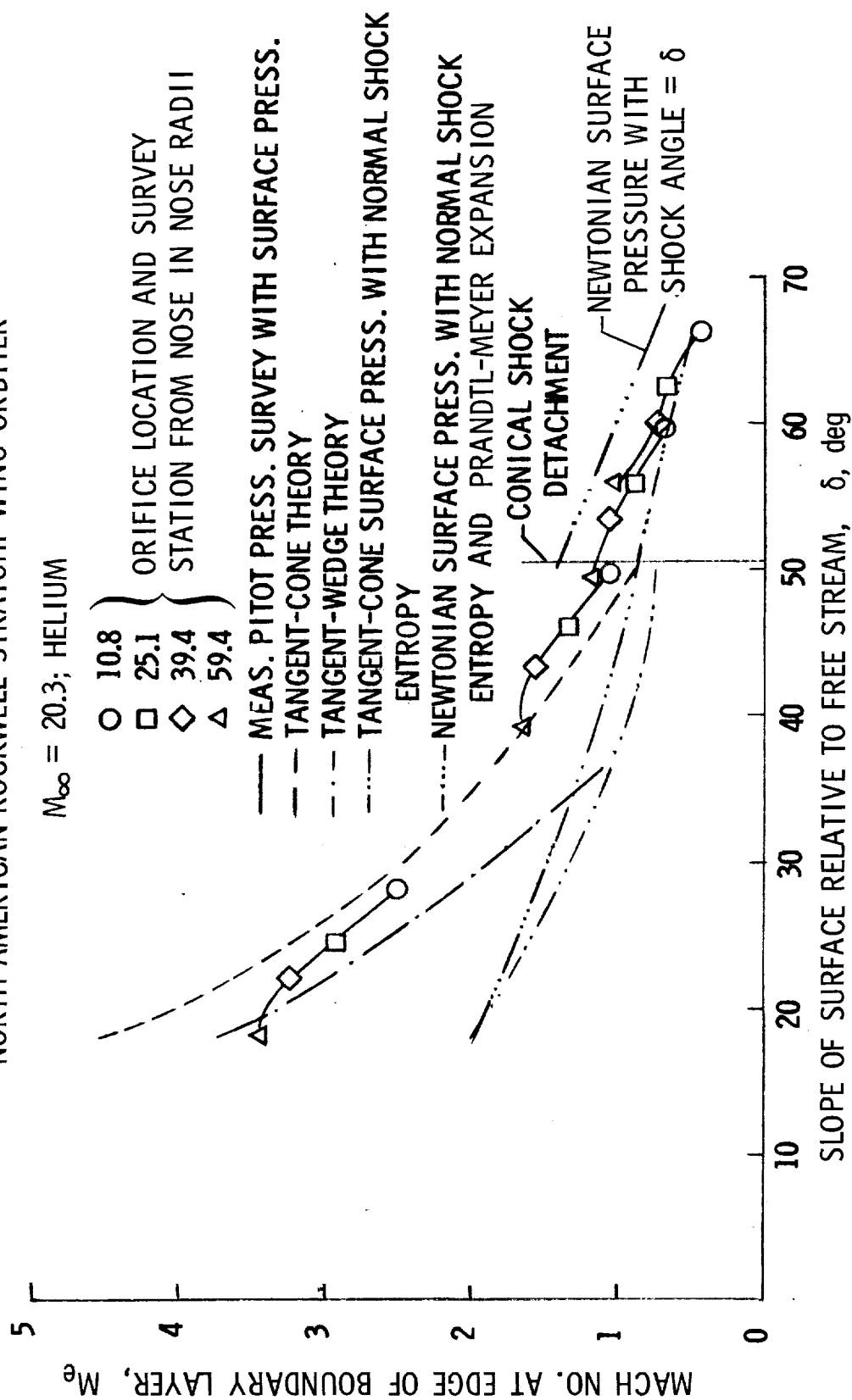


Figure 14

APPENDIX B - Concluded
BOUNDARY-LAYER EDGE MACH NUMBER
Martin Marietta Delta-Wing Orbiter

(Figure 15)

The data for the delta-wing orbiter at Mach 6.8 in air was obtained at only 20° angle of attack. However, as shown in figure 15, the Mach number at the edge of the boundary layer also agrees with the tangent-cone estimate.

BOUNDARY-LAYER EDGE MACH NUMBER MARTIN MARIETTA DELTA-WING ORBITER

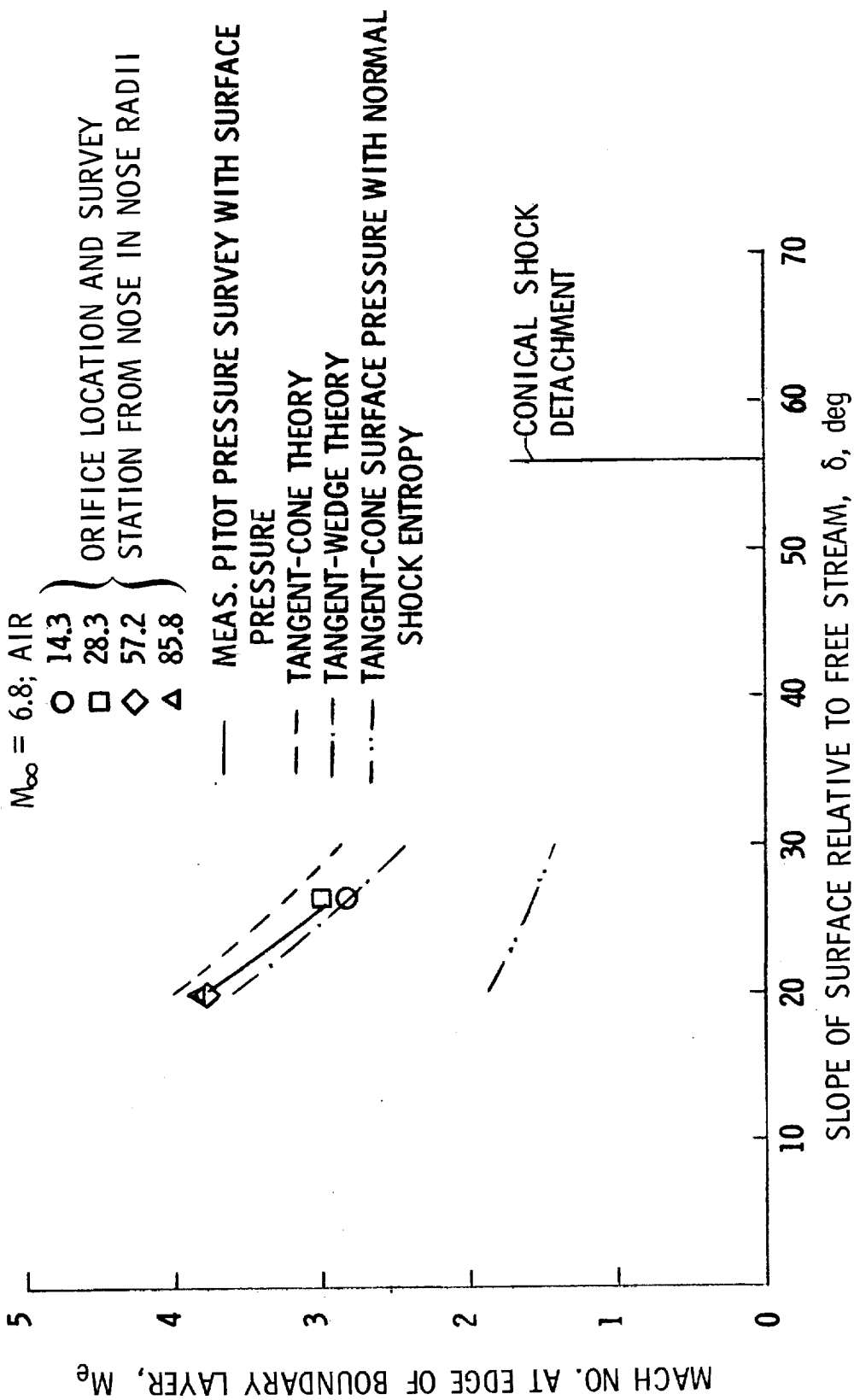


Figure 15

REFERENCES

1. Hefner, Jerry N.: Boundary-Layer Transition for Space-Shuttle-Type Configurations at Angles of Attack. NASA TM X-2254, 1971.
2. Bertram, Mitchel H.; and Beckwith, Ivan E.: NASA-Langley Boundary Layer Transition Investigations. Boundary Layer Transition Study Group Meeting, William D. McCauley, ed., BSD-TR-67-213, Vol III, U.S. Air Force, Aug. 1967, pp. 18-i - 18-73. (Available from DDC as AD 384 006.)

A NUMERICAL PROCEDURE TO CALCULATE THE
INVISCID FLOW FIELD ABOUT A
SPACE SHUTTLE ORBITER TRAVELING AT A
SUPERSONIC/HYPERSONIC VELOCITY

By B. Grossman, F. Marconi, Jr., and G. Moretti

Grumman Aerospace Corporation, Bethpage, New York

A NUMERICAL PROCEDURE TO CALCULATE THE INVISCID FLOW FIELD
ABOUT A SPACE SHUTTLE ORBITER TRAVELING AT
A SUPERSONIC/HYPERSONIC VELOCITY

By B. Grossman, F. Marconi, Jr., and G. Moretti*
Grumman Aerospace Corporation, Bethpage, New York

SUMMARY

We have developed a technique for computing the complete inviscid, three-dimensional flow field about a vehicle flying at supersonic speed at an angle of attack. The flow field in the vicinity of the stagnation point at the nose of the body is determined using a three-dimensional, time-dependent blunt body program. The asymptotic steady-state values of this flow field are then used as starting conditions for a supersonic, steady-state numerical calculation. This computation utilizes a three-dimensional, finite-difference "marching" technique which determined the flow field downstream of the nose of the vehicle where the flow is supersonic. Within the physical model of an inviscid, perfect gas, the complete coupled calculation provides an approximation which uniformly converges to the exact solution and does not rely on artificial damping or on any other arbitrary numerical feature. The bow shock wave is computed as a discontinuity obeying the Rankine-Hugoniot relations. Special provisions are made for computing the flow field in the entropy layer. The accuracy of the technique is confirmed by comparison of the results of the numerical calculation to available test data on several simple three-dimensional geometries such as sharp elliptic cones, and blunted cones at angle of attack.

We have found the agreement with experimental results to be excellent. Applications of the program are made for a typical shuttle orbiter delta lifting body configuration at angle of attack. The numerical flow field results yield important design information such as the pressure distribution on the vehicle surface, effectiveness of control surfaces and the determination of boundary-layer edge properties.

*Professor, Polytechnic Institute of Brooklyn, Farmingdale, N.Y.;
Grumman Aerospace Consultant.

INTRODUCTION

It is well known that the design of a thermal protection system on a shuttle orbiter requires a detailed knowledge of the pressure and heat transfer distribution on the vehicle surface throughout its entire range of flight. Presently, this information is obtained from experimental data. Unfortunately, these experiments are extremely costly, time consuming and cannot be run over the full range of Reynolds number, Mach number and stagnation enthalpy.

On the other hand, an efficient, accurate numerical evaluation of the flow field is far from being available. Aside from the problems related to viscous and real gas effects, difficulties arise because of the size of the vehicle and its complicated geometry. Such difficulties are better analyzed by assuming a simplified model of the gas, that is, perfect and inviscid. We believe that a computational program which determines the inviscid flow around a shuttle orbiter is urgently needed as the first step towards a more sophisticated computation which will describe the viscous flow behavior. In addition, the results of the inviscid computation can be used as a background for a preliminary study of viscous effects using the classical boundary layer approach.

We have, thus, decided to provide a computational technique for inviscid flow to satisfy the following requirements:

- (i) the accuracy is controlled and can be estimated a priori, in order to provide the designer with reliable data;
- (ii) the computer running time is reduced to a minimum, and in any event, within the

order of minutes, so that runs are inexpensive and many runs can be made

in the design phase of a project;

- (iii) realistic geometries can be computed with a minimal of input to the program and without changing the basic computational routines.

APPROACH TO THE INVISCID PROBLEM

(Figure 1)

Shown in the figure is a sketch of a typical shuttle orbiter configuration at a moderate angle of attack with its enveloping bow shock wave. The flow field in the vicinity of the nose (Region I) is characterized by a Mach number which varies from subsonic to supersonic. Because the mathematical nature of the governing inviscid equations is mixed (elliptic/hyperbolic), the most effective method of solution consists of solving the unsteady equations of motion and computing until a steady state is reached. This approach is well known and is termed the Time-Dependent Blunt Body solution.

In contrast the flow field downstream of the nose (Region II) is entirely supersonic. The solution of the equations here is more simply obtained from the steady flow equations provided the flow remains supersonic. We might note here that at higher angles of attack (on the order of 40° or more) the subsonic region on the windward face of the body will cover the entire bottom of the vehicle and the solution over the complete body must be computed as a time dependent blunt body problem. We will now discuss the techniques used in Regions I and II in greater detail.

BASIC APPROACH TO INVISCID PROBLEM

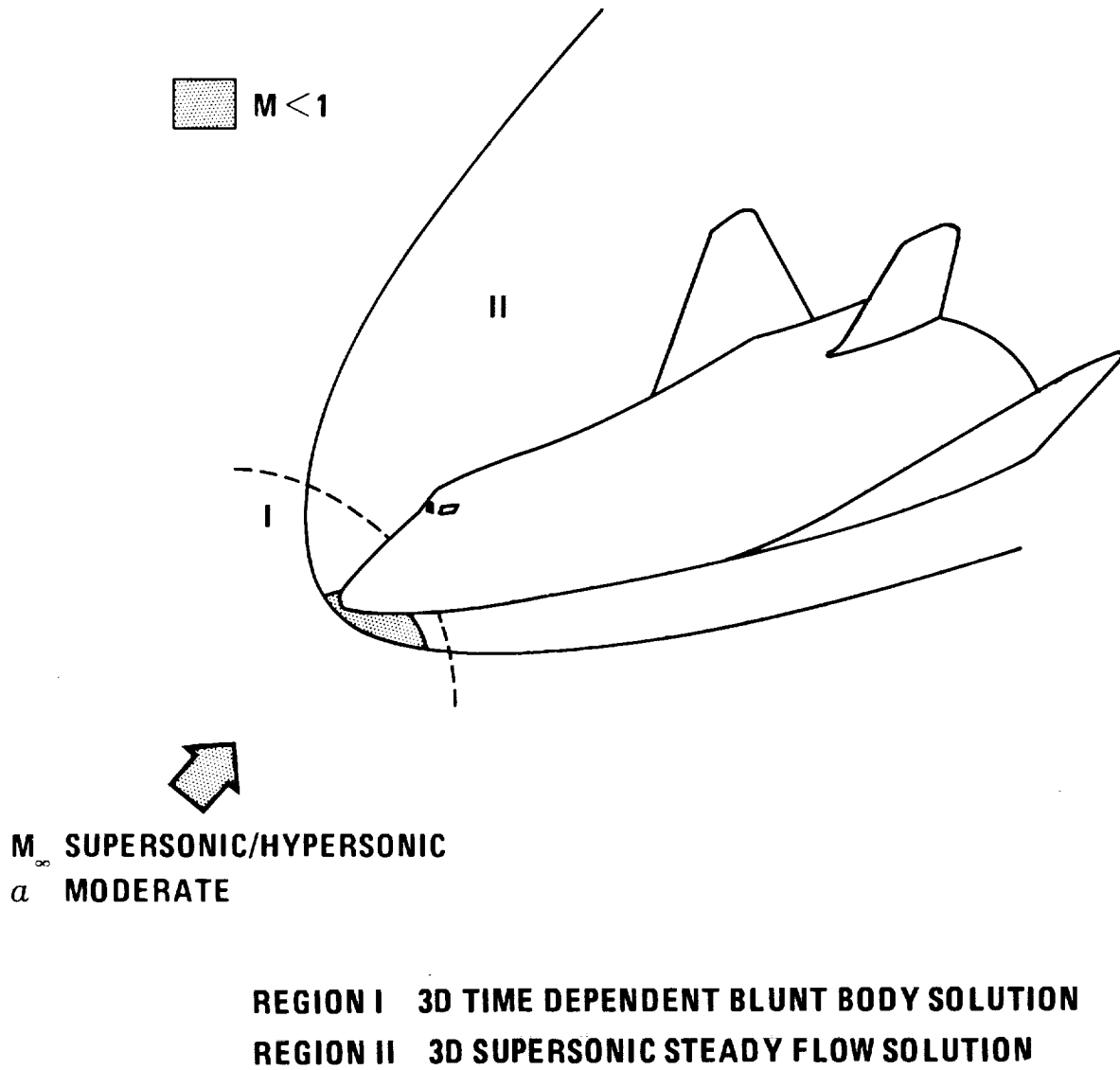


Figure 1

TIME-DEPENDENT BLUNT BODY PROBLEM

(Figure 2)

The basic philosophy of this computation follows the technique developed by Moretti in 1966 (ref. 1) for the two-dimensional or axisymmetric blunt body problem. This approach is characterized by its high levels of accuracy and efficiency. We have illustrated here a modification of this program which handles arbitrary three-dimensional nose shapes at angle of attack. The shock shape over a typical shuttle nose shape at $M = 10$ and $\alpha = 20^\circ$ is shown here for a plane of symmetry and a cross-sectional view. An important feature of this computation is the wind axis oriented spherical coordinate system which allows us to perform the calculation in the smallest possible region and which automatically adjusts this region for varying angles of attack. The bow shock wave is treated as a discontinuity which has been shown to be necessary for an accurate and efficient computation. For example, a steady state is reached for a typical three-dimensional calculation in approximately 600-800 time steps using 8 points in the radial direction (between the shock and the body), 9 points in the θ direction and 6 points in the ϕ direction. This computer run takes approximately 6-8 minutes on the CDC 6600.

TIME-DEPENDENT BLUNT BODY COMPUTATION

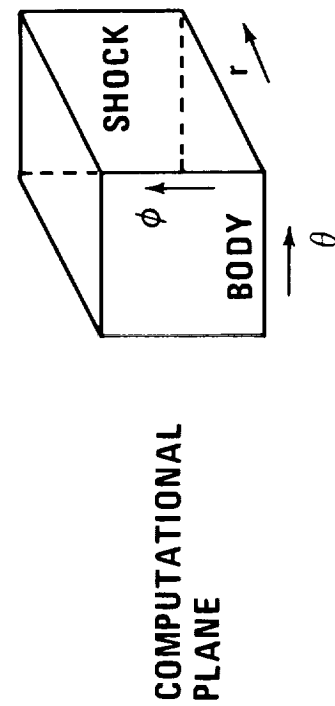
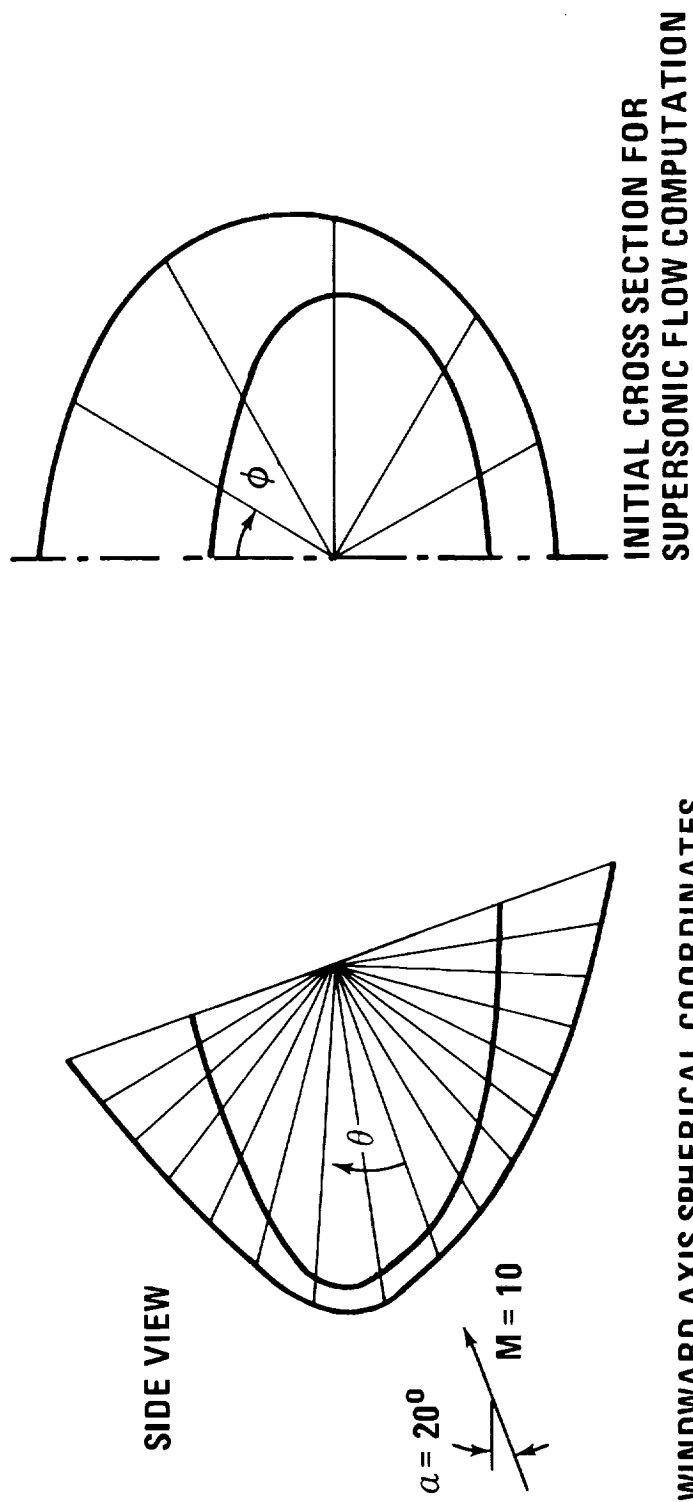


Figure 2

SUPERSONIC STEADY FLOW SOLUTION

(Figure 3)

We feel that the most effective way of performing the computation downstream of the nose of the vehicle where the flow is supersonic in the axial direction is to use a three-dimensional finite-difference "marching" technique. This method is characterized by its overall simplicity in coding and debugging. Accuracy is maintained by using a second-order non-dissipative finite-difference scheme and by treating all shock waves as discontinuities satisfying the Rankine-Hugoniot relations. This treatment of shock waves and the use of optimal mesh point locations between the bow shock and the body, which are coordinate surfaces, provide for a highly efficient calculation. We have developed techniques for easily handling complicated three-dimensional shuttle orbiter geometries. Definitely, our techniques are not restricted to simple body shapes. Also special considerations in the vicinity of the entropy layer allow us to perform the computation in this region accurately and with stability without resorting to any artificial damping method.

SUPERSONIC STEADY FLOW SOLUTION

FEATURES

- 3D FINITE-DIFFERENCE "MARCHING" TECHNIQUE
- SHOCK WAVES TREATED AS DISCONTINUITIES
- SHOCK AND BODY COORDINATE SURFACES
- ARBITRARY 3D GEOMETRY
- ENTROPY LAYER HANDLING

ADVANTAGES

- SIMPLICITY
- EFFICIENCY
- OPTIMAL MESH POINT LOCATION
- PROBLEMS OF INTEREST
- ACCURACY

Figure 3

GEOMETRIC CONSIDERATIONS

(Figure 4)

The type of realistic three-dimensional space shuttle geometries which our technique can handle is illustrated in the figure. The computational mesh automatically conforms to the specific geometry. A method has been developed to perform the task in a simple manner, analytically. The advantages are:

- 1) Guess work is eliminated;
- 2) Inaccurate interpolations are eliminated, since the mesh adjusts itself to the shape of the body as one proceeds stepwise along the body axis (therefore, the code remains the same in the computational plane but the coefficients in the equations change, without introducing additional truncation errors);
- 3) Mesh points are automatically concentrated in regions of steeper flow gradients (such as around the chines of the relatively flat bottomed vehicle and around wing tips and fins and therefore, the number of mesh points can be reduced to a minimum).

TYPICAL DELTA LIFTING BODY SHUTTLE ORBITER

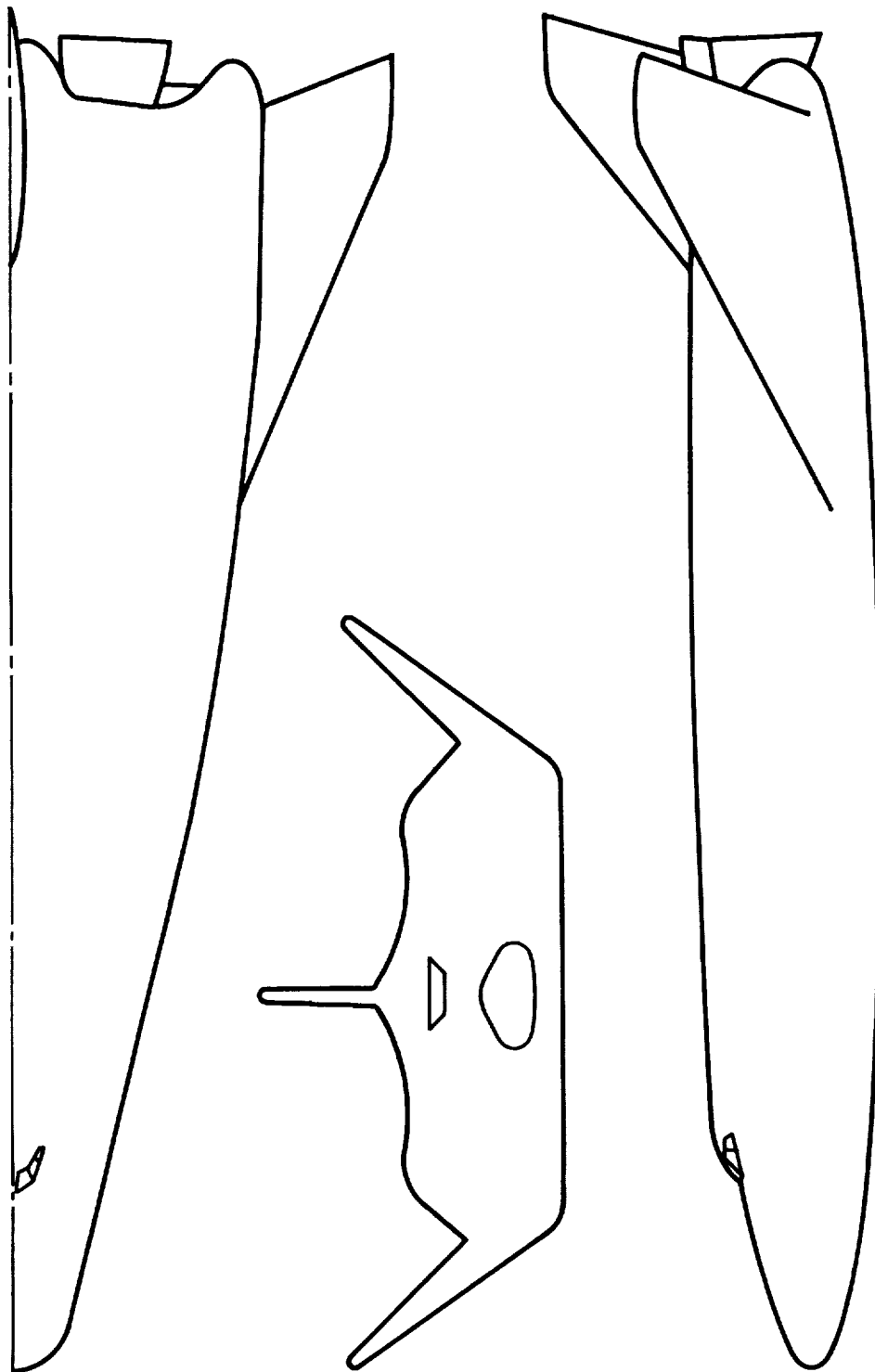


Figure 4

ELLIPTICAL CONES

(Figure 5)

As a first test case for our supersonic flow program we computed the flow field about several sharp nosed elliptical cones at zero angle of attack. The pressure coefficients on the surface of the cones is compared with the data of Jorgensen (ref. 2) and Chapkis (ref. 3), and the agreement is quite good. An interesting feature of this computation is the non-linear spacing of the mesh points concentrating them about the major axis of the elliptical cross section where the largest gradients in the flow field exist. Typical computer running times for these calculations are approximately 4 minutes using 25 points between the shock and the body and 20 points around the circumference of the body.

SURFACE PRESSURE DISTRIBUTION ON ELLIPTIC CONES

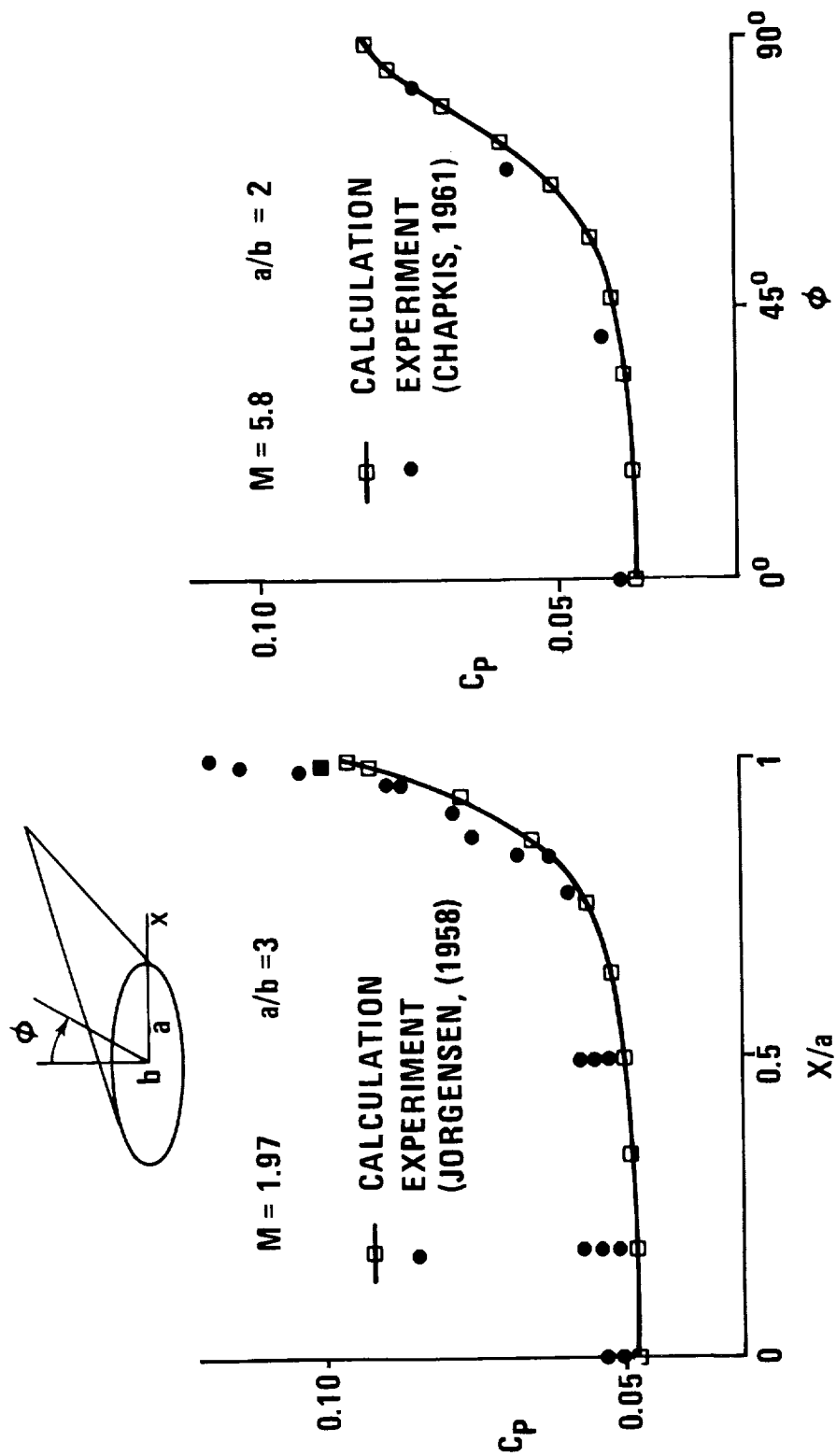


Figure 5

BLUNT CONE AT ZERO ANGLE OF ATTACK

(Figure 6)

Next, we tested the coupled blunt-body/supersonic flow program by computing the flow field about a blunt circular cone at zero angle of attack. The pressure coefficient on the body surface is plotted as a function of the axial distance along the centerline of the cone. These results are seen to compare excellently with the experimental data of Cleary (ref. 4). We also indicate a plot of the computed shock shape, sonic line and constant entropy lines. These constant entropy lines, which in this case are streamlines, clearly show the well-known entropy layer effect (a layer where the entropy varies very rapidly from the high normal shock value at the body surface to a very low oblique shock value in an extremely small radial distance away from the surface). This entropy layer requires special handling in order to avoid numerical instabilities and inaccuracies. Our approach to this problem is discussed next.

COMPUTED FLOW FIELD ON A BLUNT CONE AT $M = 10.6$

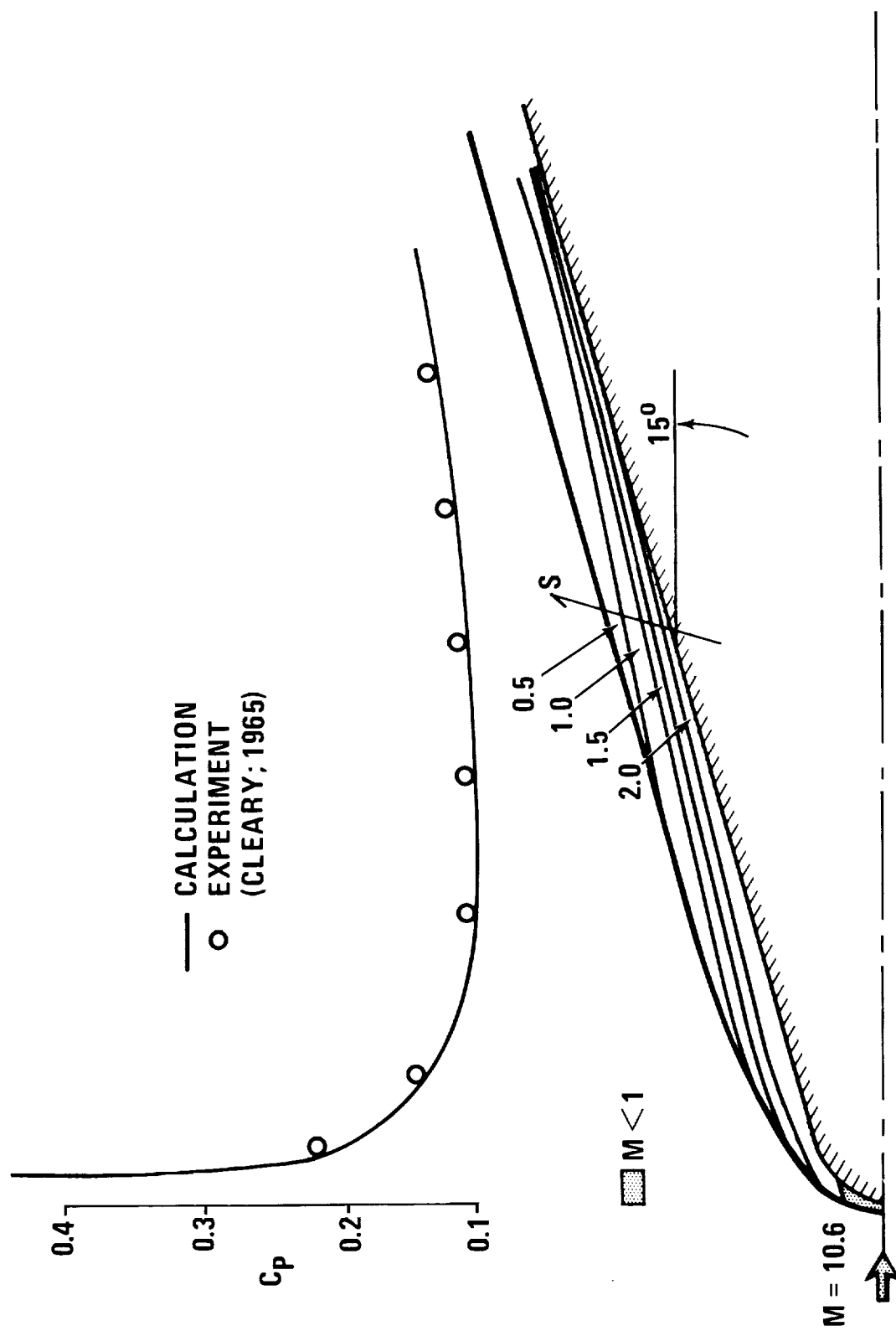


Figure 6

ENTROPY LAYER STUDY

(Figure 7)

Our approach to handling the entropy layer consists of using a radial stretching which concentrates mesh points in the region of steep entropy gradient. The stretching illustrated here automatically concentrates mesh points near the body surface and the degree of stretching is altered by varying a parameter which can be a function of the axial distance. The effect of this stretching is also illustrated here. The entropy distribution corresponding to the unstretched radial coordinate becomes unstable whereas the stretched coordinate solution yields a stable entropy distribution. The particular stretching used here concentrated about twice as many mesh points in the entropy layer than the unstretched case.

ENTROPY LAYER STUDY

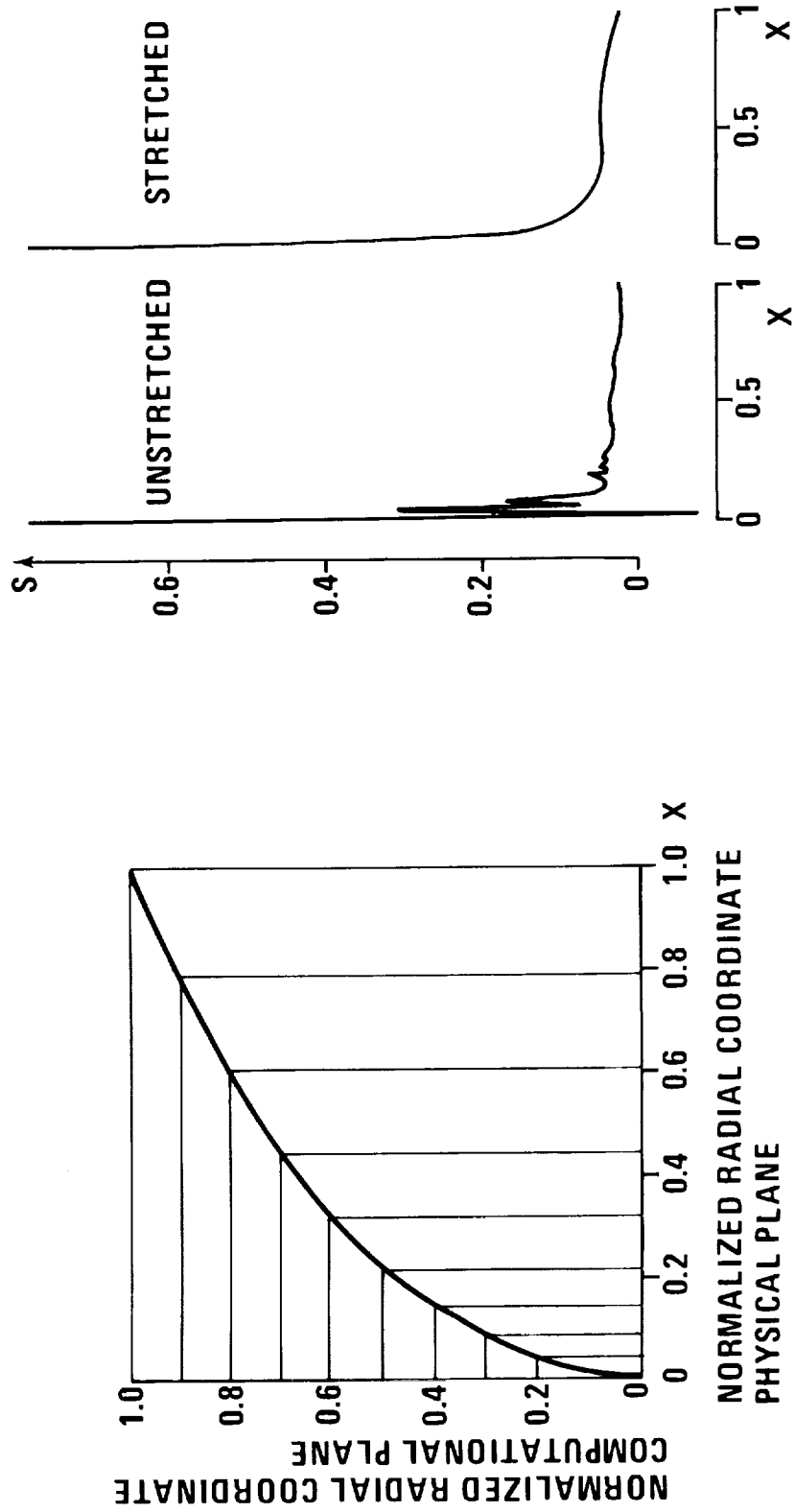


Figure 7

BLUNT CONE AT ANGLE OF ATTACK

(Figures 8 and 9)

Next we performed a computation on a blunt cone at angle of attack in order to test our three dimensional coupled blunt body/supersonic flow computation. The pressure distribution on a blunt 15° cone at $M = 10$ and $\alpha = 10^\circ$ is plotted as a function of the axial coordinate on both the windward and leeward surfaces. These results are compared to the experimental data of J.W. Cleary, 1965 and the agreement is seen to be excellent for both the solution in the blunt body region and the supersonic flow region downstream of the nose. We also indicate a plot of the computed shock shape, sonic lines and constant entropy lines on the windward face. The supersonic flow portion of this computation took about 7.5 min to calculate 20 nose radii downstream using 25 mesh points between the shock and the body and 20 mesh points around the circumference of the body (from $0-180^\circ$).

COMPUTED SURFACE PRESSURE DISTRIBUTION

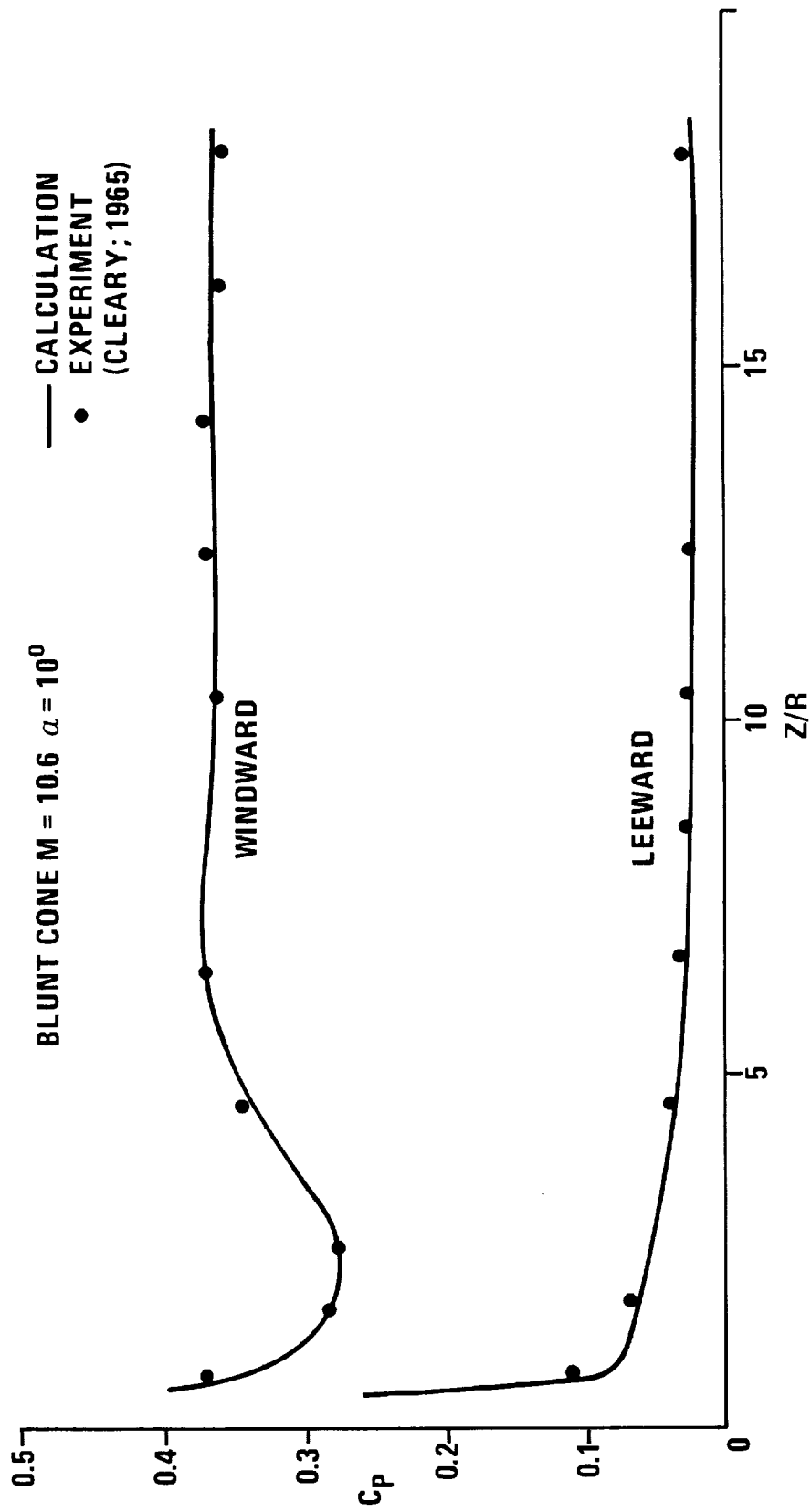
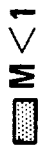


Figure 8



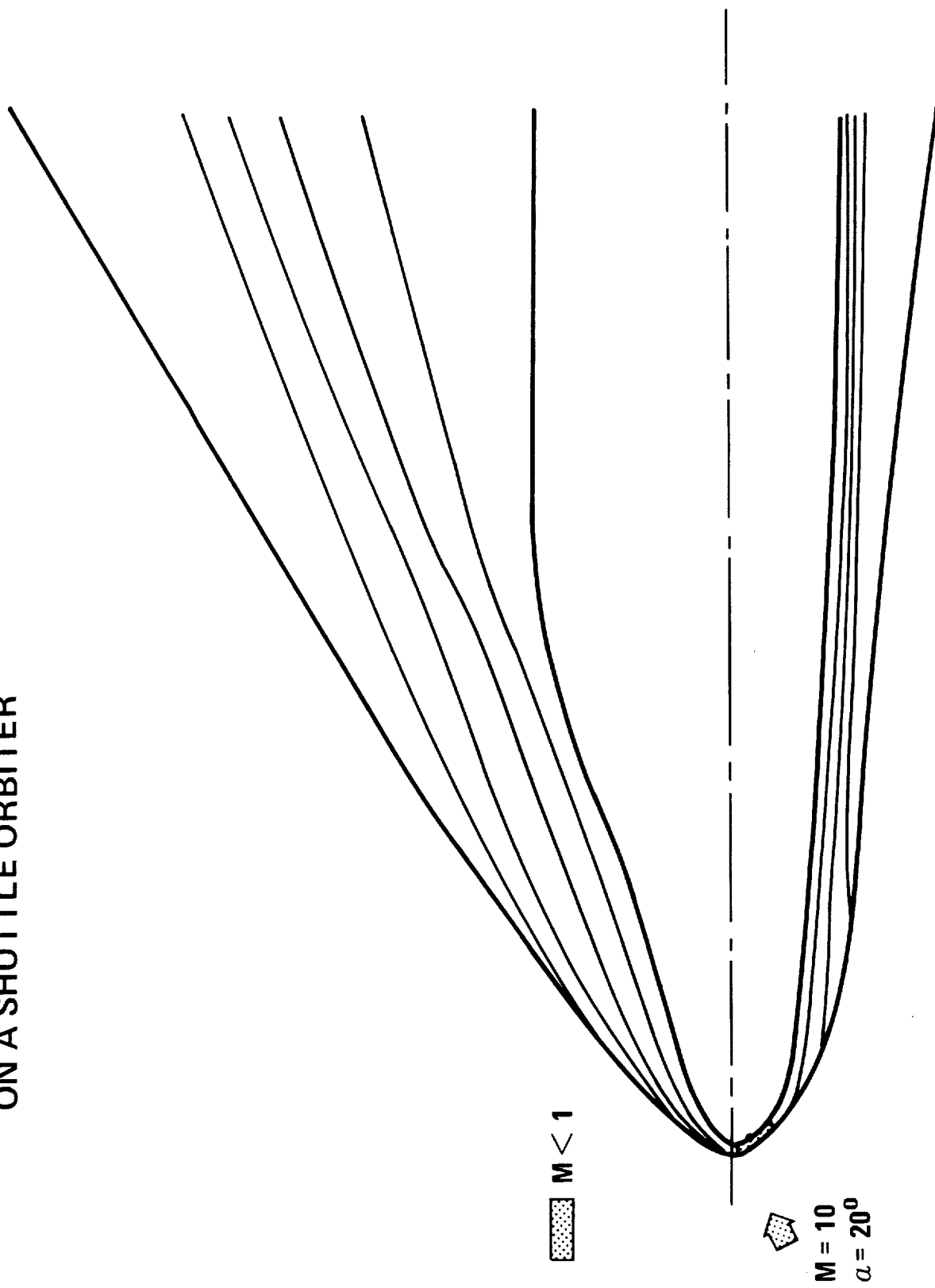
179

SHUTTLE ORBITER CALCULATION AT ANGLE OF ATTACK

(Figure 10)

Our next step in the development of this technique consisted of performing a computation about the fore portion of a typical space shuttle orbiter to indicate our capability of handling fully three-dimensional geometries. Illustrated here are the computed shock shape, sonic lines and constant entropy lines in the plane of symmetry of the vehicle at $M = 10$ and $\alpha = 20^\circ$. The geometry chosen has a relatively smooth shape to avoid problems with imbedded shock waves at this time. We have illustrated the lines of constant entropy since these would be necessary in order to determine the properties at the outer edge of the boundary layer. More information on this flow field is discussed in the next plot.

COMPUTED SHOCK SHAPE AND CONSTANT ENTROPY LINES ON A SHUTTLE ORBITER



PRESSURE DISTRIBUTION AROUND A SHUTTLE ORBITER

(Figure 11)

Here is a plot of the pressure distribution on several cross-sections of the vehicle surface. The value of the surface pressure is shown measured in a direction normal to the cross-section. We see the large high pressure region on the windward surface of the vehicle and the rapid expansion to the leeward surface. The compression on the leeward surface due to the canopy can also be noted. Downstream of the nose, the expansion on the leeward surface causes the cross flow to become supersonic and since the cross flow velocity must vanish at the plane of symmetry, an imbedded shock wave will form. We feel that in order to retain the accuracy and efficiency of this computation this imbedded shock wave must be treated as a discontinuity and not smeared over several mesh points using artificial viscosity. The techniques to handle imbedded shocks in this manner have been developed in conjunction with our work on time-dependent transonic flows and will be implemented into this program in the near future. Once this imbedded shock computation has been implemented, we can go on to a calculation of a shuttle vehicle with protruding wings and fins.

COMPUTED PRESSURE CROSS-SECTIONS ON A SHUTTLE ORBITER AT $M = 10$ AND $\alpha = 20^\circ$

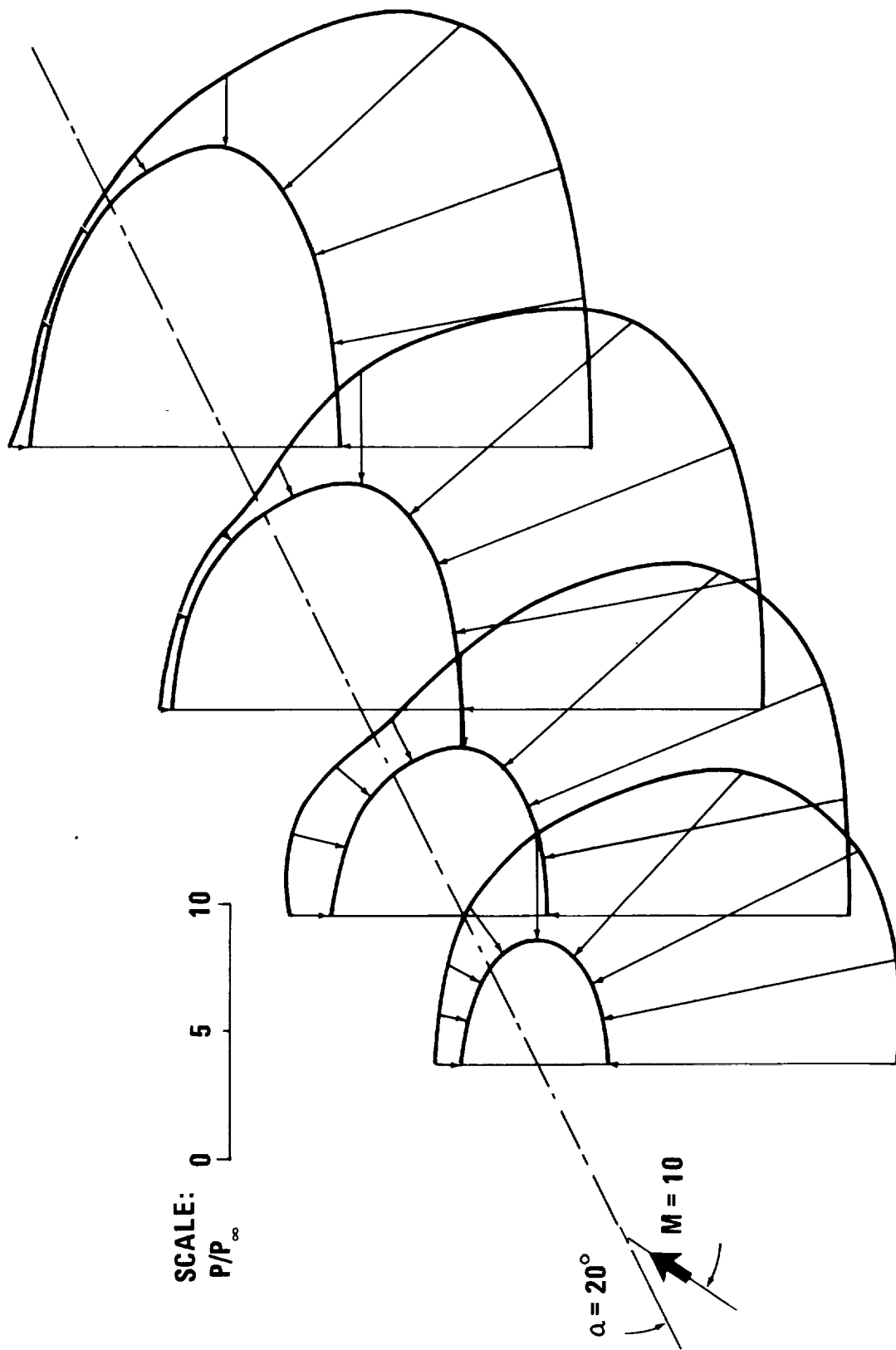


Figure 11

REFERENCES

1. Moretti, Gino; and Abbott, Michael: A Time-Dependent Computational Method for Blunt Body Flows.
AIAA J., vol. 4, no. 12, Dec. 1966, pp. 2136-2141.
2. Jorgensen, Ieland H.: Elliptic Cones Alone and With Wings at Supersonic Speeds. NACA Rept. 1376, 1958. (Supersedes NACA TN 4045.)
3. Chapkis, Robert L.: Hypersonic Flow Over an Elliptic Cone: Theory and Experiment. J. Aerosp. Sci., vol. 28, no. 11, Nov. 1961, pp. 844-854.
4. Cleary, Joseph W.: An Experimental and Theoretical Investigation of the Pressure Distribution and Flow Fields of Blunted Cones at Hypersonic Mach Numbers. NASA TN D-2969, 1965.

SHOCK INTERFERENCE HEATING AND DENSITY-RATIO EFFECTS

PART I - FLOW FIELD VISUALIZATION, THERMOCOUPLE MEASUREMENTS, AND ANALYSIS

By H. Lee Seegmiller
NASA Ames Research Center
Moffett Field, California

INTRODUCTION

Shock interference heating effects are an area of concern in the technology of the space shuttle. These interference effects are in general not well understood and are observed for a wide range of conditions and configurations. During launch, interference heating will occur at various locations on both orbiter and booster. Interference flow has been observed on the deflected tip rudder of a delta configuration and can be expected to occur if a ventral fin is required for lateral-directional stability. Configurations which have canard surfaces or wings of low sweep, such as the straight-wing orbiter proposed by Manned Spacecraft Center (MSC), encounter wing-fuselage shock interference effects. Some initial results of an investigation of this problem were presented in reference 1. More recently, measurements and analysis have been undertaken to provide an increased understanding of the shock-interference phenomena; the results will be presented in this paper.

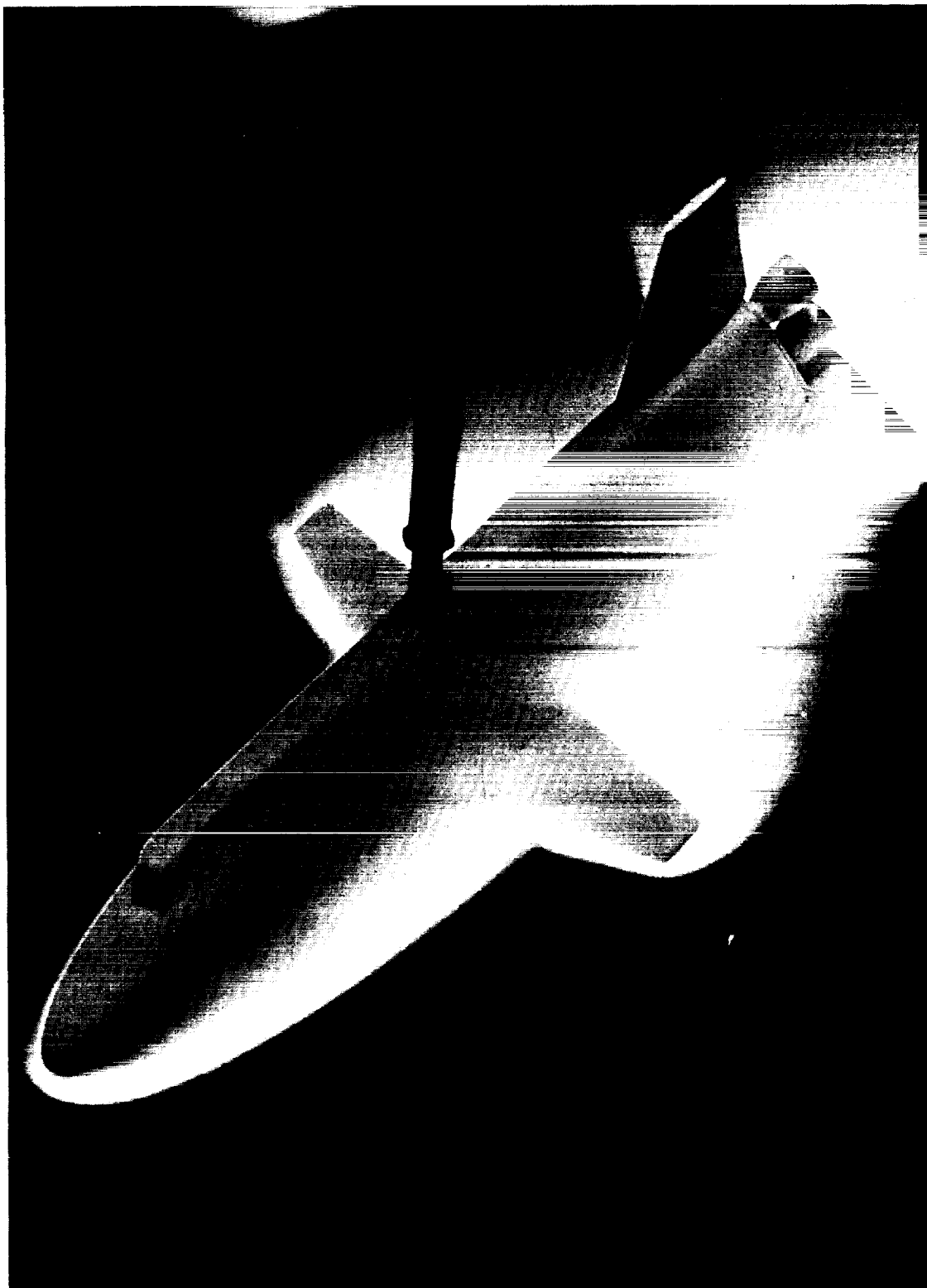
ORBITER SHOCK LAYER FLOW

(Slide 1)

The incandescent shock layer flow about a model of the MSC orbiter is shown in this photograph. Evidence of shock interference effects may be seen at the juncture of the fuselage and wing shock layers. The attitude shown here is 60° which corresponds to a nominal low-cross-range entry for this vehicle.

ORBITER SHOCK LAYER FLOW

$\alpha = 60^\circ$ $M_\infty = 13$ $H_0 = 18.6 \times 10^6 \text{ J/kg (8000 Btu/lb)}$



Slide 1

SHADOWGRAPH OF ORBITER

(Slide 2)

The intersecting fuselage-wing shock waves are shown in this shadowgraph. At this attitude of 50° the inboard wing flow which has passed through the fuselage shock is still supersonic although some deceleration and turning have occurred. Both the transmitted fuselage shock and an inward interference shock may be seen at the intersection point.

SHADOWGRAPH OF ORBITER

$\alpha = 50^\circ$ $M_\infty = 7.4$ $Re_L = 3 \times 10^6$



Slide 2

WINDWARD SURFACE FLOW VISUALIZATION

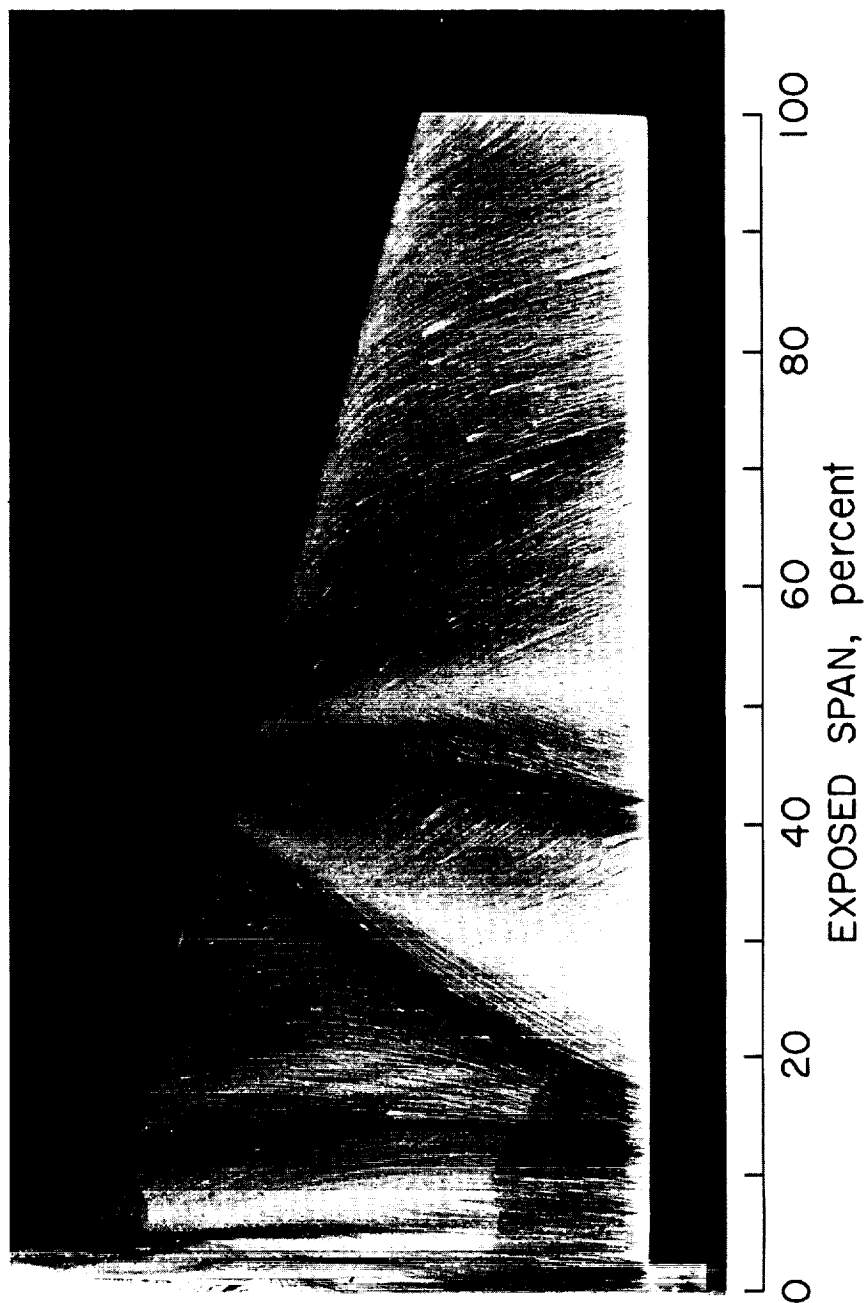
 $(\alpha = 40^\circ)$

(Slide 3)

Two interference regions are shown in this surface flow visualization photograph. The innermost or root region arises from conflict between the fuselage and wing flow at the wing root. Although significant local heating effects have been found in this region, it is believed that proper filleting of the wing-fuselage juncture could reduce this heating. The outer or shock interference region is composed of three structures; two similar shock-boundary-layer interactions and a shear region impingement. The sketches in slide 4 will assist in the explanation of these features.

WINDWARD SURFACE FLOW VISUALIZATION

$\alpha = 40^\circ$ $M_\infty = 7.4$ $Re_L = 1 \times 10^6$



Slide 3

PROPOSED FLOW MODEL

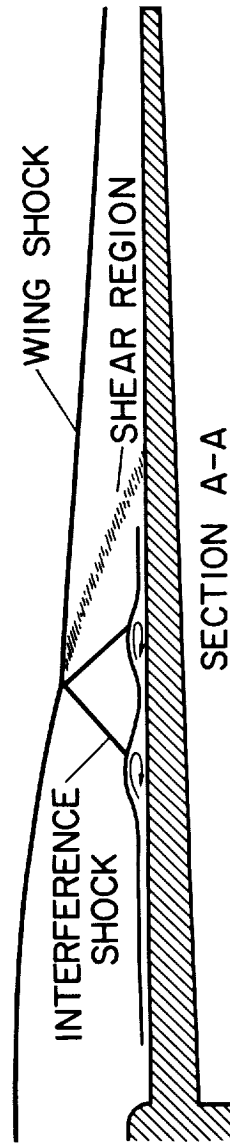
(Slide 4)

A tracing of the flow visualization photograph is used to provide a proposed interpretation of the essential features of the shock interference region. Lines of separation and attachment are found for each of the two impinging shocks. It must be noted that the impinging shocks are oblique to the wing flow streamlines. The streamlines in the separated flow region are also oblique to the lines of separation and attachment. The increasing width of the separation region which occurs as the flow approaches the trailing edge results from the increasing boundary-layer thickness. The influence of the shear region impingement is seen in the convergence of the streamlines outboard of the impinging fuselage shock. The effect of this shear region flow impingement was found to be small from tests of a phase-change paint model.

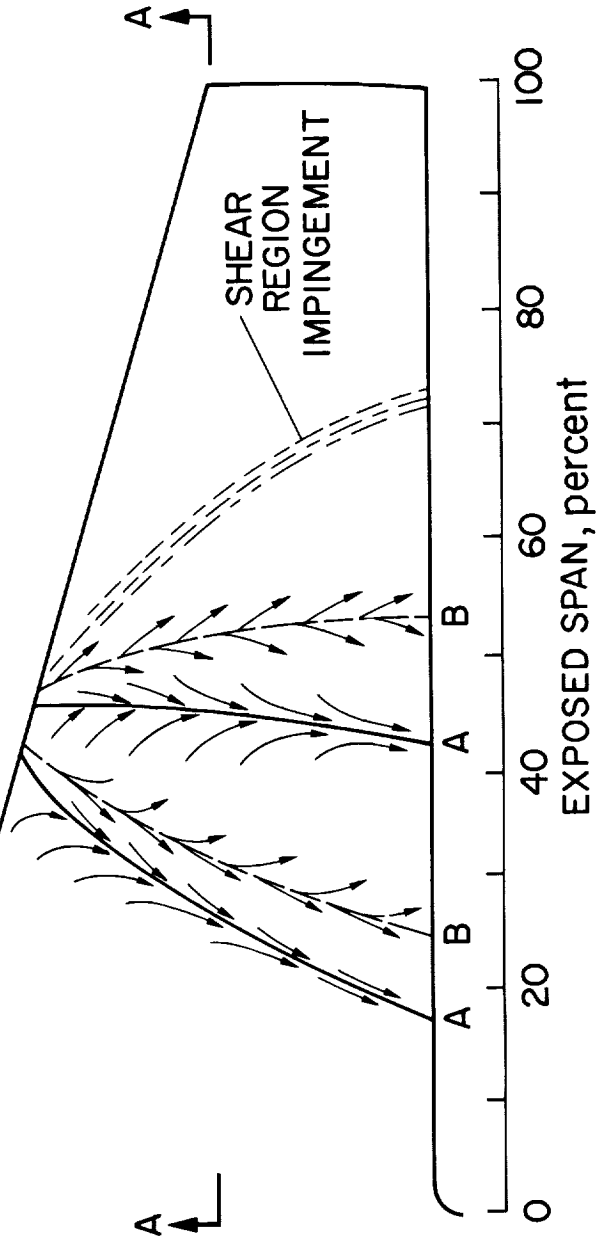
Wing-fuselage shock interference effects may be conveniently considered as a two-part phenomenon. At the leading edge, heating results from flow which has been processed by passage through multiple shocks and stagnated at some location on the forward surface. Aft of this stagnation region more conventional shock--boundary-layer interactions are found although the shocks are oblique to the flow.

PROPOSED FLOW MODEL

$\alpha = 40^\circ$ $M_\infty = 7.4$ $Re_L = 1 \times 10^6$



A = LINES OF SEPARATION
B = LINES OF ATTACHMENT



Slide 4

SPANWISE HEATING DISTRIBUTION

(Slide 5)

The graph of heat transfer to the wing at this 40° angle of attack shows the peaks associated with the impingement of the fuselage and interference shocks. The locations of the lines of attachment and separation which were obtained from the flow visualization photographs are seen to correspond quite well with the heating distribution. All heating rates shown in this paper are made dimensionless by taking the ratio of the measured value to the stagnation value for a sphere having a radius equal to $\frac{1}{150}$ of the length of the model.

SPANWISE HEATING DISTRIBUTION

$\alpha = 40^\circ$

$M_\infty = 7.4$

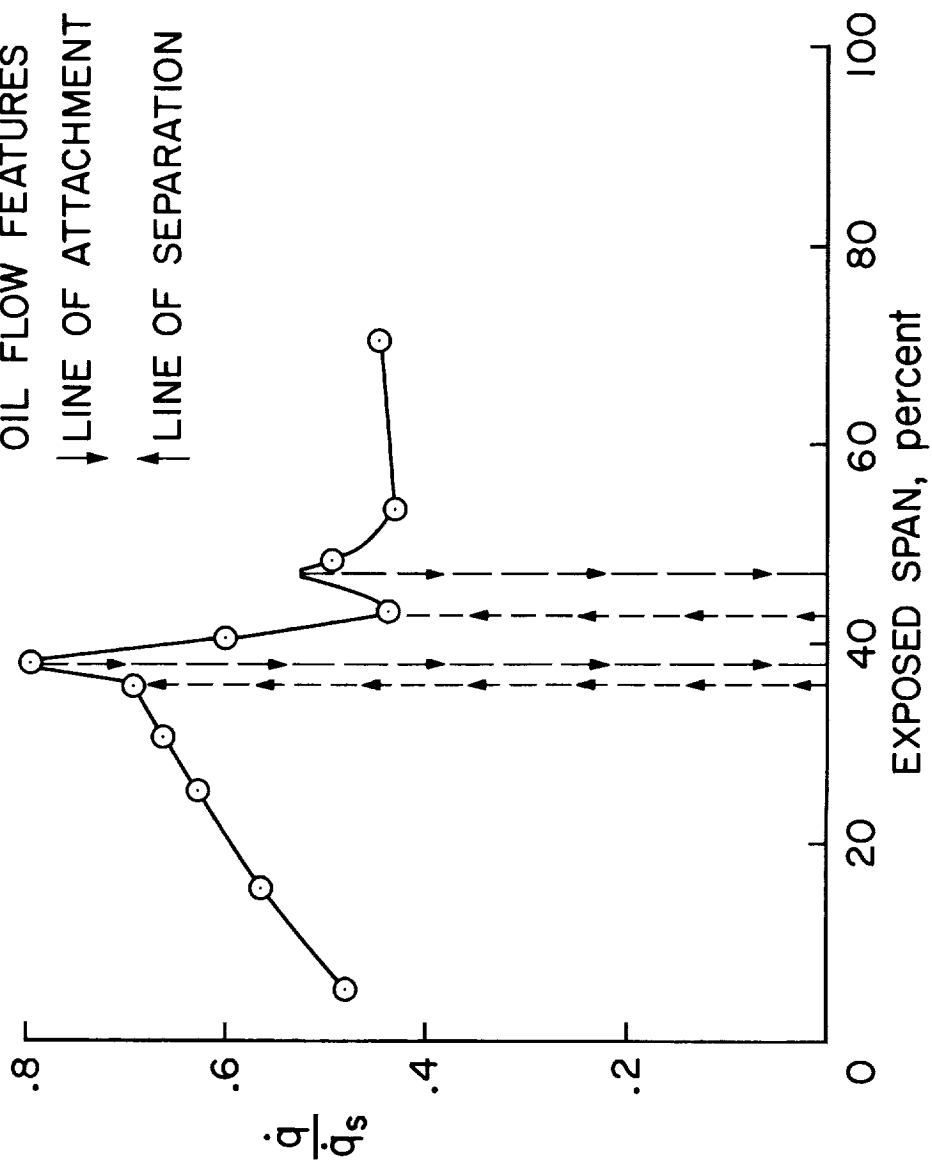
$Re_L = 1 \times 10^6$

5% CHORD

OIL FLOW FEATURES

↓ LINE OF ATTACHMENT

↑ LINE OF SEPARATION



Slide 5

WINDWARD SURFACE FLOW VISUALIZATION

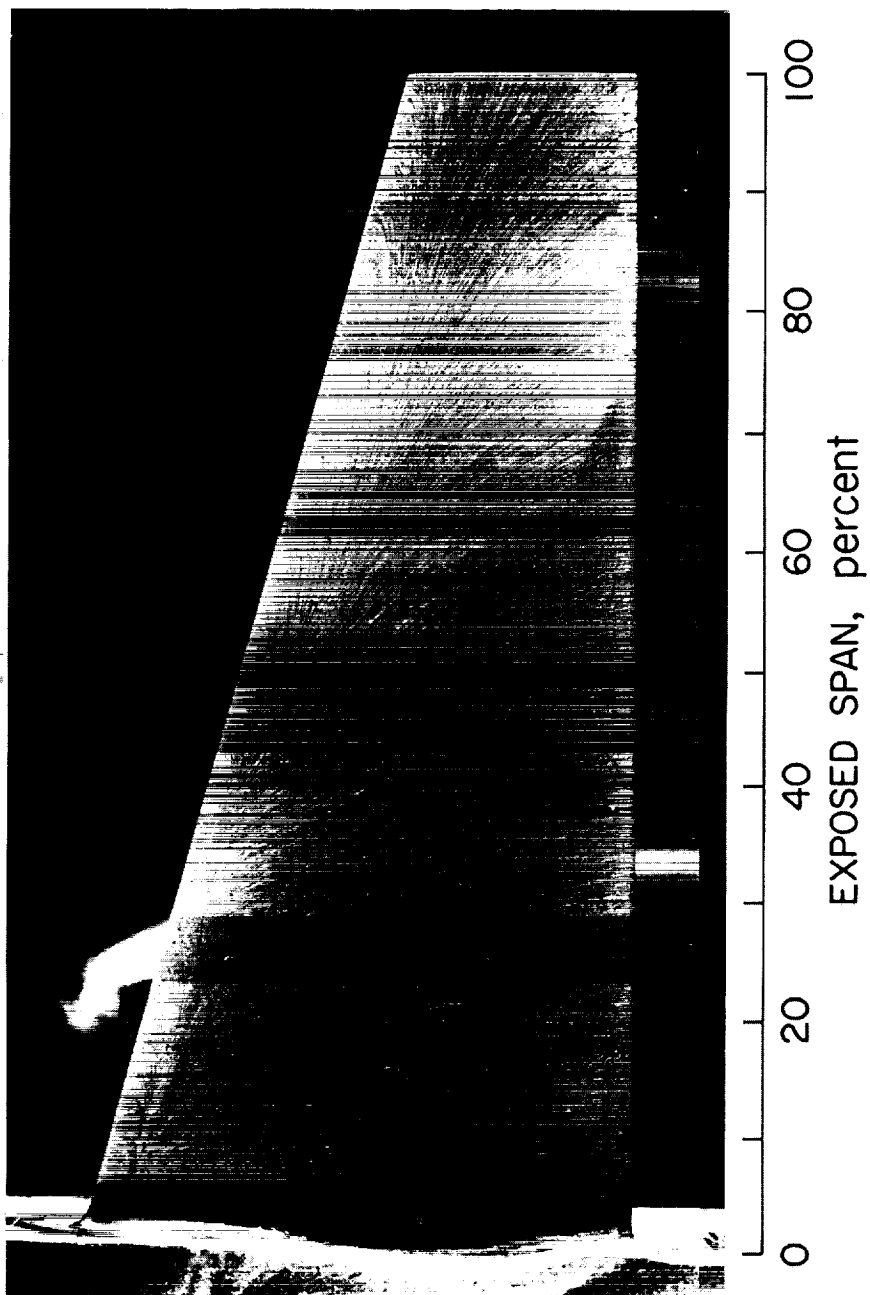
 $(\alpha = 60^\circ)$

(Slide 6)

The wing surface flow patterns at this higher angle of attack show that the fuselage and interference shocks are no longer sufficiently strong to cause the shock--boundary-layer interaction which was noted at $\alpha = 40^\circ$. The effect of the interference in the stagnation flow may be noted, however, in the distortion of the wing stagnation line near the 40% span position. A root interference region may also be seen at the leading edge near the fuselage. A graph of the stagnation line position and a sketch of the stagnation line flow are shown in slide 7.

WINDWARD SURFACE FLOW VISUALIZATION

$\alpha = 60^\circ$ $M_\infty = 7.4$ $Re_L = 3 \times 10^6$



Slide 6

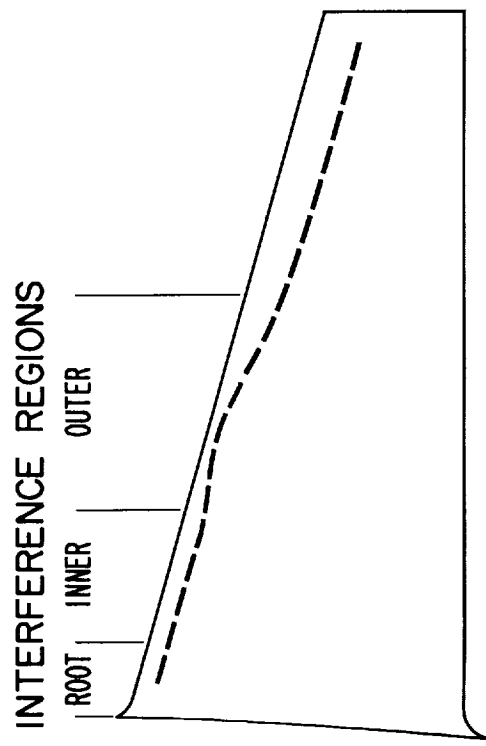
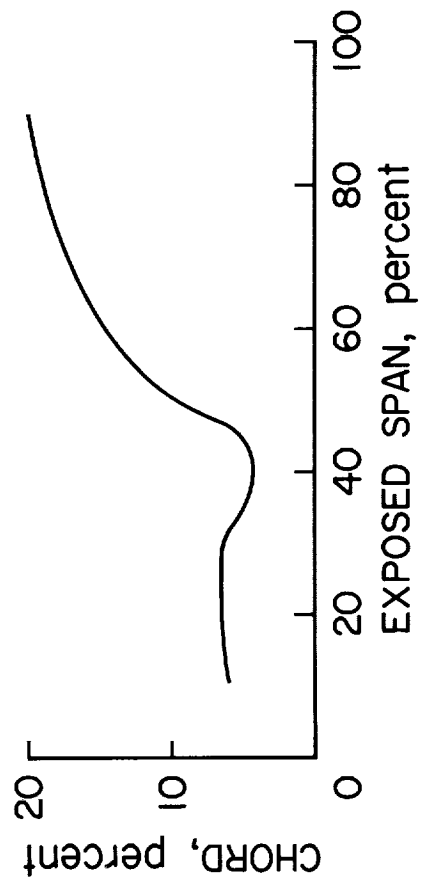
WING STAGNATION LINE POSITION

(Slide 7)

In the fuselage-shock-dominated flow between 10% and 30% span, the wing stagnation line position is relatively constant at about 7% of chord from the leading edge. The most forward location of the stagnation line occurs at about the 40% span location. Outboard of this position the stagnation line moves aft as the influence of the wing shock predominates. Using the results of other flow visualization photographs, a plot of the stagnation line position at the 70% span location (i.e., in the essentially interference-free region) was obtained for angles of attack from 18° to 80° . The measured stagnation position in the interference region is considered to correspond to an "equivalent" local angle of attack, that is, an angle resulting from the flow passing through the interference shock system. An increase in stagnation heating can be expected in regions of reduced local α because of the increased velocity gradients associated with the decreasing leading-edge radius.

WING STAGNATION LINE POSITION

$\alpha = 60^\circ$ $M_\infty = 7.4$ $Re_L = 3 \times 10^6$



Slide 7

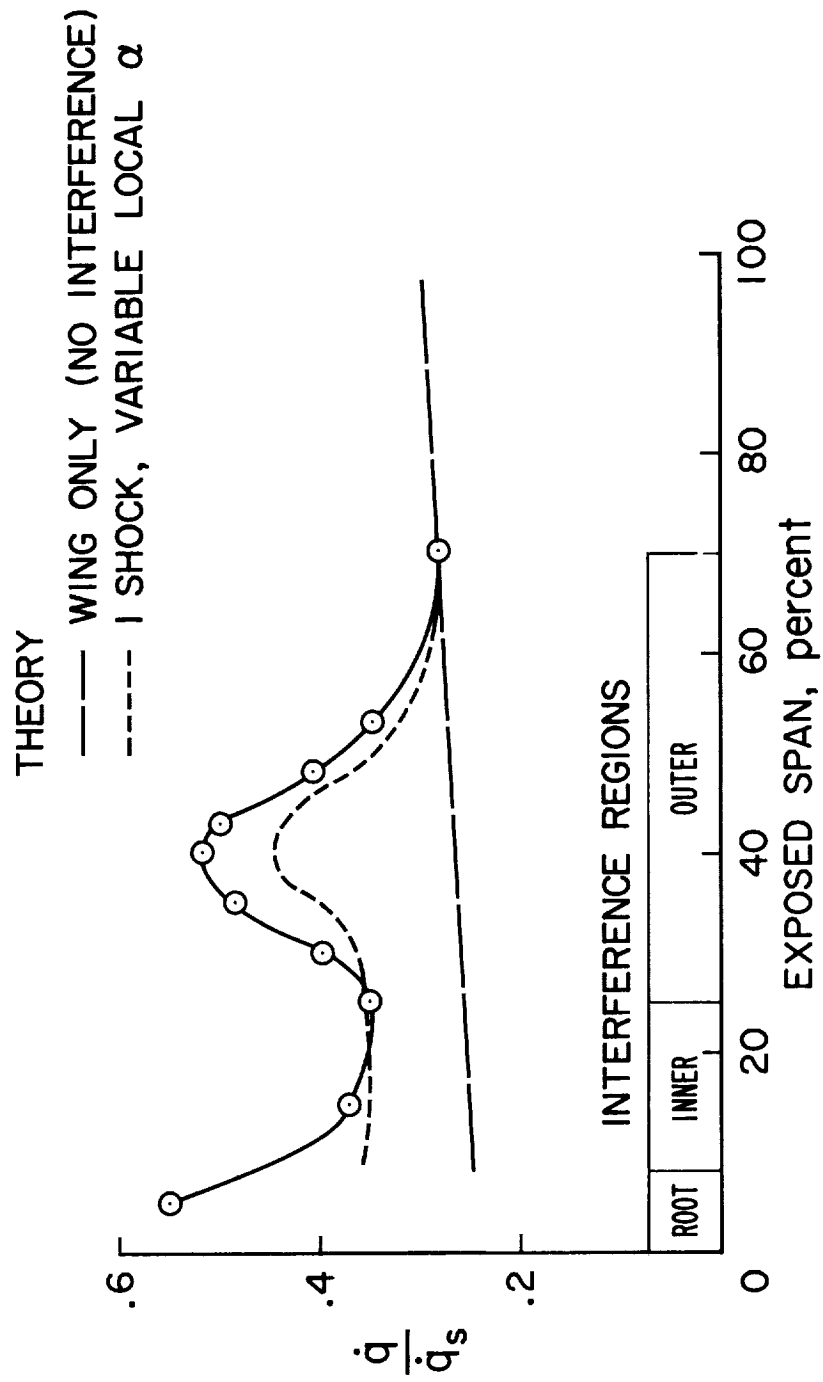
COMPARISON OF PREDICTED AND MEASURED INTERFERENCE HEATING

(Slide 8)

A predicted heating distribution obtained from the local angles of attack and the pressures associated with the required turning angles for a single shock is compared with the measured values. The local α theory predicts the level of heating in the inner or fuselage-shock-dominated flow and shows the trend in the outer or shock interference region quite well. The level is expected to be somewhat low, as seen, because of the single-shock assumption. Multiple-shock theory would of course require knowledge of the actual shock angles. It is interesting to note that at this high angle of attack (60°) maximum heating occurs in the root interference region.

COMPARISON OF PREDICTED AND MEASURED INTERFERENCE HEATING

$\alpha = 60^\circ$ $M_\infty = 7.4$ $Re_L = 1 \times 10^6$
5% CHORD



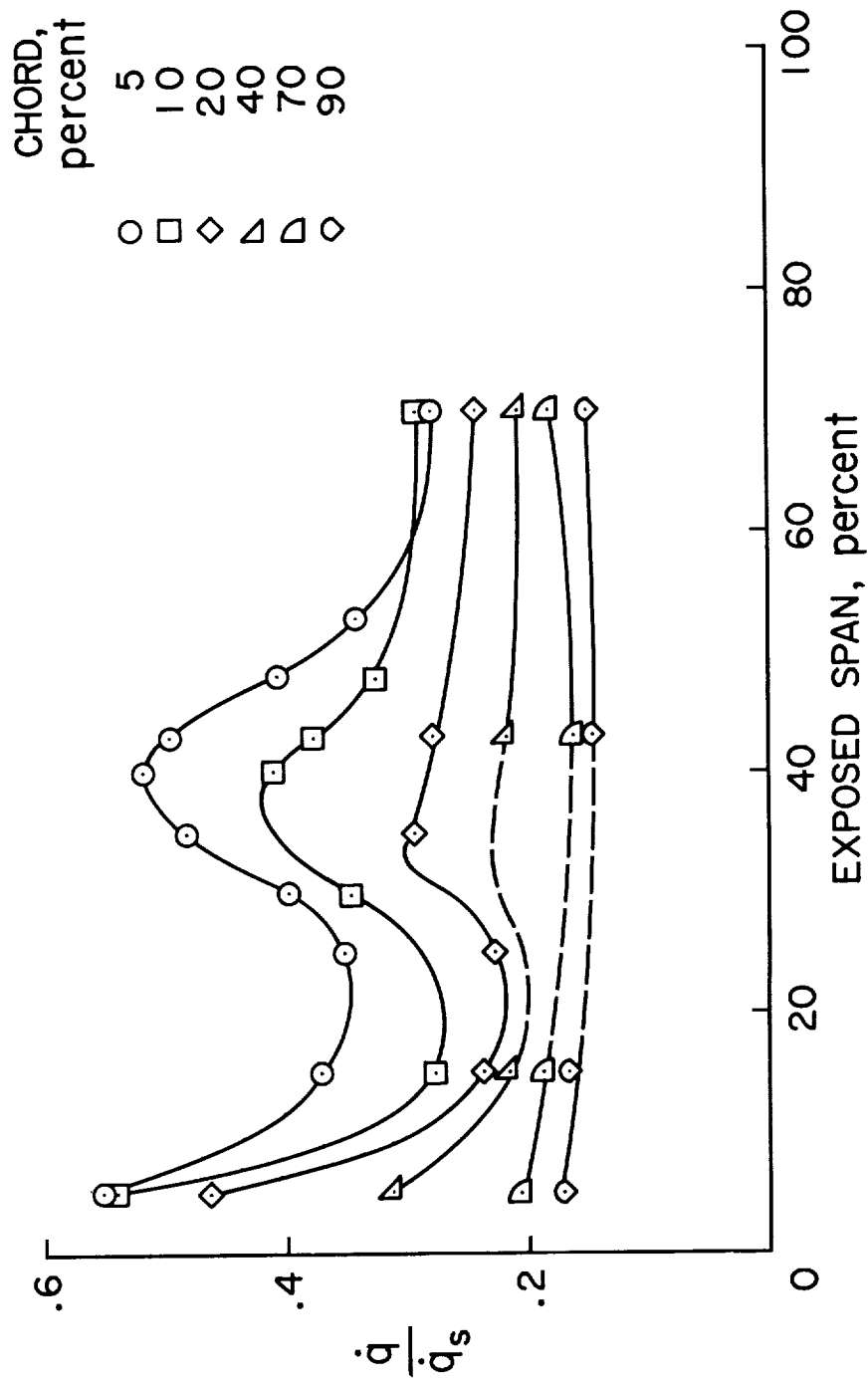
Slide 8

SPANWISE HEATING DISTRIBUTIONS

(Slide 9)

The major shock interference heating effects at 60° angle of attack occur on the wing between about 25% and 55% span and forward of the 30% chord location. It is noteworthy that this is only about 10% of the wing lower surface area. Significant root interaction heating is also found forward of the 40% chord location on the inner 10% of the span (an additional 5% of the wing area). It is believed, however, that careful filleting could reduce these root heating effects.

SPANWISE HEATING DISTRIBUTIONS $\alpha = 60^\circ$ $M_\infty = 7.4$ $Re_\tau = 1 \times 10^6$



Slide 9

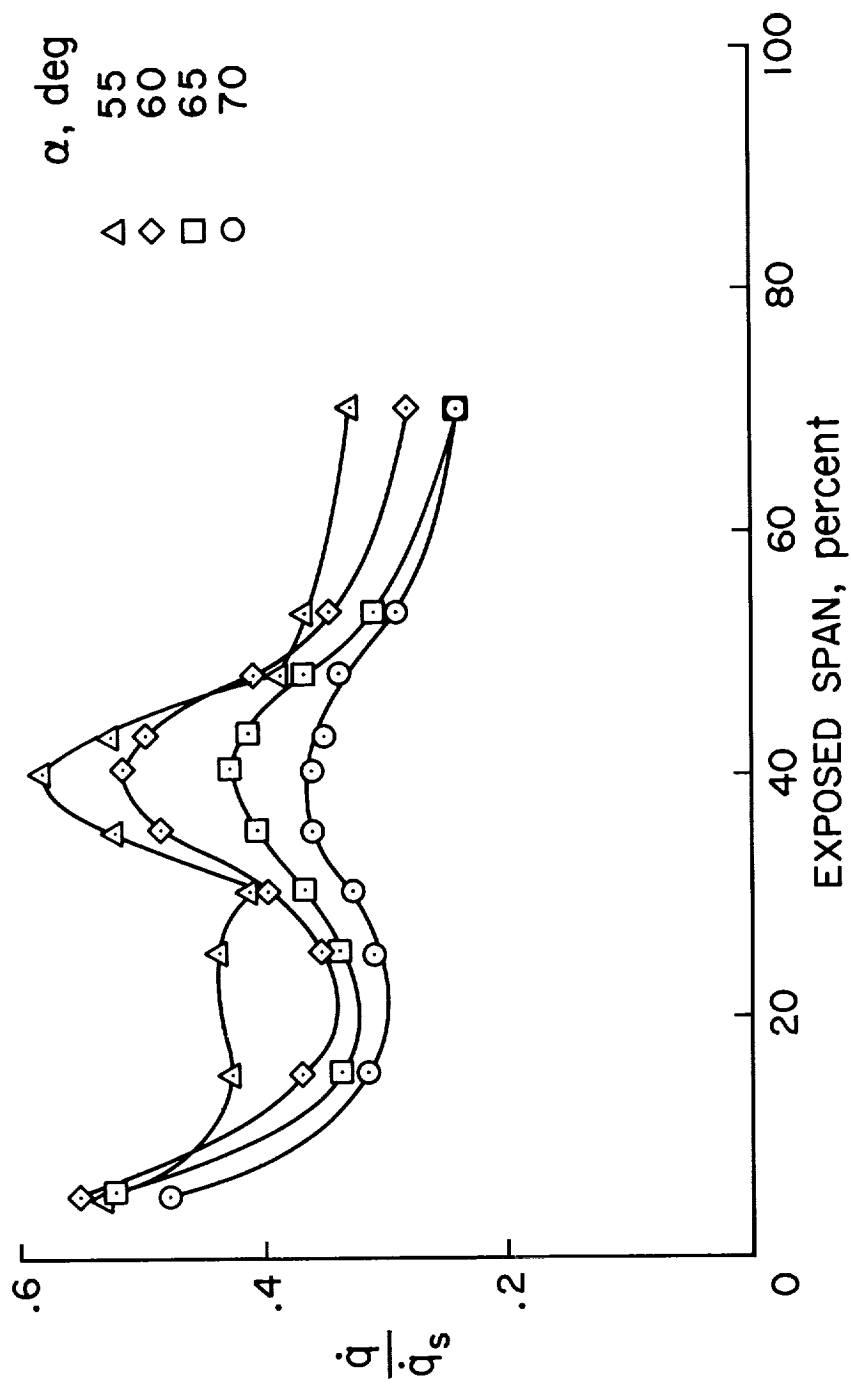
EFFECT OF ANGLE OF ATTACK ON WING HEATING

(Slide 10)

The magnitude of the shock interference heating decreases significantly with increasing angle of attack. Root heating effects, however, are relatively insensitive to attitude and exceed the shock interference values at angles of attack greater than 55° .

EFFECT OF ANGLE OF ATTACK ON WING HEATING

$M_\infty = 7.4$ $Re_L = 1 \times 10^6$ 5% CHORD



Slide 10

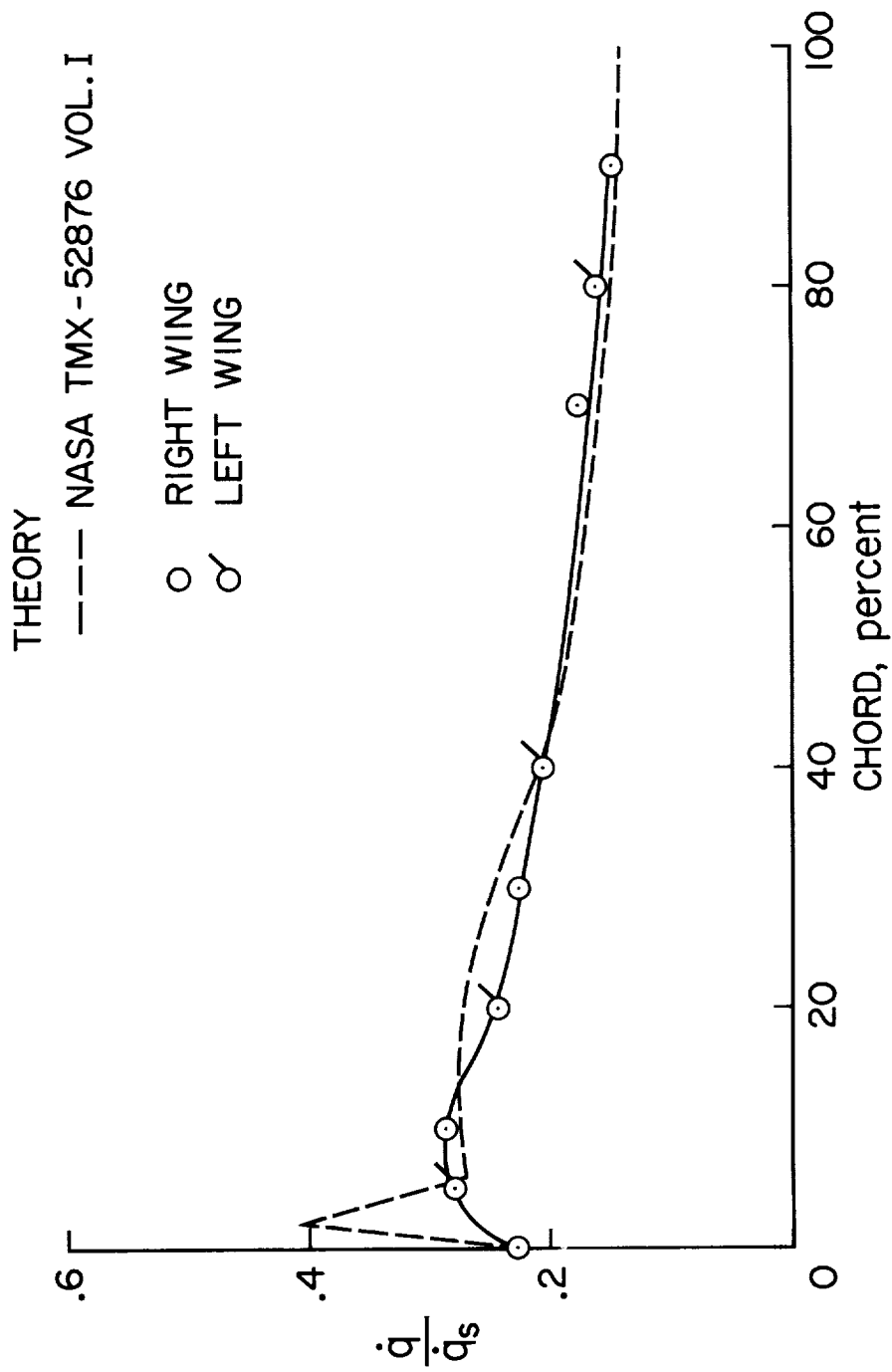
COMPARISON OF PREDICTED AND MEASURED HEATING RATES

(Slide 11)

Excellent agreement is obtained in this comparison of measured and theoretical chordwise heating distributions. At this outboard location of 70% span, the wing flow is essentially free of the influence of the fuselage. The peak in the theoretical distribution near the leading edge results from the method used in obtaining the velocity gradients used in the theory. The existence of this peak is as yet unconfirmed by measurement.

COMPARISON OF PREDICTED AND MEASURED HEATING RATES

$\alpha = 60^\circ$ $M_\infty = 7.4$ $Re_L = 1 \times 10^6$ 70% SPAN



Slide 11

SPANWISE HEATING DISTRIBUTION

(Slide 12)

The two interference heating peaks found at $\alpha = 40^\circ$ are also present here. The inner interference region heating is quite uniform and root interference heating effects are not seen.

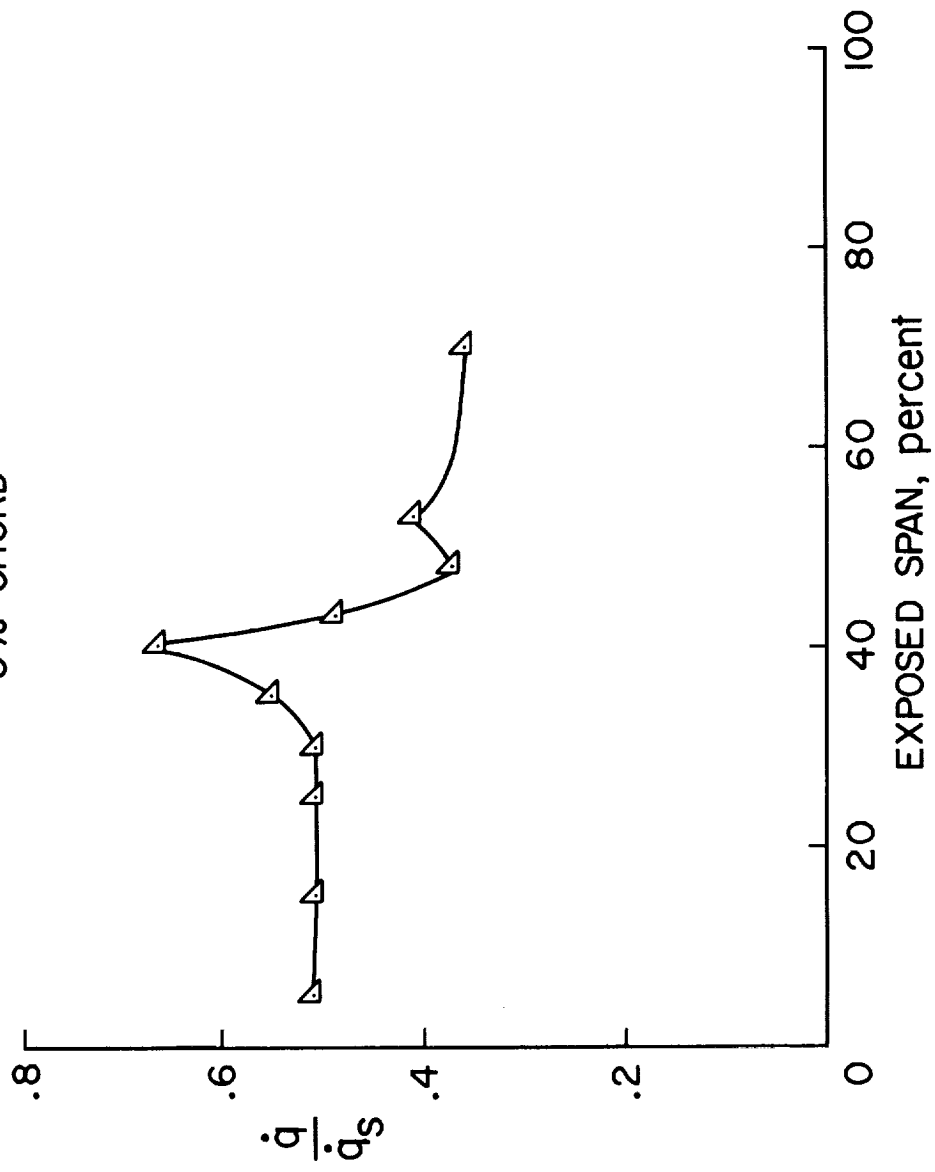
SPANWISE HEATING DISTRIBUTION

$\alpha = 50^\circ$

$M_\infty = 7.4$

$Re_L = 1 \times 10^6$

5% CHORD



Slide 12

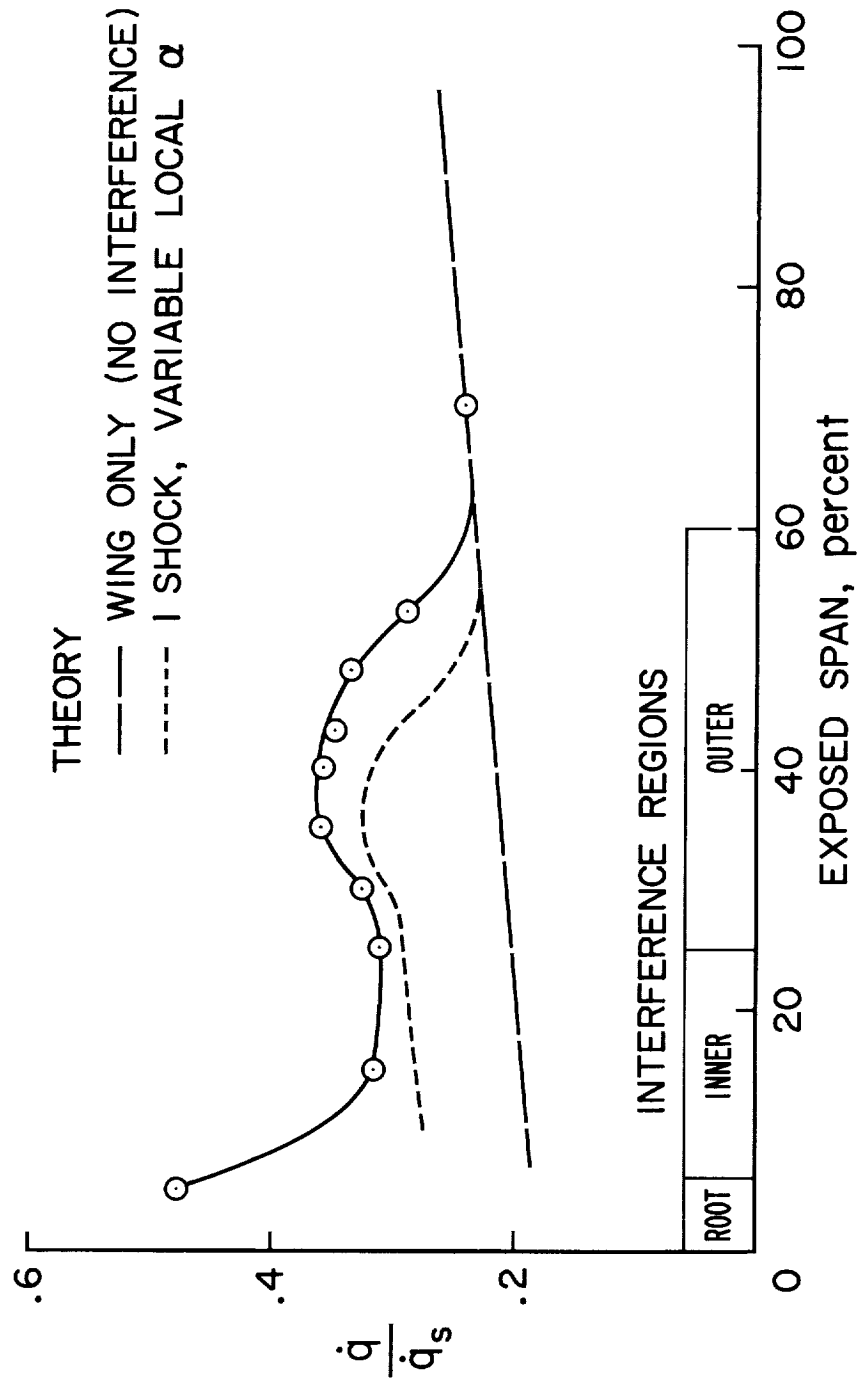
COMPARISON OF PREDICTED AND MEASURED INTERFERENCE HEATING

(Slide 13)

At this large angle of attack, shock interference heating effects are still present. The distribution of the interference heating is predicted quite well with the local α theory although the level, as expected, is somewhat low because of the reduced pressures associated with the single-shock assumption. Wing-root interference heating is approximately 25% greater than the peak shock interference value.

COMPARISON OF PREDICTED AND MEASURED INTERFERENCE HEATING

$\alpha = 70^\circ$ $M_\infty = 7.4$ $Re_z = 1 \times 10^6$
5% CHORD



Slide 13

EFFECT OF ANGLE OF ATTACK ON PEAK WING TEMPERATURES

(Slide 14)

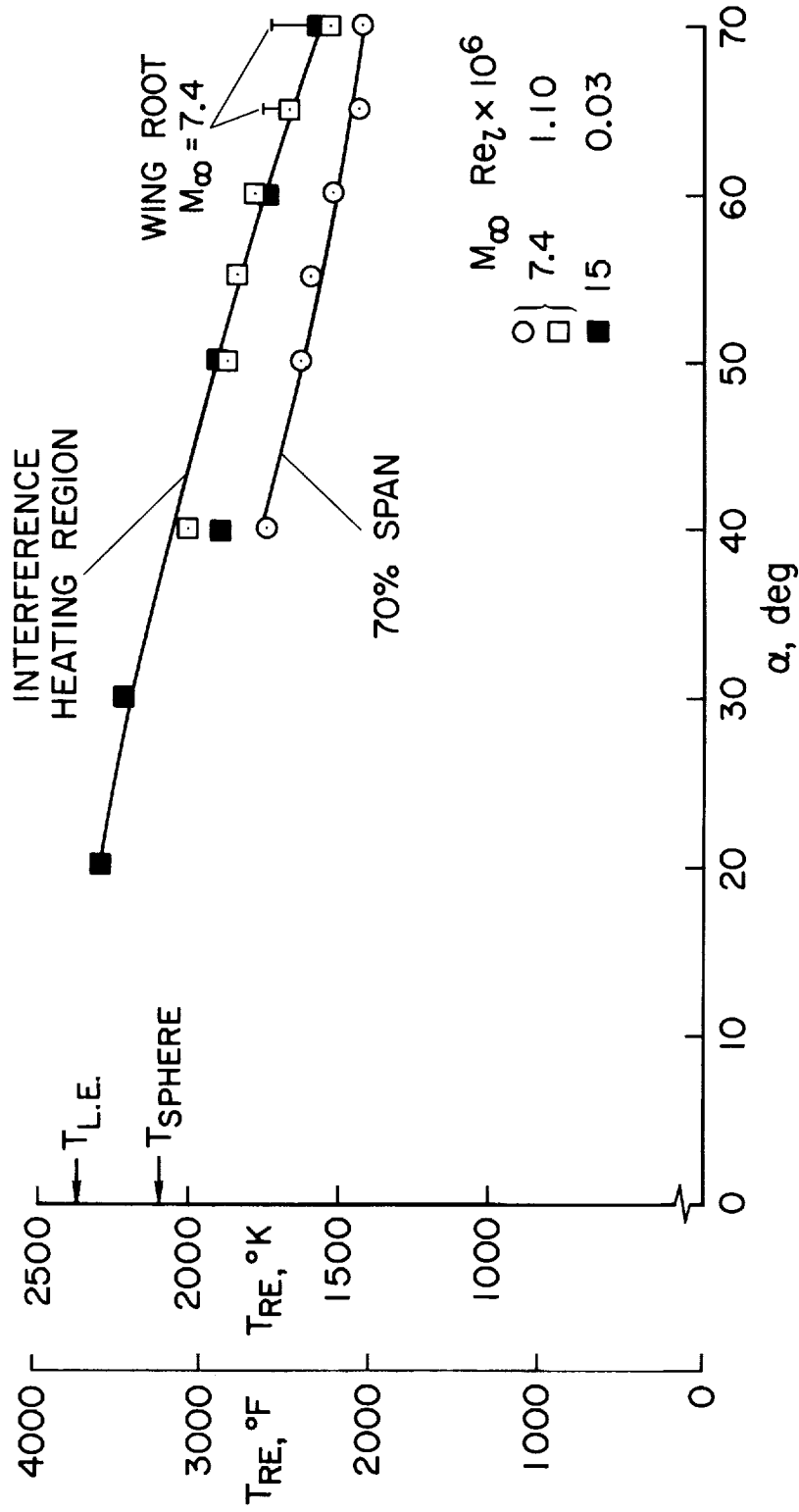
The effects of shock interference heating on the wing radiation equilibrium temperature are shown for angles of attack from 20° to 70° . These measurements, which were obtained at two widely different test conditions, represent repeated tests at yaw angles up to 3° . The model was yawed in order to sweep the interference region over the array of thermocouples and increase the probability of obtaining the peak heating value. Little difference is seen in the peak interference temperatures obtained at the two test conditions. The increase in temperature caused by the shock interference is roughly constant at about 250° K (450° F) over the α range except at $\alpha = 70^\circ$ where the increase is about 150° K (270° F). At the highest angles of attack peak temperatures occur in the root interference region next to the fuselage.

EFFECT OF ANGLE OF ATTACK ON PEAK WING TEMPERATURES

$$\dot{q}_s = 7.95 \times 10^5 \frac{\text{W}}{\text{m}^2} \quad \left(70 \frac{\text{Btu}}{\text{ft}^2 \text{ sec}} \right)$$

$$L/R_s = 150 \quad \epsilon = 0.8$$

$$R_s = 0.305 \text{ m} \quad (1.0 \text{ ft})$$



Slide 14

CONCLUSIONS

1. Wing-fuselage shock interference heating effects have been observed on a model with a wing of low sweep at angles of attack from 20° to 70° .
2. At small angles of attack both stagnation-region interference effects and shock--boundary-layer interaction effects are observed.
3. Only the stagnation-region interference effects are found at large angles of attack.
4. Stagnation-region interference effects are well predicted with a local α theory, provided the stagnation streamline is known.
5. Significant wing-root interference effects are observed. At large α root interference heating exceeds the fuselage-wing shock interference values.
6. Peak interference temperatures were found to be similar in tests conducted at $M_\infty = 7.4$, $Re_l = 1.10 \times 10^6$ and at $M_\infty = 15$, $Re_l = 0.03 \times 10^6$.

REFERENCE

1. Katzen, E. D.; Marvin, J. G.; Seegmiller, H. L.; Axelson, J. A.; Brownson, J. J.; Cleary, J. W.; Lockman, W. K.; and Kaattari, G. E.: Static Aerodynamics, Flow Fields and Aerodynamic Heating of Space Shuttle Orbiters, NASA TM X-52876, Vol. I, pp. 142-193, July 15-17, 1970.

SHOCK INTERFERENCE HEATING AND DENSITY-RATIO EFFECTS

PART II - HYPERSONIC DENSITY-RATIO EFFECTS

By James L. Hunt and Theodore R. Creel, Jr.
NASA Langley Research Center, Hampton, Virginia

INTRODUCTION

For hypersonic flow conditions, the inviscid aerodynamic characteristics of bodies at high angle of attack are determined primarily by the shock-density ratio. In flight, large density ratios across the shock result from chemical dissociation of the molecules in the high-temperature gas behind the shock and serve as an indicator of the amount of real-gas effects present. For ground tests at hypersonic Mach numbers where no dissociation occurs, the density ratio across a shock is determined by the specific-heat ratio γ of the gas (the lower γ , the higher the density ratio); thus, ground test data obtained at hypersonic Mach numbers at various values of γ can be used to simulate the trends of equilibrium real-gas effects expected in flight. The shock shape, the surface oil-flow patterns, the location of the body-shock-wing-shock intersection and, thus, the distribution of the resulting interference heating patterns on a low-cross-range shuttle configuration are investigated in this paper by obtaining data in several facilities at $\gamma = 1.67$, 1.4, and 1.12 with normal-shock density ratios of 3.9, 5.6 to 5.9, and 12, respectively.

DENSITY RATIO ACROSS NORMAL SHOCK ALONG SHUTTLE TRAJECTORIES

(Figure 1)

Equilibrium normal-shock density ratios encountered along two shuttle orbiter trajectories are given in figure 1. The normal-shock density ratio at peak heating is approximately 18 on the low-cross-range orbiter trajectory ($\alpha = 60^\circ$); it is nearer 17 for the high-cross-range orbiter ($\alpha = 22^\circ$). Since, in the earth's atmosphere, a density ratio greater than 6 indicates molecular dissociation, the potential for real-gas effects along both these trajectories is large.

Flow visualization, oil flow, and phase-change heat-transfer data were obtained on a truncated MSC (Manned Spacecraft Center) straight-wing orbiter at angles of attack of 40° , 52° , and 60° in helium ($\rho_2/\rho_1 \approx 3.9$) and nitrogen ($\rho_2/\rho_1 \approx 5.9$) for a Mach number of 20 and in air ($\rho_2/\rho_1 \approx 5.7$) for a Mach number of 8; thus, both γ and Mach number were isolated as variables. Also, flow visualization photographs and oil-flow patterns were obtained on the truncated orbiter in CF_4 (tetrafluoromethane) at a Mach number of 6 ($\rho_2/\rho_1 \approx 12$). Although, the normal-shock density ratios in the flows in which most tests were performed ($\rho_2/\rho_1 \approx 3.9$, 5.6 , and 5.9) are lower than those encountered in flight where real-gas effects are prevalent ($\rho_2/\rho_1 \approx 9$ to 18), the trends detected in this investigation in going from a density ratio of 3.9 to 5.9 along with supplementary data at a density ratio of 12 should help infer the trends which real-gas effects will take in flight.

DENSITY RATIO ACROSS NORMAL SHOCK ALONG SHUTTLE TRAJECTORIES

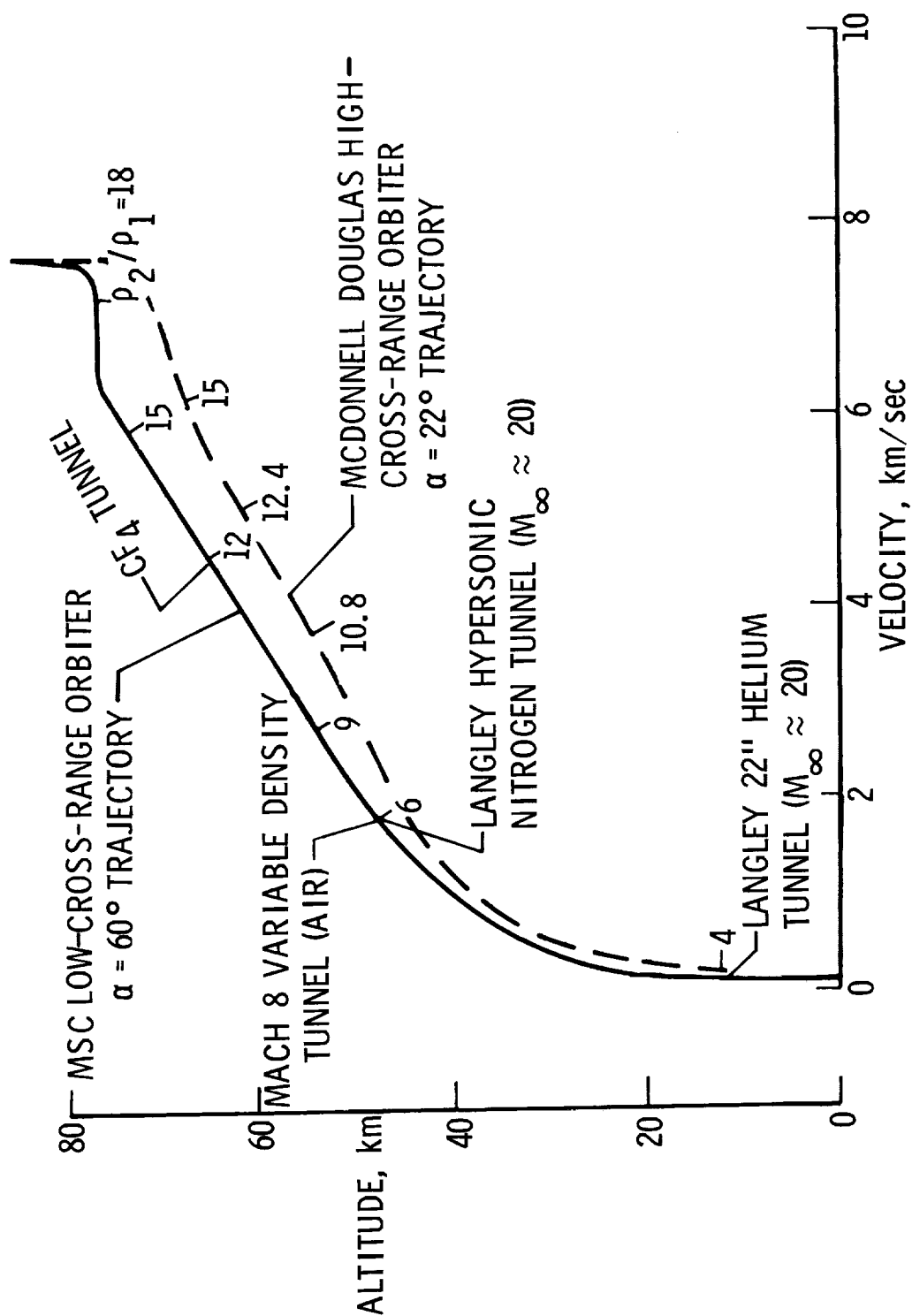


Figure 1

COMPARISON OF SHOCK PATTERNS IN AIR AND CF_4

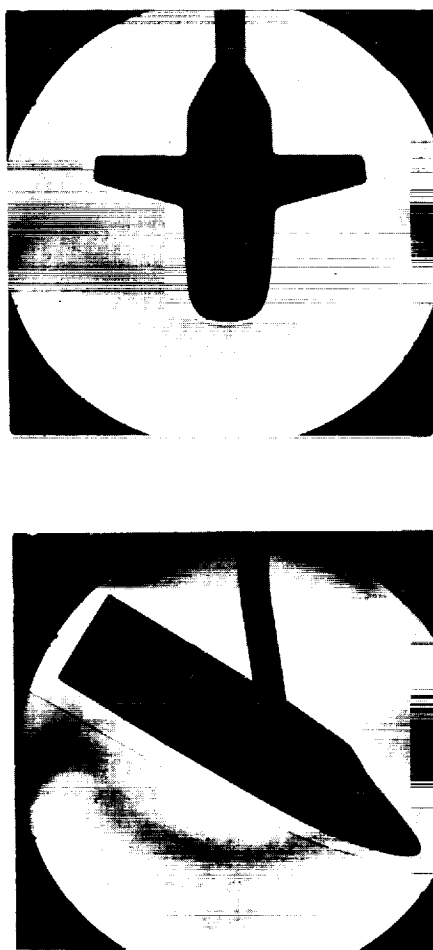
(Figure 2)

An example of the influence of density ratio on the inviscid flow field of a truncated MSC straight-wing orbiter is shown in the schlieren and shadowgraph photographs for a Mach number of 8 in air and 6 in CF_4 with density ratios of 5.6 and 12, respectively. The profile views show the body shock much closer to the fuselage in CF_4 than in air yet the wing shock bulges out further than the body shock in air while the wing shock lies inside the body shock in CF_4 . The photographs taken normal to the wing span show the body shock impinging the wing much closer inboard to the body in CF_4 ($\rho_2/\rho_1 \approx 12$) than in air ($\rho_2/\rho_1 \approx 5.6$) and the wing shock standoff distance in CF_4 to be about 1/4 that in air; thus, a significant change is indicated in the flow field over the wings.

COMPARISON OF SHOCK PATTERNS IN AIR AND CF₄ TRUNCATED STRAIGHT WING ORBITER, $\alpha = 60^\circ$



AIR: $M_\infty \approx 8$, $\gamma = 1.40$, $p_2/p_1 \approx 5.6$



CF₄: $M_\infty \approx 6$, $\gamma \approx 1.12$, $p_2/p_1 \approx 12$

Figure 2

TRUNCATED MSC ORBITER IN HELIUM AT MACH 20

(Figure 3)

The manner in which the truncated orbiter flow field changes with increasing angle of attack is shown in the electron beam photographs of figure 3. These photographs were taken in the Langley 22-inch helium tunnel ($\rho_2/\rho_1 \approx 3.9$). They show the body-shock--wing-shock intersection moving inboard along the wing span with increasing angle of attack ($\alpha = 20^\circ$ to 40°). However, between 40° and 50° angle of attack, the flow field about the wing has undergone a change similar to that shown in figure 2 between the flows for density ratios of 12 and 5.6; that is, the wing shock standoff distance has suddenly increased very greatly. In other words, the flow field in helium ($\rho_2/\rho_1 \approx 3.9$) at 50° angle of attack is very similar to that in air ($\rho_2/\rho_1 \approx 5.6$) at 60° angle of attack. In figure 2, this flow-field change occurs when the angle of attack is held constant and the density ratio decreased. In figure 3, this same type flow-field change occurs when the density ratio is held constant and the angle of attack increased.

TRUNCATED MSC ORBITER IN HELIUM AT MACH 20

$$\rho_2/\rho_1 \approx 3.9$$

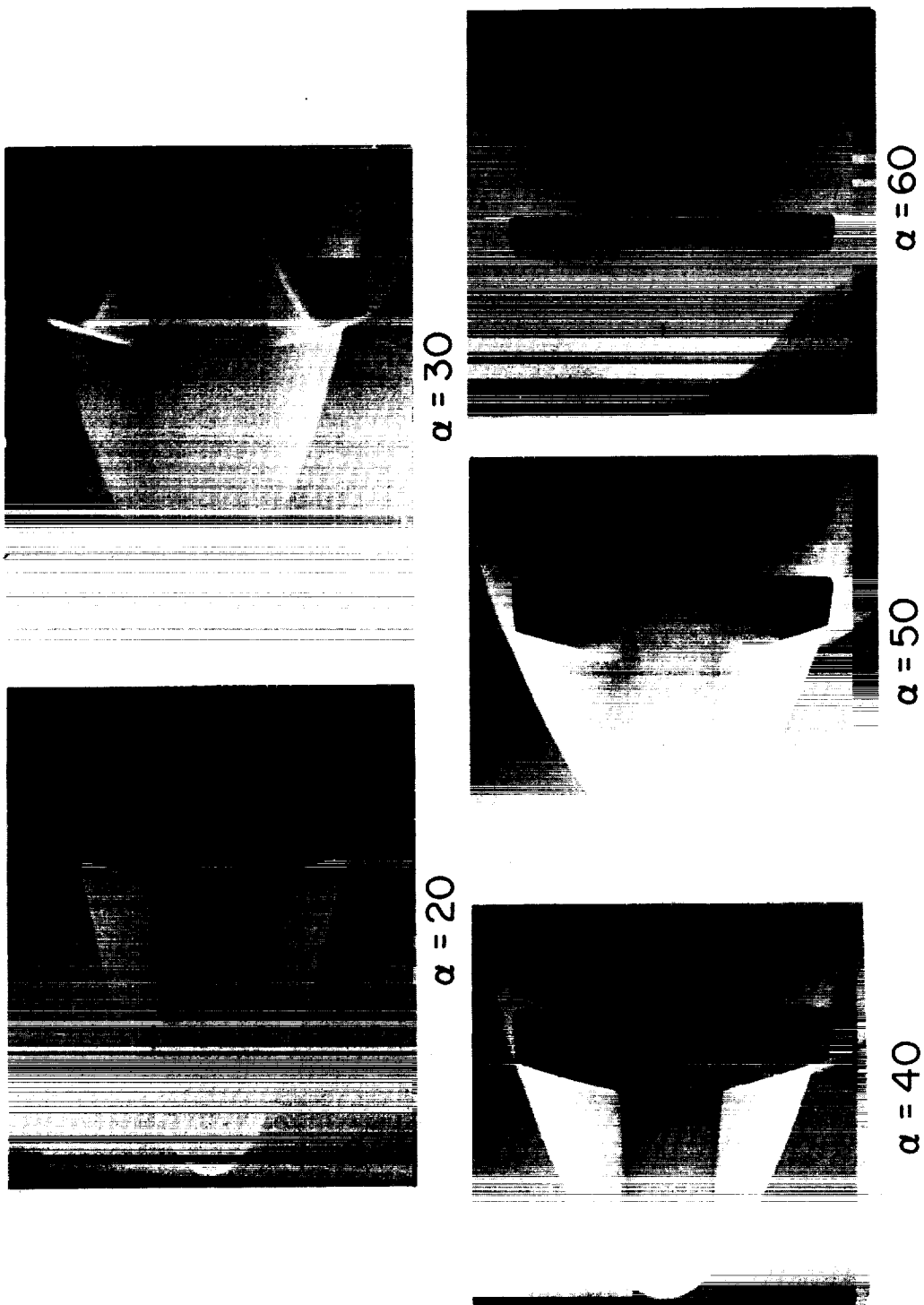


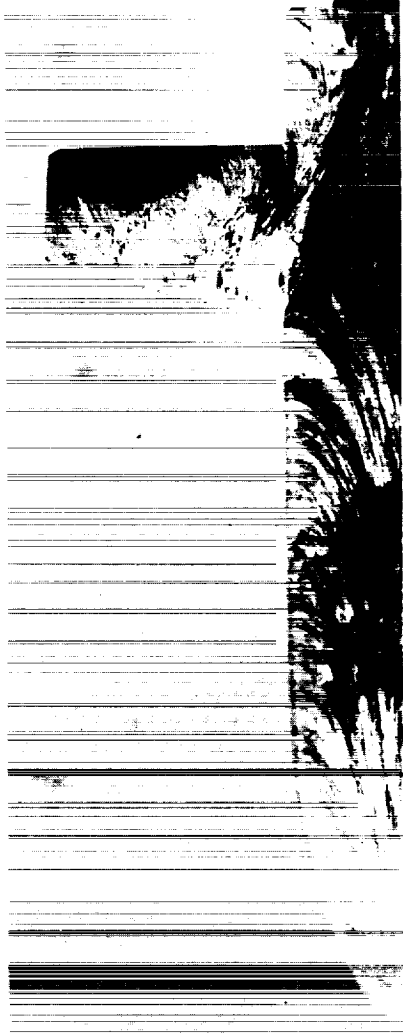
Figure 3

OIL FLOW ON TRUNCATED MSC ORBITER AT MACH 20, $\alpha = 40^\circ$

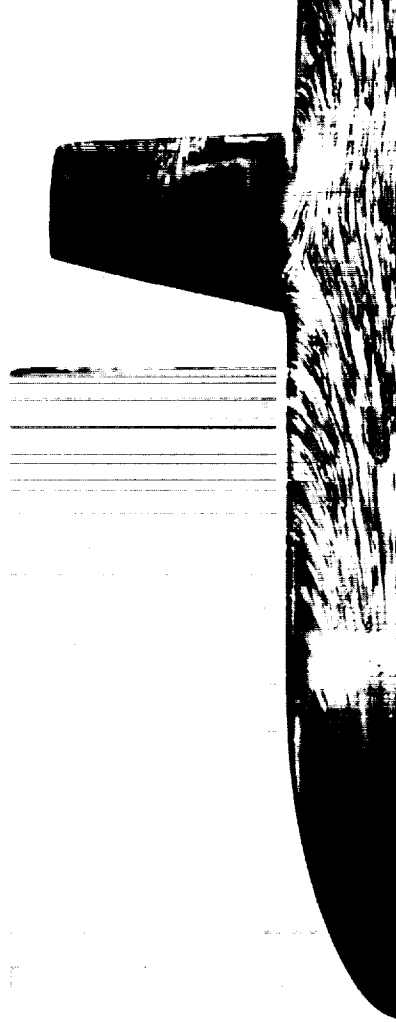
(Figure 4)

Oil-flow patterns obtained in helium ($\rho_2/\rho_1 \approx 3.9$) and nitrogen ($\rho_2/\rho_1 \approx 5.9$) at Mach 20 for an angle of attack of 40° show the stagnation point near the apex of the orbiter at both density ratios. The effects of shock interference on the wing are clearly visible. This effect is more sharply defined at the higher density ratio with the appearance of a two-prong (V-shape) interference pattern. Also, the wing stagnation streamline is on the leading edge in both density-ratio flows at this angle of attack.

OIL FLOW ON TRUNCATED MSC ORBITER AT MACH 20



HELIUM : $M_\infty \approx 20$, $\alpha = 40^\circ$, $\rho_2/\rho_1 \approx 3.9$



NITROGEN : $M_\infty \approx 20$, $\alpha = 40^\circ$, $\rho_2/\rho_1 \approx 5.9$

Figure 4

OIL FLOW ON TRUNCATED MSC ORBITER AT MACH 20, $\alpha = 52^\circ$

(Figure 5)

Similar patterns on the truncated orbiter obtained in helium ($\rho_2/\rho_1 \approx 3.9$) and nitrogen ($\rho_2/\rho_1 \approx 5.9$) at Mach 20 for an angle of attack of 52° show that the stagnation point in the flow with the lower density ratio has moved a significant distance farther downstream than at the higher ratio. On the fuselage, the oil-flow patterns show a greater divergence of the viscous streamlines near the edges of the body in the lower density-ratio flow. The oil-flow patterns on the wing at the lower density ratio show a sharp contrast to those at $\alpha = 40^\circ$ (fig. 4). There is no significant evidence of body-shock-wing-shock interference on the wing and the wing stagnation line has moved downstream of the wing leading edge. At the higher density ratio (5.9), however, the stagnation line is still on the wing leading edge, and shock impingement interference effects are still apparent but are less severe and further inboard than those for 40° angle of attack.

OIL FLOW ON TRUNCATED MSC ORBITER AT MACH 20

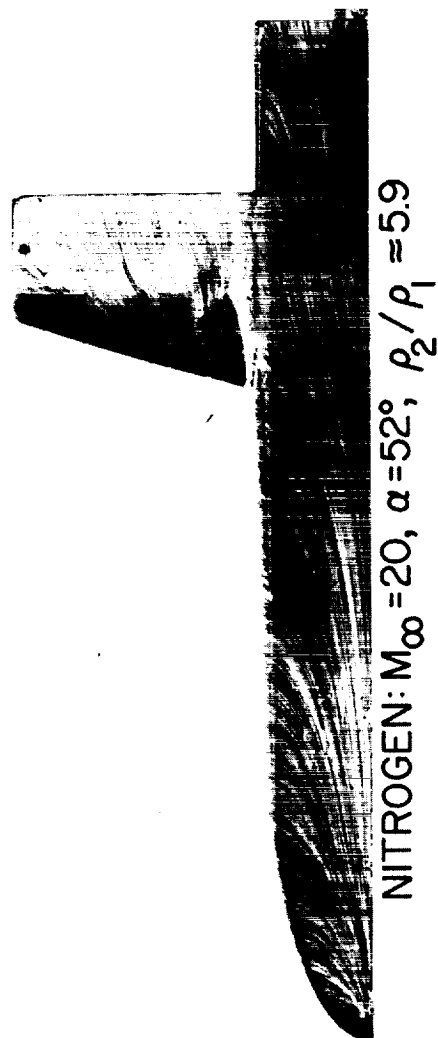
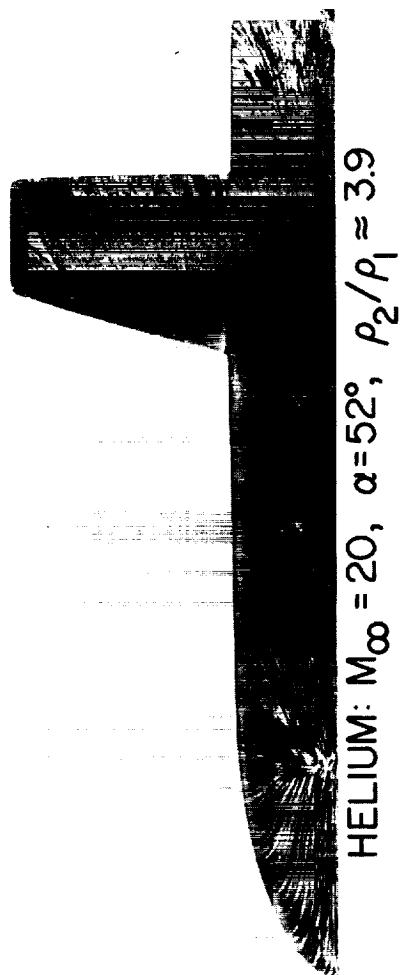


Figure 5

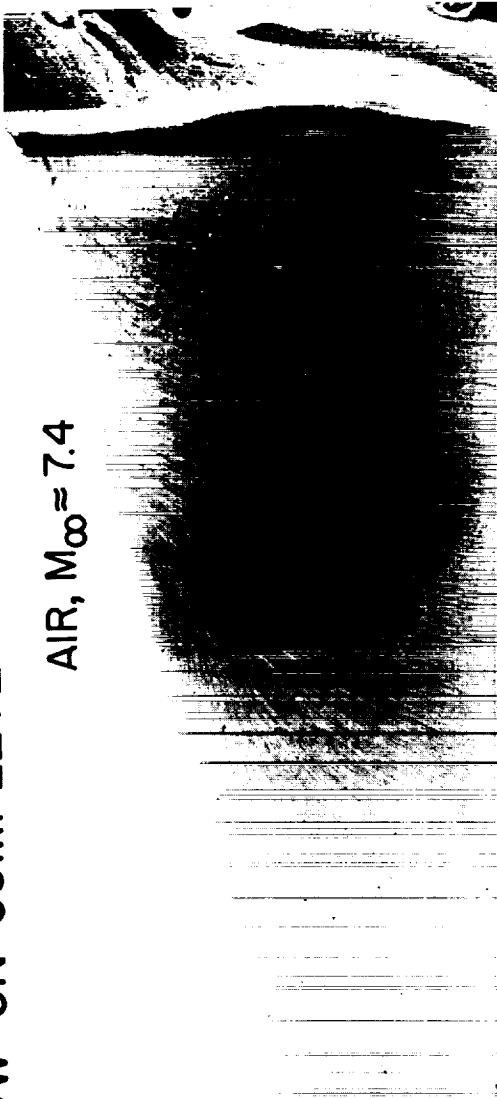
OIL FLOW ON COMPLETE AND TRUNCATED WING AT $\alpha = 60^\circ$

(Figure 6)

Oil-flow patterns obtained at 60° angle of attack in air at Mach 7.4 ($\rho_2/\rho_1 \approx 5.5$) by H. Lee Seegmiller on a model of the complete MSC orbiter and in nitrogen at Mach 20 ($\rho_2/\rho_1 \approx 5.9$) on a truncated model show no significant effects of bow shock impingement. The stagnation line on the wing is essentially at the same location in both photographs — slightly downstream of the leading edge. However, the stagnation line on the complete wing does show a bend near the truncation point of the short wing. This phenomena is discussed by H. Lee Seegmiller in Part I of this paper. This comparison of the complete configurations to that for the truncated wing and similar comparisons at smaller angles of attack indicate no significant effects of the shorter wing on the body-shock—wing-shock impingement trends.

OIL FLOW ON COMPLETE AND TRUNCATED WING AT $\alpha = 60^\circ$

AIR, $M_\infty \approx 7.4$



N_2 , $M_\infty \approx 20$



Figure 6

OIL FLOW ON TRUNCATED MSC ORBITER IN CF_4

(Figure 7)

The shock intersection effects on the truncated wing in CF_4 at Mach 6 (density ratio of 12) for 50° angle of attack are similar to those for nitrogen ($\rho_2/\rho_1 \approx 5.9$) at 40° angle of attack (fig. 4), only slightly more inboard. At an angle of attack of 60° in CF_4 , the shock intersection effects on the wing still persist, though more inboard than at $\alpha = 50^\circ$. At both angles of attack for this high density ratio, the stagnation point on the fuselage remains very near the apex of the model.

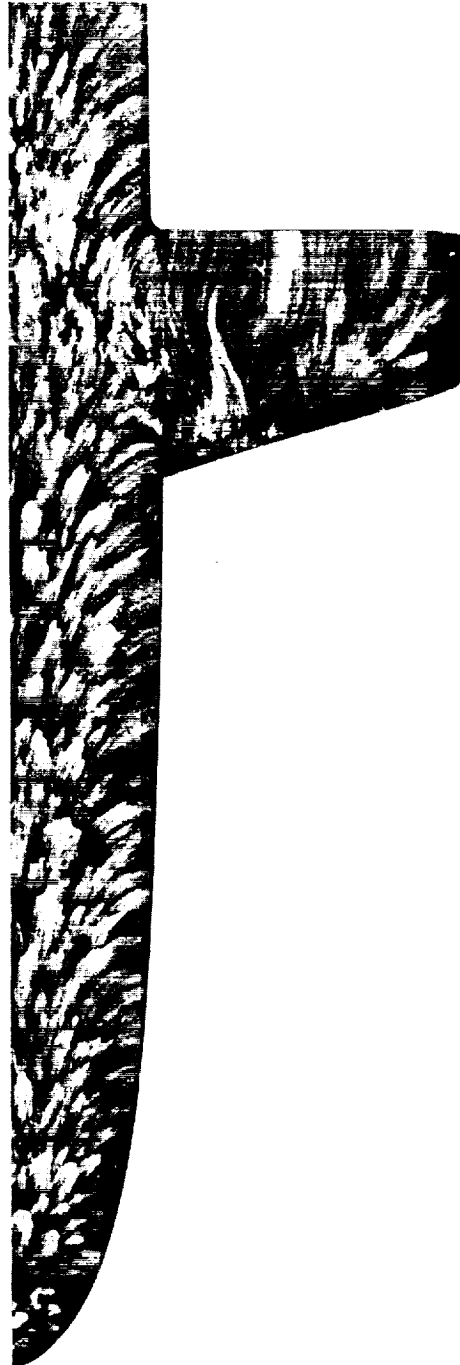
The flow visualization photographs (schlieren, shadowgraph, electron beam, and oil flow) have shown that a critical angle-of-attack range exists in each gas that is associated with a large change in the flow field in which the wing shock standoff distance is greatly increased and the local stagnation region moves off the wing leading edge toward the central portion of the wing. The angle-of-attack range at which this phenomena occurs is relatively independent of stream Mach number but shows a strong dependence on shock density ratio, that is, the larger the density ratio, the larger the angle of attack at which the flow field changeover occurs. The immediate figures and subsequent discussion concentrate on some of the effects of the density-ratio and flow-field change on the heating and aerodynamics of the MSC orbiter.

OIL FLOW ON TRUNCATED MSC ORBITER IN CF₄

$M_\infty = 6, \rho_2/\rho_1 = 12$



$\alpha = 50$



$\alpha = 60$

Figure 7

HEAT-TRANSFER-COEFFICIENT CONTOURS AT $\alpha = 40^\circ$

(Figure 8)

All heat-transfer-coefficient contours are presented in terms of the coefficient ratio h/h_g where h is the experimental local value and h_g is the theoretical value for the stagnation point of a 0.3048-meter-radius sphere scaled by the same scale factor (0.0046) as the truncated-orbiter model. An example of the density-ratio influence on the interference heating from the body-shock--wing-shock intersection can be seen by comparing the nominal heat-transfer-coefficient contours obtained on the truncated orbiter in density-ratio flows of 3.9, 5.9, and 5.6 at 40° angle of attack. The heat-transfer-coefficient distribution along the center line of the fuselage is essentially the same for each test condition shown here; however, the contours for a density ratio of 5.6 are more pointed on the fuselage than those for 3.9. Also, there is essentially no difference in the level of heating on the wing between these three test conditions. The significant difference between the contours obtained in different density-ratio flows is in the interference effects on the wings. The contours obtained in helium (Mach 20, $\rho_2/\rho_1 \approx 3.9$) show only a weak bow-shock--wing-shock interference effect. The wing-root interference is mainly inboard the wing-body junction. The contours obtained in nitrogen ($\rho_2/\rho_1 \approx 5.9$) at approximately the same Reynolds number and Mach number show a much stronger bow-shock--wing-shock interference effect. The wing-root interference is entirely outboard of the wing-body junction. The contours obtained in air (Mach 8, $\rho_2/\rho_1 \approx 5.6$) indicate a bow-shock--wing-shock interference effect similar to that for nitrogen ($\rho_2/\rho_1 \approx 5.9$). These results may be influenced somewhat by the differences in the ratio of wall temperature to total temperature T_w/T_t ; however, it is expected that this influence is minor.

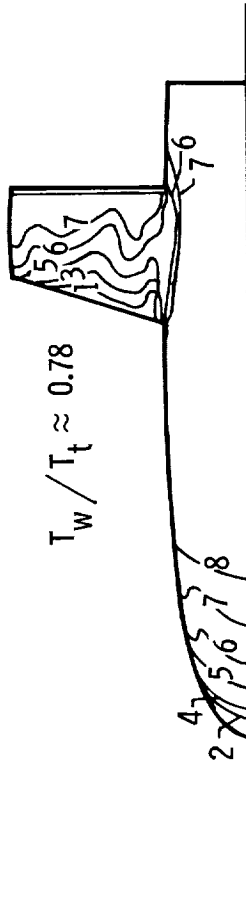
In helium ($\rho_2/\rho_1 \approx 3.9$) at $\alpha = 40^\circ$ the wing-root interference heating is approximately a factor of 2 higher than the seemingly undisturbed distribution along the wing chord between the wing-body junction and the bow-shock--wing-shock interference effects. The bow-shock--wing-shock interference heating factor (again compared to the seemingly undisturbed inboard distribution) is approximately 1.4. In air (at the same Reynolds number) the shock intersection and wing root interference heating effects are essentially the same magnitude (interference heating factor of 1.9).

HEAT-TRANSFER COEFFICIENT CONTOURS AT $\alpha = 40^\circ$

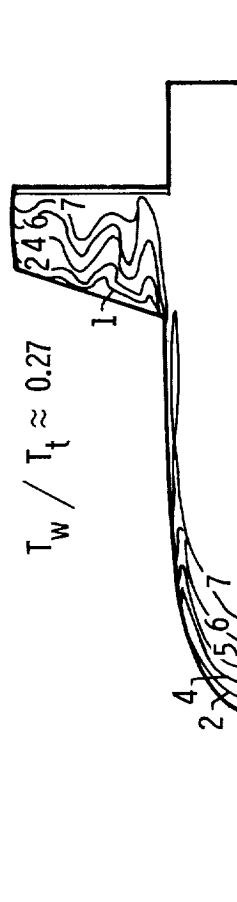
$$R_{\infty,L} = 0.92 \times 10^6$$

ISOTHERM h/h_s

1 .56
2 .34
3 .27
4 .21
5 .18
6 .14
7 .11
8 .09



1 .54
2 .32
3 .25
4 .20
5 .18
6 .14
7 .12



1 .53
2 .29
3 .24
4 .20
5 .17
6 .14

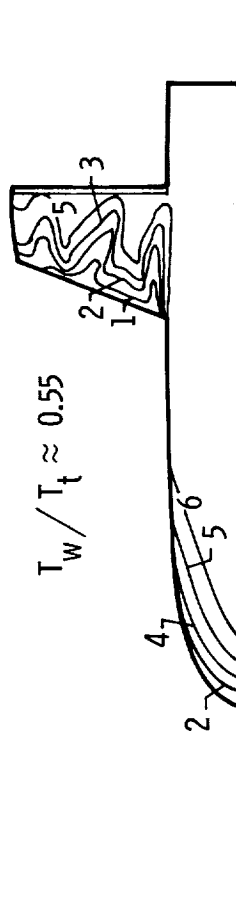


Figure 8

HEAT-TRANSFER-COEFFICIENT CONTOURS AT 60° ANGLE OF ATTACK

(Figure 9)

Heat-transfer-coefficient contours obtained on the truncated orbiter in density-ratio flows of 3.9 and 5.9 at Mach 20 and 5.6 at Mach 8 at 60° angle of attack are presented in figure 9. None of these contours show the large V-shape patterns which resulted from bow-shock--wing-shock interference effects at lower angles of attack (the critical angle-of-attack range for these density-ratio flows has been exceeded here). The distribution and level along the fuselage center line are about the same in each gas. However, the level of heating on the wing is significantly higher (almost a factor of 2) at the higher density ratios (5.9 and 5.6) than at the lower (3.9). At very high angles of attack, this trend for increasing level of heating with increasing density ratio could have significant effects for the higher density ratios expected in flight.

HEAT TRANSFER COEFFICIENT CONTOURS AT 60° ANGLE OF ATTACK

ISOTHERM h/h_s

1	.25
2	.21
3	.16
4	.14
5	.11
6	.09
1	.42
2	.32
3	.25
4	.22
5	.19
6	.17
7	.14
1	.44
2	.31
3	.28
4	.25
5	.22
6	.19
7	.15

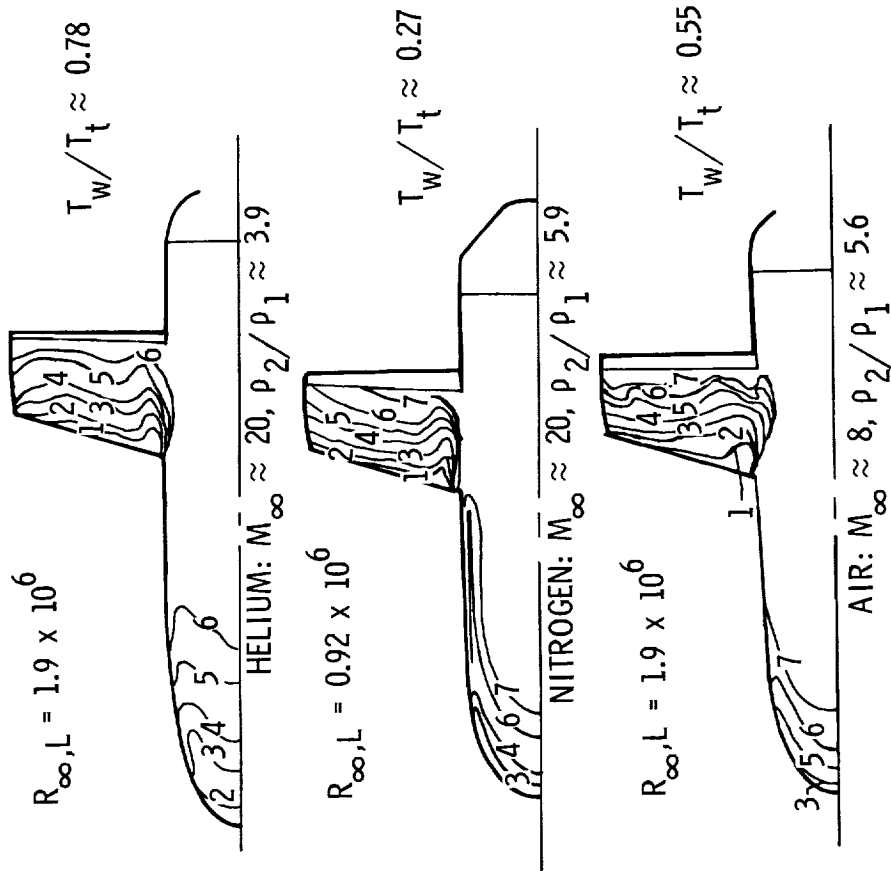


Figure 9

STAGNATION-POINT LOCATION MEASURED FROM OIL-FLOW PATTERNS

(Figure 10)

The effect of the density ratio on the flow field of the truncated orbiter is very evident in the flow visualization pictures. The measured position of the stagnation point on the fuselage as a function of angle of attack is given in figure 10 for the three density-ratio flows of this investigation. The faired data show a much larger rearward movement of the stagnation point in helium ($\rho_2/\rho_1 \approx 3.9$) than in nitrogen ($\rho_2/\rho_1 \approx 5.9$) or CF_4 ($\rho_2/\rho_1 \approx 12$) as the angle of attack increases above 40° . The faired curves for nitrogen and CF_4 are essentially parallel with the stagnation point being more rearward in nitrogen for a given angle of attack.

STAGNATION POINT LOCATION MEASURED FROM OIL FLOW PATTERNS

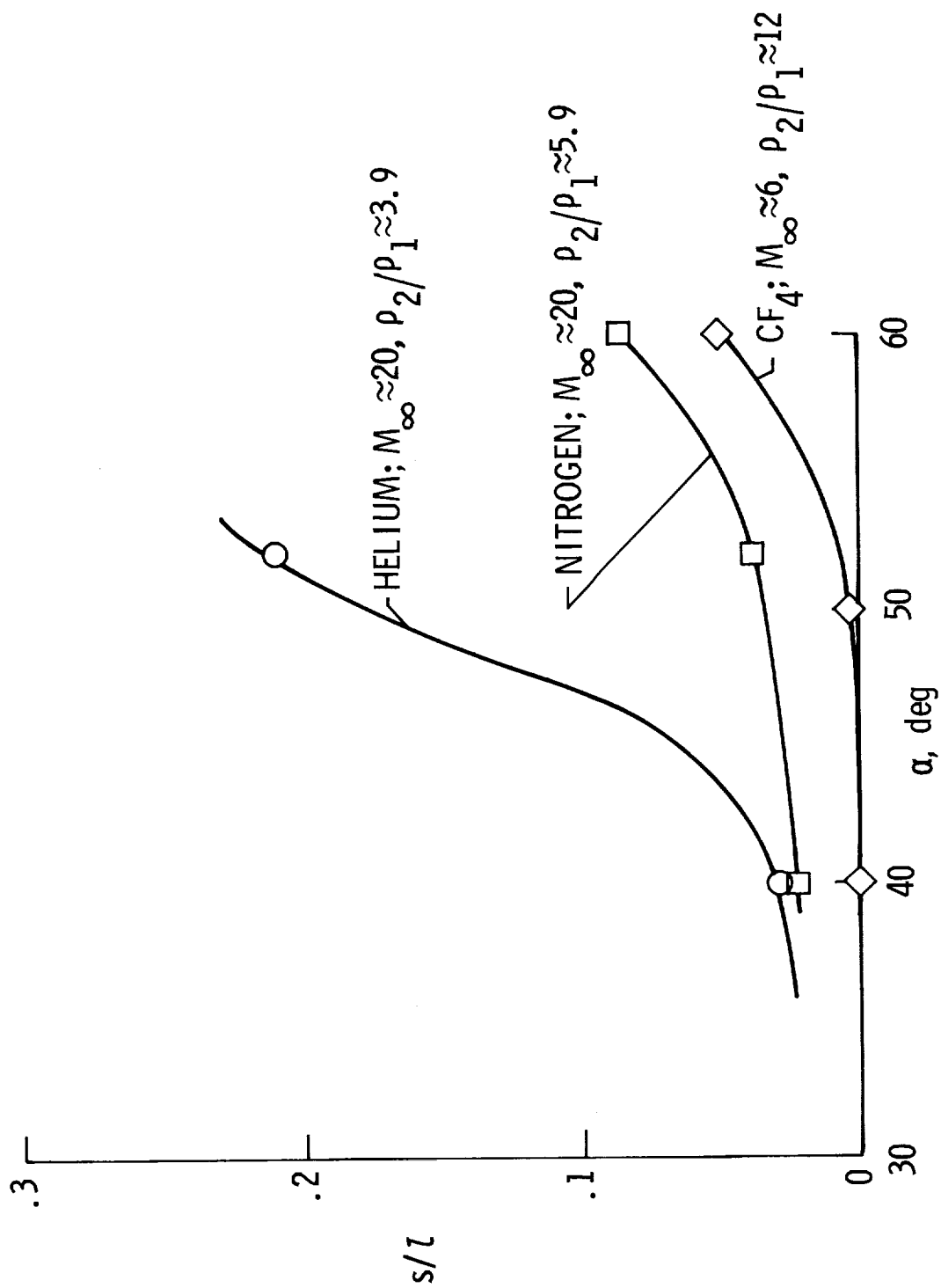


Figure 10

PITCHING MOMENT OF MSC ORBITER AT MACH 20

(Figure 11)

The rearward movement of the stagnation point on the fuselage and the stagnation line on the wing and possible similar effects on the horizontal stabilizer with decreasing density ratio is certain to affect the aerodynamics of the vehicle. Comparison of the measured pitching moments for identical complete MSC orbiter models in density-ratio flows of 3.9 (data obtained by J. P. Arrington in the Langley 22-inch helium tunnel) and 5.9 (data obtained by F. L. Clark in the Langley hypersonic nitrogen tunnel) at Mach 20 shows significant differences at the higher angles of attack ($\alpha \geq 40^\circ$). The divergence of the two curves becomes large at approximately the angle-of-attack range where the large change in the flow field occurs at the lower density ratio. This change is indicated by the rearward shift of the stagnation point on the fuselage and shift of the local stagnation line from the leading edge toward the center of the wing.

PITCHING MOMENT OF MSC ORBITER AT MACH 20

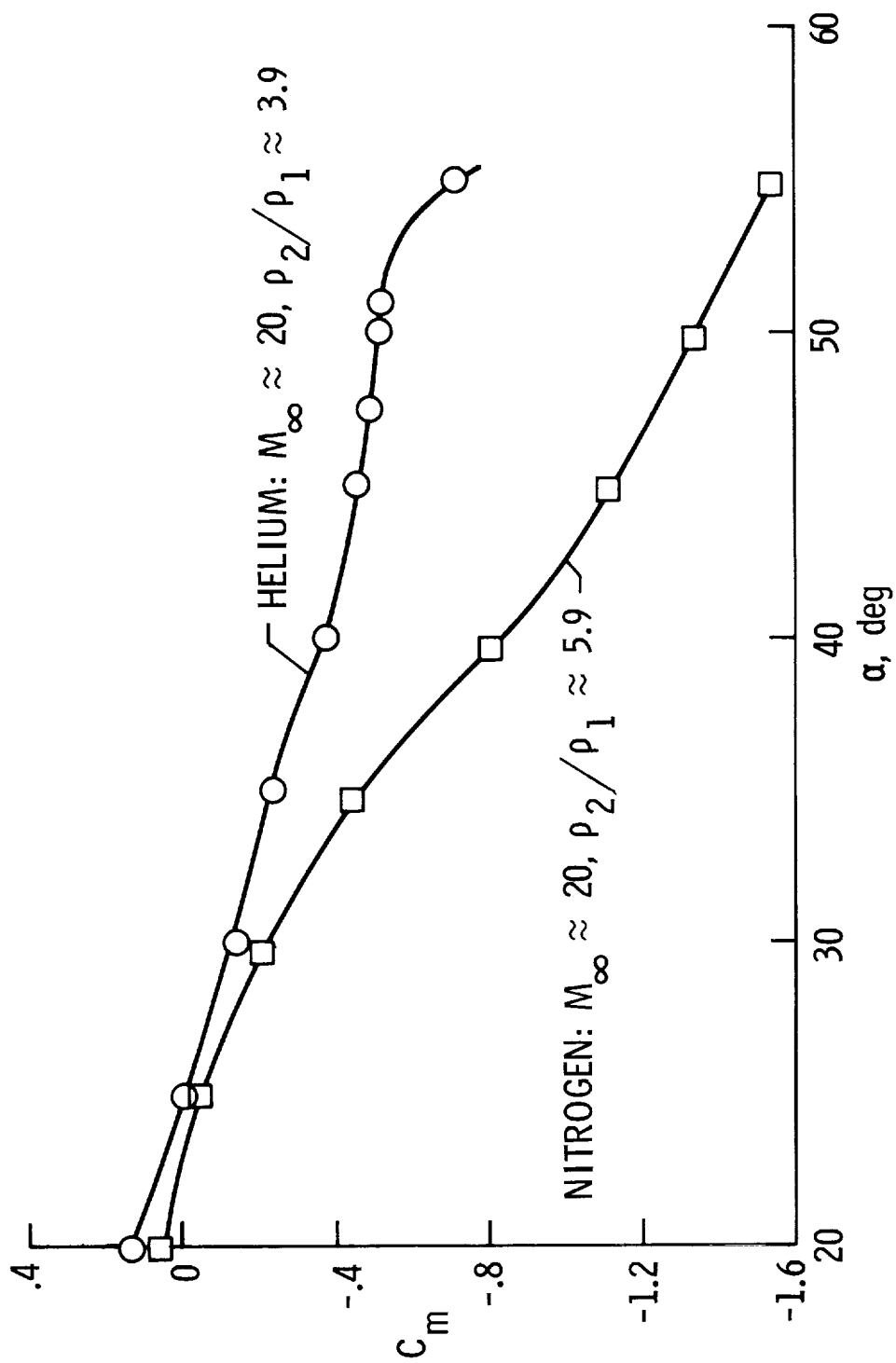


Figure 11

HIGH-CROSS-RANGE ORBITER, $\alpha = 40^\circ$

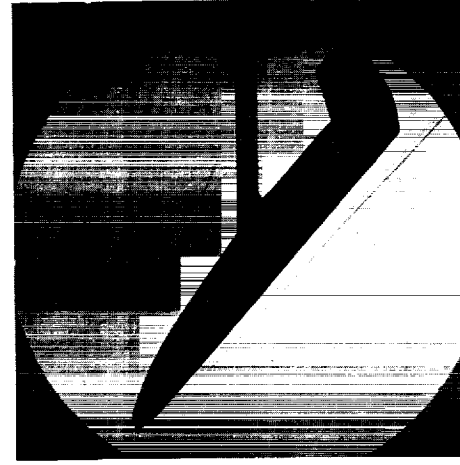
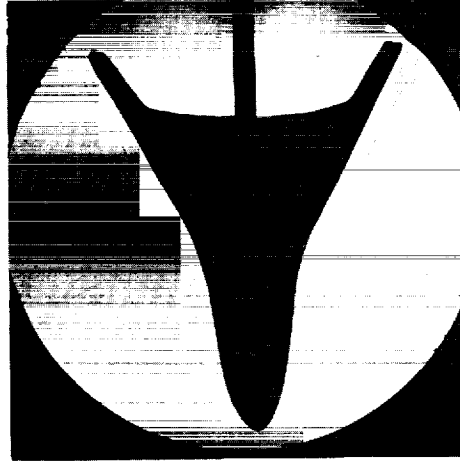
(Figure 12)

The photographs of figure 12 illustrate some possible shock-density-ratio effects on a high-cross-range orbiter. The primary bow shock is much closer to the body at the high density ratio. In addition the plan view indicates that the tip fins may not be free from shock impingement effects at high density ratios.

HIGH CROSS RANGE ORBITER, $\alpha = 40^\circ$



AIR: $M_\infty \approx 8$, $\gamma = 1.4$, $\rho_2/\rho_1 \approx 5.6$



CF4: $M_\infty \approx 6$, $\gamma \approx 1.12$, $\rho_1/\rho_2 \approx 12$

Figure 12

CONCLUSIONS

The primary conclusions pertaining to hypersonic shock-density-ratio effects on the MSC straight-wing orbiter are as follows:

1. Body-shock-wing-shock intersection moves inboard along the wing span with increasing angle of attack until at some critical angle-of-attack range where the flow field changes and the shock impingement effects do not appear to significantly affect the wing heating patterns. This critical angle-of-attack range is associated with a large change in the inviscid flow in which the wing shock standoff distance is greatly increased and the local stagnation region moves from the wing leading edge toward the central portion of the wing.
2. The angle of attack α at which this phenomena occurs is relatively independent of stream Mach number but shows a strong dependence on shock density ratio or specific-heat ratio. In helium (density ratio of 3.9) the changeover occurs between 40° and 50° angle of attack; in air (density ratio of 5.6) it occurs between 50° and 60° ; and in CF_4 (density ratio of 12) it has not yet occurred at $\alpha = 60^\circ$.
3. Since most of the present flight heating predictions for 60° angle of attack are based on measured data in air at $\alpha = 60^\circ$, they may considerably underpredict the rates that will occur in flight at the high shock density ratios.
4. Tests on an identical model in helium (density ratio of 3.9) and nitrogen (density ratio of 5.9) at Mach 20 indicate a significant difference in the pitching-moment curve for high angles of attack ($\alpha > 40^\circ$) which is apparently due to the shock density-ratio effects on the flow field.

5. The trends (conclusions 1 to 4) that real-gas effects will take in flight were indicated by a simulation in which the equilibrium shock-density ratio was varied by testing in various ideal-gas facilities having different specific-heat ratios. This simulation showed some rather drastic effects, but there are two important points which must be noted. First, these effects are strongly configuration-dependent. The straight-wing orbiter with its imbedded shock system is very sensitive to shock-density-ratio effects. Second, these effects are strongly angle-of-attack dependent. Even on the complex straight-wing orbiter, almost all of the significant shock-density-ratio effects occurred for angles of attack in excess of 40° . Therefore, for the present high-cross-range configuration which reenters at lower angles of attack and is essentially free of imbedded shocks, real-gas shock-density-ratio effects will be less significant than those shown herein for the straight-wing low-cross-range orbiter.

SHOCK INTERFERENCE HEATING ON THE SPACE SHUTTLE BOOSTER DURING ASCENT

By O. Brevig and C. Young

Convair Aerospace Division of General Dynamics, San Diego, California

INTRODUCTION

One area experiencing the most severe aerodynamic heating on the Space Shuttle booster is unquestionably the upper surface during ascent. This effect is due to shock impingement on the booster top surface from the orbiter bow shock and resulting shock wave system set up by the booster and orbiter bow shocks. The location and magnitude of the resulting hot spots are functions of orbiter and booster geometry, orbiter position relative to the booster, Mach number, and angle of attack.

To obtain heat transfer data on the booster during ascent, tests were run on the mated configuration in the NASA-LRC 18-inch Variable-Density Hypersonic Wind Tunnel, the NASA-Ames 3.5-foot Hypersonic Wind Tunnel, and the NASA-LRC Unitary Plan Wind Tunnel.

Some of the results obtained from these tests are presented in this paper. Both paint phase-change and thermocouple test results will be discussed. While the paint phase-change test method is of limited value as far as determining peak heat transfer rates due to shock interference, carefully conducted thermocouple tests can give a better estimate of the peak heating values experienced by the models in the interference region.

MATED VEHICLE CONFIGURATION

(Figure 1)

Thin-skin, 0.006-scale stainless steel heat transfer models of the booster and orbiter were used for tests performed in the NASA-Ames 3.5-foot Hypersonic Wind Tunnel and the NASA-LRC Unitary Plan Wind Tunnel. This chart shows the delta-wing booster with the delta-wing orbiter in the baseline position; to the 0.006 scale, the orbiter nose is 1.34 inches ahead of the booster nose. For paint phase-change heat transfer tests conducted in the NASA-LRC 18-inch Mach 8 Variable-Density Hypersonic Wind Tunnel, the booster heat transfer models were constructed by coating RTV-60 silicone rubber over a stainless steel skeleton; the orbiter was made of stycast. The scale for these models was 0.0035 of actual size.

MATED VEHICLE CONFIGURATION

Side View - Baseline Position

DELTA WING ORBITER



DELTA WING BOOSTER

Figure 1

SEQUENCE OF SHADOWGRAPHS

(Figure 2)

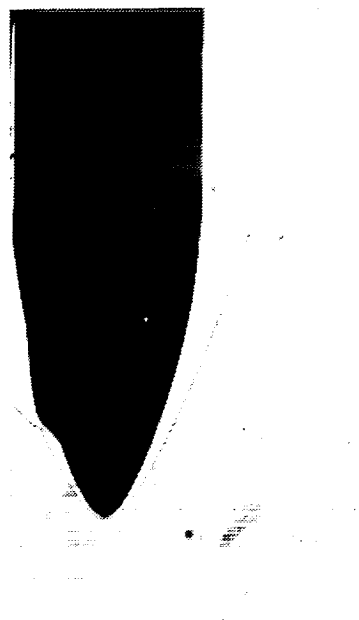
Several shadowgraphs are shown to illustrate some important features about the shock system impinging upon the booster top surface.

These shadowgraphs were taken at the NASA-Ames 3.5-foot Hypersonic Wind Tunnel at a free-stream Mach number of 7.4. For the booster alone it can be seen that the booster bow shock strikes the upper portion of the canopy.

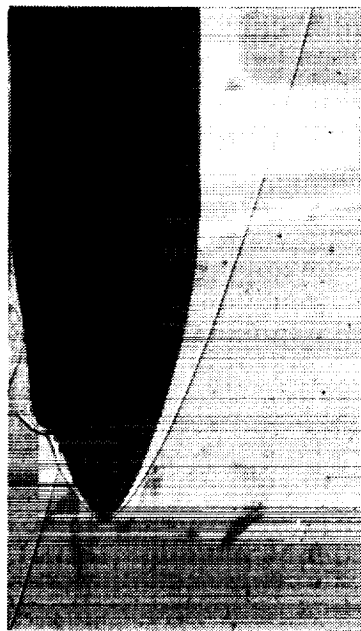
In case of the mated configuration, three positions of the orbiter are shown, with the orbiter bow shock impinging ahead of the booster canopy, on the booster canopy, and behind the booster canopy. Also, the shock pattern set up in the gap region is clearly visible.

SEQUENCE OF SHADOWGRAPHS

MATED TEST AT NASA AMES 3.5 FT. HWT $M = 7.6$, $Re = 3.5 \times 10^6/FT.$



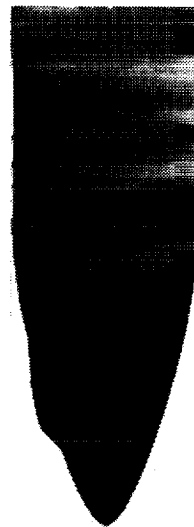
BOOSTER ALONE - $\alpha = 0^\circ$



MATED — SW. ORBITER — $\alpha = 0$



MATED — D.W. ORBITER — $\alpha = -5$



MATED — SW. ORBITER — $\alpha = 0$

Figure 2

SEQUENCE OF SHADOWGRAPHS

(Figure 3)

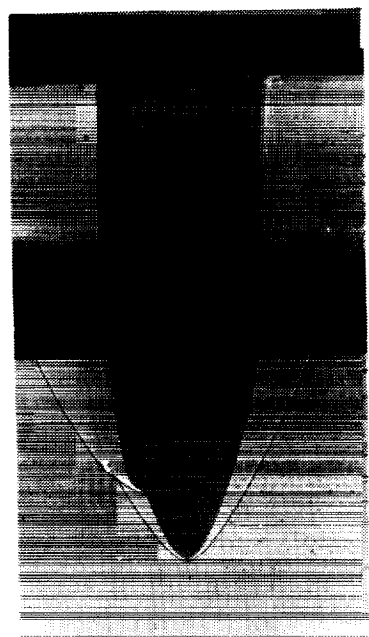
In this illustration, the shadowgraphs obtained from the heat transfer tests conducted at the NASA-LRC Unitary Plan Wind Tunnel are shown. For these tests the free-stream Mach numbers were 3.7 and 2.5.

For booster alone, the bow shock standoff distance increases with decreasing Mach number, and the bow shock does not impinge upon the canopy as was the case for Mach 7.4.

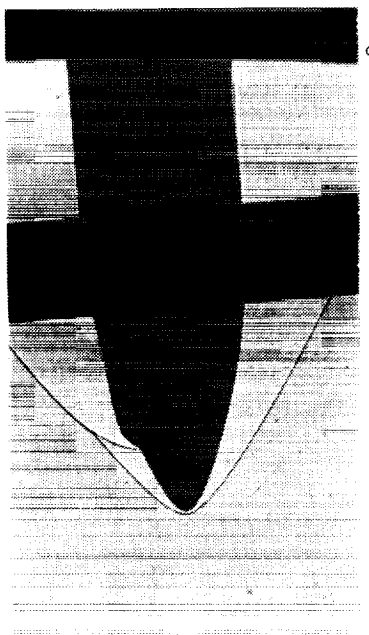
Also shown are typical shock patterns in the gap region between the booster and orbiter at Mach 3.7 and 2.5 for the orbiter in the baseline position.

SEQUENCE OF SHADOWGRAPHS

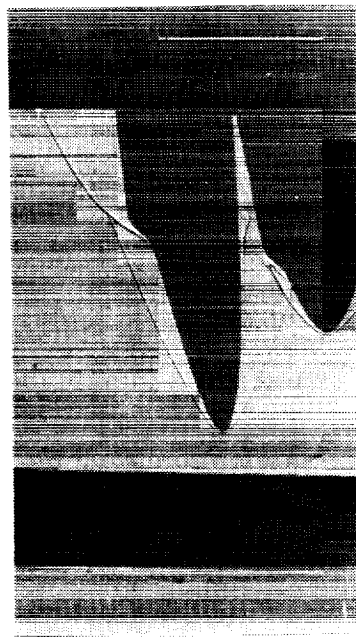
MATED TEST AT NASA-LRC UPWT — $Re = 3. \times 10^6/FT. (9.85 \times 10^6/m)$



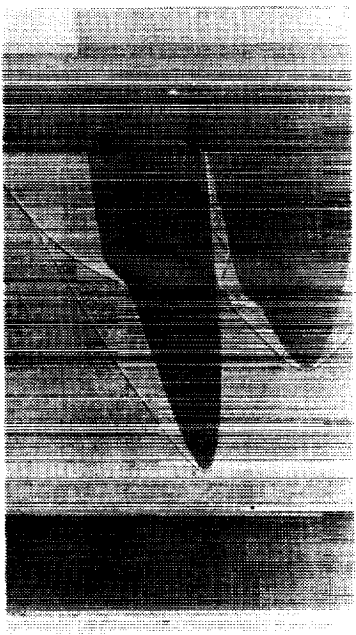
BOOSTER ALONE $M_{\infty} = 3.70, \alpha = 0^{\circ}$



BOOSTER ALONE $M_{\infty} = 2.5, \alpha = 0^{\circ}$



MATED — $M_{\infty} = 3.70, \alpha = -5^{\circ}$



MATED — $M_{\infty} = 2.5, \alpha = -5^{\circ}$

Figure 3

SEQUENCE OF PAINT PHASE-CHANGE PATTERNS

(Figure 4)

Two sets of photographs obtained from the phase-change tests are shown. The difference between these two tests is the orbiter position. As the model-wall temperature increases during the test, the coating changes phase at a selected temperature and becomes transparent. By photographing the model in the test section during the test, heat transfer rates were obtained from the isothermal melt lines recorded on 35 mm film.

The dark regions on the photographs indicate higher heating than the white. Also, the earlier a region becomes dark during the test, the higher the heating rate.

In each case, the first picture shows a few sharp dark spots occurring on the booster top surface at the canopy and behind the canopy region. These are areas of extremely high heating rates due to shock impingement. It should be pointed out that these spots or melt lines were also visible on the first frame of film which showed the model in the tunnel free stream. This is usually defined to be the initial time ($t = 0$); however, for the purpose of these tests, this frame was defined to be equal to time, $t = 0.1$ second to obtain a finite heat transfer rate.

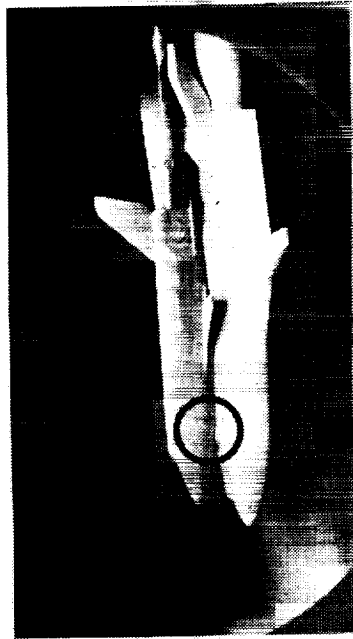
The second picture in each case shows the paint contours or melt lines after 3.0 seconds into the test. Several areas of high heating rates due to shock interference are now clearly visible.

A relative magnitude of the heating rates on the booster upper surface can be visualized by comparing the melt lines developing on the booster top surface with those developing on the bottom surface.

From these pictures, the location of the areas of high heating rates due to shock impingement is clearly indicated.

SEQUENCE OF PAINT PHASE-CHANGE PATTERNS

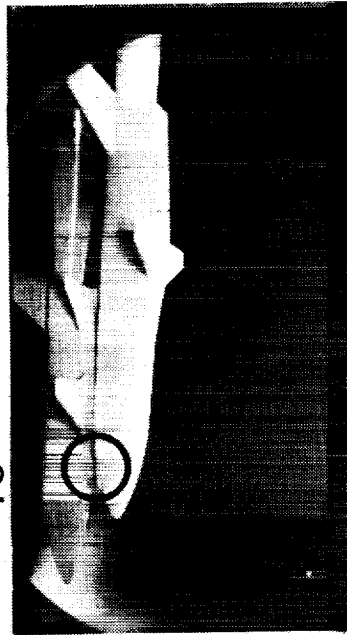
MATED TEST AT NASA LRC MACH 8 VD HWT



TIME = 0.2 SEC.
 $T_{PC} = 533^{\circ} K (300^{\circ} F)$



TIME = 3.0 SEC.



TIME = 0.2 SEC.
 $T_{PC} = 533^{\circ} K (300^{\circ} F)$



TIME = 3.0 SEC.

Figure 4

TYPICAL PAINT PHASE-CHANGE TEST RESULTS

(Figure 5)

To obtain the heat transfer coefficients on the booster from the paint phase-change melt lines, the governing transient one-dimensional heat conduction equation must be solved with appropriate initial and boundary conditions. A typical solution to this equation is shown for silicone rubber and stycast, respectively, assuming a paint phase-change temperature of 533°K (300°F). The heat transfer coefficient ($\text{watts}/\text{cm}^2 \text{ sec.}$) nondimensionalized with the stagnation heat transfer rate to a 1.15 cm (0.0035 ft.) radius sphere is plotted versus time.

From the film isothermal melt-lines and the curve for silicone rubber, typical isothermal transfer-rate lines on the booster are also shown.

It is quite obvious that from the data shown, the peak heat transfer coefficient due to shock impingement cannot be determined very accurately by this method due to the errors involved in determining the initial time ($t=0$) and the fact that the isotherm melt lines were visible on the very first picture frame. This would indicate an infinite heat transfer coefficient. However, due to the errors involved, relatively long times (one second) are required for this particular paint to obtain heat transfer coefficients within 10% accuracy or less.

A paint with higher phase-change temperature would allow a better estimate of the high heat transfer coefficients associated with shock interference heating. However, our use of a 644°K (700°F) paint for entry heat transfer tests was not successful due to optical difficulties with a semiclear yellow paint and black-and-white film.

TYPICAL PAINT PHASE-CHANGE TEST RESULTS **Booster Paint Isoheat-Transfer Lines During Ascent**

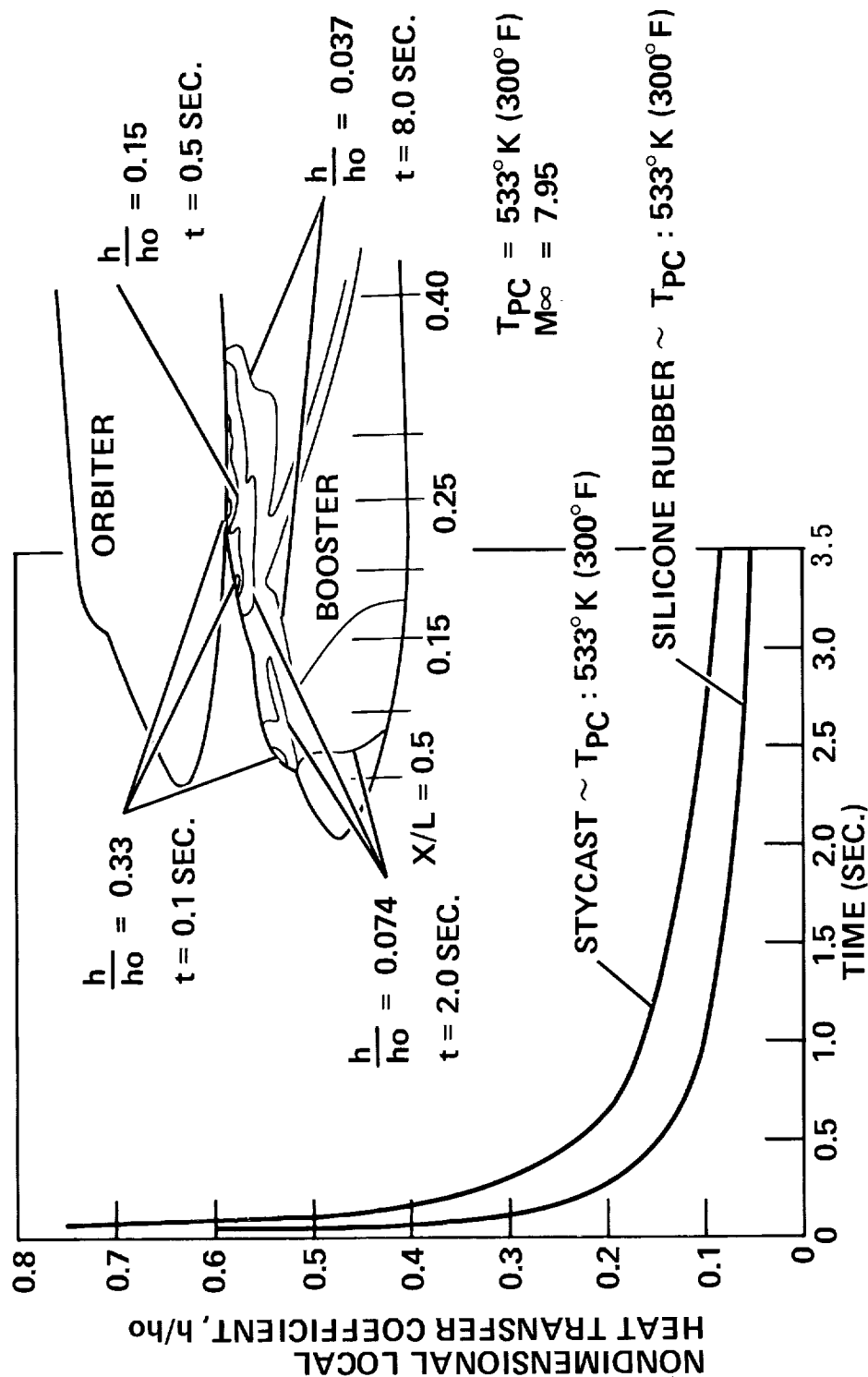


Figure 5

HEATING RATE DISTRIBUTION ON BOOSTER TOP AND BOTTOM CENTERLINE DURING ASCENT

(Figure 6)

From the isoheat-transfer rate contours on the booster obtained from the paint tests, the heat transfer coefficient distribution on the booster top and bottom surfaces can be plotted versus the nondimensionalized booster length, as shown.

The relative position of the orbiter to the booster for this particular case is also indicated. The angle of attack was 0° , the Mach number 7.95, and unit Reynolds number $1.3 \times 10^7/\text{m}$ ($3.96 \times 10^6/\text{ft.}$). Three hot spots due to shock impingement on the booster top surface are evident. The booster bow shock impinges on the canopy and the orbiter bow shock hits the booster top surface behind the canopy at an axial distance of 18% from the booster nose. A second shock is seen to impinge on the booster top surface at an axial distance of 24%.

From this slide it can be seen that the peak heat transfer coefficients on the top surface center line due to shock interference are at least 6 to 14 times that on the bottom centerline depending on axial distance. However, as already pointed out, the absolute magnitude of the peak heat transfer coefficients cannot be estimated accurately.

HEATING RATE DISTRIBUTION ON BOOSTER TOP & BOTTOM CENTERLINE DURING ASCENT

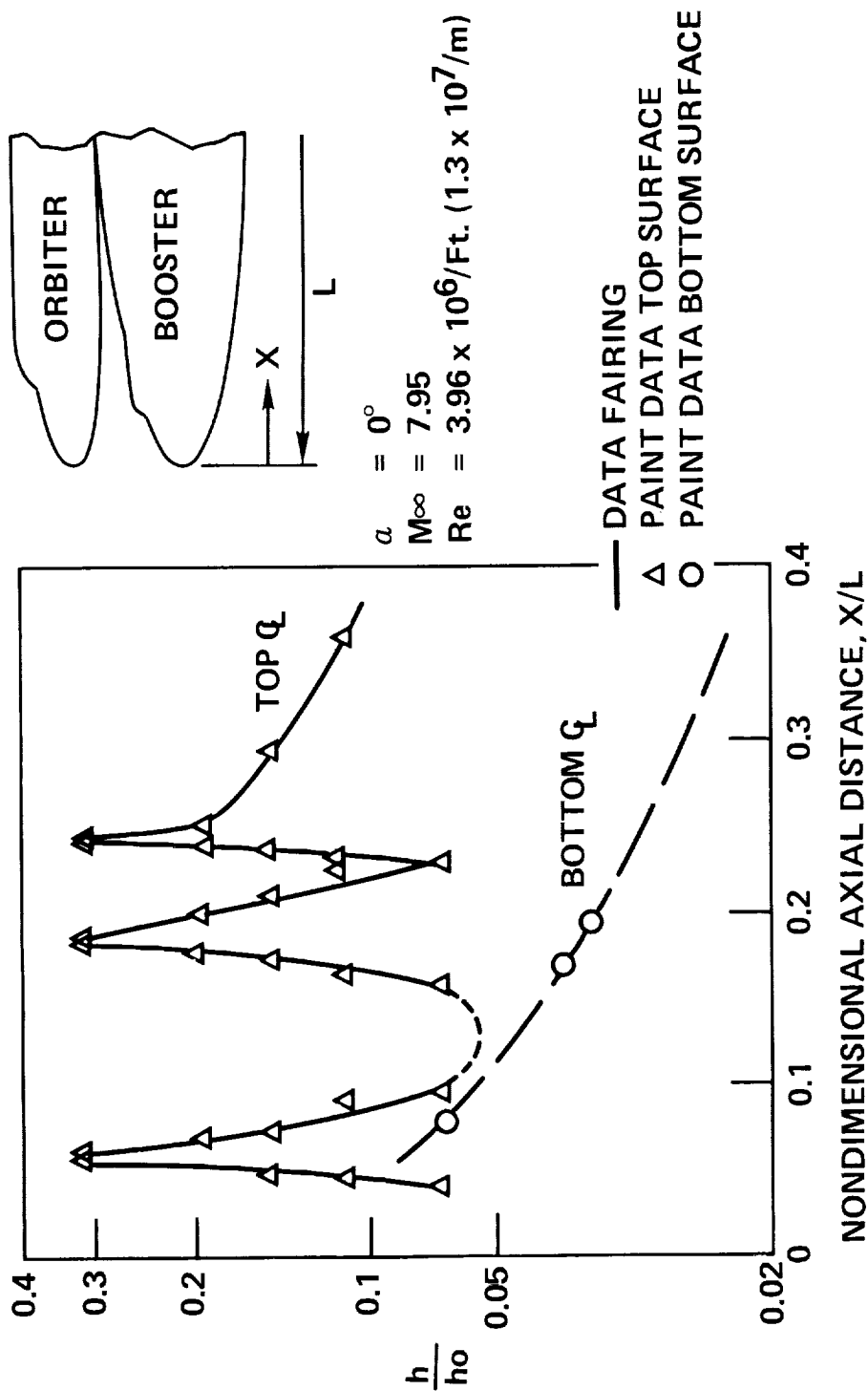


Figure 6

HEATING RATE DISTRIBUTION ON BOOSTER TOP AND BOTTOM CENTERLINE DURING ASCENT

(Figure 7)

This illustration shows the effect of changing angle of attack upon the heat transfer distribution on the upper surface during ascent.

As compared with the previous illustration, the effect of changing the angle of attack from 0° to -5° is to change the shock pattern in the gap regions between the orbiter and booster. Thus, two shocks are apparent behind the orbiter bow shock. The difference in the peak heat transfer coefficients due to shock impingement cannot be assessed. However, from thermocouple tests on the booster alone, a 20% increase in the heat transfer rate on the canopy was noted at -5° angle of attack, and a free-stream Mach number of 7.4 as compared to 0° angle of attack.

HEATING RATE DISTRIBUTION ON BOOSTER TOP & BOTTOM CENTERLINE DURING ASCENT

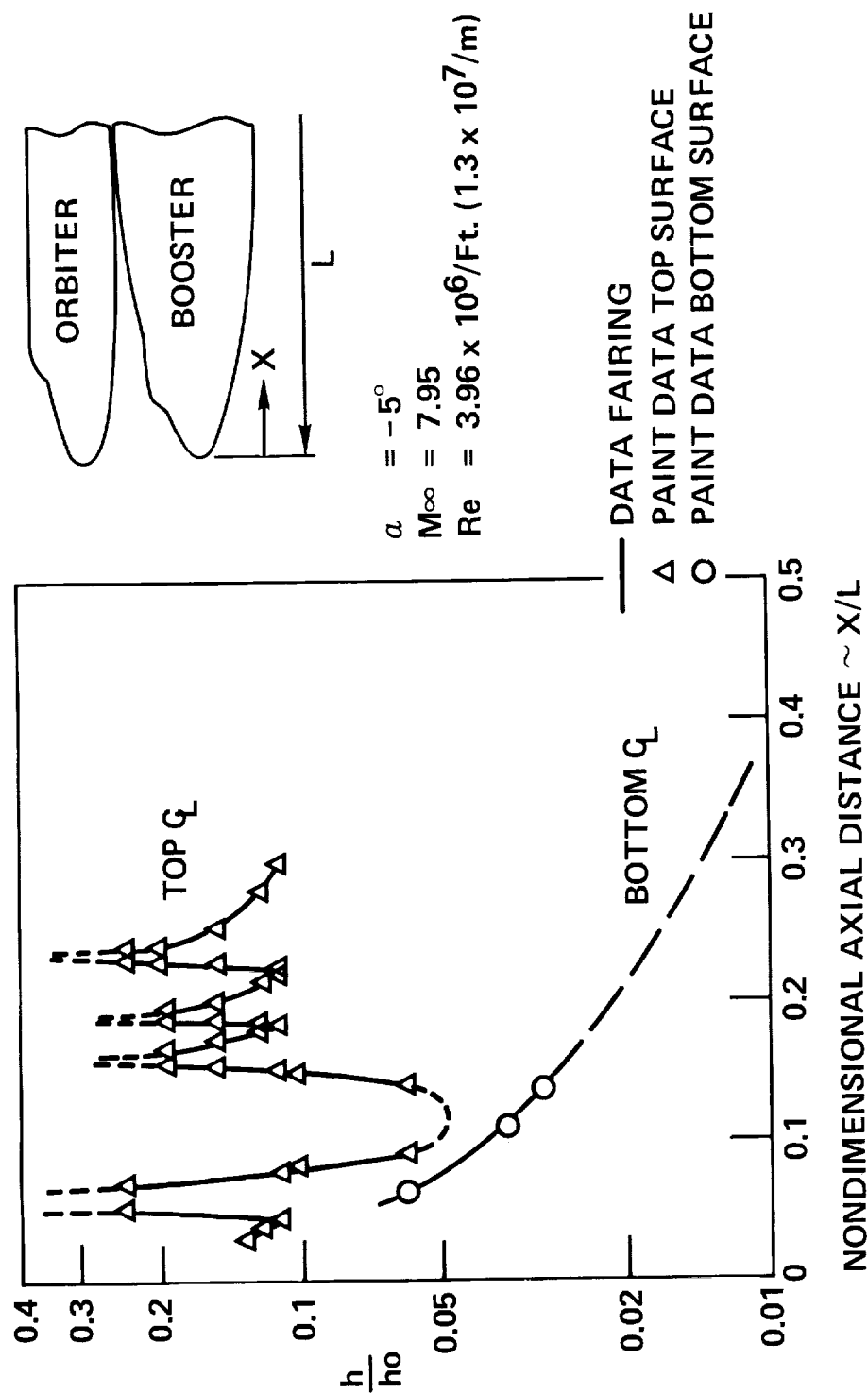


Figure 7

ASCENT HEATING (BOOSTER ONLY)

(Figure 8)

A correlation between paint phase-change and thermocouple heat transfer rate data is shown for booster alone at 0° angle of attack. The heat transfer rate distribution on the top surface is indicated by triangles while the round symbols show the heat transfer distribution on the lower surface. Paint data is indicated by open symbols, while the filled symbols show thermocouple data.

Interference heating on the canopy due to the booster bow shock is strongly evident. Also, the heat transfer coefficients on the lower surface were predicted reasonably well with laminar tangent cone-Prandtl Meyer expansion theory.

Reasonably good correlation between paint and thermocouple data was obtained when the thermocouples were corrected for conduction errors. Also, due to the narrow region of the hot spots on the booster top surface due to shock interference, an extremely small spacing of the thermocouples is required to measure the true peak heating rates.

ASCENT HEATING - (BOOSTER ONLY) **Correlation of Paint & Thermocouple Test Data**

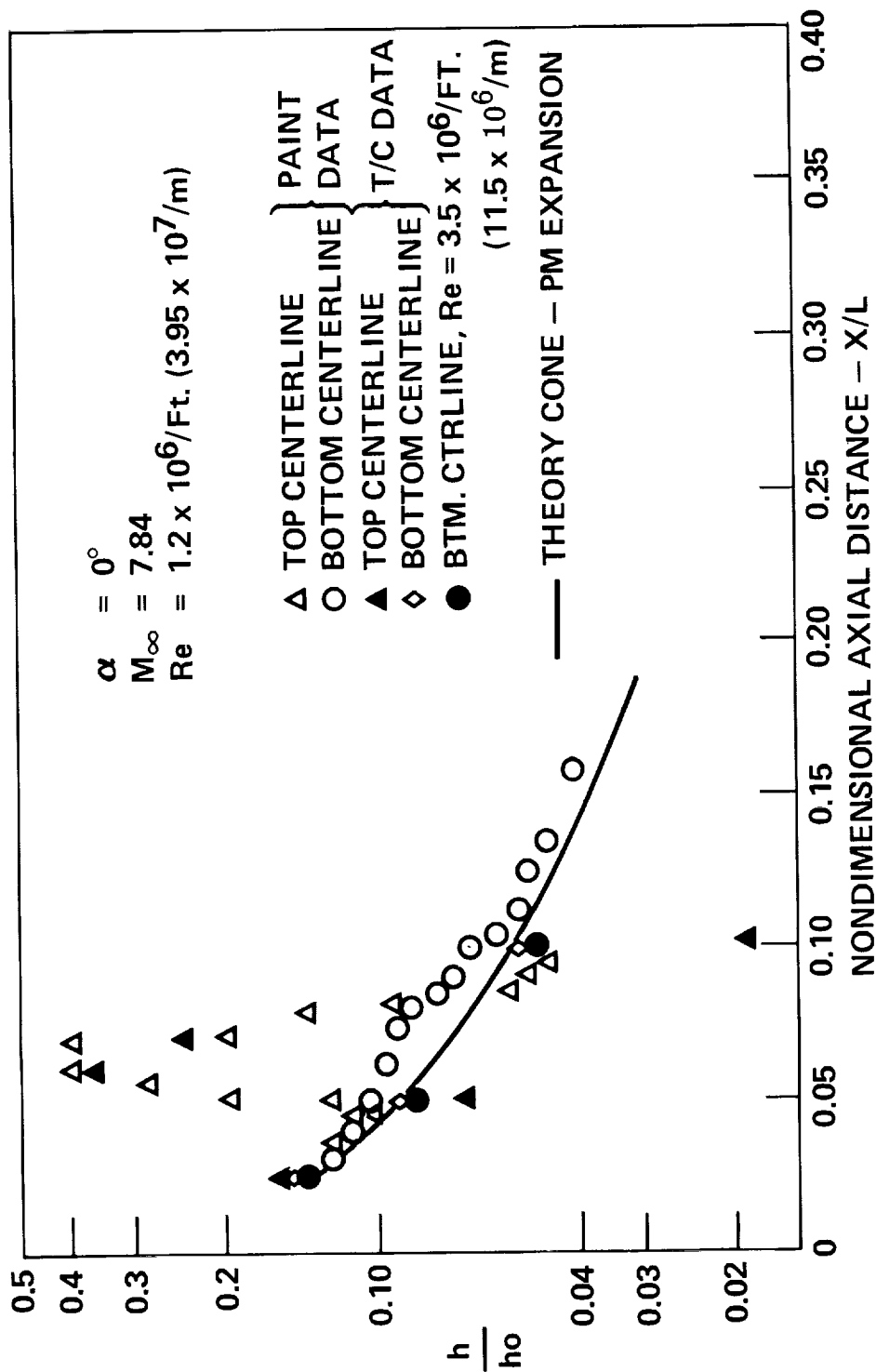


Figure 8

EFFECT OF ORBITER POSITION ON CANOPY HEATING

(Figure 9)

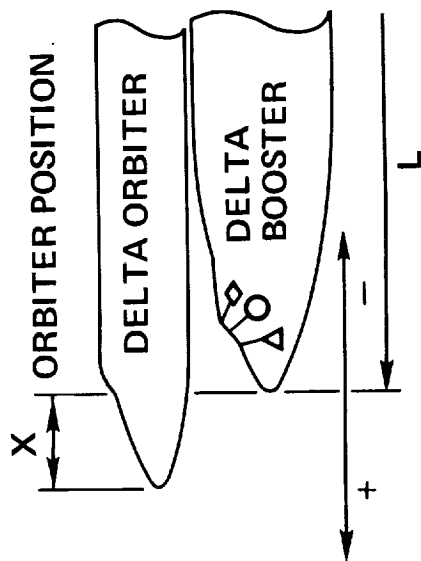
In an effort to determine the effect of the orbiter bow shock impinging upon the booster canopy, a series of tests was repeated whereby the orbiter bow shock was driven over the three thermocouples on the booster canopy as indicated.

The local heat transfer rate measured by the thermocouples corrected for conduction errors and nondimensionalized by the stagnation heating to a one-foot radius sphere to 0.006 scale is plotted versus relative orbiter position, X , nondimensionalized by the booster length.

As the orbiter moves from left to right as indicated, a rapid increase in the heat transfer rates is noted when the orbiter shock strikes the booster canopy. The open symbols are for an angle of attack of 0° . The filled symbols are for an angle of attack of -5° . As evidenced from the shadowgraphs, the orbiter shock impinges directly on the thermocouple located in the center of the canopy windshield in this case. Also, a heat transfer rate about 1.3 times that of the stagnation heating of a one-foot-radius sphere (0.006 scale) was obtained. This is about three times the heat transfer rate measured on the canopy due to impingement from the booster bow shock alone, and about 20 times the heating transfer rate on the lower surface at the same station at an angle of attack of 0° .

Due to the orbiter bow shock impinging upon the booster top surface and due to the reflection of the booster and orbiter bow shocks from the orbiter and booster surfaces, a multiple shock system will be set up in the gap between the orbiter and booster. To detect the peak heating rates with thermocouples necessitates a very close spacing. However, due to the finite spacing required, these peaks may be missed. By careful testing using both paint techniques and shadowgraphs, coupled with the thermocouple method discussed above, a better estimate of the peak heating rates on the booster top surface during ascent should be obtained.

EFFECT OF ORBITER POSITION ON CANOPY HEATING



AMES 3.5 FT. HWT, T/C DATA

$M_\infty = 7.4$

$Re = 3.5 \times 10^6/FT. (11.5 \times 10^6/m)$

$\circ \Delta \diamond \quad \alpha = 0^\circ$

$\bullet \blacktriangle \blacklozenge \quad \alpha = -5^\circ$

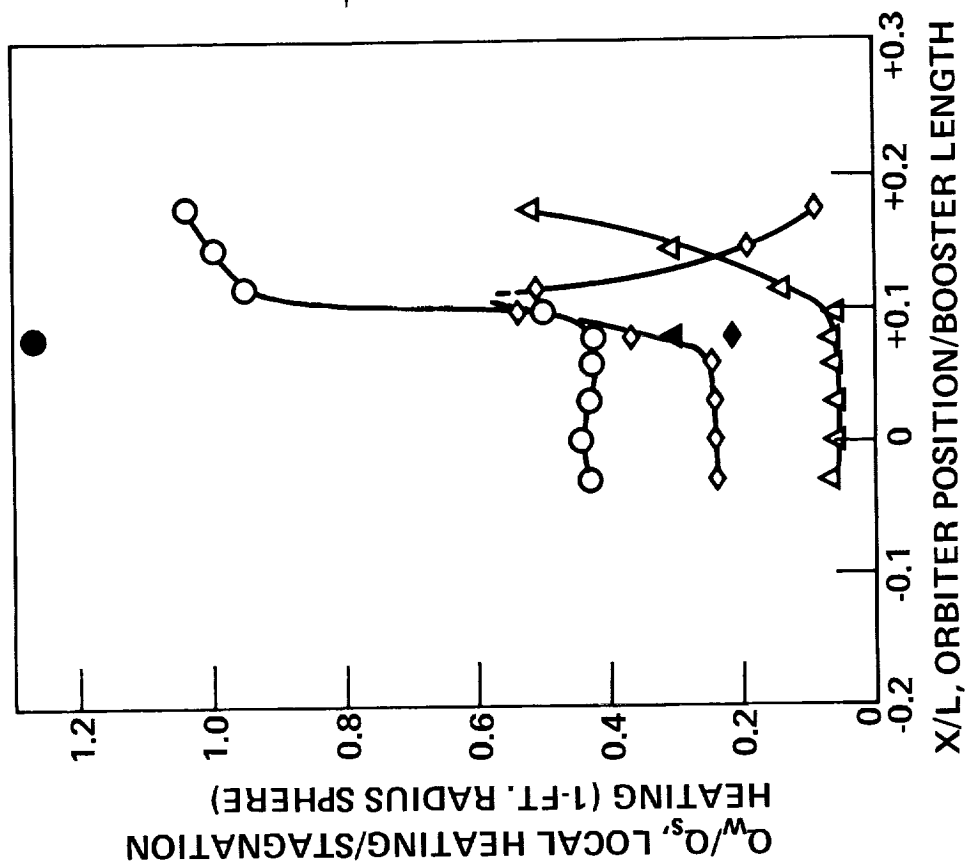


Figure 9

EFFECT OF MACH NUMBER ON GAP HEATING

(Figure 10)

Shown here is the effect of free-stream Mach number upon the heat transfer coefficients measured in the gap between the booster and orbiter for the orbiter in the baseline position.

The heat transfer coefficients for the mated configuration are nondimensionalized, with the heat transfer coefficients obtained for the booster alone and plotted versus nondimensionalized booster length.

The angle of attack was 0° ; free-stream Mach numbers and free-stream unit Reynolds numbers were as indicated.

Despite the large spacing between the thermocouples, the free-stream Mach number has a strong effect upon the gap heating. A closer spacing of the thermocouples, however, will give a better indication of the true gap heating, since for the present tests the peak heating rates were missed.

EFFECT OF MACH NUMBER ON GAP HEATING

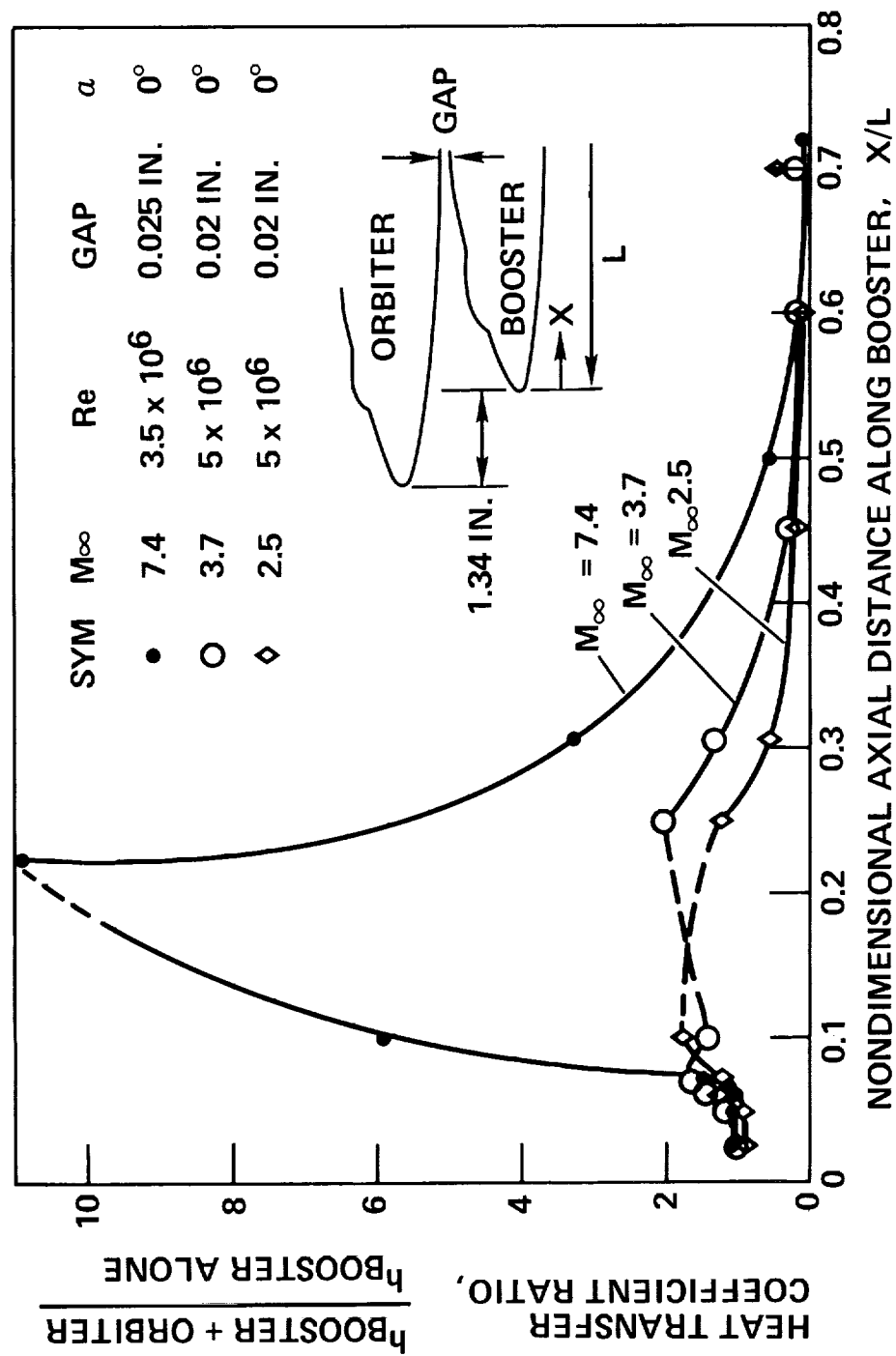


Figure 10

CONCLUSIONS

Several conclusions can be drawn concerning the interference heating on the booster top surface during ascent.

1. Due to the shock pattern set up by the orbiter and booster bow shocks in the gap region, the booster experiences high localized heating rates due to shock impingement.
2. Except for the regions of high localized heating rates due to shock impingement, a reasonable correlation between paint phase-change and thermocouple heat transfer rate test data was obtained.
3. In the areas of high localized heating due to shock impingement, the paint phase-change test data cannot be used accurately to measure the peak heat transfer rates. Thermocouples must be used in order to measure these peaks.
4. Interference heating in the gap region increases with increasing free-stream Mach number.

LEE-SIDE HEATING INVESTIGATIONS

PART I - EXPERIMENTAL LEE-SIDE HEATING STUDIES ON A DELTA-WING ORBITER

By Jerry N. Hefner and Allen H. Whitehead, Jr.
NASA Langley Research Center, Hampton, Virginia

INTRODUCTION

This paper presents results from a lee-surface heating investigation at Mach 6 on a delta-wing orbiter. The heating for this configuration is compared with limited lee-surface heating data on a straight-wing orbiter. The effects of Reynolds number and angle of attack on the magnitude and distribution of the lee-surface heating are shown as well as a brief discussion of the applicability of these wind-tunnel results to flight.

SURFACE FLOW AND HEATING ON DELTA-WING ORBITTER

(Figures 1 and 2)

Surface flow and heating distributions are shown for angles of attack (α) of 20° and 40° at a free-stream Mach number (M_∞) of 6 and a free-stream Reynolds number based on model length ($R_{\infty,L}$) of 5.2×10^6 . The lines of constant heating are given as the ratio of local heat-transfer coefficient (h) to the stagnation heat-transfer coefficient (h_{ref}) on a 0.305-m- (1-foot-) radius sphere scaled by the same factor as the model. The "featherlike" regions shown on the oil-flow photographs indicate the presence of vortices. The feather indicates a region of high shear and, by analogy, of high heating caused by the impingement of the vortices onto the lee surface.

Note that the vortices occur at both the high and the low angles of attack with the maximum lee-surface heating occurring on the meridian in the vicinity of the nose. The observation that the maximum heating induced by the vortices occurs near the nose region suggests that nose shaping and bluntness play a dominant role in the formation of these vortices. Further evidence of this is given by some unpublished results obtained in the Langley 11-inch hypersonic tunnel by Allen H. Whitehead, Jr., and Mitchel H. Bertram which show that, on a sharp flat delta wing at relatively low incidence, proper contouring of the nose region can eliminate or reduce the unfavorable effects resulting from the vortices. This result, although not directly applicable to the blunt-nose shuttle configurations, does offer hope that the proper shaping of the shuttle nose can reduce or eliminate the effect of the vortex. Studies are needed to examine the effect of nose shaping and bluntness on the vortex generation and, consequently, heating on shuttlelike geometries.

SURFACE FLOW AND HEATING ON DELTA-WING ORBITER

$M_\infty = 6$, $R_{\infty,L} = 5.2 \times 10^6$, $\alpha = 20^\circ$

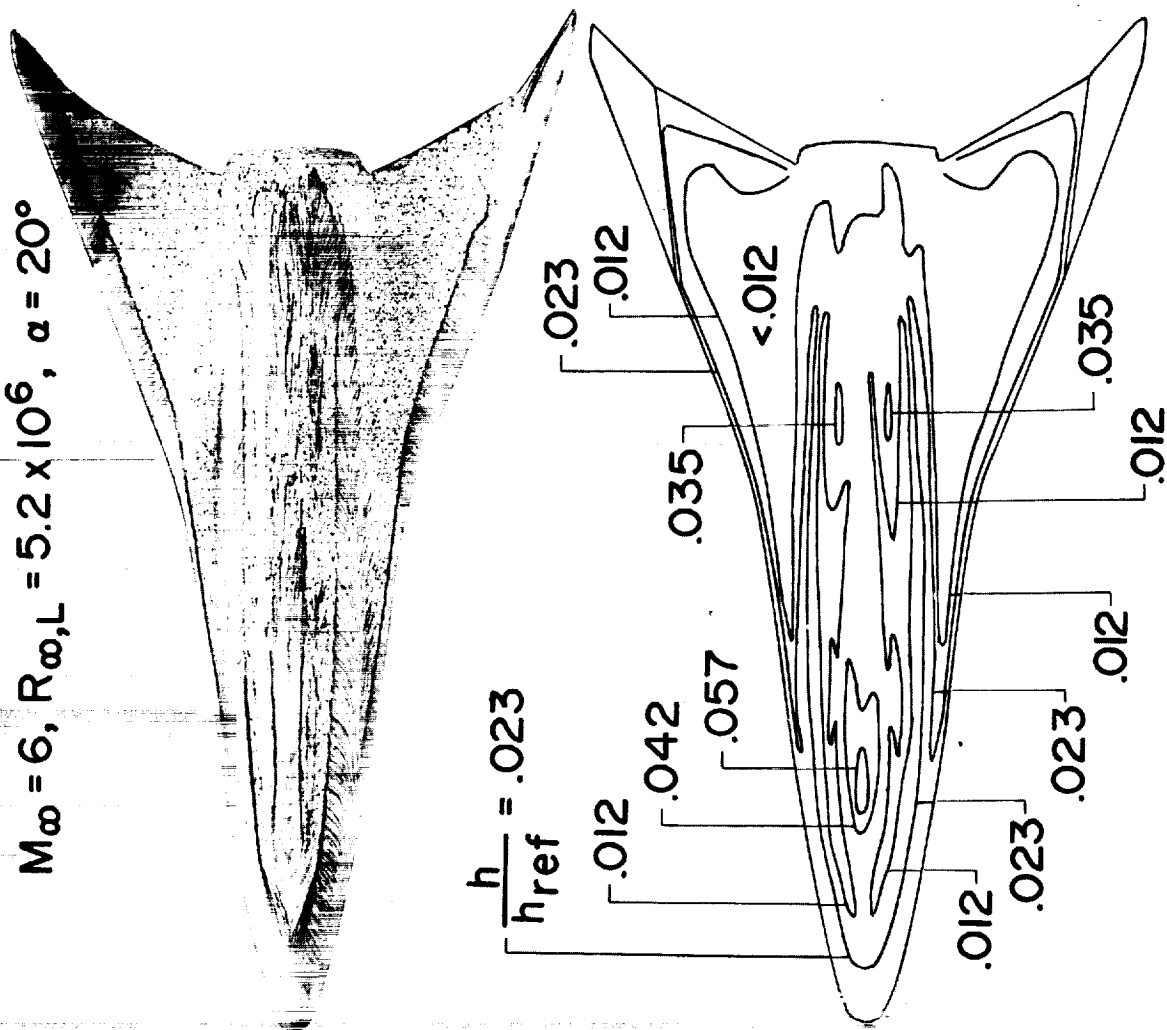


Figure 1

SURFACE FLOW AND HEATING ON DELTA-WING ORBITER

$M_\infty = 6$, $R_\infty L = 5.2 \times 10^6$, $\alpha = 40^\circ$

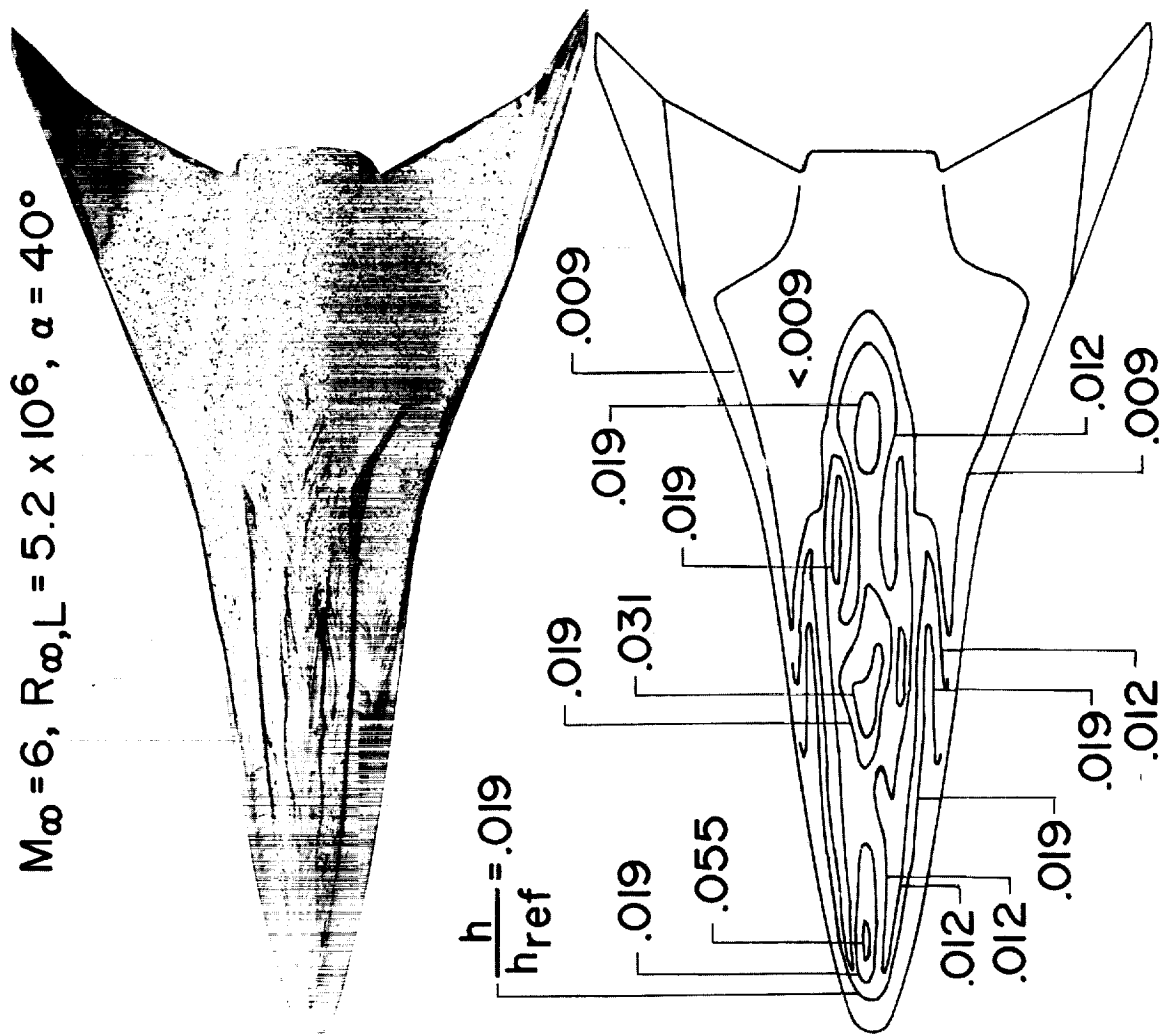


Figure 2

(Figure 3)

As indicated in the two previous figures, the maximum lee-surface heating occurs along the center line or meridian. The magnitude and distribution of this heating is shown as a function of the ratio of surface distance to the overall model length (x_s/L) for angles of attack between 20° and 50° . The zero-angle-of-attack heating is shown so that a comparison with the angle-of-attack heating can be made. Note the relatively large regions where the lee-surface meridian heating exceeds that at zero angle of attack. Again note that the maximum lee-surface heating occurs in the vicinity of the nose.

As the angle of attack increases from 20° to 50° , several heating peaks develop along the lee meridian. This first peak represents the maximum lee-surface heating and increases only slightly with increasing angle of attack. In contrast, the position of the peak heating moves forward significantly with increasing angle of attack, especially at angles of attack between 20° and 35° .

Some calculations of the radiation equilibrium surface temperatures (T_w) for 20° angle of attack were made by assuming an emissivity of 0.8 and a maximum heat-transfer rate (\dot{q}_{max}) of 38.70×10^{-4} watt/m²-°K (80 Btu/ft²-sec-°R) for a typical 1500-nautical-mile cross-range trajectory (ref. 1). The resulting temperatures ranged from 727° K (1309° R) to a peak of 1107° K (1992° R). The existence of this extremely severe heating dictates further studies of vortex-induced peak heating on particular shuttle configurations.

It has been suggested that the lee-surface or upper surface heating can be calculated by two-dimensional laminar or turbulent theory (for present study, Monaghan (ref. 2) or Spalding-Chi (ref. 3), respectively), assuming an attached flow in the cross-flow plane (ref. 4). This approach predicts neither the magnitude nor the trend of the experimental results. In fact, since much of the flow on the lee surface is separated and vortex-dominated, agreement between data and theory should not be expected.

Lee-surface heating data obtained for only selected longitudinal stations are of limited benefit in defining the lee-side flow phenomena, since the lee-meridian heating is nonuniform and since the maximum heating occurs near the nose. Furthermore, many investigations may have failed to obtain the maximum lee-surface heating since data, sufficiently close to the nose, were not obtained.

CENTER-LINE LEE-SURFACE HEATING AT ANGLE OF ATTACK

$M_\infty = 6$; $R_\infty L = 5.2 \times 10^6$; $h_{ref} = .042 \times 10^{-4} \text{ W/m}^2 \cdot \text{K} (.086 \text{ Btu/ft}^2 \cdot \text{sec} \cdot \text{R})$

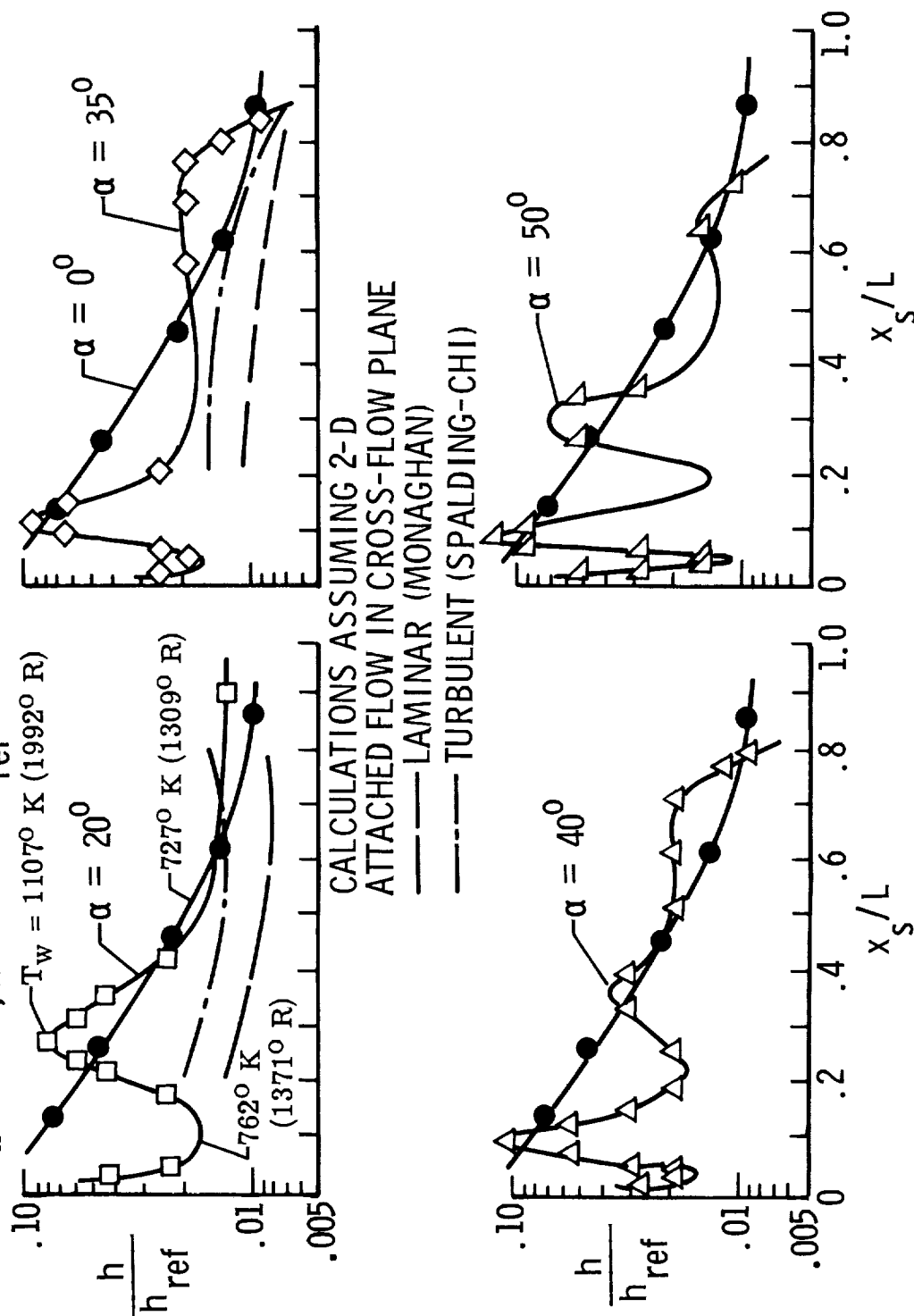


Figure 3

REGIONS OF INCREASED HEATING ON LEE SURFACE

(Figure 4)

This figure illustrates the regions on the lee surface of the delta-wing orbiter where the heating is greater than that at zero angle of attack. The upper half of the model planform shows the increased heating regions for $\alpha = 40^\circ$, whereas the bottom half shows the higher heating regions for $\alpha = 20^\circ$. The "fingerlike" projections of these heating areas are attributed to the vortex impingement onto the lee surface at angle of attack. Note that the peak heating near the nose of the configuration at $\alpha = 40^\circ$ is confined to a small area.

REGIONS OF INCREASED HEATING ON LEE SURFACE

$$M_{\infty} = 6, R_{\infty, L} = 5.2 \times 10^6$$

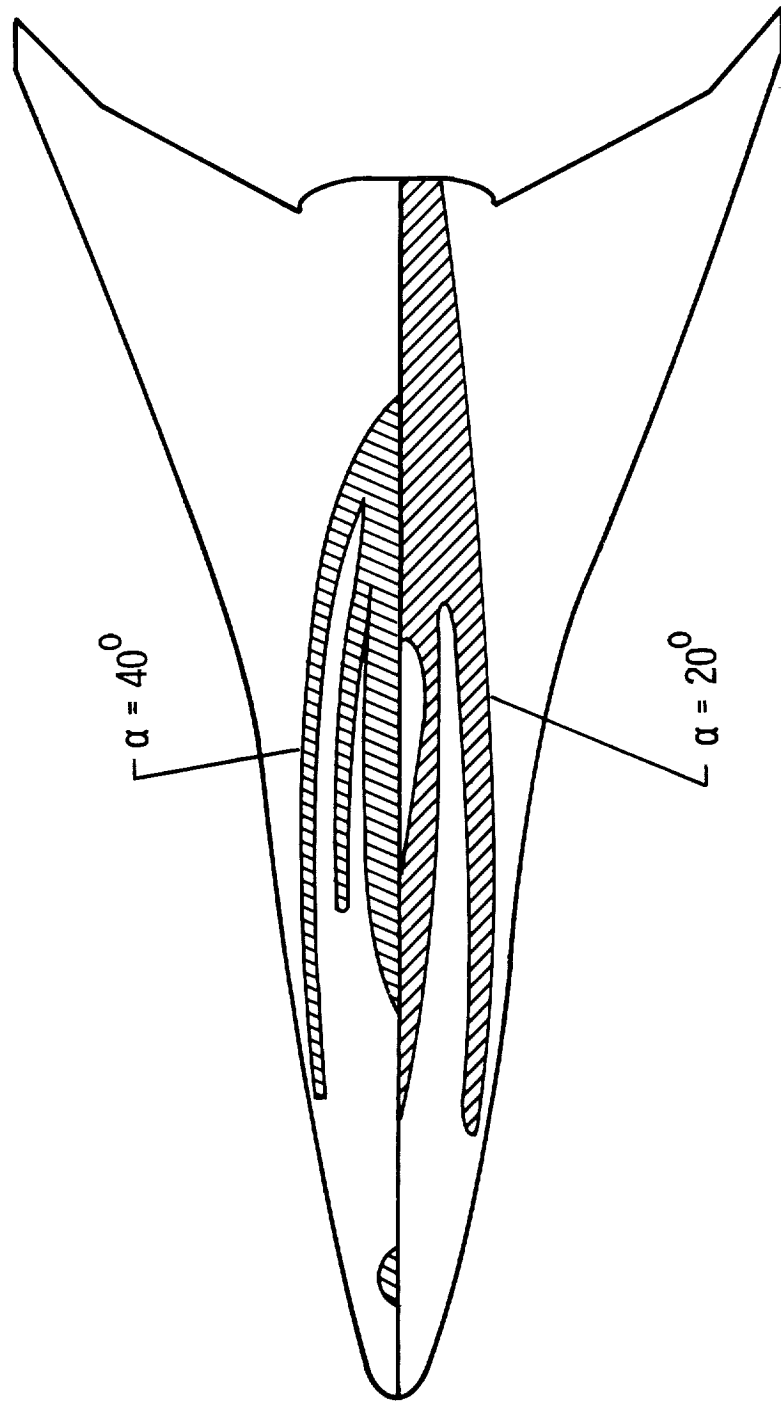


Figure 4

EFFECT OF REYNOLDS NUMBER ON CENTER-LINE LEE-SURFACE HEATING

(Figures 5 and 6)

Reynolds number is a significant parameter since it strongly influences the severity of the lee-surface heating. For the present tests, increasing Reynolds number increases the peak heating on the lee-surface meridian in the vicinity of the nose and decreases the heating on the lee meridian over the aft section of the configuration.

An unqualified interpretation of the Reynolds number influence on the peak heating in the nose region is not possible at this time; however, the increase in heating could possibly be attributed to boundary-layer or shear-layer transition prior to vortex impingement. An examination of heat-transfer data on a delta-wing orbiter at $M_\infty = 8$ and $\alpha = 20^\circ$ (ref. 5) suggests that transition on the windward surface has a strong influence on the magnitude of the lee-surface peak heating. This is a plausible result since the present oil-flow studies indicate that the flow on the lee surface originated on the windward surface. The Mach 8 results show that at the lowest Reynolds number, the transition position on the windward surface is downstream of the peak heating location on the lee surface. At the highest Reynolds number, the transition position on the windward surface is fixed in the vicinity of the peak heating location on the lee surface. The latter case would likely produce transitional or turbulent separation with a resultant higher heating rate at reattachment in the neighborhood of the lee meridian. While not conclusive, this result indicates that transition could be responsible for the variation in peak heating with Reynolds number. Further studies are needed to isolate the specific effect of

EFFECT OF REYNOLDS NUMBER ON CENTER-LINE LEE-SURFACE HEATING

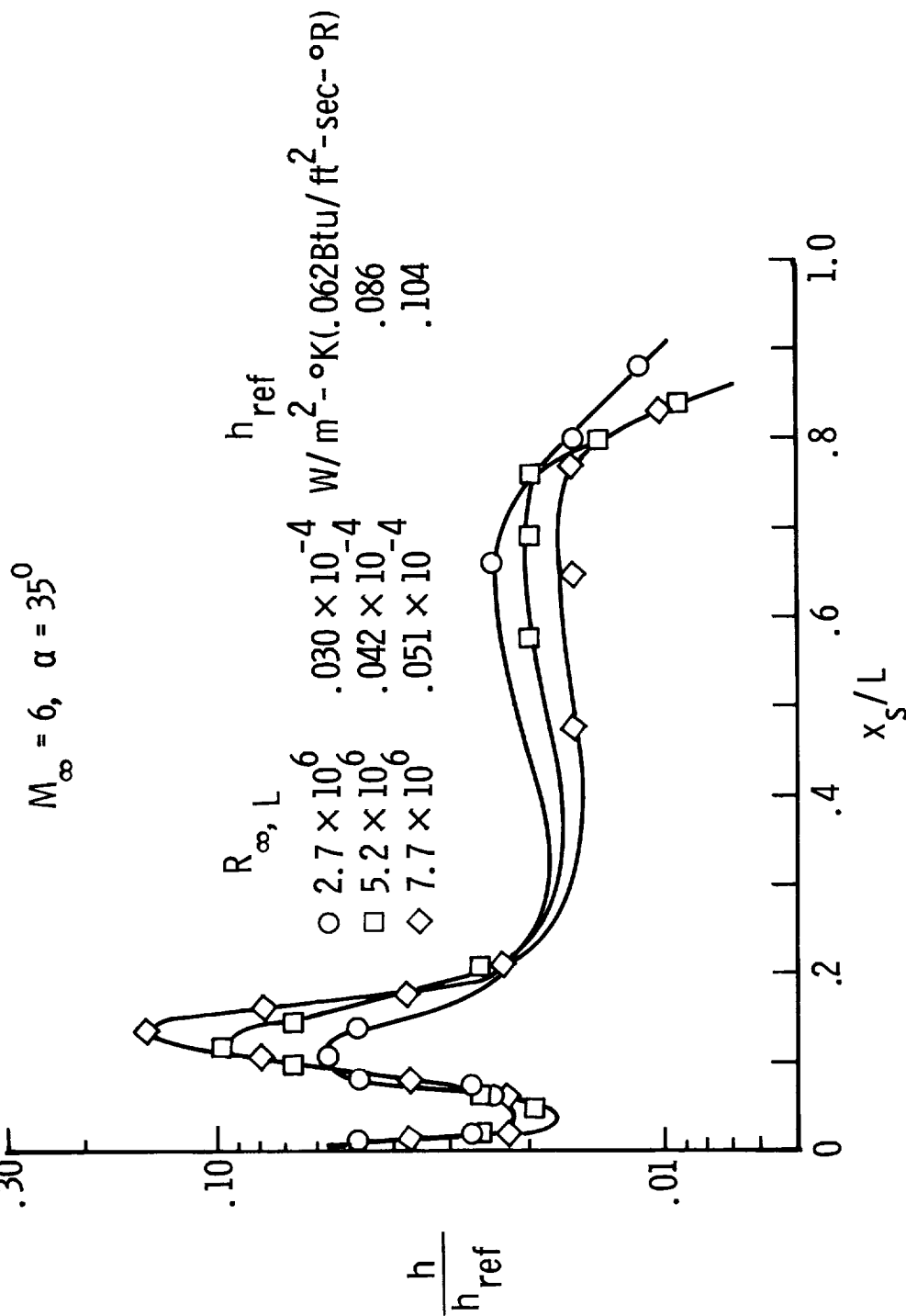


Figure 5

EFFECT OF REYNOLDS NUMBER ON CENTER-LINE LEE-SURFACE HEATING - Concluded

Reynolds number on the peak heating on the lee surface since there is no reason to expect that the strength of the vortex is independent of Reynolds number even when the general state of the boundary layer remains unchanged.

The magnitude of the lee-surface peak heating is more sensitive to Reynolds number than to angle of attack, whereas the location of the peak heating is more sensitive to angle of attack.

Oil-flow studies show separated flow over the aft section of the configuration (heating decreasing with increasing Reynolds number). Static pressures in this area were found to decrease with increasing Reynolds number. This behavior is indicative of transitional base flow separation (ref. 6) and helps to explain the decrease in heating with increasing Reynolds number.

EFFECT OF REYNOLDS NUMBER ON CENTER-LINE LEE-SURFACE HEATING

$$M_\infty = 6, R_{\infty, L} = 5.2 \times 10^6, \alpha = 35^\circ$$

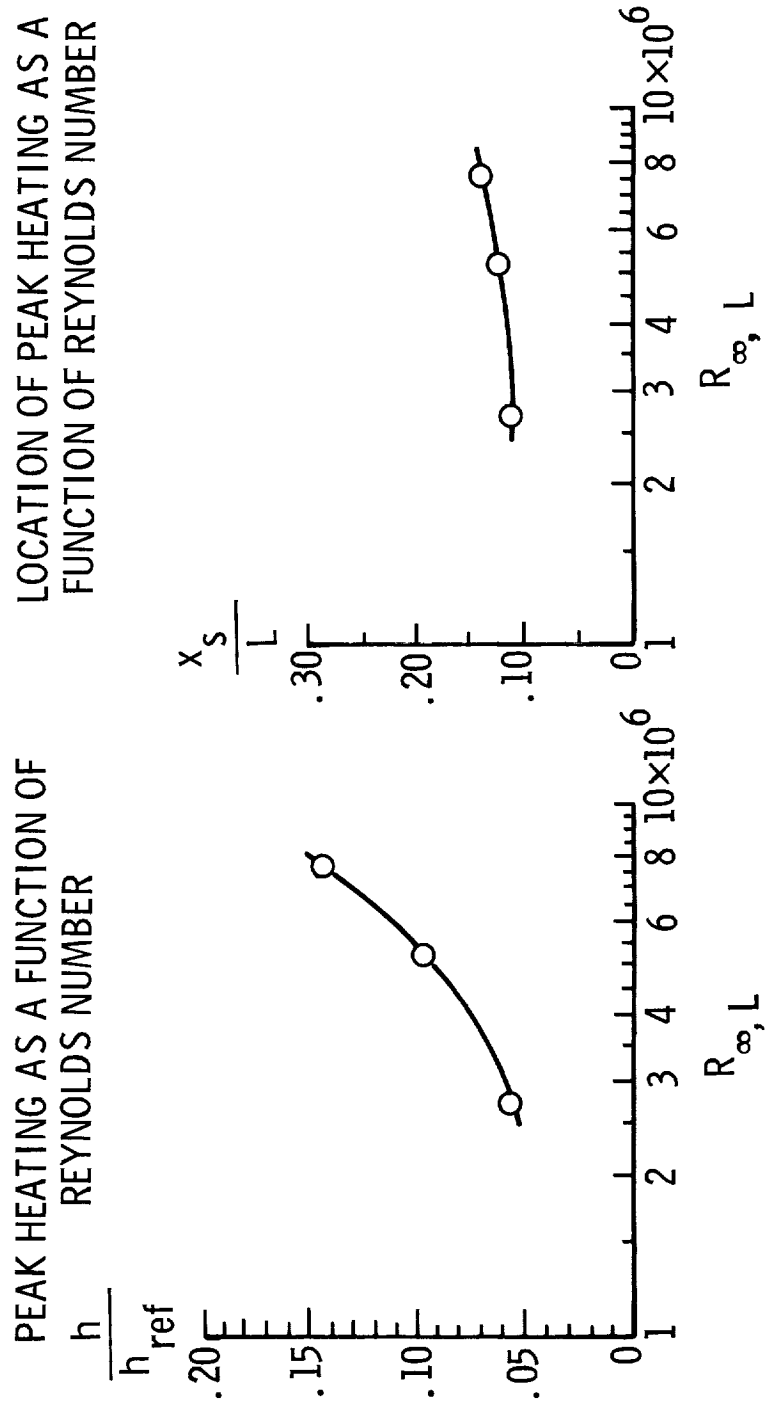


Figure 6

LEE-SURFACE HEATING ON CENTER-LINE OF A DELTA-WING
AND A STRAIGHT-WING ORBITER

(Figure 7)

This figure shows the effect of the gross difference in geometry on the magnitude and distribution of the lee-surface heating on the meridian of two shuttle configurations. The maximum heating peaks on the upper surface of the straight-wing orbiter occur at zero angle of attack whereas on the delta-wing orbiter the maximum heating peaks occur at an angle of 50° for the present test conditions. The heating on the straight-wing orbiter is affected by canopy-induced shock—boundary-layer interaction over the forward portion of the fuselage and by transition and the dorsal fin over the aft portion.

LEE-SURFACE HEATING ON CENTER-LINE OF A DELTA-WING AND A STRAIGHT-WING ORBITER

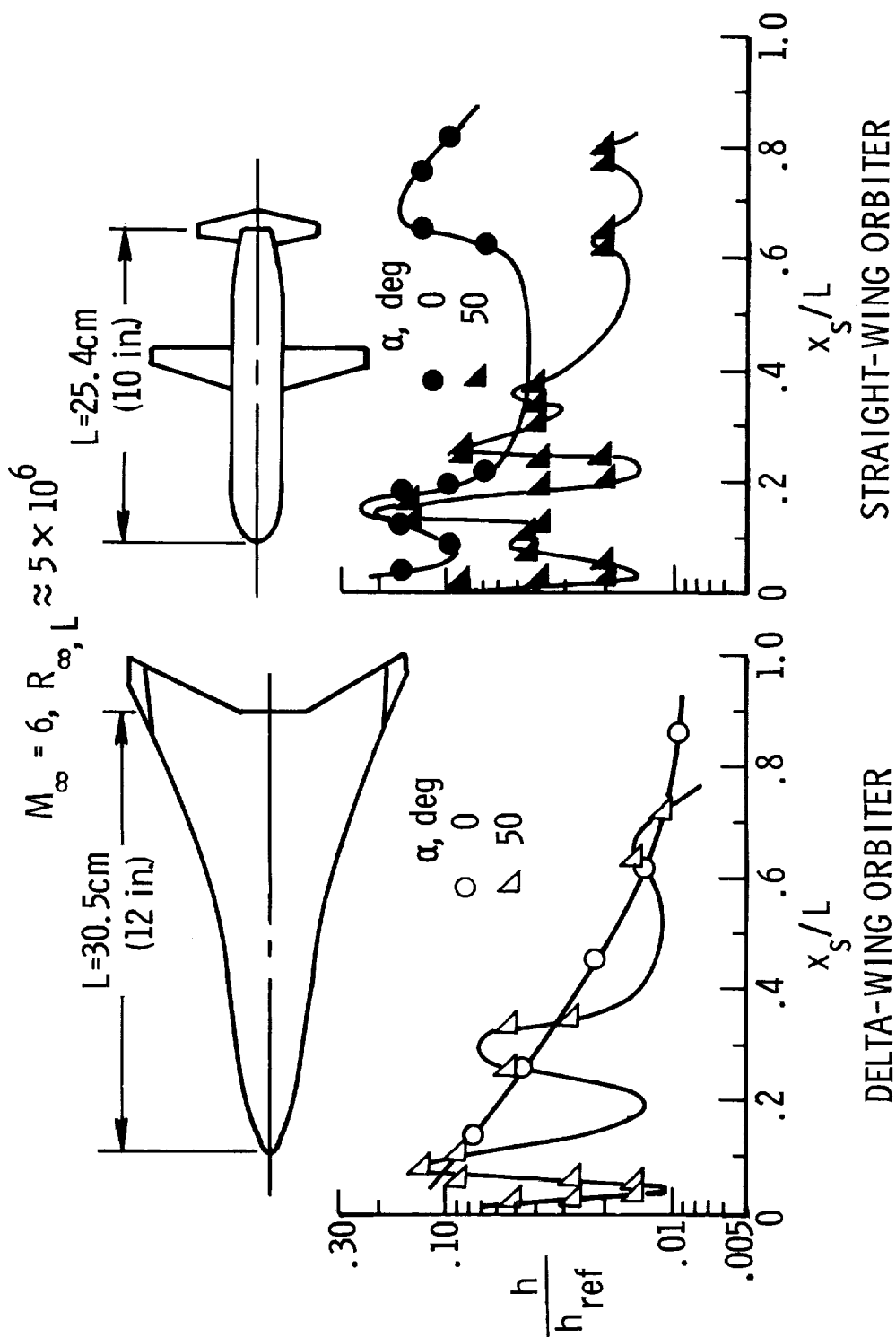


Figure 7

CALCULATED CENTER-LINE SURFACE TEMPERATURE
FOR TWO SHUTTLE GEOMETRIES

(Figure 8)

The surface temperatures on the straight-wing orbiter are substantially greater than those on the delta-wing orbiter at $\alpha = 50^\circ$. These calculated temperatures are based on a maximum stagnation heating obtained for a low cross-range trajectory (ref. 7). All the temperatures calculated exceed the structural limits for titanium.

CALCULATED CENTER-LINE SURFACE TEMPERATURES FOR TWO SHUTTLE GEOMETRIES

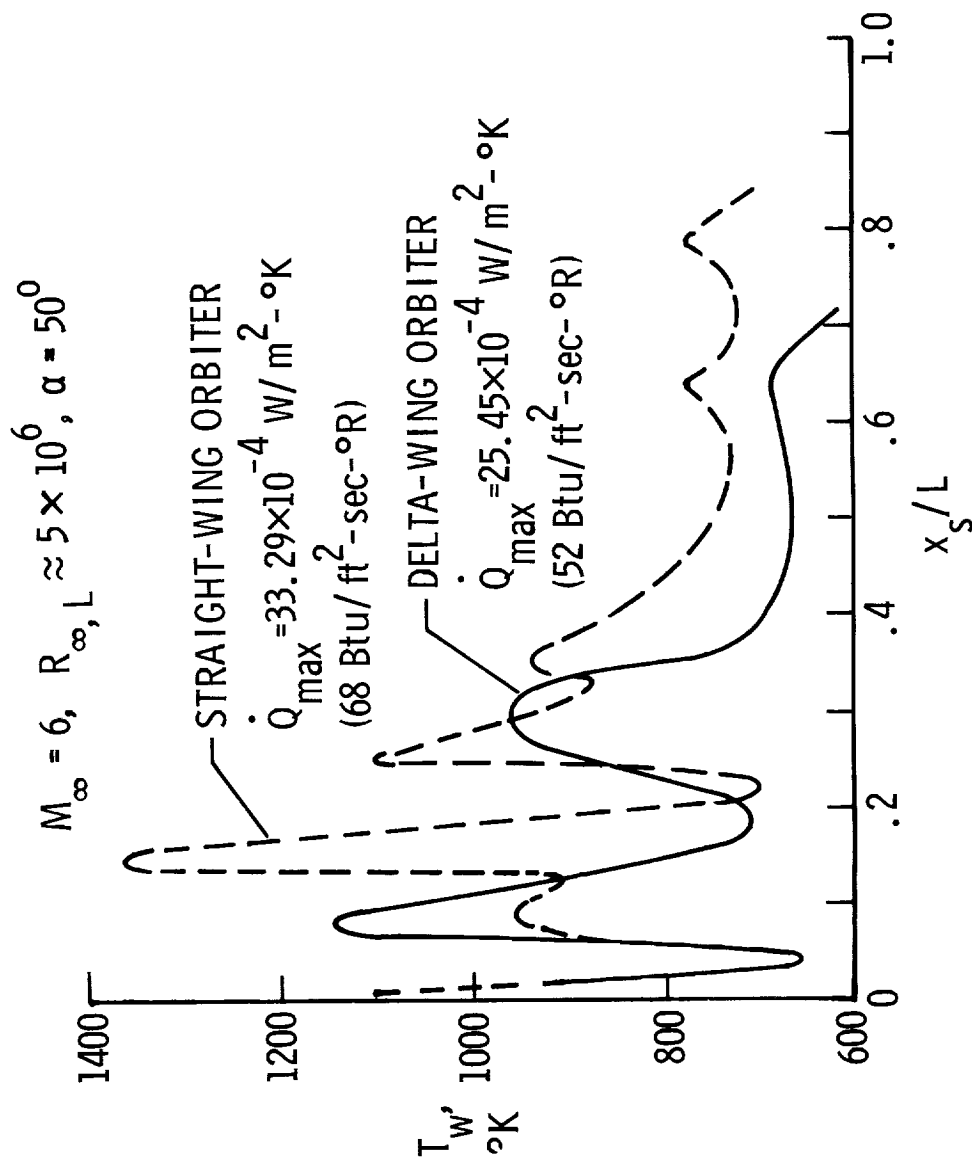


Figure 8

WIND-TUNNEL AND PROJECTED FLIGHT ENVIRONMENTS FOR DELTA-WING ORBITER

(Figure 9)

In the analysis of lee-surface heating for the shuttle, consideration must be given to the question of the applicability of the present results to flight conditions. Test conditions for pertinent wind-tunnel tests (present tests, ref. 5, and unpublished Ames and Langley tests) on high cross-range orbiters are shown and compared with a flight envelope for the full-scale orbiter. The lee-surface heating at Mach 8 displayed characteristics like those indicated from the present study. At Mach 7.4 and 20, no heating data were obtained; however, oil-flow studies indicated separation and reattachment patterns (including vortices) quite similar to those observed in the present tests. The conditions for these wind-tunnel tests encompass a wide variation in both Reynolds number and Mach number and are close to the projected flight conditions; therefore, vortex impingement on the lee surface similar to that found in the present tests should be expected in flight. The prediction of the vortex-induced heating peaks is, however, beyond the present state of the art. It is mandatory, then, that limited lee-surface heating data be obtained in wind-tunnel tests at a sufficiently high Mach number and low surface-temperature ratio with a Reynolds number range representative of the projected flight environment so that generality of the heating results can be conclusively determined. It is also particularly important to obtain higher Mach number lee-surface heating data, since the maximum windward-surface heating will occur at the higher Mach numbers and the effect of Mach number presently is unknown.

WIND-TUNNEL AND PROJECTED FLIGHT ENVIRONMENTS FOR DELTA-WING ORBITER

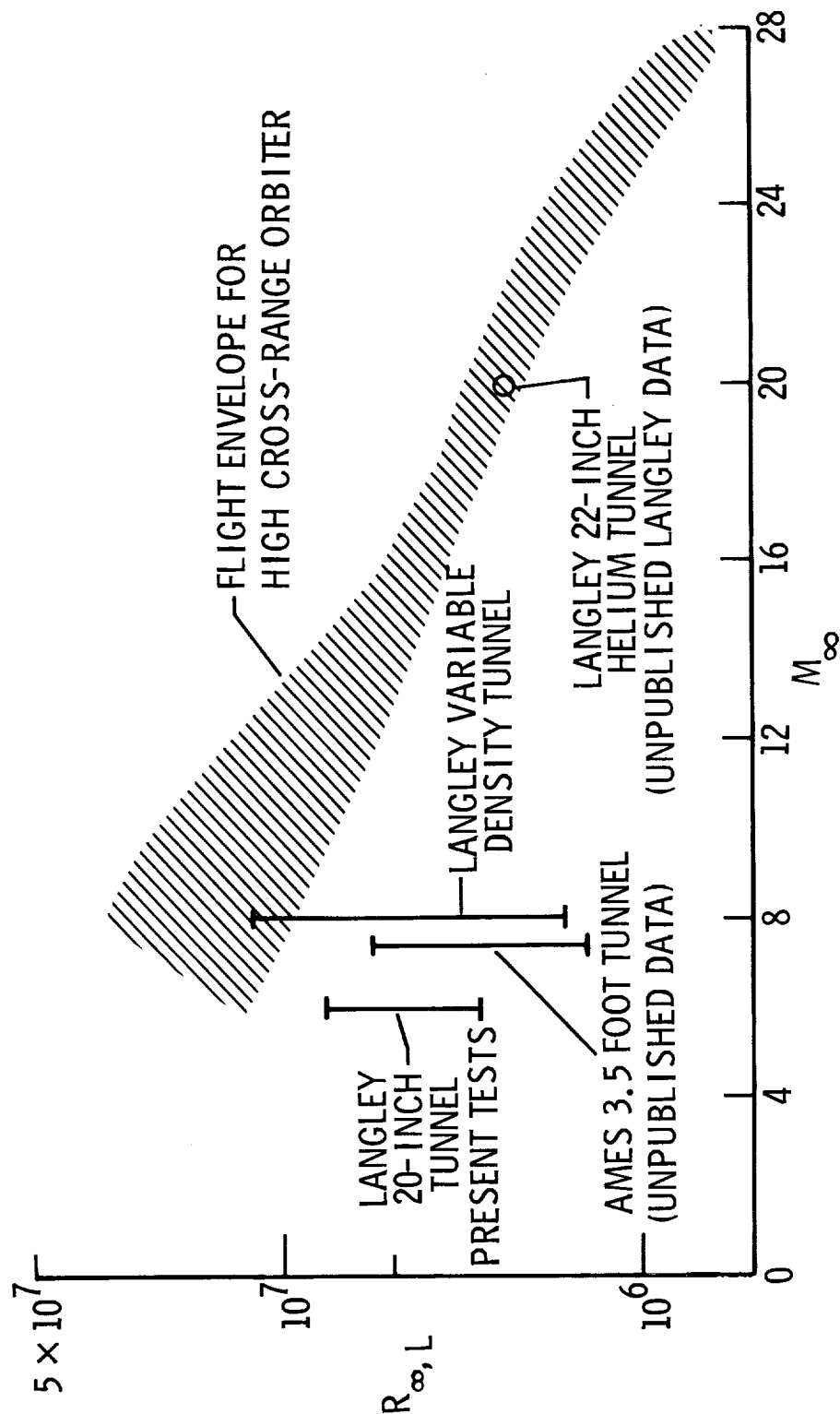


Figure 9

CONCLUSIONS

Some of the results of an experimental lee-surface heating investigation on a delta-wing orbiter are presented with the following conclusions:

1. Vortex impingement on the lee surface causes relatively large areas of the lee surface to have heating levels greater than that found on the upper surface at zero angle of attack.
2. The magnitude of the peak heating on the lee-surface meridian is found to be more sensitive to Reynolds number than to angle of attack. However, the location of the peak heating is more sensitive to angle of attack than to Reynolds number.
3. Maximum lee-surface heating occurs in the vicinity of the nose. This result, in conjunction with some basic fluid mechanics studies, suggests that judicious shaping of the nose region might reduce the heating caused by the vortex impingement.
4. Impingement of vortices on the lee-surface of the delta-wing orbiter can be expected in flight; however, lee-surface heating data at a substantially higher Mach number are needed to establish the heating levels in vortex-influenced regions. Furthermore, experimental studies are required to isolate the specific effect of Reynolds number on heating and to examine the effect of nose shaping and bluntness on the vortex generation and, consequently, heating on shuttlelike geometries.

REFERENCES

1. Arrington, James P.: Entry Maneuver/Aerothermodynamic Interactions for High Cross-Range Candidate Orbiters. Space Transportation System Technology Symposium, NASA TM X-52876, Vol. I, 1970, pp. 509-530.
2. Monaghan, R. J.: An Approximate Solution of the Compressible Laminar Boundary Layer on a Flat Plate. R. & M. No. 2760, Brit. A.R.C., 1953.
3. Neal, Luther, Jr.; and Bertram, Mitchel H.: Turbulent-Skin-Friction and Heat-Transfer Charts Adapted From the Spalding and Chi Method. NASA TM D-3969, 1967.
4. Guard, F. L.; and Schultz, H. D.: Space Shuttle Aerodynamic Heating Considerations. [Preprint] 70-HT/SpT-16, ASME, June 1970.
5. Connor, L. E.: Heat Transfer Tests of the Lockheed Space Shuttle Orbiter Configuration Conducted at the Langley Research Center Mach 8 Variable Density Tunnel. TM 54/20-241, Lockheed Missiles & Space Co., Dec. 1969.
6. Hama, Francis R.: Experimental Investigations of Wedge Base Pressure and Lip Shock. Tech. Rep. No. 32-1033 (Contract No. NAS 7-100), Jet Propulsion Lab., California Inst. Technol., Dec. 1, 1966. (Available as NASA CR-81031.)
7. Henderson, Arthur; Dunavant, James C.; and Jones, Robert A.: Heating Studies on Manned Space Shuttle Concepts. NASA paper presented at the Space Technology and Heat Transfer Conference ASME (Los Angeles, Calif.), June 21-24, 1970.

LEESIDE HEATING INVESTIGATIONS

Part II - Leeside Heating Investigations of Simple Body-Like Configurations

By George Maisie
Grumman Aerospace Corporation, Bethpage, New York

SUMMARY

An investigation was conducted to characterize the leeside aerodynamic heating of various shapes flying hypersonically at an angle of attack. In particular, attention was focussed on the problem of intense heating resulting from reattachment of leading-edge vortices on the lee side of the bodies. The present investigation consisted of (1) correlation and comparison of available leeside heating data and (2) an experimental program to clarify some questions related to the vortical flow phenomenon. In the correlation of available data on circular cones, a strong Reynolds number dependence has been observed. In the wind tunnel study, the effect of increase in cross sectional area on vortical heating was examined. Secondly, an attempt was made to establish the angles of attack at which the flow about elongated bodies becomes two dimensional in the cross-flow plane, i.e., negligible axial components. To answer these questions, heat transfer and oil flow models were tested in the Grumman hypersonic wind tunnel.

INTRODUCTION

It was pointed out in paper no. 9-I, vol. I of this compilation that leeside heating on lifting reentry vehicles can be a serious problem. What makes it even more serious is that reliable methods, either analytical or experimental, are not yet available to evaluate the magnitude of leeside heating during reentry.

To gain a better understanding of the leeside heating problem, a two-part investigation was conducted at Grumman. First, an attempt was made to correlate the data already available in the open literature; and, secondly, a wind tunnel test program was conducted to answer some important questions about the nature of vortical flow on the lee side of vehicles.

CORRELATION AND COMPARISON OF AVAILABLE DATA

A considerable amount of data on leeside aerodynamic heating is already available in the open literature. The models that have been tested range from simple bodies such as the circular cones and delta wings to more complex reentry vehicles. The present discussion will be limited to circular cones.

CIRCULAR CONES
(Slide 1)

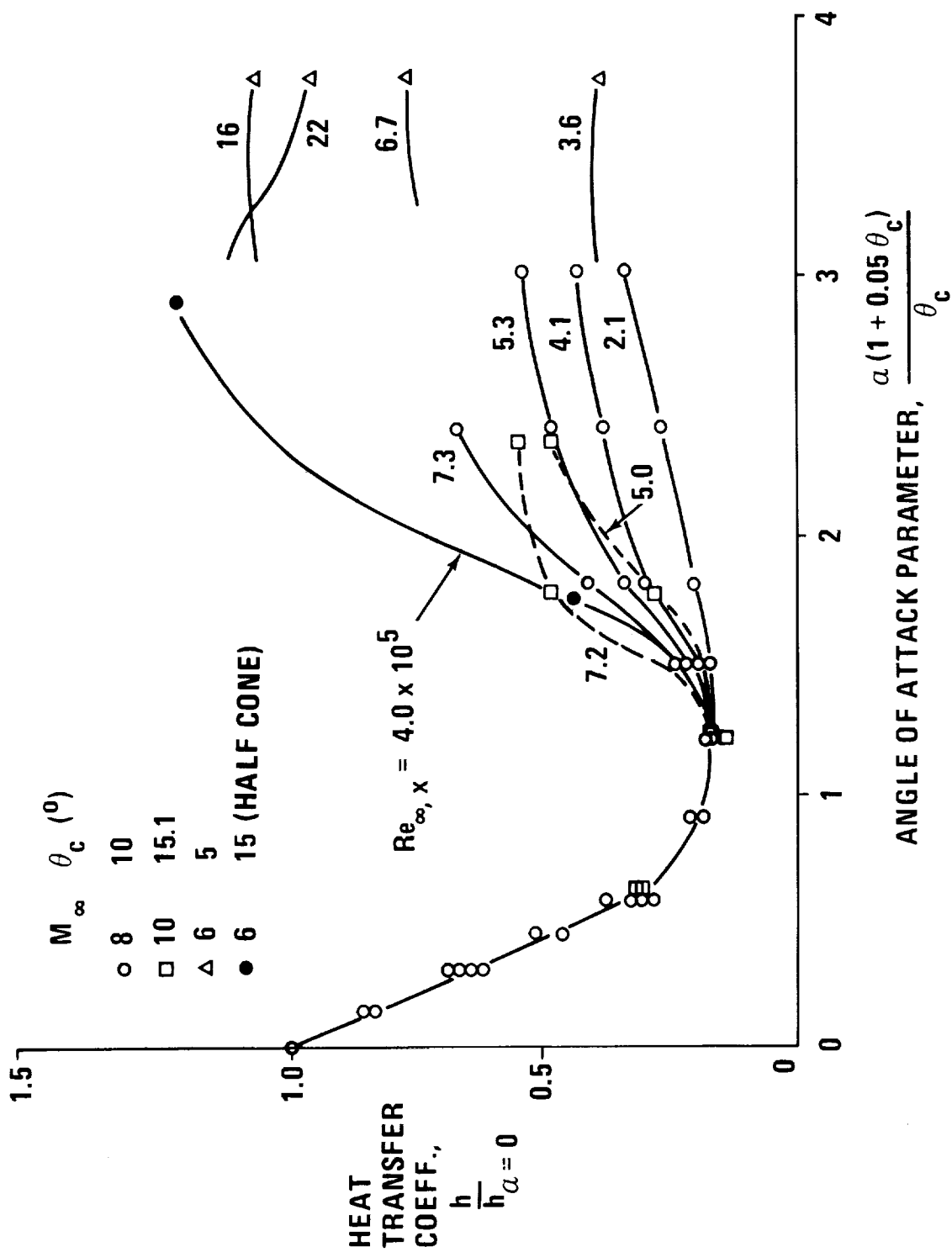
The circular cone in itself is probably not a practical shape for the shuttle; however, these data are worth examining as will be seen below. In attempting to correlate the cone results, a number of different ways to plot the data were tried. The most successful of these is shown in Slide 1. The heat transfer coefficient on the leeside centerline is normalized by the heat transfer coefficient at zero angle of attack ($\alpha = 0^\circ$). The abscissa is basically a relative incidence parameter, i.e., ratio of α to the cone half angle (θ_c). The factor $(1 + 0.05\theta_c)$ is an additional weighting factor which accounts for the differences in the cone half angle. The curves in this slide illustrate very graphically what occurs on the lee side as α is increased. Initially, there is a reduction in the leeside heat transfer coefficient due to the weaker shock and lower densities on the top surface of the cone. A minimum is reached when the angle of attack parameter is 1.2. This corresponds approximately to the condition where the leeward generator of the cone is aligned with the flow. Beyond this point the top surface is in the aerodynamic shadow, and Newtonian flow assumptions would predict negligible heat transfer. In reality, however, the heat transfer coefficient increases significantly at higher angles of attack due to the reattachment of vortical flow.

The data presented in this slide (from Refs. 1-4) cover a free-stream Mach number M_∞ range of 6 to 10 and a free-stream Reynolds number, based on the distance from the cone apex, $Re_{\infty, x}$ range of 2.1×10^5 to 2.2×10^6 . The cone half angles are 5, 10 and 15°.

Perhaps the most significant point to be noted here is the Reynolds number dependence. In the attached region the heat transfer coefficients collapse on a single curve. In the vortical region there is a very significant Reynolds number dependence. This is in addition to the normal $\sqrt{\text{Re}}$ increase which is already accounted for in the normalized h . This means that when wind tunnel tests are used to evaluate shuttle leeside heating, these tests must be conducted at the proper Reynolds numbers. If this is not possible due to facility limitations, techniques must be developed for extrapolating the data to flight Reynolds numbers.

As far as the Mach number dependence is concerned, the correlation should not be misinterpreted. Although the Mach number ranged from 6 to 10, the cone angles also changed and in such a way that the post-shock Mach numbers were approximately equal. Additional data at higher Mach numbers are needed to establish the dependence of vortical heating on Mach number.

There is one additional point to be made in this slide. In addition to the results from three sets of cone data which correlate quite well (open symbols), the graph shows some data for a half cone (filled symbol). The half-cone is oriented with the flat surface on the bottom, and ∞ is taken as zero when this surface is aligned with the flow. It is seen that, under comparable flow conditions, the leeside heating is much more intense on the half cone than on the full cones. It appears that the sharp edges on the half-cone are in some way responsible for the difference. It might be mentioned that recent (unpublished) tests at Ames Research Center with slender square pyramids indicated similar trends. The amplification of heat transfer on the leeside was much greater than for cones under comparable test conditions.



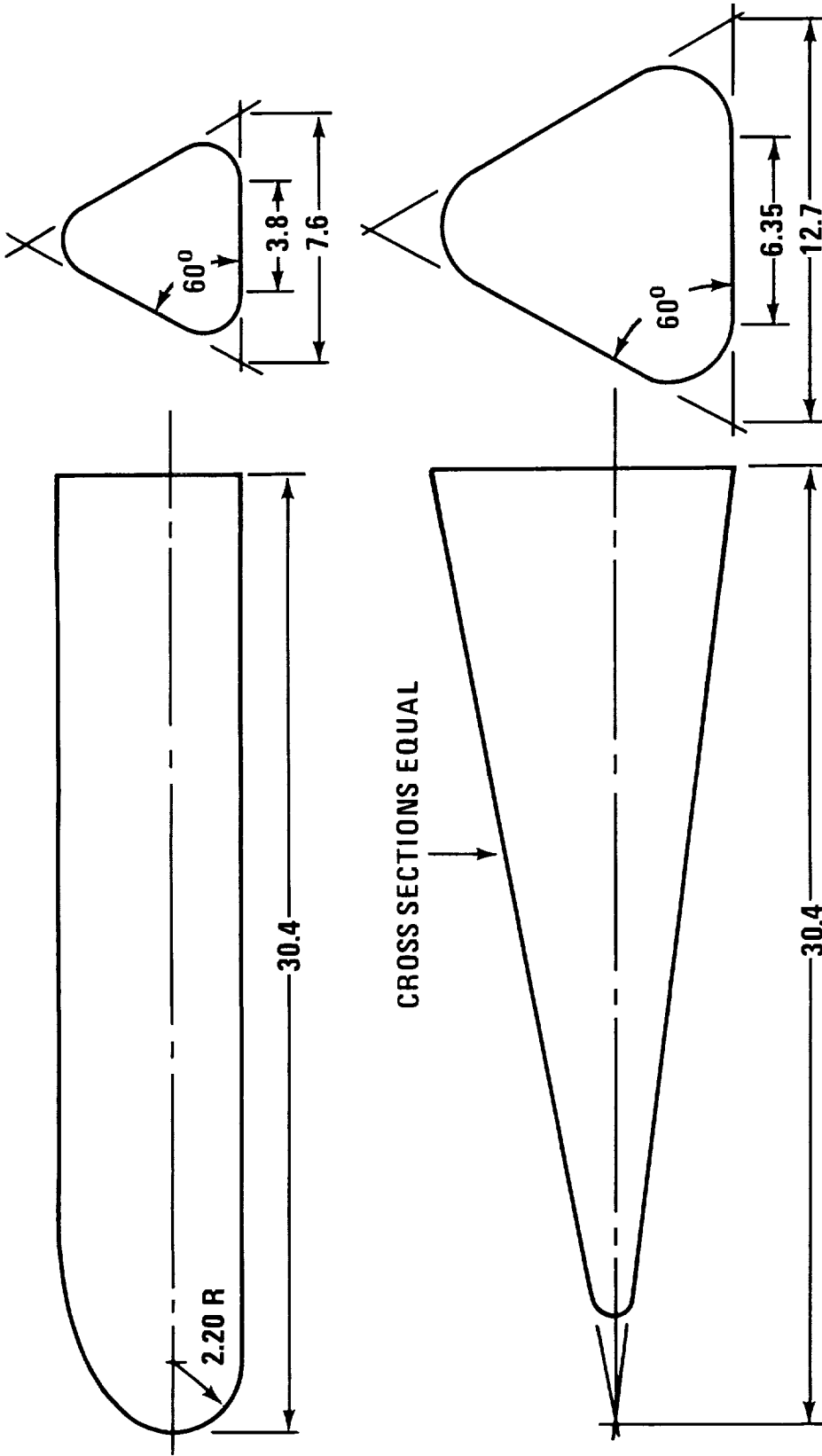
HEAT TRANSFER COEFFICIENT ON LEE SIDE OF CIRCULAR CONES

Slide 1

WIND TUNNEL TEST PROGRAM
(Slide 2)

As the second part of this investigation, a series of tests were conducted in the Grumman hypersonic wind tunnel. The models used in these tests are shown in Slide 2. One of the models in cylindrical, the other pyramidal. The cross sections are similar and, in fact, identical near the middle station of the pyramidal body.

Both models were tested at Mach 8, at a Reynolds number of 0.5×10^6 and at angles of attack ranging from 0 to 55° . Heat transfer coefficients were measured using the phase-change paint technique developed by Jones and Hunt (Ref. 5) and surface streamline patterns were obtained using the oil flow technique.



TEST MODELS

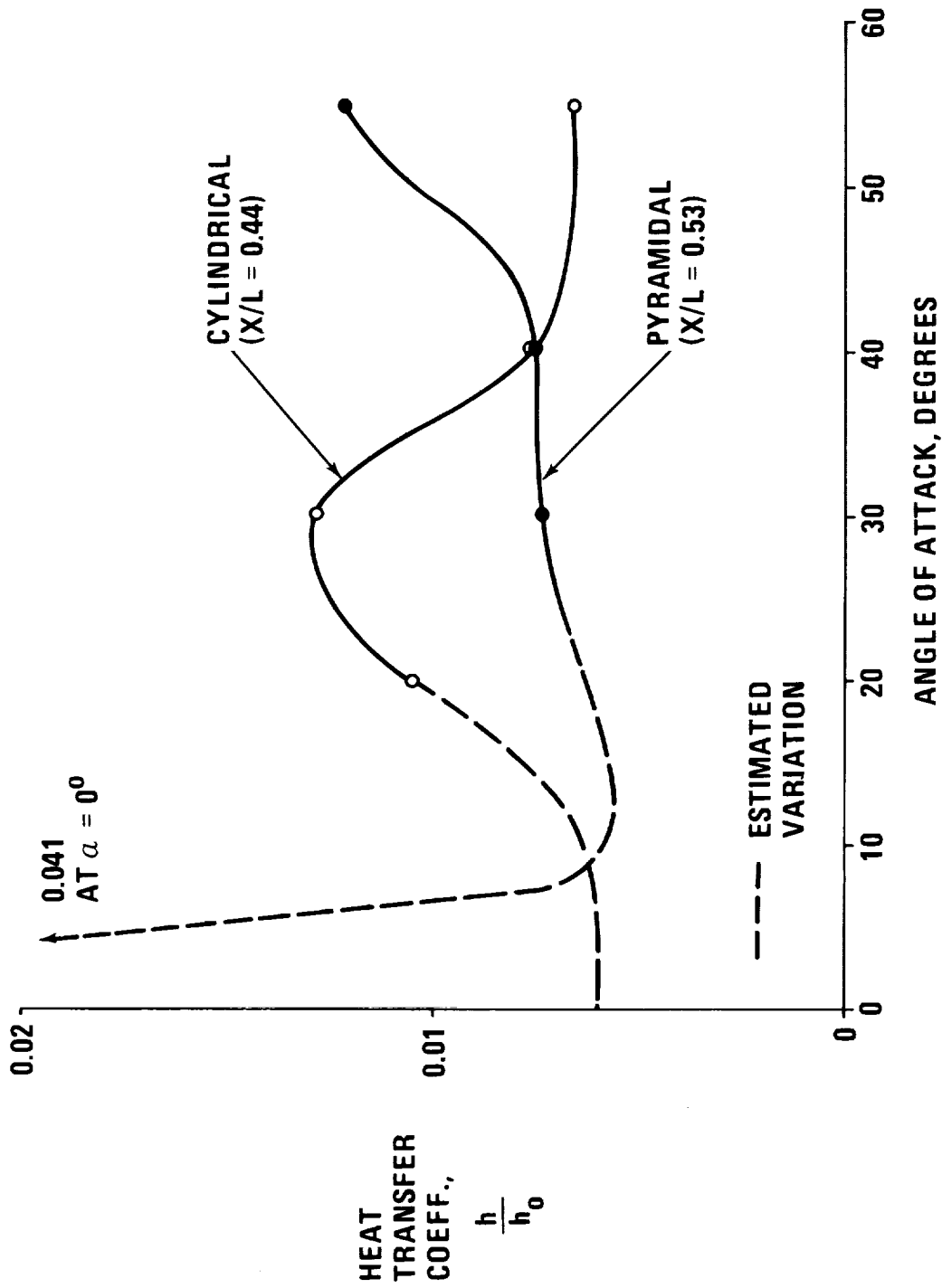
Slide 2

MEASURED HEAT TRANSFER COEFFICIENTS
(Slide 3)

Slide 3 shows the measured leeside heat transfer coefficients for the two models plotted against the angle of attack. (For convenience, the heat transfer coefficients have been normalized by the stagnation point heat transfer coefficient on a 2 mm sphere.) The body stations for which these data are shown were selected such that the cross sectional areas, as well as the running-length Reynolds numbers are equal.

Comparison of the two curves indicates that the variation of the leeside heat transfer coefficient with angle of attack is very different for the two shapes. The results for the cylindrical model indicate maximum leeside heat transfer at an angle of attack of about 30° . At angles of attack greater than 40° , the heat transfer coefficient appears to level off, probably indicating full separation.

The data for the pyramidal shape indicate just the opposite trends. The leeside heat transfer coefficient drops to low values at moderate angles of attack and then increases again as the angle of attack is increased to 55° .



LEESIDE HEAT TRANSFER COEFFICIENTS AT MODEL STATIONS WITH EQUAL CROSS SECTIONAL AREAS AND RUNNING-LENGTH REYNOLDS NUMBERS

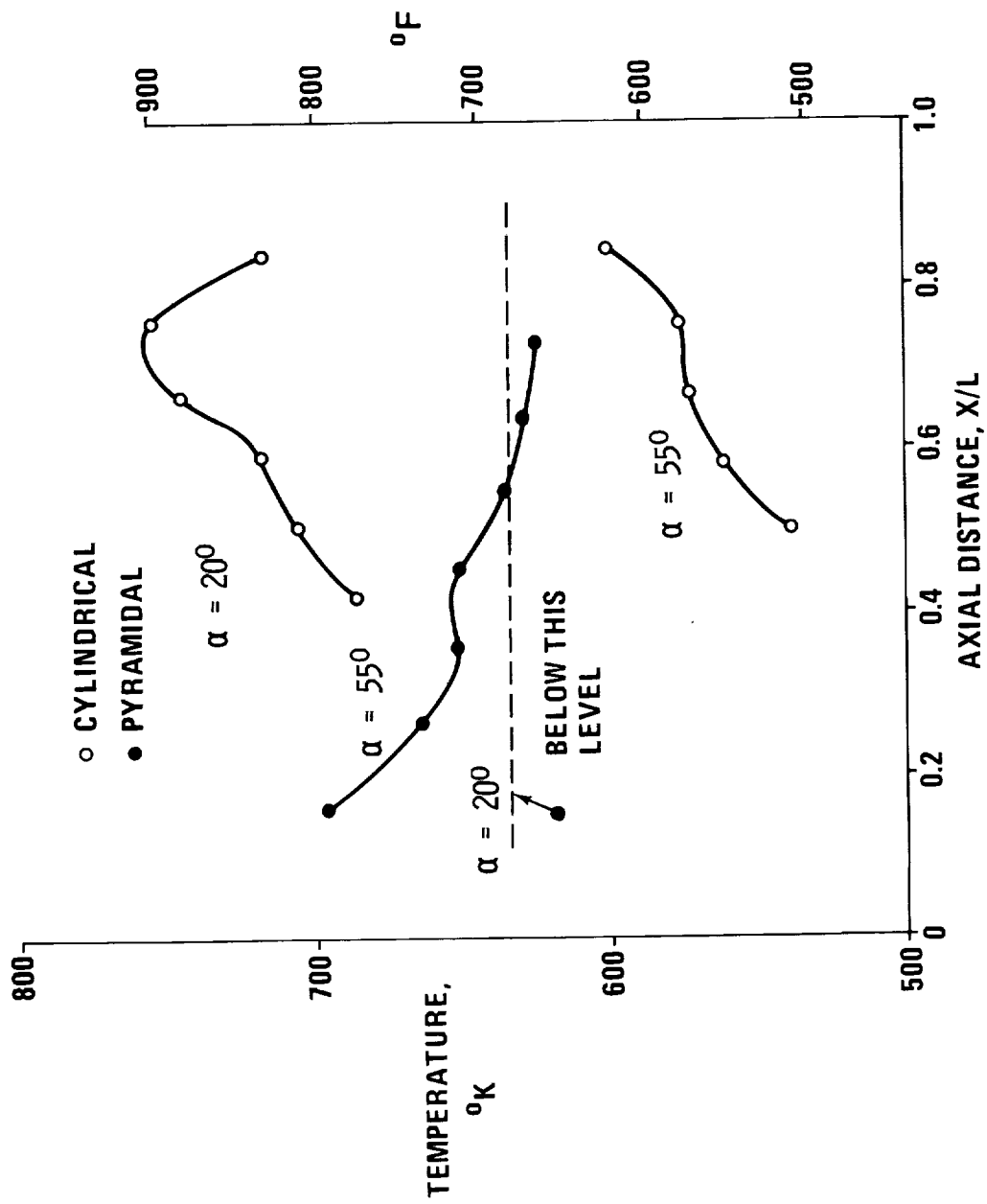
RADIATION EQUILIBRIUM TEMPERATURE
(Slide 4)

It might be of interest to consider what the measured heat transfer coefficients would mean in terms of skin temperatures during reentry. If the models were scaled up to 50 meters in length and reentered from orbit along high and low cross range trajectories (Ref. 6), the radiation equilibrium temperature shown in Slide 4 would result.

In performing these calculations the usual procedure of scaling h by the square root of Reynolds number was followed. As was mentioned earlier, there is great uncertainty in using this type of scaling on the lee side; however, in the absence of actual Reynolds number dependence it was necessary to use this simplified analysis.

The calculations show that the cylindrical vehicle experiences very moderate leeside temperatures during high angle-of-attack reentry. During low angle-of-attack reentry the leeside skin temperatures are considerably higher. The pyramidal body, on the other hand, shows just the opposite trends.

Although the overall temperature range indicated in Slide 4 is not great, the data presented do straddle the 600°K line, which is the maximum temperature limit for a load-carrying titanium structure. Thus, choice of either the cylindrical or pyramidal shape could make the difference between being able to use an unprotected load-carrying titanium structure or having to either protect it or change it to a heavier material.



MAXIMUM RADIATION EQUILIBRIUM TEMPERATURES DURING REENTRY

OIL FLOW AROUND CYLINDRICAL BODY AT $\alpha = 20^\circ$
(Slide 5)

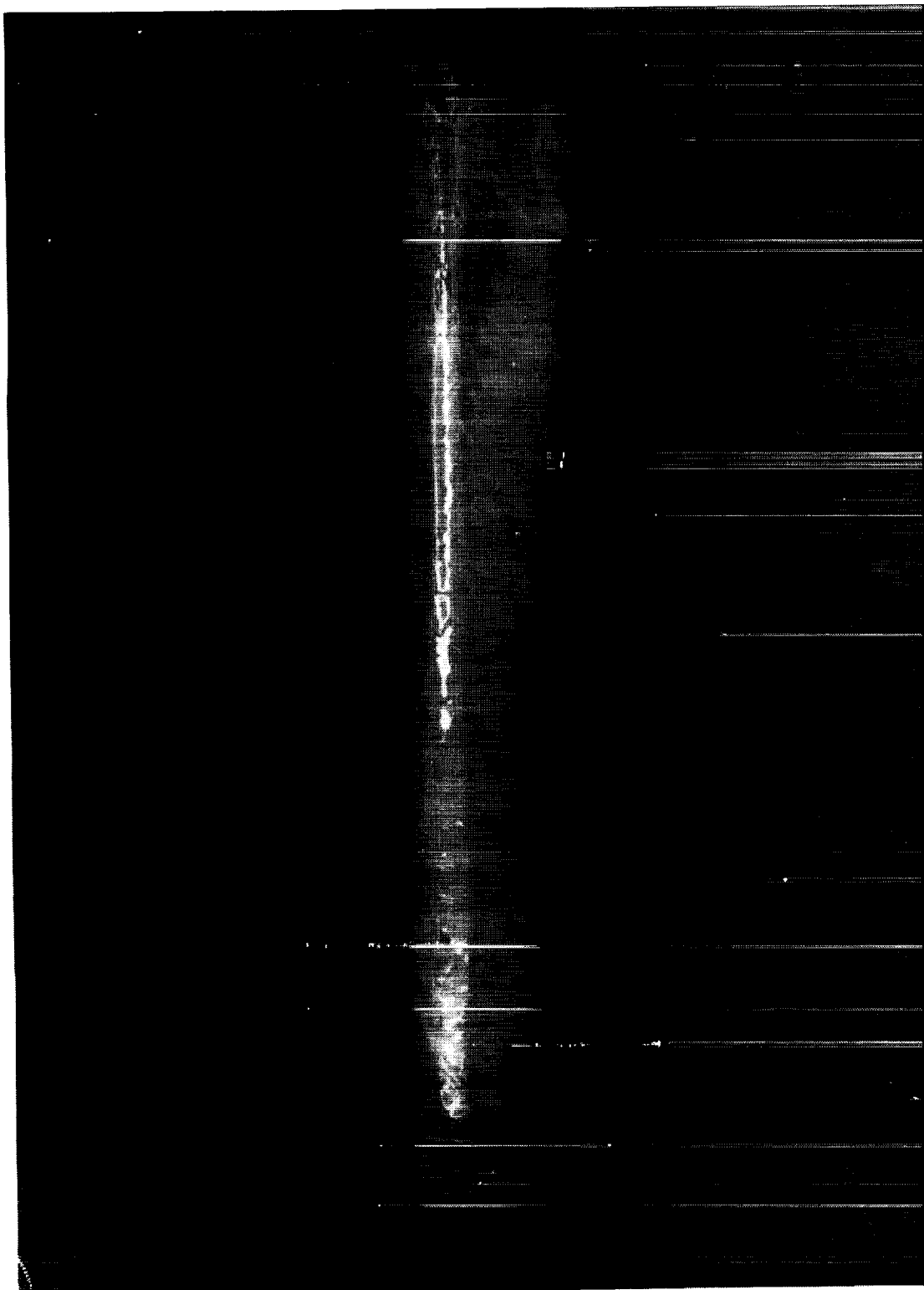
Slide 5 shows some results from the oil flow studies. In this case the cylindrical body was tested at an angle of attack of 20° . The dark areas on the model indicate regions of high shear. Significant reattachment is evident on the lee side.

OIL FLOW AT $\alpha = 20^\circ$ FOR A CYLINDRICAL BODY

Slide 5

OIL FLOW AROUND CYLINDRICAL BODY AT $\alpha = 55^\circ$
(Slide 6)

When the same body was tested at an angle of attack of 55° , the lee side appeared to be fully separated with no indication of vortical reattachment. Also, the flow appeared to be nearly two dimensional in the cross-flow plane.



OIL FLOW AT $\alpha = 55^\circ$ FOR A CYLINDRICAL BODY

Slide 6

OIL FLOW AROUND PYRAMIDAL BODY AT $\alpha = 20^\circ$
 (Slide 7)

Slide 7 shows the results with the pyramidal body at $\alpha = 20^\circ$. There is only slight evidence of vortical reattachment.



OIL FLOW AT $\alpha = 20^\circ$ FOR A PYRAMIDAL BODY

Slide 7

OIL FLOW AROUND PYRAMIDAL BODY AT $\alpha = 55^\circ$
(Slide 8)

With the pyramidal body at $\alpha = 55^\circ$, there is evidence of strong vortical reattachment.

The results of the oil flow studies are in qualitative agreement with heat transfer measurement in the sense that strong vortical reattachment is associated with a high heat transfer coefficient.



OIL FLOW AT $\alpha = 55^\circ$ FOR A PYRAMIDAL BODY

Slide 8

SUMMARY OF RESULTS

The major findings of the wind tunnel investigation can be summarized as follows:

1. The growth of the lateral dimensions of the body in addition to the nose shape and bluntness appears to have a strong influence on the nature of vortical flow and leeward heat transfer.
2. At the highest angle of attack used in these tests, that is, 55° with reference to the body axis, flow about the cylindrical body was essentially two dimensional. At the same angle of attack, the pyramidal body still indicated strong vortical reattachment.

REFERENCES

1. Tracy, R.R., "Hypersonic Flow Over a Yawed Circular Cone", Hypersonic Res. Proj. Memo No. 69, (Contract No. DA-31-124-ARO(D)-33) Graduate Aeronautical Lab., California Inst. of Technol., August 1, 1963.
2. Dearing, J.D., "Laminar Heat-Transfer Distributions for a Blunted-Cone, Cone-Frustrum Reentry Configuration at Mach 10," NASA TN D-5146, April 1969.
3. Feldhuhn, R.H. and Pasiuk, L., "An Experimental Investigation of the Aerodynamic Characteristics of Slender Hypersonic Vehicles at High Angles of Attack", NOL Tech. Rept. 68-52, May 1968.
4. Borovay, V.J., Davlet - Kildeev, R.Z., and Ryshkova, M.V., "Experimental Study of Heat Transfer on Lifting Body Surface in Supersonic Stream", in Heat Transfer 1970, Vol. 3, Proceeding of the Fourth International Heat Transfer Conference, Paris-Versailles, 1970, Verein Deutscher Ingenieure, Dusseldorf (1970).
5. Jones, R.A. and Hunt, J.L., "Use of Fusible Temperature Indicators for Obtaining Quantitative Aerodynamic Heat Transfer Data", NASA TR R-230, February 1966.
6. Proposal to Accomplish Phase B, Space Shuttle Program, Grumman Aerospace Corporation, 30 March 1970.

STATIC AND DYNAMIC AERODYNAMICS OF SPACE SHUTTLE VEHICLES

by

Victor L. Peterson, Elliott D. Katzen, John A. Axelson, Jack J. Brownson,
Donald L. Ciffone, Joseph W. Cleary, Peter F. Intrieri,
Gerald N. Malcolm and Jack A. Mellenthin

NASA Ames Research Center, Moffett Field, California

OBJECTIVES

(Figure 1)

Highlights of the Ames Research Center effort in support of the aerodynamic development of space shuttle vehicles will be presented in this paper. Specific objectives of the paper are presented in figure 1. A large number of models of space shuttle vehicles have been tested at Ames over wide ranges of Mach number, Reynolds number and angle of attack. Aerodynamic data have been obtained for orbiters, boosters and launch configurations. Including variations to baseline shapes, over 100 configurations have been tested thus far. From these tests, answers to previously identified fundamental aerodynamic flow problems are being obtained. For example, at the Space Transportation System Technology Symposium in July 1970, it was pointed out that at $M = .25$ there were large effects of body chine radius and Reynolds number on the pitching moments of a straight-wing orbiter at high angles of attack. A further analysis of these effects is presented by Thomas B. Sellers (paper no. 13 of volume I of this compilation). It is our intent to sort out effects of Mach number, as well as chine radius and Reynolds number, on the aerodynamics of space shuttle vehicles at high angles of attack. Another facet of configuration shaping that will be discussed is a comparison of the aerodynamics of delta-wing orbiters having single and twin vertical tails. In addition, new criteria for aerodynamic stability of space shuttle vehicles will be presented. These criteria now include the trajectory effects of varying dynamic pressure and Mach number. Finally, apparatus will be described for obtaining the identified dynamic derivatives.

OBJECTIVES

- DESCRIBE THE WIDE RANGE OF CONFIGURATIONS TESTED
- SORT OUT EFFECTS OF BODY CHINE RADIUS, REYNOLDS NUMBER AND MACH NUMBER ON HIGH ANGLE OF ATTACK AERODYNAMICS
- COMPARE AERODYNAMICS OF DELTA-WING ORBITERS HAVING SINGLE AND TWIN TAILS
- PRESENT NEW CRITERIA FOR AERODYNAMIC STABILITY
- DESCRIBE APPARATUS FOR OBTAINING DYNAMIC DERIVATIVES

Figure 1

McDONNELL DOUGLAS STRAIGHT-WING ORBITER

(Figure 2)

The model of the McDonnell Douglas straight-wing orbiter shown in figure 2 was tested with and without a folding wing. The foldable wing had the same aspect ratio (~ 7.0) as the fixed wing but shorter span. Low-speed tests were made with and without cruise engines deployed. Various combinations of horizontal tail incidence and elevator angles were investigated. The moveable rudder is visible in the photograph. Some tests were made with different chine radii on the body nose.

MCDONNELL DOUGLAS STRAIGHT-WING ORBITER

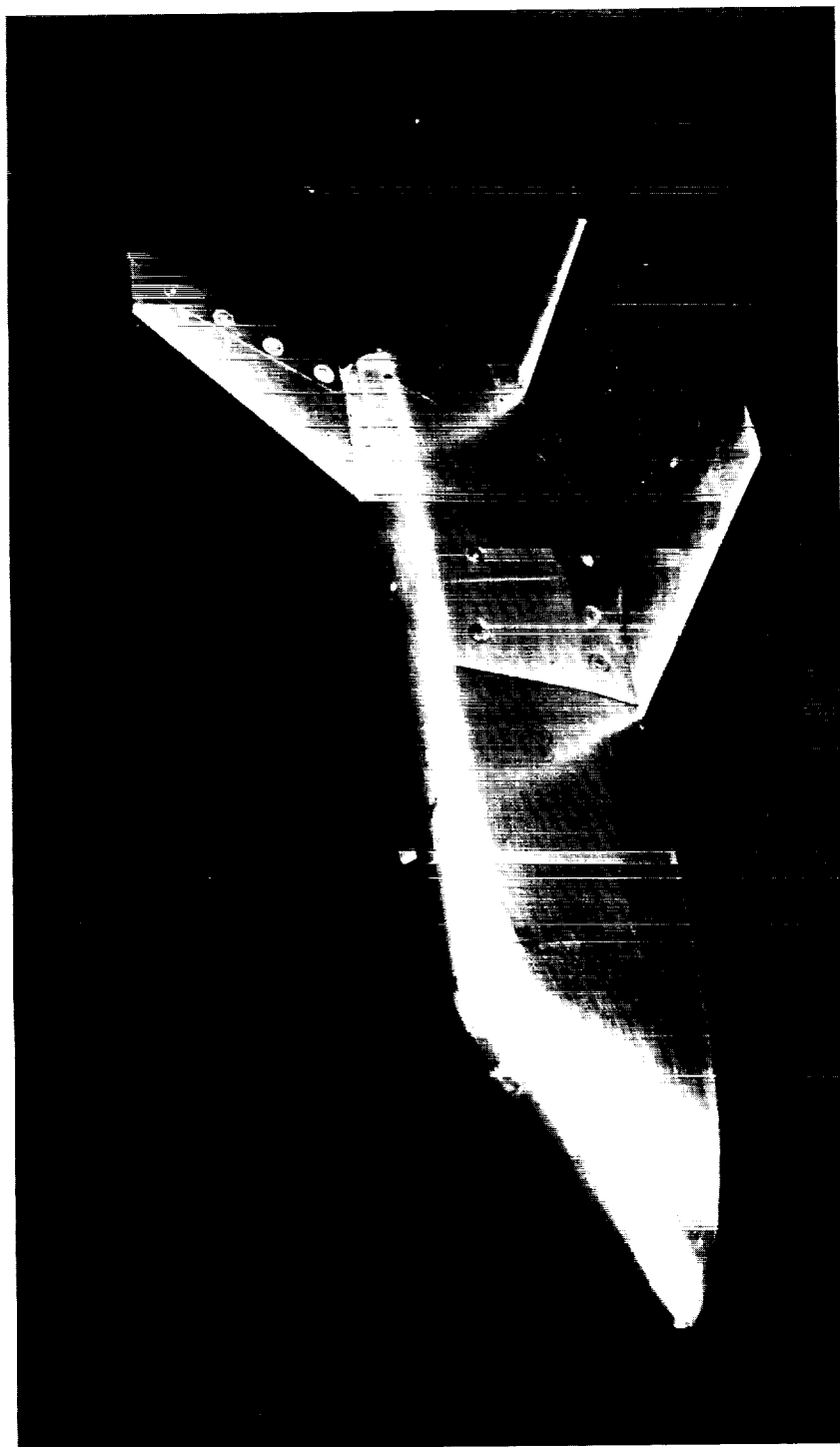


Figure 2

McDONNELL DOUGLAS DELTA-WING ORBITER
TWIN VERTICAL TAILS

(Figure 3)

A model of an early version of the McDonnell Douglas delta-wing orbiter with wing-tip-mounted vertical tails is shown in figure 3. Limited tests were made with various combinations of inboard elevon and outboard aileron deflection angles.

MCDONNELL DOUGLAS DELTA-WING ORBITER TWIN VERTICAL TAILS

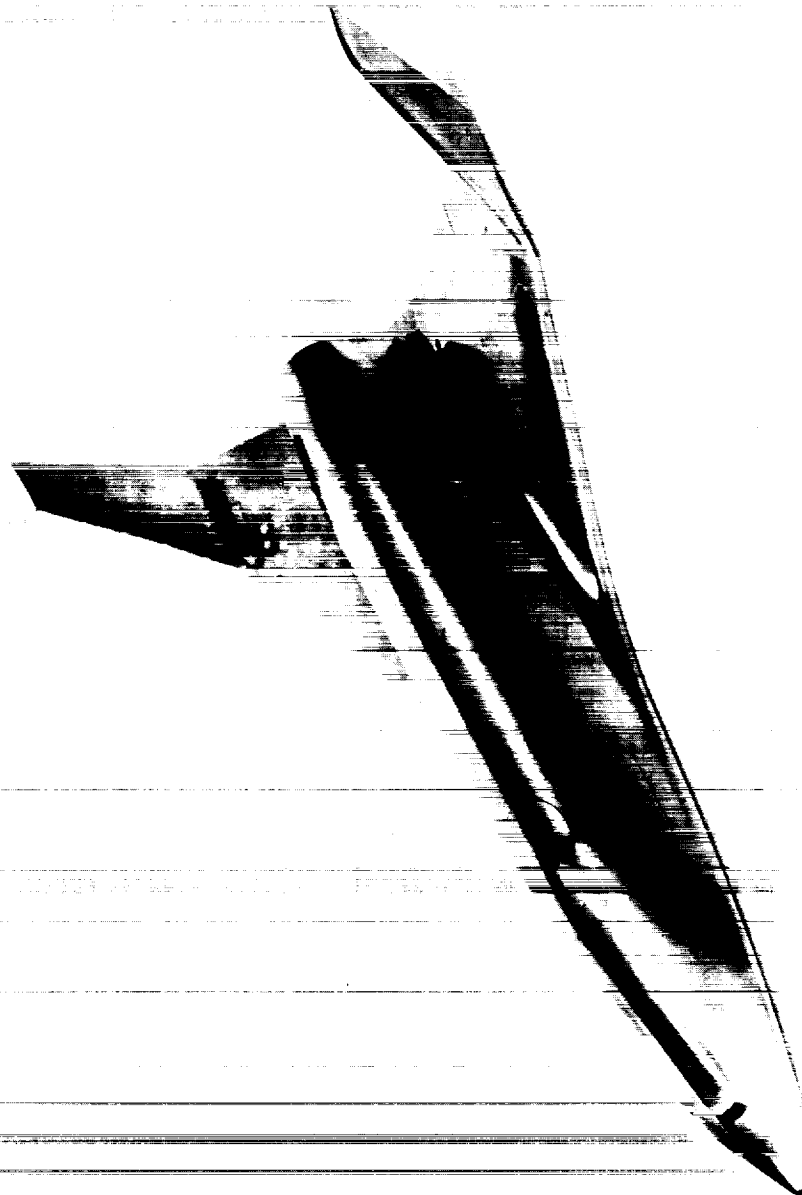


Figure 3

McDONNELL DOUGLAS DELTA-WING ORBITER
CENTERLINE VERTICAL TAIL

(Figure 4)

The model shown in figure 4 is a later version of the McDonnell Douglas delta-wing orbiter. The twin vertical tails shown in the previous figure have been removed and a centerline vertical tail added. The added wing tip fairing increased the span of the outboard ailerons over that of the earlier configuration. Also shown in the photograph is the added deflectable body flap.

MCDONNELL DOUGLAS DELTA-WING ORBITER
CENTERLINE VERTICAL TAIL



Figure 4

McDONNELL DOUGLAS/MARTIN LAUNCH CONFIGURATION
JET-FLAP-CANARD HIGH-WING BOOSTER AND STRAIGHT-WING ORBITER

(Figure 5)

The McDonnell Douglas/Martin launch configuration shown in figure 5 is comprised of a high-wing booster with jet-flap canard and the fixed-straight-wing orbiter. The model was tested with various combinations of booster elevon, aileron and rudder deflections.

MCDONNELL DOUGLAS/MARTIN LAUNCH CONFIGURATION
JET-FLAP-CANARD HIGH-WING BOOSTER AND STRAIGHT-WING ORBITER

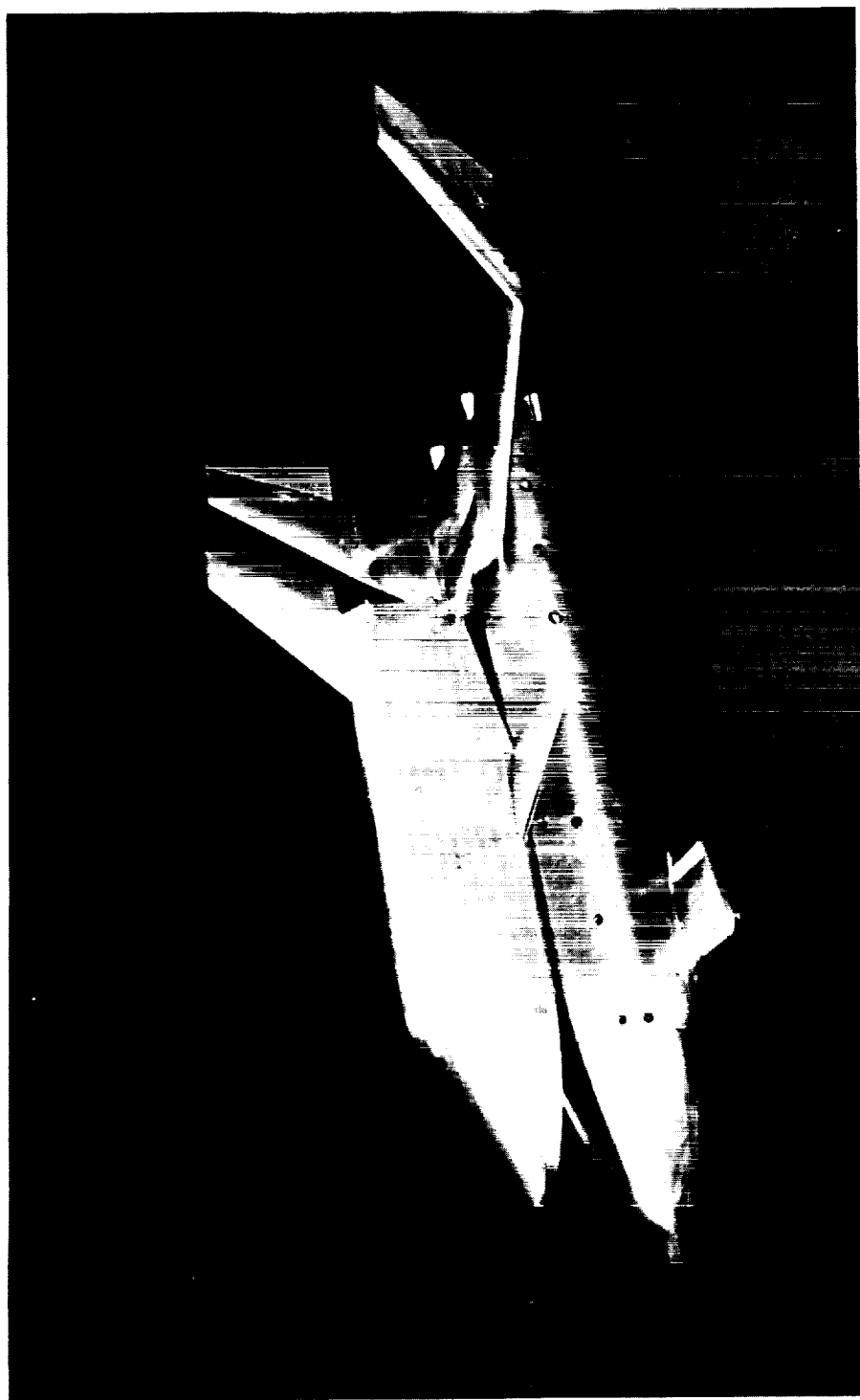


Figure 5

McDONNELL DOUGLAS/MARTIN LAUNCH CONFIGURATION
AERO-CANARD LOW-WING BOOSTER AND DELTA-WING ORBITER

(Figure 6)

The McDonnell Douglas/Martin launch configuration shown in figure 6 is comprised of a low-wing booster with aerodynamic canard and the single-tail version of the delta-wing orbiter. The canard incidence angle was not varied; aerodynamic control is provided by deflecting elevons, ailerons and rudder on the booster.

MCDONNELL DOUGLAS / MARTIN LAUNCH CONFIGURATION
AERO-CANARD LOW-WING BOOSTER AND DELTA-WING ORBITER

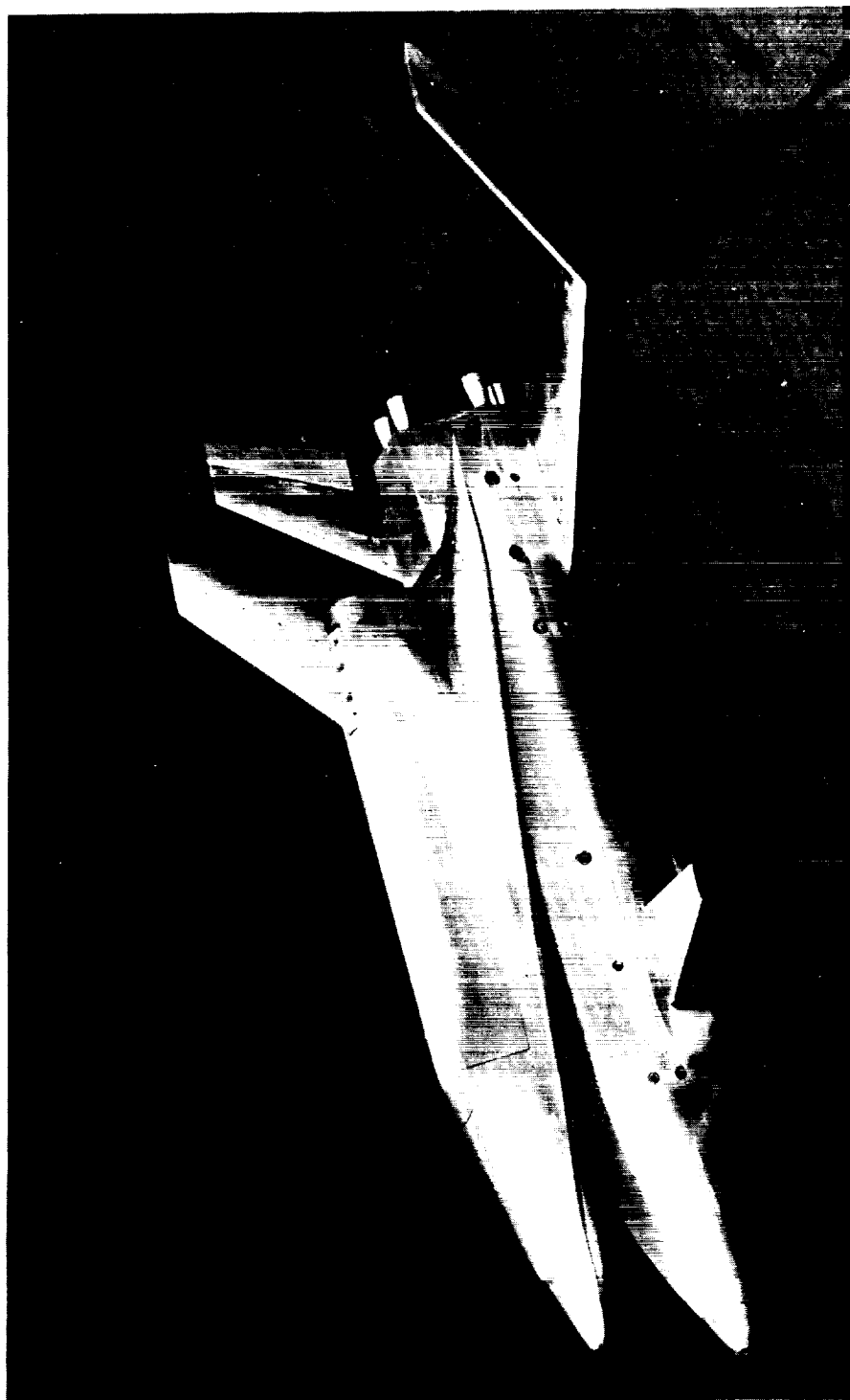


Figure 6

NORTH AMERICAN ROCKWELL STRAIGHT-WING ORBITER
LOW-POSITION HORIZONTAL TAIL

(Figure 7)

One version of the North American Rockwell straight-wing orbiter with horizontal tail in the low position is shown in figure 7. Configuration variables investigated at Ames include two different nose shapes and three different horizontal tail arrangements. The incidence of each of the horizontal tails was varied as well as elevator angle.

NORTH AMERICAN ROCKWELL STRAIGHT-WING ORBITER
LOW-POSITION HORIZONTAL TAIL



Figure 7

NORTH AMERICAN ROCKWELL STRAIGHT-WING ORBITER
MID-POSITION HORIZONTAL TAIL

(Figure 8)

- Another version of the North American Rockwell straight-wing orbiter is shown in figure 8. In this view, the horizontal tail is shown in the mid-body position.

NORTH AMERICAN ROCKWELL STRAIGHT-WING ORBITER
MID-POSITION HORIZONTAL TAIL

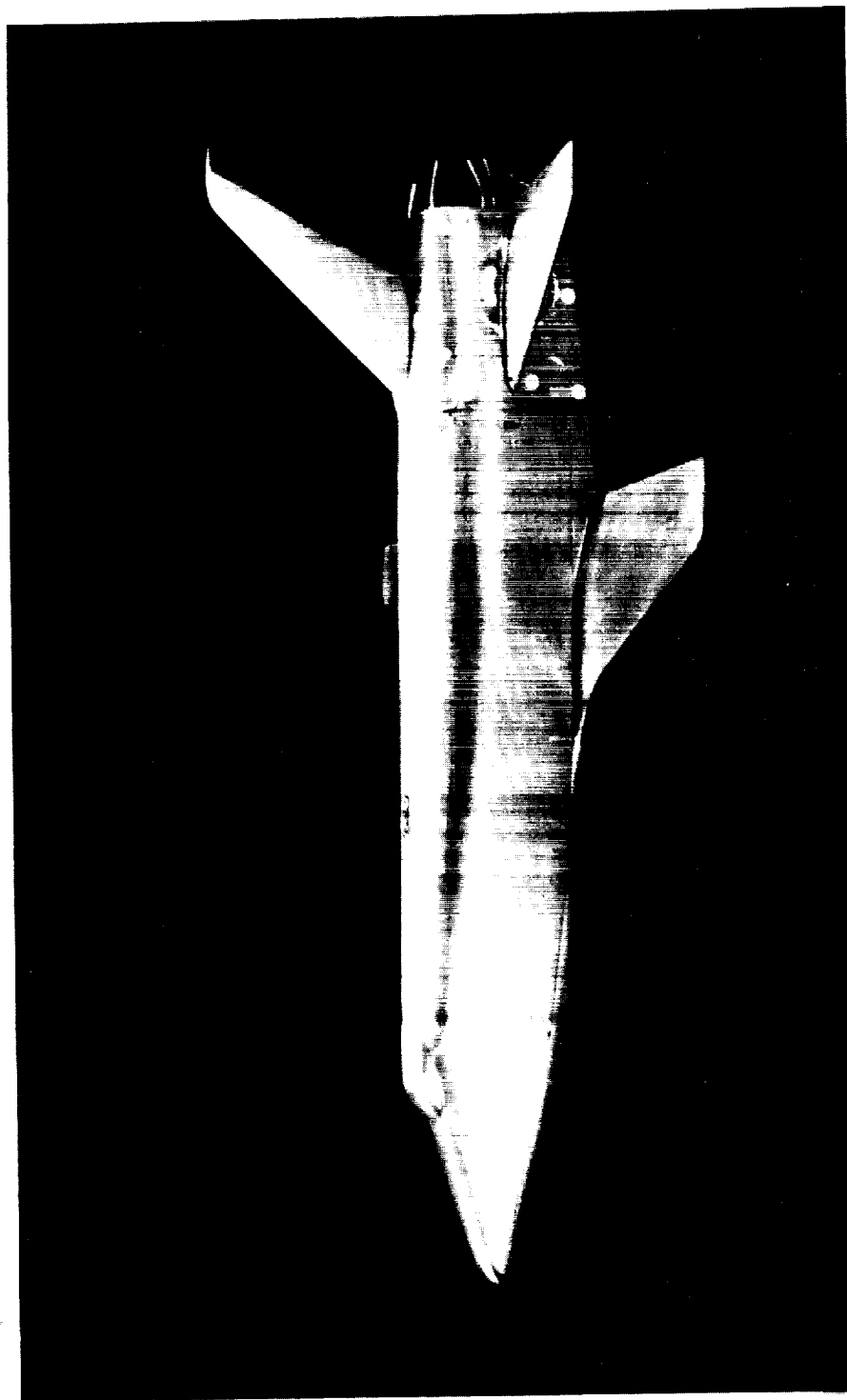


Figure 8

NORTH AMERICAN ROCKWELL DELTA-WING ORBITER
TWIN VERTICAL TAILS

(Figure 9)

One version of the North American Rockwell delta-wing orbiter with twin vertical tails is shown in figure 9. Configuration variables investigated at Ames include wing and vertical tail planform, tail cant and toe-in angles and elevon and rudder deflection angles.

NORTH AMERICAN ROCKWELL DELTA-WING ORBITER
TWIN VERTICAL TAILS

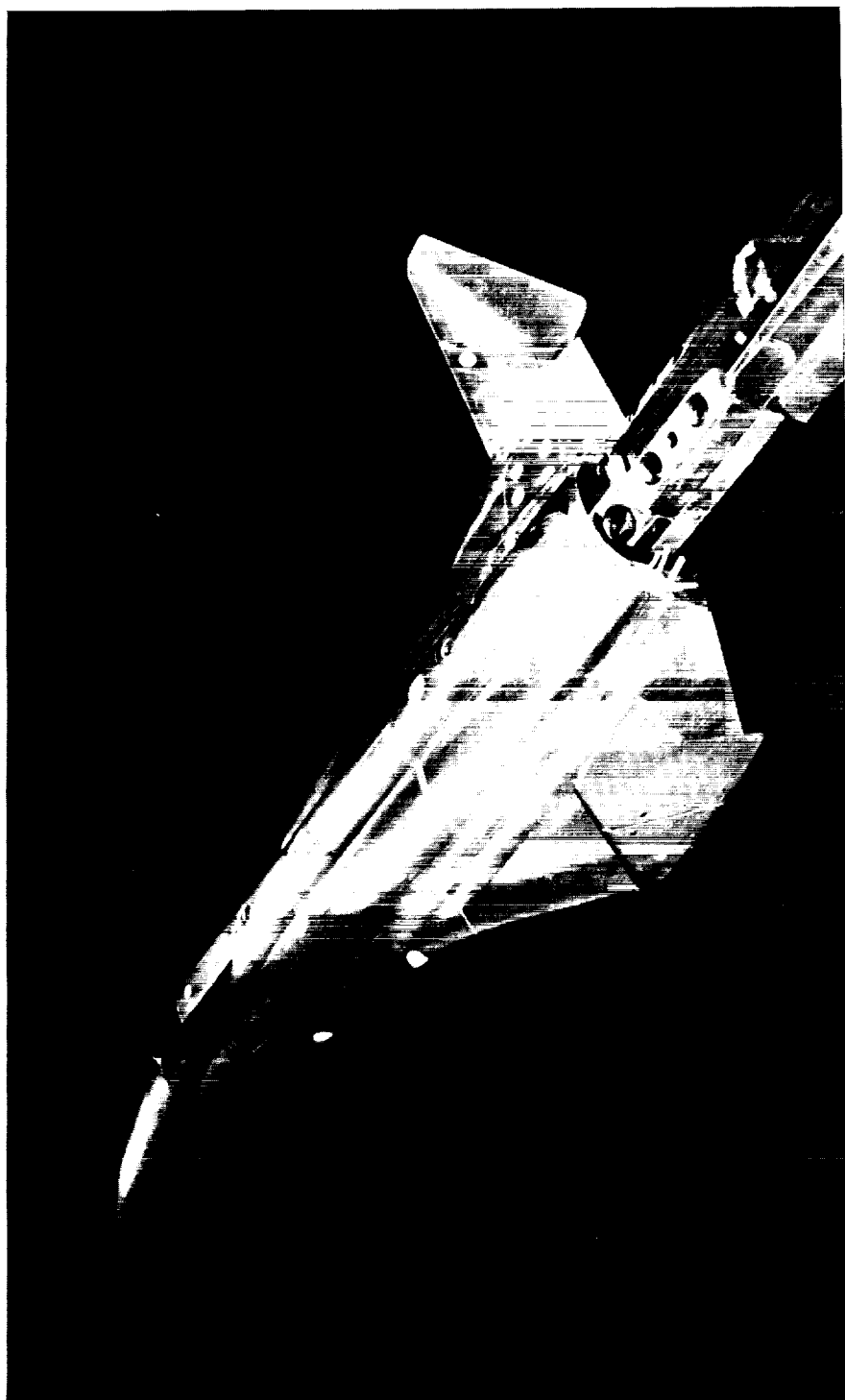


Figure 9

NORTH AMERICAN ROCKWELL DELTA-WING ORBITER
CENTERLINE VERTICAL TAIL WITH 5° FLARED RUDDER

(Figure 10)

A model of the North American Rockwell delta-wing orbiter with vertical tail on the body centerline is shown in figure 10. This photograph shows how the outboard portion of the wing was changed when the wing-tip-mounted vertical tails were eliminated. Several different rudder flare angles were investigated.

NORTH AMERICAN ROCKWELL DELTA-WING ORBITER
CENTERLINE VERTICAL TAIL WITH 5° FLARED RUDDER

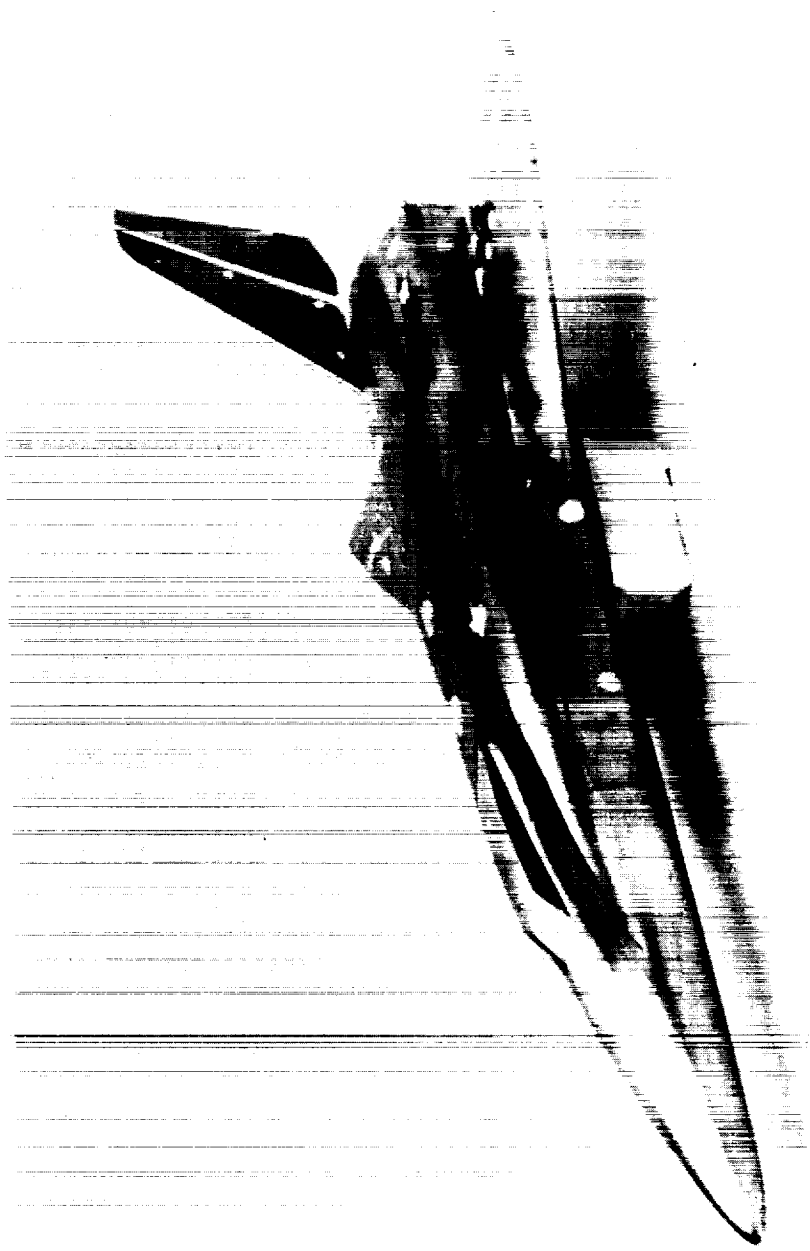


Figure 10

NORTH AMERICAN ROCKWELL DELTA-WING ORBITER
CENTERLINE VERTICAL TAIL WITH 5° FLARED RUDDER

(Figure 11)

The North American Rockwell delta-wing orbiter model shown in figure 11 has more sharply pointed wing tips than on the wing illustrated in the previous figure. The blunt trailing edge of the vertical tail resulting from the 5° of rudder flare is clearly visible.

NORTH AMERICAN ROCKWELL DELTA-WING ORBITER
CENTERLINE VERTICAL TAIL WITH 5° FLARED RUDDER

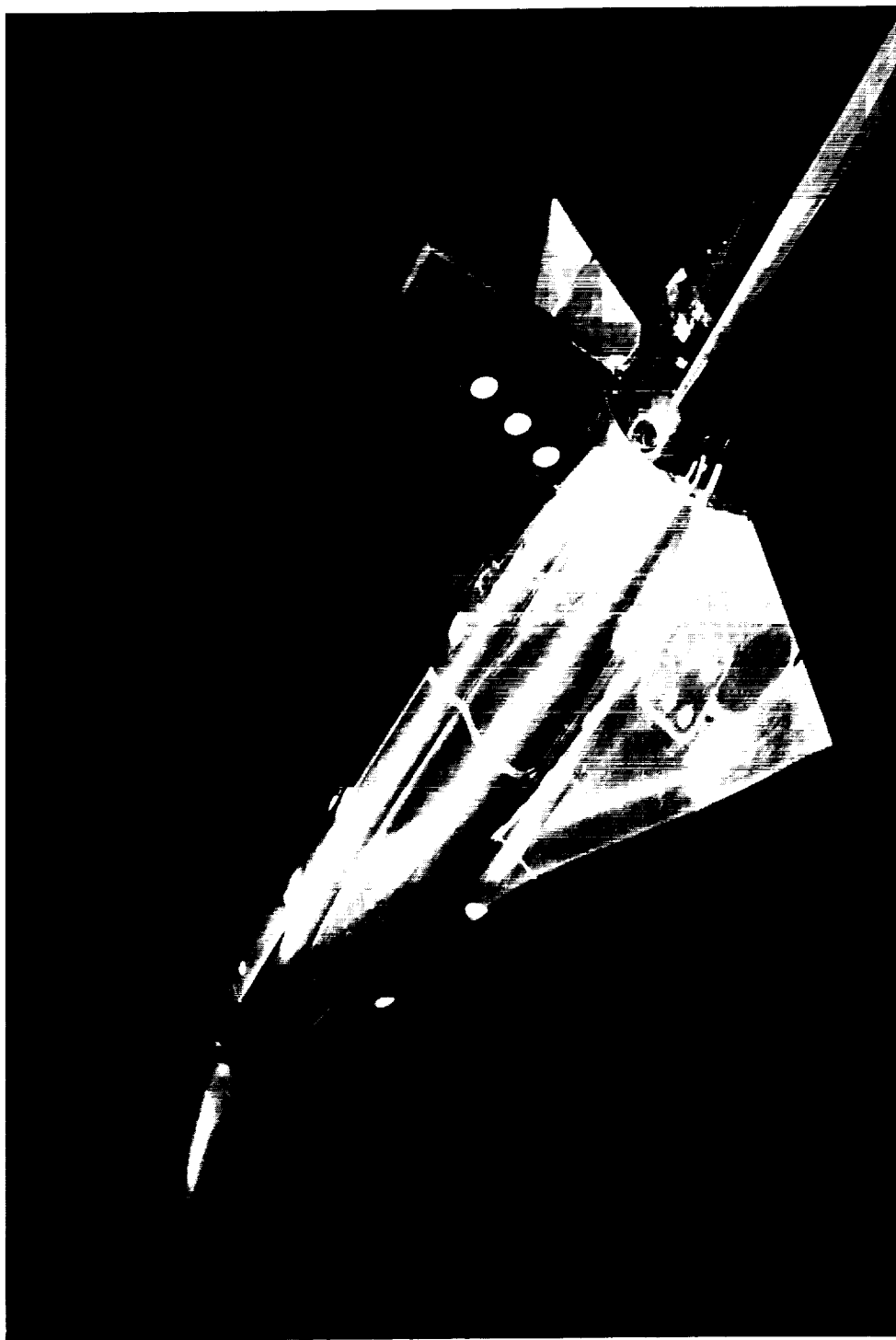


Figure 11

NORTH AMERICAN ROCKWELL DELTA-WING ORBITER
CENTERLINE VERTICAL TAIL WITH 20° FLARED RUDDER

(Figure 12)

The photograph of the North American Rockwell delta-wing orbiter model shown in figure 12 is presented to illustrate the 20° (40° included angle) flared rudder on the vertical tail.

NORTH AMERICAN ROCKWELL DELTA-WING ORBITER
CENTERLINE VERTICAL TAIL WITH 20° FLARED RUDDER

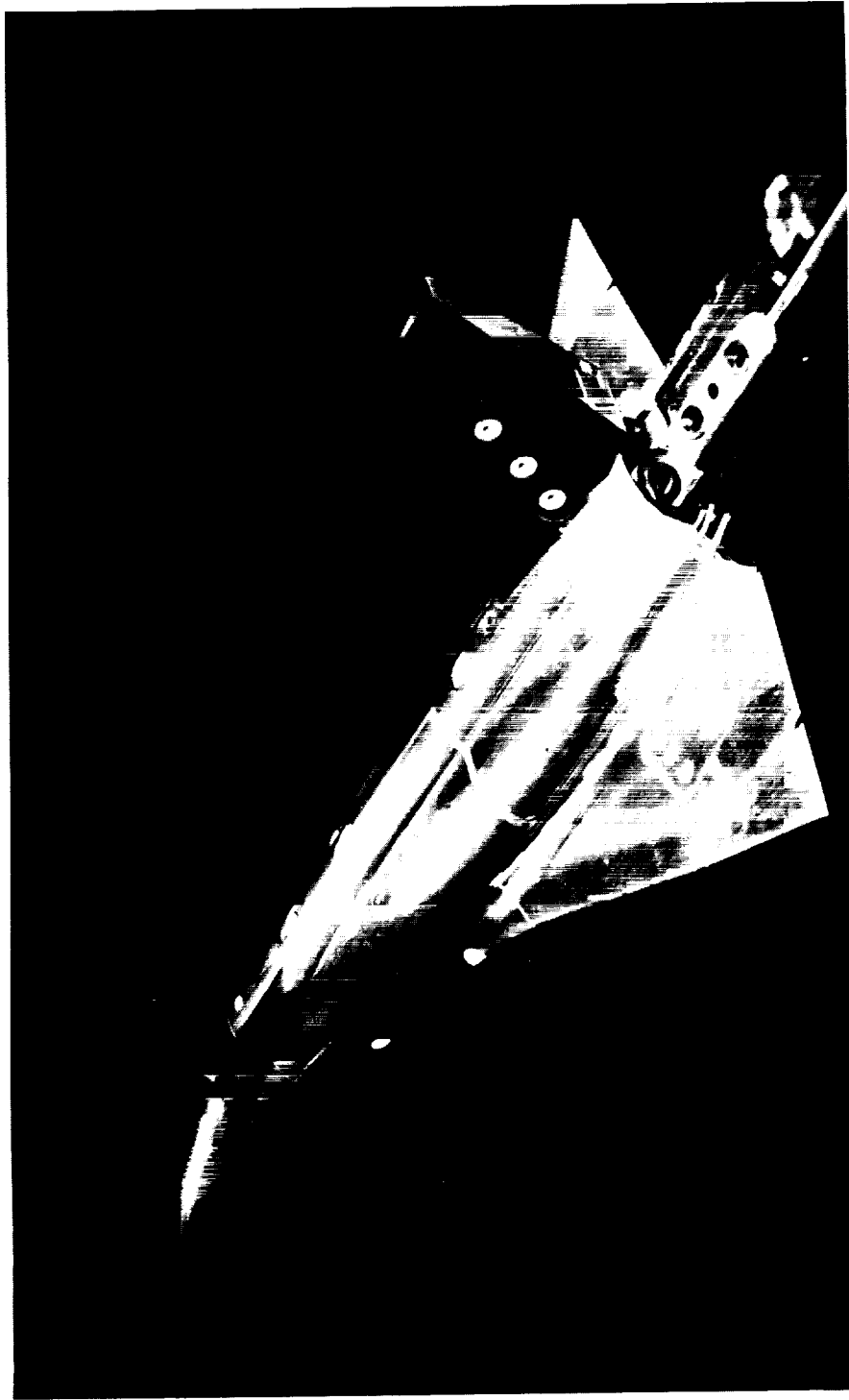


Figure 12

GENERAL DYNAMICS DELTA-WING BOOSTER

(Figure 13)

Figure 13 is a lower surface view of a General Dynamics delta-wing booster model. The model has a vertical tail mounted on the top of the fuselage. Pressures were measured on the body, wing and vertical tail.

GENERAL DYNAMICS DELTA - WING BOOSTER

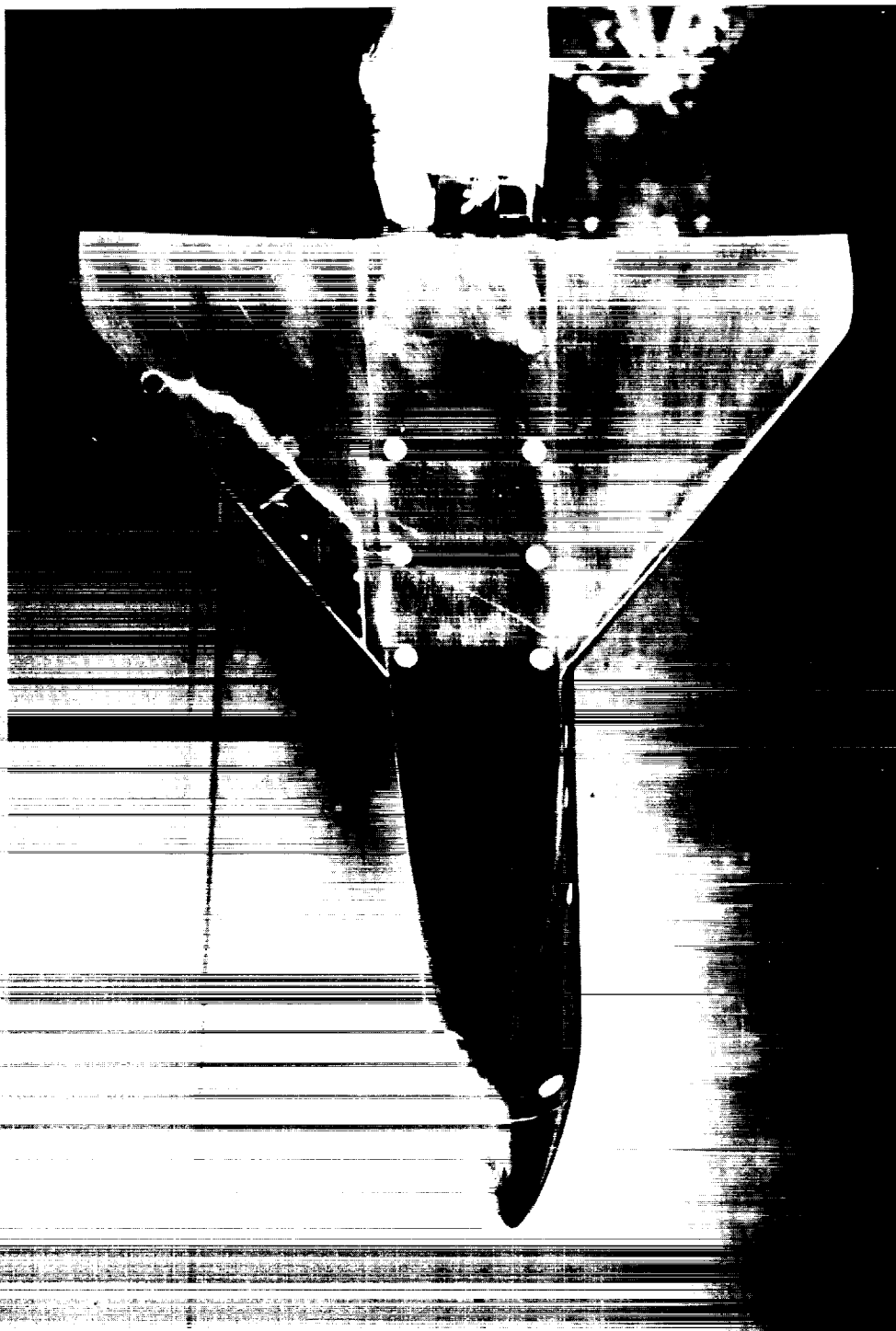


Figure 13

NORTH AMERICAN ROCKWELL/GENERAL DYNAMICS
LAUNCH CONFIGURATION
STRAIGHT-WING BOOSTER AND DELTA-WING ORBITER

(Figure 14)

One version of the North American Rockwell/General Dynamics launch configuration employing a straight-wing booster is shown in figure 14. In addition to varying the orbiter location and incidence relative to the booster, the tail arrangement on the booster was varied. The alternate arrangement consisted of a horizontal tail and a centerline-mounted vertical tail.

NORTH AMERICAN ROCKWELL / GENERAL DYNAMICS
LAUNCH CONFIGURATION
STRAIGHT-WING BOOSTER AND DELTA - WING ORBITER

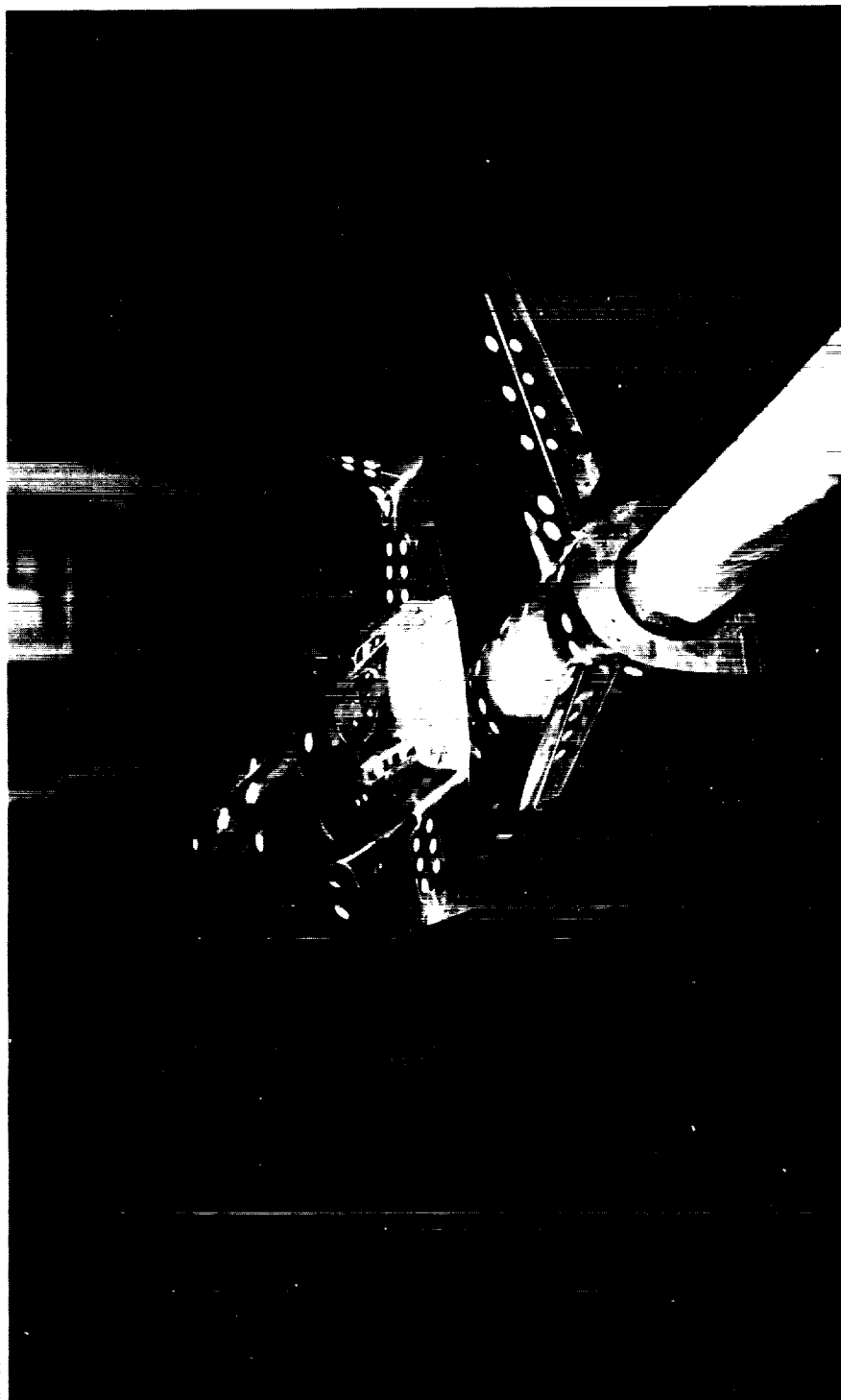


Figure 14

SUMMARY OF CONFIGURATION VARIABLES
AND TEST CONDITIONS INVESTIGATED

(Figure 15)

The photographs shown in figures 2 through 14 were selected to illustrate the wide range of configurations being investigated. Wind-tunnel data were obtained for all of these models and a number of other ones at the Ames Research Center. A summary of the configuration variables and test conditions investigated is presented in figure 15. From unpublished data a number of aerodynamic effects of configuration shaping that are common to straight- and delta-wing concepts are emerging. Only a few of those being investigated are discussed in this paper.

SUMMARY OF CONFIGURATION VARIABLES AND TEST CONDITIONS INVESTIGATED

BODY

- CROSS SECTIONAL SHAPE
- NOSE SHAPE
- CHINE RADIUS

WING

- PLANFORM - STRAIGHT, DELTA, TRAPEZOIDAL
- LOCATION - LONGITUDINAL AND VERTICAL

HORIZONTAL TAIL

- LOCATION (LOW AND MID POSITIONS) AND SIZE
- FIXED AND ALL MOVEABLE
- PLANFORM

VERTICAL TAIL

- PLANFORM
- ARRANGEMENT - TWIN AND SINGLE
- FLARED AND UNFLARED

CONTROLS

- CANARD
- WING TRAILING EDGE
- ELEVATORS
- RUDDERS
- AILERONS

LAUNCH CONFIGURATIONS

- ORBITER POSITION ON BOOSTER

TEST CONDITIONS

- MACH NUMBER, 0.25 - 7.4
- LENGTH REYNOLDS NUMBER, 1 TO 20×10^6
- ATTITUDE, $0 \leq \alpha \leq 70^\circ$ AND $0 \leq \beta \leq 15^\circ$

Figure 15

EFFECTS OF BODY CHINE RADIUS
ON AERODYNAMICS OF SHUTTLE FUSELAGE

(Figure 16)

Figure 16 shows the effect of body chine radius on the high angle of attack normal-force and pitching-moment coefficients for Mach numbers of 0.3, 0.6 and 1.35. The results, for body alone, are for a Reynolds number of 2.5×10^6 , based on body width. As might be expected from the early work of Polhamus (reference 1) on the drag of two-dimensional cylinders, chine radius has a large effect on the normal-force and pitching-moment coefficients at $M = 0.3$. Increasing chine radius (or streamlining) reduces the cross-flow drag coefficient and thereby decreases the normal-force coefficients at high angles of attack. The effect of chine radius decreases as the Mach number is increased. The reason for this trend is that at subsonic speeds the normal force results primarily from wake drag which is sensitive to small amounts of forebody streamlining, while at supersonic speeds the normal force is primarily forebody drag which is not sensitive to small amounts of streamlining.

EFFECT OF BODY CHINE RADIUS ON AERODYNAMICS OF SHUTTLE FUSELAGE

$Re_d = 2.5 \times 10^6$

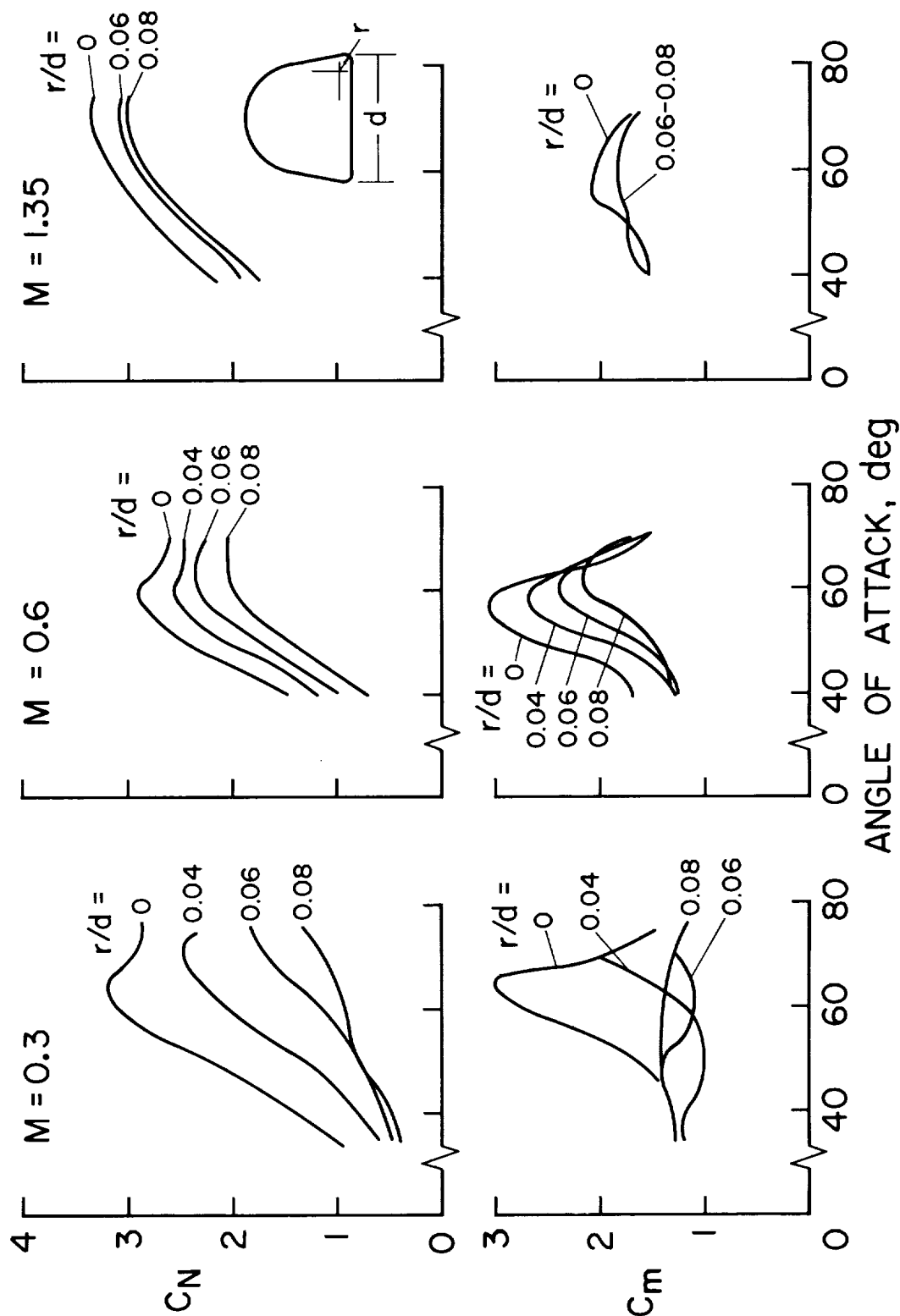


Figure 16

EFFECT OF REYNOLDS NUMBER
ON AERODYNAMICS OF SHUTTLE FUSELAGE

(Figure 17)

The effect of Reynolds number on the high angle of attack normal-force and pitching-moment coefficients of a body alone are presented in figure 17. Data are shown for two chine radii, 0 and 0.06 of the body width. For the model with sharp corners, increasing the Reynolds number by a factor of 3 or 4 had very little effect. For the rounded corner model, changes in Reynolds number had large effects only at $M = 0.3$. It should be noted that the curves of pitching-moment coefficient at $M = 0.6$ resemble those at $M = 0.3$ for the model with sharp corners and the model with round corners at the lower Reynolds numbers; i.e., high cross-flow drag of the nose and pitch up is indicated. These effects are attributed to changes in the way the flow separates in the cross-flow plane as it passes around the body. With sharp corners, the flow has fixed edges from which to separate. The resulting wake does not close behind the body and the cross-flow drag corresponds to that high value for subcritical Reynolds numbers. At $M = 0.3$ with a small amount of corner rounding, the flow remains attached for further distances around the body as Reynolds number is increased. The wake closes more and more until finally, for sufficiently high Reynolds number, the cross-flow drag corresponds to that low value for supercritical Reynolds number. Larger amounts of corner rounding and increasing Mach number reduce the Reynolds number required to obtain supercritical flow with attendant low values of cross-flow drag.

EFFECT OF REYNOLDS NUMBER ON AERODYNAMICS OF SHUTTLE FUSELAGE

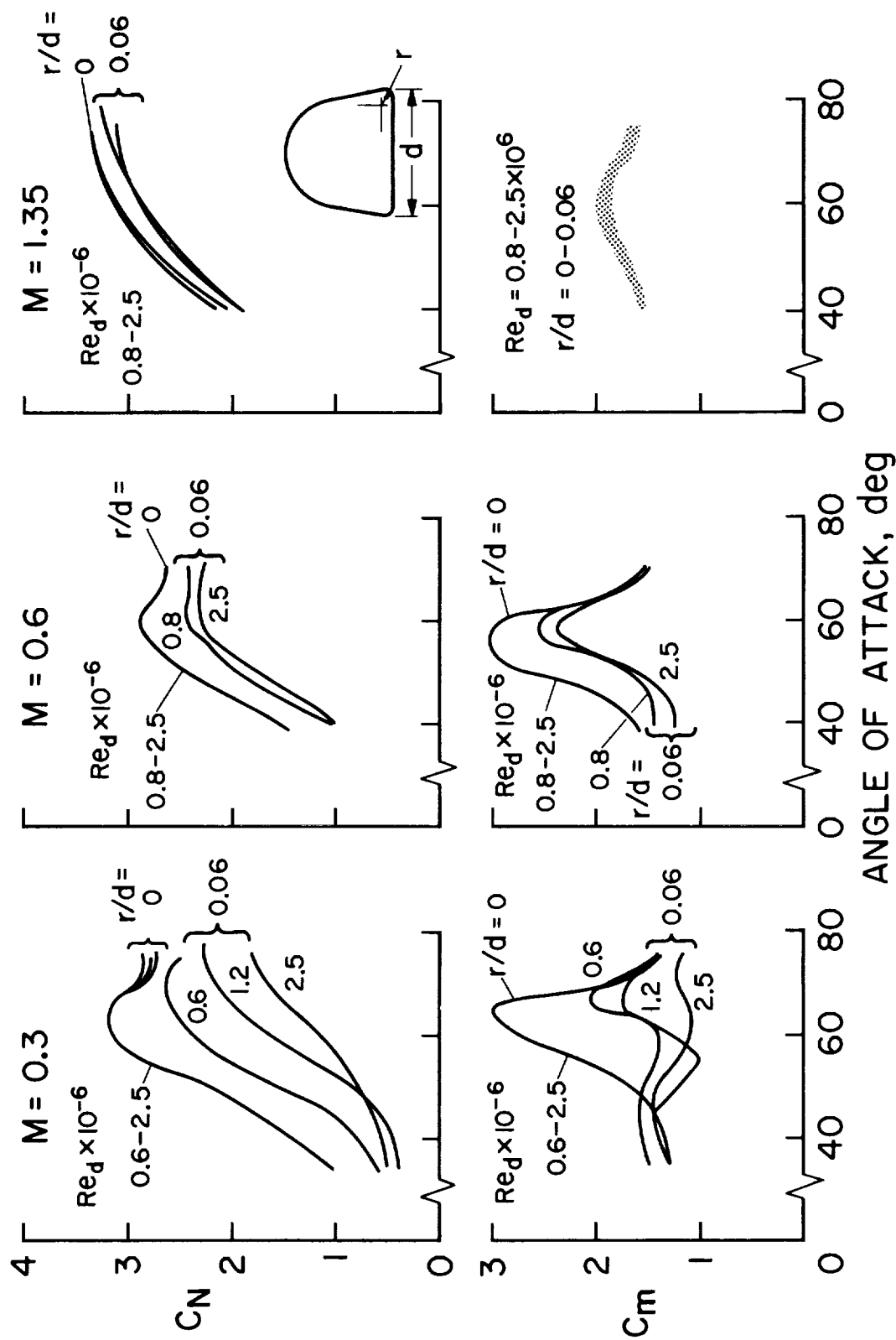


Figure 17

EFFECT OF MACH NUMBER
ON PITCHING MOMENT OF STRAIGHT-WING ORBITER

(Figure 18)

The body alone results discussed in figures 16 and 17 are reflected in figure 18 showing the effect of Mach number on the pitching-moment coefficient of a straight-wing orbiter having well-rounded corners on the fuselage. At $M = 0.6$ the tendency toward pitch up at high angles of attack, independent of Reynolds number, might make it difficult to initiate the transition from high to low angles of attack with aerodynamic controls. This pitch-up tendency at $M = 0.6$, which is attributed to the aerodynamics of the body nose, is also present in results for delta-wing shuttle vehicles. However, it is of less concern for delta-wing shapes since initiation of transition from high to low angles of attack probably would occur at supersonic speeds for these vehicles. The changing character of the pitching-moment curves at high angle of attack as Mach number is increased, i.e., no hump at $M = 0.25$, large hump at $M = 0.6$ and diminishing hump for increasing supersonic Mach number, is attributed to two effects. One is the transonic cross-flow drag rise of the body nose. The other is the reducing dominance of the body nose normal force as the center of pressure of the configuration shifts rearward toward the centroid of planform area with increasing Mach number.

EFFECT OF MACH NUMBER ON PITCHING MOMENT OF STRAIGHT-WING ORBITER

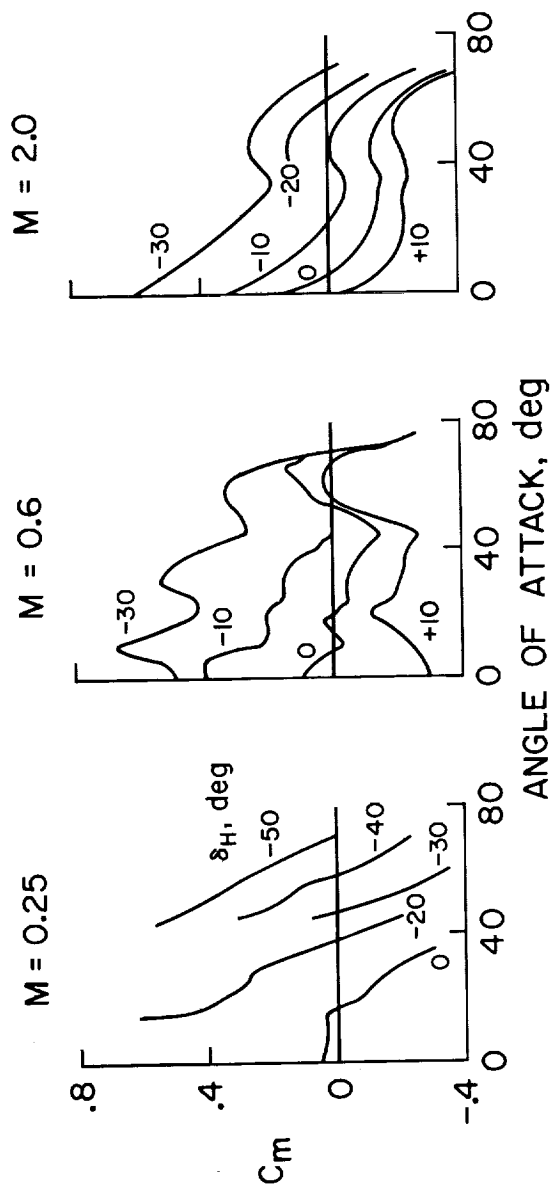


Figure 18

COMPARISON OF SINGLE AND TWIN TAILS
DELTA-WING ORBITER

(Figure 19)

Figure 19 compares the lateral-directional characteristics of a delta-wing orbiter with no vertical tail, single (centerline) vertical tail and twin vertical tails. Data for two rudder flare angles, 5° and 20°, are shown for the single tail; the results are presented for a Mach number of 7.4. At high angles of attack, positive dihedral effect ($C_{lb\beta} < 0$) overcomes directional instability ($C_{nb\beta} < 0$) in the relationship

$$C_{n\beta}^* = C_{nb\beta} \cos \alpha - \frac{I_Z}{I_X} C_{lb\beta} \sin \alpha$$

to provide static stability even with no vertical tail. For flight at angles of attack near $(L/D)_{\max}$ at hypersonic speed either a single tail with a flare angle greater than 20° or a twin tail is required for stability.

COMPARISON OF SINGLE AND TWIN TAILS DELTA-WING ORBITER

$$M_{\infty} = 7.4$$

$$\frac{I_Z}{I_X} = 4.3$$

$$C_{n\beta}^* = C_{nb\beta} \cos \alpha - \frac{I_Z}{I_X} C_{lb\beta} \sin \alpha$$

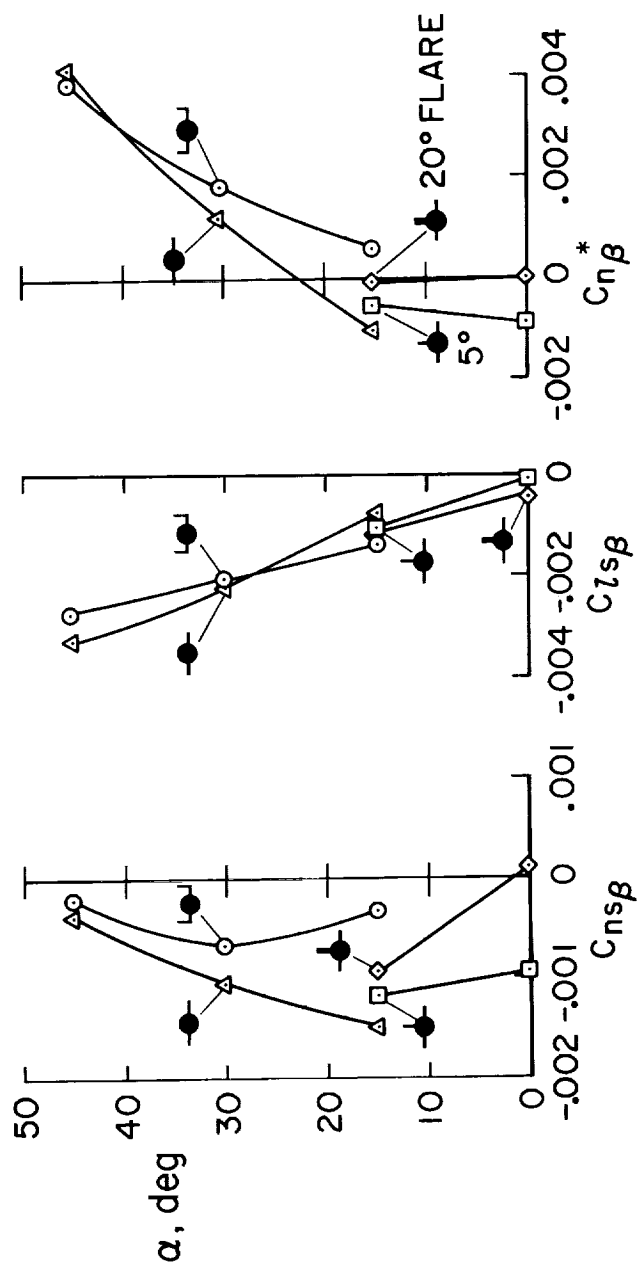


Figure 19

COMPARISON OF SINGLE AND TWIN TAILS
DELTA-WING ORBITER

(Figure 20)

Figure 20 indicates that in the subsonic and supersonic speed range at zero angle of attack, the single vertical tail provides greater stability for the delta-wing orbiter than does the twin tail. The implication can be drawn from the results that if the transition from high to low angles of attack were delayed from hypersonic to supersonic speeds, the complexity of twin tails or large flare angles might be avoided.

COMPARISON OF SINGLE AND TWIN TAILS DELTA-WING ORBITER

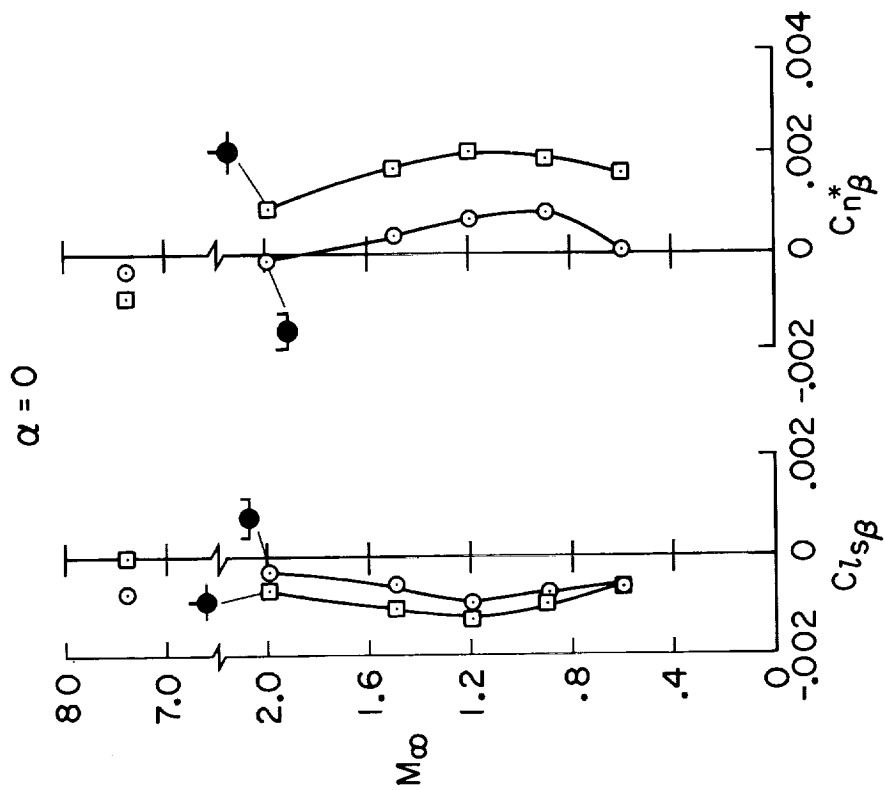


Figure 20

COMPARISON OF SINGLE AND TWIN TAILS
DELTA-WING ORBITER

(Figure 21)

Pitching-moment coefficients of a delta-wing orbiter are compared for single and twin tails in figure 21. At $M = 0.6$, a pitch up occurs near $\alpha = 10^\circ$ for the model with twin tails. It is believed that the pitch up results from flow separation and loss of lift on the wing near the fins. There appears to be no such problem for the centerline tail. Differences in the pitching-moment curves for the two types of vertical tails disappear as the Mach number is increased.

COMPARISON OF SINGLE AND TWIN TAILS DELTA-WING ORBITER

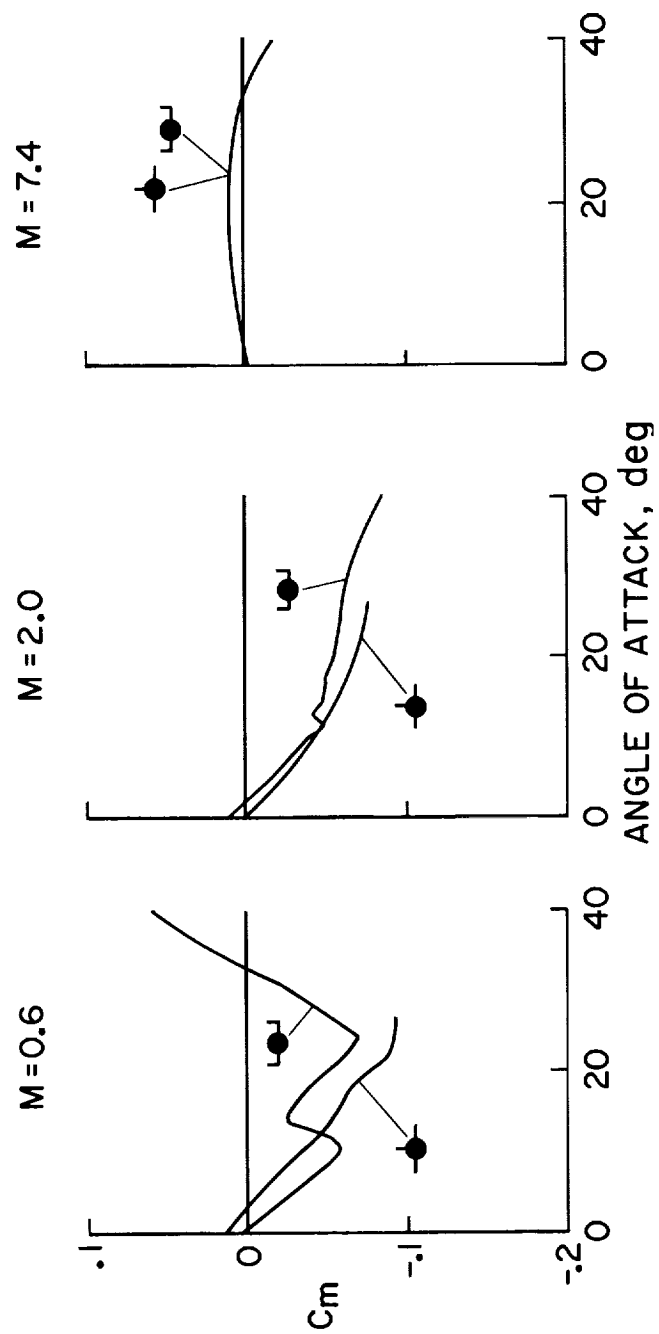


Figure 21

EFFECT OF VERTICAL TAIL FLARE
ON LIFT-DRAG RATIO DELTA-WING ORBITER

(Figure 22)

Figure 22 shows the penalty in L/D that would be incurred by flaring of the vertical tail if no provision is made for reducing the flare at the lower speeds. The reduction in L/D is mainly a result of the base drag associated with the blunt trailing edges.

EFFECT OF VERTICAL TAIL FLARE ON LIFT-DRAG RATIO DELTA-WING ORBITER

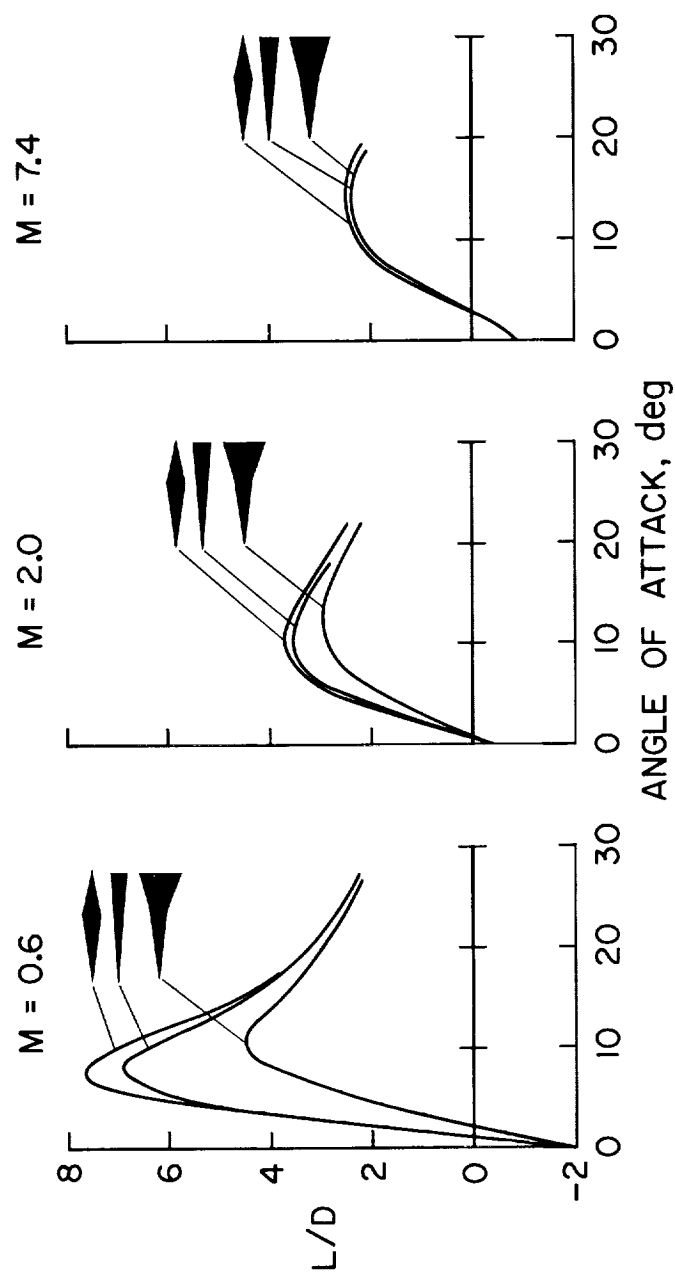


Figure 22

LONGITUDINAL STABILITY CRITERIA

(Figure 23)

Although the orbiter and booster elements of the space shuttle are airplane-like vehicles, they traverse rapidly ascending and descending paths through the atmosphere. Therefore, as is the case for missiles, it can be anticipated that aerodynamic stability criteria should include effects of varying dynamic pressure and Mach number. Longitudinal stability criteria including these effects are presented in figure 23. These criteria were derived by Sommer and Tobak in reference 2. They are presented here to illustrate the additional conditions imposed by a non constant flight environment. Of course, static aerodynamic stability about the trim angle of attack ($C_{m_\alpha} < 0$) is required to obtain an oscillatory motion. The second equation shows how much aerodynamic damping in pitch is needed to cause oscillatory motion to decay with aerodynamic controls fixed. It can be seen that the smaller the slope of the lift curve, evaluated at the trim angle of attack, is, the more damping in pitch is needed. For flight at $C_{L_{\max}}$ no benefit is derived from the lift-curve slope. At hypersonic speeds dC_{m_α}/dM_∞ is essentially zero and C_{L_α} is nearly constant. For this situation less aerodynamic damping is required when dynamic pressure is increasing while more damping is required when dynamic pressure is decreasing. At low supersonic and transonic speeds C_{m_α} changes rapidly with Mach number and reaches a maximum value near a Mach number of unity. In this flight regime the varying C_{m_α} either will be beneficial or detrimental depending upon whether the speed is increasing or decreasing and whether the Mach number is above or below one.

LONGITUDINAL STABILITY CRITERIA

FOR OSCILLATORY MOTION:

$$C_{m\dot{\alpha}} < 0$$

FOR DECAY OF OSCILLATORY MODE:

$$C_{m\dot{q}} + C_{m\dot{\alpha}} < \frac{I_Y}{m l^2} \left\{ C_{L\alpha} + \frac{m}{\rho A l} \left[\frac{dq/ds}{q} + M_\infty \frac{dv/ds}{V} \right] \frac{dC_{m\alpha}/dM_\infty}{C_{m\alpha}} \right\}$$

WHERE

$$\frac{dq/ds}{q} = \frac{\rho A l}{m} \left[-C_D + \frac{W}{A} \sin \gamma \left(\frac{1}{q} + \frac{\beta}{g \rho} \right) \right]$$

$$\frac{dv/ds}{V} = \frac{\rho A l}{2m} \left(-C_D + \frac{W}{qA} \sin \gamma \right)$$

$$S = (\text{DISTANCE ALONG FLIGHT PATH})/l$$

Figure 23

LATERAL-DIRECTIONAL STABILITY CRITERIA

(Figure 24)

In order to assure static lateral-directional stability, the criterion given in figure 24 must be satisfied. The form of the criterion includes both of the criteria given previously by Wawrzyniak in reference 3 and Manke, et.al. in reference 4. Wawrzyniak's criterion results when it can be assumed that $\frac{I_{XZ}}{I_X} \ll \cot \alpha$ and $\frac{I_{XZ}}{I_Z} \ll \tan \alpha$ so that $a \approx 1$ and $b \approx \frac{I_Z}{I_X} \tan \alpha$.

Then, the criterion can be written $C_{n\beta} \cos \alpha - \frac{I_Z}{I_X} C_{l\beta} \sin \alpha > 0$. On the other hand, when the angle of attack is small so that $\sin \alpha \approx \alpha$, $\cos \approx 1$, such as it is for the lifting body class of vehicles including the M-2, HL-10 and X-24, then the criterion can be written as

$C_{n\beta} - \frac{I_Z}{I_X} C_{l\beta} (\alpha - \frac{I_{XZ}}{I_Z}) > 0$ as given by Manke, et.al. in reference 4. Lifting body flight tests have shown that aircraft stability remains acceptable so long as this latter criterion is satisfied even though $C_{n\beta}$ is negative. Although the criterion has a different form for shuttle vehicles flying at higher angles of attack, this experience with lifting bodies lends support to the validity of the more general form of $C_{n\beta}^*$.

LATERAL-DIRECTIONAL STABILITY CRITERIA

FOR OSCILLATORY MOTION:

$$C_{n\beta}^* > 0$$

WHERE

$$C_{n\beta}^* = aC_{n\beta} - bC_{l\beta}$$

$$a = 1 - \tan \alpha \frac{I_{xz}}{I_x}$$

$$b = \frac{I_z}{I_x} \tan \alpha - \frac{I_{xz}}{I_x}$$

Figure 24

LATERAL-DIRECTIONAL STABILITY CRITERIA

(Figure 25)

Previously unpublished criteria for decay of the first and second order mode motions, respectively, including effects of varying dynamic pressure and Mach number are given in figure 25. These criteria were derived by Tobak using an approach similar to that discussed in reference 21 in which the longitudinal criteria were derived. It is assumed in the derivation that $\alpha = \text{const.}$, $q \approx 0$, so that the roll and yaw equations of motion become uncoupled from the pitch equation. The right hand side of the first equation is analogous to the result presented in figure 23 for decay of the longitudinal oscillatory mode. The quantities a and b are defined in figure 24. Note that the right side of the equation for decay of the first order mode is zero for constant velocity flight. The derivatives $C_{n\dot{\phi}}$ and $C_{l\dot{\phi}}$ are the rate of change with $\dot{\phi}/V$, evaluated at $\dot{\phi} = 0$, of the yawing- and rolling-moment coefficients, respectively, that would be measured in steady coning motion with α , β and $\dot{\phi}$ set at constant values. Analysis of the equations presented in this figure to determine which terms are most significant for shuttle vehicles now is underway. Also, consideration is being given to the definition of wind-tunnel experiments necessary for measuring the various derivatives appearing in the equations. Results of this work are shown in the next figures.

LATERAL-DIRECTIONAL STABILITY CRITERIA

FOR DECAY OF OSCILLATORY MODE:

$$\frac{I_Z}{I_X} C_{nD2} - C_{nD1} < \frac{I_Z}{m\lambda^2} \left\{ -C_{Y\beta} + \frac{m}{\rho A l} \left[\frac{dq/ds}{q} + M_\infty \frac{dv/ds}{V} \right] \frac{dC_{n\beta}^*/dM_\infty}{C_{n\beta}^*} \right\}$$

WHERE

$$C_{nD1} = a C_{nD} - b C_{lD}$$

$$C_{nD} = -(C_{nr} - \cos \sigma C_{n\dot{\beta}})$$

$$C_{lD} = -(C_{lr} - \cos \sigma C_{l\dot{\beta}})$$

$$\cos \sigma C_{nD2} = \left(C_{l\beta} + \frac{I_{XZ}}{I_Z} C_{n\beta} \right) \left(\frac{a C_{n\dot{\varphi}} - b C_{l\dot{\varphi}}}{a C_{n\beta} - b C_{l\beta}} \right)$$

σ = RESULTANT INCIDENCE ANGLE

FOR DECAY OF FIRST ORDER MODE:

$$\frac{C_{n\beta} C_{l\dot{\varphi}} - C_{l\beta} C_{n\dot{\varphi}}}{\cos \sigma C_{n\beta}^*} < \frac{2 I_X}{\rho A l^3} \frac{dv/ds}{V} \left(1 + M_\infty \frac{dC_{n\beta}^*/dM_\infty}{C_{n\beta}^*} \right)$$

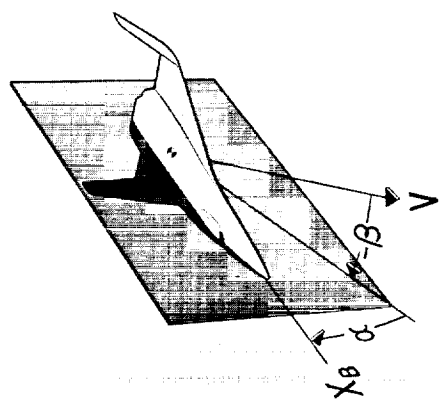
Figure 25

BASIC MOTIONS IN BODY AXES

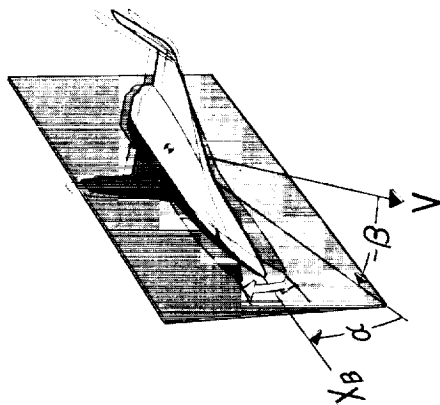
(Figure 26)

In a series of earlier papers, references 5 through 8, Tobak and his associates formulated aerodynamic force and moment systems for bodies of revolution which do not depend on a linearity assumption and are capable of accounting for the coupling between motions that may occur during large amplitude nonplanar motions. This work has just been extended to include non axisymmetric bodies (e.g., shuttlecraft) and results are presented in reference 9. It has been shown, in body axes, that moment contributions from the four characteristic motions pictured in figure 26 are required to completely specify the nonlinear moment system for arbitrary motions. For wind-tunnel tests in the body axes system, two kinds of apparatus are needed. One is a coning apparatus capable of measuring moment contributions due both to steady angle of attack and sideslip and coning at constant α and β . It is noted that all forces and moments measured with this device are steady quantities even under coning conditions so that a conventional static balance can be used in the model. The other device needed is a damping apparatus capable of measuring pitch, yaw and roll moments due to small oscillations about fixed angles of attack with sideslip angle constant (damping in pitch) and due to small oscillations about fixed angles of yaw with angle of attack constant (damping in yaw).

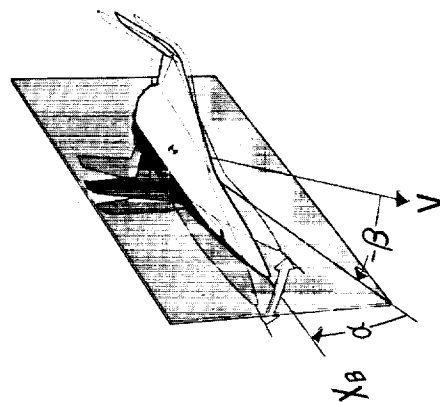
BASIC MOTIONS IN BODY AXES



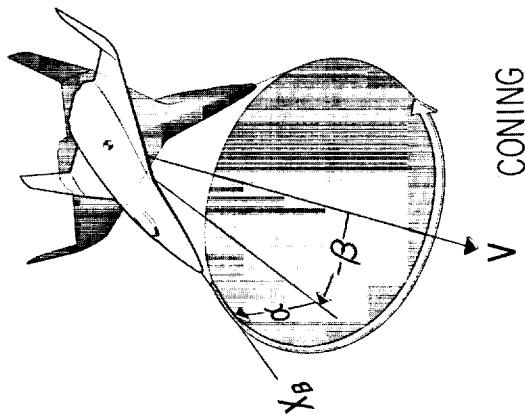
STEADY ANGLE OF ATTACK AND SIDESLIP



DAMPING IN PITCH



DAMPING IN YAW



CONING

Figure 26

BASIC MOTIONS IN AERODYNAMIC AXES

(Figure 27)

The four characteristic motions in the aerodynamic axes system are shown in figure 27. Wind-tunnel tests in this axes system require the same two pieces of apparatus needed to produce the characteristic motions in body axes except that the coning device must also be capable of producing small oscillations in roll about various constant incidence and roll angles. The damping in roll experiment in this axis system replaces the damping in yaw experiment in the body axis system.

BASIC MOTIONS IN AERODYNAMIC AXES

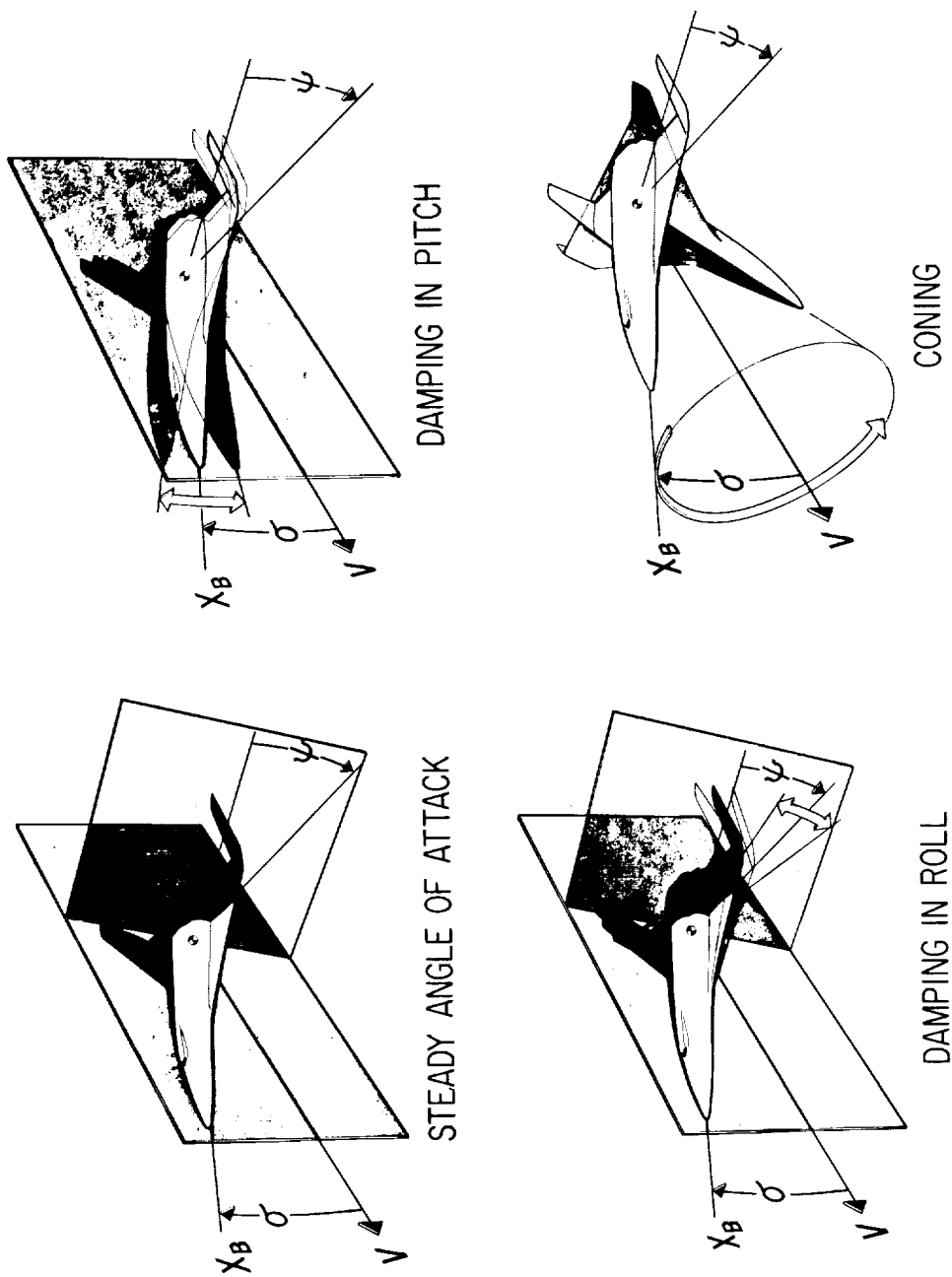


Figure 27

CONING APPARATUS FOR WIND-TUNNEL EXPERIMENTS

(Figure 28)

An apparatus designed to produce coning motion is shown in figure 28. A motor drives the apparatus about an axis parallel to the wind-tunnel flow. For illustrative purposes a model of a shuttle orbiter is shown installed on the apparatus although shuttle models have not yet been tested on this device. However, experiments have been performed with cones and results presented in reference 26 confirm the validity of the test technique. Prior to conducting experiments to measure all of the rotary derivatives for shuttle vehicles, computer simulations of vehicle motions should be made to determine which of the many dynamic derivatives have the greatest influence on flight behavior.

CONING APPARATUS FOR WIND-TUNNEL EXPERIMENTS



Figure 28

SUMMARY

(Figure 29)

Some highlights of the Ames Research Center effort in support of the aerodynamic development of space shuttle vehicles have been presented, and results are summarized in figure 29. Photographs of some of the models tested at Ames were presented to illustrate the scope of configuration variables investigated. Data obtained for these models are being analyzed to provide answers to fundamental flow problems and to guide configuration shaping; some of the findings have been presented in this paper. In addition to analyses of wind-tunnel data, analytic investigations are being performed. These studies have provided new criteria for aerodynamic stability of space shuttle vehicles which include effects of varying dynamic pressure and Mach number. Finally, methods for experimentally determining dynamic stability derivatives have been identified.

SUMMARY

- AERODYNAMIC DATA HAVE BEEN OBTAINED FOR A WIDE RANGE OF CONFIGURATIONS AND TEST CONDITIONS
- AT VERY HIGH ANGLES OF ATTACK ($> 45^\circ$) :
 - INFLUENCE OF BODY CHINE RADIUS AND REYNOLDS NUMBER MOST IMPORTANT AT SUBSONIC SPEEDS
 - PITCH-UP TENDENCY AT TRANSONIC SPEEDS, INDEPENDENT OF REYNOLDS NUMBER, MIGHT INFLUENCE CHOICE OF MACH NUMBER FOR INITIATION OF TRANSITION FROM HIGH TO LOW ANGLES OF ATTACK
 - LATERAL-DIRECTIONAL STABILITY RELATIVELY INDEPENDENT OF VERTICAL SURFACES (TWIN, SINGLE, OR NONE)
- FLIGHT NEAR $(L/D)_{\max}$:
 - LARGE FLARE ANGLE ON SINGLE VERTICAL TAIL MIGHT BE REQUIRED FOR LATERAL-DIRECTIONAL STABILITY AT HYPERSONIC SPEEDS
- CRITERIA FOR AERODYNAMIC STABILITY OF SPACE SHUTTLE VEHICLES SHOULD INCLUDE EFFECTS OF VARYING DYNAMIC PRESSURE AND MACH NUMBER.
- A METHOD FOR OBTAINING DYNAMIC DERIVATIVES HAS BEEN IDENTIFIED

Figure 29

NOTATION

A	wing reference area
b	wing reference span
C_D	drag coefficient, drag/qA
C_L	lift coefficient, lift/qA
C_l	rolling-moment coefficient, $\frac{\text{rolling moment}}{qAb}$
C_m	pitching-moment coefficient, $\frac{\text{pitching moment}}{qAc}$
C_N	normal force coefficient, $\frac{\text{normal force}}{qA}$
C_n	yawing-moment coefficient, $\frac{\text{yawing moment}}{qAb}$
$C_{n_\beta}^*$	effective lateral-directional stability derivative (figure 24)
C_Y	dimensionless lateral-force component lying in the plane containing β and directed normal to the plane containing C_L and V , $\frac{\text{lateral force}}{qA}$
\bar{c}	wing reference mean aerodynamic chord
D	drag force
d	effective body width

g	acceleration due to gravity
I_X, I_Y, I_Z	moments of inertia with respect to body axes
I_{XZ}	product of inertia with respect to body axes
L	lift force
l	reference length
m	mass
M, M_∞	Mach number
q	dynamic pressure, also pitching velocity
r	local radius, also yawing velocity
Re_d	Reynolds number based on d
s	dimensionless distance along flight path (figure 23)
V	speed
W	weight
X, Y, Z	body reference axes
α	angle of attack (figure 26)
β	angle of sideslip (figure 26)
γ	flight path angle, positive below local horizontal
δ_H	horizontal tail deflection, positive with trailing edge down
ρ	atmosphere density
σ	resultant incidence angle (figure 27)

$\dot{\phi}$	coning rate of X axis about velocity vector
ψ	angular inclination from the crossflow velocity vector of the Z axis (figure 27)

Subscripts

b	body axes
max	maximum value
s	stability axes
α	$\partial () / \partial \alpha$
β	$\partial () / \partial \beta$
$\dot{\alpha}$	$\partial () / \partial \dot{\alpha} \frac{1}{V}$
$\dot{\beta}$	$\partial () / \partial \dot{\beta} \frac{1}{V}$
q	$\partial () / \partial q \frac{1}{V}$
r	$\partial () / \partial r \frac{1}{V}$
$\dot{\phi}$	$\partial () / \partial \dot{\phi} \frac{1}{V}$

REFERENCES

1. Polhamus, Edward C.: Effect of Flow Incidence and Reynolds Number on Low-Speed Aerodynamic Characteristics of Several Noncircular Cylinders with Applications to Directional Stability and Spinning. NASA TR R-29, 1959.
2. Sommer, Simon C. and Tobak, Murray: Study of the Oscillatory Motion of Manned Vehicles Entering the Earth's Atmosphere. NASA Memo 3-2-59A, 1959.
3. Wawrzyniak, M.E.: To What Extent Should Space Shuttle Stability and Control be Provided Through Stability Augmentation? Space Transportation System Technology Symposium I - Aerothermodynamics and Configurations, NASA TMX-52876, Volume I, July 15-17, 1970.
4. Manke, John A., Retelle, John P., and Kempel, Robert W.: Assessment of Lifting Body Vehicle Handling Qualities. Symposium on Flight Test Results Pertaining to the Space Shuttlecraft, NASA TMX-2101, October, 1970.
5. Tobak, M. and Pearson, W.E.: A Study of Nonlinear Longitudinal Dynamic Stability. NASA TR R-209, 1964.
6. Tobak, M., Schiff, L.B., and Peterson, V.L.: Aerodynamics of Bodies of Revolution in Coning Motion. AIAA Journal, Volume 7, No. 1, January 1969, pp. 95-99.
7. Schiff, L.B. and Tobak, M.: Results from a New Wind-Tunnel Apparatus for Studying Coning and Spinning Motions of Bodies of Revolution. AIAA Journal, Volume 8, No. 11, November, 1970, pp. 1953-1957.
8. Levy, L.L., Jr. and Tobak, M.: Nonlinear Aerodynamics of Bodies of Revolution in Free Flight. AIAA Journal, Volume 8, No. 12, December, 1970, pp. 2168-2171.
9. Tobak, M. and Schiff, L.B.: A Nonlinear Aerodynamic Moment Formulation and Its Implications for Dynamic Stability Testing. AIAA Paper 71-275, Albuquerque, New Mexico, 1971.

CONTROL AND HANDLING QUALITIES OF SPACE SHUTTLE ORBITERS

By Richard W. Powell, James J. Adams, and Lawrence W. Brown
NASA Langley Research Center, Hampton, Va.

INTRODUCTION

In keeping with the recent decision in the shuttle program to focus on the high-cross-range orbiters, the portion of the effort on low-cross-range orbiters has been redirected. However, the results of certain analyses conducted on the low-cross-range orbiters are of continuing interest. For example, most of the current booster concepts conduct their suborbital entry in the low-cross-range, high-angle-of-attack mode. With these applications in mind, the first part of this paper will discuss analyses of the α transition of a low-cross-range orbiter in the terminal portion of the trajectory.

\bar{c}	mean aerodynamic chord
C_{Lmax}	maximum lift coefficient
C_l	rolling-moment coefficient
$C_{l\beta} = \frac{\partial C_l}{\partial \beta}$	
C_m	pitching-moment coefficient
$C_{m\alpha}$	slope of pitching-moment curve, $\frac{\partial C_m}{\partial \alpha}$
$C_{mq} = \frac{\partial C_m}{\partial (q\bar{c}/2V)}$	
C_n	yawing-moment coefficient
$C_{n\beta} = \frac{\partial C_n}{\partial \beta}$	
$(C_{n\beta})_{dyn} = C_{n\beta} \cos \alpha - \frac{I_z}{I_x} C_{l\beta} \sin \alpha$	
h	altitude
I_x, I_z	moments of inertia
K_p, K_r, K_β	feedback gains
$(L/D)_{max}$	maximum lift-drag ratio
M	Mach number

M_x, M_z	moments about roll and yaw axes, respectively
p	roll velocity
q	pitch velocity
r	yaw velocity
t	time
V	velocity
α	angle of attack
β	angle of sideslip
$\dot{\beta} = \frac{d\beta}{dt}$	
δ_H	horizontal-tail deflection
ϵ_β	error in $\dot{\beta}$
ϵ_ϕ	error in bank angle
ϕ	bank angle
ϕ_c	commanded bank angle

$C_{L_{max}}$ REENTRY TRAJECTORIES OF STRAIGHT-WING ORBITERS
COMPARING SUPERSONIC AND SUBSONIC TRANSITION MANEUVERS

(Figure 1)

For the straight-wing orbiter, the handling qualities presented are based on the characteristics of the North American Rockwell (NAR) L3OG phase "B" design.

Along the baseline reentry trajectory proposed for this orbiter, the entry angle of attack is maintained down to subsonic speed before pitching to a cruise attitude, at an altitude of approximately 15 km (50 000 feet). The second trajectory shown corresponds to transition initiated at $M = 2$, at an altitude of 36 km (120 000 feet). These trajectories are also shown in terms of altitude and time where it is noted that the supersonic transition provides a substantial increase in gliding flight time over the subsonic transition.

COMPARISON OF $C_{L_{max}}$ REENTRY TRAJECTORIES OF STRAIGHT-WING ORBITER SUPERSONIC AND SUBSONIC TRANSITION MANEUVERS

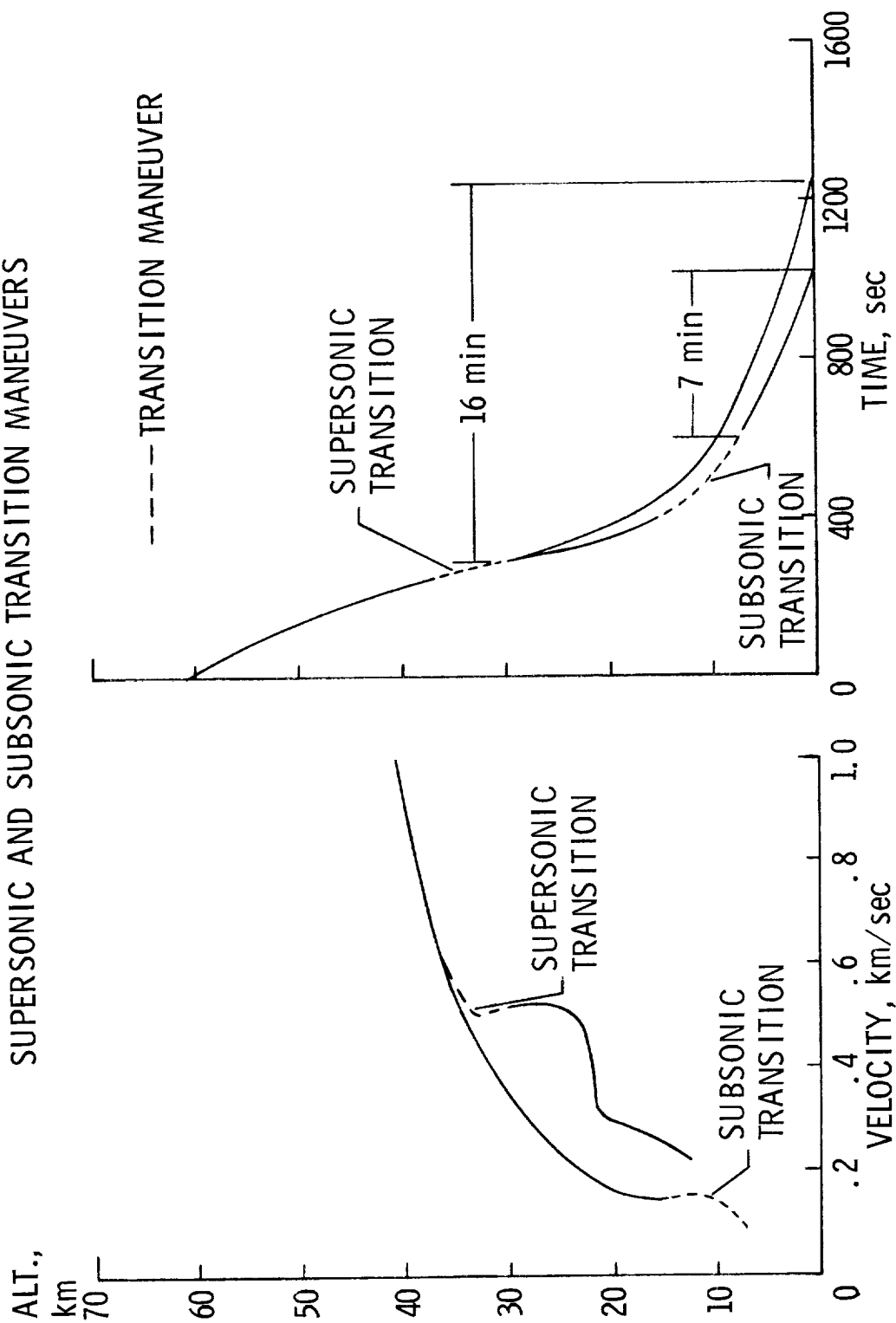


Figure 1

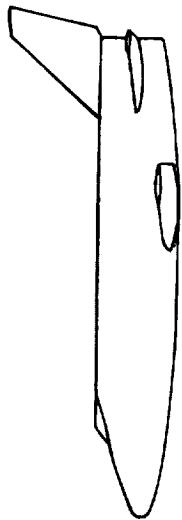
LONGITUDINAL STABILITY CHARACTERISTICS OF THE NAR 130G STRAIGHT-WING ORBITER

(Figure 2)

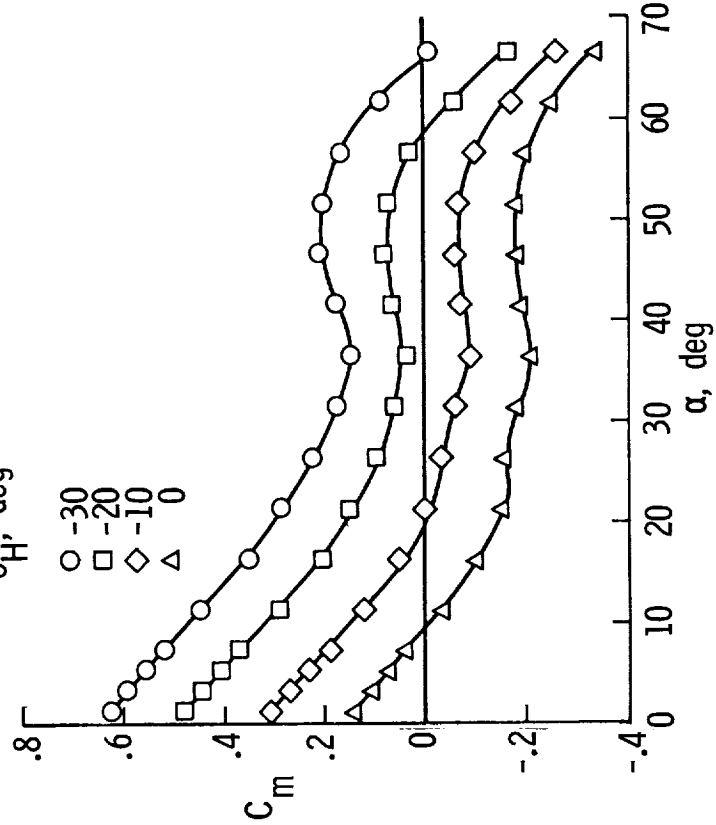
Supersonic pitching-moment characteristics of the NAR 130G straight-wing orbiter are presented on the left side of the figure. At supersonic speeds, this configuration is **statically stable** (C_{m_α} negative) in both the high and low α ranges but slightly unstable in a limited intermediate region. The even spacing of the curves for various tail angles indicate uniform control power throughout the angle-of-attack range. In addition, control authority is sufficient to perform the α transition maneuver using only aerodynamic controls.

Corresponding subsonic characteristics are presented on the right side of the figure. At high subsonic Mach number, this instability increases, as indicated by the high C_{m_α} of the $M = 0.6$ curves; at lower Mach numbers, however, the instability disappears. Although the control power is quite variable in the low α range, it should be adequate to perform the α transition maneuver at low subsonic speeds.

LONGITUDINAL STABILITY CHARACTERISTICS OF NAR 130G STRAIGHT-WING ORBITER



SUPERSONIC
 $M = 2.0$ (LANGLEY)
 δ_H , deg



SUBSONIC
 δ_H , deg
 $M = 0.6$ (AMES) $M = 0.4$ (LANGLEY)

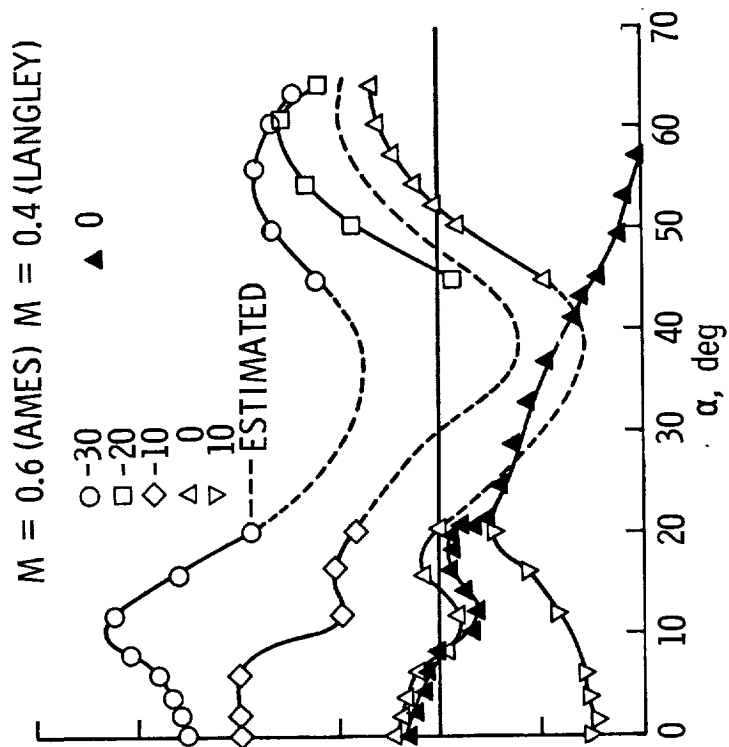


Figure 2

THEORETICAL TRAJECTORY AND MOTION ANALYSIS OF A $M = 2.0$
 α TRANSITION MANEUVER OF THE NAR 130G STRAIGHT-WING ORBITER

(Figure 3)

To determine the major characteristics of the supersonic transition maneuver, a three degree of freedom analysis was performed. This study showed that a two-step horizontal tail deflection program would provide a gradual transition. In addition, enough natural damping (C_{mq}) is available so that the maneuver would offer little difficulty even for an unaugmented vehicle. This maneuver results in an altitude loss of ≈ 6 km (20 000 feet) and a net velocity loss of 0.1 km/sec (300 feet/sec).

Since the subsonic transition maneuver has been demonstrated by others to be smooth and well damped, no further analysis of it was made.

THEORETICAL TRAJECTORY AND MOTION ANALYSIS

M = 2.0 α TRANSITION MANEUVER OF NAR 130G STRAIGHT-WING ORBITER

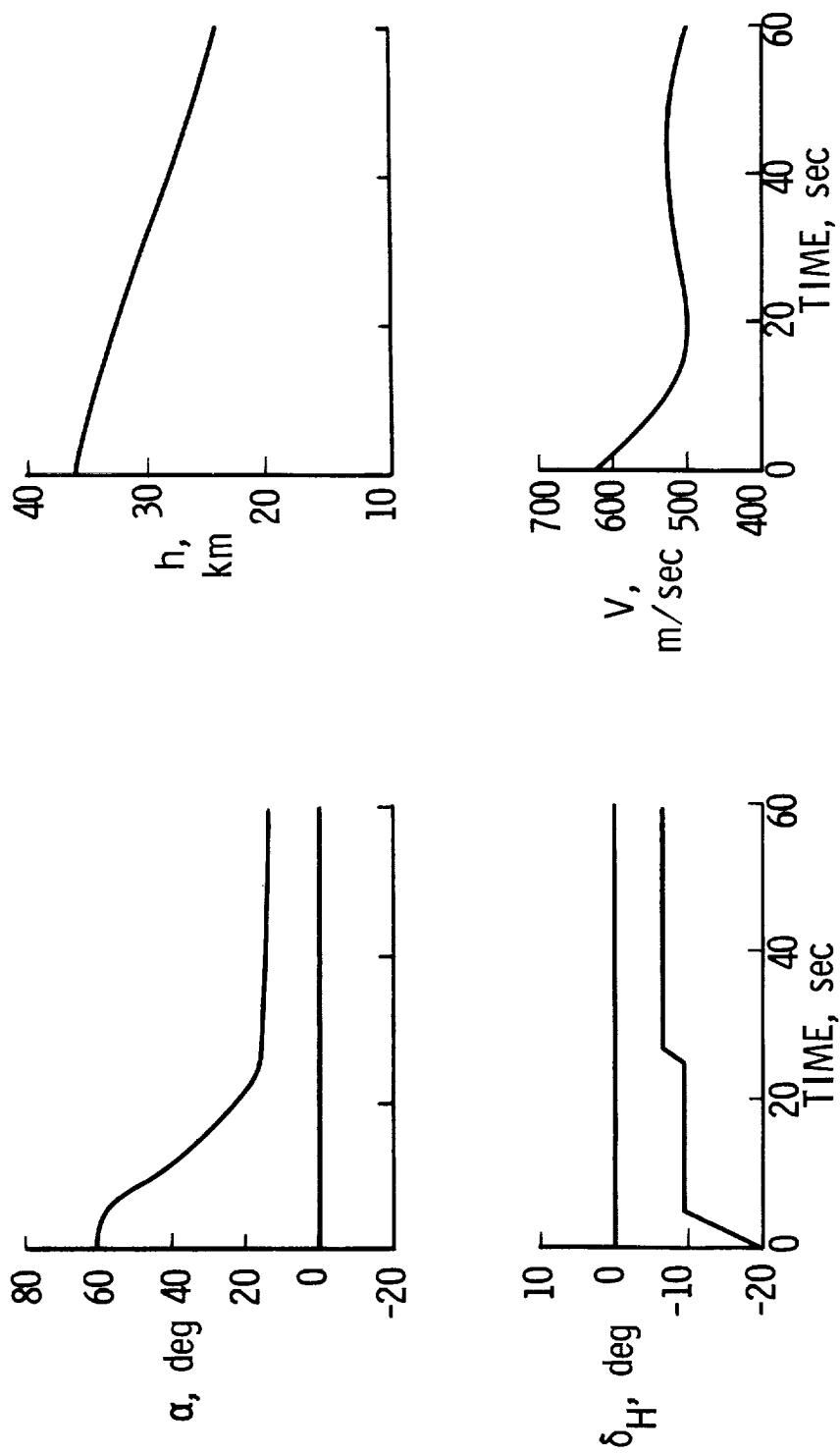


Figure 3

LATERAL DIRECTIONAL STABILITY OF THE NAR 130G STRAIGHT-WING ORBITER

(Figure 4)

The lateral directional characteristics are summarized in terms of $(C_{n\beta})_{dyn}$. The parameter combines the static aerodynamic and inertia characteristics to provide a first order approximation to the Dutch roll frequency. A positive value of $(C_{n\beta})_{dyn}$ is desired whereas negative values indicate aperiodic roots, one of which is divergent. It should be noted that $(C_{n\beta})_{dyn}$ does not by itself predict the level of stability. Used in the complete equations of motion, however, the values shown indicate that the lateral directional characteristics of this vehicle are satisfactory subsonically ($M = 0.6$) at all α 's without augmentation, but that some stability augmentation is required supersonically at the low α 's.

LATERAL DIRECTIONAL STABILITY NAR 130G STRAIGHT-WING ORBITER

$$(C_{n_\beta})_{\text{dyn}} = C_{n_\beta} \cos \alpha - (I_z/I_x) C_{l_\beta} \sin \alpha$$

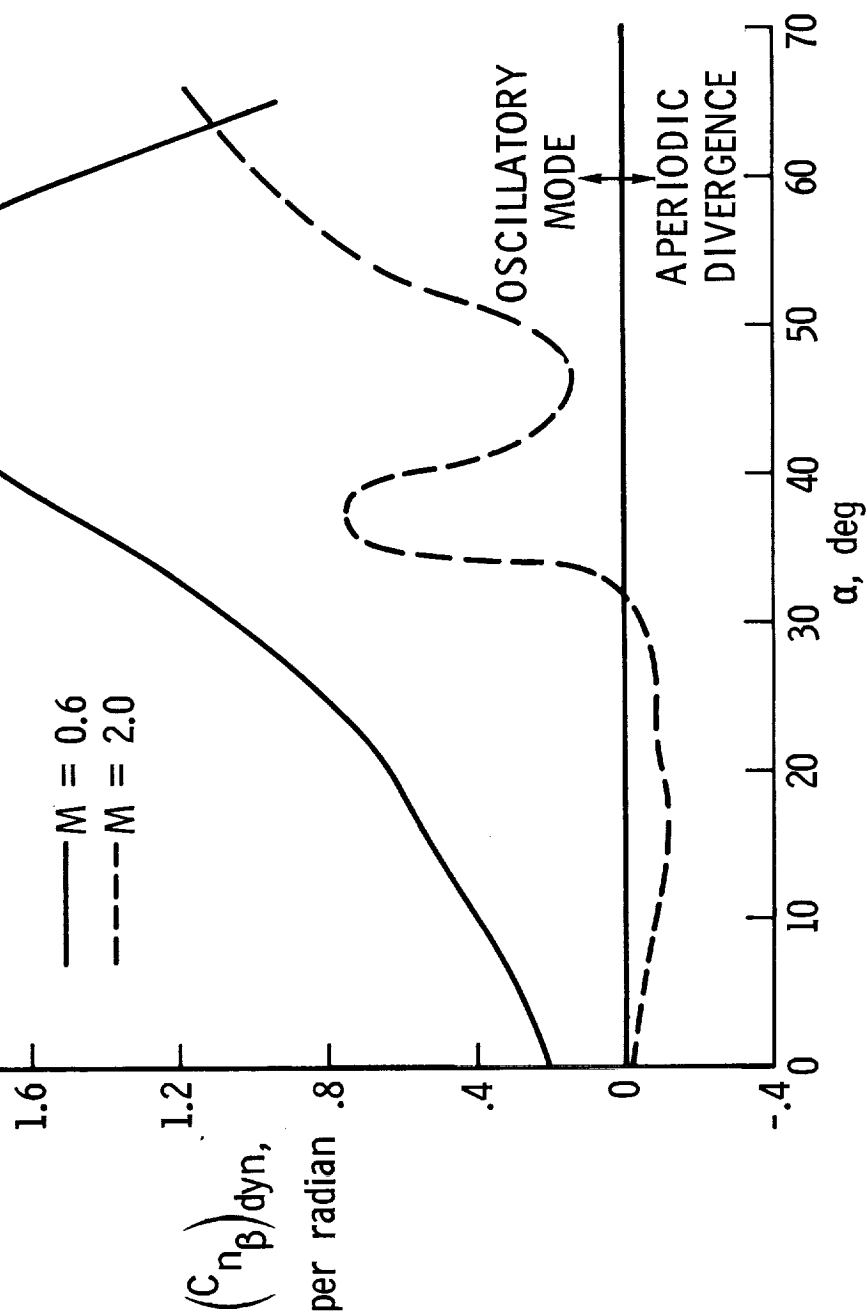


Figure 4

PILOTED SIMULATION HANDLING QUALITIES EVALUATION OF α TRANSITION MANEUVERS OF NAR 130G STRAIGHT-WING ORBITER

(Figure 5)

The handling qualities associated with supersonic transition were studied on a six degree of freedom piloted simulator. The vehicle was provided both aerodynamic and reaction jet control; augmentation was limited to pitch damping and RCS* feedbacks. Noting that transition at $M = 4.0$ and at $M = 2.0$ offered the same degree of difficulty in the pitch plane, the simulator studies were performed at the higher Mach number to have more time to study problems associated with low α flight. As predicted, if there is no lateral disturbance, the maneuver is easily performed supersonically. However, when the pilot was required to perform a heading change, lateral directional instabilities appeared. Typical Cooper-Harper pilot ratings for both the subsonic and supersonic maneuver are shown. The rating system is graduated in values from 1 to 10, where 1 indicates excellent flying qualities, and 10 indicates the vehicle is unflyable, a rating less than 4 is desirable. When artificial improvement of $C_{L\beta}$ was added, the pilot ratings for the supersonic maneuver improved substantially. Another measure of the relative stability of the two maneuvers is the RCS fuel usage. The initial indications are that if this vehicle flies the trajectory dictated by the supersonic maneuver with a RCS control authority of $2^\circ/\text{sec}^2$, it will use 70 percent more fuel (300 kg) than along the subsonic trajectory.

*Reaction Control System.

PILOTED SIMULATION HANDLING QUALITIES EVALUATION α TRANSITION MANEUVERS OF NAR 130G STRAIGHT-WING ORBITER

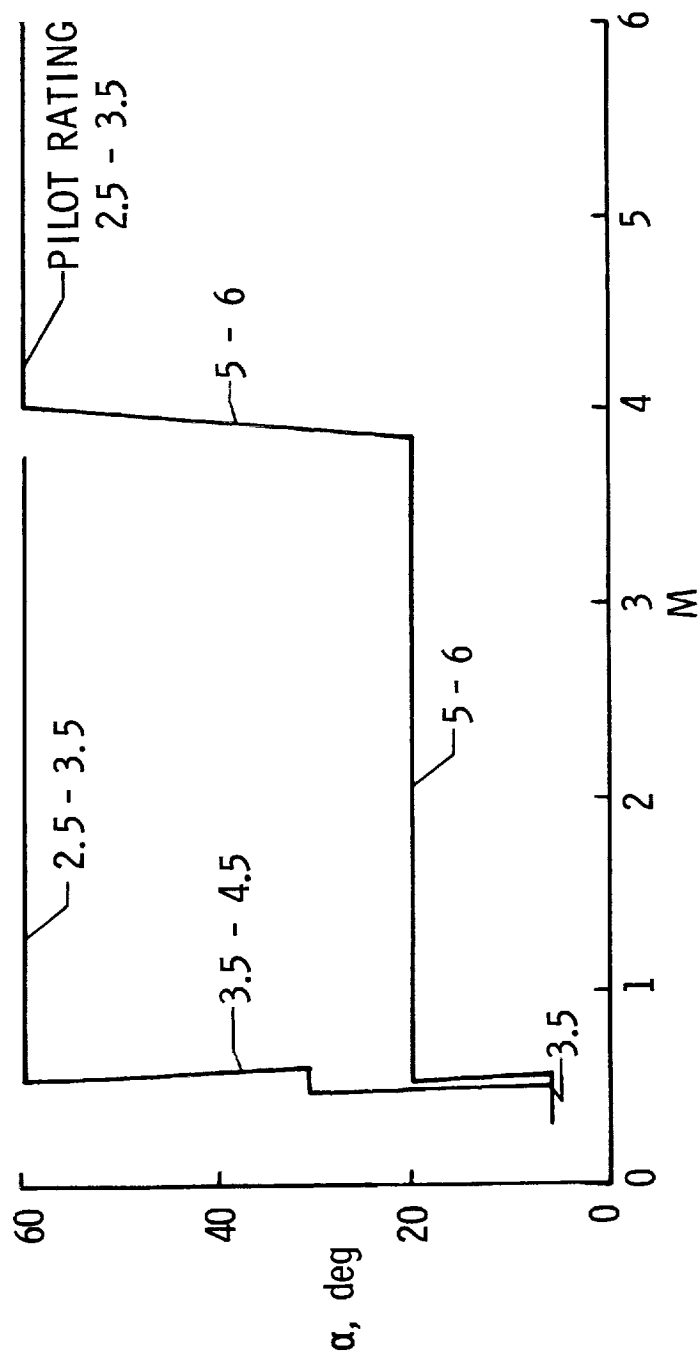


Figure 5

DELTA-WING ORBITER STABILITY AND CONTROL ACTIVITIES

(Figure 6)

The recent change in phase "B" ground rules precluded the determination of the augmentation or configuration changes necessary to provide good handling qualities for the supersonic transition. All attention is now directed toward the delta-wing configuration. The program being followed is wind-tunnel evaluation of performance, stability, and control of both in-house and contractor's configurations throughout the speed range. Once these are complete, dynamic motion and handling qualities calculations will be made and verified on a simulator.

A limited discussion of one of the control system studies now in progress, namely, the effect of fin location and size and control system characteristics on the vehicle's ability to execute a bank angle command, follows.

DELTA-WING ORBITER STABILITY AND CONTROL ACTIVITIES

- WIND TUNNEL EVALUATION OF PERFORMANCE, STABILITY AND CONTROL
- DYNAMIC MOTION CALCULATIONS
- HANDLING QUALITY CALCULATIONS
- MANNED, FIXED-BASE, 6-DEGREE OF FREEDOM SIMULATOR INVESTIGATIONS

Figure 6

BANK-ANGLE CONTROL SYSTEM CHARACTERISTICS

(Figure 7)

Initial studies indicate that the aerodynamic control of the delta-wing configuration will require supplemental reaction jets in roll and yaw.

Two automatic bank-angle control systems were studied, one using roll jets as the primary control, the other using yaw jets. The controlling parameters and final values used in each one are:

Primary Control by Roll Jets

$$\epsilon_{\phi} = (\phi_c - \phi) - K_p p$$

$$\epsilon_{\beta} = p \tan \alpha - r + K_{\beta} \beta$$

$$M_x/I_x = 5.2^\circ/\text{sec}^2, \quad M_z/I_z = 4^\circ/\text{sec}^2$$

$$K_p = 1 \text{ sec}, \quad K_{\beta} = 2 \text{ sec}^{-1}$$

$$\text{Deadband} = \pm 2 \text{ deg } (\epsilon_{\phi}), \pm 2 \text{ deg/sec } (\epsilon_{\beta})$$

where ϕ_c is the commanded bank angle, and K_p , K_r , K_{β} are feedback gains.

A three degree of freedom analogue simulation was conducted using these values for a commanded bank-angle change of 30° for a vehicle flying at $(L/D)_{\max}$ at 67 km (220 000 feet). The values of $C_{n_{\beta}}$ and $C_{l_{\beta}}$ were varied to simulate an orbiter with tip fins, one with a center vertical, and one with a small center vertical such that $(C_{n_{\beta}})_{\text{dyn}}$ was negative.

For this angle of attack, the primary control of bank angle by roll jets is more efficient since the roll authority necessary is only half that required by the other method.

Similar studies combining reaction jets with other aerodynamic controls are in progress. Results from these and other studies will provide the input for further evaluation of handling qualities in programs similar to those followed in the analysis of the straight-wing orbiter.

Primary Control by Yaw Jets

$$\epsilon_{\phi} = (\phi_c - \phi) - K_r r$$

$$\epsilon_{\beta} = r \cot \alpha - p$$

$$M_x/I_x = 12^\circ/\text{sec}^2, \quad M_z/I_z = 4^\circ/\text{sec}^2$$

$$K_r = 2 \text{ sec}$$

$$\text{Deadband} = \pm 2 \text{ deg } (\epsilon_{\phi}), \pm 2 \text{ deg/sec } (\epsilon_{\beta})$$

BANK-ANGLE CONTROL SYSTEM CHARACTERISTICS

— BANK-ANGLE CONTROL WITH ROLL JETS
 --- BANK-ANGLE CONTROL WITH YAW JETS

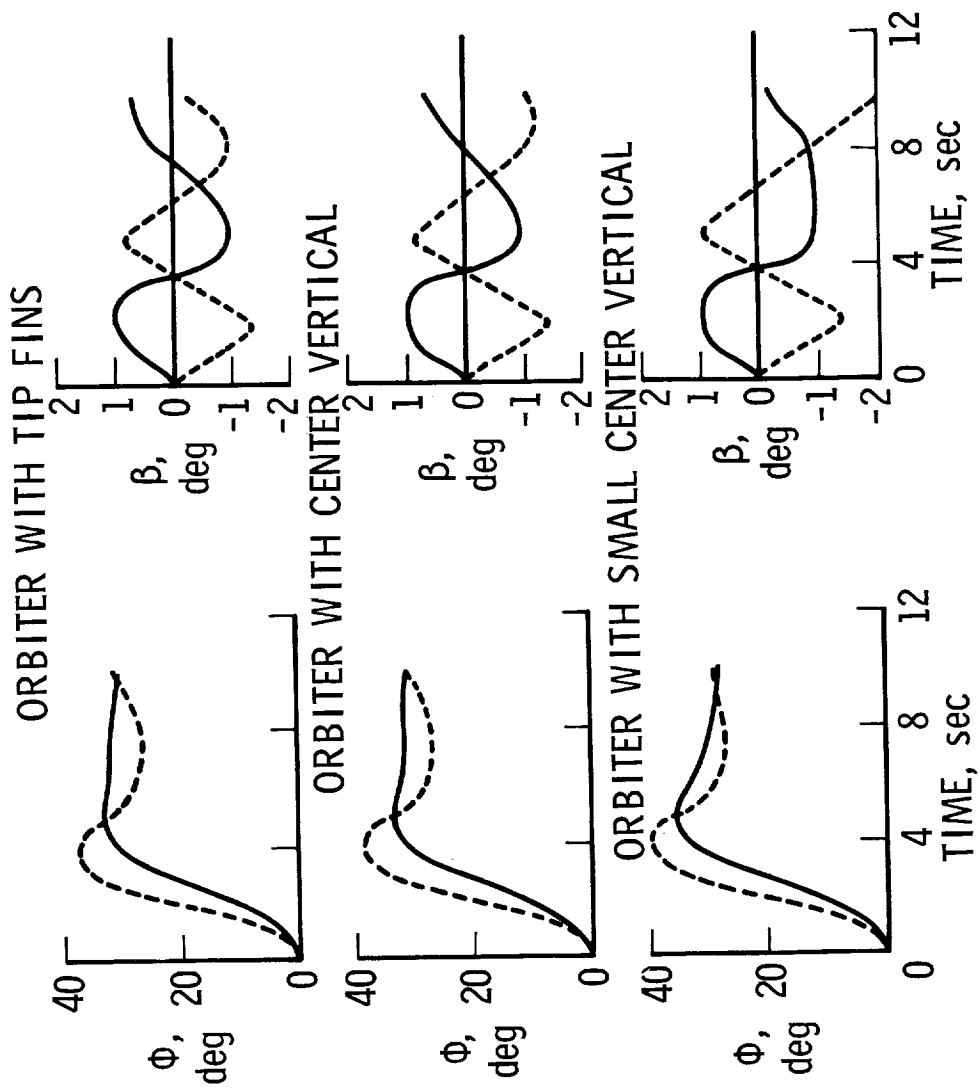


Figure 7

PLUME IMPINGEMENT DURING SEPARATION OF A TWO-STAGE SPACE SHUTTLE VEHICLE

By Ivy Fossler, NASA Manned Spacecraft Center, Houston, Texas

and

Robert Prozan, Lockheed Missiles and Space Company, Huntsville, Alabama

INTRODUCTION

To date, manned spacecraft have been designed with little regard to plume-impingement effects, with the result that hardware changes and scheduling problems have been encountered well into the flight phase of the vehicles. The preliminary design of a two-stage reusable logistics vehicle — the space shuttle vehicle (SSV) — is now in progress in the National Aeronautics and Space Administration (NASA). As a result of past experience, it was decided that plume-impingement effects should be considered in the design of the SSV so that potential problems could be identified early in the program.

Historically, the separation sequence of launch vehicle stages has been designed solely to safeguard the upper stages during such maneuvers; this was the natural consequence of the expendable-boosters approach to vehicle design. For reusable boosters, however, the effects of the staging sequence on the exhausted stage are significant because control of the stage must be maintained. In addition, damage, particularly that caused by impingement heating, must be prevented. Thus, the plume-impingement forces and heating loads on the booster (first stage) resulting from the ignition of the orbiter (second stage) main engines are important considerations in the stage-separation design. Orbiter-engine ignition in close proximity to the booster can cause high heating loads as well as significant forces and moments on the booster. Large separation distances, however, introduce undesirable performance penalties as a result of the delay in orbiter ignition.

For these reasons, the significance of the plume-impingement problem during staging must be assessed in the determination of an optimum separation trajectory. This optimum trajectory should provide an acceptable trade-off between the effect on the vehicle design necessary to withstand the plume-impingement environment and the resultant penalties in system performance and operation.

SPACE SHUTTLE LAUNCH CONFIGURATION
(Table I)

A NASA Manned Spacecraft Center (MSC) in-house concept of the two-stage space shuttle was used for this study. The mass characteristics and staging conditions are listed in table I.

SPACE SHUTTLE MASS PROPERTIES AND TRAJECTORY CONDITIONS

Mass properties and trajectory conditions	Booster	Orbiter
Weight, kg (lb)	208 017 (458 600)	283 450 (624 900)
Inertia, kg-m ² (slug-ft ²)		
I _{xx}	9.3 × 10 ⁶ (6.84 × 10 ⁶)	1.9 × 10 ⁶ (1.43 × 10 ⁶)
I _{yy}	67.49 × 10 ⁶ (49.62 × 10 ⁶)	33.12 × 10 ⁶ (24.35 × 10 ⁶)
I _{zz}	72.28 × 10 ⁶ (53.15 × 10 ⁶)	28.78 × 10 ⁶ (21.16 × 10 ⁶)
Altitude, km (ft)	82.30 (270 × 10 ³)	82.30 (270 × 10 ³)
Mach number	10.8	10.8
Flight path, deg	8.1	6.2
Azimuth, deg	38.9	38.9
Bank, deg	0	0
Angle of attack, deg2	-1.7
Angle of sideslip, deg	0	0
Dynamic pressure, N/m ² (lb/ft ²)	52.67 (1.1)	52.67 (1.1)

TABLE I

SIMULATION OF THE MSC SPACE SHUTTLE CONFIGURATION

EXHAUST-PLUME IMPINGEMENT
(Figure 1)

The simulation of the MSC SSV configuration that was used in the plume-impingement analysis is shown in figure 1. A computer program (ref. 1) was used to perform the necessary calculations. This program accepts as input magnetic-tape data representing an assembly of simple shapes (which simulate the vehicle) and an axisymmetric rocket-exhaust plume. The MSC booster was simulated using a cone for the nose section (a paraboloid has since been added), a cylinder for the top surface of the fuselage, and flat plates for the fuselage sides. An airfoil-geometry-subshape calculation was used for the wings and the vertical and horizontal tails. Each subshape was then subdivided into a number of elemental areas for the impingement analysis.

It should be noted that the MSC configuration is remarkably well simulated by these subshapes, particularly when the paraboloidal nose calculation is used. The main areas in which the simulated vehicle deviates from the actual external configuration are in the vicinity of the cockpit, the bottom of the vehicle (which is shaded anyway), and small cutout areas on the horizontal tail.

In the MSC configuration, the orbiter has two rocket engines mounted vertically in close proximity to each other. The exhaust plumes from these engines interact, giving rise to a three-dimensional flow field. A definition of this exhaust field is necessary to predict the environment that acts on the booster. Several factors must be considered in making a decision regarding the theoretical approach to the exhaust-plume definition. The factors are (1) state-of-the-art prediction methods, (2) economy of solution technique, and (3) confidence in the final result.

For this study, the use of three-dimensional plume solutions, such as those in references 2 and 3, appeared to be prohibitively expensive in computer time, particularly when the state of flux of the engine design was considered. Another stumbling block to using one of these analyses is the fact that the impingement solution itself is limited to an axisymmetric flow field. To consider a three-dimensional solution to the plume/plume-interaction problem also meant considering development of an attendant plume-impingement calculation. It was for these reasons that an axisymmetric-jet approximation was chosen for the plume definition.

SIMULATION OF MSC CONFIGURATION FOR IMPINGEMENT CALCULATIONS

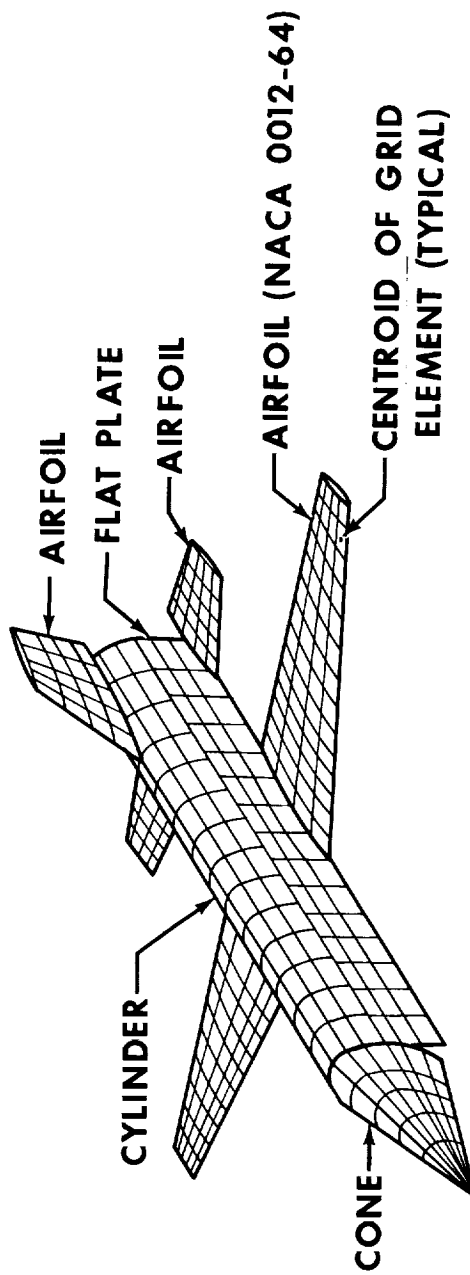


Figure 1

AXIAL AND NORMAL FORCES ON THE BOOSTER AND THE PITCHING MOMENT
OF THE BOOSTER CAUSED BY ORBITER EXHAUST-PLUME IMPINGEMENT
(Figures 2, 3, and 4)

Plots of the calculated impingement forces and moments for full-thrust operation of the orbiter are given in figures 2, 3, and 4. The results shown are for 0° relative roll, pitch, and yaw displacements. The vertical tail is exposed to impingement at all times; in general, as axial distance increases, the fuselage, horizontal tails, wings, and finally the nose portion of the vehicle become exposed. The moments are calculated with respect to the booster nose and are considerably reduced when referenced to the booster center of gravity (c.g.).

The impingement force and moment results were produced by integrating the local impact pressure over the entire vehicle. The Newtonian impact theory, as modified for moderate- to low-impingement angles by the experimental results given in reference 4, was used to determine the local impact pressure. Details of the entire impingement-analysis procedure are contained in reference 5.

BOOSTER AXIAL FORCE CAUSED BY ORBITER-EXHAUST PLUME IMPINGEMENT

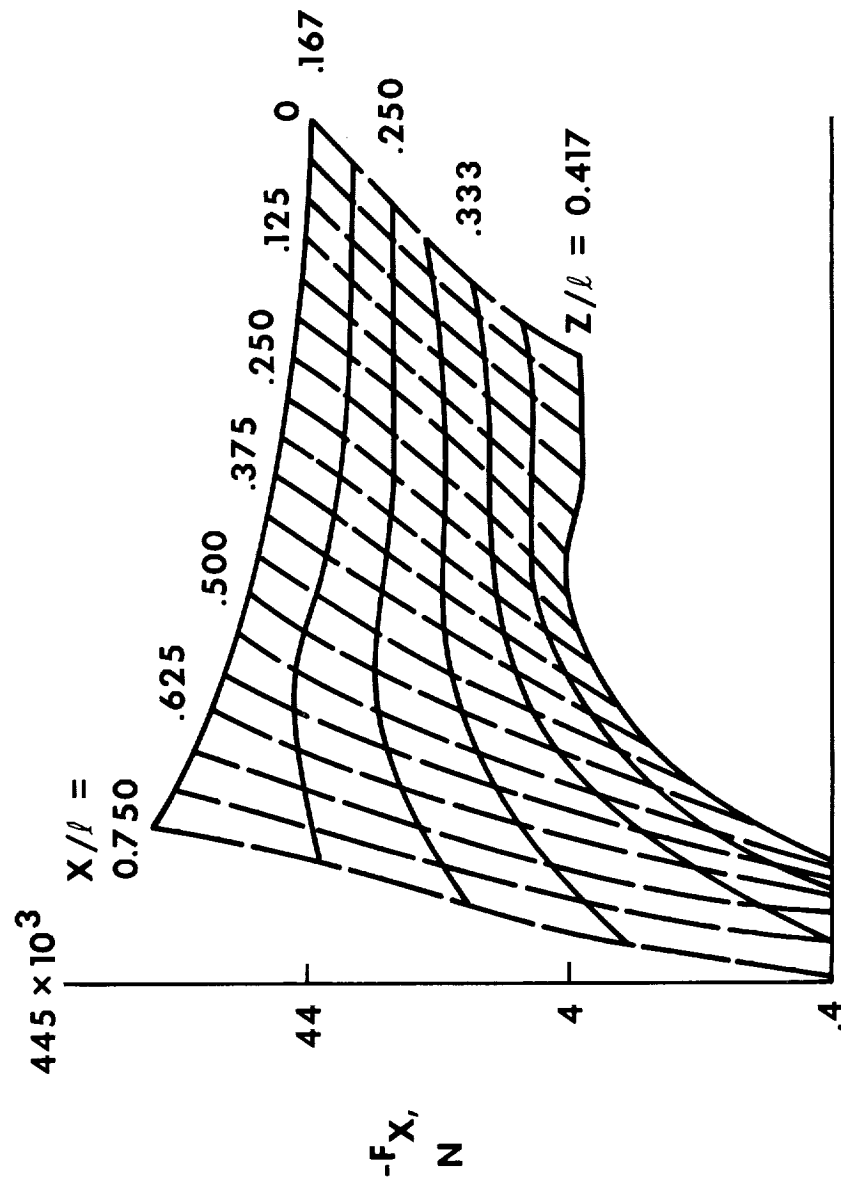


Figure 2

**BOOSTER
NORMAL
FORCE
CAUSED
BY
ORBITER-
EXHAUST PLUME
IMPINGEMENT**

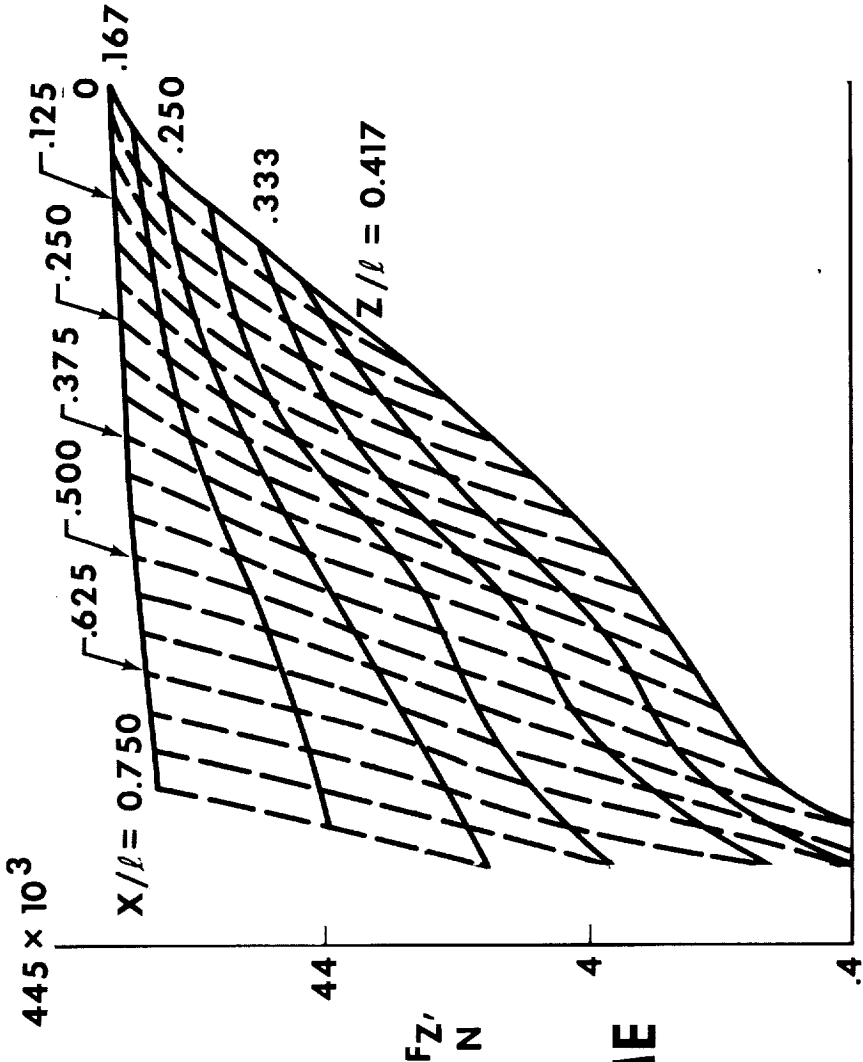


Figure 3

BOOSTER PITCHING MOMENT CAUSED BY ORBITER- EXHAUST PLUME IMPINGEMENT

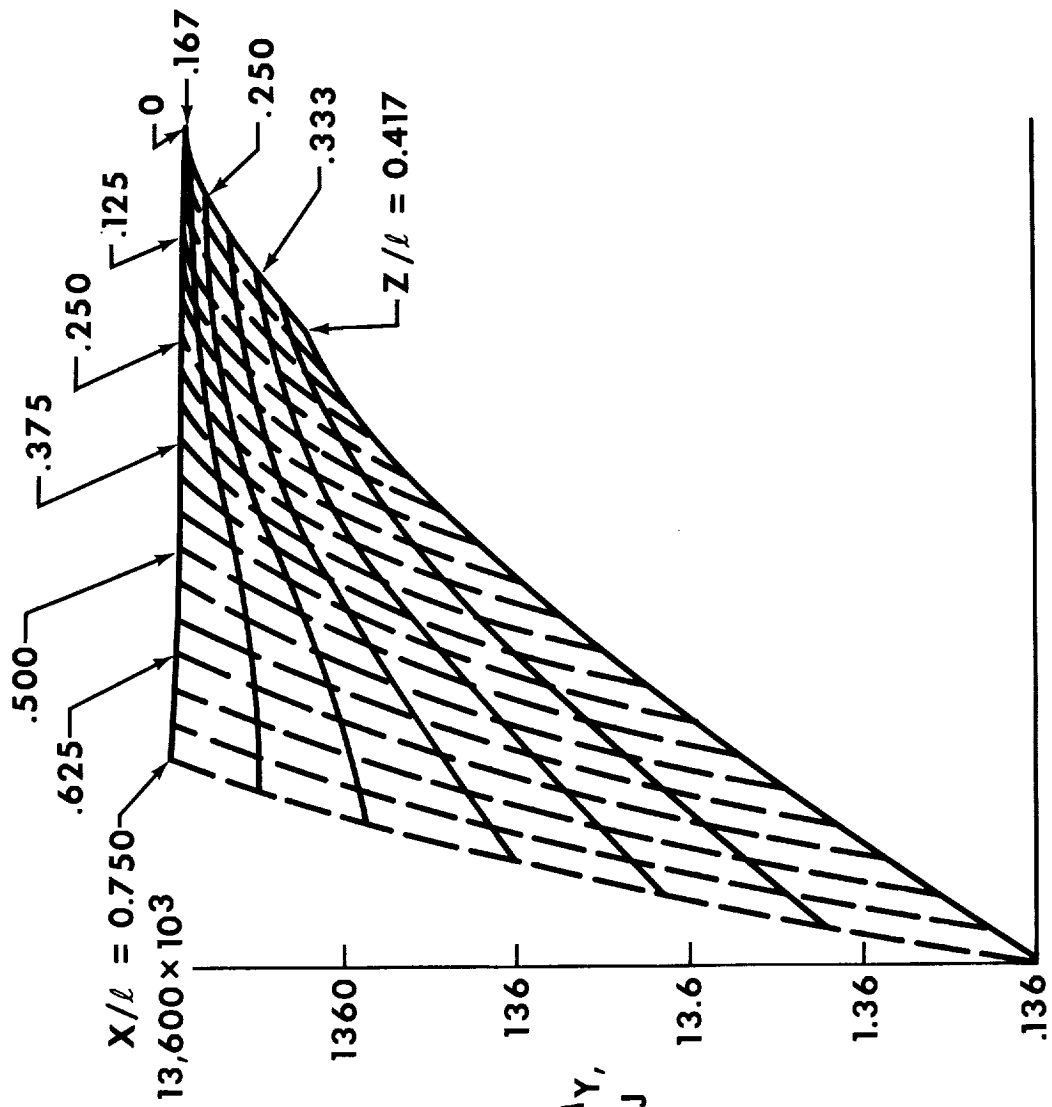


Figure 4

HEATING-RATE CONTOURS ON THE VERTICAL TAIL
(Figure 5)

Details of the methods used to calculate the plume-impingement heating rates are presented in reference 5. Briefly, yawed infinite-cylinder theories were used to predict the stagnation-line heat-transfer rates. Heat-transfer-distribution functions that are strongly dependent on the ratio of the local pressure to stagnation-line pressure were used to predict heat-transfer rates off the stagnation lines. Worst-case heating rates on the vertical tail ($x/l = -0.667$, $z/l = 0.167$) are shown in figure 5. It should be noted that these rates are turbulent heating rates with the orbiter engines operating at full thrust.

HEATING-RATE CONTOURS ON THE VERTICAL TAIL

($X/\ell = -0.667$ AND $Z/\ell = 0.167$) (FULL THRUST)

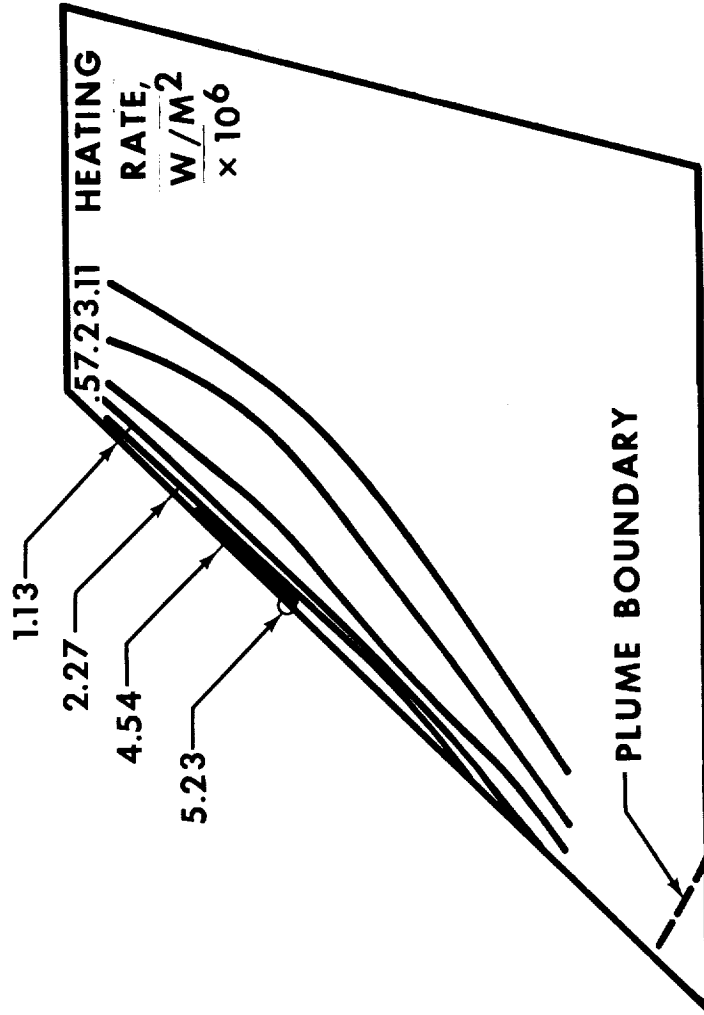


Figure 5

PLUME EFFECTS ON SEPARATION TRAJECTORIES (Figure 6)

During the design phase of the SSV, all conditions are dynamic. To determine the possible severity of plume impingement, a set of representative conditions for a nominal staging was selected for study. The effects of plume impingement on vehicle dynamics, on heating rates, and on heat loads were investigated using these conditions. The results obtained should be indicative for other similar situations, and trends should be established that will be of benefit in future studies. The aerodynamics used were hypersonic, interference-free data for each vehicle.

Two methods were used to integrate the plume forces and moments into the trajectory program. Initially, a matrix of plume forces and moments was determined using the plume-impingement program (PLIMP) (ref. 1). The forces and moments (ref. 5) were derived as a function of the booster location relative to the orbiter engines and were based on a plume at a 86.3-kilometer (283 000-foot) altitude with an external Mach number of 12.08 and an area expansion ratio, $A/A^* = 200$. By the time this matrix had been determined, the engine specifications had been changed and the expansion ratio had been set at 155. Because staging conditions and booster geometry were also varying, it was evident that a flexible technique was required to simulate plume impingement. To accomplish this objective, the PLIMP was incorporated into a trajectory program. Calls are made to the PLIMP at selected intervals in the trajectory program, and plume forces and moments are determined and returned to the trajectory calculations. Data for heating calculations are written on tape for future evaluation. Only if the engines, external flow field, or booster configuration change are any modifications necessary, and these modifications are relatively simple.

The magnitude of the forces and moments experienced by the booster is affected by the orbiter-engine thrust level, which builds during the initial portion of the trajectory. This thrust-buildup time history affects the trajectory and the magnitudes of the plume-impingement forces, moments, and heating rates. Two thrust-buildup time histories of 7 and 4 seconds were used in this study. The cases to be presented are illustrated in figure 6.

SEPARATION TRAJECTORY STUDIES

CASE	INITIAL $\dot{\theta}$, DEG/SEC	PLUME IMPINGEMENT		THRUST- BUILDUP TIME, SEC
		NONE	COMBINED MATRIX PROGRAMS	
A	0		X	7
B	0	X		7
C	0		X	4
D	-3.6		X	7
E	0		X	4

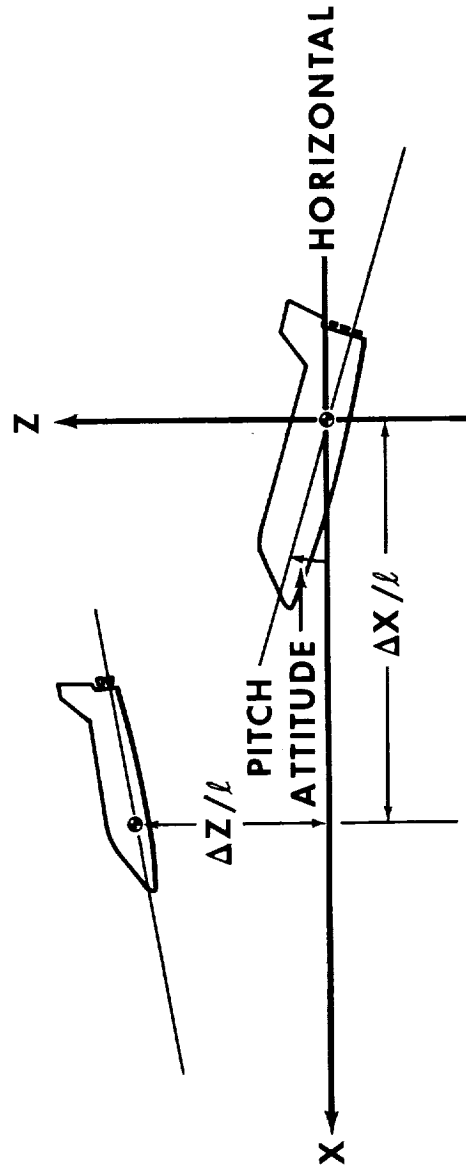


Figure 6

RELATIVE EFFECTS OF PLUME IMPINGEMENT AND AERODYNAMICS

ON A SEPARATION TRAJECTORY (Figures 7 and 8)

To determine the relative importance of the plume forces and moments requires comparisons with the other forces and moments affecting the vehicles. The most significant comparison is with the vehicle aerodynamics. Because of the low dynamic pressure at the nominal staging altitude, the aerodynamic forces and moments acting on the booster are small relative to the plume forces and moments, as illustrated in figure 7, which shows the axial forces, normal forces, and pitching moments experienced by the booster as a result of aerodynamics and plume impingement. These data were taken from a trajectory (case A) that used the 7-second thrust-buildup curve and that had ignition occurring immediately upon attach-mechanism release. The booster pitch attitude, pitch rate, and displacement relative to the orbiter are shown in figure 8 for this trajectory. Also shown on this figure are the conditions (case B) that exist when the plume forces and moments are not considered. In case A, the matrix of impingement data was used. These data were established for booster pitch attitudes of $+5^\circ$, 0° , and -5° relative to the plume center line. For larger dispersions, the data were held constant. Thus, beyond 6 seconds, the data used for case A are less accurate than earlier in the trajectory.

As indicated in figure 8, the major effects of the plume impingement for this trajectory are the changes in the pitch attitude and in the pitch rate of the booster. Failure to account for this attitude change could be crucial to the separation maneuver.

PLUME AND AERODYNAMIC FORCES AND MOMENTS

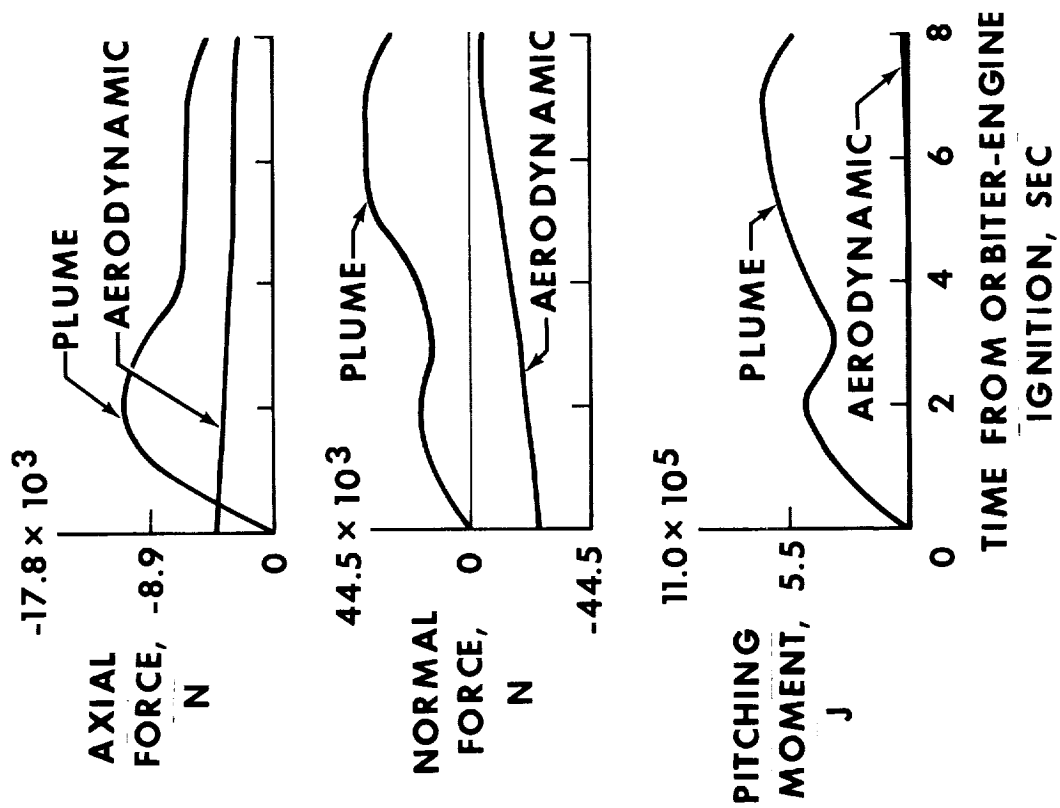


Figure 7

BOOSTER PITCH ATTITUDE, PITCH RATE, AND POSITION RELATIVE TO THE ORBITER (CASES A AND B)

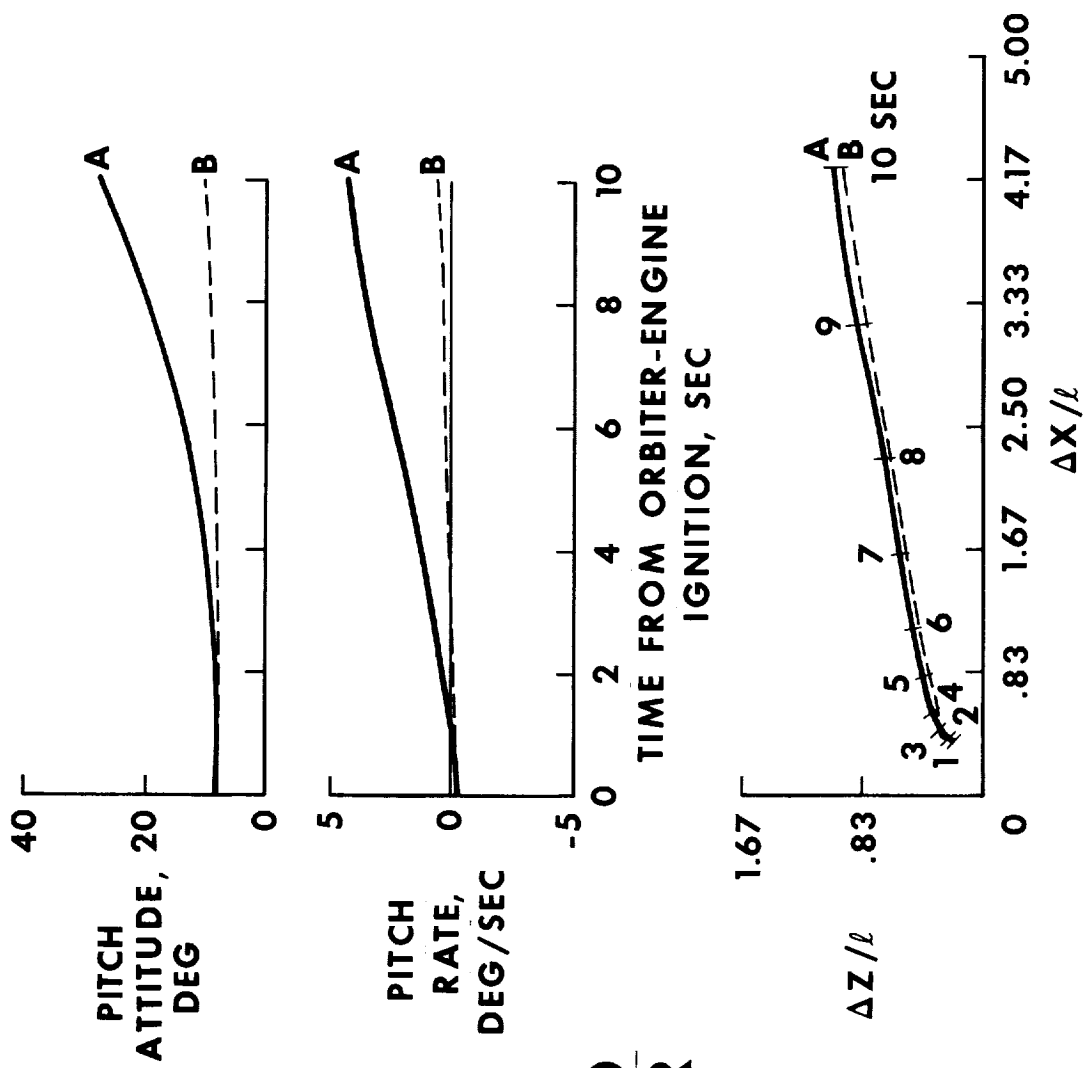


Figure 8

EFFECTS OF THRUST BUILDUP TIME ON A SEPARATION TRAJECTORY
(Figure 9)

The effects of the thrust-buildup time history on the booster trajectory and heating rates were also examined using the matrix of plume-impingement data. The variation of trajectories using the two thrust-buildup curves are shown in figure 9 (cases A and C). Heating rates for a point on the leading edge of the vertical tail were computed. Case C reached a higher peak heating rate than case A, but the integrated heat loads were similar for both cases.

BOOSTER PITCH ATTITUDE, PITCH RATE, AND POSITION RELATIVE TO THE ORBITER (CASES A AND C)

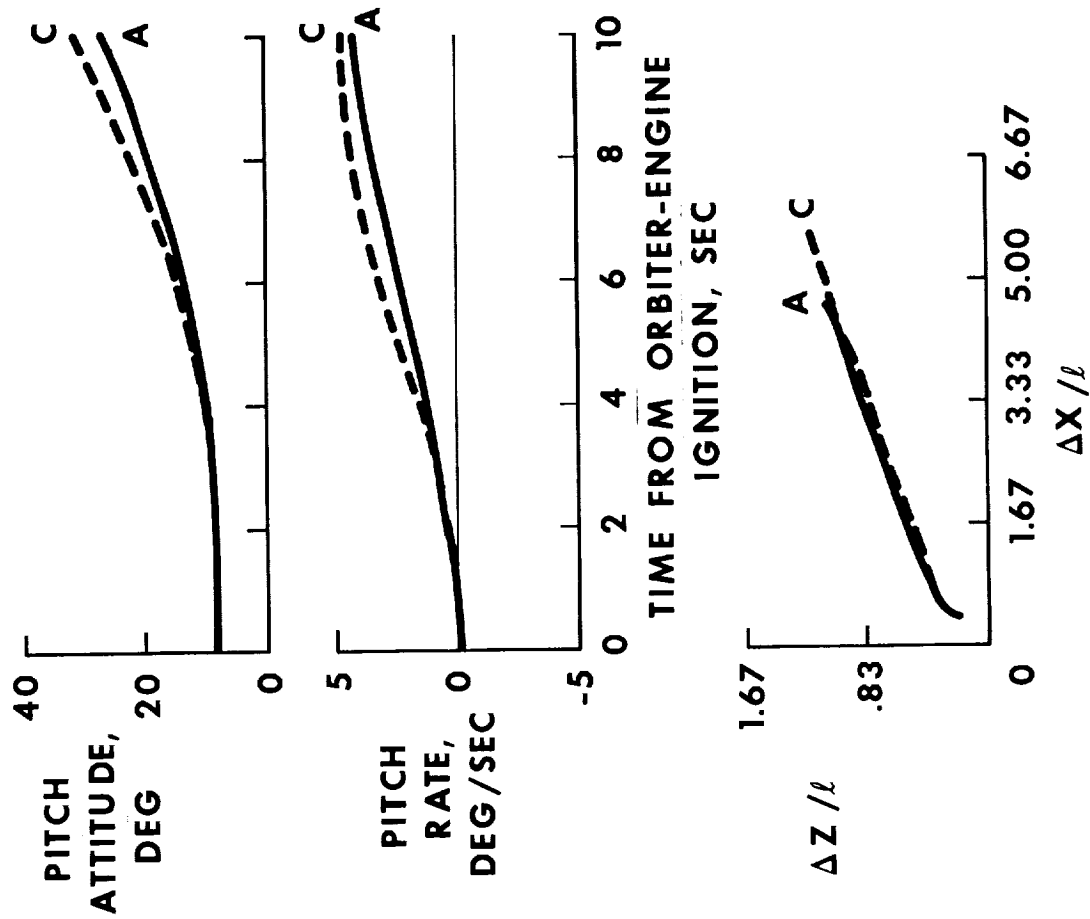


Figure 9

EFFECTS OF PLUME IMPINGEMENT FOR A TYPICAL SEPARATION SCHEME (Figure 10)

In these trajectories, a 0° pitch rate on the booster was assumed at separation. However, for most separation devices and schemes (i.e., pistons with booster-engine shutdown and reverse linkage with the booster at reduced thrust level), a negative (nose down) rate is imparted to the booster. The trajectory (case D) shown in figure 10 is for a booster with an initial pitch rate of -3.6 deg/sec and the 7-second orbiter-engine thrust buildup. Because of the plume impingement, the negative pitch rate on the booster is counteracted before 6 seconds, and a positive attitude (vehicle center line relative to horizontal) is achieved before 8 seconds. Sensitivity to dynamic pressure and proximity aerodynamics will require that detailed studies of this type be continued.

One area that this type of study could affect is that of the separator mechanism. For example, one proposed separation scheme uses a piston to separate the vehicles. This mechanism tends to produce a negative pitching moment on the booster. Nominally, to counteract this moment, rockets that increase the vehicle weight are added to the booster. As illustrated in figure 10, the plume-induced moment could be used in lieu of such rockets with no weight penalty.

Another area that would be affected by this type of study is the booster reaction control system (RCS), the design of which requires knowledge of all external forces and moments acting on the booster. Because this booster enters at a high angle of attack, the positive rate induced by the plume could be helpful in reaching the desired entry attitude and in reducing the amount of required RCS propellants. Thus, the existence of the plume effects is not necessarily detrimental to a design area but may, in fact, benefit the entire system if the effects can be well predicted.

BOOSTER PITCH ATTITUDE, PITCH RATE, AND POSITION RELATIVE TO THE ORBITER (CASE D)

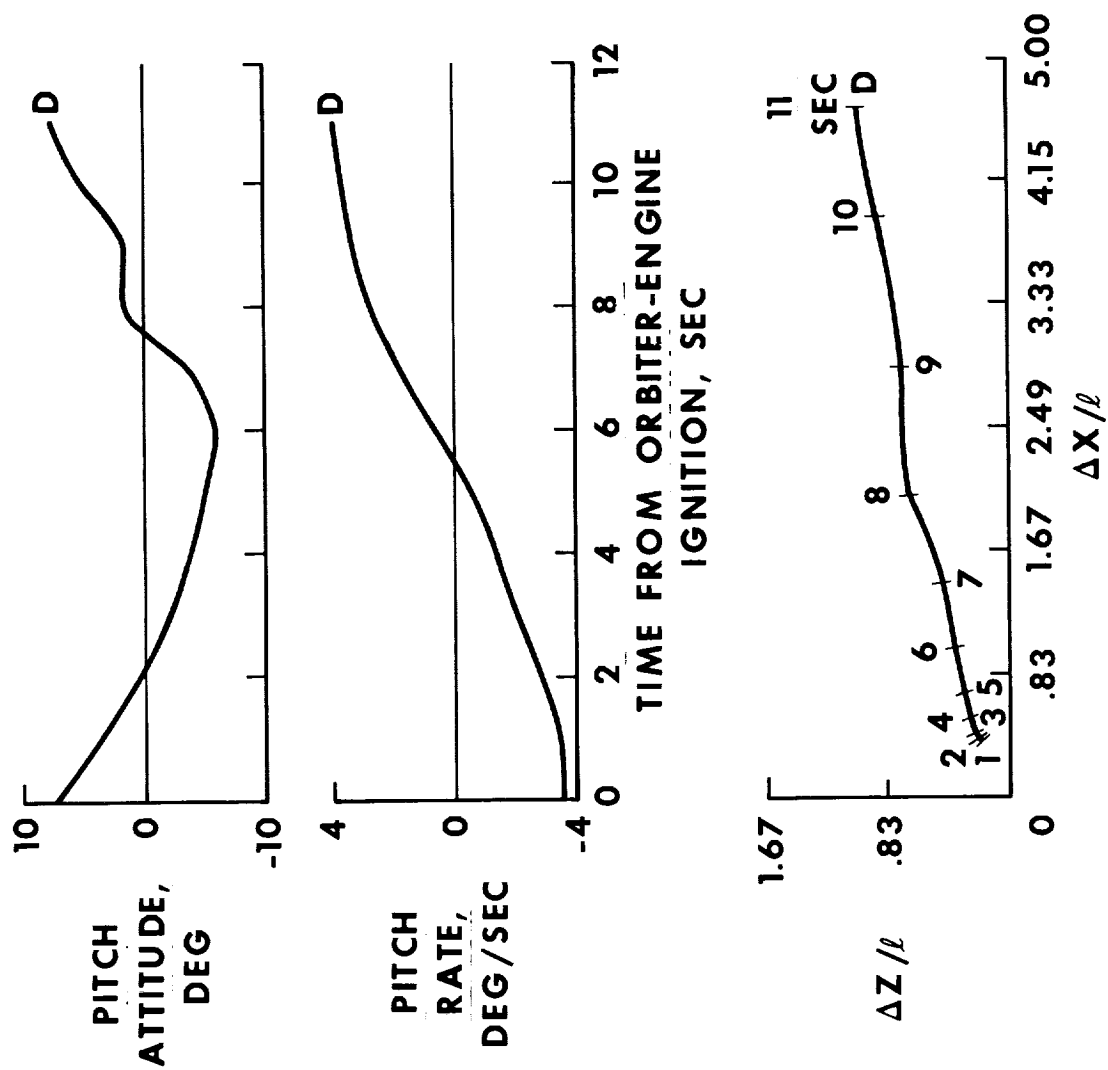


Figure 10

EFFECTS OF USING COMBINED TRAJECTORY AND PLUME-

IMPINGEMENT PROGRAMS (Figure 11)

In all the cited cases, the matrix was used to determine the plume forces and moments. To compare this technique with that which combined the PLIMP and the trajectory program, the conditions used to generate case C were repeated. In this instance (case E), the plume forces and moments were obtained by calls to the PLIMP every 0.5 second. As was noted previously, the matrix data were available to $\pm 5^\circ$ relative pitch attitude and held constant beyond this point (which on case E begins at approximately 5 seconds). The variations in trajectories between cases C and E are shown in figure 11.

To use the most recent engine data, it was necessary to change to a plume that had an $A/A^* = 155$. It was also of interest to determine the effect of assuming either external-flow or quiescent conditions. The use of the combined PLIMP and trajectory programs made this investigation relatively simple. Using the integrated program, cases were generated using plumes with $A/A^* = 155$ and external Mach numbers of 12.08 and 0. The variation in external Mach number was practically nondiscernible in the effect on the trajectory, forces, and moments.

The study of the plume-impingement forces and moments also indicated several possible problem areas, the knowledge of which will be most helpful during the early stages of vehicle design. One problem is that of vehicle yaw and roll induced by plume impingement. Under normal circumstances, the vehicle is symmetrical in the plume flow field and no yawing or rolling moments should exist. If, however, some yaw or roll is induced by other means, the plume contributes to the motion, introducing an unstable moment. Another related problem could exist for the side-by-side-mounted orbiter engines. In the event that one engine failed or that the starts of the two engines were not simultaneous, the plume impingement would introduce vehicle yaw and roll motions that would be sustained by the impingement. The magnitude of these problems is linked with the vehicle inertias, aerodynamic characteristics, and staging dynamic pressure, but knowledge of the fact that a problem could exist is very beneficial in the vehicle design phase.

BOOSTER PITCH ATTITUDE, PITCH RATE, AND POSITION RELATIVE TO THE ORBITER (CASES C AND E)

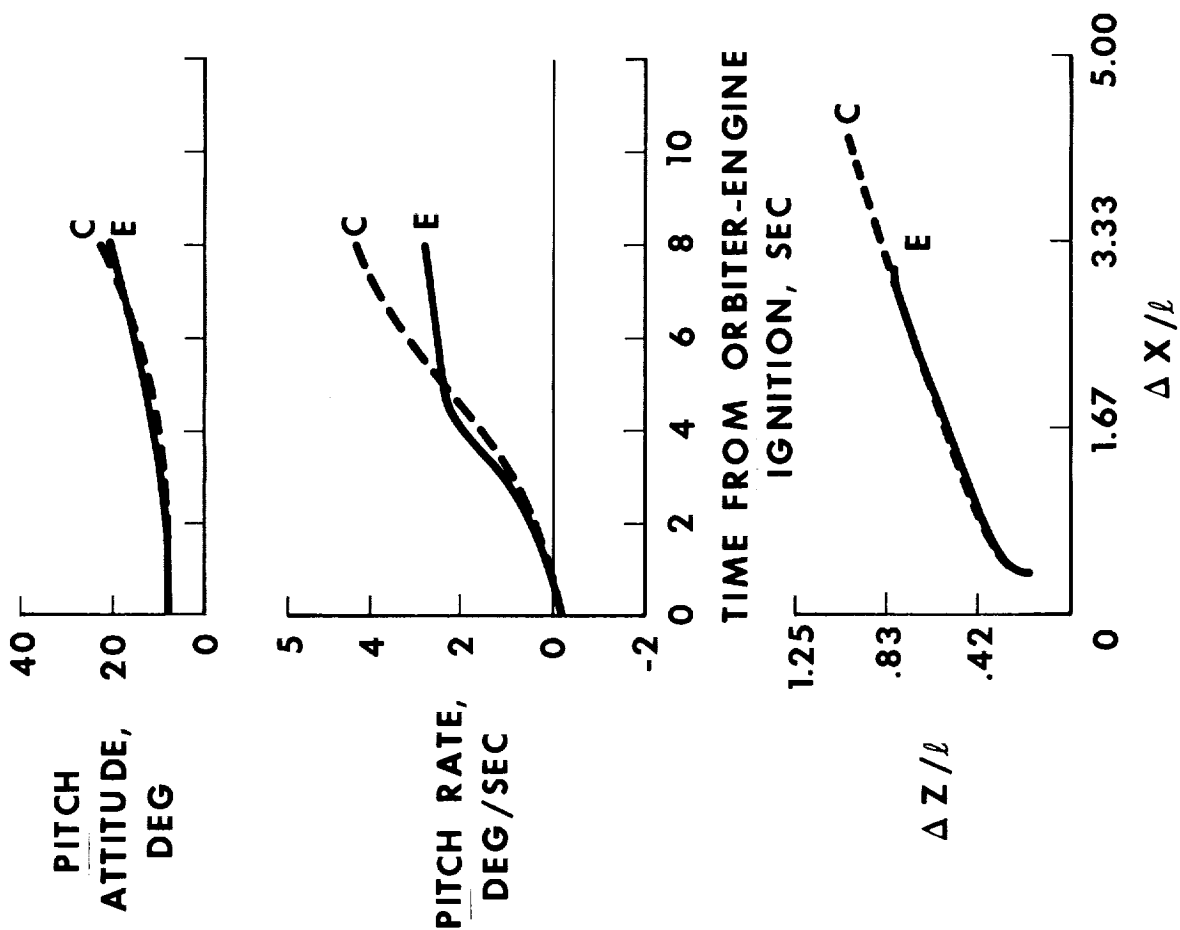


Figure 11

TRAJECTORIES USED IN THE HEATING STUDY (Figure 12)

This discussion has been concerned mainly with the plume-induced forces and moments. However, another area that requires considerable attention is that of heating sustained by the booster during separation. The heating rates that the booster can sustain are dependent on the separation sequencing, on the orbiter thrust-buildup and ignition times, and on the booster geometry. The heat loads are dependent on the trajectory (which defines the period over which heating rates exist) and on the structural and thermal materials that comprise the vehicle. To make trade-off studies concerning various separation mechanisms and sequences, the effects of plume-impingement heating must be known.

In the initial effort in this area, a simplified heating-rate calculation (ref. 6) was used that made it possible to determine sensitivity to certain parametric changes, such as ignition time and thrust-buildup time history. On the basis of these initial studies, it was learned that immediate engine ignition did not result in significantly higher heating rates than those experienced when ignition was delayed for several seconds. Each second of delay in engine-ignition time can be equated to a loss of approximately 90.71 kilograms (200 pounds) of payload in the orbiter. These studies also showed that the maximum heating rates were not significantly affected by thrust-buildup time variations.

These results, which were preliminary, were intended only to determine the sensitivity of the heating rates to various parameters. Much more detailed work (ref. 5) was possible using the PLIMP. The method used to compute the plume-impingement heating rates in this program was described briefly in a previous section. For the range of separation distances studied, only the continuum regime was encountered. Also, the heating rates thus far obtained do not include any localized effect caused by the nozzle-lip-shock/fin-bow-shock interaction phenomena.

To evaluate the severity of the heating problem, the heat loads experienced by the booster during typical trajectories must be examined. Two such trajectories that have been studied are shown in figure 12. The trajectories indicate the path of the center of the orbiter engines relative to the booster for two possible separation maneuvers. Trajectory H is representative of a staging using a piston-type separator mechanism; trajectory I is similar to a staging that uses reverse links to separate the vehicles.

TRAJECTORIES USED IN HEATING STUDY

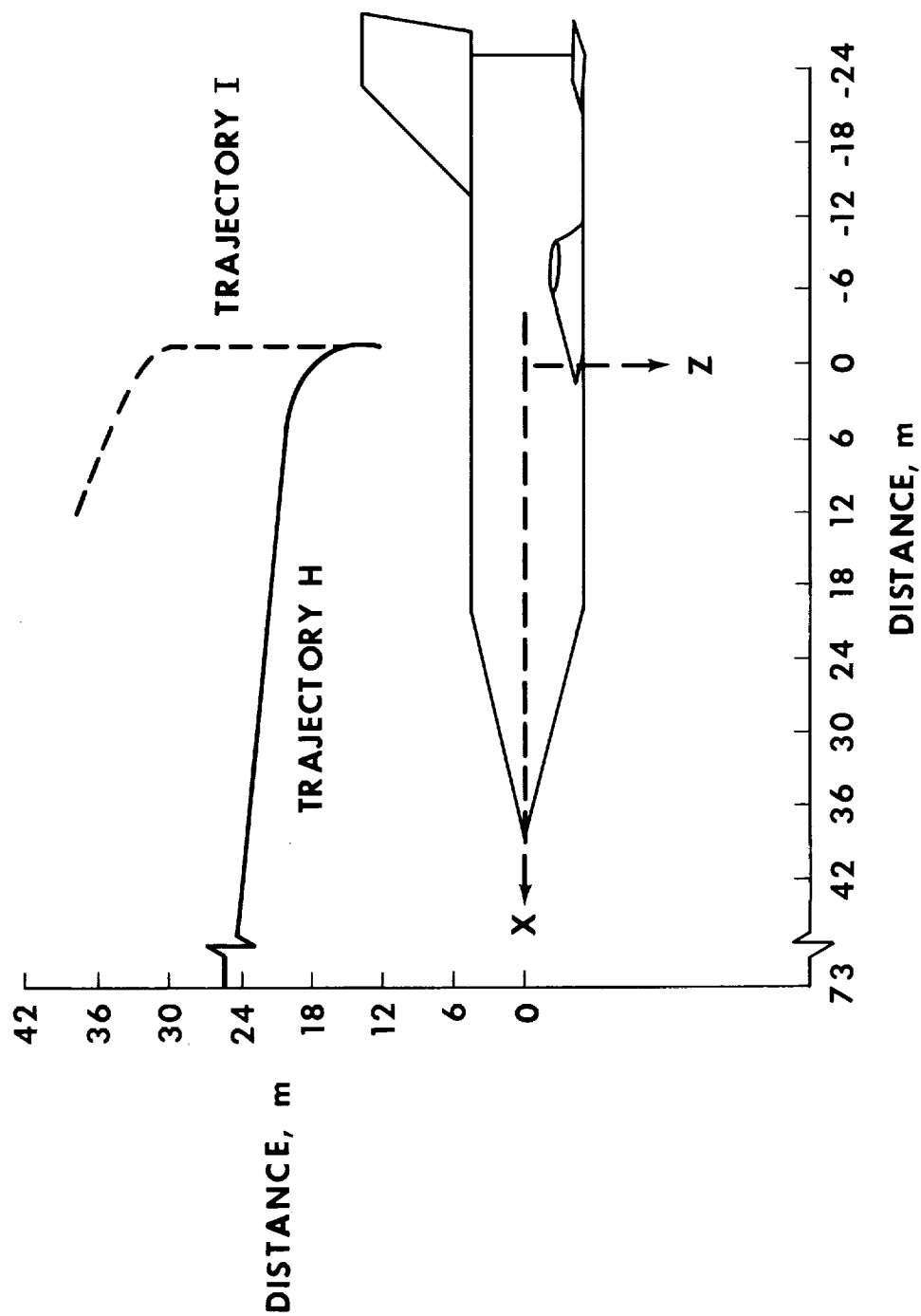


Figure 12

HEATING RATES AND SURFACE TEMPERATURES (Figure 13)

Heating-rate data obtained from the PLIMP and the 4-second thrust buildup were used to determine heating rates and loads to two points located on the booster tail. Point 1 was located on the leading edge of the tail, 0.69 meter (27 inches) below the tip; point 2 was located back 15 percent of the chord length from point 1. For point 1, a 0.0064-meter (0.25 inch) thick carbon/carbon material was used. This material extends back approximately to point 2 where a 0.00127-meter (0.05 inch) thick titanium skin was used. Flow was turbulent over these points during much of the trajectory, and this fact was considered in the heating-rate calculations. The heating-rate time histories for points 1 and 2 for both trajectories are shown in figure 13. The heating-rate data shown were for 0° pitch of the booster relative to the plume center line, which may or may not be a conservative parameter, depending upon the actual staging situation. The surface temperatures are also shown in figure 13. For both trajectories, the maximum temperatures reached are well below the structural temperature limits of 1755.4° K (2700° F) and 588.7° K (600° F) for the carbon and titanium materials, respectively. An initial temperature of 422.0° K (300° F) was assumed for this analysis.

On the booster fuselage, no heating problems were indicated, because, for trajectory I, no direct plume impingement existed on the booster ahead of the root of the vertical tail and, for trajectory H, only a very small time interval (2 to 3 seconds) of any impingement existed; this impingement was at rates of 4.54 to 6.81 kW/m² (4 to 6 Btu/ft²/sec).

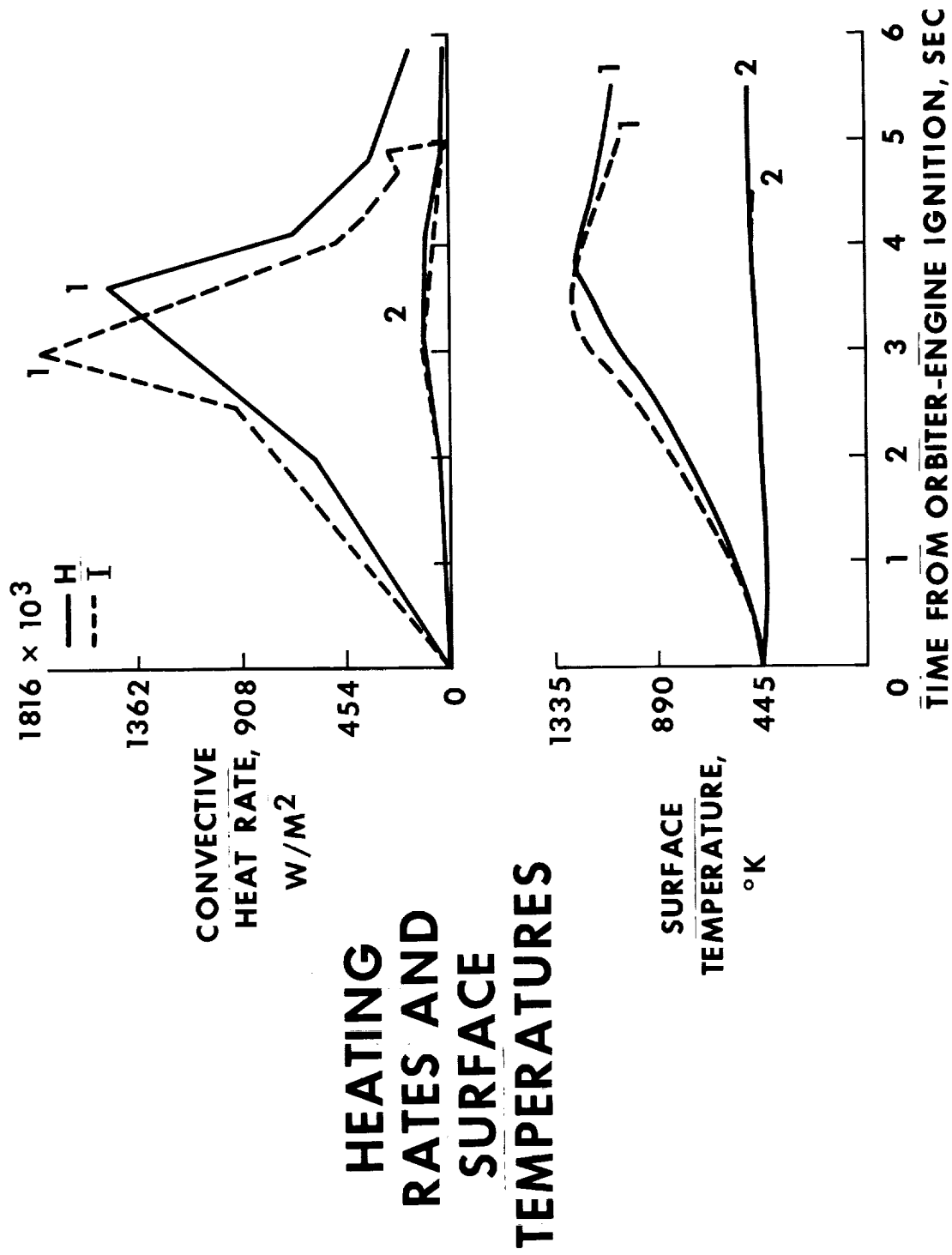


Figure 13

CONCLUDING REMARKS

The data obtained in this preliminary plume-impingement study will be used in selecting candidate separator mechanisms and separation schemes for the space shuttle vehicle. Results of this study indicate that several plume problem areas, while significant, are not detrimental to the separation maneuver. Such items as variation in thrust-buildup time history and engine-ignition time do not cause the severe plume-impingement heating problems that were once assumed. It should be noted that, in all the data presented here, the orbiter and booster were separated at, or before, the time that the orbiter engines acquired a 20-percent thrust level. Schemes that require that the vehicles remain joined until the orbiter has reached higher thrust levels must be evaluated in the same manner as the two trajectories discussed.

Some possible plume-impingement problem areas that should be considered in the space shuttle vehicle design were also identified. The possible problems that could result from a side-by-side orbiter-engine installation and the failure of recognizing plume-induced forces and moments in the sizing of the booster reaction control system are two such areas.

The study that has been made of plume impingement during stage-separation maneuvers illustrates the capability and versatility of analytical techniques applied to vehicle design. Although empirical studies and flight tests will eventually be required to verify the stage-separation maneuver, these analytical plume and trajectory studies make it possible to study a wide variety of conditions at minimal costs, both in time and in dollars.

REFERENCES

1. Wojciechowski, C. J.; and Penny, M. M.: Development of a High Altitude Plume Impingement Analysis for Calculating Heating Rates, Forces, and Moments Acting on Bodies Immersed in Rocket Exhaust Plumes. Lockheed Missiles and Space Co., Huntsville Research and Engineering Center Rept. DL62867-1, 1971.
2. Ziegler, H.; and Chu, C.: Calculation of Multiple Rocket Engine Exhaust Plumes by the Method of Characteristics. Northrop Rept. NOR-6971, Vols. 1 and 2, May 1969.
3. D'Attorre, L.; Novak, G.; Thommen, H. U.; and Trammel, V. L.: Inviscid Analysis of the Plume Created by Multiple Rocket Engines, Part II, Description of the Computer Programs. General Dynamics/Convair Rept. GD/C-DBE-66-014, May 1966. (Available as NASA CR-79741.)
4. Buck, M. L.; and McLaughlin, E. J.: A Technique for Predicting Pressure Distributions and Aerodynamic Force Coefficients for Hypersonic Winged Re-Entry Vehicles. Wright-Patterson Air Force Base Rept. ASD-TDR 63-522, Aug. 1963.
5. Wojciechowski, Carl J.; Penny, Morris M.; and Prozan, Robert J.: Space Shuttle Vehicle Rocket Plume Impingement Study for Separation Analysis, Tasks II and III, Definition and Preliminary Plume Impingement Analysis for the MSC Booster. Lockheed Missiles and Space Co., Huntsville Research and Engineering Center Rept. DL62657, Nov. 1970.
6. Penny, Morris M.; and Wojciechowski, Carl J.: Space Shuttle Vehicle Rocket Plume Impingement Study for Separation Analysis, Task I, A Program for Computing Heating Rate Indicators to Space Shuttle Vehicles. Lockheed Missiles and Space Co., Huntsville Research and Engineering Center Rept. DL62574, Oct. 1970.

CONSIDERATION OF REYNOLDS NUMBER SIMULATION
FOR SUBSONIC SHUTTLE TESTS

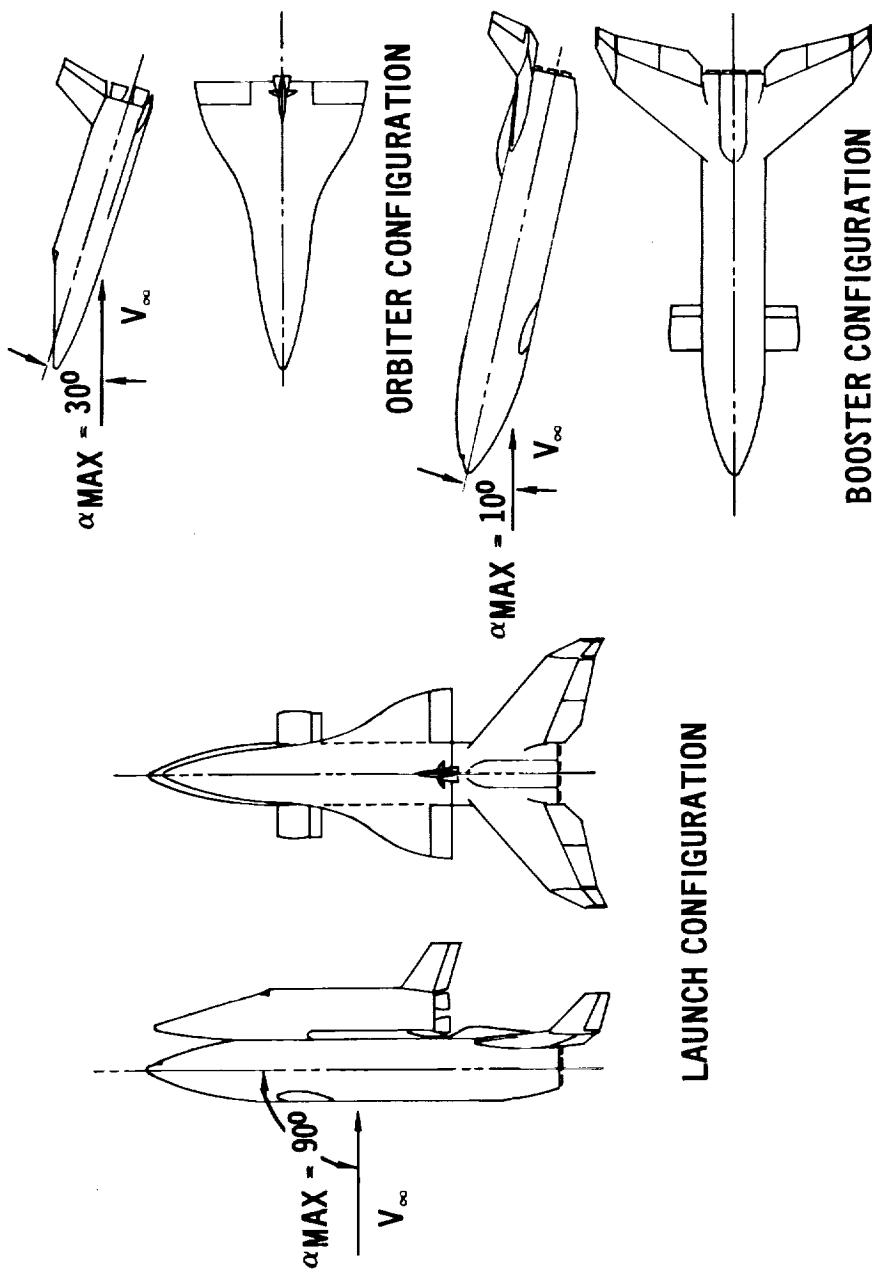
By Thomas B. Sellers
McDonnell Douglas Astronautics Company - East
St. Louis, Missouri

SPACE SHUTTLE CONFIGURATIONS AND ASSOCIATED ANGLE OF ATTACK RANGES IN SUBSONIC FLOW

(Slide 1)

One segment of the aerodynamic technology required to support the Space Shuttle Project is concerned with the acquisition of meaningful wind tunnel data for the launch (mated booster/orbiter), isolated booster, and isolated orbiter aerodynamic configurations. Each configuration has a unique maximum angle of attack - Mach number profile. The subsonic angle of attack ranges are shown in Slide 1. At subsonic speeds the booster and orbiter are limited to a maximum angle of attack of 30 degrees. Launch configuration considerations must include the 90 degree attitudes associated with the ground winds environment. Aerodynamic uncertainties associated with the high angle of attack range prompted an analytical study early in the Space Shuttle program. In that study, the flow mechanisms and aerodynamic phenomena which control the longitudinal stability of typical shuttle bodies were identified and a means for qualitatively assessing the sensitivity of the longitudinal stability to Reynolds number was developed. Although the original study was directed specifically toward the straight wing orbiter body contribution at angles of attack near 60 degrees, findings are related to, and have a definite impact on, Reynolds number simulation at lower angles, they are also directly applicable to the launch configuration in the ground winds environment. This paper summarizes the results of that study.

SPACE SHUTTLE CONFIGURATIONS AND ASSOCIATED ANGLE OF ATTACK RANGES IN SUBSONIC FLOW



Slide 1

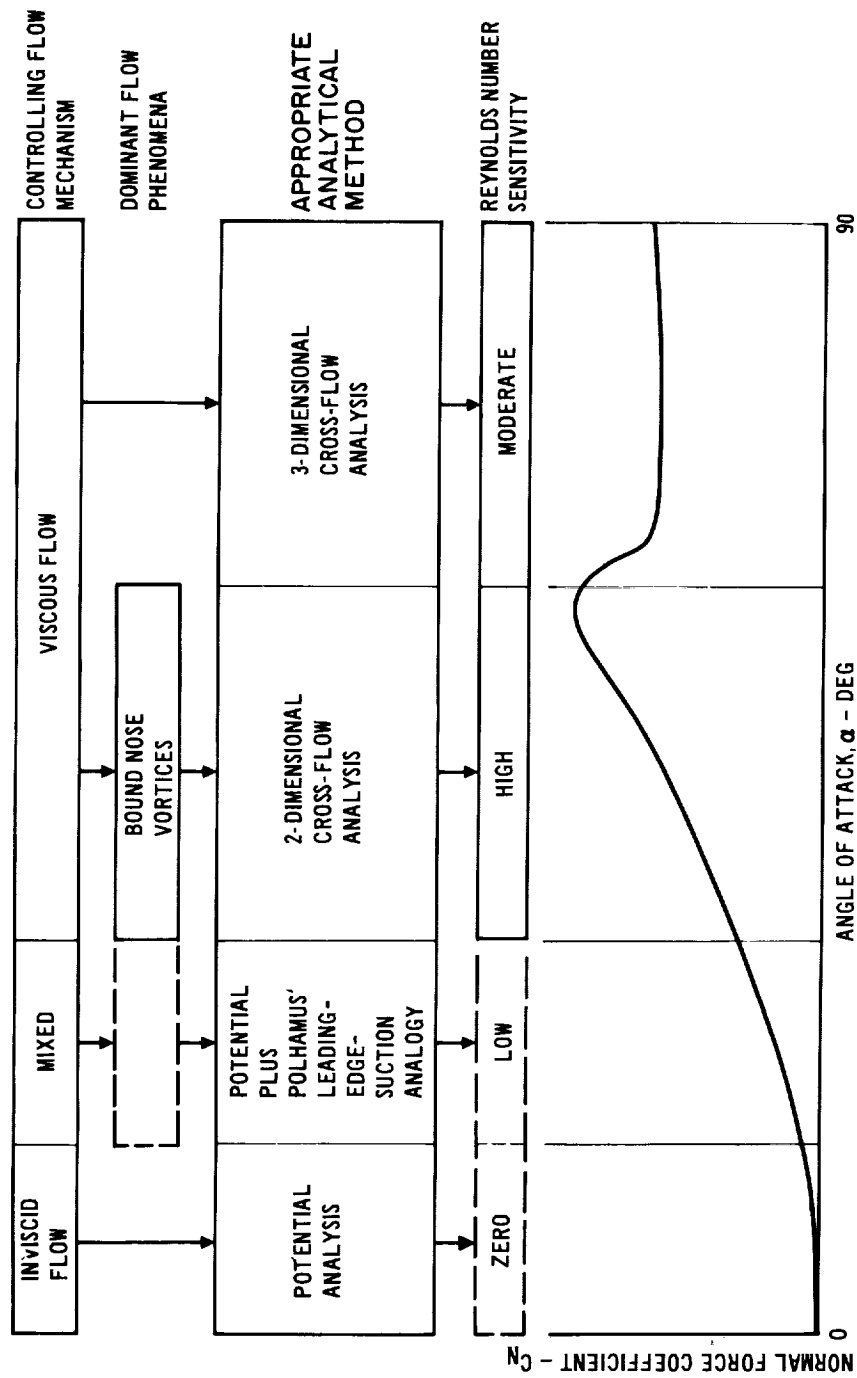
SUMMARY OF ANALYTICAL APPROACH AND PERTINENT RESULTS - BODY ALONE

(Slide 2)

From a technology viewpoint, the aerodynamic phenomena that govern body contribution to Shuttle configuration(s) longitudinal stability at angles of attack from zero to 90 degrees may be segmented as a function of angle of attack. With this overview, the total analytical approach to predicting body aerodynamic characteristics consists of a number of analyses, each of which is associated with a particular angle regime. At the angle of attack interfaces, however, solutions must be continuous, or a flow mechanism must be identified that accounts for any discontinuity in aerodynamic forces and moments.

The detailed scheme of this analysis is to (1) identify the controlling mechanisms and aerodynamic phenomena, (2) divide the total angle of attack range into appropriate regimes according to (1), (3) develop and/or select analytical methods that adequately predict existing experimental results within each angle regime, and (4) exercise these methods to indicate qualitatively the sensitivity of longitudinal stability to variations in Reynolds number. In achieving these objectives separate low angle and high angle of attack analyses were conducted. Slide 2 illustrates the approach and summarizes the findings in relation to typical body normal force data. Near zero angle of attack the flow is essentially potential and the stability is insensitive to viscous effects. At sufficiently high angles of attack, viscous cross-flow becomes predominant, a transition regime which exhibits characteristics of both acts as an interface between these extremes. The formation of the two bound nose vortices is coincident with a discernible viscous contribution to the normal force. Further increases in angle of attack increases the relative influence of the nose vortices and, at intermediate angles of attack, these vortices dominate the flow field. At some high angle of attack, approaching 90 degrees, the nose vortices break down and a true cross-flow condition exists. During the study, analytical methods applicable to each regime shown were selected or developed. Exercising these methods produced a data base which established the Reynolds number sensitivities shown. The remainder of this paper is devoted to developing the analyses that lead to establishing these Reynolds number sensitivities. The effect of the bound nose vortices on the flow field is discussed first.

ANALYTICAL APPROACH AND SUMMARY OF RESULTS



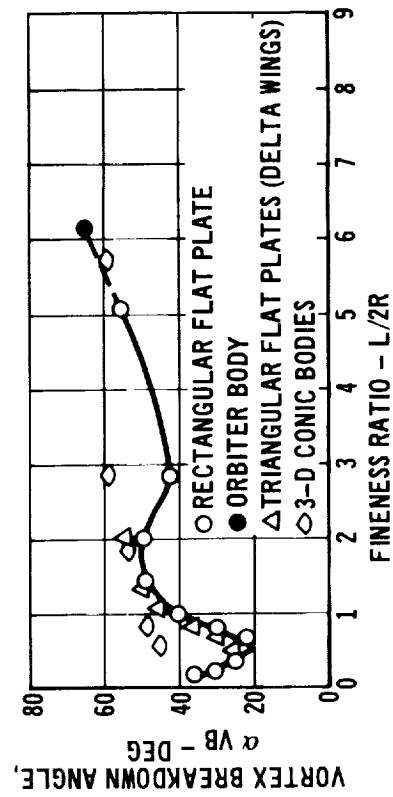
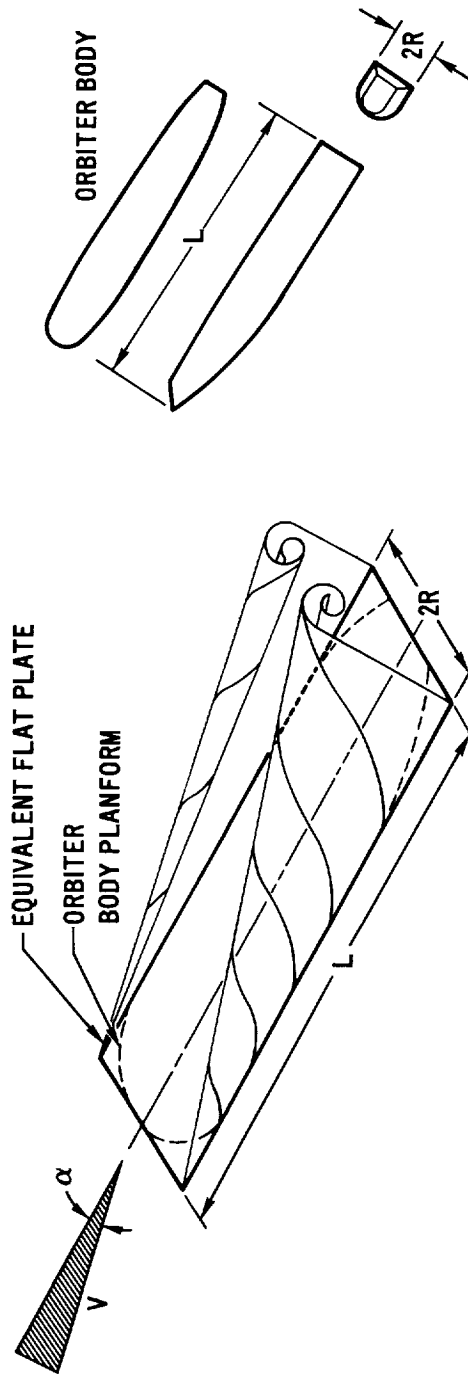
Slide 2

VORTEX FLOW OVER BODIES AT HIGH ANGLES OF ATTACK

(Slide 3)

At high angles of attack, the straight wing orbiter body shown in Slide 3 is considered to exhibit aerodynamic characteristics similar to a rectangular flat plate of equal $L/2R$. Surveying existing studies of flow over rectangular and delta shaped flat plates shows that, at moderate angles of attack, the flow field is dominated by two bound nose vortices which maintain attached flow to relatively high angles of attack^{(1),(2)}. At still higher angles these vortices break down, and the attached flow is no longer present. This characteristic is shown in the lower portion of the slide, which relates the nose vortex breakdown angle to fineness ratio. The generality of this phenomenon is supported by the delta flat plate and conic body data. On the basis of that comparison, it would be predicted that the nose vortices over the orbiter body would break down at an angle of attack near 63 degrees, which agrees with the orbiter data. At angles of attack up to 63 degrees, the flow is attached, the body nose vortices isolate the body leading and trailing edges, and a two-dimensional cross-flow analysis is valid from some intermediate angle of attack up to vortex break down.

VORTEX FLOW OVER BODIES AT HIGH ANGLES OF ATTACK

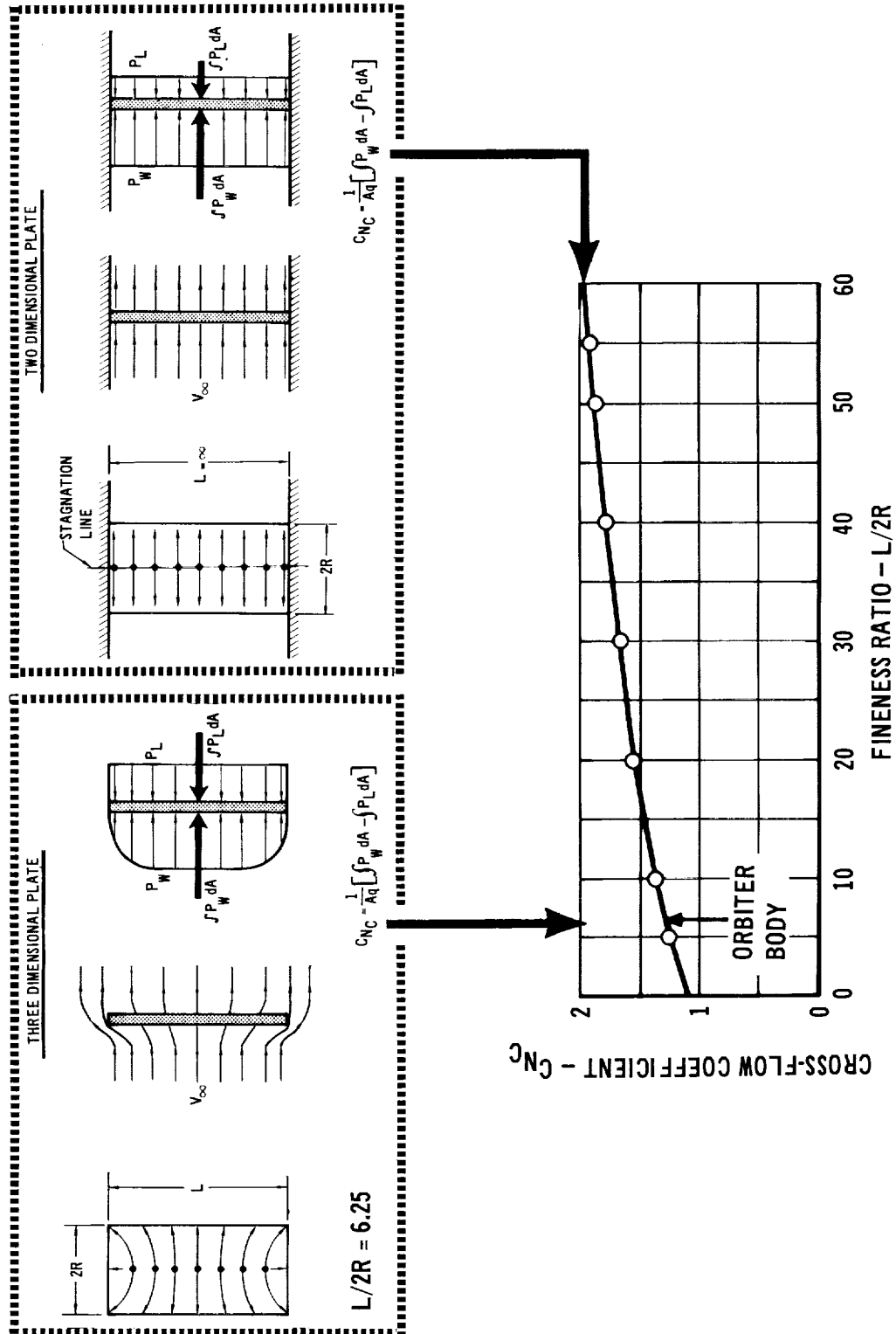


LEADING- AND TRAILING-EDGE EFFECTS ON CROSS-FLOW COEFFICIENTS

(Slide 4)

At angles greater than 63 degrees, the flow over the orbiter body is similar to the flow over a 3-dimensional rectangular flat plate mounted normal to the freestream velocity. This effect is indicated in Slide 4. Qualitatively, the flow around the body leading and trailing edges influences (increases) the leeward pressure, resulting in a cross-flow coefficient that is smaller than the two-dimensional value. The cross-flow coefficient is shown to be dependent upon fineness ratio. The three-dimensional cross-flow coefficient at $L/2R$ of 6.25 compares well with the orbiter data obtained in wind tunnel tests at high angles of attack.

LEADING- AND TRAILING-EDGE EFFECTS ON CROSS-FLOW COEFFICIENTS



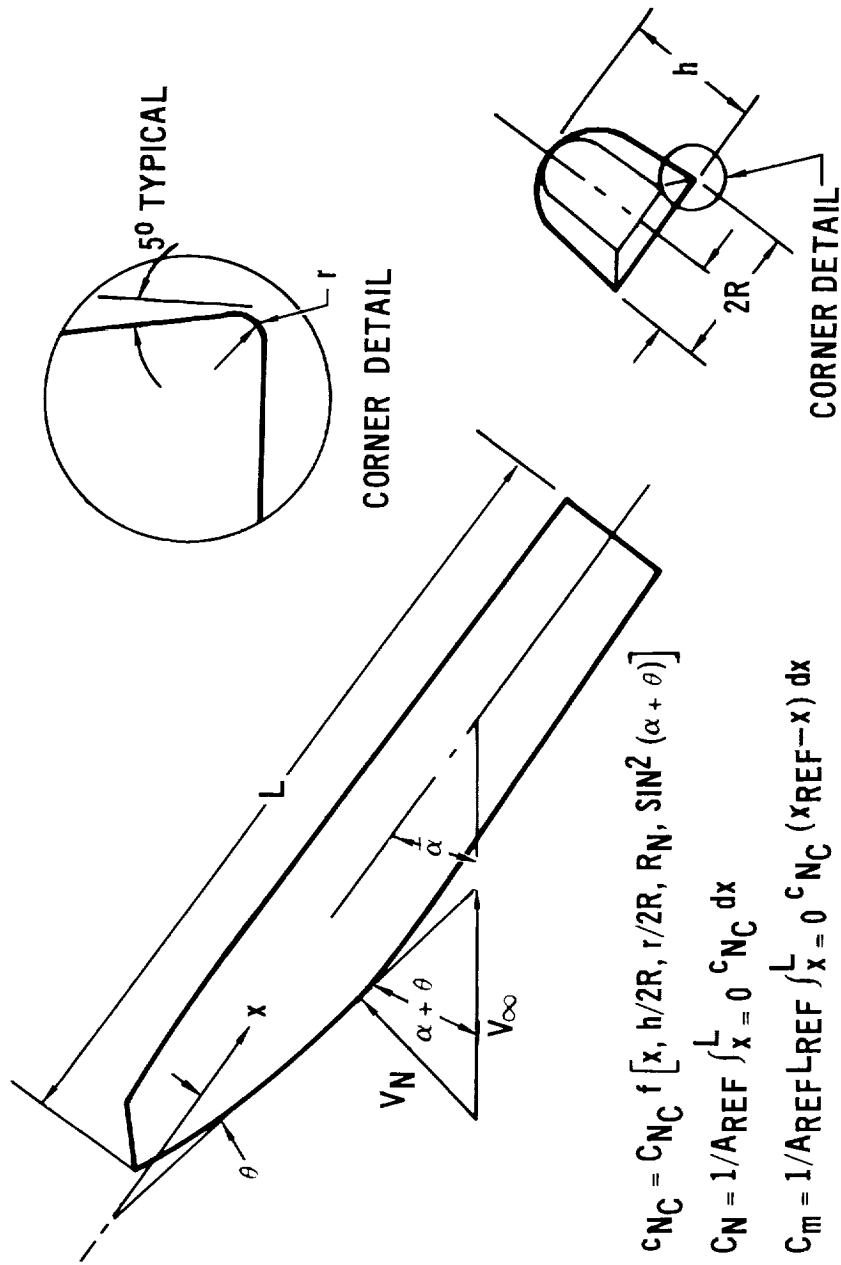
Slide 4

CROSS-FLOW ANALYSIS

(Slide 5)

According to the original approach, cross-flow analyses are used to predict longitudinal stability above some unspecified angle of attack. For the straight wing orbiter body, this lower boundary on angle of attack was selected as 30 degrees which is the minimum angle of attack at which cross-flow calculations compared favorably with experiment. The cross-flow analytical technique is shown here. Longitudinal distributions of experimental cross-flow coefficients are required as inputs. Depending upon the particular angle of attack, cross-flow coefficients are either two- or three-dimensional values.

CROSS-FLOW ANALYSIS



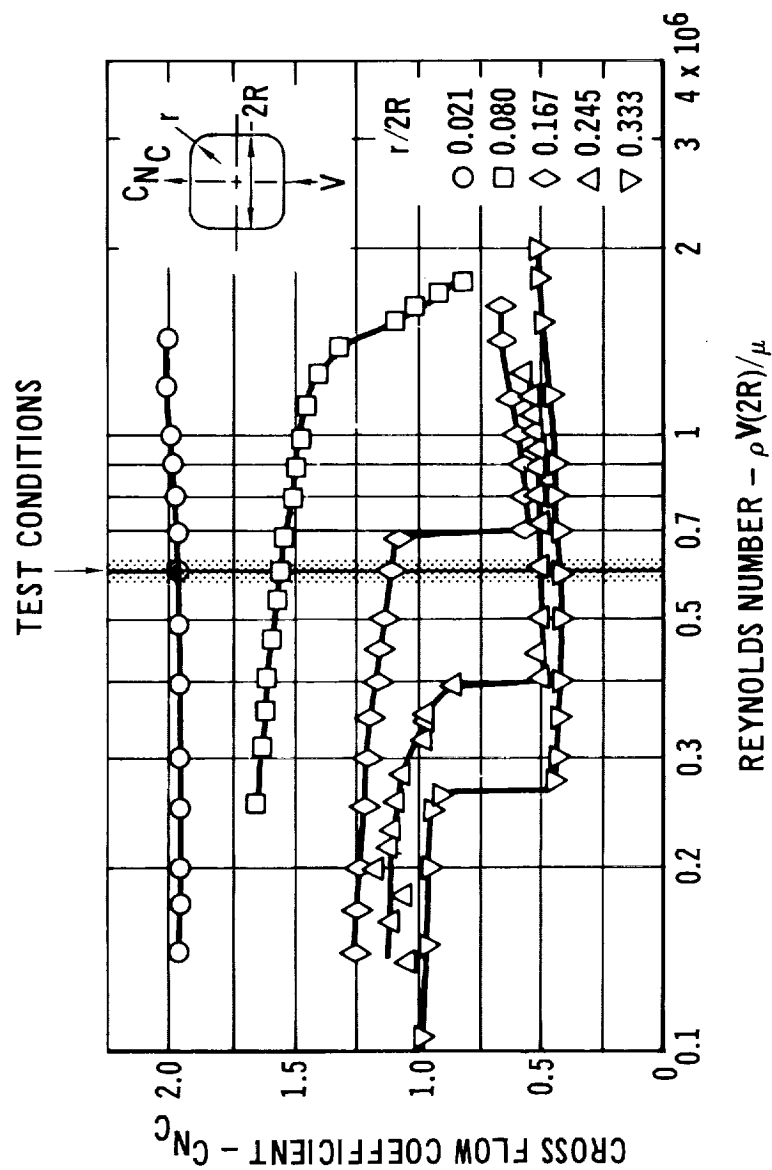
Slide 5

EXISTING 2-DIMENSIONAL CROSS-FLOW COEFFICIENT DATA

(Slide 6)

The two-dimensional cross-flow coefficients⁽³⁾ used in the calculations are shown, and test conditions for the experimental results are included. These data are for square cylinders, which approximate the orbiter body cross-sectional shape. The orbiter model had a sharp corner, $r/2R = 0$; therefore, a constant laminar cross-flow coefficient was used in the calculations. A three-dimensional cross-flow coefficient for the orbiter body was assumed to be equal to the cross-flow coefficient of a flat plate, with a fineness ratio equal to that of the orbiter body, Slide 4.

EXISTING 2-D CROSS-FLOW COEFFICIENT DATA



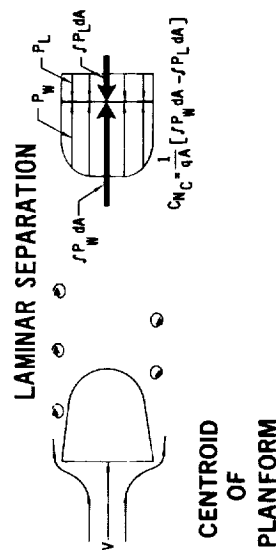
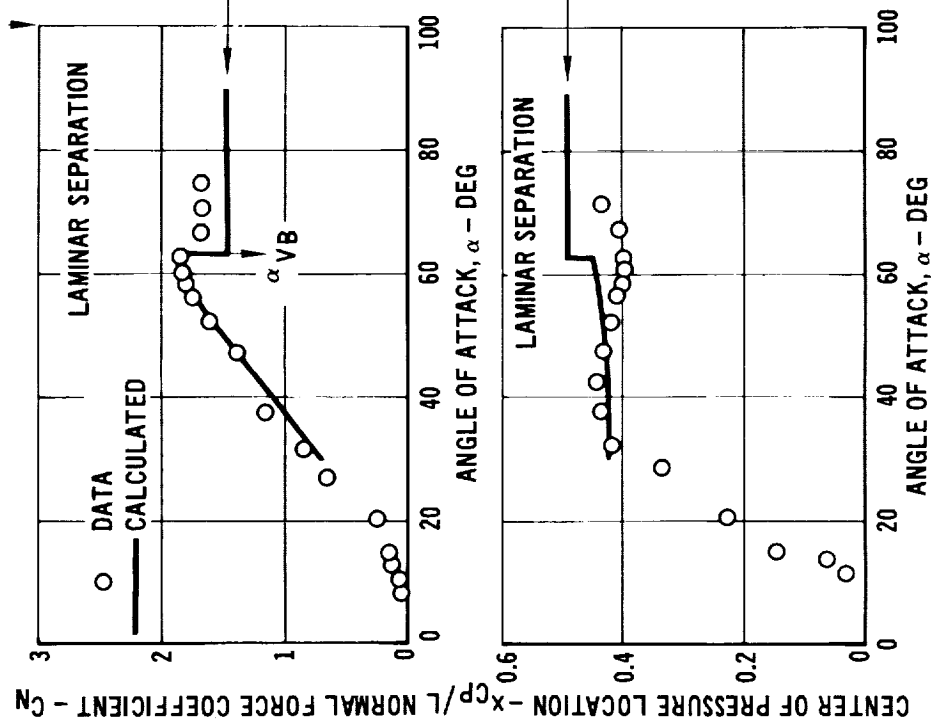
Slide 6

COMPARISON OF CROSS-FLOW ANALYSIS WITH EXPERIMENTAL DATA

(Slide 7)

Variation of predicted normal force, pitching moment, and center of pressure with angle of attack is obtained by combining a two-dimensional cross-flow analysis (laminar) with the vortex breakdown angle, and applying the 90 degree three-dimensional cross-flow coefficient at higher angles of attack. These calculations are compared with the experiment in this slide. Agreement is sufficient to validate the analytical method for estimating full scale flight characteristics. The calculations, however, require two- and three-dimensional cross-flow data for cylinders with cross-sectional shapes similar to the orbiter body at full scale Reynolds numbers.

COMPARISON OF CROSS-FLOW ANALYSIS WITH EXPERIMENTAL DATA

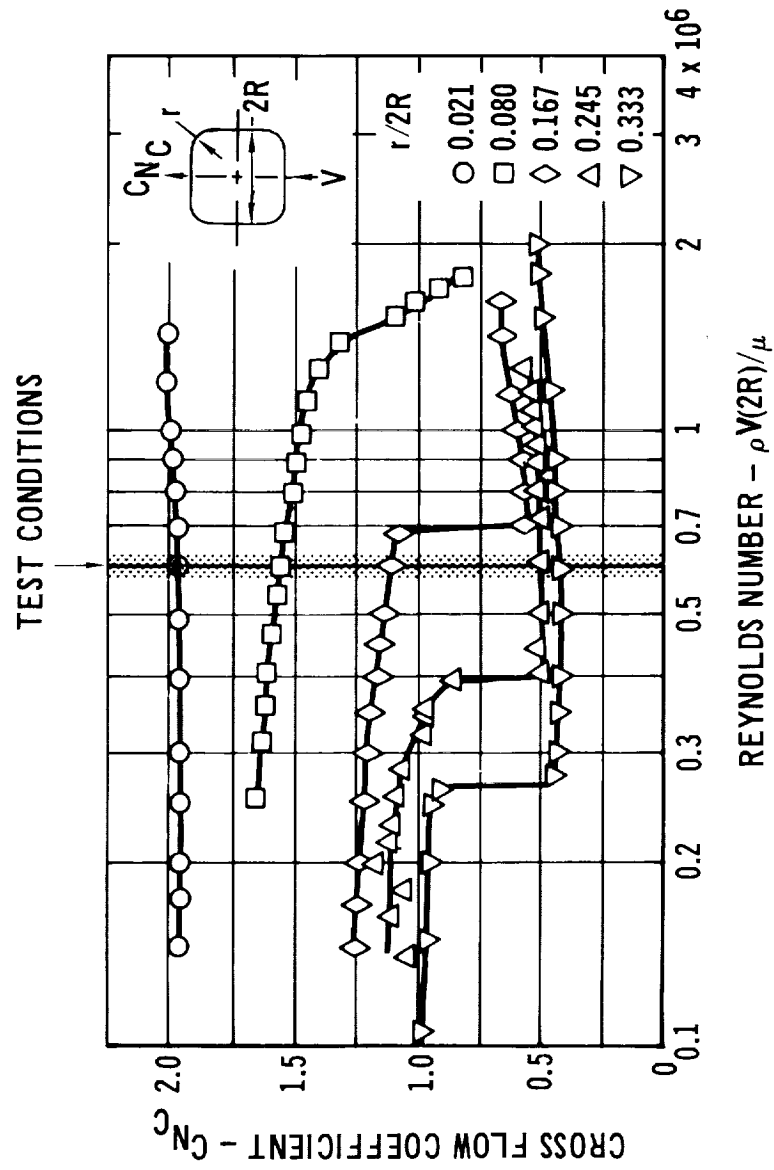


EXISTING 2-DIMENSIONAL CROSS-FLOW COEFFICIENT DATA

(Slide 8)

The two-dimensional cross-flow data base used in the analysis is shown in this slide. The subsonic full scale straight wing orbiter flight conditions include Reynolds numbers up to 20×10^6 , based on body width. This Reynolds number range is beyond the scope of the experimental data base currently available. These data show that the cross-flow coefficients are sensitive to both Reynolds number and corner radius. The large decreases in cross-flow coefficients with increasing Reynolds number result from a change from a laminar to a turbulent boundary layer at the point of separation. Based on these data for bodies with corner radii of interest ($r/2R \approx .015$), the critical Reynolds number (turbulent boundary layer at separation) is difficult, if not impossible, to predict with any degree of confidence. Therefore, a meaningful extrapolation of these data for a corner radius ratio of 0.015 is not practical. However, based on understanding the basic controlling mechanisms, the magnitude of the turbulent cross-flow coefficient may be estimated. Cross-flow analysis based on these estimated turbulent cross-flow coefficients will define the uncertainties in the aerodynamic characteristics which are associated with deficiencies in test Reynolds number simulation.

EXISTING 2-D CROSS-FLOW COEFFICIENT DATA



Slide 8

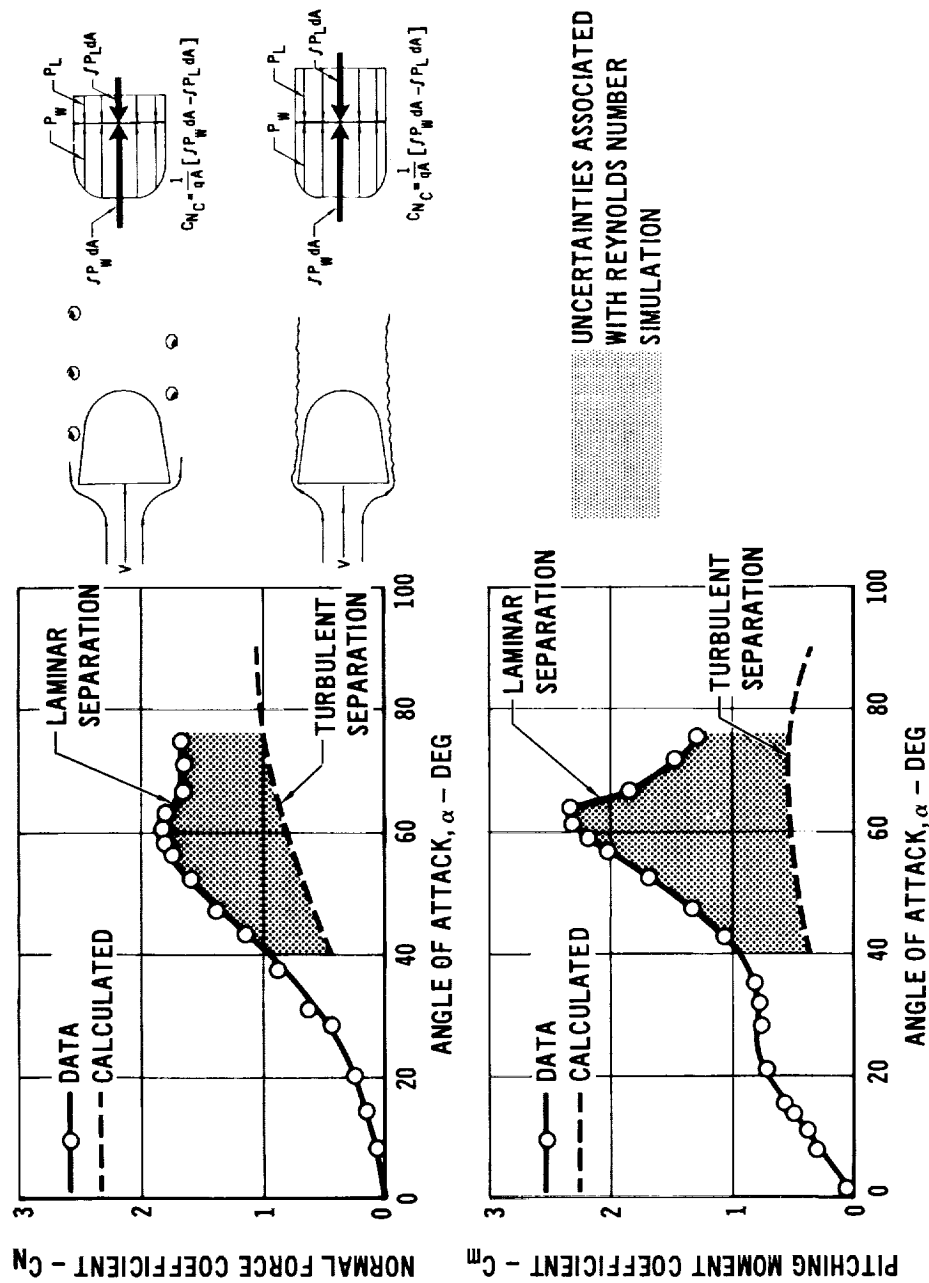
UNCERTAINTIES IN LONGITUDINAL STABILITY ASSOCIATED WITH REYNOLDS NUMBER

(Slide 9)

Turbulent cross-flow coefficients were estimated for this purpose by assuming that flat windward surface drag was unaffected by leeside pressure, and that leeward surface pressure is equal to the leeside pressure of a two-dimensional circular cylinder with a turbulent boundary layer at separation⁽⁴⁾. This assumption is shown schematically, together with the results of the turbulent cross-flow analysis.

The data points were obtained with a laminar separation. They represent the maximum level of normal force, while the turbulent analysis represents the minimum possible normal force. As shown, a normal force error of 50 percent, and a greater error in pitching moment, may result from test Reynolds number deficiencies. For Space Shuttle applications, the use of subscale data to predict full scale flight characteristics at high angles of attack may result in an unacceptable level of stability, or impose unrealistic control requirements.

UNCERTAINTIES IN LONGITUDINAL STABILITY ASSOCIATED WITH REYNOLDS NUMBER



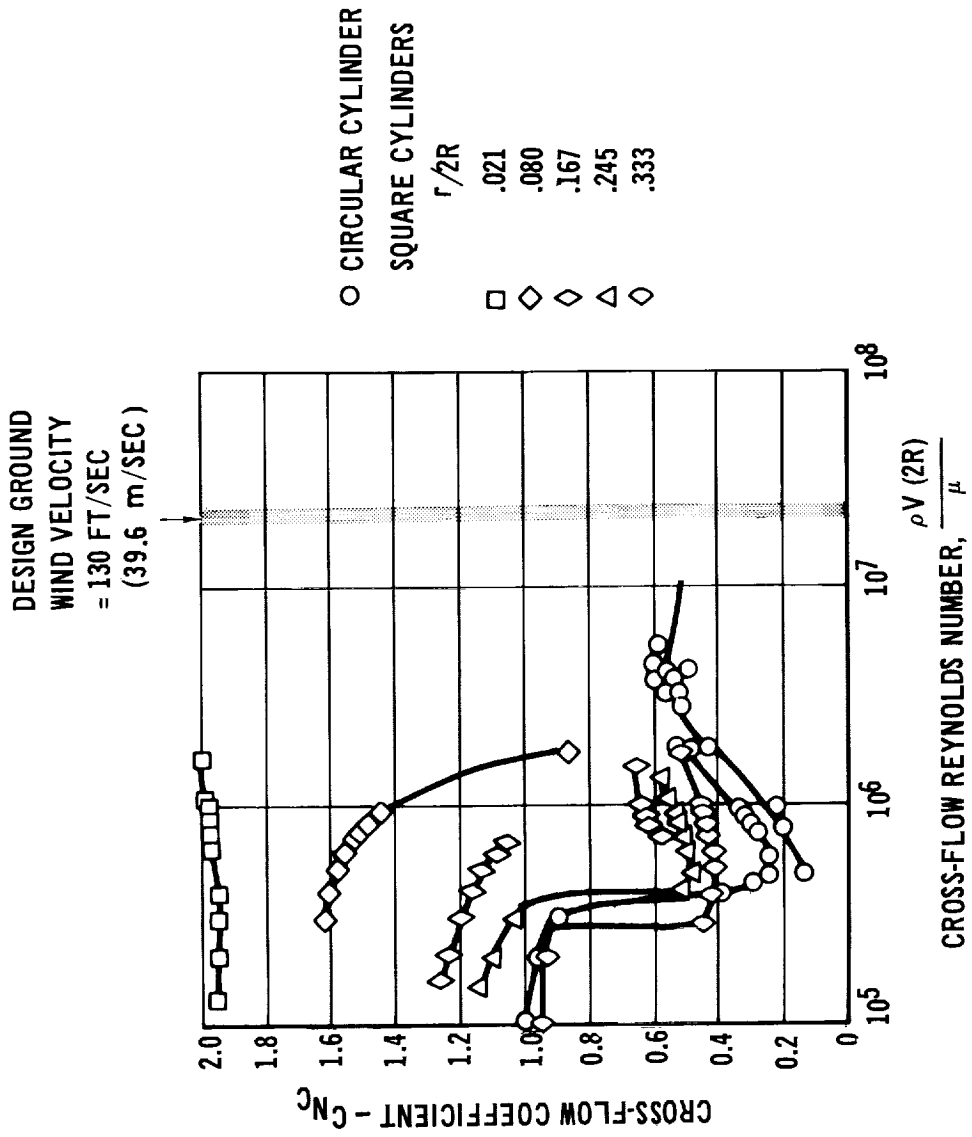
Slide 9

QUALITATIVE EFFECTS OF REYNOLDS NUMBER

(Slide 10)

For bodies at high angles of attack in subsonic flow, two-dimensional cross-flow coefficients have been shown to be valid indicators of both the level of normal force and the sensitivity of the stability of the total body to Reynolds number. The current state-of-the-art Reynolds number simulation requirements for conducting wind tunnel tests of the launch configuration in the ground winds environment, therefore, are summarized in Slide 10. The composite launch configuration consists of bodies with circular and "D" cross-section shapes; design ground winds velocity spectrum results in cross-flow Reynolds numbers from zero to approximately 20 million, based on body diameter. The higher range of Reynolds numbers exceeds the scope of the present data base. Furthermore, the achievement of full scale Reynolds numbers with present test facilities is very questionable. In order to assess the effect of these anticipated simulation deficiencies, it is recommended that the 2-dimensional, non-circular cylinder data base be increased to include the critical Reynolds number. Increasing the corner radius to achieve pseudo-turbulent conditions implies detailed knowledge beyond the data base and may only be justified by increasing the data base to higher Reynolds number. Three-dimensional effects tend to reduce difference between laminar and turbulent cross-flow coefficients. This tendency was accounted for by assigning a moderate Reynolds number sensitivity factor at angles of attack near 90 degrees, and a high sensitivity at the intermediate angles. These observations emphasize the importance of considering body cross-section shape in defining Reynolds number simulation requirements for high angle of attack wind tunnel testing.

QUALITATIVE EFFECTS OF REYNOLDS NUMBER



Slide 10

DATA BASE FOR EVALUATING POLHAMUS' LEADING-EDGE-SUCTION ANALOGY

(Slide 11)

The method selected for predicting the longitudinal stability of the orbiter body at low angles of attack is the lifting surface theory plus Polhamus' leading-edge-suction analogy. This technique is identical to Polhamus' work⁽⁵⁾, except that the vortex lift component is applied at an angle of attack other than zero. The particular angle is dependent upon body cross-sectional shape. The validity of this approach is supported by the data base summarized here. A wide range of elliptical cross-section bodies are included (6 to 9), and additional unpublished LRC data for trapezoidal cross-section bodies will be used to increase this data base.

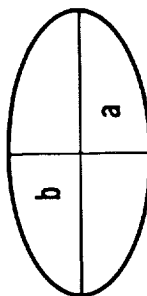
DATA BASE FOR EVALUATING POLHAMUS' LEADING-EDGE-SUCTION ANALOGY

NASA LIFTING BODY TEST DATA, NASA TN D-1149, 1963, 2622, 3203

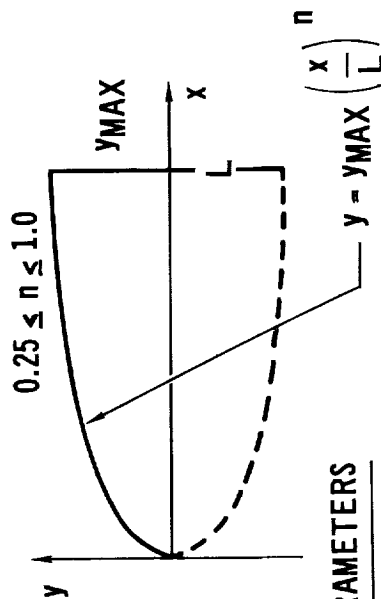
BODY GEOMETRY

ELLIPTICAL CROSS SECTION

$$0.4 \leq a/b \leq 3.0$$



POWER-LAW PLANFORM



BODY THICKNESS PARAMETERS

$$\text{FINENESS RATIO} = \frac{L}{d_b}; \quad d_b = 2 \sqrt{(ab)\text{BASE}}$$

$$\text{THICKNESS RATIO} = a/b$$

BODY PLANFORM PARAMETER

ASPECT RATIO

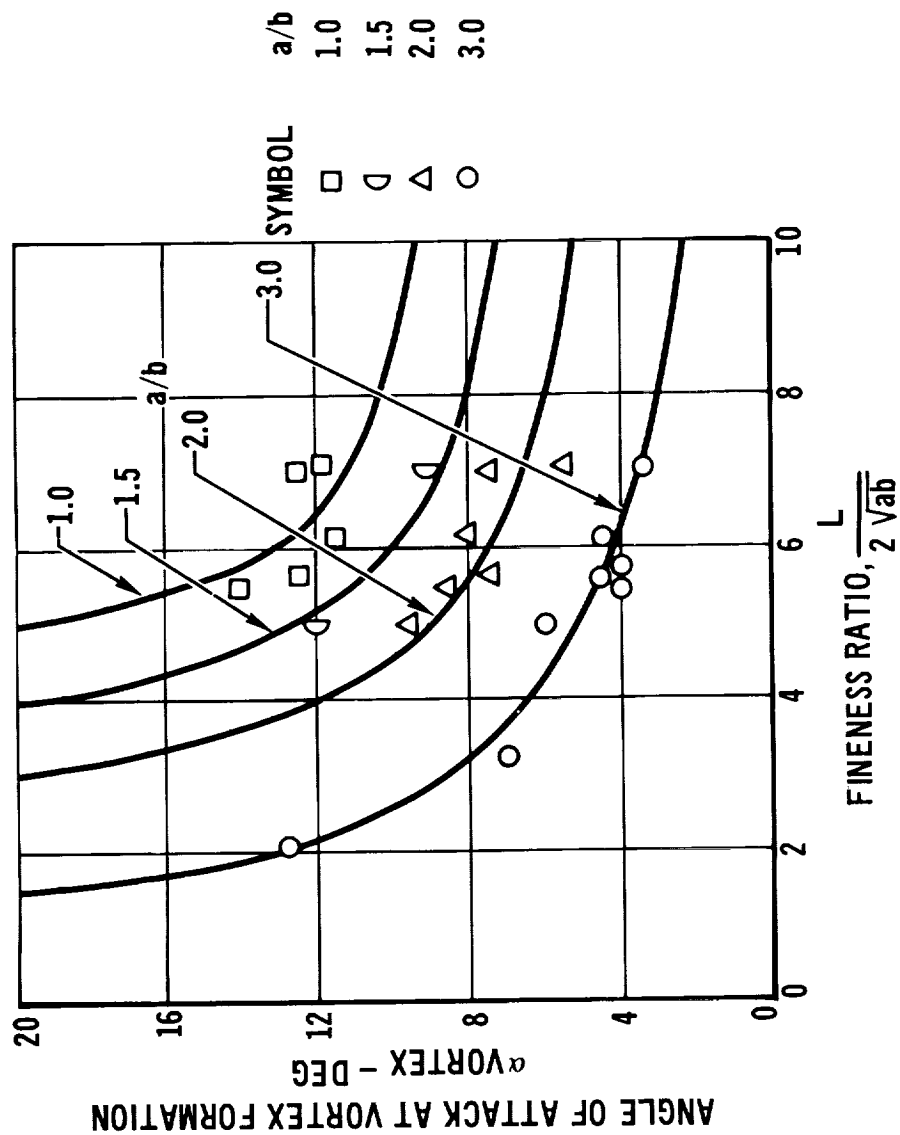
Slide 11

ANGLE OF ATTACK AT VORTEX FORMATION ELLIPTICAL CROSS-SECTION BODIES

(Slide 12)

The data base shown on the previous slide is the source of the correlation shown here. The angle of attack at vortex formation was determined by comparing calculated potential lift with experimental data, and selecting that angle of attack at which potential lift deviated from experimental data.

ANGLE OF ATTACK AT VORTEX FORMATION ELLIPTICAL CROSS-SECTION BODIES



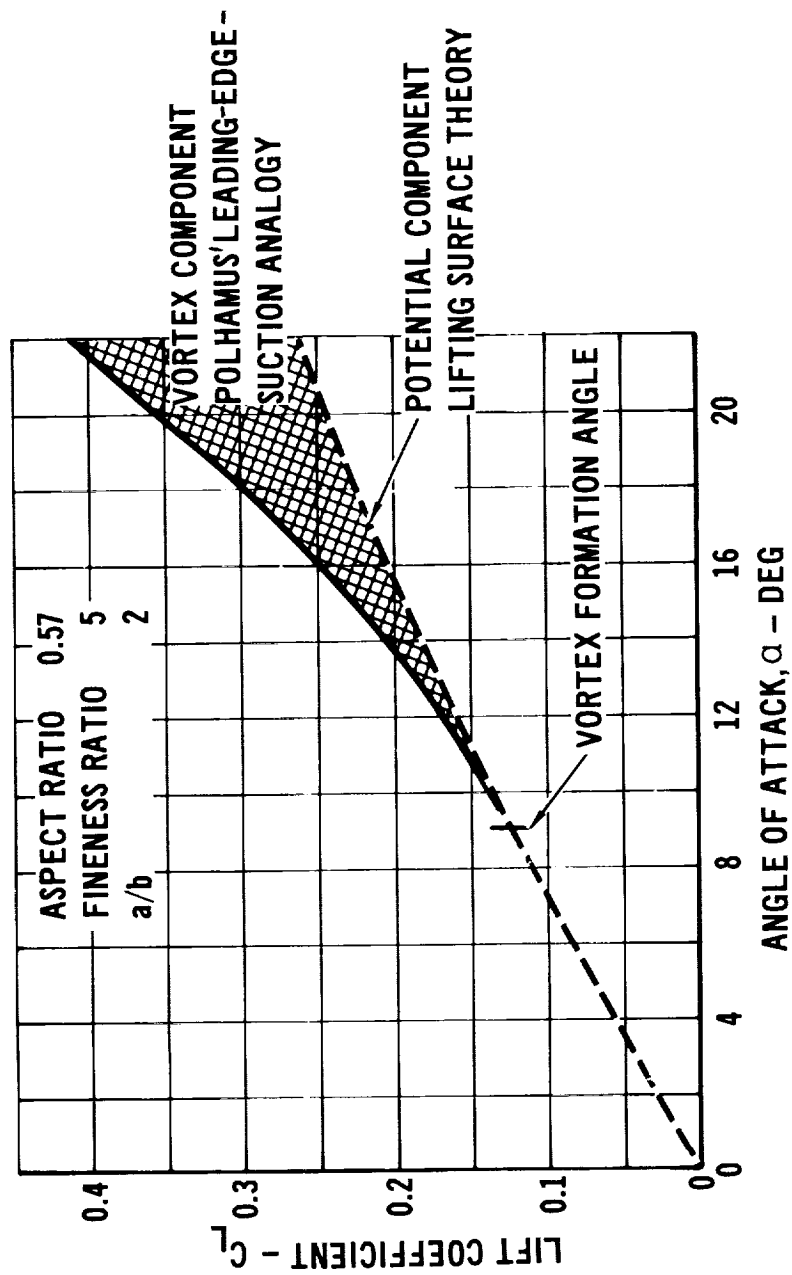
Slide 12

TYPICAL ELLIPTICAL BODY DATA

(Slide 13)

This slide presents typical elliptical body lift data. The vortex formation angle and the relative magnitudes of the potential and vortex components are shown. The vortex formation angle is the lower boundary of the mixed regime and, at that angle, the vortex component is zero. The upper boundary of the mixed regime corresponds to the minimum angle where the cross-flow component dominates. Qualitatively, then, a low Reynolds number sensitivity is an average value that is assigned to the mixed regime. Methods for quantitatively evaluating the variation in longitudinal stability with Reynolds number are not currently available.

TYPICAL ELLIPTICAL BODY DATA



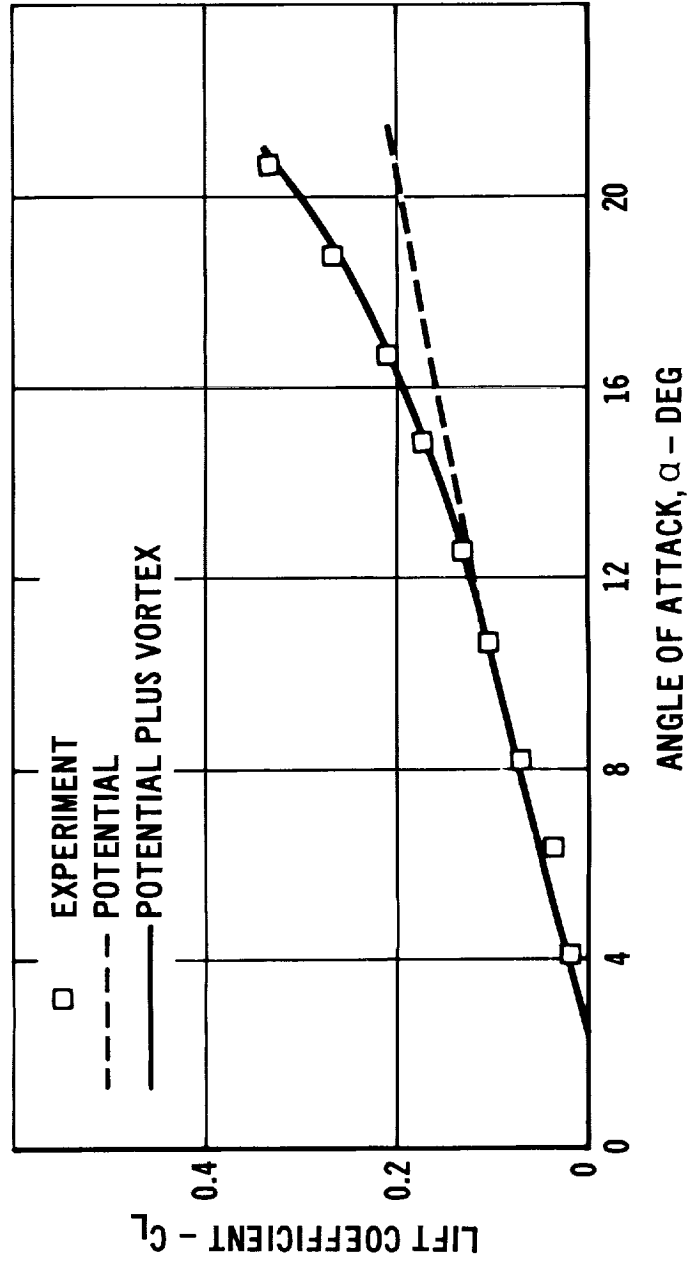
Slide 13

TYPICAL ORBITER BODY DATA OF LOW ANGLES ATTACK

(Slide 14)

A comparison of predicted lift with experiment for the isolated orbiter body in the mixed regime is shown in Slide 14. Calculations have been adjusted for the zero-lift angle of attack. With this adjustment, predicted lift compares well with the data, and similar agreement has been obtained for various non-circular bodies. Technology efforts directed toward developing methods for predicting the zero-lift angle of attack, zero-lift body pitching moment coefficient, and establishing a quantitative measure of the effects of Reynolds number for the mixed regime are needed to reduce the uncertainties in the stability data due to the lack of Reynolds number simulation.

TYPICAL ORBITER BODY DATA LOW ANGLES OF ATTACK



Slide 14

SUMMARY

The Reynolds number simulation requirements for conducting subscale wind tunnel tests of Space Shuttle aerodynamic configurations are reviewed in this paper, and conclusions are reached that apply to the acquisition of data at angles of attack from zero to 90 degrees. Methods for qualitatively evaluating effects of simulation deficiencies are presented. It is shown that uncertainties inherent in high angle of attack stability data may be greatly reduced by extending the existing two-dimensional cross-flow coefficient data base. At low angles of attack, requirements for developing methods for predicting the onset of discernible viscous components, and relating the strength of that component to Reynolds number, are cited.

REFERENCES

- (1) Winter, H.: Flow Phenomena on Plates and Airfoils of Short Span. NACA TM 798, 1936
- (2) Earnshaw, P. B. and Lawford, J. A.: Low-Speed Wind-Tunnel Experiments on a Series of Sharp-Edged Delta Wings. Brit. R&M No. 3424, March 1964
- (3) Polhamus, Edward C.: Effect of Flow Incidence and Reynolds Number on Low-Speed Aerodynamic Characteristics of Several Noncircular Cylinders With Applications to Directional Stability and Spinning. NASA TR R-29, 1959
- (4) Bursnall, William L. and Loftin, Laurence K., Jr.: Experimental Investigation of the Pressure Distribution About a Yawed Circular Cylinder in the Critical Reynolds Number Range. NACA TN 2463, 1951
- (5) Polhamus, Edward C.: A Concept of the Vortex Lift of Sharp-Edge Delta Wings Based on a Leading-Edge-Suction Analogy. NASA TN D-3767, 1966
- (6) Stivers, Louis S., Jr. and Levy, Lionel L., Jr.: Longitudinal Force and Moment Data at Mach Numbers from 0.60 to 1.40 for a Family of Elliptic Cones with Various Semiapex Angles. NASA TN D-1149, 1961
- (7) Spencer, Bernard, Jr. and Phillips, W. Pelham: Effects of Cross-Section Shape on the Low-Speed Aerodynamic Characteristics of a Low-Wave-Drag Hypersonic Body. NASA TN D-1963, 1963
- (8) Spencer, Bernard, Jr. and Phillips, W. Pelham: Transonic Aerodynamic Characteristics of a Series of Bodies Having Variations in Fineness Ratio and Cross-Sectional Ellipticity. NASA TN D-2622, 1965
- (9) Spencer, Bernard, Jr.: Transonic Aerodynamic Characteristics of a Series of Related Bodies with Cross-Sectional Ellipticity. NASA TN D-3203, 1966

CORRELATION OF SPACE SHUTTLE APPLICABLE EXPERIMENTAL
HYPERSONIC AERODYNAMIC CHARACTERISTICS WITH THEORY

Richard K. Hamilton
McDonnell Douglas Astronautics Company-EAST
St. Louis, Missouri

INTRODUCTION (Slide 1)

Hypersonic theoretical-experimental correlations of aerodynamic characteristics pertinent to Phases A and B straight and blended delta wing Shuttle designs studied by the MDC team are presented. The results substantiate the usefulness of the theoretical techniques in supporting the assessment of the hypersonic aerodynamic coefficients for Phase B shuttle designs. The use of the Hypersonic Arbitrary Body Program (HABP) also provides confidence in configurations as they are entered into the wind tunnel program. No significant hypersonic "surprises" have occurred as a result of the MDAC Phase B wind tunnel program.

Emphasis is placed on those aerodynamic characteristics which are influential with respect to the Shuttle design. Characteristics correlated are shown on the slide. Areas of exceptional agreement will be noted as well as instances where deviations exist. Oil flow visualization studies complement the analysis.

It is not the intent of this paper to imply that the HABP rigorously describes the aerodynamic phenomena. In Phase B as NASA groundrules have been altered and as design innovations dictate, the configuration has been in a state of evolution. The HABP has been instrumental in allowing for a rapid and orderly evaluation. As we enter into Phase C/D development, the use of the program will yield to extensive testing.

PERTINENT EXPERIMENTAL AERODYNAMIC CHARACTERISTICS
CORRELATED WITH THE HYPERSONIC ARBITRARY-BODY
AERODYNAMIC PROGRAM INCLUDE

- LONGITUDINAL TRIM AND STABILITY
- REYNOLDS NUMBER EFFECTS
- LIFT TO DRAG RATIO $\sim L/D$
- LIFT COEFFICIENT $\sim C_L$
- LATERAL DIRECTIONAL STABILITY, C_{n_β}, C_{l_β}
- DIFFERENTIAL CONTROL EFFECTS

Slide 1

DELTA WING CONFIGURATIONS

(Slide 2)

Correlations with respect to several vehicles of a given type are required to give sufficient scope that conclusions relative to the theoretical-experimental comparisons can be constructively drawn. For delta wing (highly swept) type designs considerable hypersonic research and testing (including flight test) has been accomplished by McDonnell Douglas in conjunction with NASA and the Air Force over the past several years. The corresponding figure presents several delta-type configurations which have been studied and for which correlations pertinent to this paper exist. The MDC Phase B, November 1970, delta orbiter (with centerline vertical) wind tunnel model tested in the Ames 3.5 ft hypersonic tunnel at a Mach number of 7.4 will be the basic delta vehicle correlated. Pertinent results from experimental-theoretical comparisons of the other delta shapes will be used in a supporting role.

The theoretical estimates were generated with the MDC Hypersonic Arbitrary-Body Aerodynamic Computer Program (HABP) developed by A. E. Gentry (Reference (1)). This program is also utilized by NASA and the Air Force as well as other industrial concerns. In this presentation (except where noted) the force calculation techniques utilized are:

- Newtonian ($K = 2$) for impact regions
- Prandtl-Meyer expansion from free stream for shadow regions
- Reference Enthalpy laminar friction
- Spalding-Chi turbulent friction

This combination of techniques has proven to be particularly applicable for delta wing shapes flying at the angles of attack required for crossrange missions.

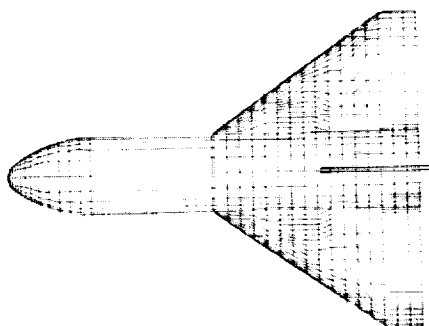
MDC HYPERSONIC CORRELATED DELTA CONFIGURATIONS



AFFDL-7MC



ASSET



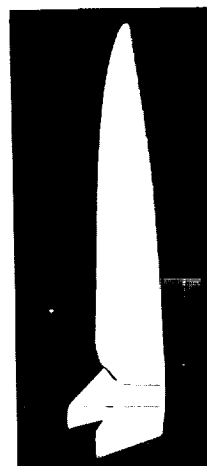
MDC-LaRC PHASE A



MDC PHASE B NOV 70



MDC SEPT 70



MMC-LaRC PHASE A

MDC-MMC BOOSTER



LONGITUDINAL STABILITY AND CONTROL

(Slide 3)

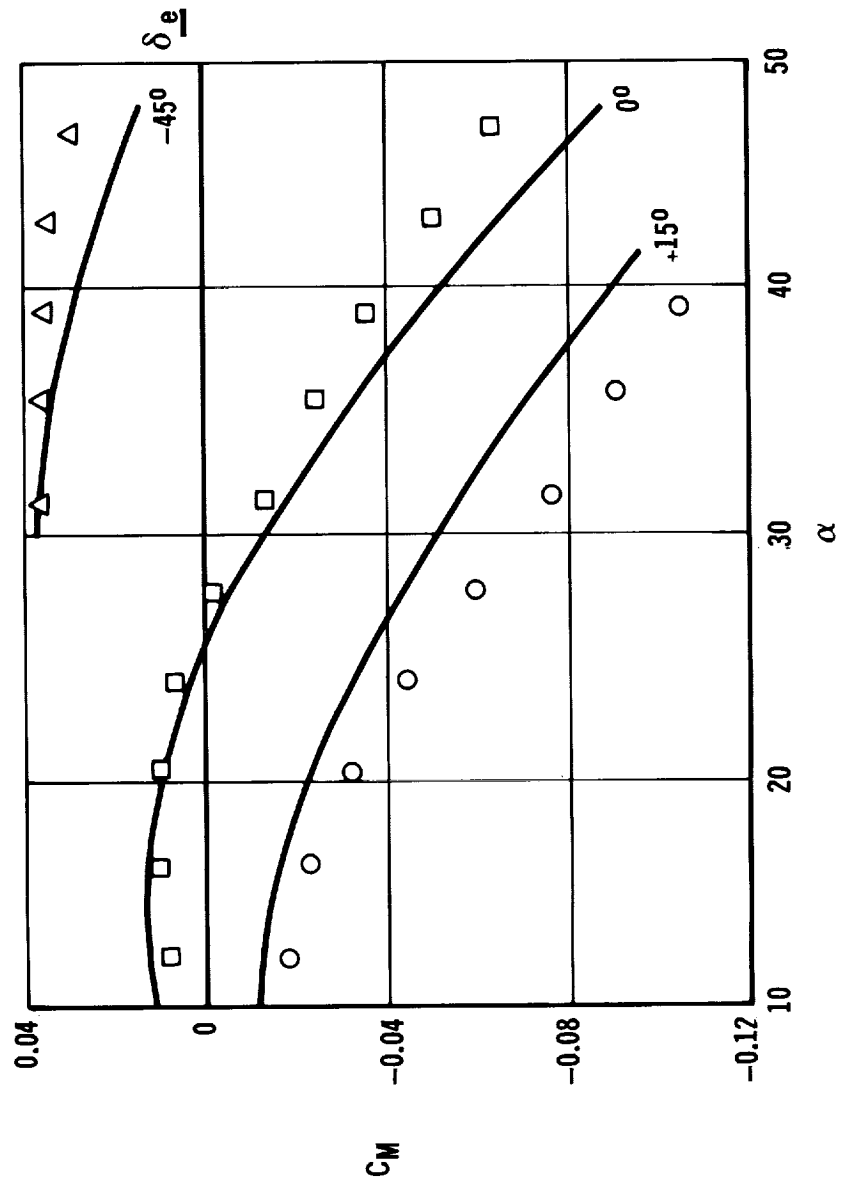
The theoretical-experimental comparison of pitching moment coefficient versus angle of attack and elevon setting is shown on the slide for our November 1970 Configuration tested in the NASA Ames Research Center 3.5 ft tunnel. The magnitude of the deviation between test and theory is typical for delta vehicles as will be shown on the next page. The trim angle of attack determined from the test data for the undeflected elevons is within 2 1/2 degrees of that predicted. The test results show a somewhat greater tolerance to center of gravity location and greater control authority than predicted. The effectivity of the trailing-edge-down ($+\delta_e$) elevons was underpredicted as expected and agrees with test correlations for our teammates (Martin Marietta Corporation) Phase A delta tested at Langley. A more detailed analysis of trailing-edge-down deflections and the phenomenon of flow separation is contained in later figures. It is noted that for a desired trim angle of attack of 20 degrees (low enough for more than sufficient L/D for the crossrange mission) the model requires about a +3 degree deflection. The largest trailing-edge-down elevon deflection requirement occurs for the aft center of gravity position which was the case for this slide.

MDAC DELTA - NOV 1970

LONGITUDINAL STABILITY COMPARISON

TEST: $M = 7.4$ NASA AMES
THEORY: HABP ———

REYNOLDS NUMBER ≈ 3.3 MILLION



LONGITUDINAL TRIM COMPARISON

(Slide 4)

Estimated trim angle of attack with undeflected elevons and the corresponding amount of control deflection required to neutralize the theoretical-experimental deviation is presented on this slide for several of the delta configurations correlated. The collation of the undeflected elevon trim angle of attack is pertinent to the shuttle since it is a frequent guideline to trim hypersonically near the nominal angle of attack with undeflected controls. With the exception of the MDC-LaRC Phase A delta comparison, the correlation is considered to be very good with only a typical 2-3 degree deviation in trim α which can be accounted for with a 1-2 degree elevon deflection. Although the deviation for the MDC-LaRC Phase A delta is considered to be a poor correlation (α_{TRIM} uncertainty 10 degrees, elevon angle 7 degrees), it fortunately did not impact the configuration design as the test data resulted in greater trim capability than predicted. However, if a deviation of this magnitude had occurred in the wrong direction for a configuration where the elevon angle was constrained (by maximum deflection capability or aerothermodynamic problems associated with trailing edge down deflections), the results could have dictated a redesign. Available correlations indicate that this is unlikely to occur as the HABP has a tendency to underpredict control authority and configurations are seldom designed for the limiting case.

TRIM COMPARISON - DELTA SHAPES

	MACH	α TRIM FOR $\delta = 0^\circ$		EQUIVALENT δ FOR PREDICTED TRIM (DEG)
		THEORY	TEST	
MDC PHASE B NOVEMBER 1970	7.4	25	27.5	+ 2
MDC PHASE B SEPTEMBER 1970	7.4	'24.5	26.5	+ 1
MMC-LaRC PHASE A DELTA ($\delta = 5^\circ$)	20	46	44	- 2
MDC-LaRC PHASE A DELTA	10	31	21	- 7
MDC-AFFDL-7 (SANS TAILS)	8	(X)	(X - 3)	-
MDC-MMC PHASE B BOOSTER	7.4	35	33	- 3

Slide 4

CONTROL SURFACE FLOW SEPARATION PHENOMENON

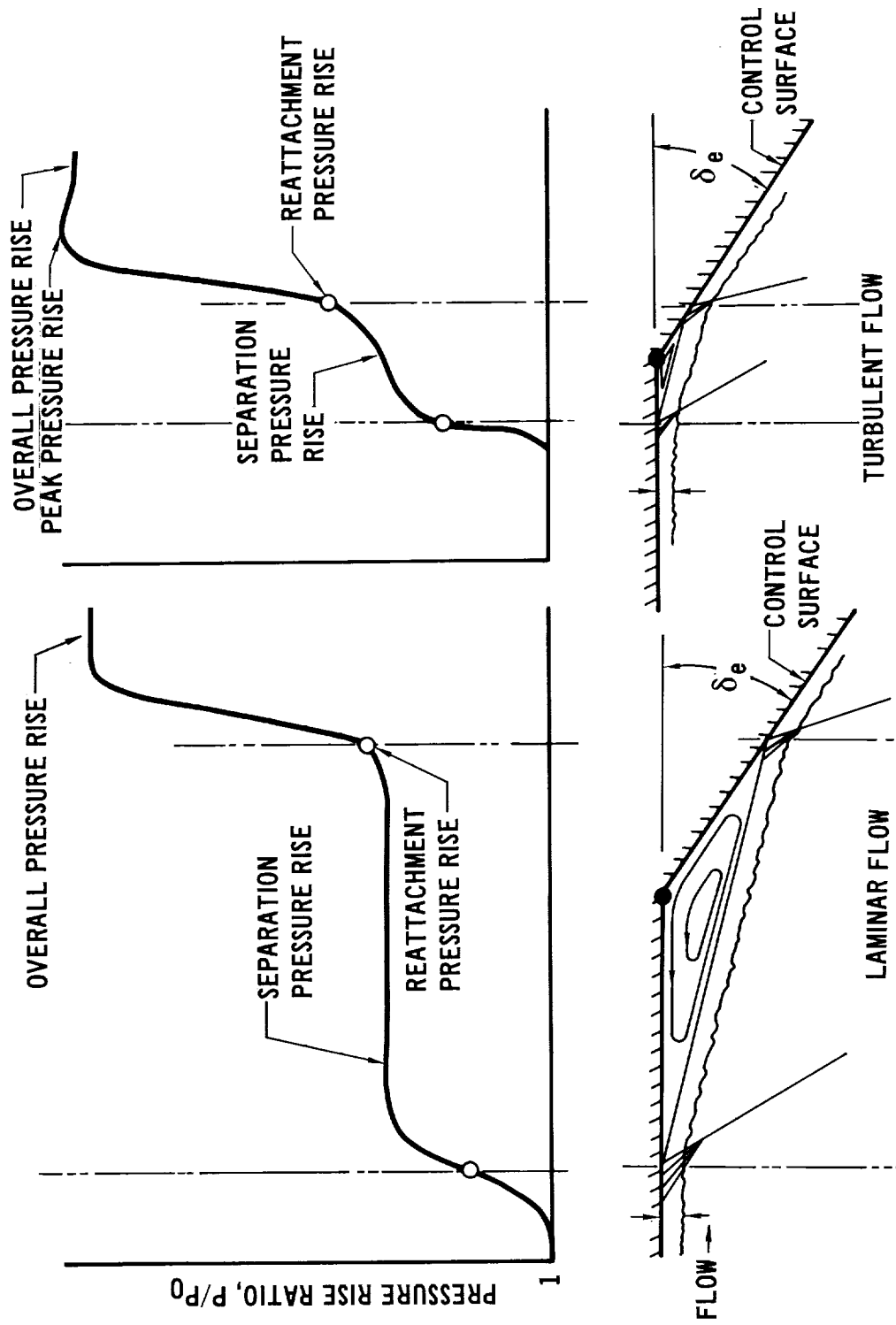
(Slide 5)

An important factor in the determination of the effectiveness of control surfaces deflected in such a manner as to compress the flow is the phenomenon of boundary layer separation. The diagrams on the slide illustrate the pressure distribution associated with this phenomenon.

As the control surface is deflected, an adverse pressure gradient is imposed upon the boundary layer. Boundary layer separation will then occur if the energy in the boundary layer is insufficient to overcome the momentum loss resulting from the adverse pressure gradient. As the control surface deflection angle increases, the final overall pressure rise after the reattachment shock increases and the flow is forced back up the boundary layer into the separated region; the length of the separated region will then increase and in the limiting case the reattachment point reaches the control surface trailing edge. Separation is more pronounced for laminar flow due to its lower energy level and may affect a large portion of the vehicle surface ahead of the elevator. As indicated on the diagram the separated region is much smaller for turbulent flow.

From the above discussion it can be anticipated that the flow separation phenomenon can have a pronounced influence on control effectiveness. Therefore, the aerodynamicist prefers to minimize control deflections that compress the flow at high speeds. However, as we develop the most efficient vehicles for performance and stability over the complete flight spectrum, this type of control requirement may result. Some interesting results and correlations relative to the flow separation phenomenon and elevator effectiveness are presented on the following slides.

CONTROL SURFACE FLOW SEPARATION



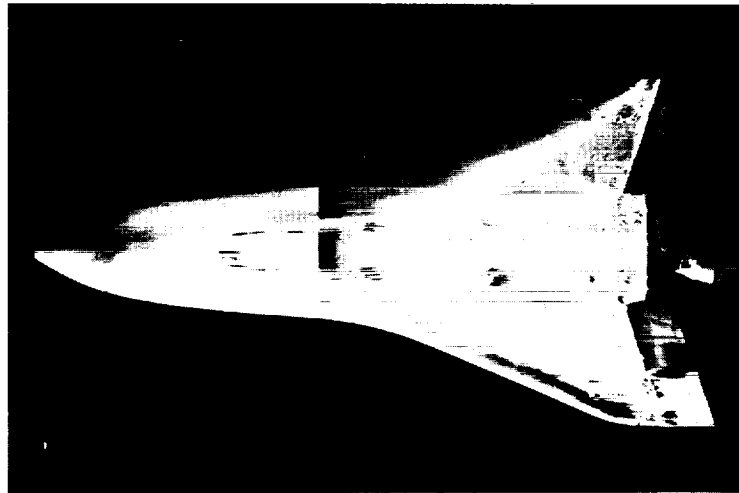
FLOW SEPARATION - OIL FLOW VISUALIZATION

(Slide 6)

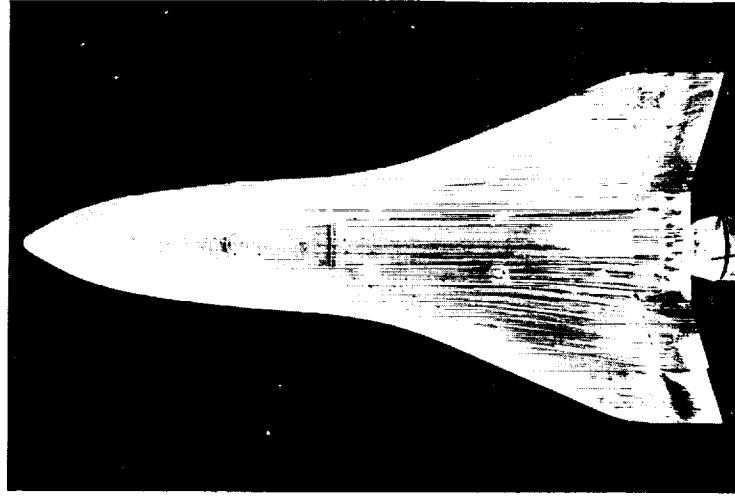
Results of oil flow visualization studies directed toward the separation phenomenon are presented on the opposite page. The photo on the left shows that for a Reynolds number of 3.3 million the flow is separated ahead of the elevon and reattaches on the elevon. On the right, for the 7.5 million Reynolds number case, the flow appears to be attached. The model angle of attack was 21 degrees and the Mach number was 7.4. This model contains five (5) segmented independent control surfaces on the aft portion of the vehicle. Control settings reading from left to right were -15, +15, +15, and +15 degrees. The two control surfaces on the left side of the vehicle in each photo represent a differentially deflected control mode; on the right side the normal longitudinal only control is shown. The purpose of these two types of deflections was to obtain as much information per run as possible since there was no flow interference between the left and right side of the vehicle.

It is noted that the elevon effectiveness and separation phenomenon are a function of Reynolds number, Mach number, wall temperature and deflection angle. Therefore, caution must be exercised in applying wind tunnel data to the flight condition. Preliminary findings at MDAC indicate that for our flight Mach-altitude-elevon angle schedule the flow in the region of the elevons is similar to the photo on the right for the attached flow case.

MDAC DELTA OIL FLOW VISUALIZATION RESULTS



SEPARATED FLOW



ATTACHED FLOW

Slide 6

LONGITUDINAL STABILITY - REYNOLDS NUMBER EFFECTS

(Slide 7)

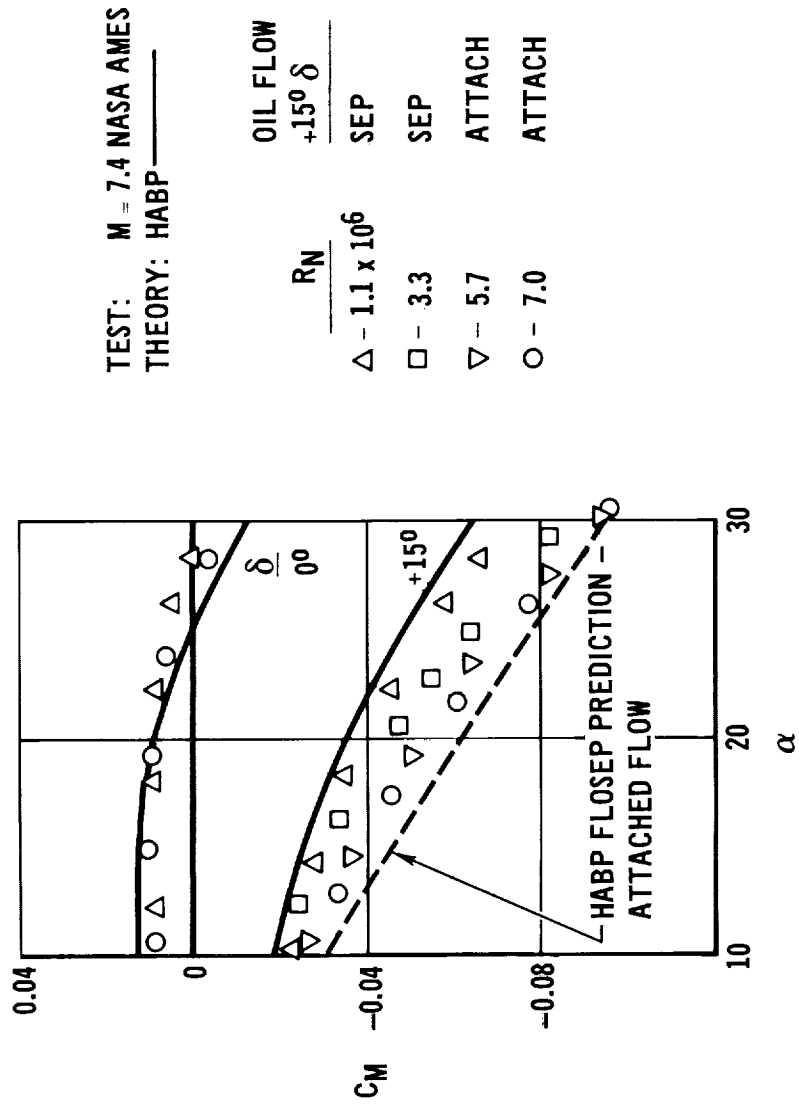
This slide presents correlations with test results relative to the phenomenon of flow separation and elevon effectivity as discussed on the preceding two pages. In the figure pitching moment coefficient is compared for the undeflected elevons and for the +15 degree deflections over a Reynolds number range of 1 million to 7 million.

The figure shows that pitching moment coefficient is invariant with Reynolds number for the undeflected elevons and as expected changes significantly for the +15 degree deflected data. The elevon effectivity is seen to increase with Reynolds number for the deflected data. As the flow becomes attached the data show very little Reynolds number sensitivity.

The basic estimating technique predicts the undeflected elevon data very adequately but as noted previously, generally underpredicts the effectivity of the positive deflected elevon. The FLOSEP option in the HABP program was utilized to predict the effectivity for the high Reynolds number case (7 million) which more closely simulates the flight condition for this Mach number. The results are shown by the dashed line. Turbulent flow conditions were specified for the predictions with a very small foresurface separated area. The elevon pressure rise due to the near coincident separation and reattachment shocks was computed based on empirical data (Reference 1). The agreement with the high Reynolds number data is better than expected. As noted on the preceding page, in addition to Reynolds number, the effectivity of the positive deflected elevons is a function of Mach number, wall temperature and deflection angle. Caution must be applied in extending the wind tunnel data to flight conditions.

MDAC DELTA - NOV 1970

REYNOLD S NUMBER EFFECTS – LONGITUDINAL TRIM



Slide 7

LIFT-TO-DRAG RATIO VERSUS ANGLE OF ATTACK

(Slide 8)

The theoretical-experimental correlation of lift-to-drag ratio (L/D) versus angle of attack is presented on this slide. This parameter (L/D) is associated with performance and is the primary guideline for the evaluation of crossrange capability for the shuttle.

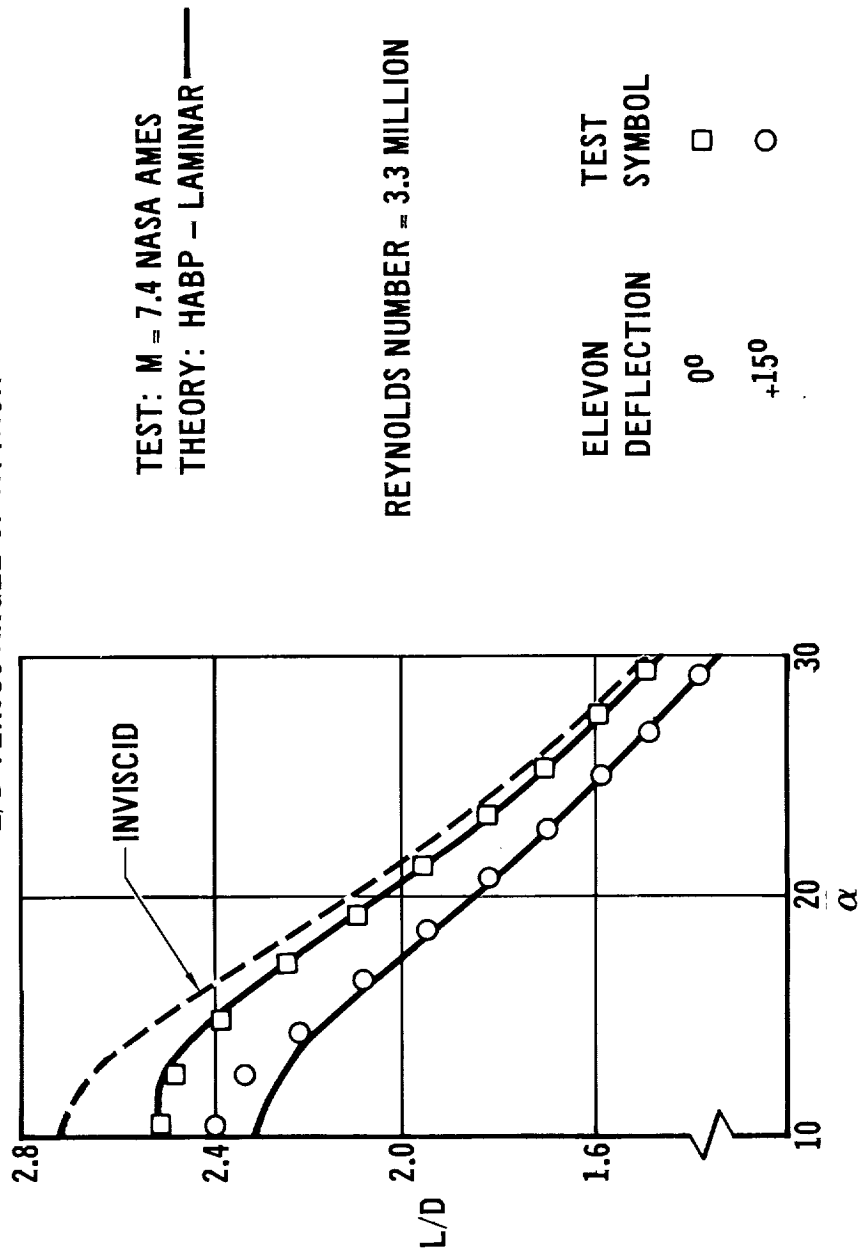
The significance of including the viscous effects (skin friction drag) is amply demonstrated by the overprediction utilizing inviscid forces only (dashed line). It is mandatory that viscous effects be included when presenting correlations of the maximum lift-to-drag ratio at hypersonic speeds for this type of vehicle. As shown the importance of friction diminishes with angle of attack. At the higher angles (~ 60 degrees) the configurational characteristics lose importance as L/D approaches a value equal to the cotangent of the angle of attack. The correlation of L/D improves with angle of attack as the normal force component becomes predominate in both lift and drag and thus much of the deviation cancels out.

The L/D correlation on the slide was better than expected with only about a 1 percent deviation over the angle of attack range for the undeflected controls.

The ability to determine trim L/D versus Mach number, altitude and angle of attack is of considerable importance to trajectory shaping and the crossrange requirement and will be discussed further on the following page.

MDAC DELTA - NOV 1970

L/D VERSUS ANGLE OF ATTACK



Slide 8

LIFT-TO-DRAG RATIO VERSUS REYNOLDS NUMBER

(Slide 9)

Lift-to-drag ratio at 20 degrees angle of attack versus Reynolds number is correlated on this slide for undeflected and +15 degree deflected elevons. The 20 degree condition is at the lower limit of the anticipated angle of attack range for hypersonic flight during crossrange attainment and was selected since it is the angle within the anticipated envelope that the viscous (Reynolds number) effects have the greatest influence. The ability to predict L/D versus Reynolds number for wind tunnel conditions is a first step in gaining confidence in the Mach-altitude L/D variation input into trajectory simulations. The correlation presented on this slide is considered to be of sufficient accuracy for Phase B purposes. The large L/D scale must be appreciated. The +15 degree deflected elevons result in a reduction in L/D of about 10 percent.

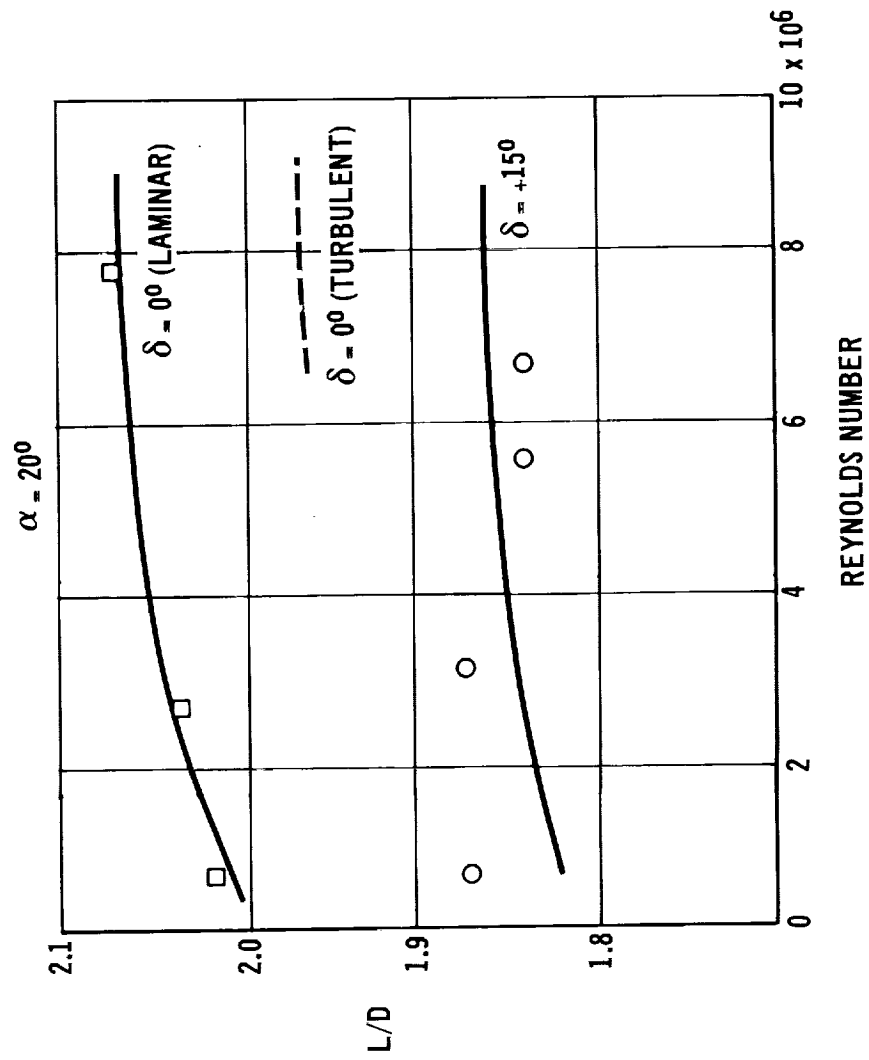
The sensitivity of L/D to predominately laminar or turbulent flow is shown by the theoretical estimates. For our simulator and trajectory analysis at MDAC we calculate L/D as a function of altitude, Mach number, angle of attack and control setting, utilizing the work of Masek (Reference 2) for the calculation of the boundary layer transition points on the vehicle.

MDAC DELTA - NOV 1970

L/D VARIATION WITH REYNOLDS NUMBER

TEST: M = 7.4 NASA AMES

THEORY: - HABP



Slide 9

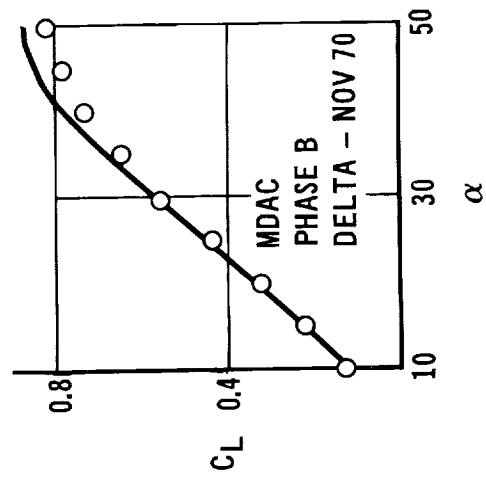
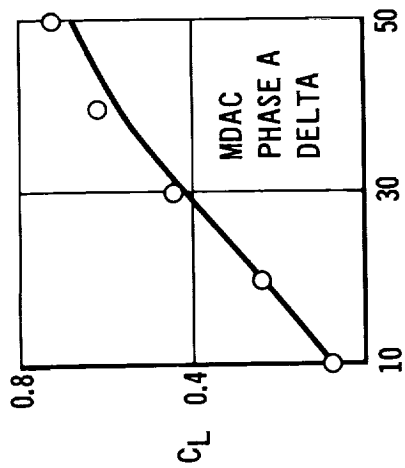
LIFT COEFFICIENT

(Slide 10)

This slide presents the general status of the theoretical-experimental correlation of lift coefficient for delta wing designs we have evaluated. Typical correlations versus angle of attack show that theory can either predict on the high or low side and can deviate with angle of attack. The percentage over (under) prediction at angles of attack representative of crossrange flight as well as that for maximum lift are shown on the right portion of the slide. An adequate estimate of lift coefficient versus Mach number and angle of attack is necessary for proper assessment of trajectory shaping and TPS weight requirements. At the lower hypersonic Mach numbers our utilization of the Prandtl-Meyer expansion from free stream for the shadowed (hidden) portions of the vehicle results in a higher lift coefficient than that given by Newtonian only. At 20 degrees angle of attack and a Mach number of 6 we predict nearly a 10 percent higher lift coefficient than Newtonian by accounting for the upper surface lift. With this technique correlations of delta shapes in the lower hypersonic Mach regime (4-7) have been encouraging.

It is observed that the prediction of lift coefficient is generally slightly on the low side when significant trailing-edge-down elevon deflections are required for trim.

DELTA WING CORRELATION - LIFT COEFFICIENT



CONFIGURATION	MACH	% OVER (UNDER) PREDICTION $\delta_e = 0^\circ$	
		$\alpha = 20$	$\alpha = 50$
MDAC DELTA NOV 70	7.4	5	10
MDAC DELTA SEPT 70	7.4	0	-
MDAC PHASE A DELTA	10	(2)	(10)
MMC PHASE A DELTA	20	(10)	(10)
FDL-7MC	18	6	-
	8	0	-
	6	(2)	-
MDC-MMC BOOSTER	7.4	-	9

LATERAL-DIRECTIONAL STABILITY DERIVATIVES

(Slide 11)

The yaw induced asymmetric flow field, vortex activity and nose and leading edge bluntness effects cause difficulty in the theoretical determination of the lateral-directional stability characteristics.

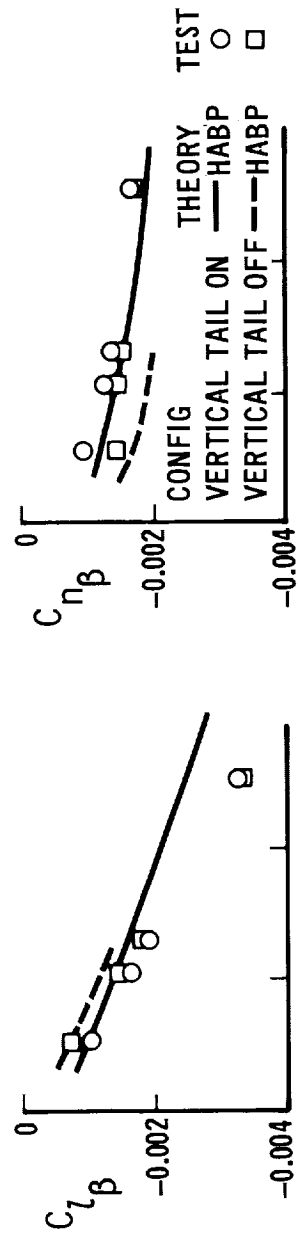
The top portion of the slide presents the results of our most recent test. The propellant requirement for reaction control is very sensitive to the values of the yawing moment coefficient derivative, $C_{\eta\beta}$ and rolling moment coefficient derivative, $C_{\xi\beta}$.

Recognizing the uncertainty of the HABP prediction of $C_{\eta\beta}$ and $C_{\xi\beta}$, the theoretical coefficients are treated as a band as shown in the lower portion of the slide for the estimates of our March 1971 configuration. The uncertainty band is based on correlations with respect to the several vehicles we have studied. The program consistently predicts a smaller effective dihedral, $C_{\xi\beta}$, than experimentally determined at angles of attack pertinent to hypersonic flight for the delta. With respect to $C_{\eta\beta}$ the program frequently results in optimistically predicting the static yaw instability. However, for our most recently tested configuration, the predictions were more pessimistic than the test results. The AFFDL-7MC correlated closely. Therefore, an uncertainty band weighted to the unstable side has evolved. Due to the previously noted under-prediction of $C_{\xi\beta}$ the program has a tendency to predict conservatively with respect to $C_{\eta\beta}$ dynamic (Reference 3). The HABP estimate of the magnitude of C_Y is slightly lower than the test results.

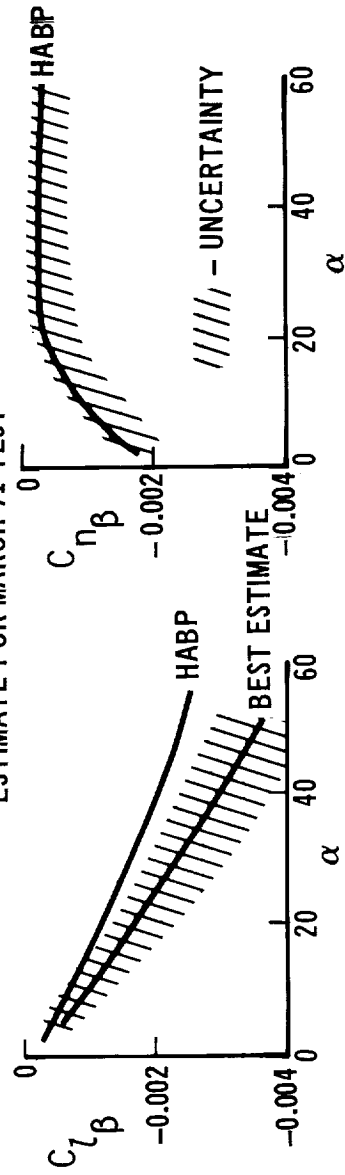
As shown the centerline vertical contribution is generally small and at angles of attack associated with the 1100 N.M. crossrange requirement is expected to be ineffective. The pretest prediction of the lateral-directional stability derivatives is currently an "art" and it is obviously important for the aerodynamicist to be associated with good fortune.

LATERAL-DIRECTIONAL STABILITY

CORRELATION OF MDAC DELTA NOV 70



ESTIMATE FOR MARCH 71 TEST



Slide 11

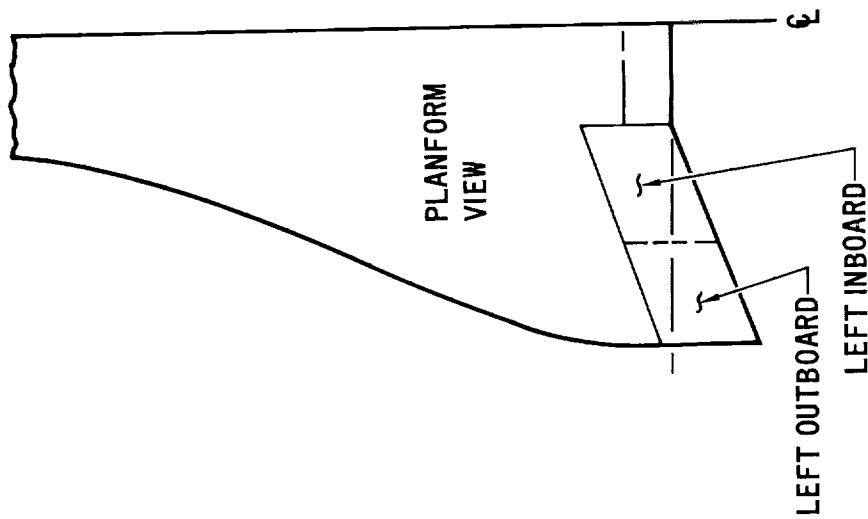
DIFFERENTIAL CONTROL DEFLECTIONS

(Slide 12)

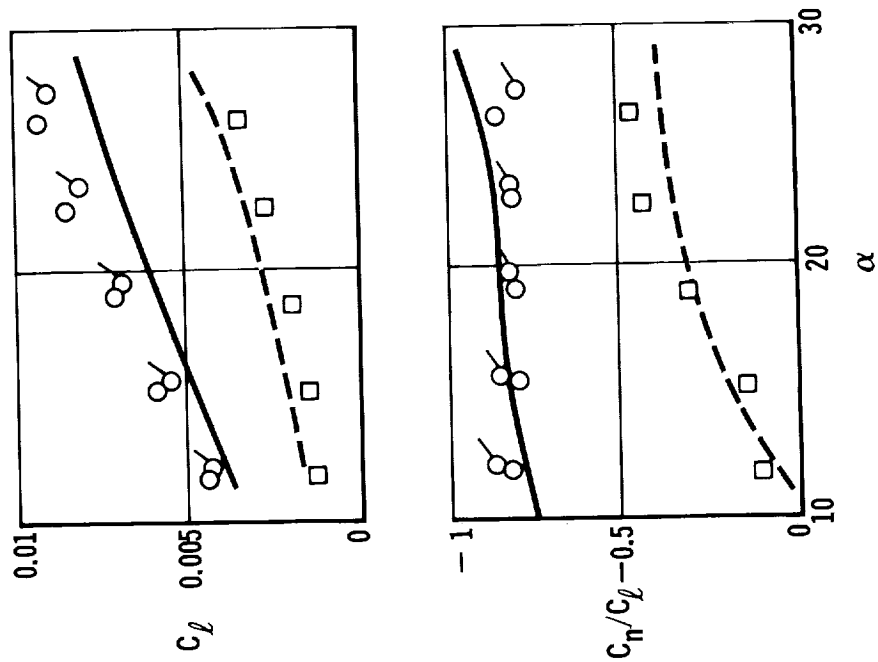
Lateral-directional control moments resulting from differential deflections of segmented outboard aileron/inboard elevator in the presence of separated and attached flows are correlated in this figure. As noted previously for this model the controls were segmented such that the outboards could be deflected independently of the inboards and thus be used for lateral directional control. The inboards would be dedicated to maintain longitudinal control.

The two cases correlated are for 15 degree differential deflections with respect to (1) a flush 0 degree initial setting and (2) a 15 degree up-outboard initial setting. For the former case the left outboard was deflected 15 degrees trailing edge up and the right outboard was deflected 15 degrees trailing edge down (compressing the flow) such that a 15 degree differential relative to the initial setting was accomplished. As noted earlier the basic technique underpredicts the effectivity of controls deflected to compress the flow and thus slightly underpredicts the induced roll moment. The correlation of yaw-to-roll ratio is considered to be adequate for Phase B. The data for the high Reynolds number (attached flow) indicated slightly less roll effectivity. Depending upon the entry guidance mode, it may be desirable to have a lower yaw to roll ratio than that for the above case, i.e., $C_{\eta}/C_{\ell} < 0.5$. It was predicted that this ratio could be obtained by differentially deflecting the outboards from an initial 15 degrees trailing-edge-up setting. The test data substantiate the theoretical estimates relative to the reduction of C_{η}/C_{ℓ} as shown on the slide. Caution must be exercised in using these data in derivative form, e.g., $C_{\ell\delta A}$, due to the non-linearity with deflection angle.

DIFFERENTIAL OUTBOARD DEFLECTIONS



TEST - NASA AMES M - 7.4
THEORY - HABP
MDAC NOV 70 DELTA



- - $\delta = 0^\circ$ INITIAL OUTBOARD SETTING
- - $\delta = -15^\circ$ INITIAL OUTBOARD SETTING
- - ATTACHED FLOW, $\delta = 0^\circ$ INITIAL

Slide 12

FIXED STRAIGHT WING CONFIGURATION

(Slide 13)

High angle of attack ($\alpha = 60^\circ$) entry with fixed straight wing configurations is a recent innovation and thus the availability of test-theory correlations is less than for the delta shape. At MDC we have studied and made comparisons relative to two geometrically different fixed straight wing shuttle designs. Model photographs are presented on the slide for the Phase A (MSC August 1969) and Phase B (MDC September 1970) shapes. Some important geometrical differences are:

(1) Wing position: Phase A - Mean aerodynamic quarter chord ($\bar{c}/4$) at 53.5 percent body length.

Phase B - $\bar{c}/4$ at 60 percent of body length.

(2) Nose Profile Shape: - see slide

(3) Horizontal Tail Shape: - Phase A - Diamond

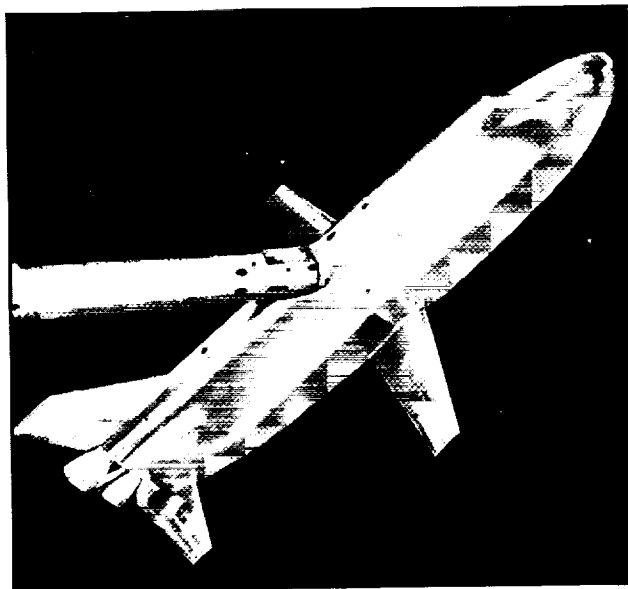
Phase B - Conventional

(4) Control Surface Deflection Technique: Phase A - elevator for trim.

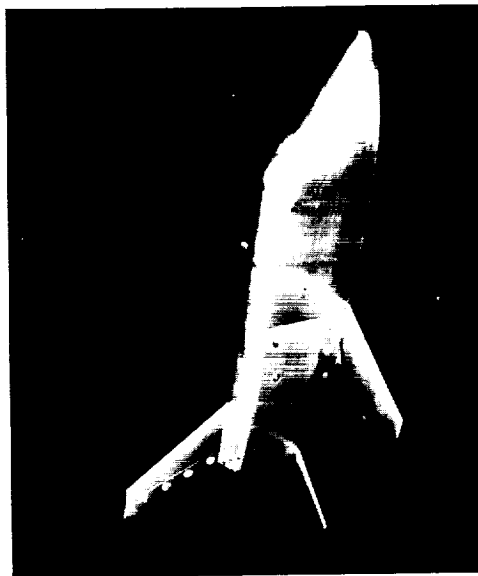
Phase B - stabilizer for trim.

Conclusions relative to the correlations for the Phase A shape were generally substantiated by the Phase B comparisons as discussed on the following pages. The correlations are primarily concerned with high angle of attack ($\alpha = 50$ to 70 degrees) data which are representative of the nominal hypersonic entry attitude. Where appropriate, pertinent low angle of attack comparisons are also included.

STRAIGHT WING MODELS



PHASE A



PHASE B

Slide 13

LONGITUDINAL STABILITY AND CONTROL

(Slide 14)

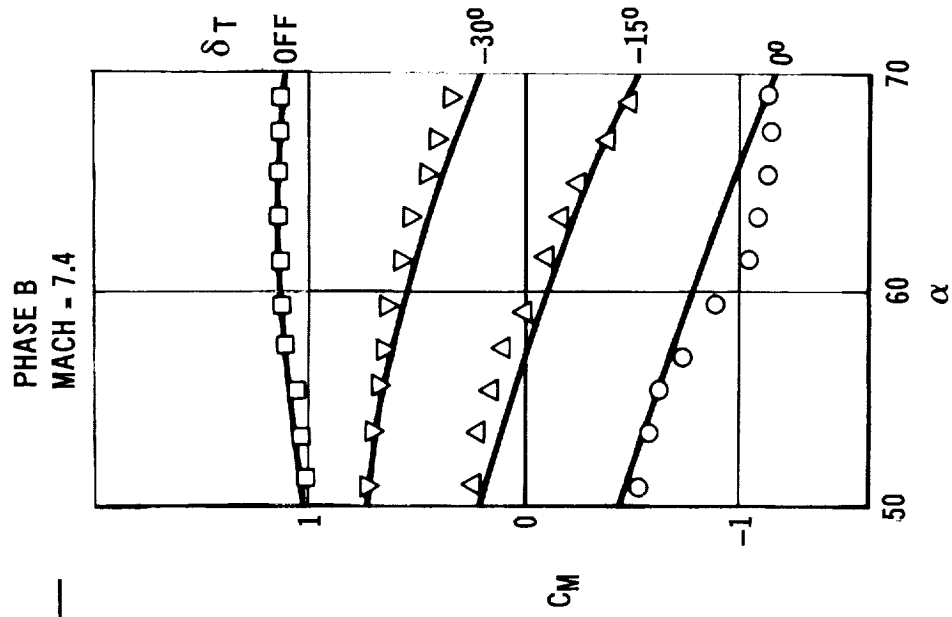
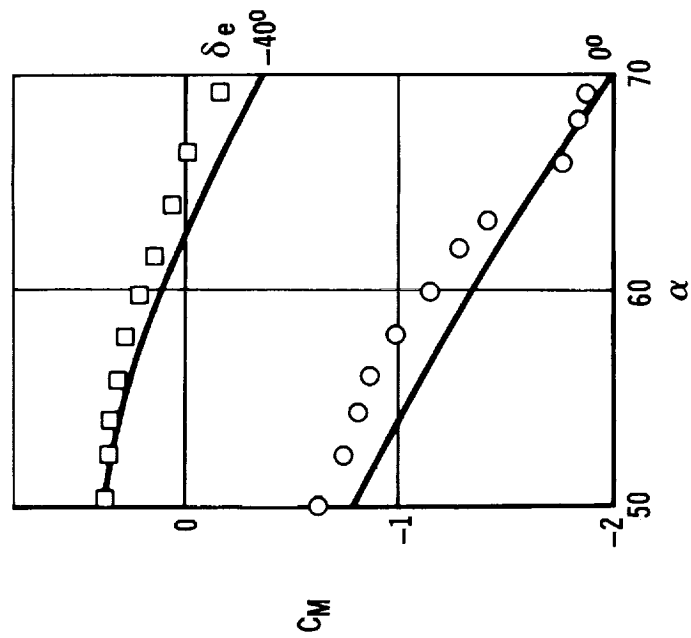
Wind tunnel test data have been obtained at Mach numbers of 6, 7.4 and 20 for the Phase A configuration and at $M = 7.4$ for the Phase B shape. For both vehicles the comparison of experimental pitching moment coefficient with the theoretical estimate has been good for the negative control settings which are representative of the trim condition. With respect to the change in stability for the undeflected controls, oil flow studies on the Phase B shape indicate a high pressure region on the undeflected horizontal tail at $\alpha = 60^\circ$ but not at $\alpha = 50^\circ$ or at $\alpha = 60^\circ$ with $\delta_T = -15^\circ$. Although the source of the problem is unknown the oil flow studies support the test-theory deviation for the $\alpha = 60^\circ$, $\delta = 0^\circ$ condition. Recent Mach 20 LaRC pressure data on the Phase A shape indicate that the presence of the wing influences pressures on the fuselage and horizontal tail. The HABP has generally predicted the incremental effect of the wing poorly. Therefore, at this time there is sufficient evidence to indicate that although the program has correlated well with respect to the trimmed trailing edge up control settings, a significant test-theory deviation could occur as a result of the phenomena noted above.

At the high angle of attack the comparison was about the same for either the full horizontal tail (δ_T) or "elevator only" (δ_e) trim as shown on the slide. At the lower angles of attack ($\alpha = 20^\circ$) where trailing edge down deflections are necessary for trim, the all moveable horizontal tail (which avoided the flow separation problem since there is no foresurface) correlated much better than the "elevator only" concept.

STRAIGHT WING LONGITUDINAL STABILITY

TEST: NASA AMES
THEORY: HABP ———

PHASE A
MACH = 7.4



Slide 14

LIFT COEFFICIENT AND LIFT-TO-DRAG RATIO

(SLIDE 15)

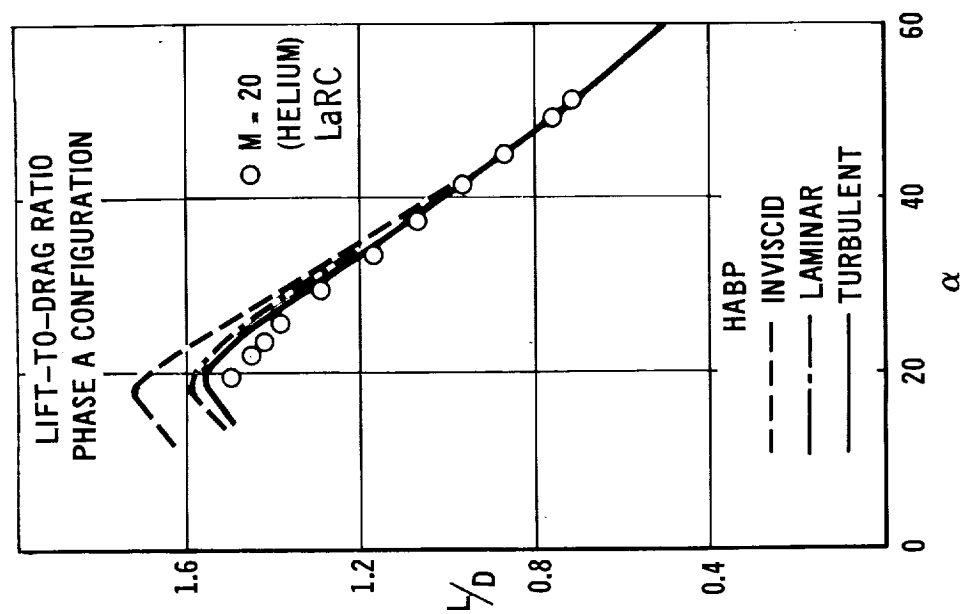
LIFT COEFFICIENT

A tabulation of the theoretical-experimental lift coefficient results is presented for the straight wing shapes at high and low angles of attack. Test-theory deviations are compared utilizing the basic technique discussed earlier as well as Newtonian theory only. The use of the Prandtl-Meyer expansion from freestream for shadowed regions results in a better correlation at the lower angles of attack while Newtonian agrees more favorably with the high angle data. It is noted that the Mach 20 data (helium) for the Phase A shape yields a maximum lift coefficient 7-8 percent higher than for the lower hypersonic Mach numbers. This is not accounted for by the theoretical techniques utilized at this time.

LIFT-TO-DRAG RATIO

The lift-to-drag ratio comparisons versus angle of attack on the slide are made for the Phase A orbiter at Mach 20 in helium. The HABP has the capability to predict viscous (friction) effects utilizing either air or helium for the media. The inviscid prediction is also shown which again emphasizes the necessity to include friction when calculating maximum lift-to-drag ratio. Although not shown here, theory (including viscous effects) overpredicted the maximum L/D for the Phase B shape by about 8 percent which is considered to be a very poor correlation. However, as noted previously at the high angle of attack ($\alpha \approx 60^\circ$) the L/D is relatively insensitive to configuration perturbations or viscous effects, and can be predicted equally well for the straight and for the delta wing.

STRAIGHT WING HYPERSONIC PERFORMANCE



LIFT COEFFICIENT

CONFIGURATION	MACH	PERCENT OVER (UNDER) PREDICTION $\delta = 0^\circ$			
		NEWTONIAN		NEWTONIAN WITH P.M. SHADOW	
		$20^\circ \alpha$	$60^\circ \alpha$	$20^\circ \alpha$	$60^\circ \alpha$
PHASE A -	20.0	(10)	(6)	(10)	(6)
PHASE A -	7.4	(8)	3	0	5
PHASE A -	6	(10)	5	0	7
PHASE B -	7.4	(10)	5	(3)	7

LATERAL-DIRECTIONAL STABILITY CHARACTERISTICS

(Slide 16)

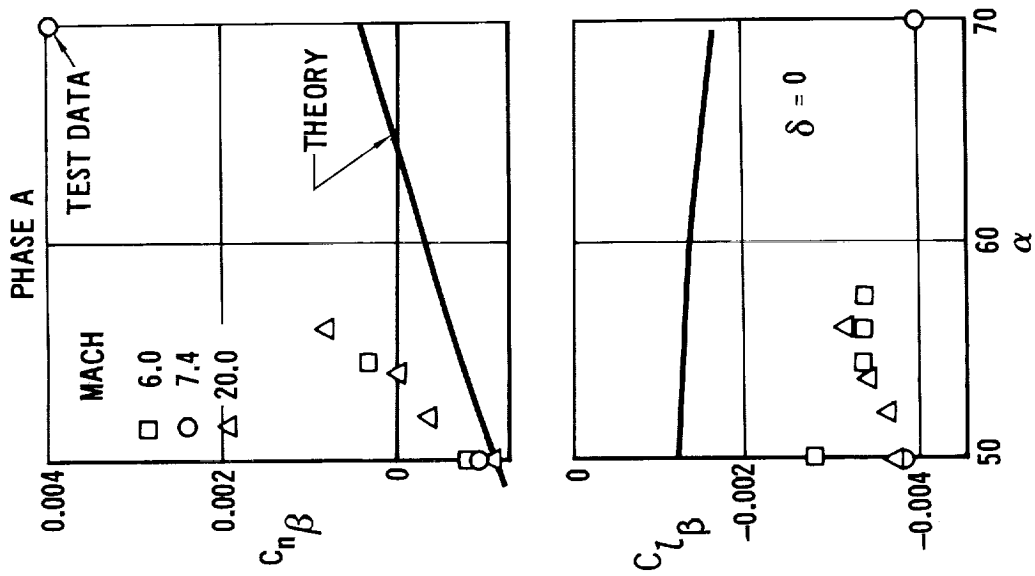
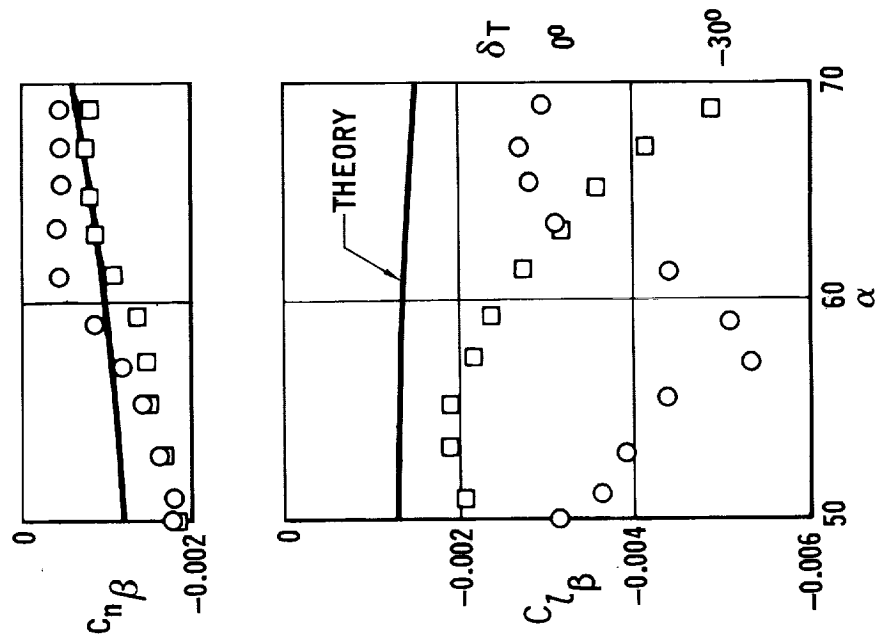
Wind tunnel data for both vehicles confirm that the theoretical techniques employed are not adequate to predict the lateral-directional stability characteristics of the straight wing orbiter. Reliance must be placed on corrections to existing test data for estimating the effects of configuration changes. Results of oil flow visualization studies applicable to this problem are presented on the next page.

Correlations of yawing moment coefficient derivative, C_{n_β} , and rolling moment coefficient derivative, C_{l_β} , are presented on the slide for both vehicles in the nominal high angle of attack range. The data for the Phase B orbiter (without vertical tail) indicate that C_{l_β} is significantly affected by control deflection angle as well as angle of attack. The theory is not a noticeable function of control setting. Although not shown, side force coefficient derivative, C_{Y_β} , varies from 50 to 300 percent greater than predicted. The relatively good correlation of yawing moment coefficient appears to be coincidental. The data for the Phase A configuration were of the same order as the Phase B shape except that yawing moment coefficient deviated significantly at the higher angles of attack apparently due to a vertical tail contribution of about +.004 at $\alpha = 70$ degrees. This phenomenon was not predicted by theory and will be discussed on the next page.

The relatively large effective dihedral, C_{l_β} , coupled with high angle of attack ($\alpha = 60^\circ$) flight, results in a very stable C_{n_β} dynamic (Reference 3). Therefore, the configuration can tolerate relatively large uncertainties with respect to the basic lateral directional derivatives. Consequently the inability of the HABP to predict the characteristics accurately has not been a significant problem for Phase B.

STRAIGHT WING LATERAL - DIRECTIONAL CHARACTERISTICS

PHASE B
(NO VERTICAL TAIL)



STRAIGHT WING OIL FLOW STUDIES

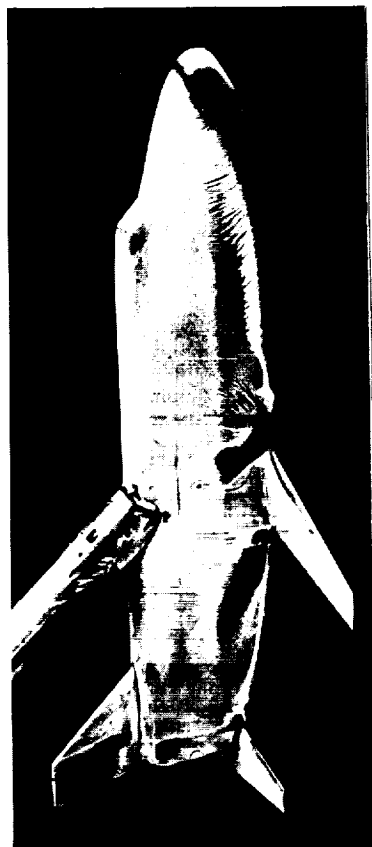
(Slide 17)

This slide presents results of oil flow visualization studies at 60 degrees angle of attack for the two straight wing shapes correlated. The Mach number is 10 for the Phase A shape and 7.4 for the Phase B vehicle. The tests were conducted at NASA Ames at a Reynolds number of about 3 million. The oil flow patterns are similar for both configurations.

The presence of the wing induces flow onto the sides of the fuselage and onto the vertical tail. Oil flow studies performed with the wing off verify that the fuselage and vertical tail "scrubbing" results from the presence of the wing. The same phenomenon occurs at the root leading edge of the horizontal tail but to a lesser extent.

The HABP does not account for the induced fuselage sidewall and vertical tail pressures due to the presence of the wing and horizontal tail. This phenomenon is suspected to be a prime cause for the inability to predict the lateral-directional characteristics. A comprehensive oil flow study by Seegmiller at Ames indicates that the scrubbed area increases noticeably with angle of attack such that the vertical tail could be very effective at $\alpha = 70$ degrees. Also, as expected for attitudes in yaw, the windward side showed considerably more tail scrubbing than did the leeward. The studies imply that the lateral-directional characteristics could be a significant function of the relative position of the wing and vertical tail since the vertical tail effectiveness results from flow induced by the wing. In addition, since $C_{L\beta}$ is a strong function of horizontal tail setting (see previous slide), it is possible that the same flow mechanism that induced the longitudinal stability change also affects the lateral-directional characteristics.

STRAIGHT WING OIL FLOW



PHASE A



PHASE B

Slide 17

CONCLUDING REMARKS

(Slide 18)

The HABP has been effective in estimating the hypersonic aerodynamic characteristics of Space Shuttle designs for Phase B purposes. For Phase C/D development extensive testing is required to obtain greater accuracy. However, the HABP will be used to reduce the test matrix of independent parameters by applicable correlation of the vast amount of Phase A and B data stored in the NASA data bank.

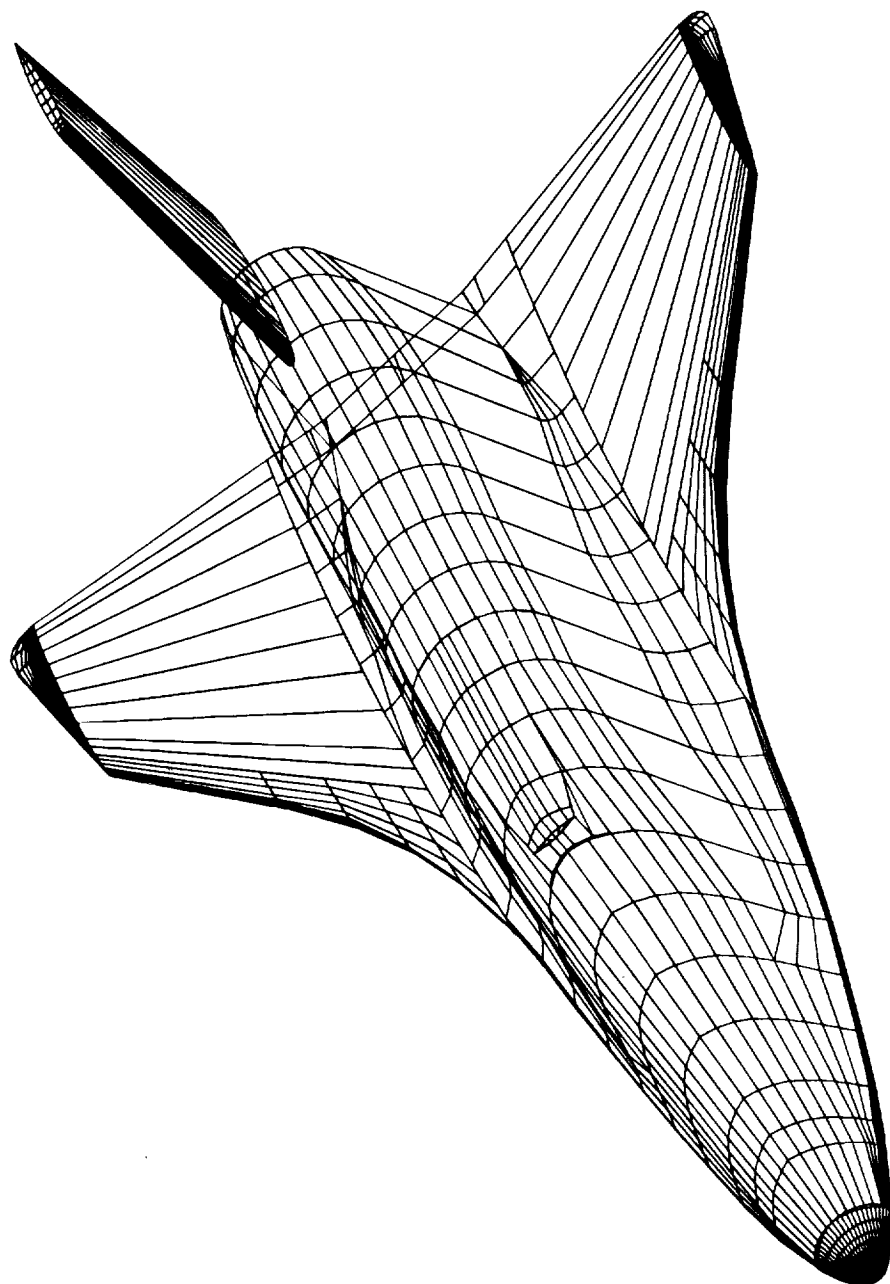
Due to the larger stable of vehicles for comparison and less likelihood of unaccounted-for component interaction, the predictions for the delta wing shapes are viewed with more confidence than those for the straight wing. The inability of the HABP to reasonably predict the lateral-directional characteristics of the straight wing was not a significant problem during Phase B due to the very stable C_{η_B} dynamic of this vehicle at 60 degrees angle of attack. The present program will not predict the effects of unusual phenomena associated with component or flow field interaction, vortex activity, jet interaction and real gas effects; thus wind tunnel and flight test must be used for final analyses.

The necessity of including viscous effects in the calculation of lift-to-drag ratio again has been amply shown. The ability of the program to calculate L/D versus Reynolds number was presented. Additional data for correlation relative to flow compressing eleven deflections will be obtained during our next test. Surface oil flow visualization results were employed to aid in the theoretical-experimental assessment.

To assure that the theoretical-experimental comparisons are pertinent, the identical model geometry and wind tunnel conditions must be utilized for the predictions. It is appropriate that the closing slide of the paper be dedicated to geometry verification with our forthcoming March 71 wind tunnel model configuration presented as drawn by the Calcomp.

MARCH 71 DELTA WING ORBITER

HABP LINES



Slide 18

REFERENCES

1. Gentry, Arvel E.; and Smyth, Douglas N.: Hypersonic Arbitrary-Body Aerodynamic Computer Program (Mark III Version). Vols. I and II. Rep. DAC 61552, (Air Force Contract Nos. F33615 67 C 1008 and F33615 67 C 1602), Douglas Aircraft Co., Apr. 1968. (Available from DDC as AD 851 811 and AD 851 812.)
2. Masek, R. V.: Boundary Layer Transition of Lifting Entry Vehicle Configurations at High Angle-of-Attack. Space Transportation System Technology Symposium, NASA TM X-52876, Vol. I, 1970, pp. 445-462.
3. Wawrzyniak, M. E.: To What Extent Should Space Shuttle Stability and Control Be Provided Through Stability Augmentation? Space Transportation System Technology Symposium, NASA TM X-52876, Vol. I, 1970, pp. 47-66.

THE DELTA BODY

A POTENTIAL SPACE SHUTTLE ORBITER

By Grover L. Alexander

Lockheed Missiles & Space Company
Sunnyvale, California

INTRODUCTION

At last year's Space Shuttle Technology Conference (Ref. 1), many technical problems were identified and the desire was expressed that solutions to some of the problems be presented at the next Technical Conference. This paper identifies a potential basis for the solutions to several of the key technical problems associated with the Space Shuttle Orbiter. That basis is the Delta Body Orbiter configuration. The points discussed are indicative of the Delta Body evolution and show how the design approach, which was born out of the technology requirements, has led to modern Delta Body designs.

THE DELTA BODY - A POTENTIAL SPACE SHUTTLE ORBITER

(Figure 1)

The Delta Body Orbiter Configuration provides a basis for the solution to many of the key Space Shuttle technology problems. The Delta Body was evolved to meet the shuttle technology requirements, is a logical result of 15 years of evolution, permits efficient space shuttle orbiter designs, is an efficient lightweight low-risk design approach, and is a potential candidate for the Space Shuttle Orbiter configuration.

THE DELTA BODY

A POTENTIAL SPACE SHUTTLE ORBITER

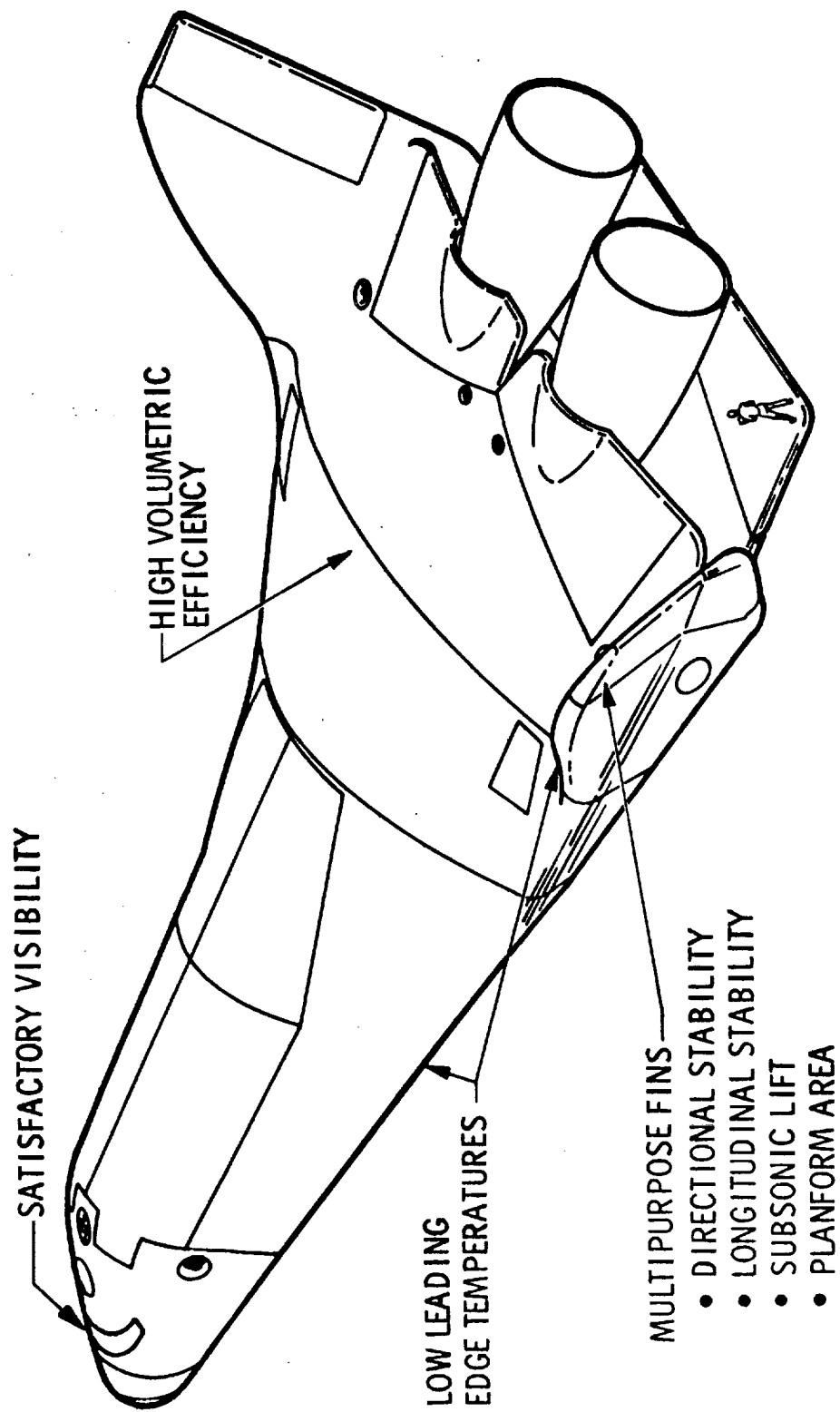


Figure 1

SPACE SHUTTLE TECHNOLOGY REQUIREMENTS - CONFIGURATION RELATED

(Figure 2)

Aerodynamic Performance - The technology requirements of today's Space Shuttle Orbiter have not changed significantly from those which led to the evolution of the Delta Body Concept. Those related directly to the orbiter configuration are indicated here. Hypersonic L/D is important to cross range capability. Delta Bodies (or lifting bodies) can develop hypersonic L/D values as high as 3.0 in practical configurations. Subsonic L/D establishes ferry efficiency and minimum approach glide path for landing approach. Present Delta Body designs exhibit subsonic L/D values of 5.8, entirely adequate for subsonic performance. Landing speed is determined to a large extent by the subsonic trimmed lift capability of the orbiter. Present Delta Body designs show high trimmed lift values resulting in landing speeds not significantly different from competing designs.

Satisfactory Flight Characteristics - Aerodynamic stability and control characteristics are determined primarily by the inherent shape of the configuration. Modern Delta Body designs exhibit aerodynamic stability and control in all three axes (stability) throughout their atmospheric flight. The resulting handling qualities are, in general, quite acceptable as demonstrated in the lifting body flight tests at Edwards Air Force Base, California. Visibility is a result of a specific design approach. Present Delta Body designs for the Space Shuttle orbiter have been tailored to provide acceptable visibility for all flight phases.

(Figure 2, Cont.)

Low Inert Weight - A driving factor that led to the evolution of Delta Body orbiter configurations is the requirement for a compact design of low wetted area. The result which has directly followed is a design of low structural weight and low thermal protection system weight. This latter factor is enhanced by the absence of shock impingement and flow interference with their associated high heating rates.

High Propulsive Efficiency - With their compact shape and high volumetric efficiency, the Delta Bodies are natural propellant carriers. This leads to high λ' values and, with proper arrangement, simple tank geometries.

The Delta Body design is particularly well suited for the Space Shuttle orbiter technology requirements.

SPACE SHUTTLE TECHNOLOGY REQUIREMENTS

CONFIGURATION RELATED

- AERODYNAMIC PERFORMANCE
 - HYPERSONIC L/D
 - SUBSONIC L/D
 - SUBSONIC C_L
- SATISFACTORY FLIGHT CHARACTERISTICS
 - STABILITY AND CONTROL
 - HANDLING QUALITIES
 - PILOT VISIBILITY
- LOW INERT WEIGHT
 - LOW STRUCTURAL WEIGHT
 - LOW TPS WEIGHT
- HIGH PROPULSIVE EFFICIENCY
 - HIGH λ'
 - EFFICIENT VOLUME

Figure 2

DELTA BODY SPACECRAFT DEVELOPMENT

(Figure 3)

Two factors most of all led to the evolution of the Delta Body design approach. These were:

1. The desire to increase leading edge sweep angle and radius to reduce aerodynamic heating levels and to reduce shock impingement,
2. The desire to have a simple compact configuration of minimum inert weight.

These desires started (in the late '50's) the search for a configuration which would combine these features into a configuration with satisfactory flight characteristics.

Since that time the search has proven extremely successful with a variety of configuration evolutions. Three of these are presently undergoing flight tests at Edwards Air Force Base with a frequency of flight operations not significantly less, at times, than that projected for the Space Shuttle itself. A vast amount of flight experience and familiarity exists, as a result of these programs. Hypersonic flight of a lifting body vehicle has also been demonstrated through flight of the SV-5. Flight with a Delta Body orbiter would not be a new experience.

DELTA BODY SPACECRAFT DEVELOPMENT

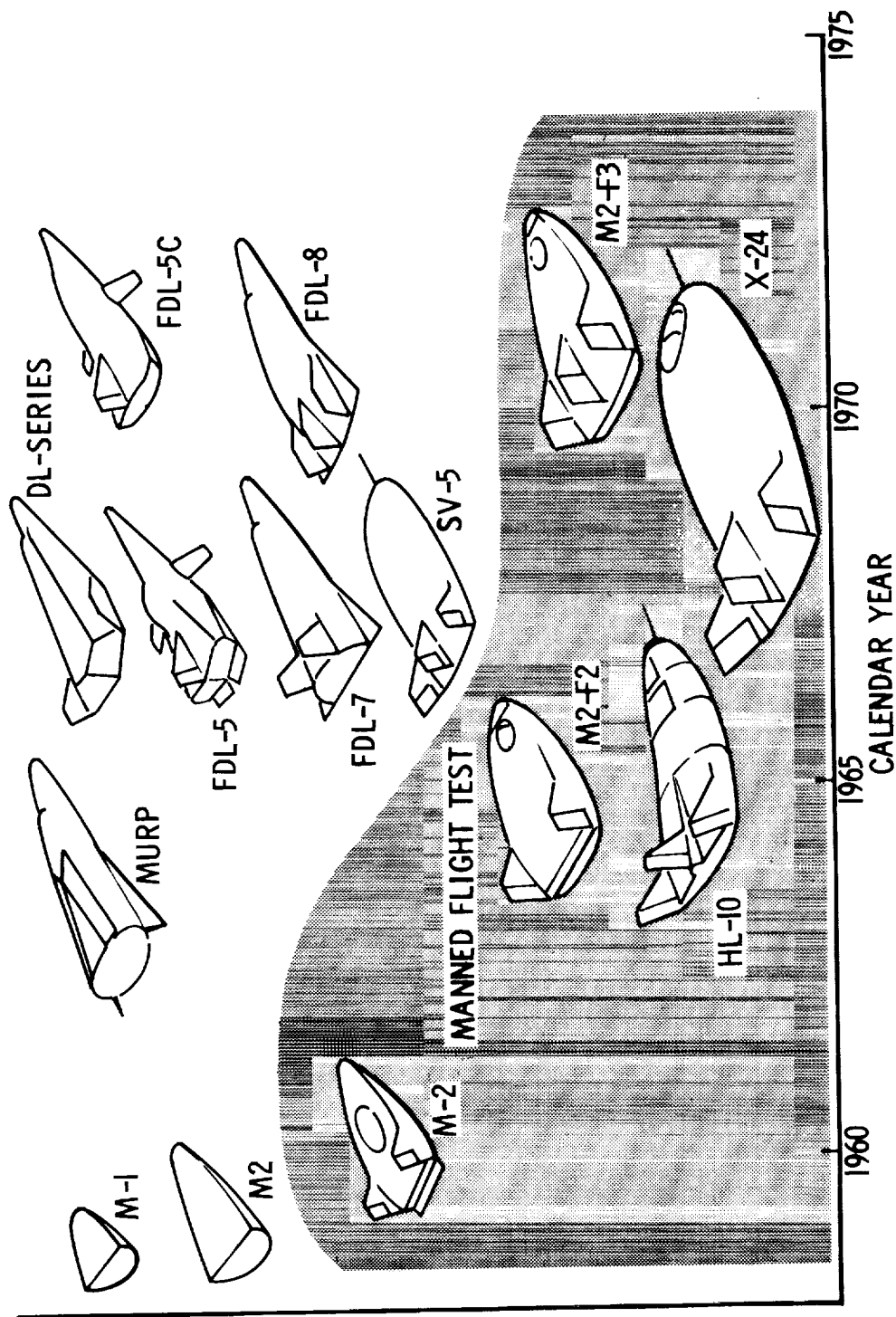


Figure 3

(Figure 3, Cont.)

The Delta Body concept and its advantageous features have been incorporated into designs for a wide range of hypersonic L/D values (1.1 for the HL-10 to 3.0 for the DL and FDL series). The inherent advantages of the concept are not restricted to a given L/D range.

The Delta Body concept is versatile and proven.

DELTA BODY ORBITER CONFIGURATION EVOLUTION

(Figure 4)

From the rich background of design information existing for Delta Bodies, attention was focused by Lockheed in 1968 on the evolution of an improved orbiter design to meet the rigorous requirements of a powered orbiter stage in a reusable launch system. The result has been a design of improved aerodynamic performance with a realistic answer for each design requirement. In particular, improvements have been achieved in configuration shaping which allow the design to exploit its advantages of volumetric efficiency, low heating rates, and compact size.

The modern Delta Body orbiter exploits its inherent advantages of volumetric efficiency and compact size while providing improved aerodynamic characteristics.

DELTA-BODY ORBITER CONFIGURATION EVOLUTION

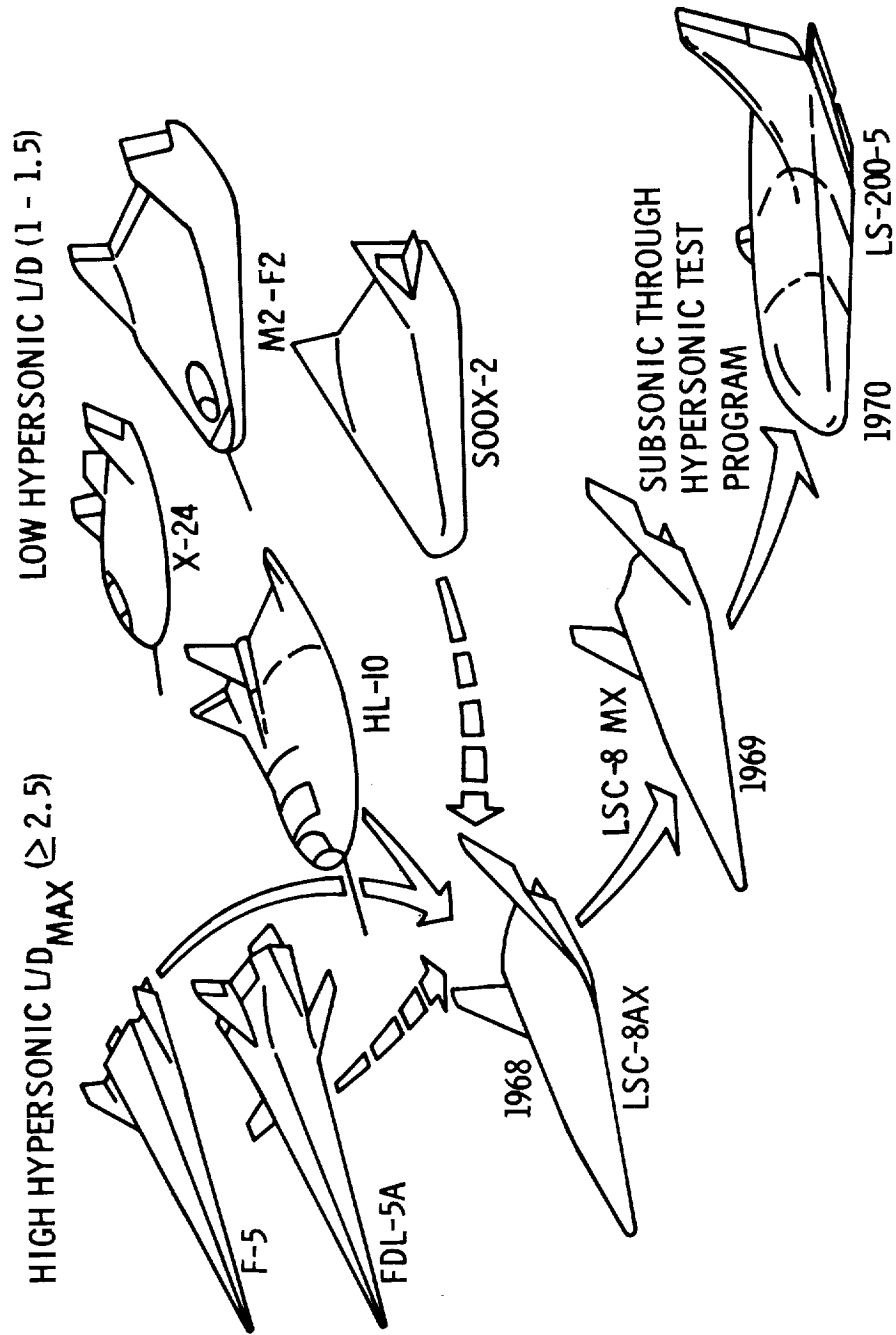


Figure 4

(Figure 5)

The development of the Delta Body orbiter has been supported and substantiated by extensive wind tunnel testing. Lockheed has performed over 3,000 hours of aerodynamic and aerothermodynamic testing on Delta Body configurations. Many tests have been performed on parametric variations of promising configurations. Tests such as the one indicated have explored the variations of every key geometric element including body cross-section shape, body camber, leading edge sweep, leading edge radius, fin shape, fin size, fin orientation, control surface size, control surface shape, and control surface orientation. These parametric test data have been supplemented with comparable thermodynamic, materials, structural, and design data to achieve a complete data bank of design information for the Delta Body Orbiter.

An extensive parametric data bank exists for the confident development and assessment of the Delta Body orbiter.

PARAMETRIC WIND TUNNEL MODEL - DELTA-BODY

- LTV 7 FT BY 10 FT SUBSONIC WIND TUNNEL
- TEST CONDITIONS
 - MACH NUMBER = 0.24
 - ANGLES-OF-ATTACK = -10° \rightarrow $+30^{\circ}$
 - SIDESLIP ANGLES = -10° \rightarrow $+10^{\circ}$
- TEST DURATION
 - 307 RUNS, 176 HR OCCUPANCY
- CONFIGURATION PARAMETERS
 - FIN
 - ROLLOUT
 - TOE-IN
 - AREA
 - LEADING EDGE GEOMETRY
 - WASHOUT
 - CENTER FIN
 - RUDDER DEFLECTIONS
 - BODY
 - CAMBER
 - L.E. RADIUS
 - BOAT-TAILING
 - ENGINE NOZZLES
 - TRIM FLAP DEFLECTIONS



Figure 5

BODY PARAMETERS
(Figure 6)

The wealth of parametric data for the Delta Body has been systematically examined to identify design trends and effect design improvements. Important design trades are known and the configuration can be readily modified to achieve a desired change in aerodynamic or design characteristics. In this manner every line, contour, and angle on the configuration is selected to provide the best combination of system characteristics. In addition to the aerodynamic parameters shown, similar thermodynamic and design parametric data exist.

The shaded squares indicate the more significant trades.

AERODYNAMIC CONFIGURATION PARAMETERS FOR THE BODY

	L/D _{MAX}		PITCH STABILITY		YAW STABILITY		MAX α _{TRIM}		EFFECTIVE DIHEDRAL		C _{Lα}	
	SUB	HYP	SUB	HYP	SUB	HYP	SUB	HYP	SUB	HYP	SUB	HYP
▲ SWEEP			-	-	-	-	-	-	▲	-		
▲ CAMBER	-	▲	-	▲	-	-			-	-	-	-
▲ L.E. RADIUS					▲	▼	▼	-	-	-	-	-
▲ BASE AREA			-	-	-	-	-	-	-	-	-	-
▲ ROLLOUT			-	-			-	-	-	-	-	-

▲ DENOTES INCREASE ▼ DENOTES DECREASE ■ CONFIGURATION DRIVER

Figure 6

FIN PARAMETERS

(Figure 7)

The parametric data on the aerodynamic characteristics of the Delta Body orbiter have shown the fins to be effective in providing a wide range of aerodynamic characteristics. The fins serve the multiple purposes of providing lateral-directional stability, longitudinal stability, directional control, and lift augmentation through their "end plate" effect on the aft upper body. Performing the dual purposes of fins and wings, the surfaces could appropriately be called "fings".

AERODYNAMIC CONFIGURATION PARAMETERS FOR THE FIN

	L/D _{MAX}		PITCH STABILITY		YAW STABILITY		MAX α_{TRIM}		EFFECTIVE DIHEDRAL		C _{Lα}	
	SUB	HYP	SUB	HYP	SUB	HYP	SUB	HYP	SUB	HYP	SUB	HYP
▲ SWEEP	—	▲	▼	—	■		▲	—	—	—	—	—
▲ ASPECT RATIO	▲	▼	▼	—			▼	—	■		▲	—
▲ AREA	■		▲	—	■		▼	—			▲	—
▲ TOE-IN	▼	▼	—	—			▼	—	■		—	—
▲ ROLLOUT	▲	▼	▲	▲	■		▼	▼			▲	▲
▲ L.E. RADIUS		■		—		—		—	—	—		—

▲ DENOTES INCREASE ▼ DENOTES DECREASE ■ CONFIGURATION DRIVER

Figure 7

DELTA BODY ORBITER THREE VIEW
(Figure 8)

An example of the family of Delta Body designs suitable for Space Shuttle orbiter configuration is shown in the three view figure. The compact design exploits the volumetric efficiency of the Delta Body concept by providing ample volume for design flexibility in the internal arrangement, with overall dimensions smaller than competing designs. The configuration shown can be packaged to serve as a two-stage or stage-and-one-half orbiter. This configuration is under study in the Lockheed Study of Alternate Space Shuttle Concepts under Contract NAS 8-26362 for George C. Marshall Space Flight Center.

Present designs employ a lower surface trim flap with trailing elevons. These surfaces provide pitch trim and control and roll control for high speed flight and for low angles of attack (up to maximum L/D) during low speed flight (landing). A set of upper surface flaps provide for pitch trim and control and added roll control for transonic and subsonic (landing flare) flight. Rudders and yaw dampers provide directional stability and control throughout the flight range. In addition, differential rudder settings can be selectively employed to improve stability and performance characteristics.

A design tail-scrrape angle of 22° is provided to permit a wide range of landing attitudes. The nose section is shaped to provide acceptable pilot visibility for all landing altitudes.

Practical efficient Delta Body orbiter designs have been defined and are being evaluated.

DELTA BODY ORBITER THREE VIEW

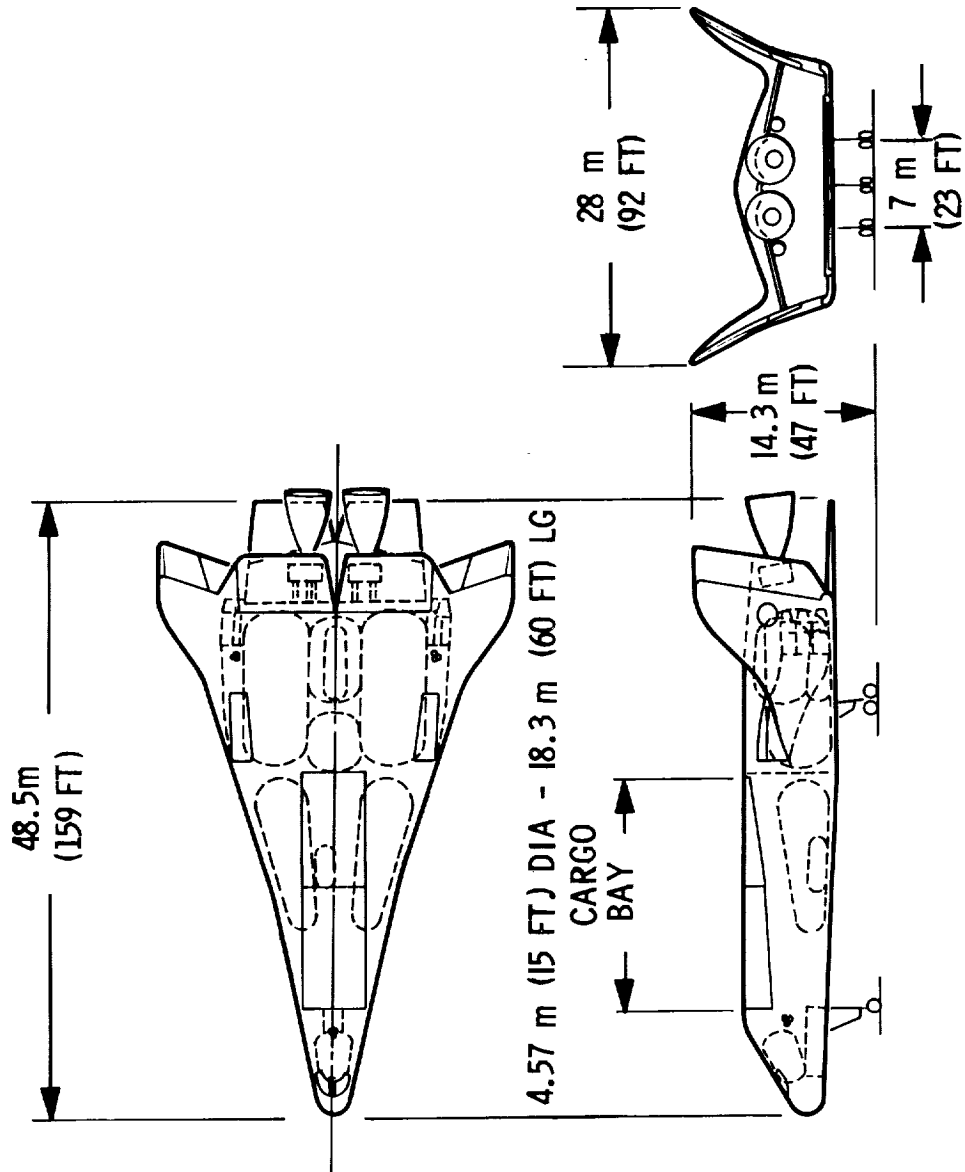


Figure 8

STATIC STABILITY (Figure 9)

The aerodynamic flexibility of the Delta Body orbiter has permitted the observance of a simple groundrule in its aerodynamic development. That ground rule is "Neutral or positive aerodynamic stability in all three axes (stability) throughout the required aerodynamic flight spectrum with aerodynamic trim and control". This ground rule is essential to the selection of early design concepts to assure that during the final development of the configuration, adequate performance and handling qualities can be provided without undue sophistication in the flight control and stability augmentation system. With this ground rule, major configuration changes to correct deficiencies discovered late in the development program (with the associated increases in development cost) can be avoided. The Delta Body design approach permits adherence to this ground rule without large weight penalties. This is due to the facts that (1) a large portion of the inherent aerodynamic stability is provided by effective body shaping and (2) the fins (or "fingers") serve several purposes (directional stability, longitudinal stability, directional control, longitudinal trim, and lift augmentation through their effectiveness as end plates) - consequently, the stability is established by adding a relatively small set of aerodynamic surfaces.

The curves show that neutral or better pitch and yaw stability has been designed into the Delta Body orbiter for all anticipated flight conditions and for far aft center-of-gravity locations characteristic of Space Shuttle orbiter (in this case a Stage-and-One-Half orbiter).

The Delta Body concept permits design with three axis aerodynamic stability and control, reducing development risk, and schedule slippage due to late configuration fixes during the development program.

It is not necessary (with the Delta Body concept) to sacrifice aerodynamic stability to achieve a compact orbiter design.

STATIC STABILITY

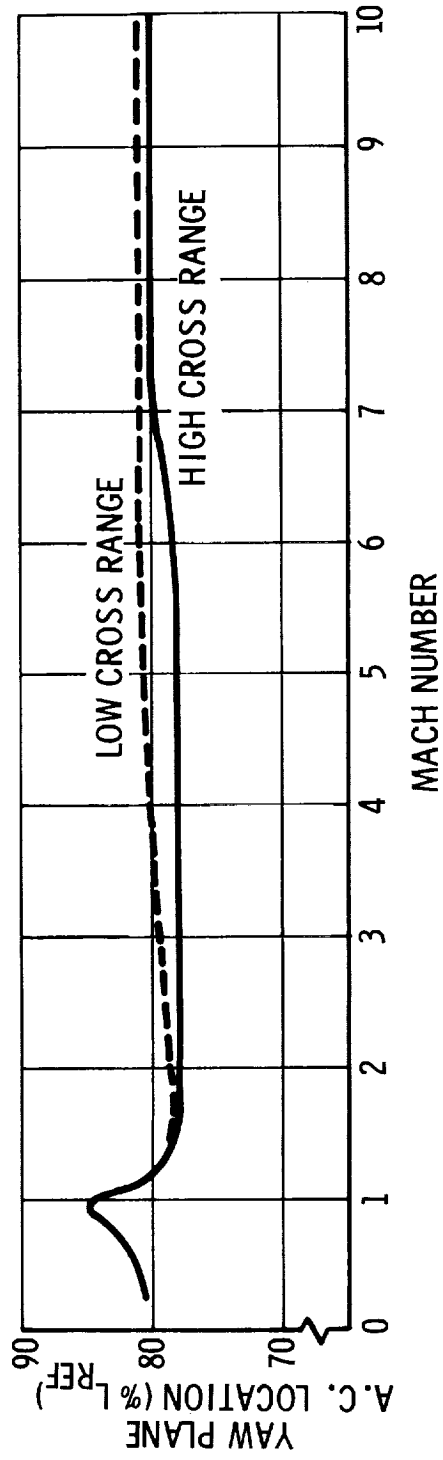
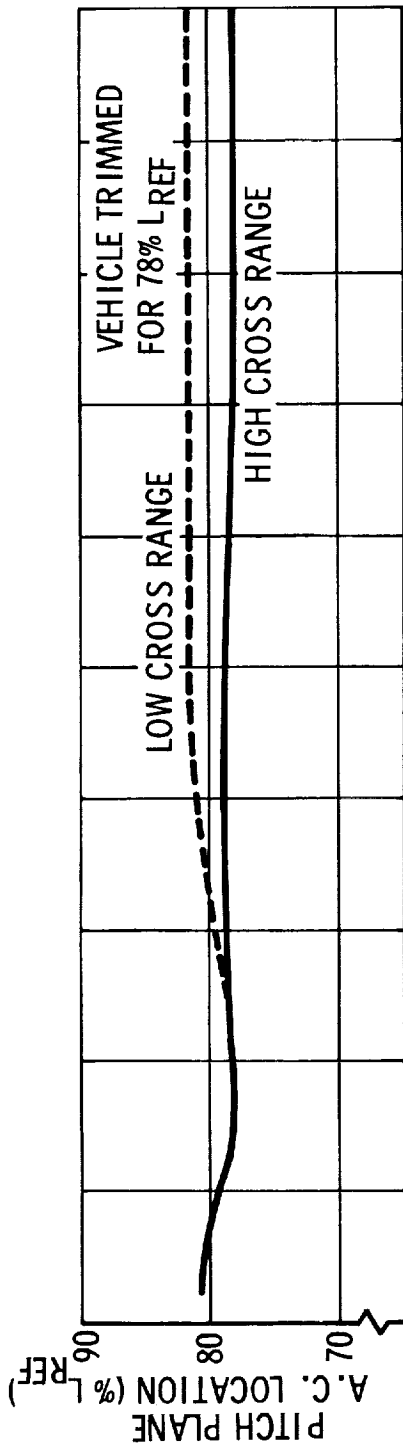


Figure 9

UNAugMENTED SUBSONIC HANDLING QUALITIES

(Figure 10)

Parameter plane analyses of the Delta Body orbiter concept has indicated that the configuration will have excellent handling qualities when compared with most of the relative handling qualities criteria, the only major exception being that of the damping in Dutch roll. This deficiency may be common to the Space Shuttle orbiter concepts where their directional-to-roll stability ratio is low as is the roll inertia-to-yaw inertia ratio. The aerodynamic flexibility of the Delta Body design offers several solutions to this deficiency, such as damping by aileron deflection (and/or yaw dampers).

The Delta Body orbiter is presently being simulated by Lockheed under contract to NASA Manned Spacecraft Center (NAS-9-111459) to further verify the concept handling characteristics during low speed flight.

Level 1 handling quality characteristics are predicted for the Delta Body orbiter for most large transport category criteria. Aerodynamic design flexibility offers cures for any deficiencies which may exist.

UNAUGMENTED SUBSONIC HANDLING QUALITIES

<u>MODE</u>	<u>CRITERIA</u>	<u>RATING*</u>
LONGITUDINAL		
• SHORT PERIOD	DAMPING RATIO	LEVEL 1
	NATURAL FREQUENCY	LEVEL 2
• PHUGOID	DAMPING RATIO	LEVEL 1
LATERAL/DIRECTIONAL		
• ROLL	ROLL MODE TIME CONSTANT	LEVEL 1
	NATURAL FREQUENCY	LEVEL 1
• DUTCH ROLL	DAMPING RATIO	UNACCEPTABLE (REQUIRES AUGMENTATION)
CONTROL		
• LANDING APPROACH	VERTICAL VS ANGULAR ACCELERATION FOR MAX PITCH CONTROL	LEVEL 1
• SIDESLIP TRIM FOR 30 KNOTS SIDEWIND	β TRIM VS AILERON DEFLECTION	LEVEL 1
• 30 DEG ROLL IN 2 SEC	δ_A VS ROLL RATE	LEVEL 1

*HEAVY TRANSPORT, CLASS III, MIL-F-8785B (ref. 2)

Figure 10

AERODYNAMIC PERFORMANCE

(Figure 11)

The configuration shown in Figure 8 has been configured to provide cross-range capability of up to 1500 nautical miles. The required maximum lift-to-drag ratio of 1.7 has been provided for hypersonic flight conditions.

For subsonic flight the maximum subsonic lift-to-drag ratio had, until recently, been conservatively predicted at 4.5, a value proven adequate for the power-off landings during the NASA Flight Research Center lifting body flights. Recent wind tunnel test data indicate considerably higher lift-to-drag ratios. The data indicated show a maximum trimmed lift-to-drag value of 5.65 at 14° angle of attack. This extrapolates to a free flight value of 5.8. (All lift-to-drag ratio values indicated are for the aerodynamically trimmed case.)

The high subsonic lift-to-drag ratios result partially from the approach used to trim the vehicle. The lower surface trim flap and control surfaces are deflected upward to achieve trim, and effectively streamline the flow over the large base area. The apparent aerodynamic base area is therefore greatly reduced from that of the actual base area. Consequently, trim is achieved with reduced axial force and improved L/D values in contrast with the trim losses associated with winged bodies.

The normal operating ranges of angle of attack are indicated for the subsonic and hypersonic regimes. The subsonic range provides adequate approach control and landing flare capability. The hypersonic range permits modulation of the configuration's cross-range capability to achieve high or low cross-range values ($0.6 \leq L/D \leq 1.7$).

The Delta Body has a high performance capability and operational flexibility.

AERODYNAMIC PERFORMANCE

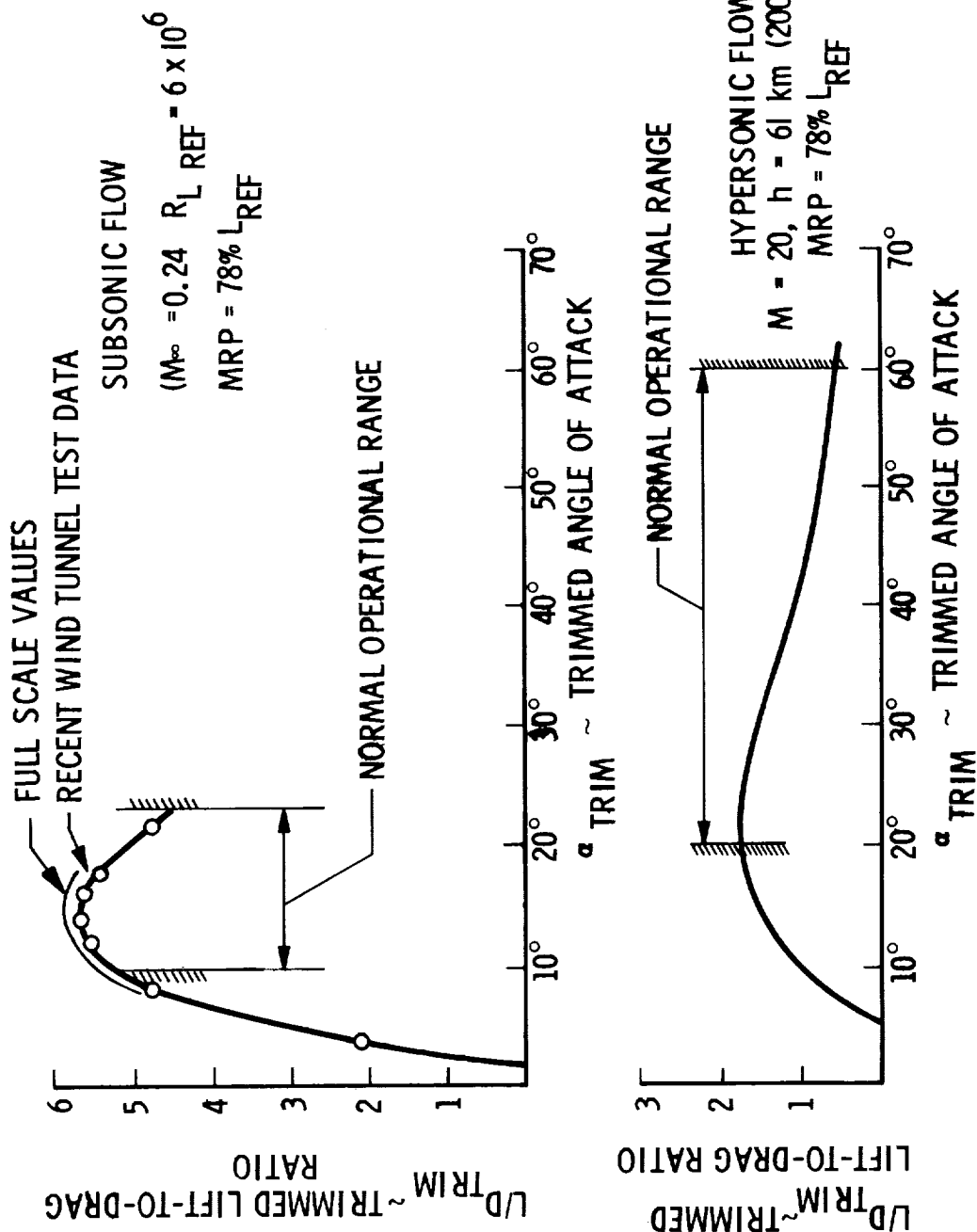


Figure 11

DELTA BODY/DELTA WING-BODY GEOMETRIC COMPARISON

(Figure 12)

A comparison of configurations reveals that the Delta Body configuration is smaller in length, span, and height than a comparable base-line Delta Wing-Body orbiter presently under study in the Phase B program. The larger cross-section area of the Delta Body is apparent in the end view. Potentially more favorable visibility characteristics are attributable to the Delta Body design with its steep nose angle, although a similar angle is possible as a revision to the Delta Wing-Body design.

The Delta Body configuration provides a compact Space Shuttle orbiter design.

DELTA BODY/DELTA WING-BODY GEOMETRIC COMPARISON

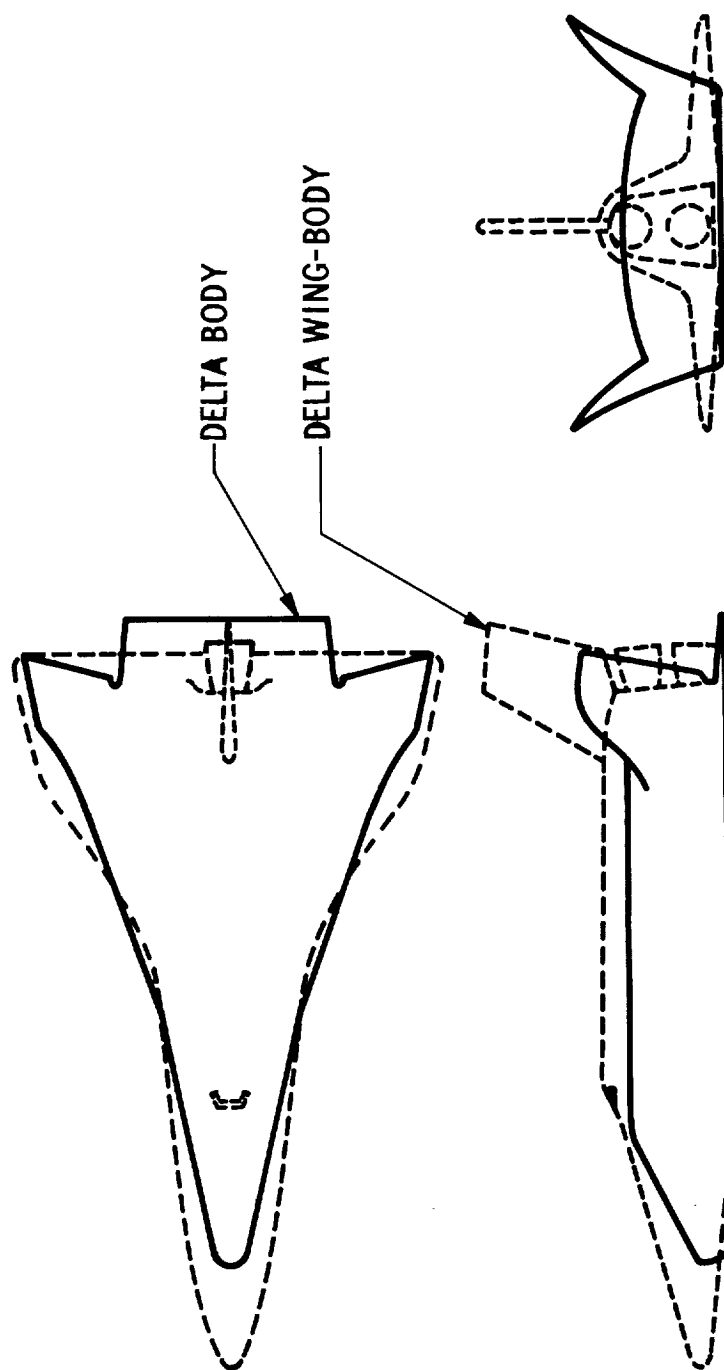


Figure 12

LANDING SPEED AND ATTITUDE COMPARISON

(Figure 13)

Preliminary considerations of landing speeds and attitude show little difference between Delta Body and Delta Wing-Body values. Recent wind tunnel data were used to compute the respective landing speeds. The values shown reflect weights for the two-stage Space Shuttle orbiter landing with the payload in.

Experience with the lifting bodies at the NASA Flight Research Center indicates the pilots' preference to land at speeds high enough to provide good control rather than minimum speeds. Consequently, it is reasonable to expect that the Space Shuttle orbiters will land at speeds of approximately 180 knots and at attitudes near 15° angle of attack. The Delta Body design has provided ample pilot visibility for the required landing conditions.

Flight tests at the Flight Research Center would support the acceptance of these characteristics for Space Shuttle operations.

The Delta Body landing conditions are acceptable for the Space Shuttle operations and essentially equivalent to those of the Delta Wing-Body.

LANDING SPEEDS AND TOUCHDOWN ATTITUDE COMPARISON

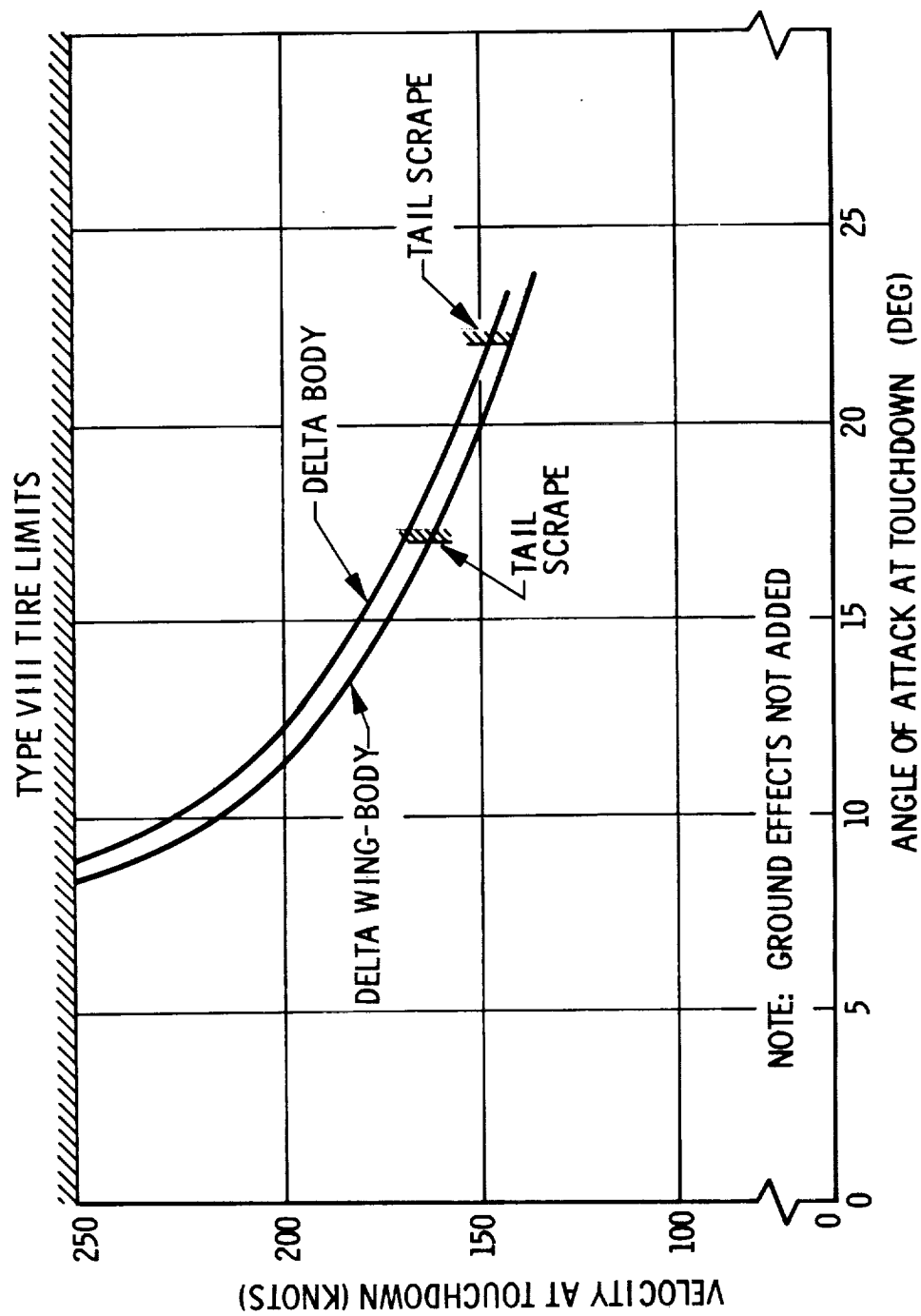


Figure 13

COMPARISON OF VOLUME VARIATION WITH LENGTH

(Figure 14)

The relative compactness of the Delta Body design results from the inherent volumetric efficiency of the configuration and the design steps taken to employ that volume. Comparing with the baseline Delta Wing-Body configuration shown in figure 12, a Delta Body fuselage packaged for the two-stage Space Shuttle orbiter is 39.4 m (129.5 feet) long as compared with the 48.3 m (158.3 feet) long fuselage of the Delta Wing-Body baseline.

Of considerable importance is the fact that the small Delta Body size has been achieved while employing non-integral internal tanks of no greater complexity than simple conical tanks of circular cross section.

The total volumes of the configuration compare closely. The Delta Body is seen to have little unusable volume. In recent designs, 80 percent of the available volume is occupied, leaving ample access for inspection, maintenance and repair.

COMPARISON OF FUSELAGE VOLUME VARIATION WITH LENGTH

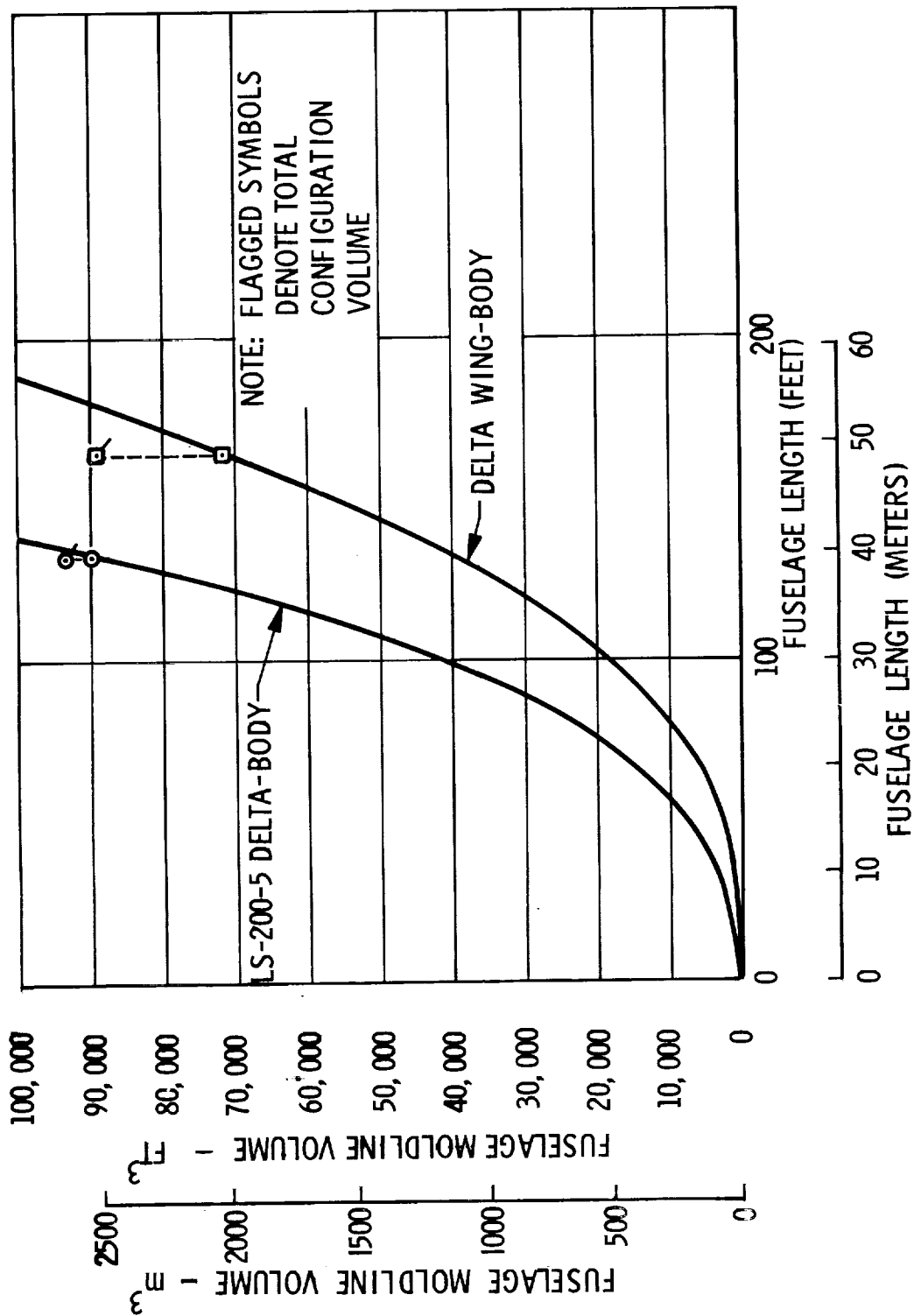


Figure 14

VOLUMETRIC EFFICIENCY COMPARISON

(Figure 15)

A significant advantage of the Delta Body design is its reduced wetted area necessary to contain the required volume for the Space Shuttle orbiter. An index of merit is the ratio of volume contained per unit of wetted area since wetted area is directly related to structural (and thermal protection system) weight. Recent total volume numbers for the Two-Stage Delta Body orbiter, the Delta Wing-Body with tip fins, and the Delta Wing-Body with a center fin only are $2,648 \text{ m}^3$ ($93,492 \text{ ft}^3$), $2,384 \text{ m}^3$ ($84,241 \text{ ft}^3$) and $2,532 \text{ m}^3$ ($89,485 \text{ ft}^3$), respectively. Corresponding wetted areas are $1,750 \text{ m}^2$ ($18,835 \text{ ft}^2$), $2,087 \text{ m}^2$ ($22,462 \text{ ft}^2$), and $1,860 \text{ m}^2$ ($20,019 \text{ ft}^2$). The ratios are indicated in the figure. The efficiency of the Delta Body configuration is seen to be 10% to 25% greater than the Delta Wing configuration with corresponding center fin and tip fin configurations.

The increased efficiency of the center finned Delta Wing-Body configuration over the Delta Wing-Body with tip fins is achieved at the expense of reduced directional yaw stability at hypersonic and supersonic speeds.

Body structure and wing and fin surface unit weights are typically 17.1 kg/m^2 (3.5 pounds per square foot). The potential differences in the Delta Body and Delta Wing-Body inert weights due to reduced surface area are therefore 1,878 kg (4,140 lb) (center fin) and 5,761 kg (12,700 lb) (tip fins) in favor of the Delta Body. An equivalent savings in thermal protection system weight is obtained with the Delta Body.

The reduced surface area of the Delta Body configuration can result in reduced structural and thermal protection system weights.

VOLUMETRIC EFFICIENCY COMPARISON

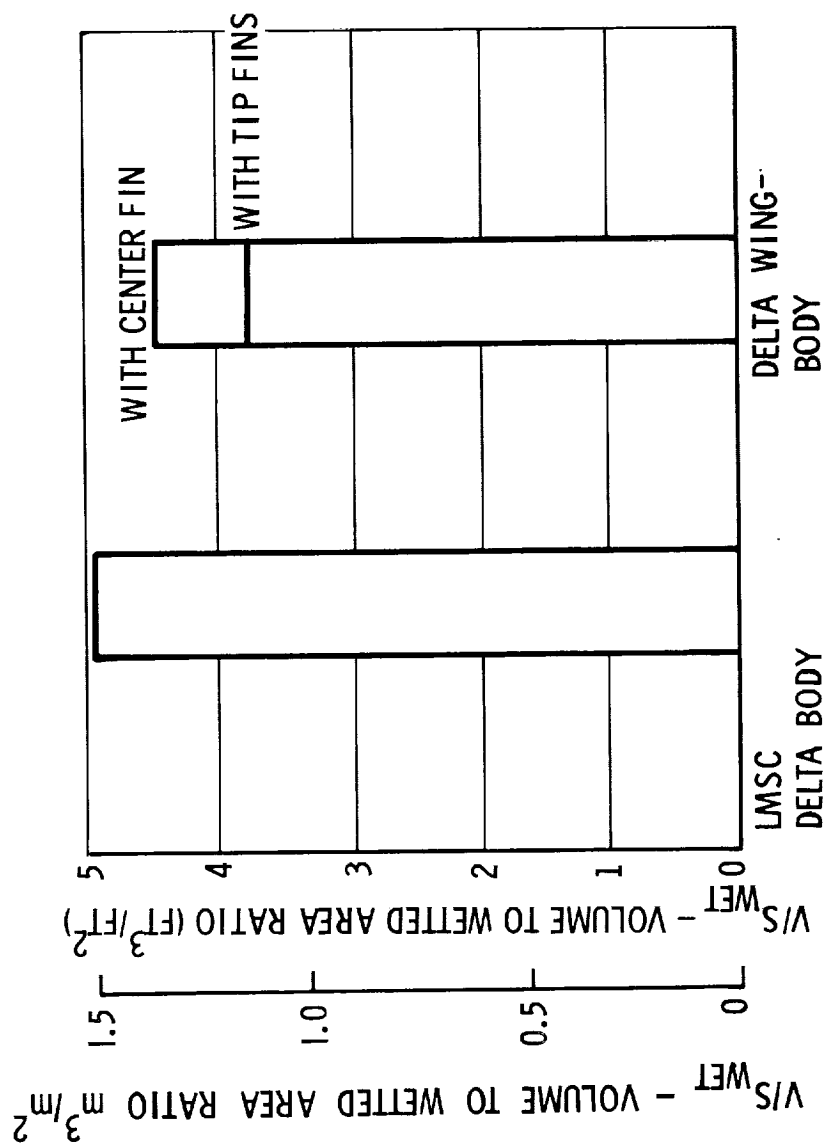


Figure 15

PEAK TEMPERATURE ISOTHERMS - DELTA BODY
(Figure 16)

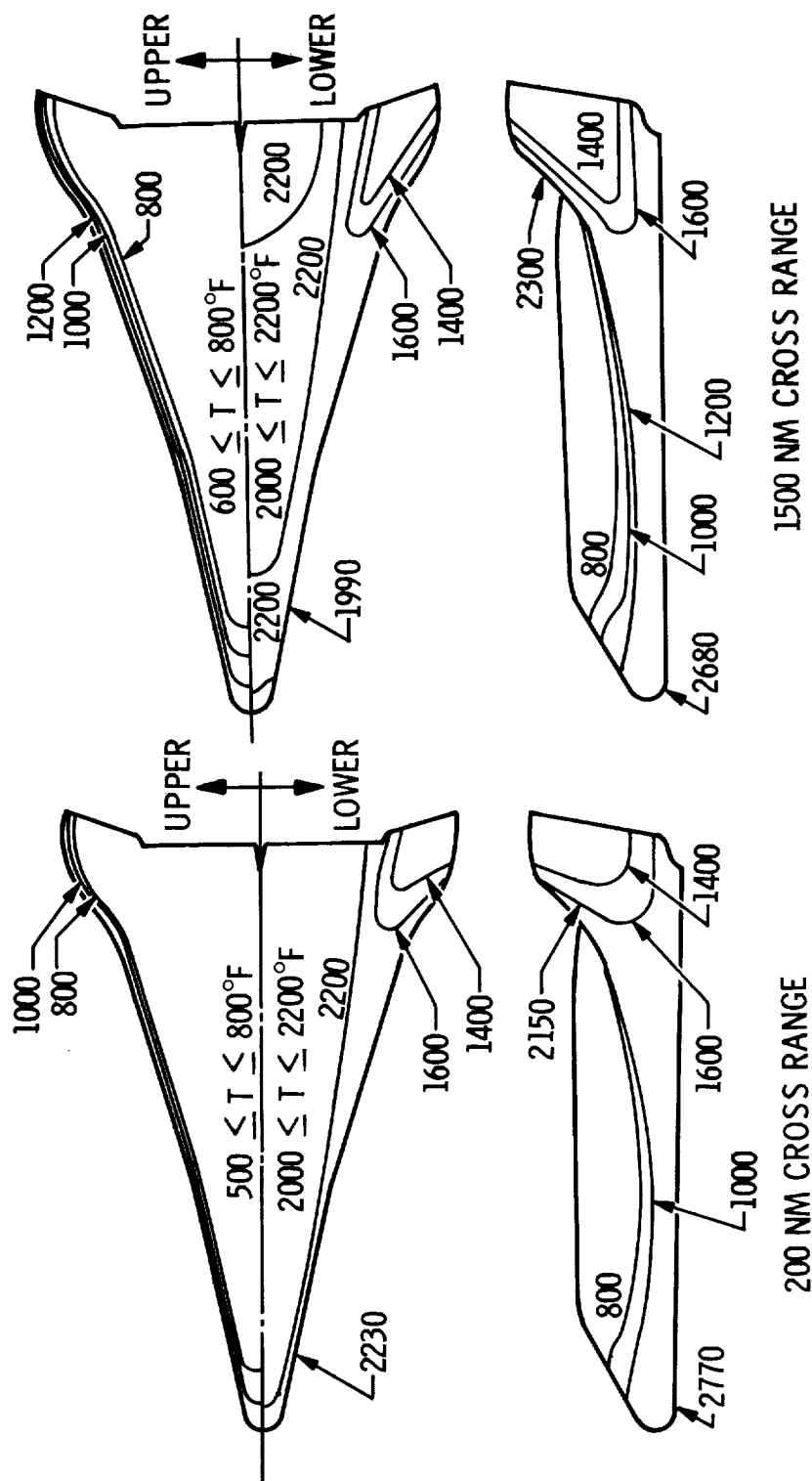
The smooth contours of the Delta Body result in low aerodynamic heating rates and correspondingly low surface temperatures. This is a direct result of the inherent Delta Body philosophy of swept leading edges and large leading edge radii.

The contours show a distinct absence of shock impingement and its associated high heating rates. In addition, there is a lack of high temperature gradients. Consequently, the design of the thermal protection system for the Delta Body would be simplified as compared to the TPS system for the Delta Wing-Body with its potential shock impingements and high leading edge temperatures.

One feature of the Delta Body is the relative insensitivity of heating distribution and level with angle of attack [when the trajectory is constrained to not exceed a given temperature $T = 1533^{\circ}\text{K}$ (2300°F)]. The resulting temperature distributions for the 200 nautical mile cross range ($\alpha \approx 52^{\circ}$) and the 1500 nautical mile cross range ($\alpha \approx 25^{\circ}$) trajectories are shown to be quite similar, again simplifying the TPS design and providing a versatile design. Insulation requirements increase with time of flight (cross-range).

The Delta Body design results in no shock impingement, low temperature levels and simplified thermal protection system requirements.

PEAK TEMPERATURE ISOTHERMS – DELTA BODY



NOTE:
TO CONVERT TO $^{\circ}\text{K}$, $^{\circ}\text{K} = (5/9)^{\circ}\text{F} + 459.67$

Figure 16

SURFACE TEMPERATURE COMPARISON

(Figure 17)

With only the nose cap (0.5% of wetted area) experiencing high temperature levels ($T > 1644^{\circ}\text{K}$, 2500°F), the Delta Body design offers maximum TPS reusability potential using external insulation or metallic materials presently under development.

Competing systems involve significant areas (up to 5% for the Delta Wing-Body) with temperatures greater than 1644°K (2500°F). Although ablatives and certain high temperature materials allow consideration of initial flights at these temperatures, the desired degree of reusability (100 flights) is jeopardized. Lack of reusability can seriously increase operational costs.

The Delta Body offers maximum reusability potential for the Space Shuttle orbiter thermal protection system.

SURFACE TEMPERATURE COMPARISON

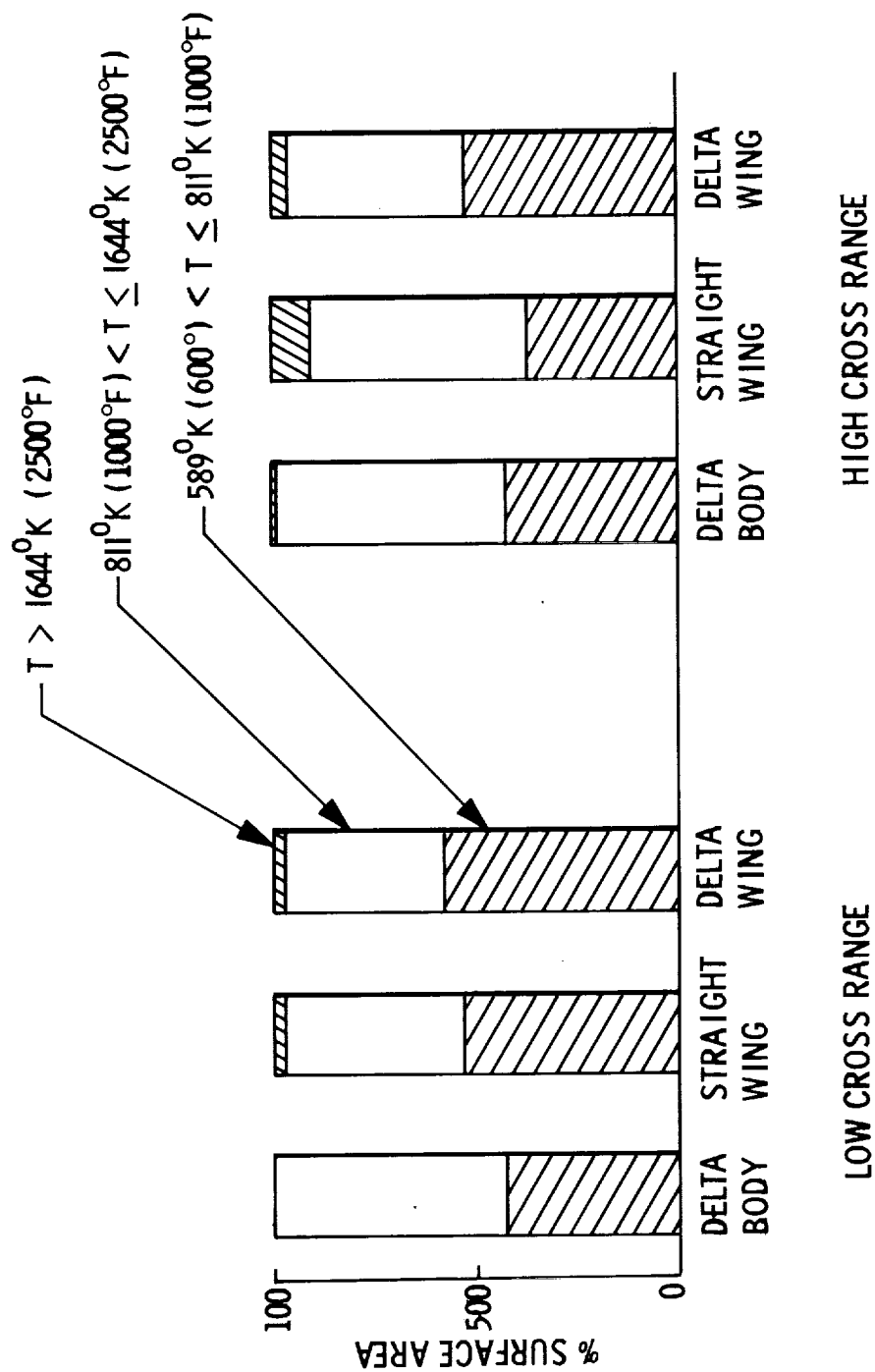


Figure 17

ONE-AND-ONE-HALF-STAGE ORBITER PRIMARY STRUCTURE - DELTA BODY
(Figure 18)

The compact size and large body cross-sections of the Delta Body orbiter design affords many structural advantages.

- Low body line loads (use aluminum for primary structure)
- Short load paths (mass concentrated aft)
- Inertial and aerodynamic loadings tend to maximize where the available fuselage cross section maximizes (low line loads)
- Reduced aerodynamic surfaces with high line loads
- Nonintegral tanks

These advantages are inherent in the configuration and afford advantages to either the two-stage or stage-and-one-half orbiter designs.

The Delta Body has many features which contribute to low structural weight and reduced design complexity.

ONE-AND-ONE-HALF-STAGE ORBITER PRIMARY STRUCTURE – DELTA BODY

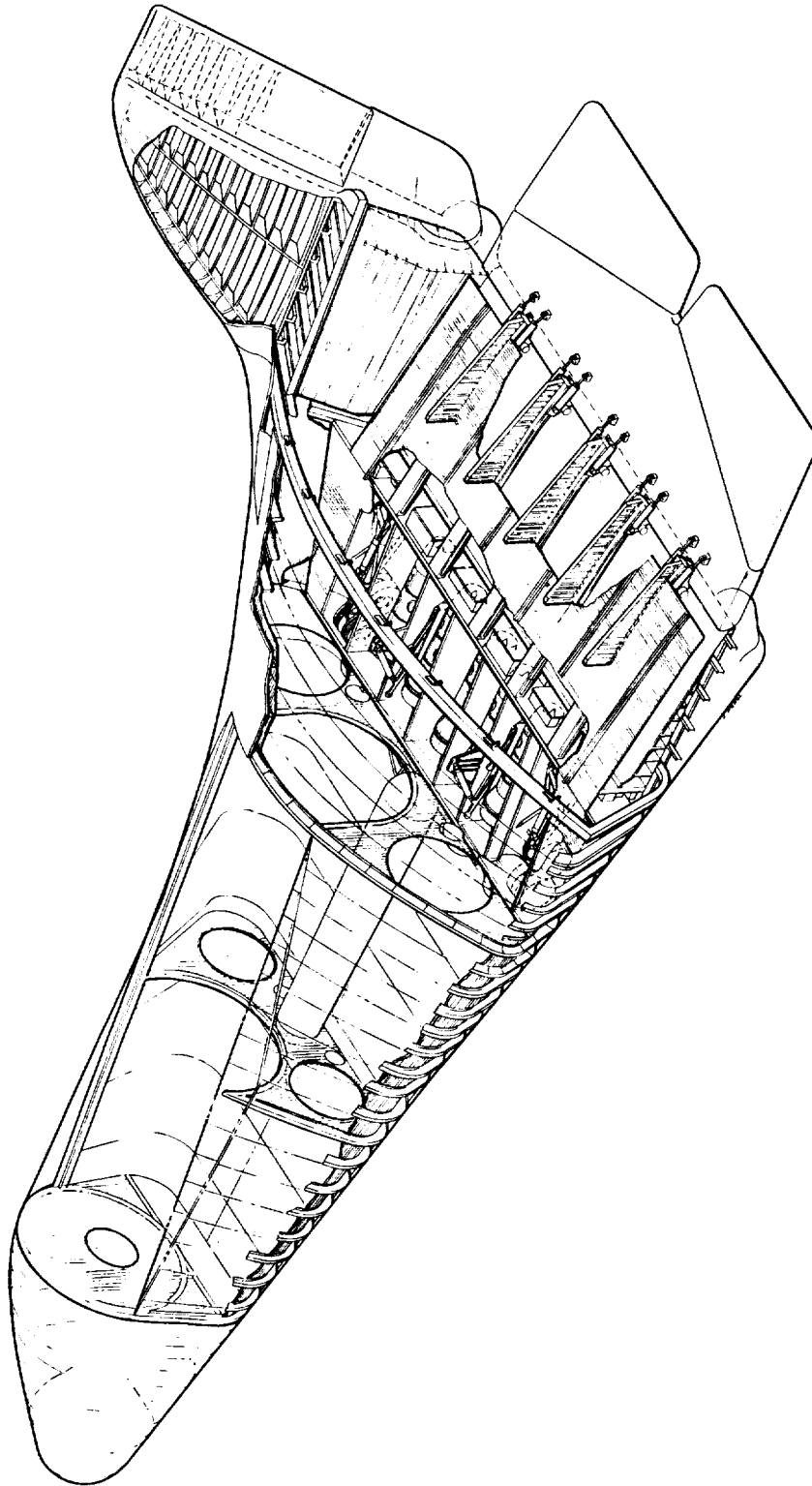


Figure 18

PRODUCTION BREAKDOWN - DELTA BODY
(Figure 19)

The simplified structural design features of the Delta Body orbiter will permit development and manufacturing to proceed on a modular basis with no undue complexity required to coordinate the system elements. This is true for either the two-stage or stage-and-one-half orbiter designs. Avoiding integral tanks, the structural system and propulsion system developments can proceed relatively independent of each other. This should greatly simplify development and scheduling. In addition, the incorporation of technology advances into one of the systems (tanks for instance) can proceed with no impact on the other (body structure).

The Delta Body design can reduce development risk.

DELTA-BODY MAJOR STRUCTURAL BREAKDOWN

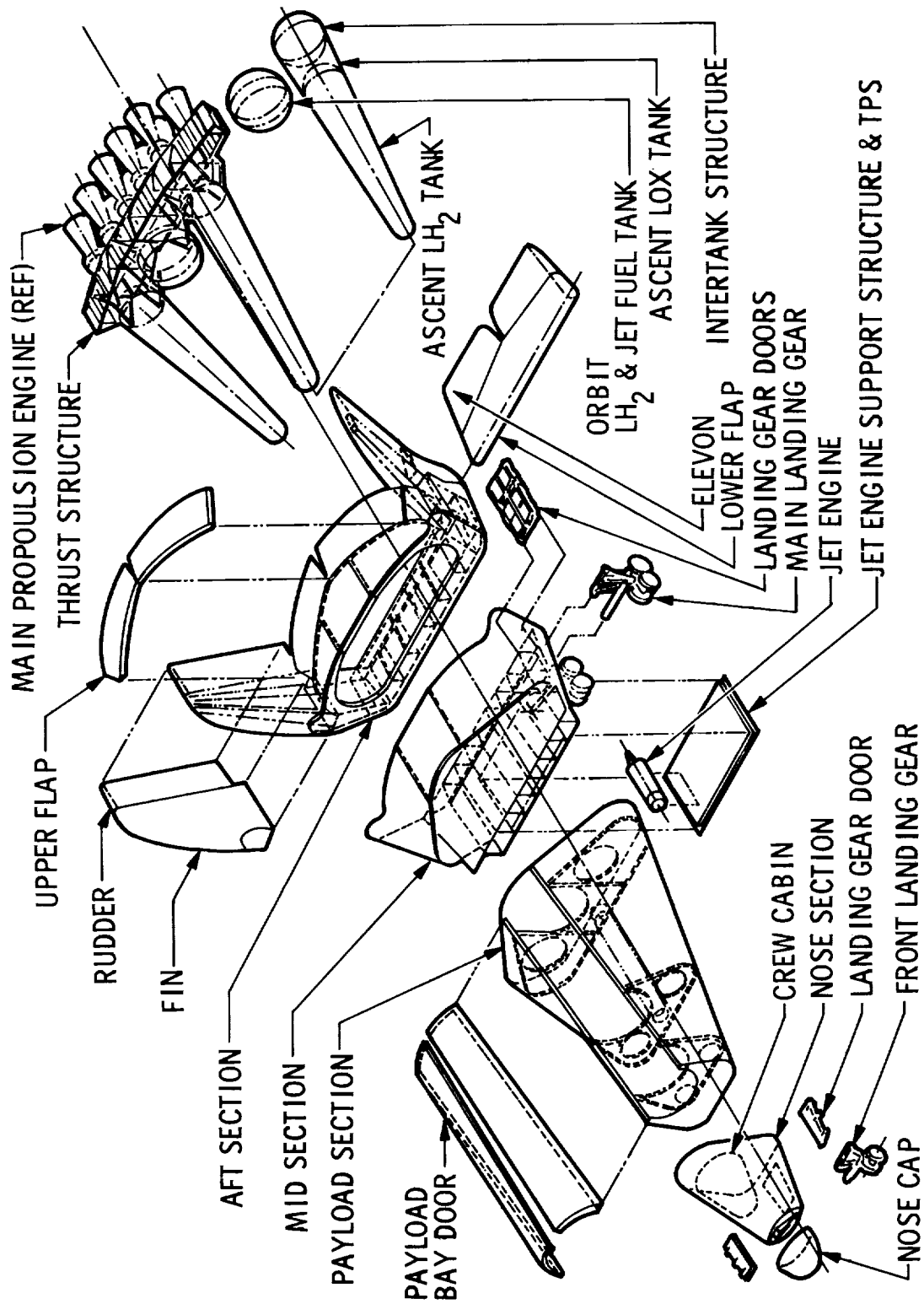


Figure 19

DELTA BODY/DELTA WING-BODY COMPARISON - TWO STAGE ORBITER

(Figure 20)

The Delta Body design approach is seen to have many potential advantages over the contemporary Delta Wing-Body design approach. This comparison reflects the two design approaches being worked to the same ground rules (Phase B) and to reasonably comparable depth. While the characteristics of each design are expected to change with further definition, the relative features are not expected to change significantly.

Properly exploited, the Delta Body design can yield an efficient Space Shuttle orbiter.

DELTA BODY/DELTA WING-BODY COMPARISON TWO-STAGE ORBITER

SIZE: (OVERALL DIMENSIONS)	DELTA BODY		DELTA WING-BODY (CENTER FIN)	
	LENGTH	SPAN	HEIGHT	DRY WT. VOLUME WEETED AREA
	48.5 m (159 ft)	28.0 m (91.83 ft)	11.1 m (36.4 ft)	94,305 kg (207908 lb) 2648 m ³ (93492 ft ³) 1750 m ² (18835 ft ²)
λ'	0.711		0.698	
THERMODYNAMICS/TPS FLOW FIELD	Predictable, No Shock Impingement		Flow Interference and Shock Impingement on Leading Edge	
TEMPERATURES	Total Surface (Except Nose Cap 0.46%). Less Than 1644° K (2500° F)		1/4 of Surface Area Above 1644° K (2500° F)	
LEADING EDGE	T ≤ 1533° K (2300° F)		T ≥ 1977° K (3100° F)	
LANDING: TOUCHDOWN VELOCITY (POWER OFF)	180 Knots		180 Knots	
MINIMUM GLIDE SLOPE	9.94° (L/D = 5.8)		9° (L/D = 6.5)	
STABILITY	All axis aerodynamic trim, control, and static stability at α , δ require required throughout aerodynamic flight regime.		Directionally unstable (static) hypersonic/supersonic ($C_{N\beta}$ is stable) $C_{N\beta}$ dynamic	

Figure 20

CONCLUDING REMARKS

The Delta Body orbiter is a potential candidate for the Space Shuttle orbiter. The advantages of using the Delta Body design approach are

1. Bow shock impingement and flow interference is avoided
2. Only the nose cap sees surface temperatures above 1644°K (2500°F), therefore the TPS can be fully reusable with the proposed materials.
3. Static aerodynamic stability and control is provided for all three axes during atmospheric flight - the configuration has sufficient aerodynamic performance.
4. Low structural weight is achieved without resorting to integral tanks.
5. The concept provides a simple development/manufacturing approach.
6. Fifteen years of background evolution supports the concept.
7. The Delta/Body Space Shuttle orbiter will perform the Space Shuttle mission.

REFERENCES

1. "Space Transportation System Technology Symposium", NASA TM X-52876, NASA Lewis Research Center, Cleveland, Ohio, July 15-17, 1970.
2. "Flying Qualities of Piloted Airplanes", Military Specification MIL-F-8785B(ASG), Aug. 7, 1969.

SPACE SHUTTLE SEPARATION SYSTEM

By

Frank Jarlett

Convair Aerospace Division of General Dynamics, San Diego, California

SYSTEM REQUIREMENTS

(Figure 1)

The separation system can possibly be a major technology problem area -- mainly because parallel staging of large, fully reusable vehicles has not been proven in any existing aircraft or space launch vehicle. After liftoff, the booster and orbiter must separate routinely and without damage to either vehicle to accomplish: reusability of both stages, crew and passenger safety, and payload delivery or recovery.

SYSTEM REQUIREMENTS

ORBITER & BOOSTER MUST SEPARATE FOR:

- STAGE REUSABILITY
- CREW & PASSENGER SAFETY
- PAYLOAD DELIVERY/RECOVERY

NORMAL & ABORT MISSIONS

Figure 1

STUDY APPROACH

(Figure 2)

The objective of this trade study was to compare several candidate separation system concepts, and then to select those features that best meet the requirements for separation. At the start of the study, it was recognized that there were strong interfaces among aerodynamics, mass properties, dynamics, attitude control, propulsion, thermodynamics, plume impingement, loads and structure. In addition, recommendations from concurrent studies on abort, safety, reliability, orbiter position on booster, structural arrangement, propulsion and ground operations were included as they became available and are part of the evaluation of the candidate concepts. Initially, concepts were sized and evaluated for normal staging. Concepts capable of early separation (aborted missions) were then evaluated and penalties derived. This was followed by evaluation of the concepts and selection of the best system.

STUDY APPROACH

CONCEPTS:	LINKS, ROCKETS, PISTONS, RAILS
SIMULATION:	6-DEG.-OF-FREEDOM COMPUTER PROGRAM, 2 BODY , CONSTRAINED, THRUST SCHEDULE, AERODYNAMICS, INERTIAS, GUIDANCE & CONTROL
EVALUATION:	RELATIVE MOTION, ACCELERATIONS, LOADS, BEST PHASING DISTANCE VS. TIME, WEIGHTS, EARLY SEPARATION CAPABILITY, FAILURE TOLERANCE

Figure 2

SEPARATION DYNAMICS

(Figure 3)

A primary tool in the evaluation of the various separation concepts was a digital computer program. This program determined the relative motion of each vehicle while allowing six degrees of freedom for each body and for appropriate schedules of inertia, aerodynamic, thrust and attitude control forces, plus any constraints by linkages or rails. The output of the program displayed separation clearances, rates, accelerations, loads, etc., in both analytical and line plot forms.

SEPARATION DYNAMICS Computer Program

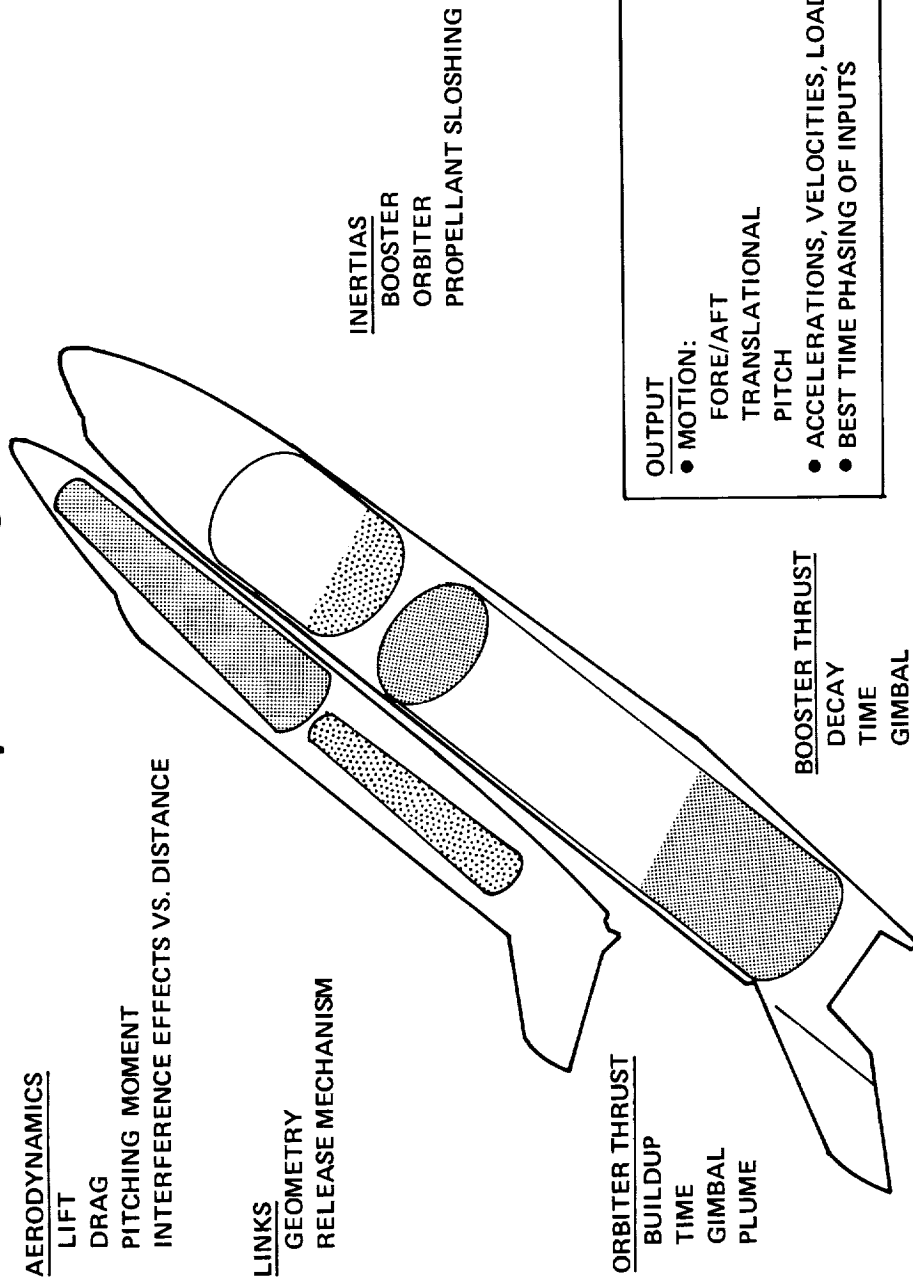


Figure 3

INTERCONNECT LOADS

(Figure 4)

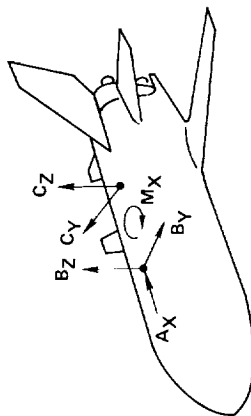
Early in the study it became apparent that aerodynamic/inertia loads occurring during mated flight required heavy fittings, frames and longerons in both booster and orbiter. Since the structural attachment must be broken during separation, there is a strong interface between the attachment structure components and the separation system.

The highest load occurs at maximum longitudinal acceleration of the booster and approximates $3g \times 76,000 \text{ lb}$ (34,500 kg). This load could be taken at either the forward or the aft attachment. However, because the orbiter is six times more sensitive to weight growth than the booster, it is lighter to transfer this load at the forward attach point since it is close to the liquid oxygen tank (and hence the c.g.) of the orbiter.

Maximum loads normal to the waterline of the vehicles are roughly 225,000 pounds (102,000 kg) tension at the front attachment and 478,000 pounds (218,000 kg) compression at the rear attachment. Since these large loads require heavy bulkheads, the internal arrangements of the propellant tanks and other major components restrict the location of these major bulkheads. The orbiter is located at that fore-aft position which gives it the shortest and lightest load path between these major bulkheads.

The weight of the attachment structure in the booster is approximately 10,300 pounds (4,680 kg) at the forward attach and 2,100 pounds (955 kg) at the aft attach point.

INTERCONNECTION LOADS Limit



CONDITION	A _X (LB)	B _Y (LB)	B _Z (LB)	C _Y (LB)	C _Z (LB)	M _X (10 ⁶ IN.-LB)
LIFT OFF + GROUND WINDS	HEAD WIND	1,192,675		137,618		-181,561
	TAIL WIND	1,192,675			-208,215	
	SIDE WIND	1,192,675	±18,951	142,214	±6,285	±8,572
MAXIMUM α, θ	HEAD WIND	1,679,105		190,819		158,410
	TAIL WIND	1,484,122		225,431	-478,613	
MAXIMUM β, ϕ		1,638,850	±15,508	208,740	±97,435	±24,486
	HEAD WIND	2,309,718		143,578		-372,008
3g MAX. THRUST	TAIL WIND	2,312,791		169,384		-385,929
3g BOOSTER BURNOUT		2,272,182		57,604		-369,624

1 LB = 4.448 NEWTONS
1 IN.-LB = 0.1130 METER-NEWTON

Figure 4

LATERAL ROCKETS

(Figure 5)

Thrust scheduling is shown in the upper right corner. Sequentially, the booster thrust is reduced to zero, the separation rockets are ignited and the orbiter is released. After separation has started the orbiter engines are ignited. The orbiter engines thus require 0-g start capability.

The thrusters produce 161,600 lb -sec (719,000 Newton-sec) of impulse and are angled to avoid direct impingement on the orbiter; 100,000 lb -sec (440,000 Newton-sec) of impulse is produced normal to the booster waterline. Redundancy is provided by ripple firing any four out of five rockets at each location. Four empty casings, plus one full casing, are returned every flight by the booster. The thrusters are on the booster in preference to the orbiter because (1) the booster weight is only 0.7 the weight of the orbiter, and (2) the weight of the carry-back rocket and casings degrades performance only one sixth as much as if they were on the orbiter.

For the assumed level of rocket impulse of 100,000 lb -sec (440,000 Newton-sec), separation is very effective and the chances of recontact are small. At release, the relative acceleration is 6.1 ft/sec^2 (1.86 m/sec^2) and after three seconds the closest point between orbiter and booster is 22 feet (6.7 m). (Note that in reality the booster moves away from the orbiter; however, the relative position is correct.)

LATERAL ROCKETS

ROCKETS = 150,000 LB x 1 SEC
 660,000 NEWTONS x 1 SEC
 EQUIV. = 100,000 LB.
 440,000 NEWTONS
 SEPARATION FORCE NEWTONS 8.8

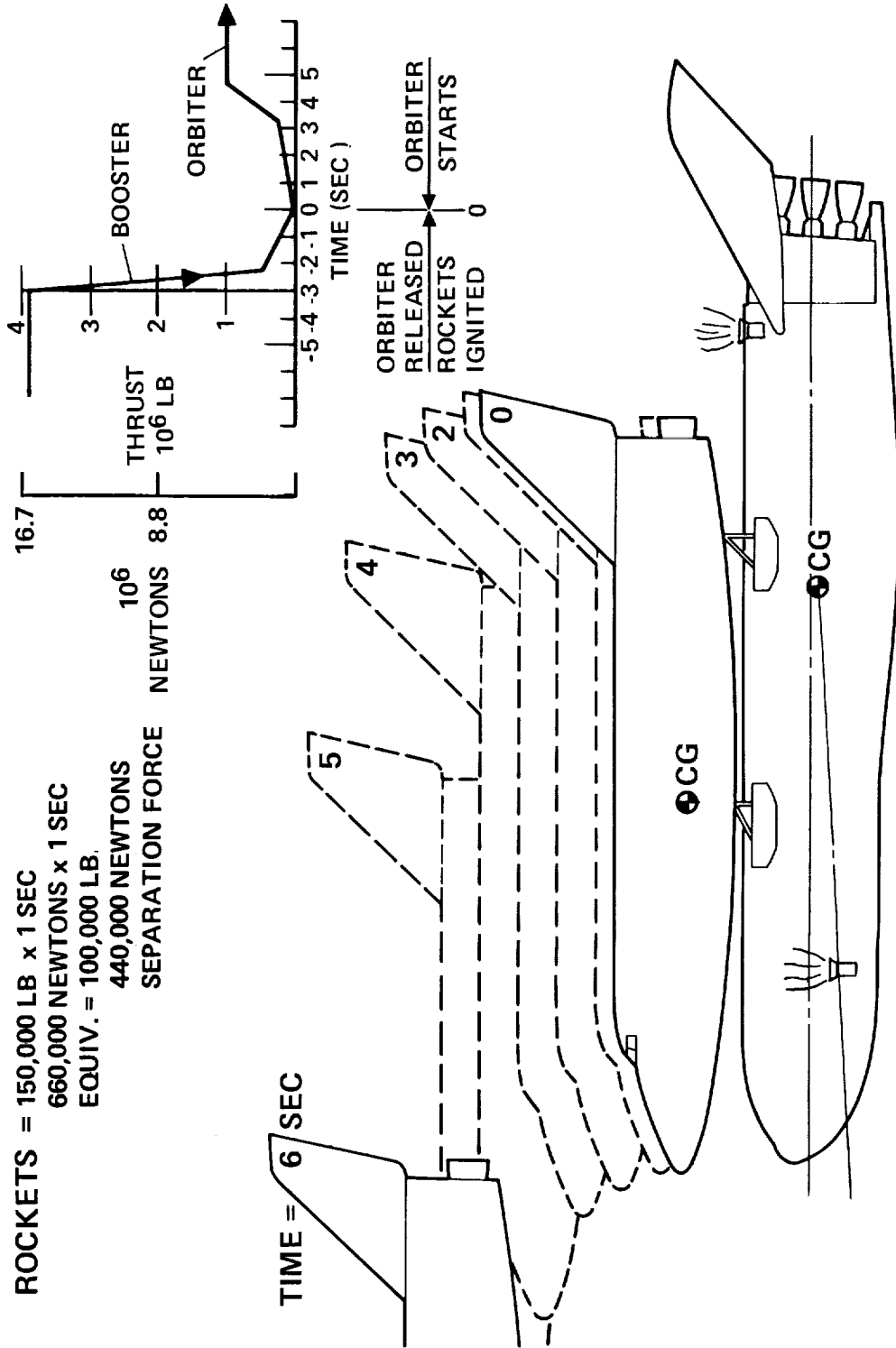


Figure 5

PISTON

(Figure 6)

The system was sized to give 100,000 lb.-sec. (440,000 Newton-sec) of impulse. This requires a 3,000-psi (207×10^6 Newtons/sq.m) gas generator, 10-inch diameter (25 cm diameter) by 60-inch stroke (152 cm stroke). Because the piston is inherently limited in its ability to take side load, the booster and orbiter rocket engines are not thrusting throughout the one second of piston extension. The thrust scheduling is shown in the upper right corner; one second of coast time at zero thrust is shown.

The piston is located on the planform centerline of both vehicles. The fore-aft location was chosen so that the piston force is directly through the orbiter cg. The reaction on the booster is ahead of its cg; the booster, therefore, has a pitchdown rate of 7° per second at separation.

Diagram illustrating the pitch motion of a ship over a 6-second period. The ship is shown in a side profile, with the center of gravity (CG) marked. The pitch angle is indicated by a curved arrow at the stern, labeled "PITCH DOWN RATE 7°/SEC (ACS LIMIT)". The time axis is labeled "TIME (SEC)" and ranges from -6 to 7. The piston actuates at time 0, and the end of the stroke is marked at time 1. The ship's pitch is shown in six stages (0 to 5) as dashed outlines, indicating a downward pitch motion.

551

RAILS

(Figure 7)

The concept uses orbiter thrust to accelerate along rails attached to the booster. The rails are inclined 5° to the booster centerline. Orbiter thrust is applied parallel with the rail. Because of the low orbiter cg, this puts a large nosedown moment on the orbiter which in turn puts a large nosedown load on the booster. At separation, the booster has a nosedown angular velocity of 9.8 deg/sec .

Because the thrust/weight of the orbiter is relatively low, the transverse acceleration up the inclined rail is also low. Consequently, the separation distance between the vehicles is much worse than for the rocket and piston concepts.

Timing is particularly critical. If separation is initiated earlier than that shown on the thrust schedule in the upper right corner, the orbiter is unable to accelerate forward. If separation is initiated later than shown, the booster will have an even higher pitchdown rate after separation.

Compared with the rocket and piston concepts, the rail concept has a poorer separation trajectory.

RAILS

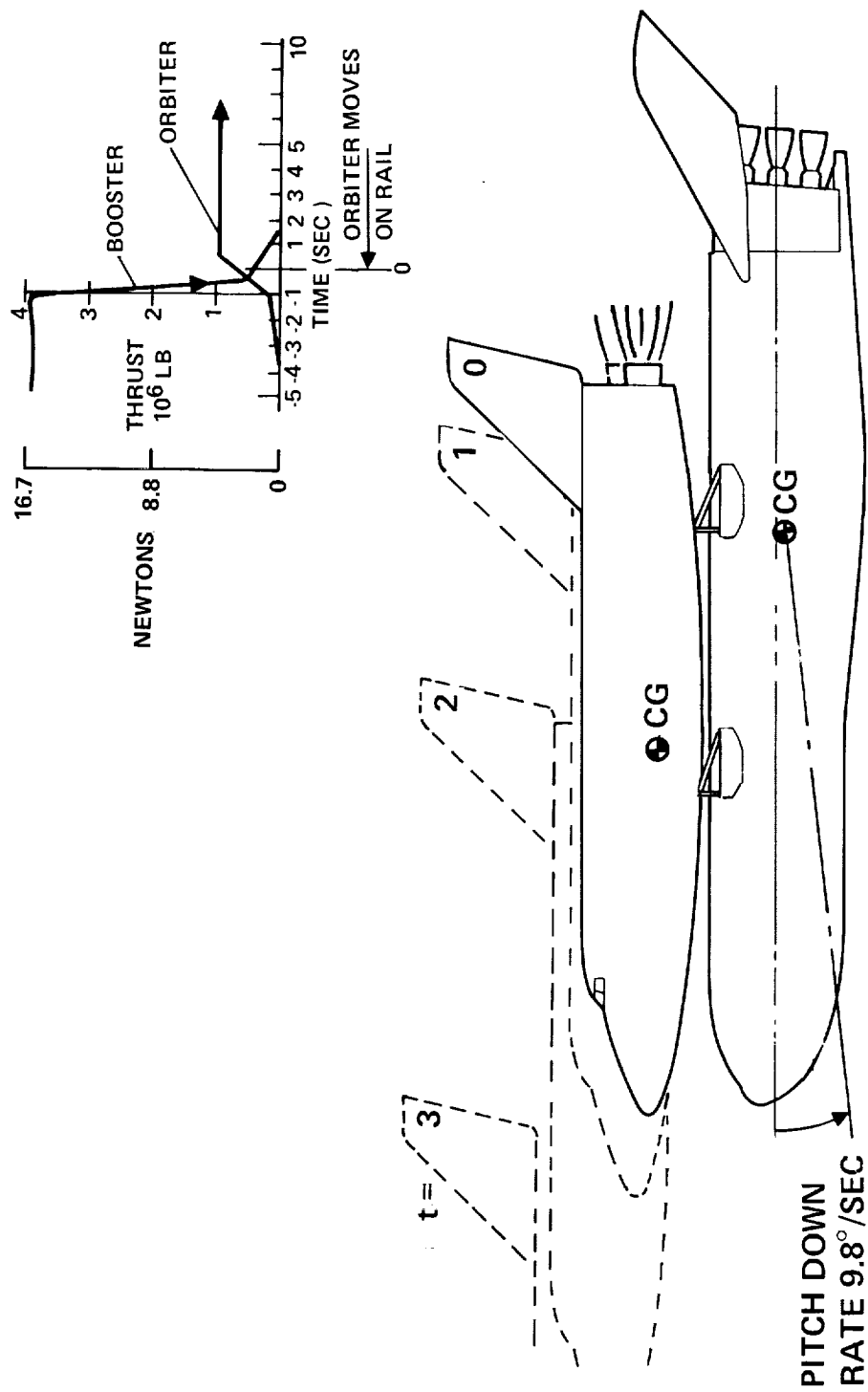


Figure 7

LINKS USING ORBITER THRUST

(Figure 8)

This concept is similar to the rail concept except that rotating links are used to provide the transverse acceleration forces. Thrust scheduling is shown in the upper right corner. The overlapping and timing requirements are similar to that discussed for the rail concept. Gimbals for the booster engines are significant as the effective cg moves towards the booster centerline during movement of the separation linkage.

Separation is initiated by breaking the vertical connection at each fore and aft attachment point. The increasing thrust/weight of the orbiter rotates the links and provides a transverse velocity when the orbiter subsequently releases from the links.

Pitchdown rates are partly compensated by orbiter engine gimbaling, however, at separation the booster has a nosedown angular velocity of $3^\circ/\text{sec}$.

Throughout the separation maneuver, loads in the links are much less than those occurring during the boost phase.

LINKS Using Booster Thrust

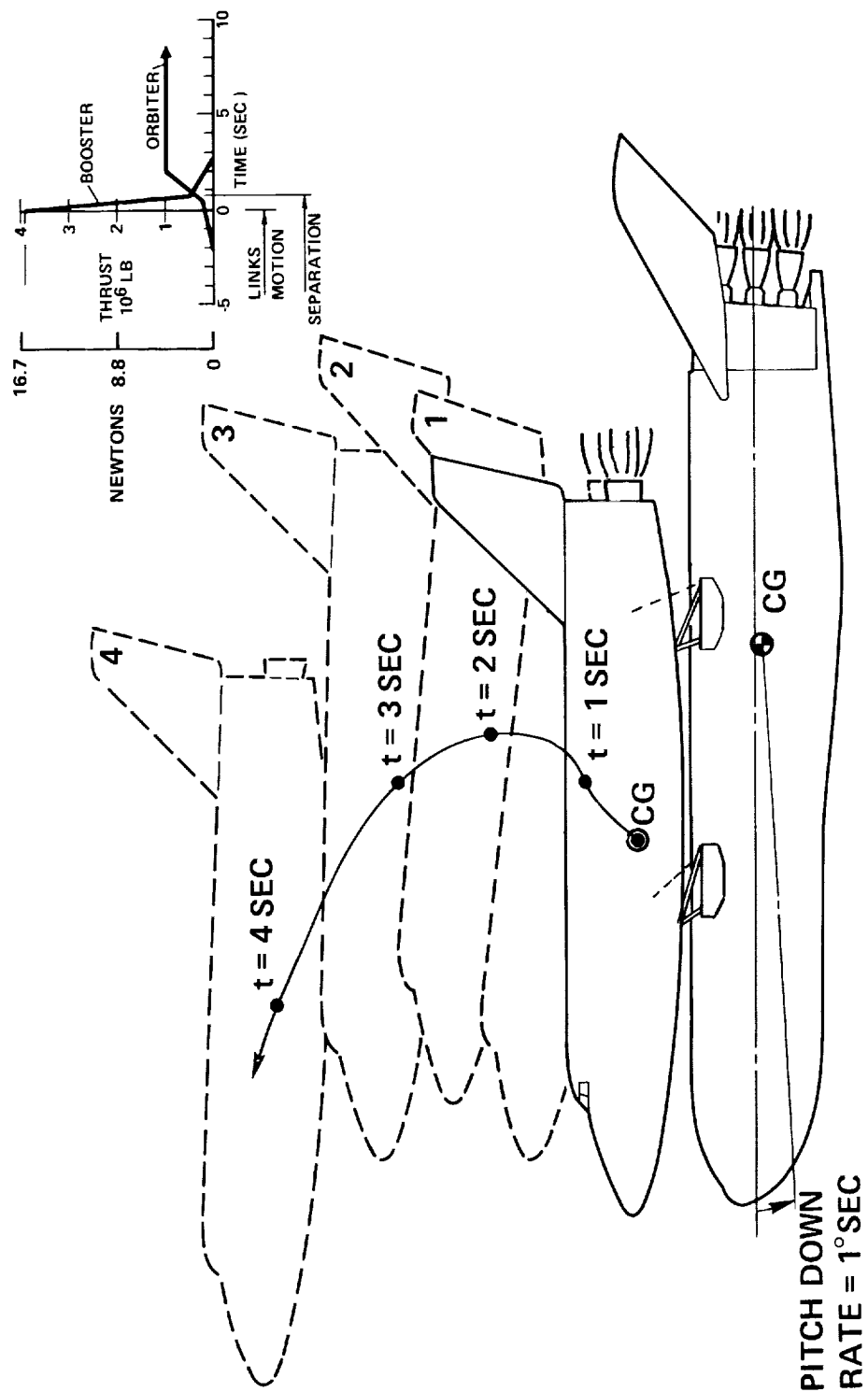


Figure 9

SEPARATION DISTANCE VS. TIME

(Figure 10)

Using trajectory data given in the previous five figures, separation distances for all concepts are shown. The distance referred to is the closest point between booster and orbiter. Links using orbiter thrust and the rail concepts both have poor initial separation trajectories and the chances of recontact are relatively high. Piston and rocket concepts are equal since both assume 100,000 lb -sec (440,000 Newton-sec) of separation impulse. Links using booster thrust provide the best separation trajectory. This is because booster thrust inherently provides much higher forces than the other concepts.

LINKS Using Orbiter Thrust

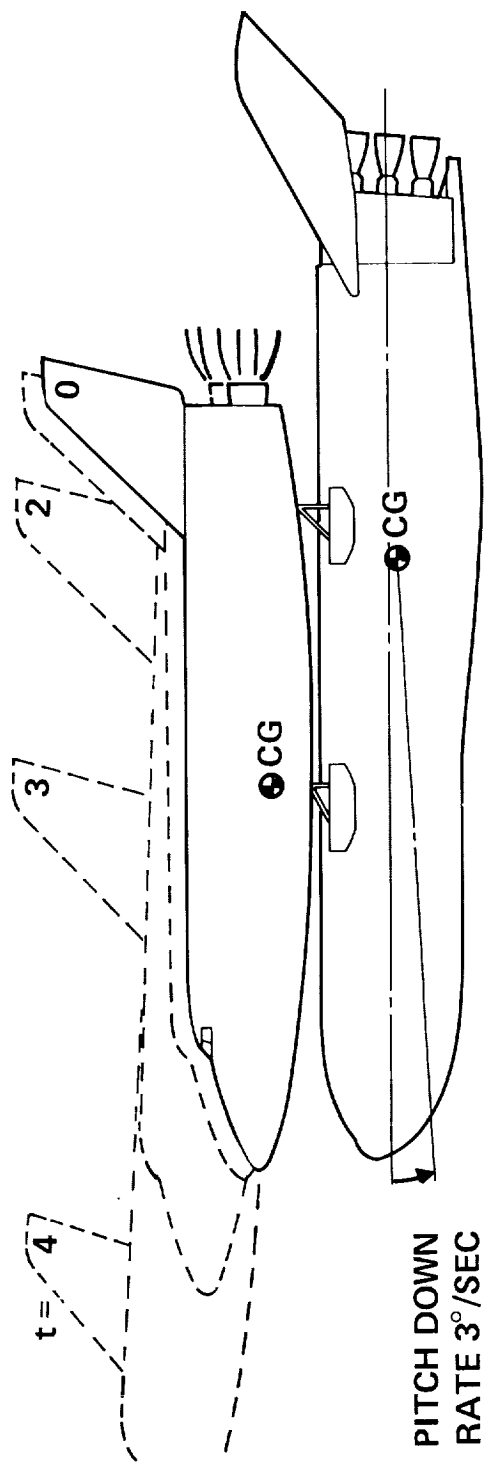
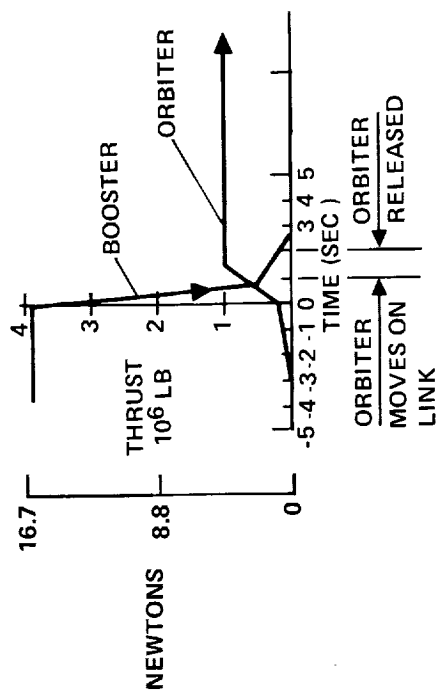


Figure 8

LINKS USING BOOSTER THRUST

(Figure 9)

The concept is similar to that described on the previous page, except that the inclined links are reversed. At start of separation the vertical connection is broken and the links are free to rotate. Since booster thrust is approximately five times greater than orbiter thrust, the separation trajectory is much better than when orbiter thrust is used. Because of the high thrust/weight of the booster, the orbiter thrust level is not significant.

Thrust scheduling is shown in the upper right-hand corner, with separation being initiated at the start of the booster engine thrust tail off. Booster pitchdown rate is only 1° per second because the available gimbal authority of the booster engines is large.

Loads in the links are much higher than for the other link concept; however, they can be kept within the loads experienced during the boost phase.

At release the separating velocity is 13 fps (4 m/sec); three seconds after release, the closest point between booster and orbiter is 60 feet (18.3 m).

SEPARATION DISTANCE VS. TIME

SEPARATION
DISTANCE

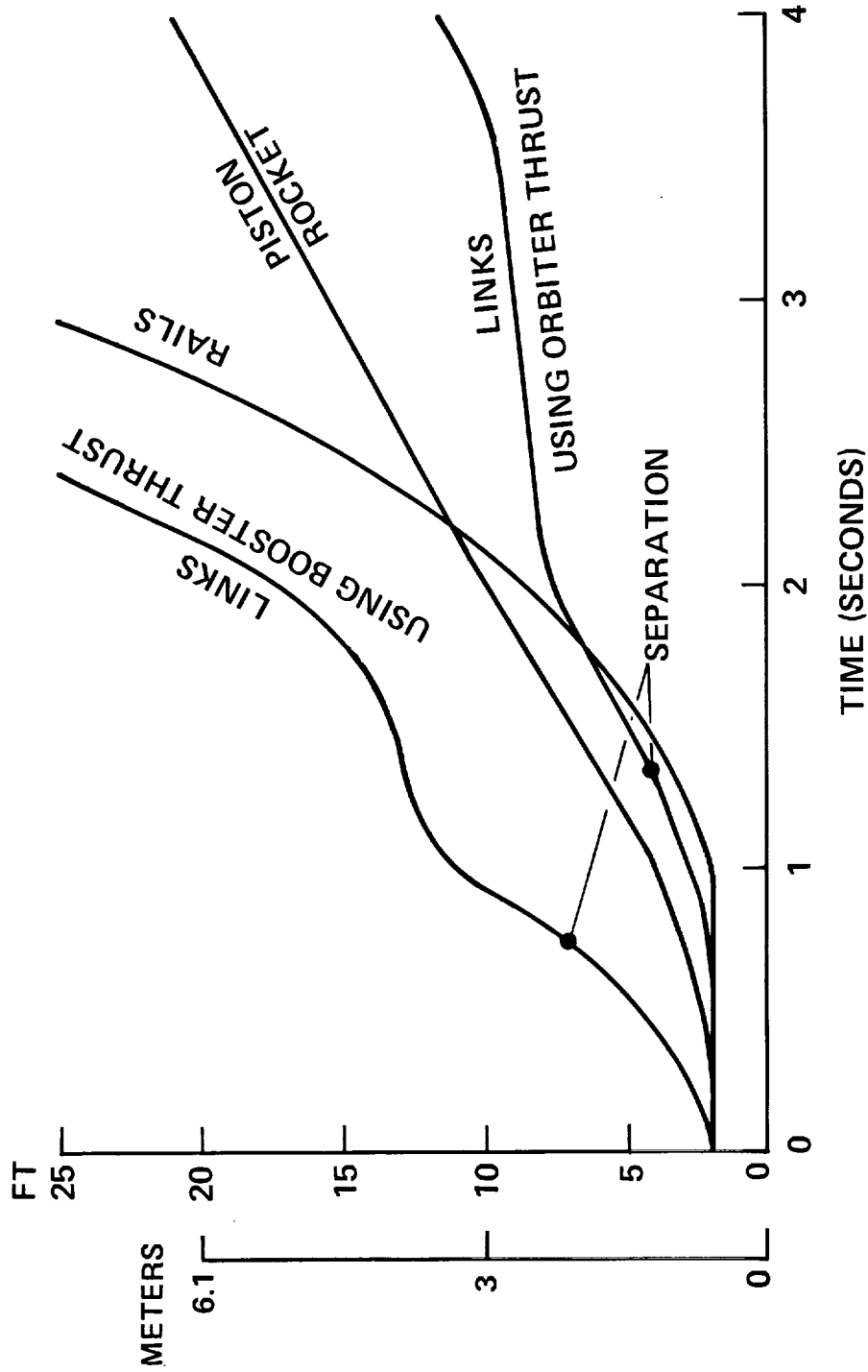


Figure 10

SEPARATION SCHEME WEIGHTS

(Figure 11)

This shows the weights of each separation concept. In each instance, the weight of structure to attach the booster to the orbiter is much greater than the weight of the system that separates the booster from the orbiter. The coast time for the lateral rocket and piston concepts (calculated from the sensitivity value of 1,200 pounds (540 kg) of booster inert weight per second of coast time) results in a significant penalty to these two concepts. The data show that the weight penalties due to attachment and to coast time are much greater than the weights for separation.

SEPARATION SCHEME WEIGHTS

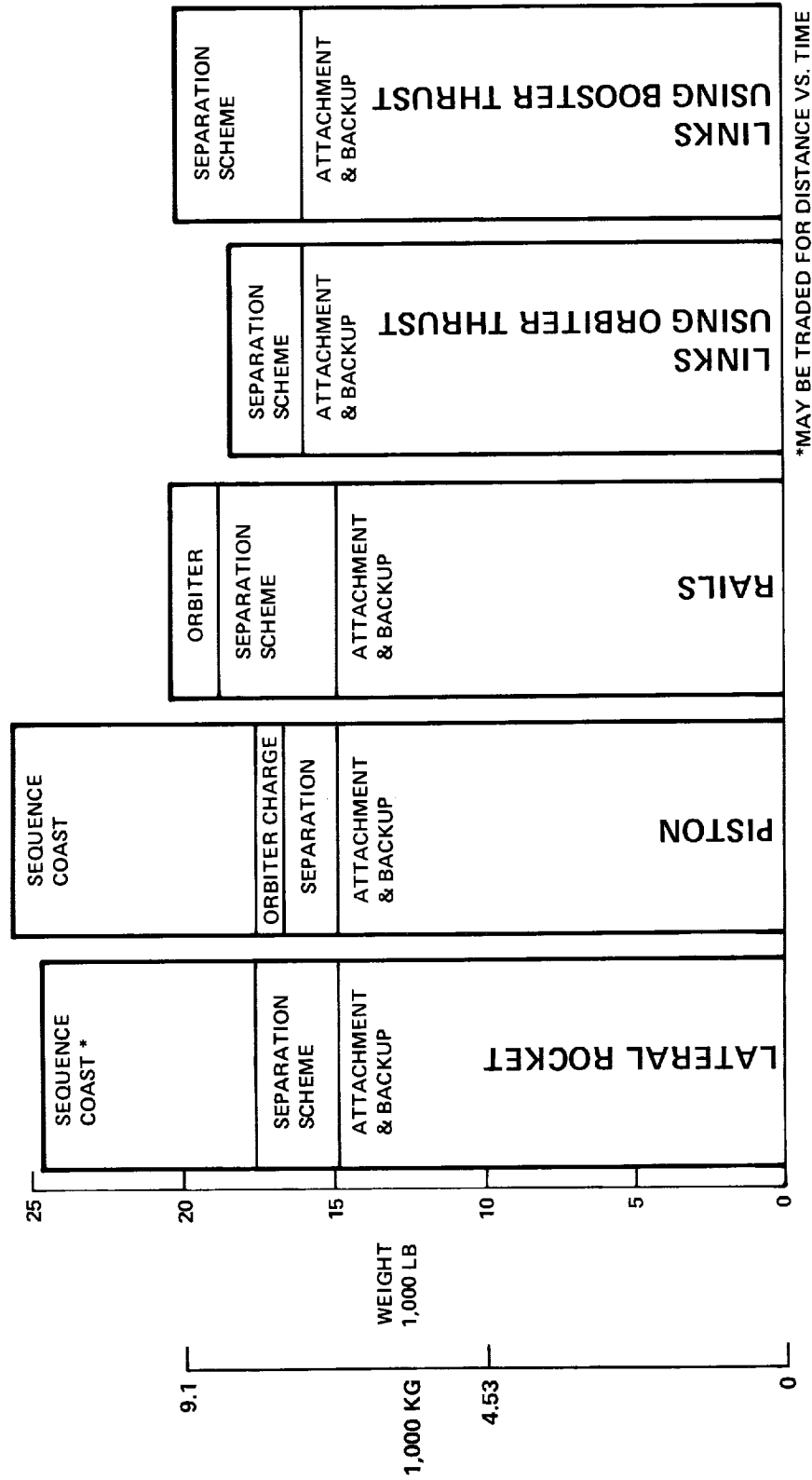


Figure 11

FAILURE MODES

(Figure 12)

A significant feature of each concept is its tolerance to failures. This chart indicates the consequences of various failure modes.

The rocket concept cannot tolerate full or partial booster thrust since the booster vertical fin will impact the orbiter. Early release of the attachment will have the same consequences. The piston is intolerant of both booster thrust, orbiter thrust, and early or late release since differential accelerations between booster and orbiter will bend the rod of the extending piston.

Rails are intolerant of booster thrust, zero orbiter thrust and early release because all of these prevent the orbiter from accelerating along the rails. Because of the relatively poor separation trajectory, incorrect attitude control by the rocket engine gimbal system of either the booster or the orbiter could result in recontact.

All comments given above for the rail concept are equally applicable to the link concept that uses orbiter thrust.

The link concept that uses booster thrust cannot tolerate total thrust loss of the booster rocket engines, nor failure of the attitude control gimbal system of the booster engines.

The rocket concept and link concept using booster thrust are most tolerant to the types of failures assumed.

FAILURE MODES

		ROCKET	PISTON	RAILS	LINKS ORB. THR.	LINKS BST. THR.
BOOSTER THRUST	FULL	X	X	X	X	
	PARTIAL	X	X	X	X	
	ZERO					X
ORBITER THRUST	FULL		X			
	PARTIAL ZERO		X	X	X	
RELEASE	EARLY	X	X	X	X	
	LATE		X			X
ATT. CONT.	BOOSTER			X	X	X
	ORBITER			X	X	

X NON SAFE SEPARATION

Figure 12

VERTICAL LEADING EDGE HEATING

(Figure 13)

This shows the results of an analysis of the plume heating of the orbiter engine on the leading edge of the vertical fin of the booster. Shown are the thrust time history for the worst concept (links) and the approximate boundary of the plume. The graph shows the temperature at the spanwise location of the fin leading edge that is in line with the centerline of the orbiter engines before separation. Even with thin leading edge gages, the temperatures are well within the capabilities of TD NiCr material. The points at the right side of the graph show that the temperature rise would be about 200° F (366 K) for each additional second that the orbiter remains on the booster.

VERTICAL LEADING EDGE HEATING LINKS

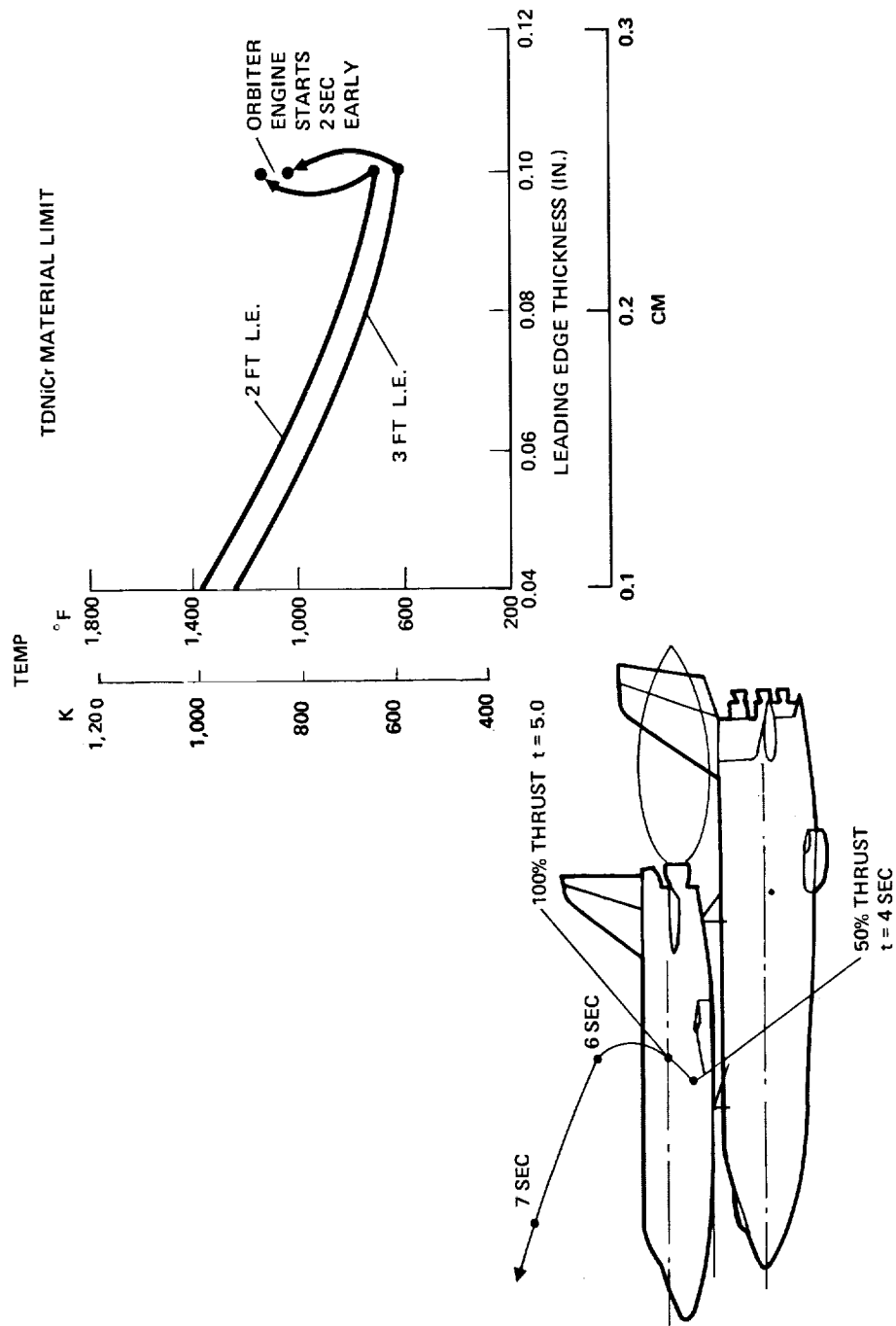


Figure 13

COMPARISON NORMAL STAGING

(Figure 14)

This chart summarizes data given in preceding pages. Because of coast time, the rocket and piston concepts are heavier than the others. Rails and links using orbiter thrust have poor separation distances. Rocket and piston concepts require zero g start of the orbiter engine. Because they react ahead of the cg of the booster, the piston, rails and links using orbiter thrust concepts give high post-separation pitchdown rates to the booster. These three concepts are also less tolerant to failure modes.

The most significant adverse feature of the comparison is that the two concepts that use orbiter thrust to provide the separation energy do not provide adequate separation distances and are not failure tolerant. The other three concepts are satisfactory; the links using the booster thrust concept are slightly superior.

COMPARISON Normal Staging

	ROCKET	PISTON	RAILS	LINKS ORB. THRST	LINKS BSTR. THRST
WEIGHTS			✓	✓	✓
DISTANCE	✓	✓			✓
ORB. ENG. START AT POS. g			✓	✓	✓
BOOSTER PITCHDOWN	✓				✓
FAILURE MODES	✓				✓

✓ GOOD

Figure 14

ABORT AT MAXIMUM αq

(Figure 15)

If separation is initiated at maximum dynamic pressure, the loads shown are being transmitted through the interconnect structure. Since the booster is thrusting, the orbiter, if released, would decelerate aft and crash into the fin of the booster. Wind shears at max αq conditions result in the loading conditions shown. Under headwind conditions, the airloads will tend to separate the orbiter, however, in the tail wind case, a large tail-down reaction opposes separation.

The chart also shows that parts of the orbiter and booster structure are designed at maximum αq . If either booster or the orbiter experiences an increase in local angle of attack, then either the structure will fail or it must be beefed up to carry the additional loads. Ideally, the separation system should prevent both booster and orbiter from increasing its angle of attack throughout the separation trajectory maneuvers.

ABORT AT MAX. α q

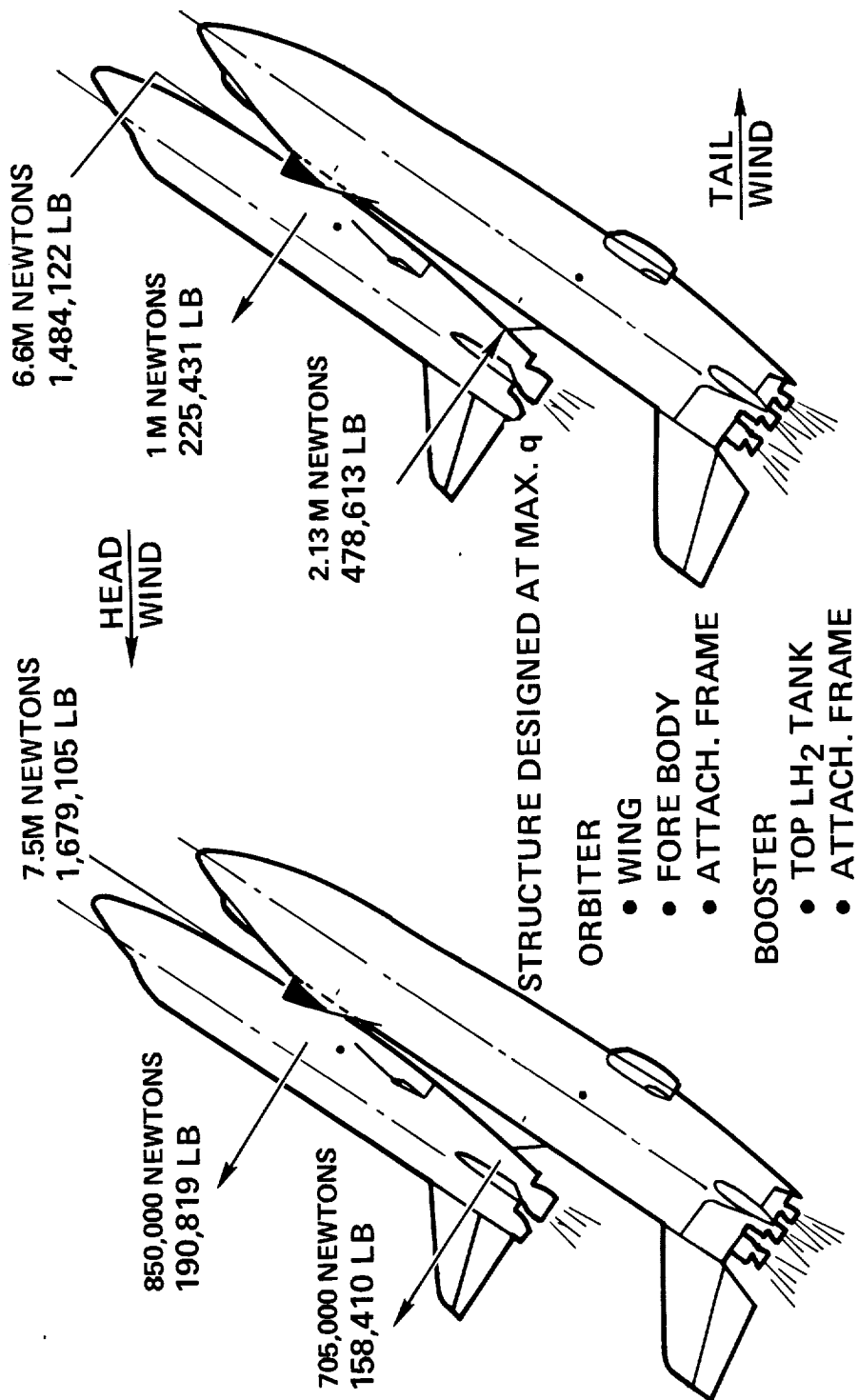


Figure 15

PROBLEMS & PENALTIES

ABORT AT MAX αq

(Figure 16)

Concepts that use orbiter thrust are totally inadequate in providing acceptable separation at maximum αq because of the relatively low thrust/weight of the orbiter. The piston and rocket concept incur significant weight penalties because they have to be resized upward by a factor of 6 to overcome the heavier booster weight plus aerodynamic forces. Additionally, the piston reaction pitches the booster into higher aerodynamic loadings.

PROBLEMS & PENALTIES

Abort at Max. αq

	ROCKET	PISTON	RAILS	LINKS ORB. THRST.	LINKS BSTR. THRUST
BOOSTER THRUST	* 43%	43%	0	0	100%
ORB. ENGINE AT MAX. THRUST	YES	YES	YES	YES	NOT CRIT.
RELATIVE FORE/AFT ACCEL.	SAME	SAME			
SEPARATION TRAJECTORY			NOT ACCEPTABLE		
BOOSTER ATTITUDE	PARTIAL	NOT ACCEPTABLE			
Δ WEIGHT PENALTY	2,720 KG	910 KG ORB. 2,040 KG BSTR.			SMALL

* ALTERNATIVE = NEG. g RESTART FOR BOOSTER & ORBITER ENGINES

Figure 16

ABORT
IMMEDIATELY OFF PAD - ROCKETS/PISTONS
(Figure 17)

The abort situation postulated is one that demands separation as quickly as possible just after liftoff. The malfunction is assumed to occur when the mated configuration has just lifted off and is one second into the flight. Under these conditions, the orbiter cannot be released immediately because the booster would continue to accelerate and crash its fin into the orbiter. The orbiter would also fall back on the pad, damaging the pad and destroying the booster by fire and explosion. Terminating booster thrust will have similar consequences.

It is, therefore, paramount that the booster keep thrusting and that the orbiter engine be accelerated to the maximum available thrust level before separation is initiated. Further, it is important that each stage continue to accelerate away from the pad for at least 18 seconds. Otherwise, the overpressure due to ground impact of one stage will also destroy the other. Ground winds, tower clearance, low available thrust/weight on each stage, and plume heating are additional factors that complicate separation at this point in the trajectory. Immediately at alarm, the orbiter engines are started while the booster engines are maintained at maximum thrust. Because both concepts are intolerant of differential longitudinal accelerations, the booster thrust must be reduced to about 65% of maximum thrust so that the axial acceleration of booster and orbiter are equal. Both have a thrust/weight ≈ 1.1 . The separation system is then activated. To produce a separation trajectory similar to that shown at normal staging a separation thrust of about six times that required at normal staging is required. The links using the booster thrust concept (not shown) are superior under these abort conditions because maximum booster thrust is maintained throughout the separation sequence. This provides maximum altitude and maximum gimbal authority during the separation maneuvers.

ABORT Immediately off Pad - Rockets/Pistons

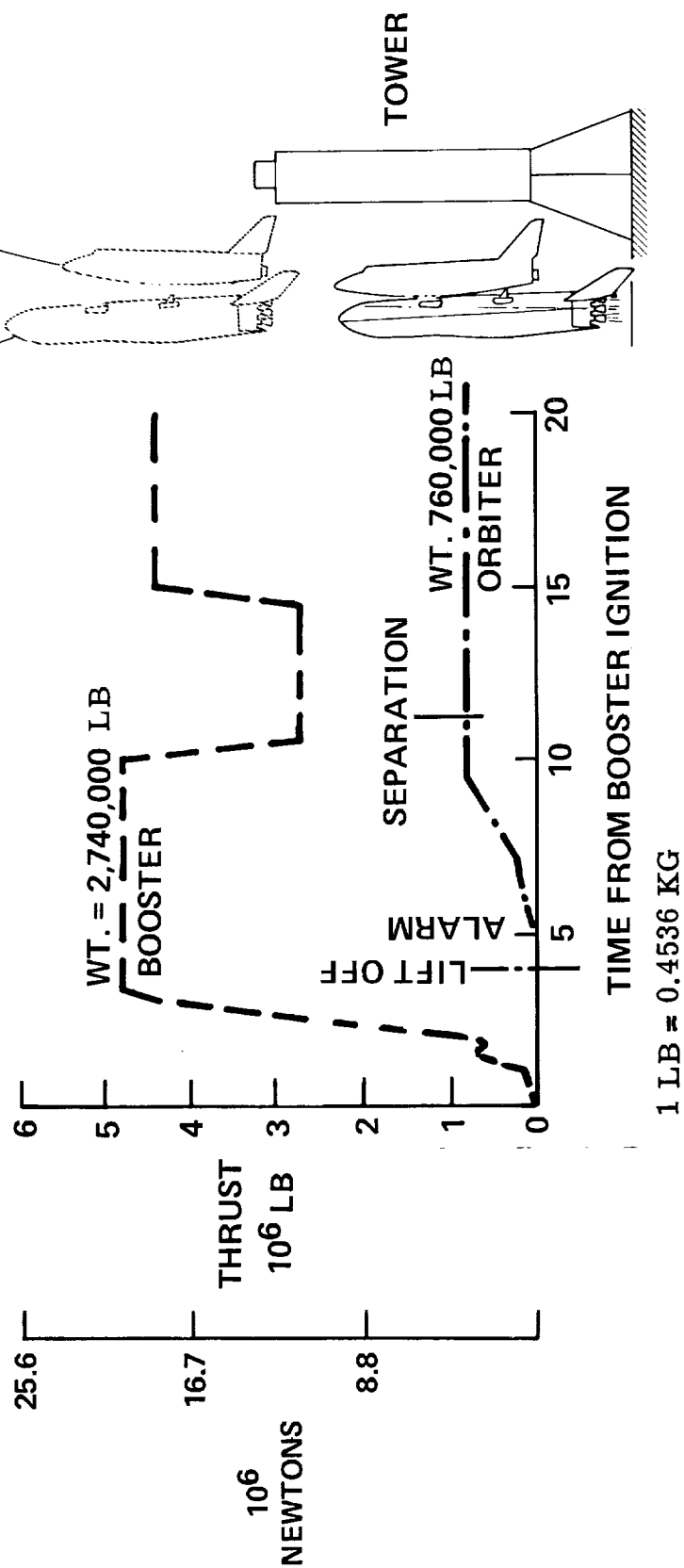


Figure 17

PLUME HEATING
ABORT IMMEDIATELY OFF PAD

(Figure 18)

This chart shows the temperature of the booster fin leading edge for the separation trajectory given on the previous page. Temperatures during abort off the pad are much higher than those experienced during normal staging. This is because of the slower separation trajectory and smaller concentrated plume for the low altitude case.

PLUME HEATING **Abort Immediately off Pad**

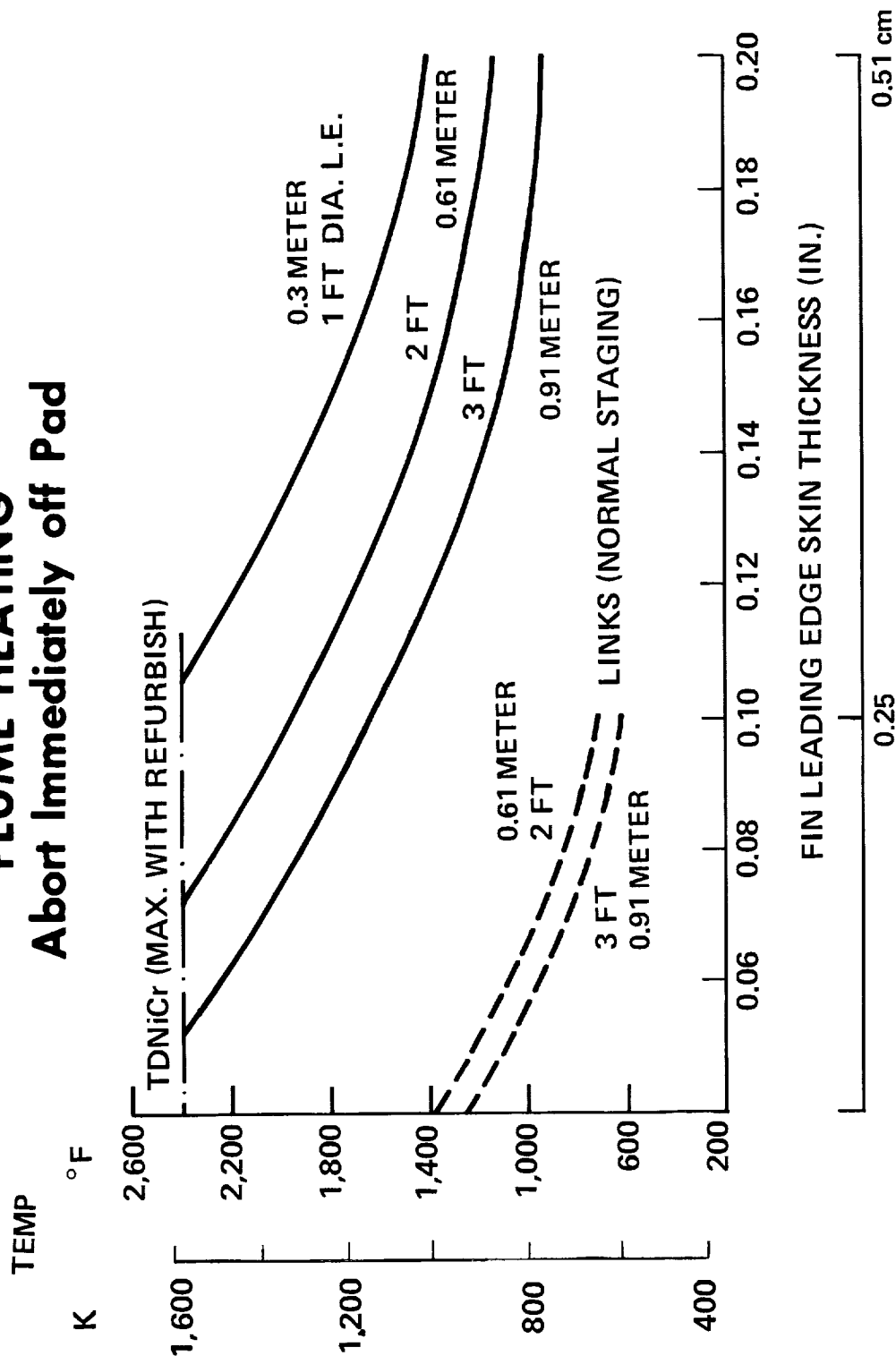


Figure 18

PROBLEMS & PENALTIES
ABORT IMMEDIATELY OFF PAD

(Figure 19)

Concepts that use orbiter thrust are not acceptable because the booster engines have to be throttled back, making attitude control in the presence of ground winds very difficult. Piston and rocket concepts incur weight penalties over that required for normal staging mainly because of the higher weight of the booster. The link using booster thrust concept has an acceptable separation trajectory, has no weight penalty, and requires no booster throttling.

PROBLEMS & PENALTIES **Abort Immediately off Pad**

	ROCKET	PISTON	RAILS	LINKS ORB. THRST.	LINKS BSTR. THRST.
BOOSTER THRUST	65%	65%	58%	58%	100%
ORBITER ENGINE START	<div> <div>← FULL THRUST NEEDED →</div> </div>				
RELATIVE FORE/AFT ACCEL.	SAME	SAME	MAX. POS.	MAX. POS.	NOT CRIT.
SEPARATION TRAJECTORY		NOT ACCEPT.	POOR	POOR	
BOOSTER ATTITUDE CONTROL	POOR	POOR	NOT ACCEPTABLE		
ΔWEIGHT PENALTY	2,720 KG	910 KG ORB. 2,040 KG BSTR.	SMALL		

Figure 19

CONCLUSIONS

(Figure 20)

This table compares the main features of the five concepts at the three points in the trajectory. Concepts that use orbiter thrust are poor at normal staging and are not acceptable for abort.

Rocket and piston concepts have excellent separation characteristics at normal staging, but incur significant penalties for abort. The piston is probably not acceptable for immediate separation along the boost trajectory.

The link concept, using booster thrust, has excellent separation characteristics at normal staging. In addition, this concept has the inherent capability to provide immediate separation along the entire boost trajectory for negligible penalties.

COMPARISON

COMMON PROBLEMS: STRUCTURAL DYNAMICS, FAILURE MODES, TIMING, QUAL. TEST.

	NORMAL STAGING	ABORT AT q MAX.	ABORT IMMEDIATELY OFF PAD
ROCKET	GOOD	+2,720 KG THROTTLING	+ 2,720 KG THROTTLING
PISTON	GOOD	POOR ATTITUDE CONTROL +2,500 KG THROTTLING	POOR ATTITUDE CONTROL + 7,500 KG THROTTLING
RAILS	POOR SEPARATION	POOR SEPARATION NO ATTITUDE CONT.	POOR SEPARATION NO ATTITUDE CONTROL
LINKS (ORBITER THRUST)	POOR SEPARATION	POOR SEPARATION NO ATTITUDE CONT.	POOR SEPARATION NO ATTITUDE CONTROL
LINKS (BOOSTER THRUST)	GOOD	SMALL PENALTIES	SMALL PENALTIES

Figure 20

FLIGHT DYNAMICS OF A STRAIGHT-WING SPACE SHUTTLE BOOSTER DURING ENTRY

By L.G. Kimbrel and J.T. Patha
The Boeing Company
Seattle, Washington

INTRODUCTION

Critical problem areas are investigated for a straight-wing space shuttle booster during entry. A six-degree-of-freedom entry simulation is utilized to study vehicle dynamics and control system requirements which include attitude control propulsion system (ACPS) propellant usage requirements. Linear analysis is utilized to supplement the non-linear simulation where a critical problem requires additional definition.

Dynamics investigations include:

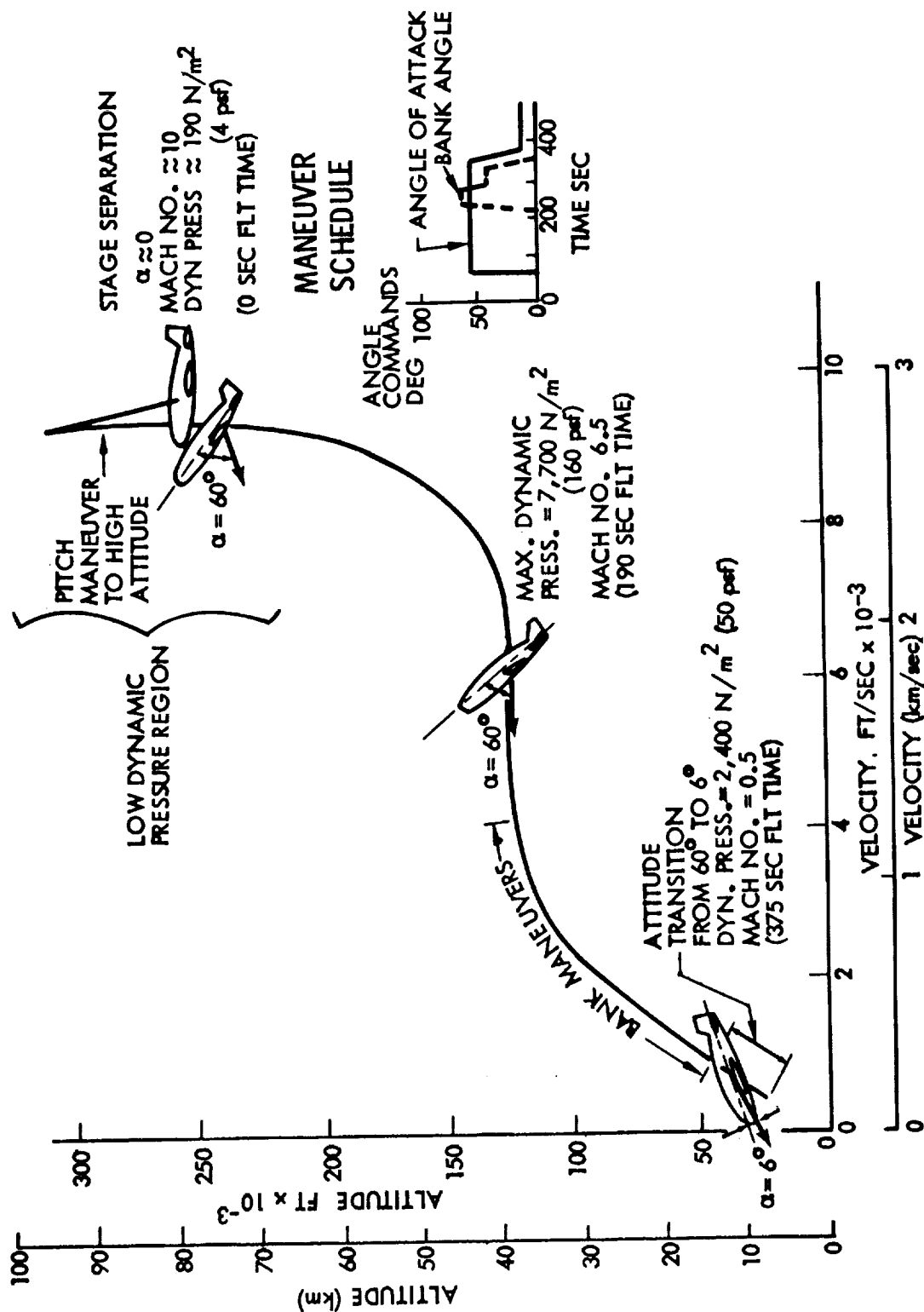
1. Variations in autopilot and guidance law including a modified Apollo control law.
2. Transition maneuver from high to low attitude angle at termination.
3. ACPS size and dead bands.
4. ACPS minimum pulse size.
5. Wind disturbance.
 - a) Wind shear
 - b) Gust
 - c) Turbulence
6. Lateral c.g. offset.
7. Different levels of aerodynamic lateral-directional stability.

FACTORS AFFECTING BOOSTER ACPs (Slide 1)

The straight-wing booster entry is characterized by high angle of attack (alpha) and relatively low dynamic pressure over most of the trajectory. Low dynamic pressure coupled with a configuration that has acceptable aerodynamic properties at high alpha and a carefully tailored autopilot allows primary vehicle control by an ACPs with minimum propellant requirements. Trajectory control is achieved by angle-of-attack and bank-angle commands. The commands are precomputed to provide the minimum booster flyback range within operational constraints, e.g., normal load factor. Six separate flight regimes may be identified during booster entry. The salient dynamic and control characteristics during these regimes are:

- 1) Low dynamic pressure, low alpha region.
 - . Attitude and attitude-rate control feedbacks required for vehicle stabilization.
 - . Large control dead bands minimize ACPs propellant requirements.
- 2) Pitch-up maneuver.
 - . Pitch rate limit required to minimize ACPs propellant usage.
- 3) Intermediate dynamic pressure, high alpha region.
 - . Pitch and roll axis: rate feedback only.
 - . Yaw axis: attitude position and rate feedback.
 - . Lateral-directional stability allows vehicle rates to remain within control dead bands and results in minimum ACPs operation.
- 4) High dynamic pressure, high alpha region.
 - . Alpha trim becomes important and ACPs provides stability about pitch trim condition.
- 5) Banking maneuver during intermediate dynamic pressure, high alpha region.
 - . During maneuvers, yaw channel drives bank maneuver best at high alpha, and roll channel dead bands must be small enough to provide acceptable coordinated maneuver.
 - . Timing of bank maneuver reduces maximum dynamic pressure and avoids excessive aerodynamic forces and moments.
- 6) Transition maneuver to low angle of attack.
 - . Attitude and attitude-rate feedback with rate limit.
 - . Avoid adverse buffet region, avoid excessively low vehicle speed in wind spike region, and provide adequate pull-out altitude margin.

FACTORS AFFECTING BOOSTER ACPS



Slide 1

REQUIRED SIMULATION DETAIL FOR BOOSTER ENTRY (Slide 2)

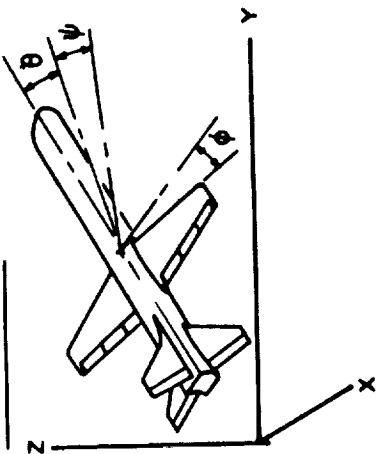
The six-degree-of-freedom space shuttle booster entry simulation is a complete representative of a vehicle with aerodynamic and reaction control. The program is used for vehicle stability verification, ACPS propellant usage computations, generalized performance trade studies, guidance, navigation, and flight control system development.

The booster entry simulation has the capability of taking into account the following effects:

- a. Three-axis guidance, navigation, and control laws with varying degree of logic representation.
- b. No restriction in magnitude of any of the angles associated with the vehicle motion.
- c. Aerodynamic and/or reaction control torque generation. Present aerodynamic control actuation system is second order with acceleration, rate, and position limits
- d. Non-linear aerodynamic forces and moments over any angle range.
- e. Rapidly varying vehicle weight, thrust, c.g., and moment of inertia
- f. Variable tolerance for all equipment and for all geometric and aerodynamic parameters (c.g. offset, thrust misalignment, gyro errors, etc.).
- g. Inertial and aerodynamic coupling.
- h. Wind effects:
 - . Gusts
 - . Shear
 - . Turbulence

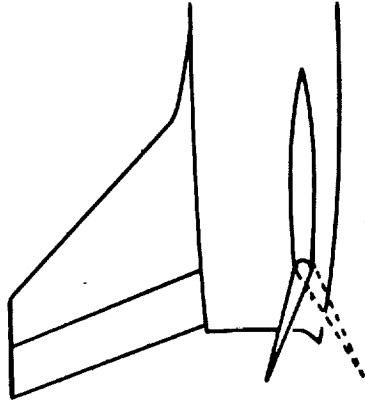
REQUIRED SIMULATION DETAIL FOR BOOSTER ENTRY

I RIGID MOTION



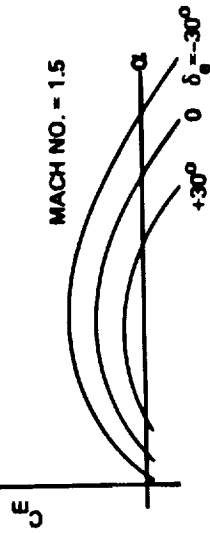
SIX RIGID BODY DEGREES OF FREEDOM WITH VARIABLE MASS PROPERTIES

II CONTROL ACTUATION



III AERODYNAMICS

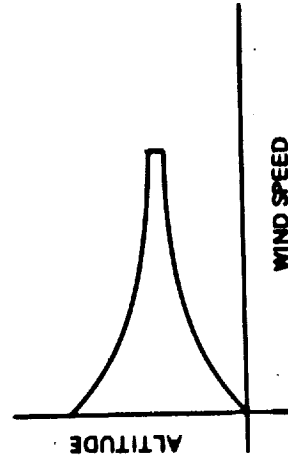
TYPICAL SIX COMPONENT FORCES AND MOMENTS ~ VARIABLE WITH MACH NUMBER



IV AUTOPILOT

- GUIDANCE STEERING COMMANDS
- ACFS
- AERODYNAMIC

V DISTURBANCES & TOLERANCES



Slide 2

TYPICAL FLIGHT DYNAMICS TIME HISTORIES (Slide 3)

586

The time histories shown are typical six-degree-of-freedom simulation machine plots. Slide 3(a) shows the normal load factor which has been constrained to approximately 5g by proper programming of the angle-of-attack command profile.

The bank angle ϕ and angle-of-attack α are shown in slide 3(b) and are the control responses to the command angles shown in slide 1.

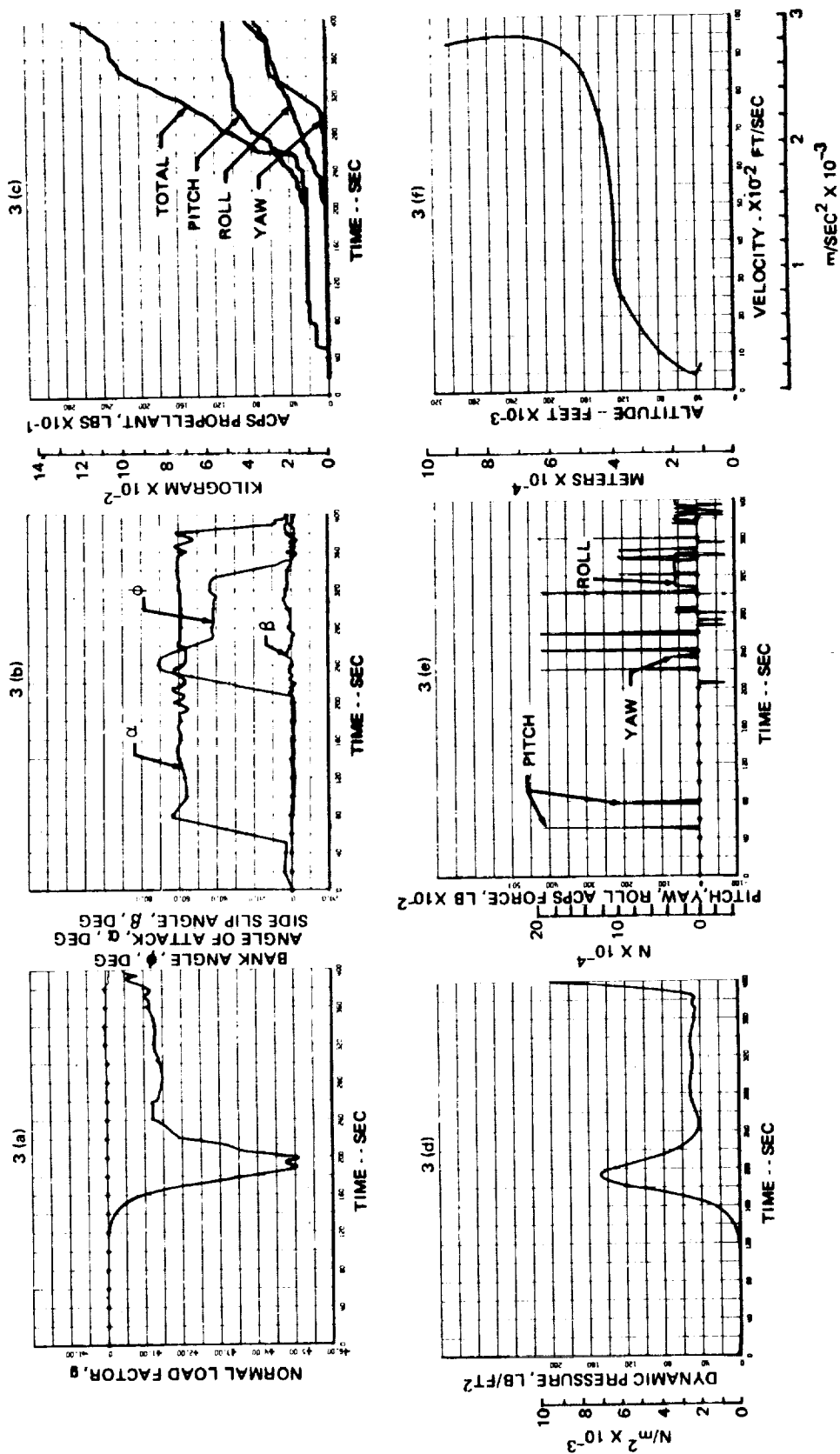
Slide 3(c) shows roll, pitch, yaw, and total ACPS propellant usage. It is noted that approximately 10% of the total propellant is used during the first half of the trajectory. During the last half 80% is used for bank maneuvers and stabilization, and 10% for transition.

Slide 3(d) shows the maximum dynamic pressure at high altitude and the second rise in dynamic pressure which results from the transition maneuver.

Slide 3(e) shows the ACPS force duty cycle for each of the three axes.

The vehicle altitude-velocity history is shown in slide 3(f). After staging, the booster is lofted to approximately 91 km (300,000 ft). Note that nearly horizontal flight is maintained during the velocity range from 2286 to 914 m/sec (7500 to 3000 ft/sec).

TYPICAL FLIGHT DYNAMICS TIME HISTORIES



Slide 3

FLIGHT CONTROL SCHEMATIC (Slide 4)

The booster entry flight control system utilizes modified Apollo logic. The logic is switched as angle of attack α becomes greater or less than 40° . The most efficient flight control system at high α was found to be bank-angle commands (δ_C) driving the yaw axis control system, with the roll axis providing rate cross-feedback that results in coordinated banking maneuvers.

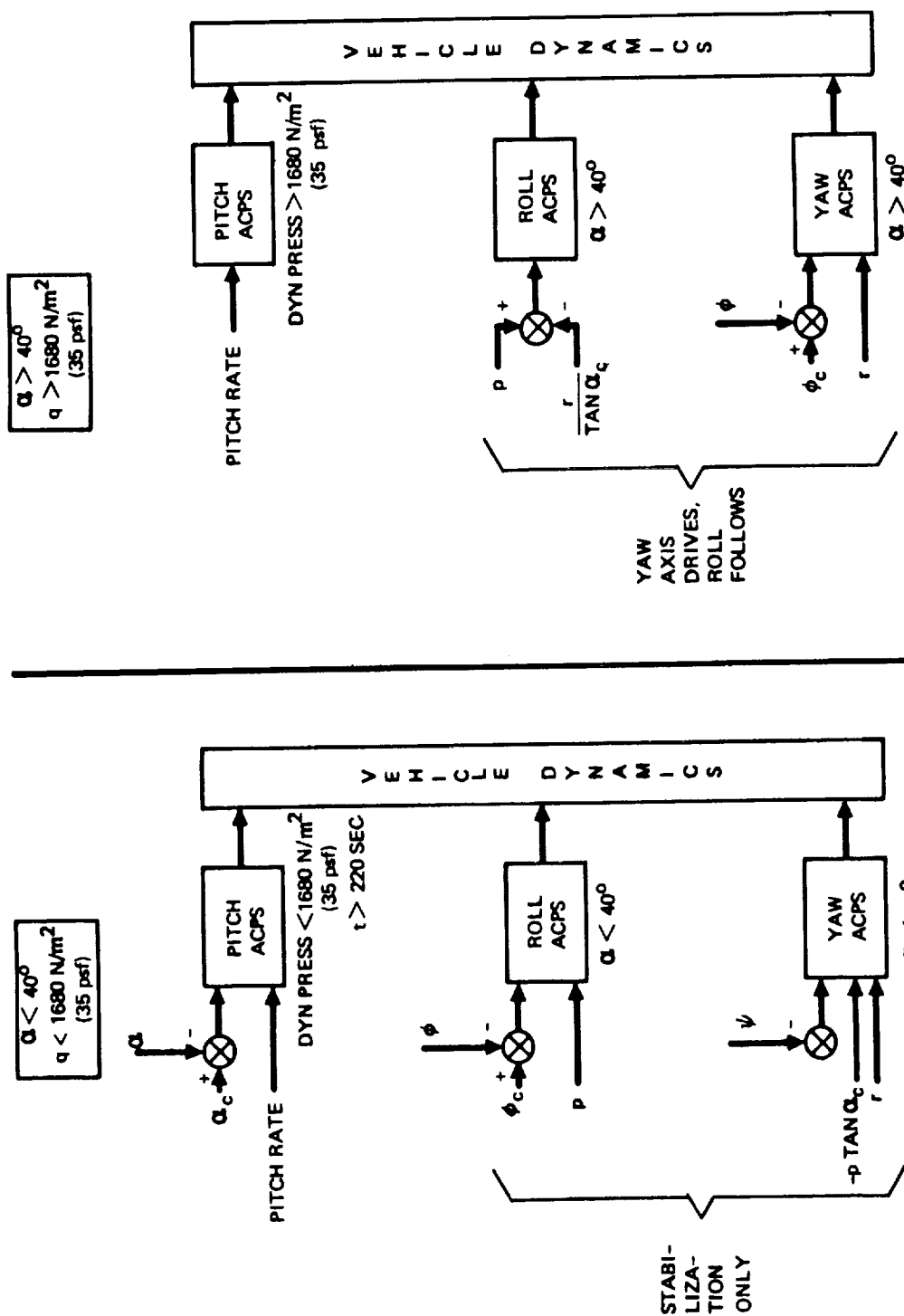
At low angle of attack, bank angle ϕ and roll rate p are fed back to the roll axis, while the yaw axis provides a cross-feed term ($p \tan \alpha_C$) to provide coordinated maneuvers.

In effect, the axis which requires the major rotation acceleration is the control driving axis, and the remaining lateral-directional axis follows and provides coordination.

To maintain stability at low dynamic pressure (less than 1676 N/m^2 (35 psf) the pitch system requires position and rate feedback. Pitch ACPS propellant is minimized for dynamic pressures greater than 1676 N/m^2 (35 psf) by utilizing the vehicle aerodynamic pitch trim capability and providing only damping through the pitch ACPS.

At time t greater than 220 sec, the pitch angle position loop is closed to augment pitch stability and provide position feedback for the pitch-down transition maneuver. Large control dead bands will allow $(C_{n\beta})$ dynamic (adequate lateral-directional stability) to minimize ACPS propellant for non-maneuvering periods of flight. However, excessively large control dead bands in the following axis will result in uncoordinated maneuvers during the maneuvering periods of flight and allow large sideslip angles and excessive ACPS propellant usage. In this study, control gain was chosen to give the optimum fixed dead bands. A more optimum system would have variable control dead bands tailored for maneuvering and non-maneuvering flight.


FLIGHT CONTROL SCHEMATIC



Slide 4

The areas in which additional major gains might be made to reduce ACPs propellant consumption are (1) proper aerodynamic configuration tailoring and (2) control law optimization.

ACPS SENSITIVITY FACTORS

	RANGE	APPROXIMATE INCREMENTAL ACPS PROPELLANT kg (lb)
• LATERAL C.G. OFFSET	0 - 0.0254 m (1.0 INCH)	230 (500)
• THRUSTER SIZE	0.5 - 1 MULTIPLIER	230 (500)
• DEAD BAND	0.5 TO 5 DEG & DEG/SEC	450 (1,000)
• CONTROL LAW	ROLL AXIS CONTROL-APOLLO CONTROL	1,820 (4,000)
• MANEUVER RATE	0.2 TO 5 DEG/SEC	230 (500)
• MIN PULSE SIZE	50 TO 160 mSEC	90 (200)
• CONFIGURATION TAIL TYPE		360 (800)
• BODY SHAPE	FLAT - ROUND	450 (1,000)
• WINDS		
SHEAR GUST	0 - 82.7 m/SEC (271 FT/SEC)	360 (800)
TURBULENCE	0 - 5.5 m/SEC (18 FT/SEC)	320 (700)
• ACPS THRUST LOSS WITH ALTITUDE	0 - 5%	90 (200)
• HIGH ATTITUDE TRANSITION MANEUVER	ACPS - AERO	540 (1,200)

Slide 5

BOOSTER ACPS PROPELLANT (Slide 6)

The effect of (changing) lateral-directional stability on ACPS propellant usage for a given straight-wing booster configuration is shown. The basic lateral-directional rotational aerodynamics are a function of side-slip angle β , angle of attack α , and Mach number; i.e.,

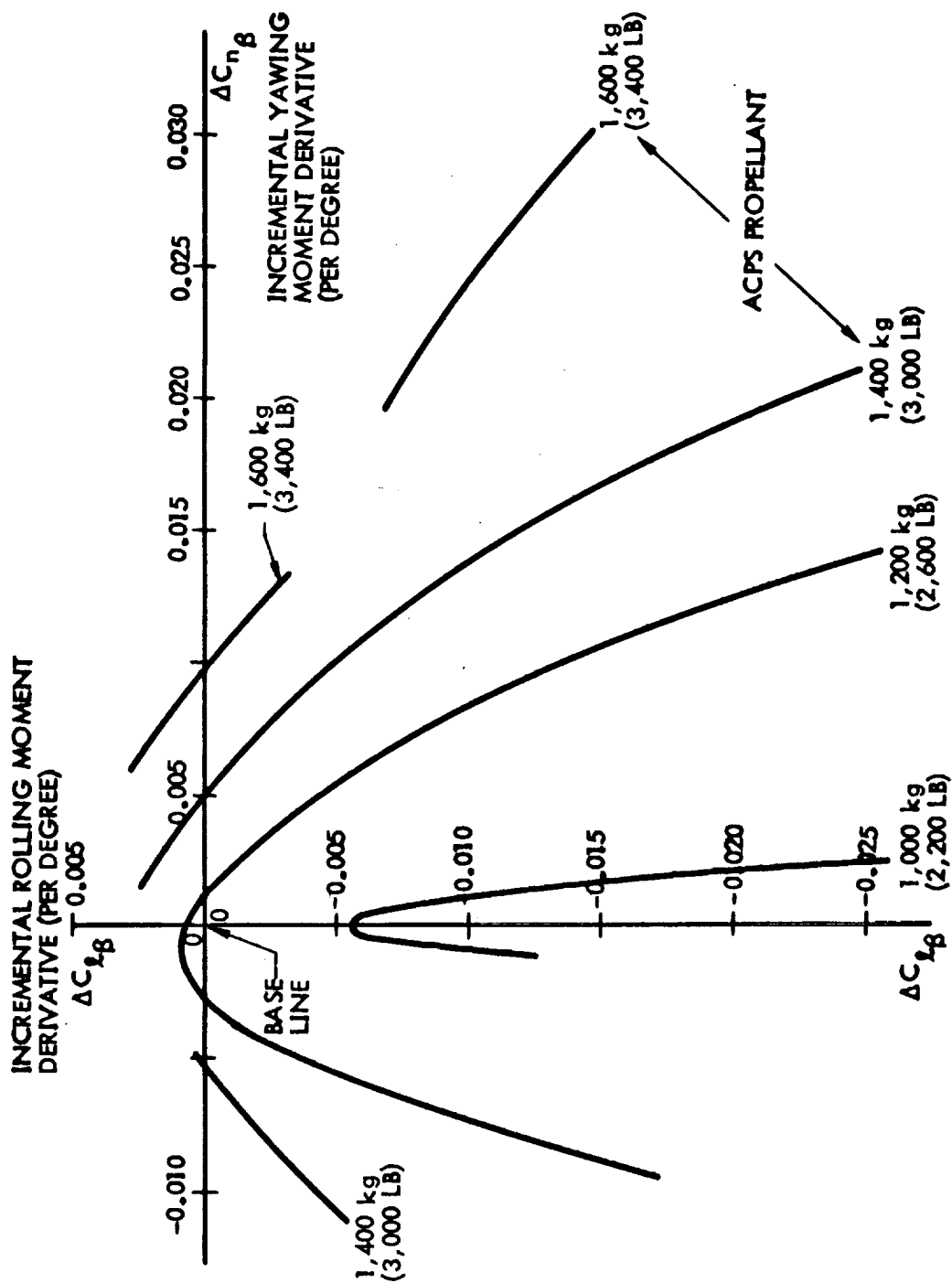
$$\left. \begin{array}{l} \text{Aerodynamic} \\ \text{controls} \\ \text{fixed} \end{array} \right\} \begin{array}{l} C_n = f_1 (\beta, \alpha, \text{Mach}) \\ C_l = f_2 (\beta, \alpha, \text{Mach}) \end{array} \quad \begin{array}{l} \text{Yawing moment coefficient} \\ \text{Rolling moment coefficient} \end{array}$$

In order to show first-order trends and gross effects, incremental changes in these coefficients have been made as a function of β only in the form

$$\begin{aligned} \Delta C_n &= C_{n\beta} \beta \\ \Delta C_l &= C_{l\beta} \beta \end{aligned}$$

The abscissa $\Delta C_{n\beta}$ is the incremental yawing moment derivative and the ordinate $\Delta C_{l\beta}$ is the incremental rolling moment derivative. Positive $\Delta C_{n\beta}$ results in increased directional stability - and negative $\Delta C_{l\beta}$ results in increased stable dihedral effect. Lines of constant ACPS propellant usage show the trend of decreasing propellant if $\Delta C_{l\beta}$ is increased negatively for a given $\Delta C_{n\beta}$. Propellant usage is increased if $\Delta C_{n\beta}$ is increased for a given $\Delta C_{l\beta}$. ACPS propellant usage is strongly dependent on the basic vehicle aerodynamic and control characteristics for a given vehicle configuration. The trends in this chart indicate the baseline configuration (i.e., $\Delta C_{n\beta}$ and $\Delta C_{l\beta} = 0$) is near optimum in terms of increasing or decreasing $\Delta C_{n\beta}$.

BOOSTER ACPS PROPELLANT

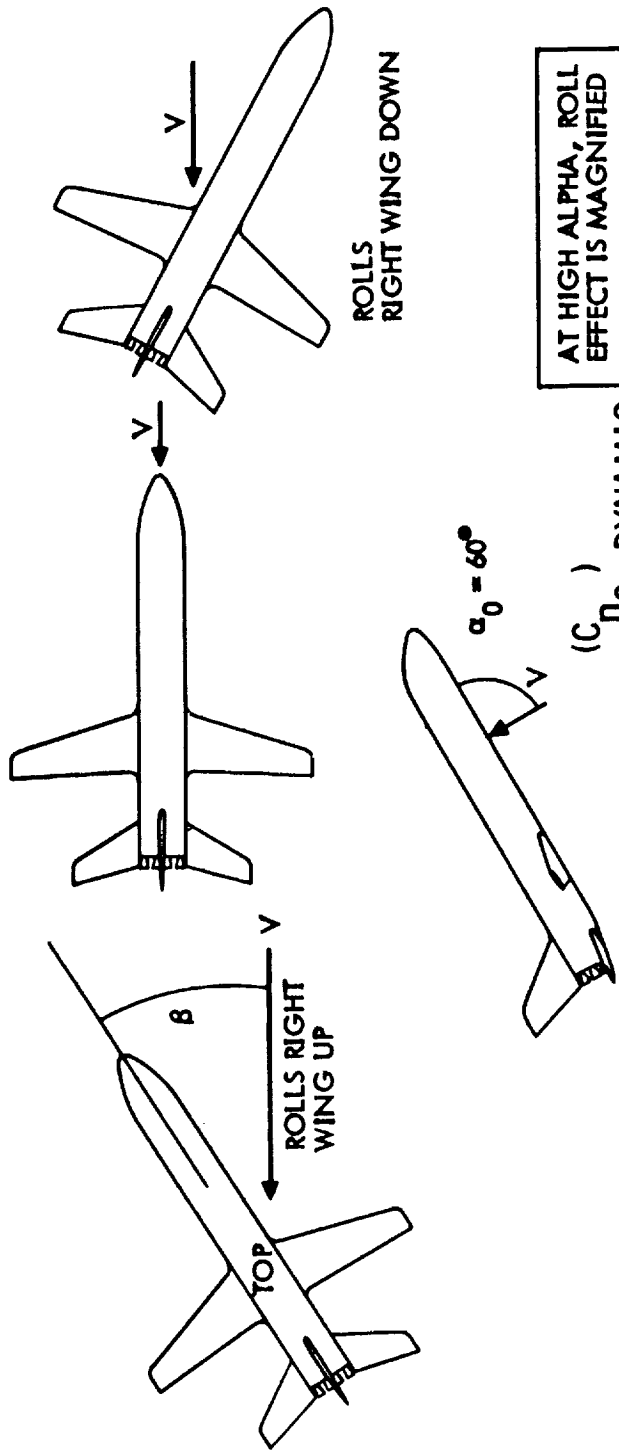


Slide 6

LATERAL-DIRECTIONAL DYNAMICS (Slide 7)

An important factor which helps determine ACPs propellant usage, control system gains, and maximum side-slip angle β is the Dutch roll frequency. The effective $C_{n\beta}$ or $(C_{n\beta})_{\text{dynamic}}$ determines Dutch roll frequency. $(C_{n\beta})_{\text{dynamic}} = 0$ is the Dutch roll stability boundary at high angle of attack. Note that for this class of vehicles the term $C_{l\beta} I_{zz}/I_{xx} \sin \alpha_0$ is a major contributor to $(C_{n\beta})_{\text{dynamic}}$ and Dutch roll frequency at large α , since $I_{zz}/I_{xx} \approx 5$ and $\sin \alpha_0 \approx 0.9$. If the lateral-directional Dutch roll frequency is set properly, the vehicle natural stability will result in small angular perturbations which lie within the control system dead bands and minimum ACPs activity will result. As will be shown in a later slide, $C_{n\beta}$ and $(C_{n\beta})_{\text{dynamic}}$ are equally important.

LATERAL—DIRECTIONAL DYNAMICS



$$\text{DUTCH ROLL FREQUENCY} = \frac{qSb}{I_{zz}} \left(C_{n_\beta} \cos \alpha_0 - C_{l_\beta} \frac{I_{zz}}{I_{xx}} \sin \alpha_0 \right)$$

DUTCH ROLL FREQUENCY, Hz	ACPS PROPELLANT	MAX SIDE SLIP ANGLE, DEG
0.1	1,800 kg (3,900 LB)	3.0
0.2	1,200 kg (2,600 LB)	0.6
0.3	1,000 kg (2,200 LB)	0.2

Slide 7

TRAJECTORY DIVERGENCE CAN RESULT FROM IMPROPER TRIM CONDITION (Slide 8)

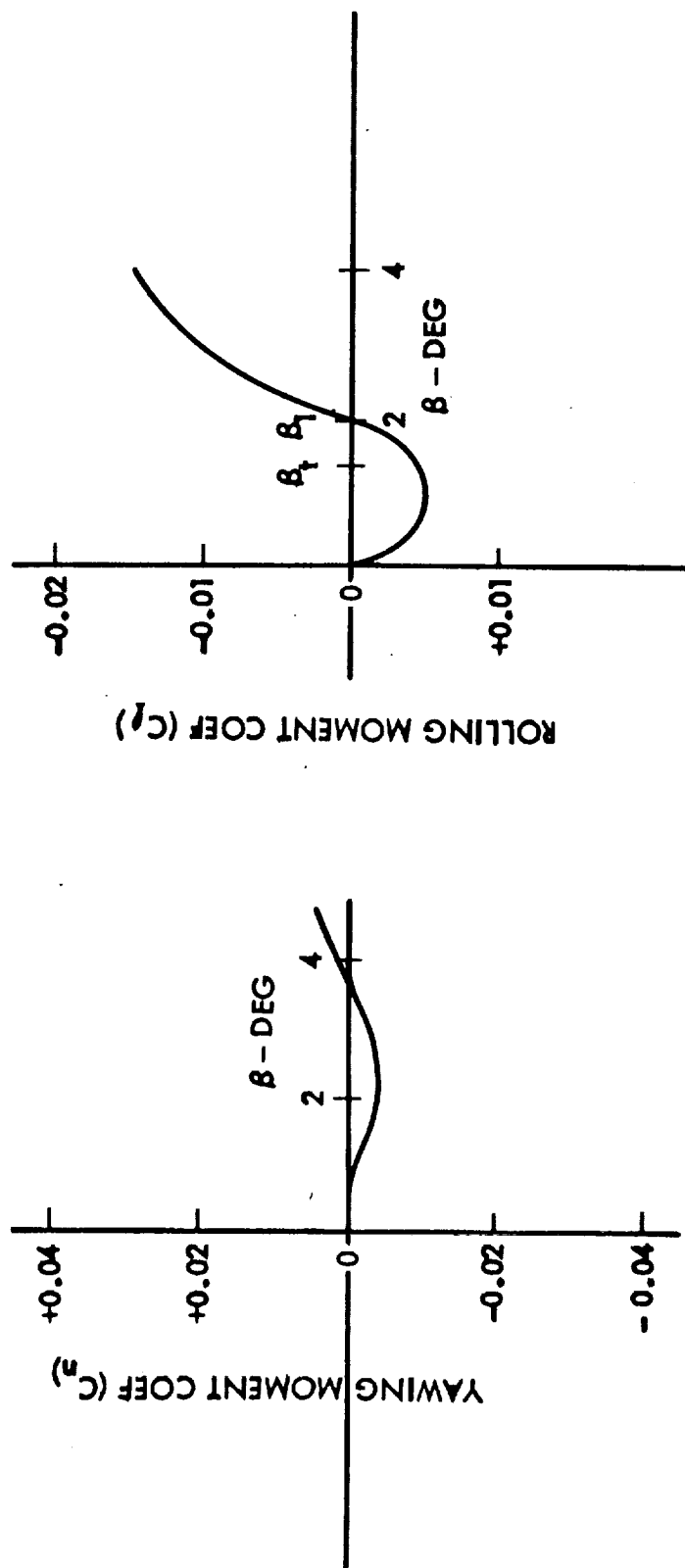
A severe trajectory instability can result for the particular configuration investigated in this study and is caused by a trim condition at approximately $\beta = 2^\circ$ in the roll degree of freedom. From the linearized lateral-directional equations of motion and the final value theorem, the expression for the trim sideslip angle β_t can be derived as shown on the slide. Typical values are:

$$I_{xx}/I_{zz} \approx 0.2$$

$$\cot \alpha_0 \approx 0.5$$

From the equation, it is seen that an increase in directional stability has only a small effect on changing the trim β from approximately 2° because of the moment-of-inertia ratio and angle-of-attack effect. Excessive directional stability at approximately constant β results in an increased yawing moment and has the effect of causing extensive trajectory and bank-angle divergence which is shown by the additional boundary in the next slide.

TRAJECTORY DIVERGENCE CAN RESULT FROM IMPROPER TRIM CONDITION



$$\beta_t = \frac{\beta}{1 - \frac{C_{n\beta} I_{xx}}{C_{l\beta} I_{zz}} \cot \alpha_0}$$

Slide 8

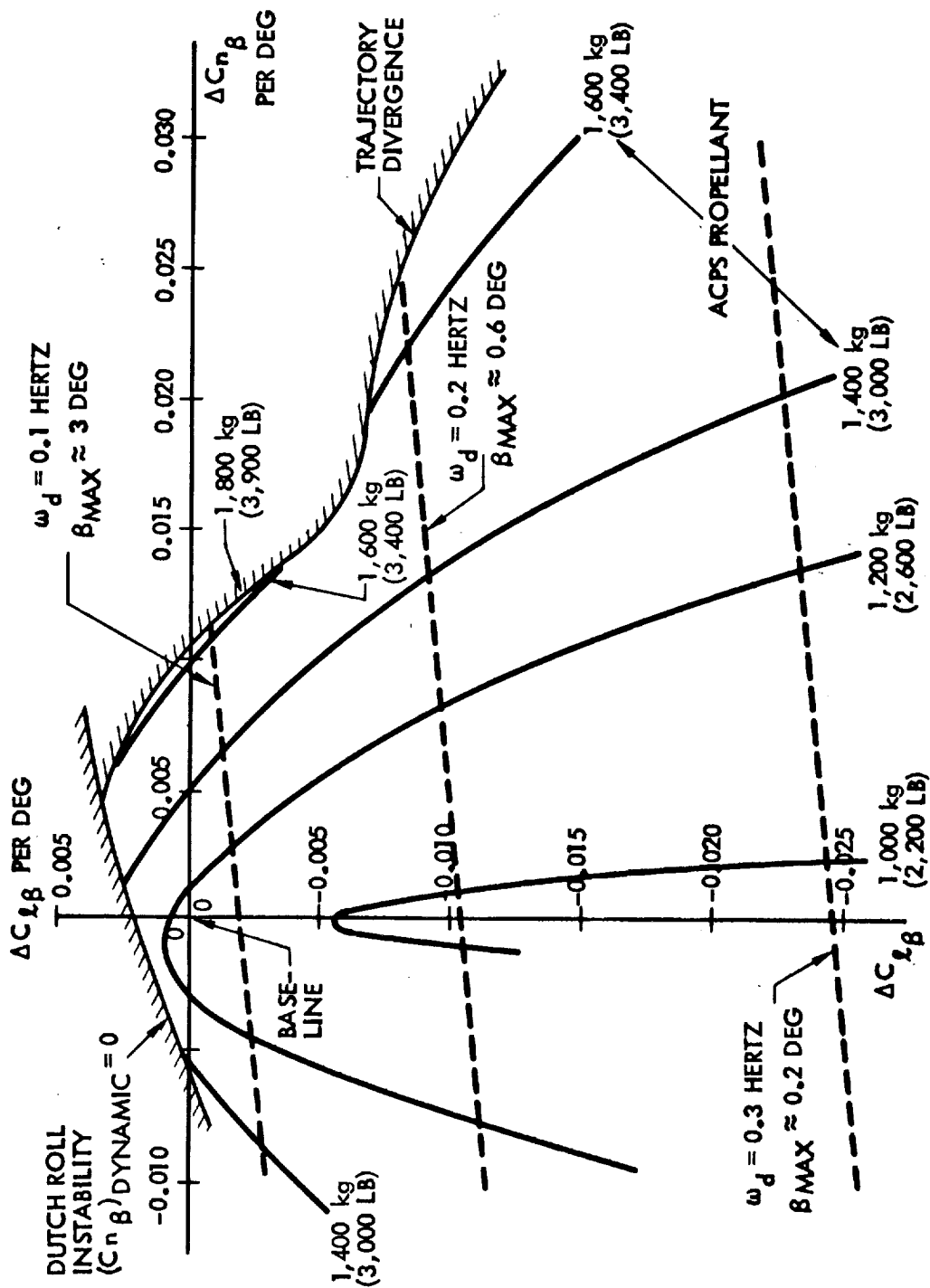
PROPER DIRECTIONAL STABILITY SAVES ACPS PROPELLANT (Slide 9)

A summary of the last three slides is shown. Lines of constant Dutch roll frequency ω_d are shown with the corresponding approximate maximum sideslip angle β . $\omega_d = 0$ represents the Dutch roll stability boundary. The lines of constant frequency were computed for dynamic pressure = 2010 N/m² (42 psf) $Q = 60^\circ$, and Mach number = 2.5, which are representative for the entry trajectory. $\Delta C_{L\beta}$ has a major influence on ω_d since at high Q the roll effect is magnified as was illustrated in the previous slide. If the configuration did not have the trim characteristic discussed in the previous slide, the lines of constant ACPS propellant usage would be more parallel to the lines of constant frequency.

Both the Dutch roll and trajectory divergence stability boundaries were determined from the six-degree-of-freedom simulation and correlated closely with the linear analysis for $(C_n \beta)_{dynamic} = 0$ and the expression for β_t .

An increase in dihedral effect would be desirable for this particular configuration during entry, but the effect on low-speed, low-angle-of-attack lateral-directional stability must be evaluated for an integrated vehicle design.

PROPER DIRECTIONAL STABILITY SAVES ACPS PROPELLANT

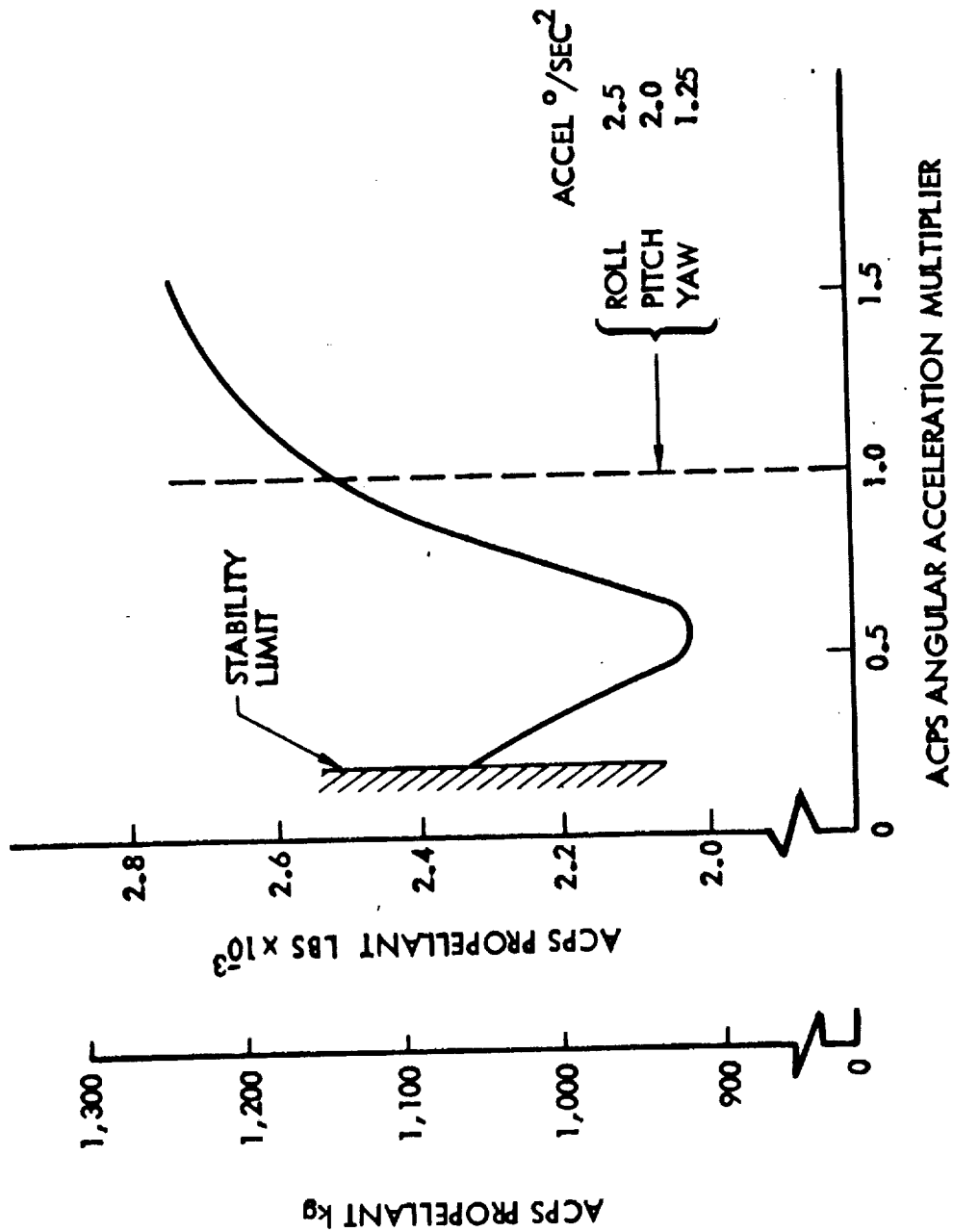


Slide 9

OPTIMUM ANGULAR ACCELERATION FOR AUTOMATIC CONTROL (Slide 10)

The ACPS propellant is a minimum for the particular configuration investigated when the ACPS thrust is reduced approximately 50%. Further reduction results in increased propellant usage because the control authority is inadequate for the aerodynamic moments during the more critical entry flight phases. Increased thruster size causes increased propellant usage due to increased limit cycle activity.

OPTIMUM ANGULAR ACCELERATION FOR AUTOMATIC CONTROL

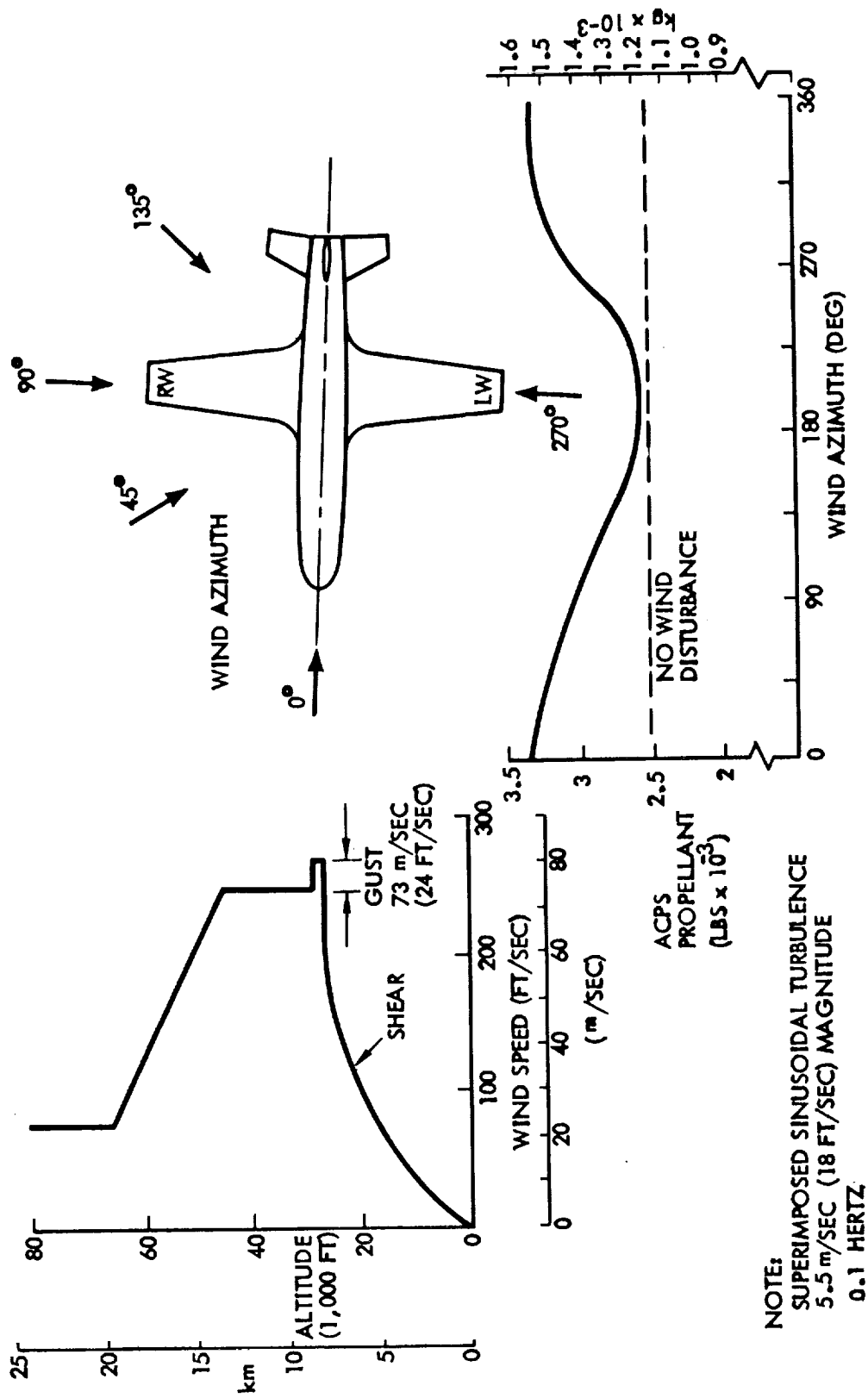


Slide 10

ENVIRONMENT (Slide 11)

A wind disturbance similar to that used for the boost phase is also utilized for entry. Different wind azimuth angles are investigated. Wind azimuth is defined in the wind direction relative to the vehicle at the time of the superimposed gust. A simple turbulent representation was superimposed on the wind shear disturbance and increased propellant usage approximately 454 kg (1000 lb) or 24% of the total. (The wind environments in this slide and slide 12 were derived from reference 1).

ENVIRONMENT



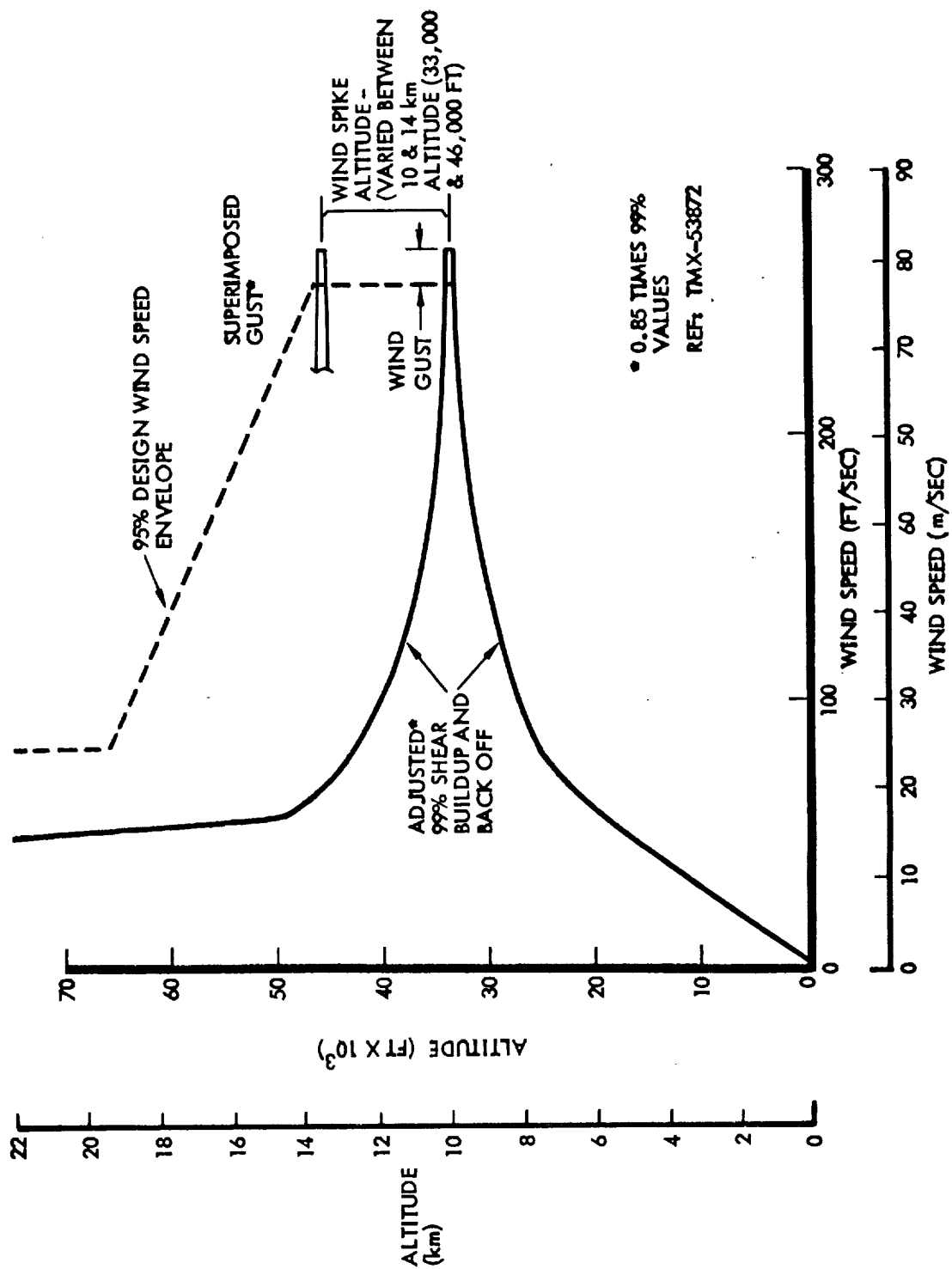
NOTE:
 SUPERIMPOSED SINUSOIDAL TURBULENCE
 5.5 m/SEC (18 FT/SEC) MAGNITUDE
 0.1 HERTZ

Slide 11

REVERSE WIND SPIKE DISTURBANCE (Slide 12)

The preceding slide shows the effect of wind azimuth. This slide shows the wind disturbance that was used to show the effect of variation in altitude at which the "wind spike" occurs. A back-off shear was also incorporated in this analysis to give the "worst case" dynamic situation.

REVERSE WIND SPIKE DISTURBANCE

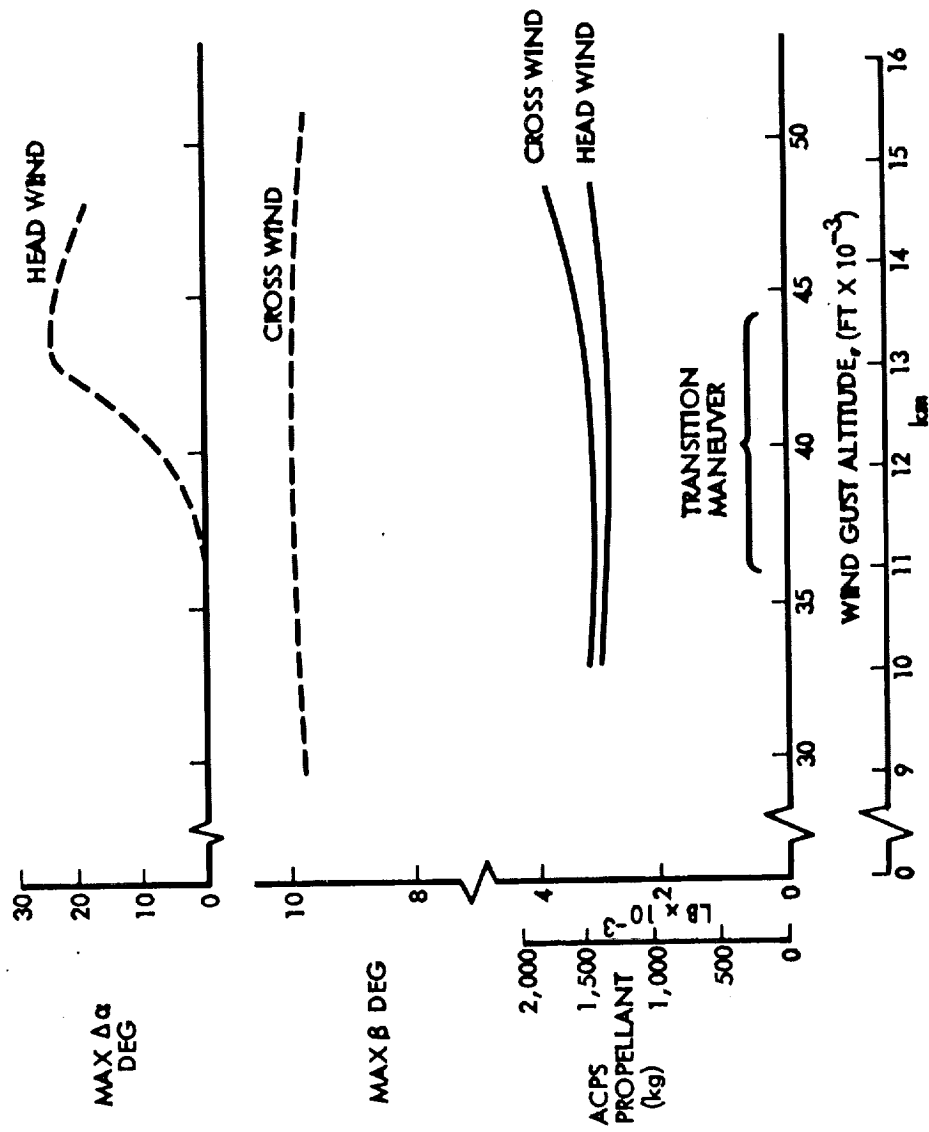


Slide 12

ALTITUDE FOR WIND DISTURBANCE DURING TRANSITION MANEUVER IS NOT CRITICAL (Slide 13)

The reverse wind disturbance was raised through the transition altitude range and found to be non-critical in terms of ACPS propellant usage or vehicle rigid body dynamics. The sideslip angle β is reduced during the wind disturbance because the control law for $\alpha > 40^\circ$ with a positive $(C_{n\beta})$ dynamic allows considerable "weather-cocking" into the wind before the gust is encountered. Other types of wind disturbances over a wider range of altitudes and more azimuth angles should be investigated before the dynamics of a straight-wing booster in the presence of wind disturbance is considered complete.

ALTITUDE FOR WIND DISTURBANCE DURING TRANSITION MANEUVER IS NOT CRITICAL



Slide 13

CONCLUDING REMARKS (Slide 14)

A modified Apollo control law was found to be optimum for ACPs propellant usage and dynamic behavior in the presence of wind disturbances. (C_{ng})dynamic is an important parameter for determining minimum ACPs propellant usage. However, the particular vehicle lateral-trim characteristics can be equally important. It appears the control system can be further optimized to reduce ACPs propellant usage by incorporating variable dead bands for different flight phases. The wind spike does not appear critical for the conditions investigated. During the transition maneuver, sideslip angles became excessive for a particular control law when the Mach number became abnormally low (≈ 0.3) and the vehicle was not allowed to weathercock. The modified Apollo control law does not appear to exhibit these undesirable characteristics.

CONCLUDING REMARKS

- MODIFIED APOLLO CONTROL LAW APPEARS TO BE BEST APPROACH
- CONFIGURATION TAILORING REDUCES ACPS PROPELLANT
- ACPS PROPELLANT FOR DISTURBANCES \approx 40% OF TOTAL REQUIREMENT
- VARIABLE ACPS SWITCHING LINES ARE DESIRABLE
- WIND SPIKE IS NOT CRITICAL FOR MACH NO. GREATER THAN 0.4

Slide 14

REFERENCE

1. Daniels, Glenn E., editor: Terrestrial Environment (Climatic) Criteria Guidelines for Use in Space Vehicle Development. NASA TM X-53872, 1969.

BOOSTER WING GEOMETRY TRADE STUDIES

By

H. G. Struck, George C. Marshall Space Flight Center
J. E. Butsko, Convair Aerospace Division of General Dynamics

INTRODUCTION

The subsonic aircraft mode of a Space Shuttle booster establishes design requirements on airbreathing engine size and flyback fuel allotment. Trade study results show the influence of wing geometry variations on the flyback systems weight (wing, jet engine and flyback fuel weight) of a canard Space Shuttle booster. The influence of such wing geometry parameters as aspect ratio, wing area, and thickness ratio is discussed.

Wing weight trends with wing geometry, obtained from conventional cargo, bomber and fighter airplane weight histories, are correlated with predicted values for Space Shuttle wings with structural span, load factor, and other design parameters taken into account.

For other than cruise performance reasons, a lower limit of wing area is defined; the influence of other phases of the booster mission profile, including launch, entry, and landing is presented. Aspect ratio, however, is influenced primarily by cruise performance and cost considerations. The influence of ground rules, such as choice of flyback fuel, headwind profile, and required range is discussed.

SCOPE

- OBJECT
 - DETERMINE WING ASPECT RATIO WITH MINIMUM FLYBACK SYSTEMS WEIGHT (FSW)
- PRIMARY CONSIDERATION
 - BOOSTER FLYBACK CRUISE PERFORMANCE
- SECONDARY CONSIDERATIONS
 - ENTRY STABILITY & TRIM
 - LANDING PERFORMANCE
 - TOTAL MISSION PERFORMANCE SENSITIVITIES
 - COST TRENDS

SCOPE (Slide 1)

The booster wing geometry trade studies have been directed toward determining the wing aspect ratio that results in minimum system weight. A parameter referred to as flyback systems weight (FSW), the sum of wing airbreathing engine and flyback fuel weights, is used to relate the influence of wing geometry on the booster flyback leg of the overall Space Shuttle mission.

However, other portions of the booster mission profile must be considered in studying wing geometry. Secondary considerations include the hypersonic entry stability and trim and landing performance characteristics of the booster, which influence wing size.

Any changes resulting from cruise optimization must be carried through the entire mission; hence, system weights can spiral. Total mission performance sensitivities reflect changes to system weight due to changes in structural weight, flyback fuel and launch drag.

GROUND RULES

- AFT WING, CANARD BOOSTER FAMILY WITH $2 < \text{ASPECT RATIO} < 8$
- AIRBREATHING ENGINE SYSTEM WITH $\text{BPR} = 0.7, 1.8$ USING JP-4 OR H_2
- CRUISE AT OPTIMUM ALTITUDE OR 10,000 FT. AGAINST 95% WIND PROFILE
- ENTRY WEIGHT = $\text{FSW} + 400,000 \text{ LB. (1,779,000 N)}$
- $\text{FSW} = W_w + W_{\text{ENG}} + W_{\text{FR}}$
 - W_w = WING STRUCTURE + TPS
 - W_{ENG} = ENGINE WEIGHT + INSTALLATION
 - W_{FR} = FUEL WEIGHT + 10% TANK & LINE WEIGHT + RESERVES

GROUND RULES

(Slide 2)

The trade study used a family of aft wing, forward canard booster configurations with aspect ratio varying between 2 and 8.

Two candidate Space Shuttle airbreathing engines were studied with bypass ratios of 0.7 and 1.8. Two different flyback fuels – kerosene (JP-4) and hydrogen (H_2) – were considered. Cruise performance was determined at optimum altitude or 10,000 ft. (3,048 m) whichever was greater. Current Space Shuttle ground rules of operation against the NASA/Kennedy Space Center 95% headwind profile were used.

For the flyback analysis trade study, the main fuselage was held at a constant size and the structure and systems were assigned a constant weight of 1,779,000 N. The entry weight of all configurations was, then, the sum of 400,000 lb. (1,779,000 N) and the FSW. The FSW (flyback system weight) is defined as

$$FSW = W_w + W_{ENG} + W_{FR}$$

where

$$W_w = \text{wing structure} + \text{TPS}$$

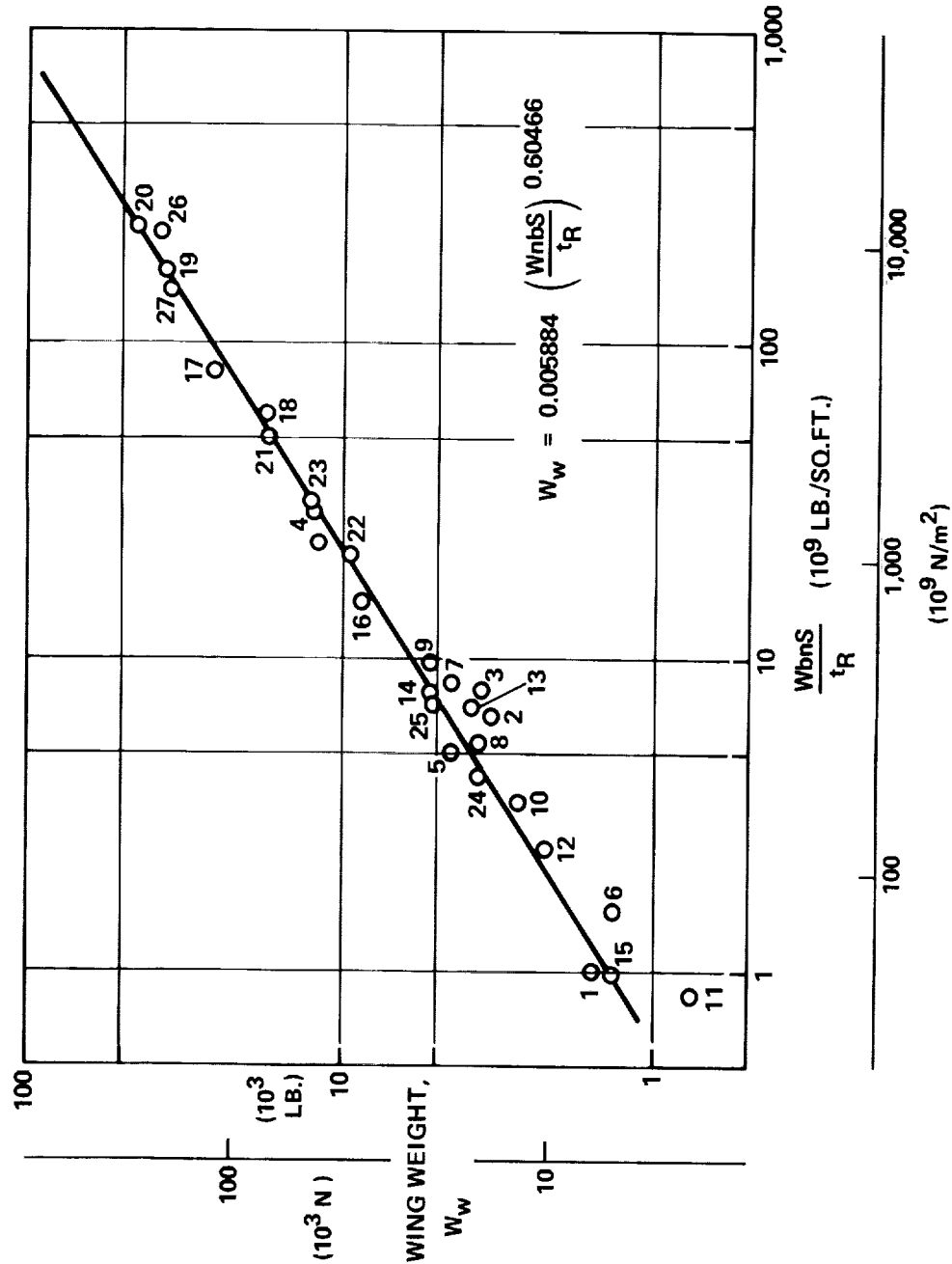
$$W_{ENG} = \text{engine weight} + \text{installation}$$

$$W_{FR} = \text{fuel weight} + 10\% \text{ tank and line weight} + \text{reserves}$$

AIRCRAFT WING WEIGHT DATA CORRELATION

DATA POINTS

1. A4D-2N
2. F-102A
3. F-106B
4. B-58A
5. F3H-2
6. F-104A
7. F-4C
8. F4H-1
9. F-105D
10. F8U-1
11. T-38A
12. F11F-1
13. F-101B
14. A-6A
15. OV-1C
16. B-66A
17. C-135A
18. 880
19. C-141A
20. B-52H
21. B-47B
22. C-118A
23. C-130A
24. C-159
25. 440
26. B-52G
27. B-70



Slide 3

AIRCRAFT WING WEIGHT DATA CORRELATION

(Slide 3)

Wing weights of a number of existing aircraft are plotted versus a term ($WnbS/t_R$), which seems to represent more the bending moment of the wing.

where

W = vehicle weight

n = design load factor

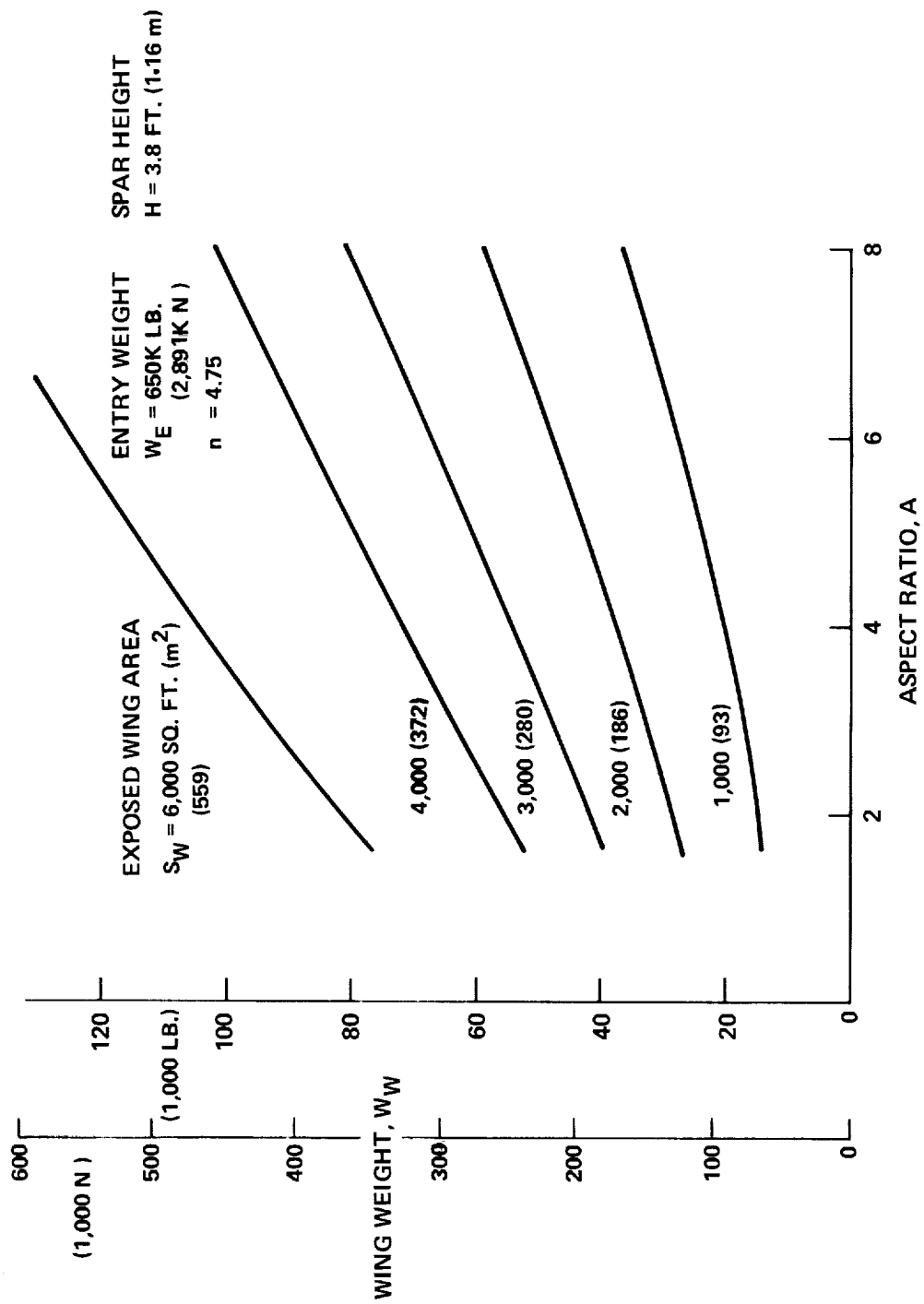
b = wing span

S = wing area

t_R = wing thickness at root

All data falls within a reasonable band around a straight line on the log-log plot.

SPACE SHUTTLE BOOSTER WING WEIGHT TRENDS



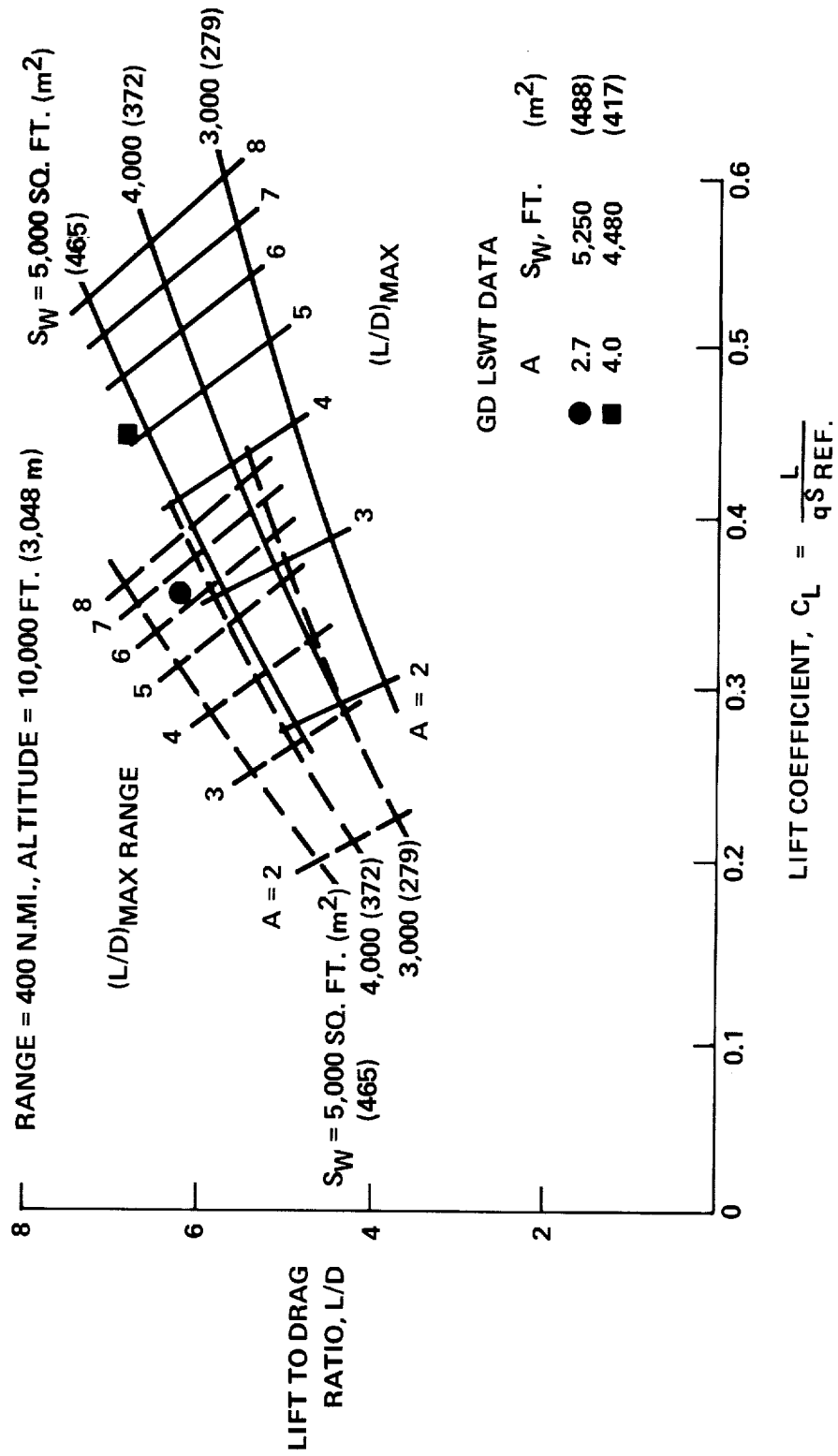
SPACE SHUTTLE BOOSTER WING WEIGHT TRENDS

(Slide 4)

The resulting wing weights are plotted as a function of the aspect ratio with the exposed wing area as parameter. For the wing weight calculation some parameters were held constant:

1. The entry weight of the booster was assumed to be $W_E = 650,000$ lb. (2,891,000 N) and invariant with aspect ratio or wing size.
2. The ultimate load factor was assumed to be $n = 4.75$.
3. The spar height was held constant at $h_s = 3.8$ ft. (1.16 m). The thickness ratios of the wings of $S_w = 3,000$ sq. ft. (279 m²) and 4,000 sq. ft. (372 m²) for instance, changed therefore from approximately $\tau = 6\%$ at an aspect ratio of $A = 2$ to approximately $\tau = 12\%$ at an aspect ratio of $A = 8$.

SPACE SHUTTLE BOOSTER CRUISE AERODYNAMICS

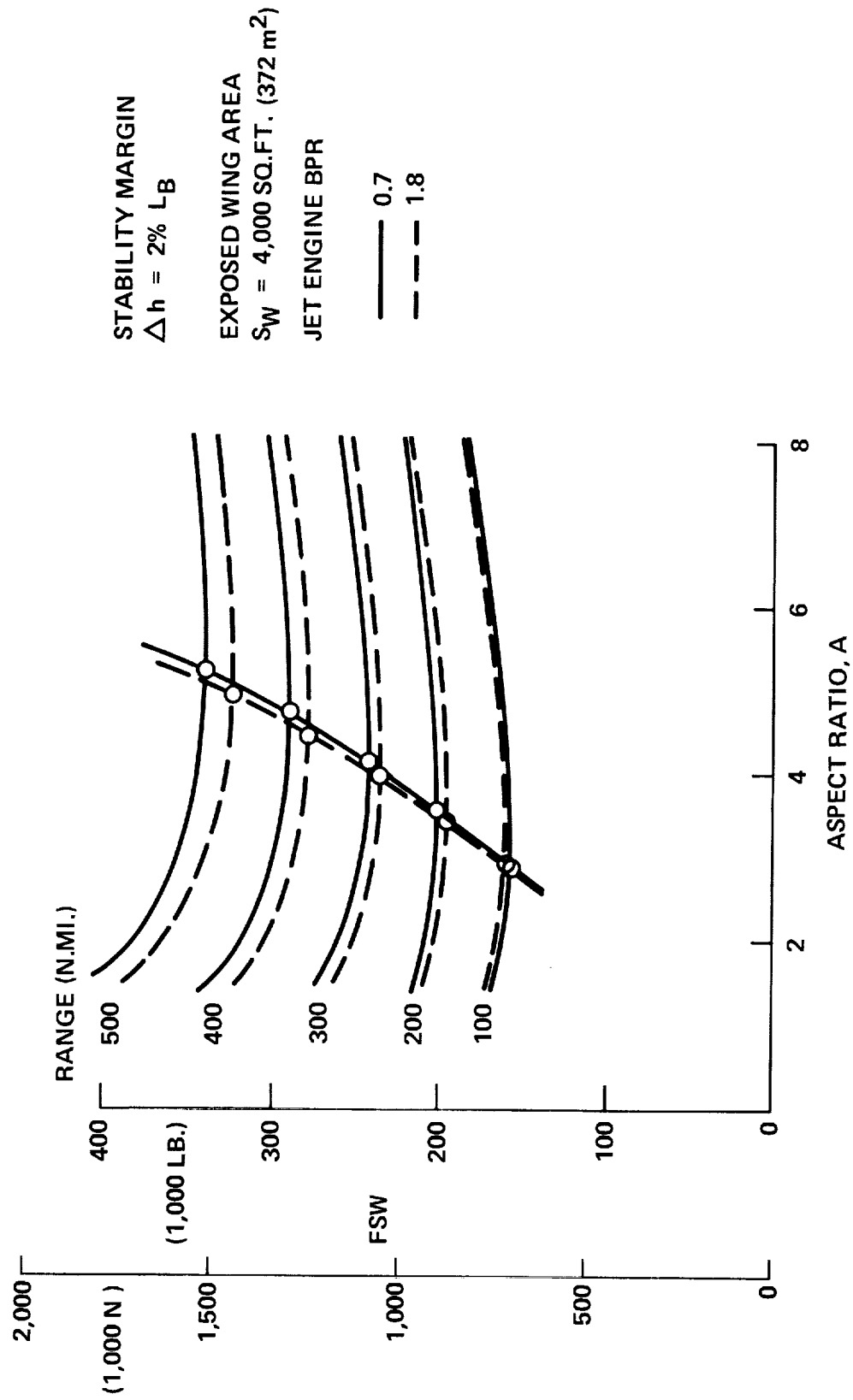


SPACE SHUTTLE BOOSTER CRUISE AERODYNAMICS (Slide 5)

The family of boosters subjected to the trade study had one fuselage of 220 ft. (67.1 m) length of constant shape and a constant canard surface of $S_c = 800$ sq. ft. (74.5 m²). The canard was mid-fuselage mounted and located at the intertank region; it is all-movable and can therefore be unloaded during hypersonic entry.

The different wings, all provided with a constant leading edge sweep of $\Lambda_{LE} = 40^\circ$ and a constant taper ratio of $\lambda = 0.4$ varied in aspect ratio from $A = 2$ to $A = 8$ and in exposed wing area from $S_w = 1,000$ sq. ft. (93.1 m²) to $S_w = 6,000$ sq. ft. (558 m²). The maximum lift to drag ratios of two configurations are compared with wind tunnel test data obtained in the General Dynamics Low Speed Wind Tunnel. We notice that the magnitude of $(L/D)_{max}$ is reasonably well reproduced. The Space Shuttle booster, however, flies generally at lower lift coefficients and therefore faster ($M \sim 0.6$) to obtain maximum range or at fixed range $R = 400$ n. mi. to obtain maximum FSW.

EFFECT OF CRUISE RANGE ON FSW



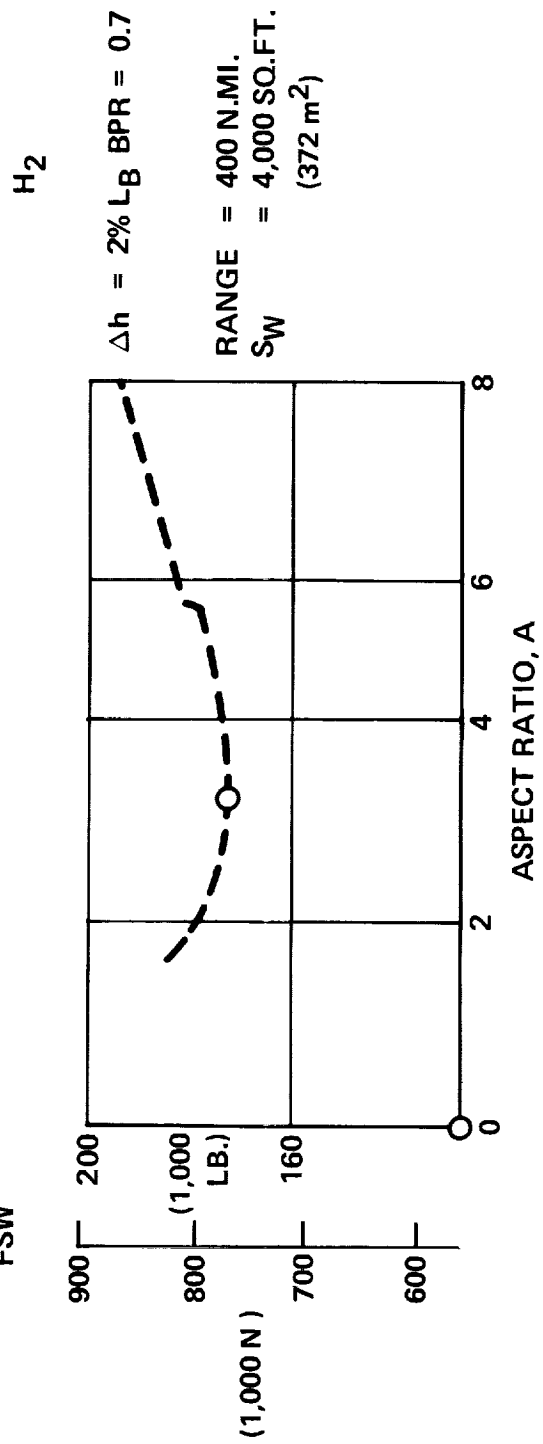
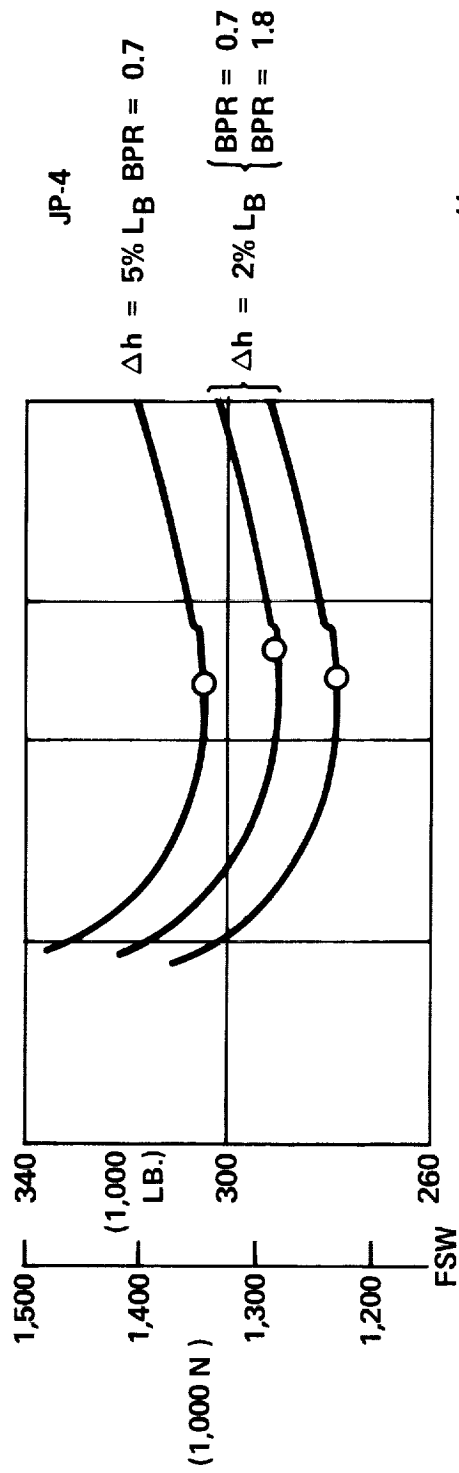
Slide 6

EFFECT OF CRUISE RANGE ON SFW (Slide 6)

The flyback systems weight of a Space Shuttle booster with a fixed exposed wing area and flyback range shows a decreasing tendency with increasing aspect ratio until a minimum is reached. At this point, increasing wing weight influences the decreasing fuel plus propulsion weight and reverses the trend of the FSW. With decreasing range, however, the minimum should occur at smaller aspect ratios since the fuel weight is proportionately less and the wing weight more dominating.

From the plot we obtain, for minimum FSW, aspect ratios ranging from $A \leq 3$ for a range of $R = 100$ n. mi. to $A \sim 5$ for a range of $R = 500$ n. mi. The influence of the bypass ratio of the jet engine on the optimum aspect ratio is small. However, the trend that higher bypass ratio engines yield smaller FSW reverses between $R = 200$ n. mi. and $R = 100$ n. mi. In this region, the smaller thrust to weight ratio of the higher bypass ratio engines plays the significant role in reversing the trend.

EFFECT OF CRUISE FUEL ON FSW



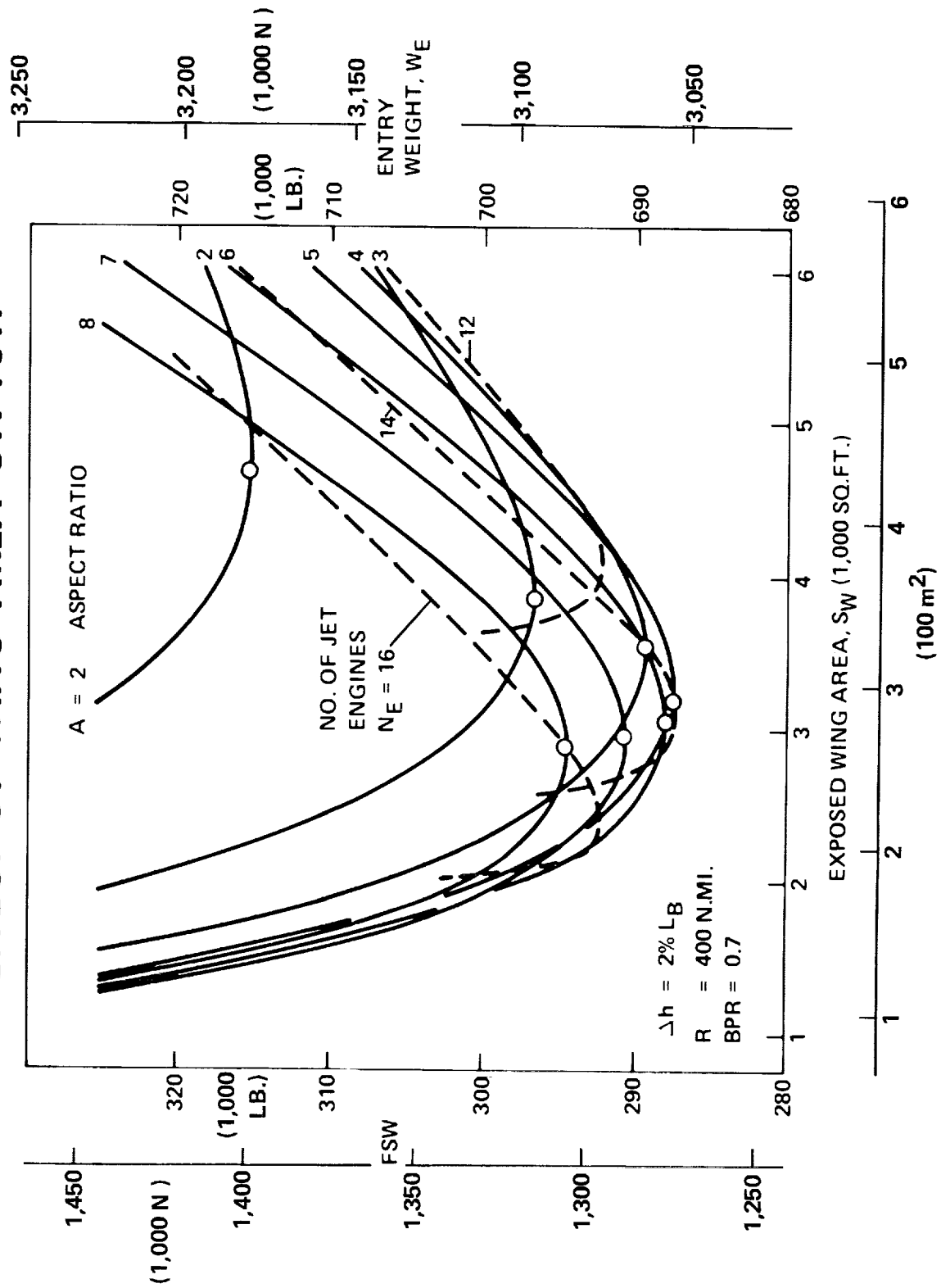
EFFECT OF CRUISE FUEL ON FSW

(Slide 7)

The FSW changes drastically when liquid hydrogen (H_2) is used as jet engine fuel instead of kerosene (JP-4). For a range of $R = 400$ n. mi. and an exposed wing area of $S_W = 4,000$ sq. ft. (372 m^2) a weight difference of approximately $\Delta W = 120,000$ lb. ($530,000 \text{ N}$) can be saved. We also notice that the minimum FSW for JP-4 occurs at approximately $\Delta A \sim 2$ units higher than the minimum FSW for hydrogen (H_2).

If we consider only JP-4 as flyback fuel we notice that the stability margin has an influence on FSW. Increasing the stability margin from $\Delta h = 2\% L_B$ to $\Delta h = 5\% L_B$ results in a FSW increase of $\Delta W = 15,000$ lb. ($67,000 \text{ N}$). On the other hand an increase in jet engine bypass ratio from $BPR = 0.7$ to $BPR = 1.8$ results in a FSW decrease of $\Delta W = 13,000$ lb. ($58,000 \text{ N}$).

EFFECT OF WING AREA ON FSW



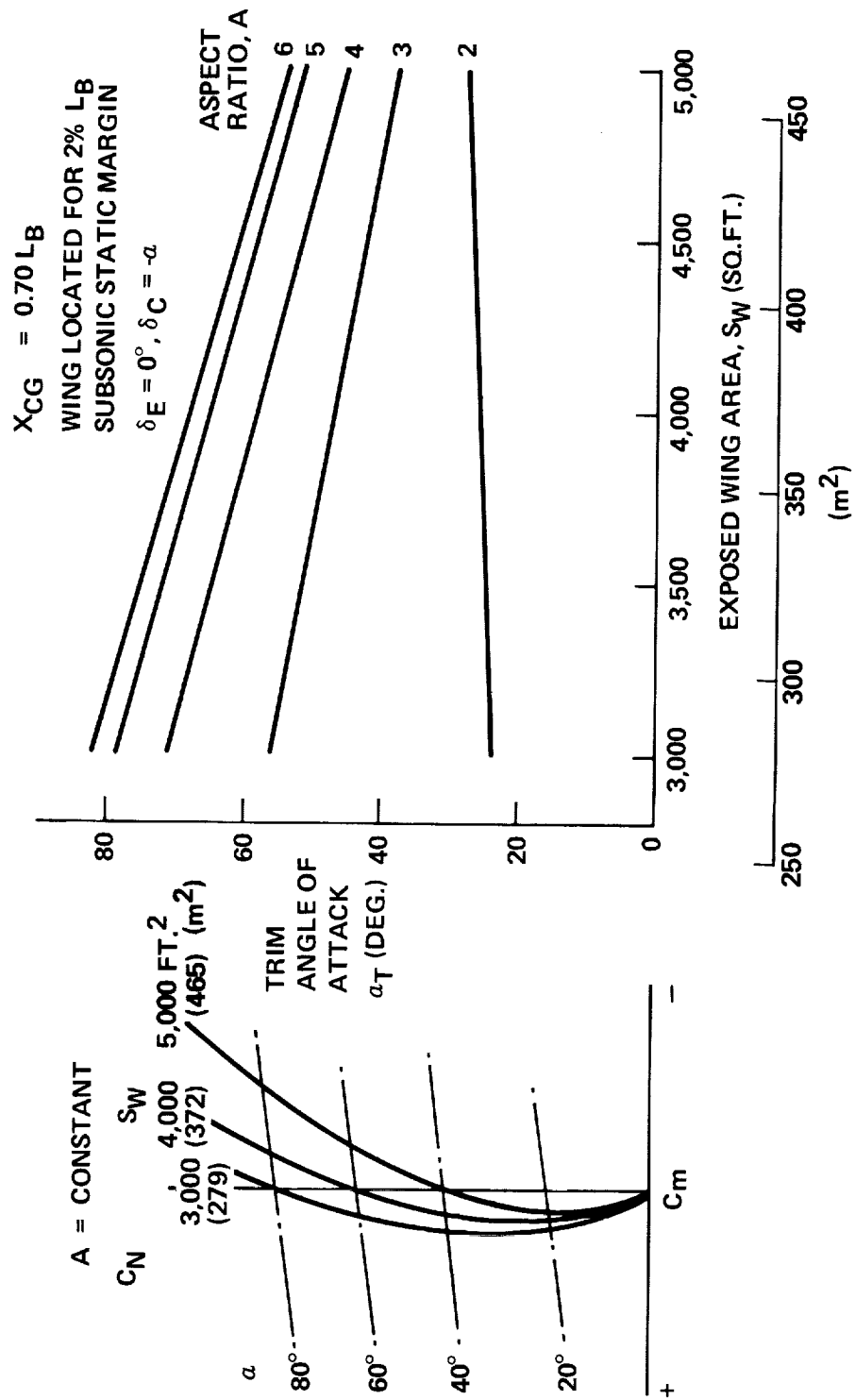
EFFECT OF WING AREA ON FSW

(Slide 8)

The flyback systems weight for a range of $R = 400$ n. mi. is plotted as a function of the exposed wing area S_w with the aspect ratio A as parameter. The optimum exposed wing area where FSW has a minimum from the flyback performance point of view decreases with increasing aspect ratio. In the neighborhood of $A = 5$ and $S_w = 3,300$ sq. ft. (307 m^2) an absolute minimum in FSW is reached, $FSW = 287,000$ lb. ($1,280,000 \text{ N}$). For higher aspect ratios and smaller exposed wing areas the FSW is increasing rapidly. The entry weight obtained by adding the FSW to a partial dry weight of $W = 400,000$ lb. ($1,779,000 \text{ N}$) is $W_E = 687,000$ lb. ($3,050,000 \text{ N}$).

Superimposed on the plot are lines of constant numbers of jet engines which have an approximate sea level static thrust of $T_{SLS} = 18,000$ lb. ($80,000 \text{ N}$). In order to fly the Space Shuttle booster at an altitude of $10,000$ ft. ($3,048 \text{ m}$), approximately $N_E = 14$ jet engines of the BPR = 0.7-type are necessary.

HYPERSONIC TRIM CONSIDERATIONS



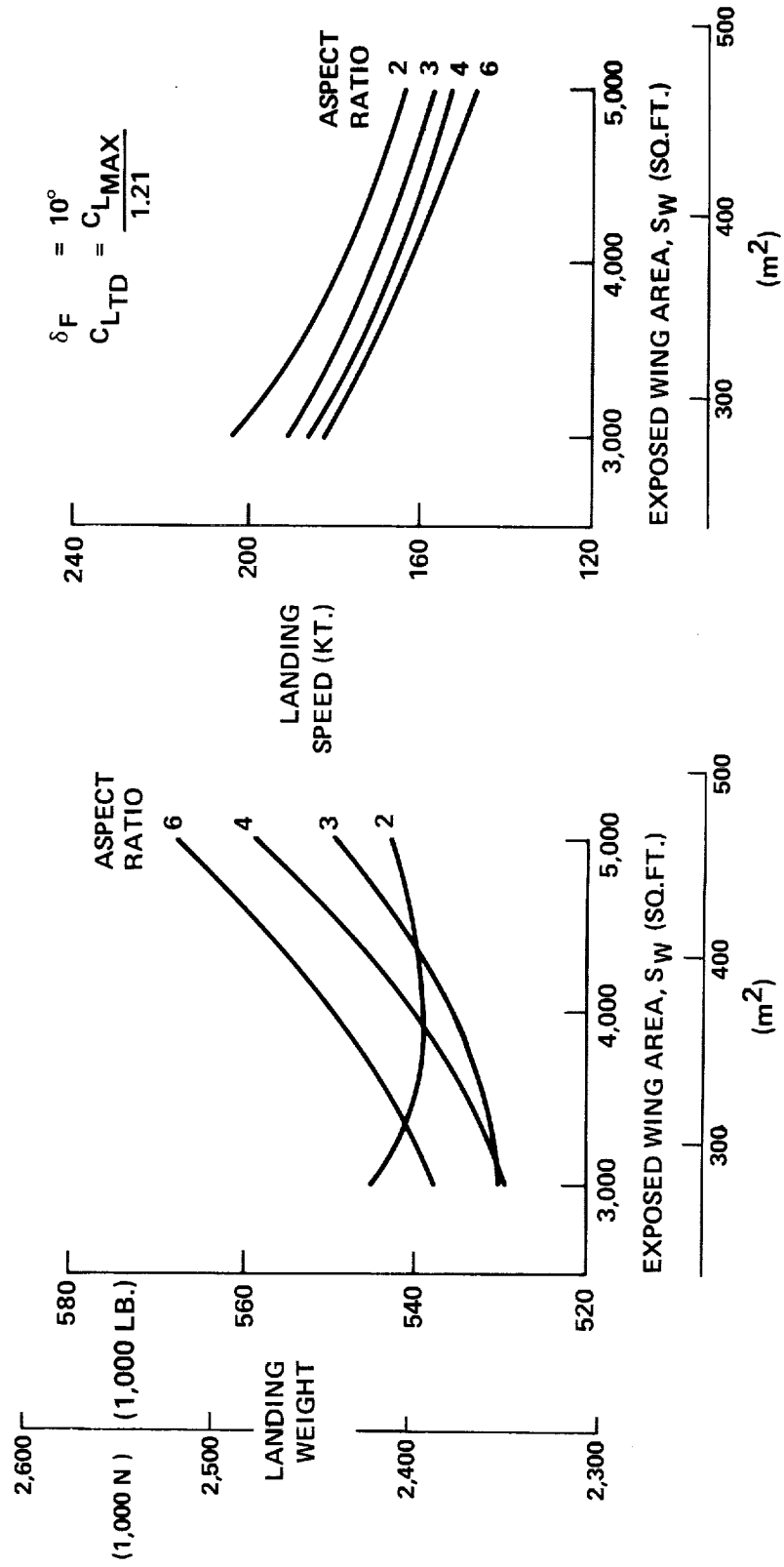
HYPERSONIC TRIM CONSIDERATIONS

(Slide 9)

The family of boosters for the trade study has the wing located to provide a subsonic stability margin of 2% of fuselage length. The resulting hypersonic stability and trim characteristics of each aspect ratio family vary with wing area, as indicated by the stability diagram (normal force versus pitching moment coefficient) shown on the left side of the slide. Typically, as area increases, the vehicle trims to progressively lower angles of attack, with the elevons neutral and the canard surfaces unloaded (aligned with the freestream). Static stability is generally not of concern; the angle of attack for neutral stability ($dC_m/dC_N = 0$) is considerably lower than that for trim.

The trim angle of attack for each family, as a function of exposed wing area, is presented. Current Space Shuttle design studies indicate that a trim angle of attack of 60° is a good compromise from heating and entry loading considerations. For the trade study, this criterion was adopted as a possible constraint to wing area.

LANDING PERFORMANCE



Slide 10

LANDING PERFORMANCE

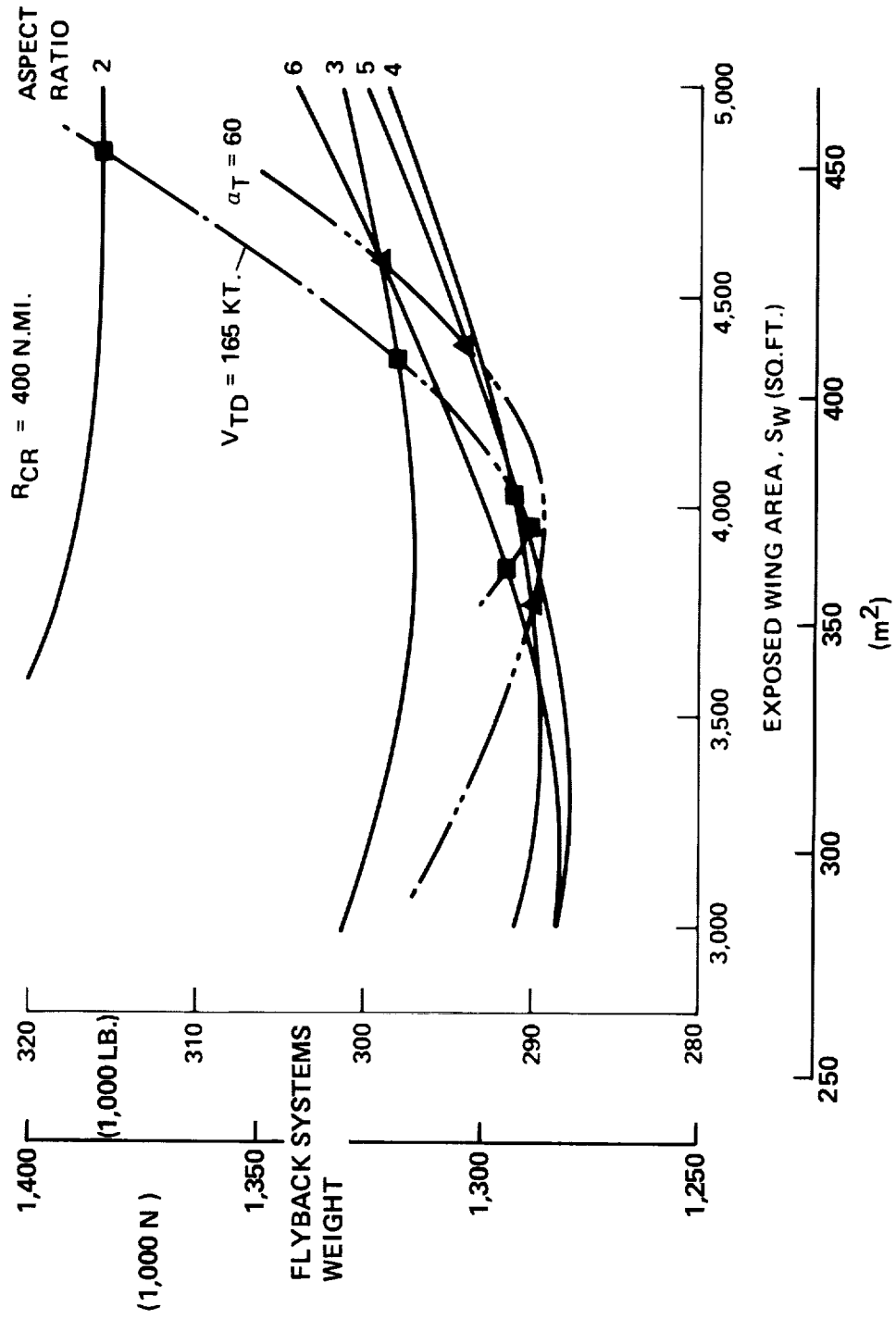
(Slide 10)

The landing weights of the family of boosters, as determined from entry weight minus cruise fuel weight, are shown. Typically, landing weight increases with aspect ratio, at constant area. due to the increase in wing structure weight. The A = 2 family has a different trend, influenced primarily by the number of engines required.

Landing performance of the family was estimated assuming the use of the elevons deflected down 10° as simple landing flaps. Stall characteristics are reflected; the higher aspect ratios are restricted to lower landing angles. However, the higher aspect ratios still have better landing performance, as indicated by lower landing speeds at the same area.

Operational considerations (gear, brake, and tire design, field lengths) indicate a landing speed of 180 knots as being maximum. To preserve a margin of safety for operations at higher landing weights and lower density (hot day, altitude) a design landing speed of 165 knots was selected for the trade study.

EFFECT OF ENTRY & LANDING ON FSW



Slide 11

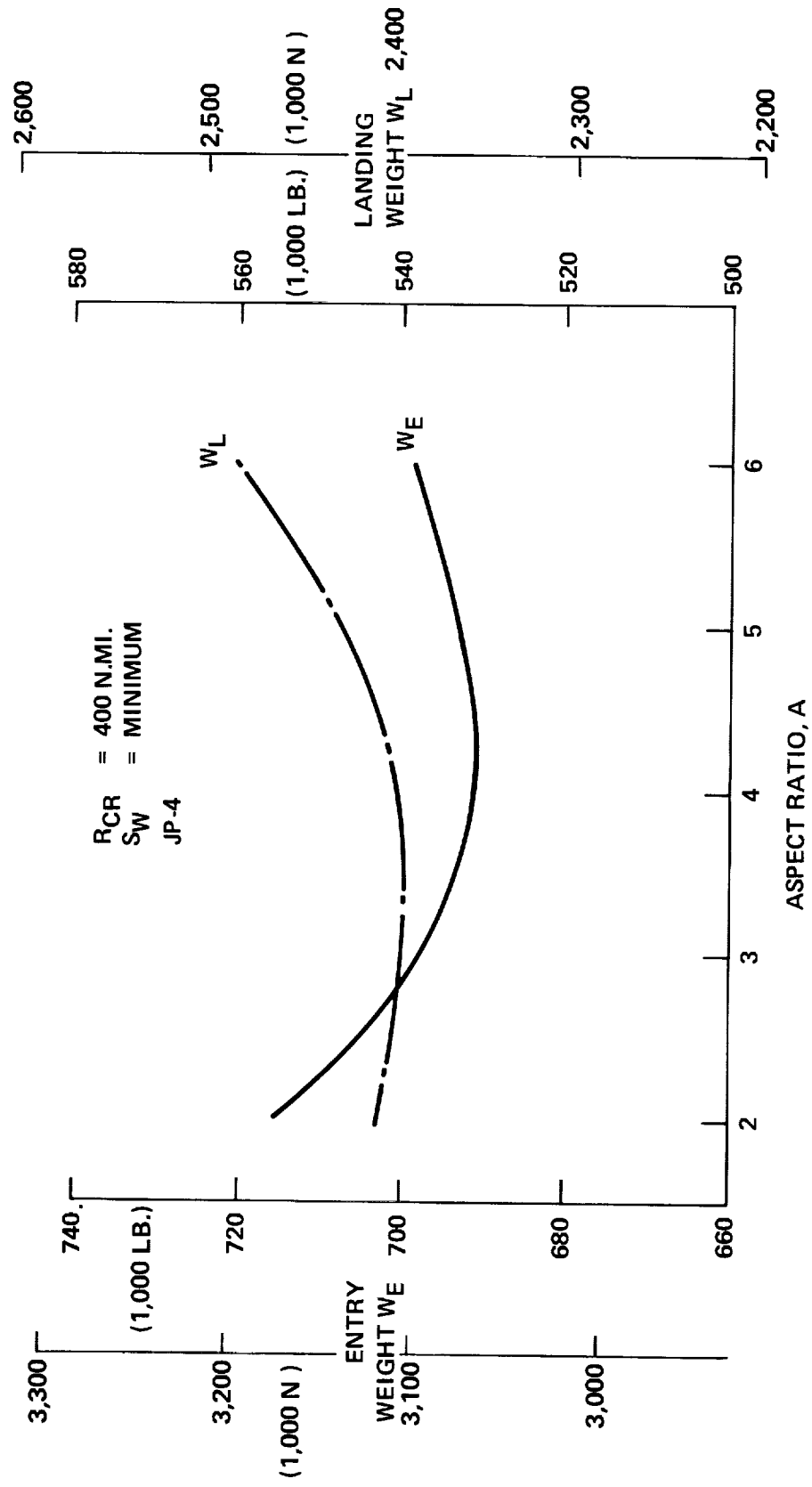
EFFECT OF ENTRY AND LANDING ON FSW

(Slide 11)

The constraints on wing area imposed by entry trim and landing performance are superimposed on the plot of FSW versus aspect ratio and wing area for $R_{CR} = 400$ n.mi. In general, these constraints prohibit attainment of the area for minimum FSW.

For aspect ratios of 5 and 6, the hypersonic trim requirement establishes minimum area. For the lower aspect ratios, the minimum wing area is established by the landing speed requirement.

WING GEOMETRY FROM FLYBACK ANALYSIS



WING GEOMETRY FROM FLYBACK ANALYSIS

(Slide 12)

The variation of entry weight (FSW + 400,000 lb. (1,779,000 N)) with aspect ratio is presented, corresponding to the wing area sized by landing or entry considerations. Minimum entry weight occurs at $A = 4$. The maximum difference in entry weight over the range from $A = 2$ and $A = 6$ is seen to be 24,000 lb. (107,000 N).

The corresponding variation in landing weight is also presented. It is indicated that minimum landing weight occurs at a lower aspect ratio, near $A = 3$.

Typical Cost Estimating Relationships (CER) used in Space Shuttle studies relate RDT&E costs to dry weight; in this case, booster landing weight. Minimum cost would appear to coincide with that for minimum landing weight. The direct cost of JP-4 is insignificant. However, the JP-4 must be carried over the entire Space Shuttle mission profile. Differences in JP-4 weight spiral total system weights, including structures. These spiraling factors are introduced by the use of total mission sensitivities.

TOTAL MISSION PERFORMANCE SENSITIVITIES

STRUCTURAL WEIGHT

$$\frac{\partial W_E}{\partial W_{STRUCT}} = 2.2 \text{ LB./LB. (N /N)} \qquad \frac{\partial W_L}{\partial W_{STRUCT}} = 2.0 \text{ LB./LB. (N /N)}$$

FLYBACK PROPELLANT

$$\frac{\partial W_E}{\partial W_{JP-4}} = 1.8 \text{ LB./LB. (N /N)} \qquad \frac{\partial W_L}{\partial W_{JP-4}} = 0.6 \text{ LB./LB. (N /N)}$$

LAUNCH DRAG

$$\frac{\partial W_E}{\partial \Delta V_{DRAG}} = 160 \text{ LB./FPS} \qquad \frac{\partial W_L}{\partial \Delta V_{DRAG}} = 120 \text{ LB./FPS}$$

(2,330 N /M/S) (1,750 N /M/S)

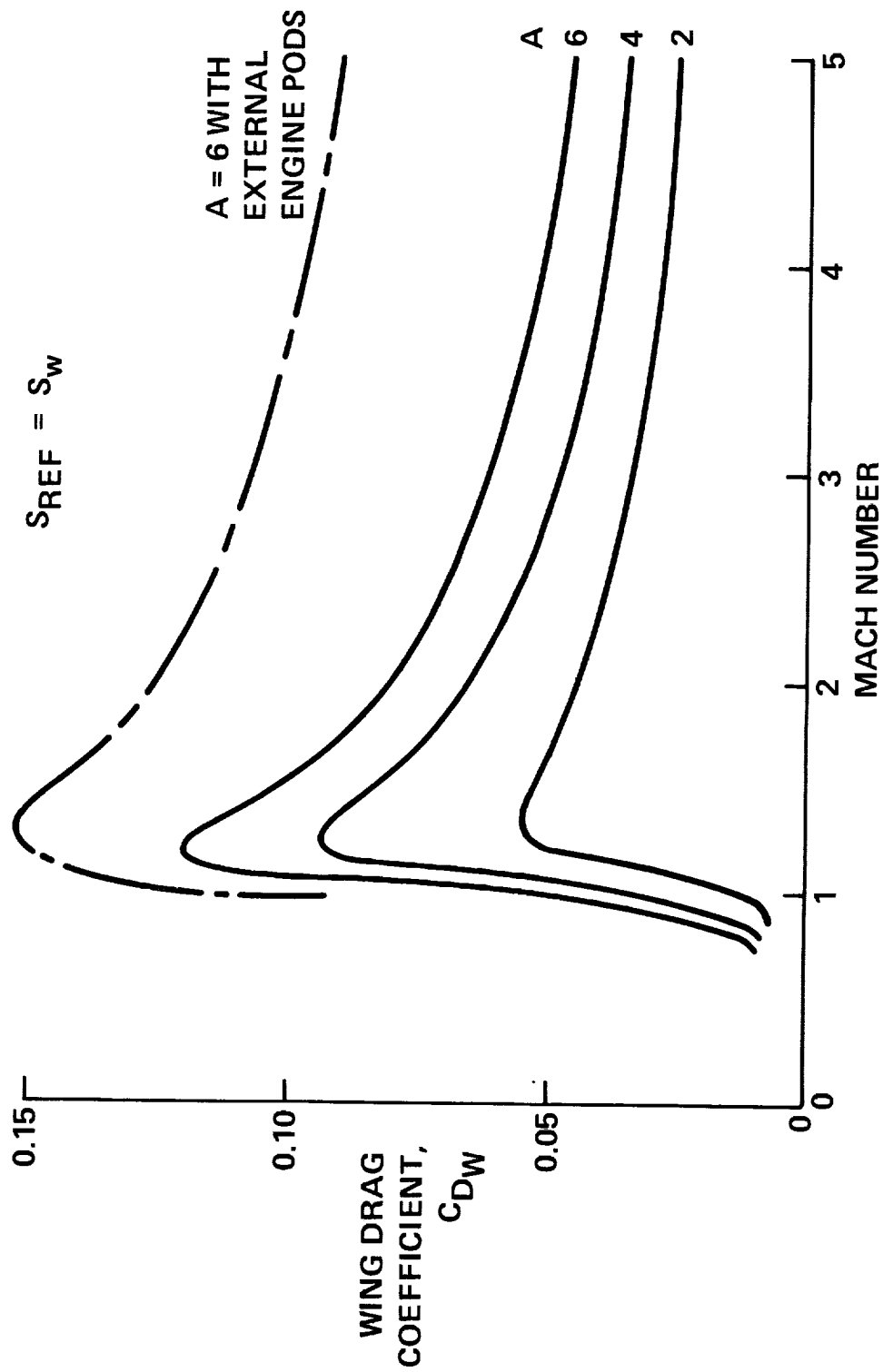
Slide 13

TOTAL MISSION PERFORMANCE SENSITIVITIES (Slide 13)

Representative sensitivities relating changes in booster entry and landing weights due to changes in structural weight, flyback propellant weight and drag velocity losses during ascent to staging are presented. These are based on holding payload constant.

The flyback analysis previously presented was based on a constant fuselage structure and systems weight (400,000 lb (1,779,000 N)). With payload fixed, the differences in the factors that contribute to FSW between configurations in the trade study should be influenced by total mission performance. The sensitivities shown allow adjustment of the flyback analysis trade study results.

WING CONTRIBUTION TO LAUNCH DRAG



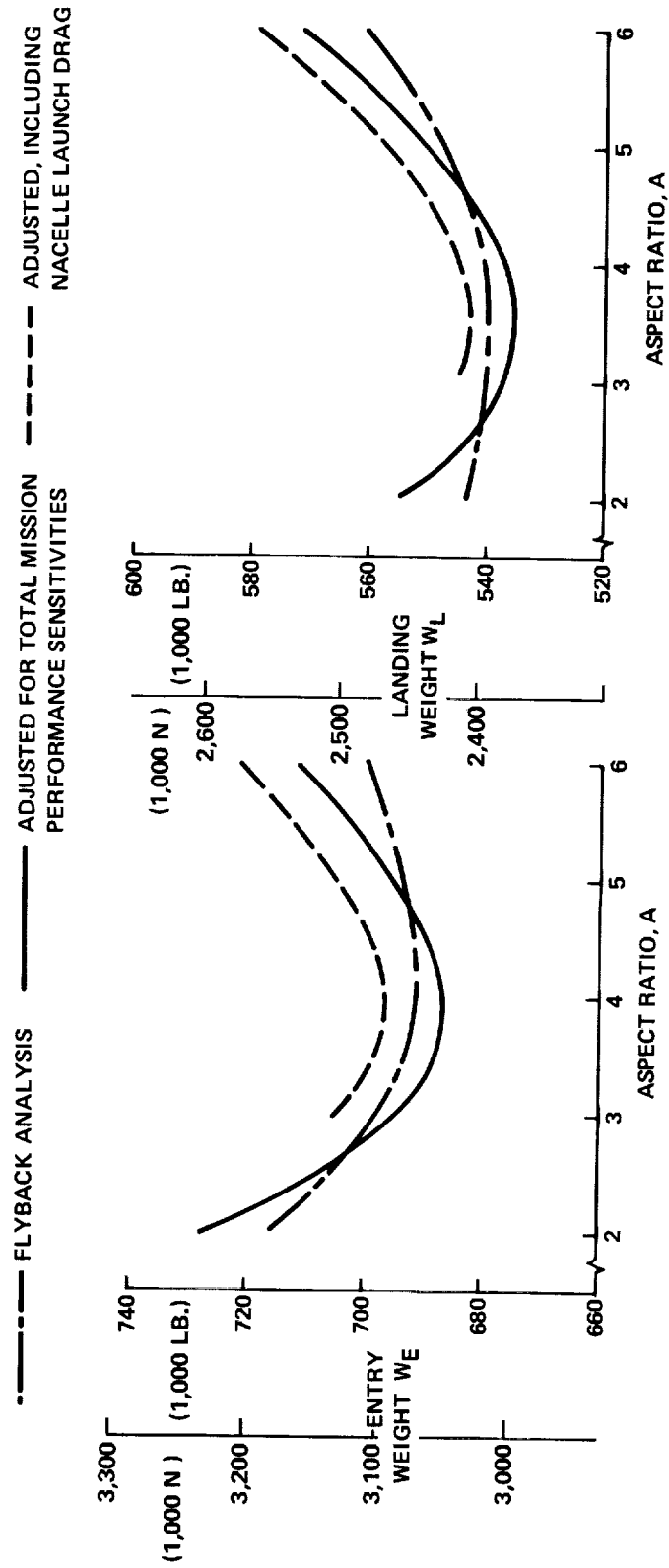
WING CONTRIBUTION TO LAUNCH DRAG

(Slide 14)

The influence of wing geometry on total mission performance of the booster includes the contribution of wing to the launch drag and, hence, drag velocity losses through staging. Presented are predicted values of the wing drag contribution over the significant ascent Mach number range, for aspect ratios of 2, 4 and 6. For the wings sized previously, the booster wing comprises from approximately 15% to 23% of the total configuration peak drag.

The lower aspect ratio wings offer a potential advantage in reducing launch drag, since the greater chord lengths may permit stowage of the airbreathing engines within the wing. The higher aspect ratios require external podding: the increase in drag due to an underwing nacelle is seen to greatly increase the launch drag contribution.

TOTAL MISSION PERFORMANCE RESULTS



TOTAL MISSION PERFORMANCE RESULTS

(Slide 15)

The effect of aspect ratio upon entry and landing weight, based on flyback analysis and with adjustment by total mission performance sensitivities, is presented. The sensitivities were applied by normalizing to the performance of the system with $A = 2.7$.

It is indicated that the differences of the original analysis are accentuated by the influence of total performance spiralling. Minimum entry weight is at $A = 3.9$, and landing weight is minimum at $A = 3.5$. If an external airbreathing engine nacelle is added to launch drag, both entry and landing weights are increased, as shown. A discontinuity is expected when the aspect ratio wing which permits internal engine stowage is reached.

As previously discussed, booster RDT&E cost estimates follow dry weight. This would indicate minimum cost at $A = 3.5$. Additional cost considerations include differences in structural complexity of wings and number of engines.

CONCLUSIONS

The results of the booster wing geometry trade study have established the following trends:

1. For the current design mission ($R_{CR} \approx 400$ n.mi., JP-4) minimum FSW occurs at an aspect ratio of 4.
2. System RDT&E cost follows dry weight; minimum landing weight occurs at an aspect ratio of 3.5.
3. Reduction of cruise range lowers aspect ratio for minimum FSW.
4. Use of H_2 fuel lowers aspect ratio for minimum FSW.

ORBITER ENTRY TRAJECTORY CONTROL

By J. McNamara and L. Weiss
Grumman Aerospace Corporation
Bethpage, New York

I. HIGH-SPEED ENTRY PHASE

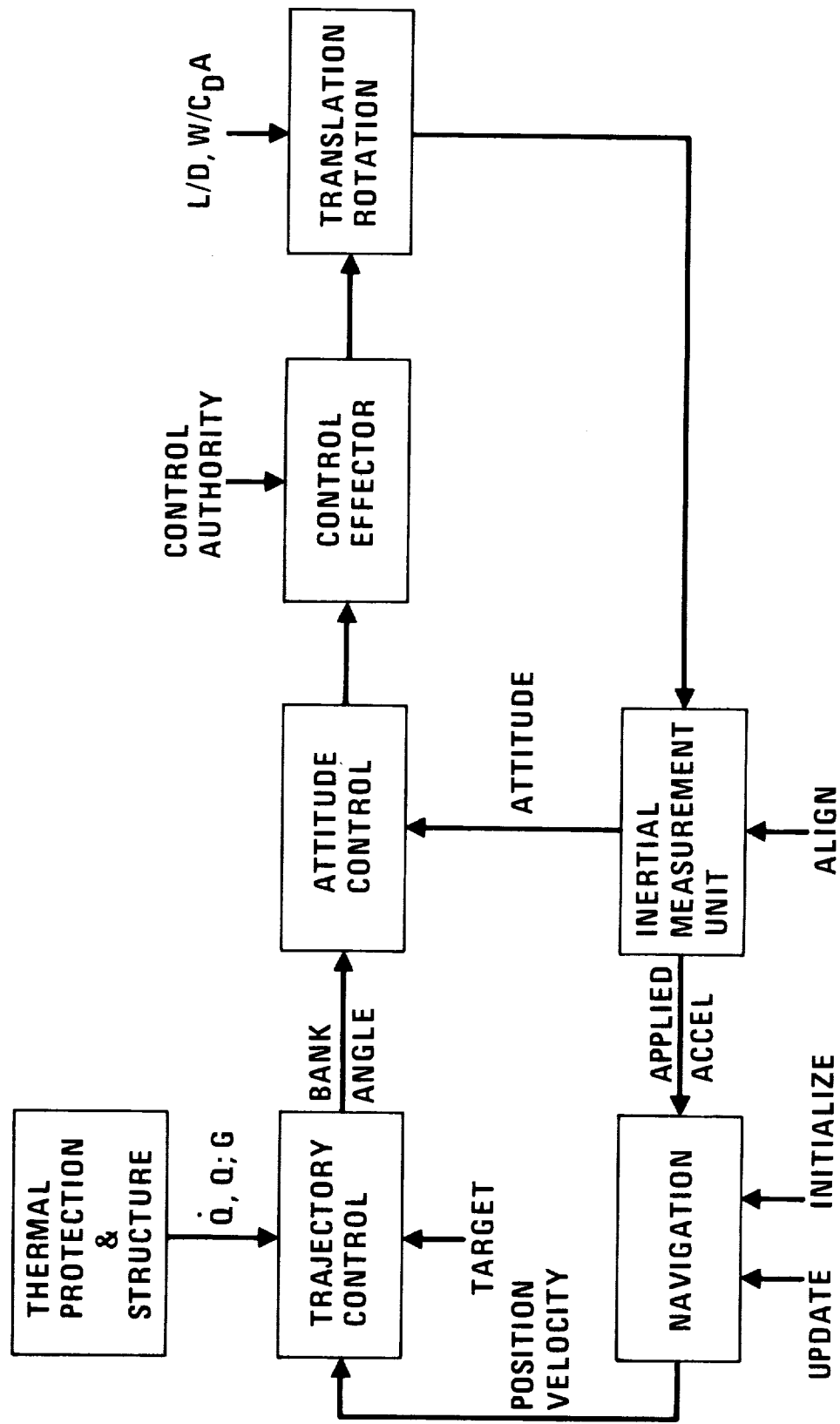
By J. McNamara

INTRODUCTION

The thermal environment experienced during entry is a major factor in the design of the Shuttle on-board Guidance Navigation and Control System. Reference heating rate profiles, characterized by a second maximum subsequent to transition to turbulent flow, penalize the weight and cost of the Thermal Protection System design for both the upper and lower vehicle surfaces.

A method of combining heat pulse shaping with control of applied acceleration and terminal targets is presented. The interaction of various system elements with thermal and load factor environment is evaluated.

TRAJECTORY CONTROL



TRAJECTORY CONTROL

(SLIDE 1)

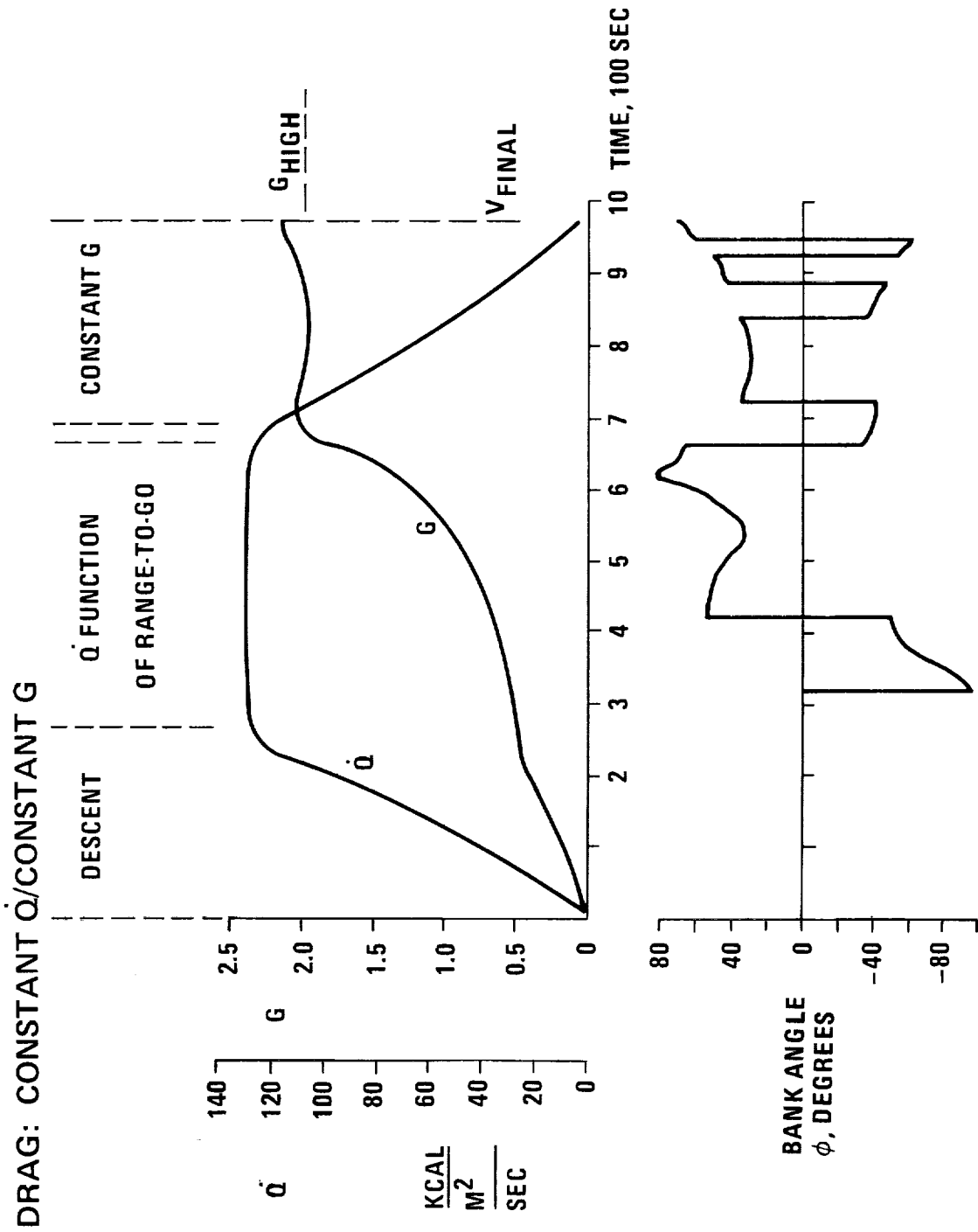
The entry is accomplished by two integrated systems: the outer guidance system with a 2 sec sample interval and the inner attitude control system with a 0.1 sec sample interval. An inertial measurement unit (IMU) provides applied acceleration and vehicle attitude, the required measurements for translational and rotational control.

The Thermal Protection and Structural Systems impose reference heating (\dot{Q}) total heat (Q), and applied acceleration (G) constraints upon the design of the trajectory. In addition to \dot{Q} , Q , and G constraints, guidance must steer to a specified target location and arrive there with the specified terminal speed.

Trajectory control is accomplished by designing a drag profile compatible with the entry constraints. Bank angle commands are then computed from the nominal drag value and the drag error. Proportional, integral, and derivative error control is employed.

Efficient and fast response to bank angle commands is required of the attitude control system.

Attitude control authority, navigation uncertainty, IMU performance, and vehicle aerodynamic uncertainty impact the effectiveness of trajectory control. Requirements for the design and operation of these systems are obtained from the study of their interaction with guidance and their impact on the \dot{Q} , Q , G , and target constraints.



DRAG: $\text{CONSTANT } \dot{Q} / \text{CONSTANT } G$

(SLIDE 2)

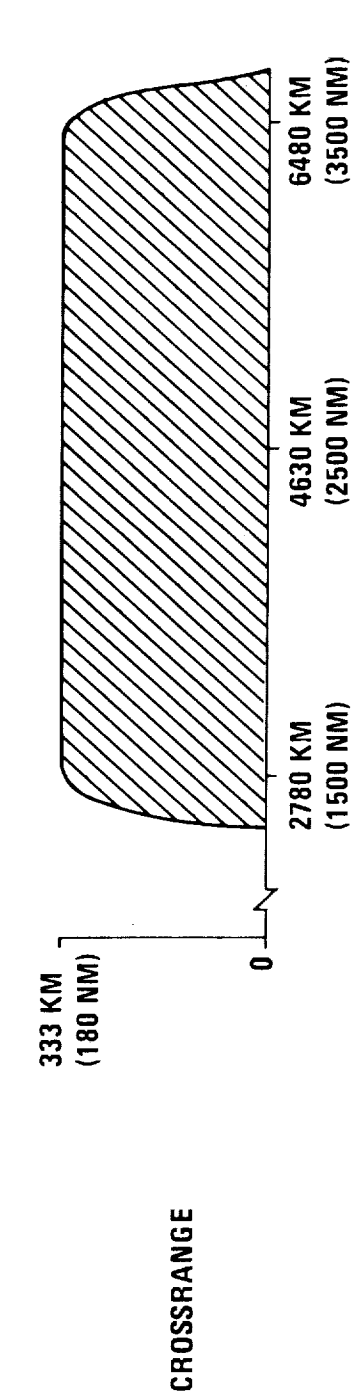
The entry is separated into four phases: (1) the descent to zero altitude rate, (2) the control of the heat flux in the stagnation region of a 0.3m (1ft) sphere (\dot{Q}), (3) the transfer from heat flux to applied acceleration (G) control, and (4) the control of G to arrive at the target latitude-longitude with the specified speed V_{FINAL} .

The desired \dot{Q} is obtained iteratively, by requiring the range of travel predicted for the final three phases to be equal to the range to the target. In addition, the G level, at the termination of the heat control phase, is constrained to be 90 percent of G_{HIGH} (the desired G level for the final phase). The \dot{Q} phase is terminated when the predicted range of travel during the last two phases is equal to the range from the present position to the target. After the transfer to G_{HIGH} has been accomplished, a new constant G value is computed every guidance interval. This G value insures the reduction of the instantaneous velocity to V_{FINAL} during the range of travel to the target.

For a 5556 km ($3,000$ nautical miles) target location, the vehicle enters with zero bank angle, rotates the lift vector out of the trajectory plane, and descends to the denser atmosphere. The descent increases G and maintains a constant \dot{Q} . The bank angle reversals are executed when the lateral excursion of the target from the trajectory plane exceeds one-half of the vehicle's estimated lateral range capability.

LOW CROSS RANGE GUIDED FOOTPRINT

- FINAL MISS DISTANCE < 3.7 KM (2 NAUT MI)
- $G_{MAX} < 2.5$



DOWNRANGE FROM ENTRY			
STAGNATION	\dot{Q}_{MAX}	KCAL/M ² /S (BTU/FT ² /S)	1500 NM
UNIT SPHERE	Q	KCAL/M ² (BTU/FT ²)	2500 NM
UNDERBODY AT 30.5M(100FT)	TEMP _{MAX}	°K (°F)	3500 NM
	Q _{UB}	KCAL/M ² (BTU/FT ²)	101 (38)
			74,000 (27,500)
			1144 (1600)
			8,100

LOW CROSS RANGE GUIDED FOOTPRINT

(SLIDE 3)

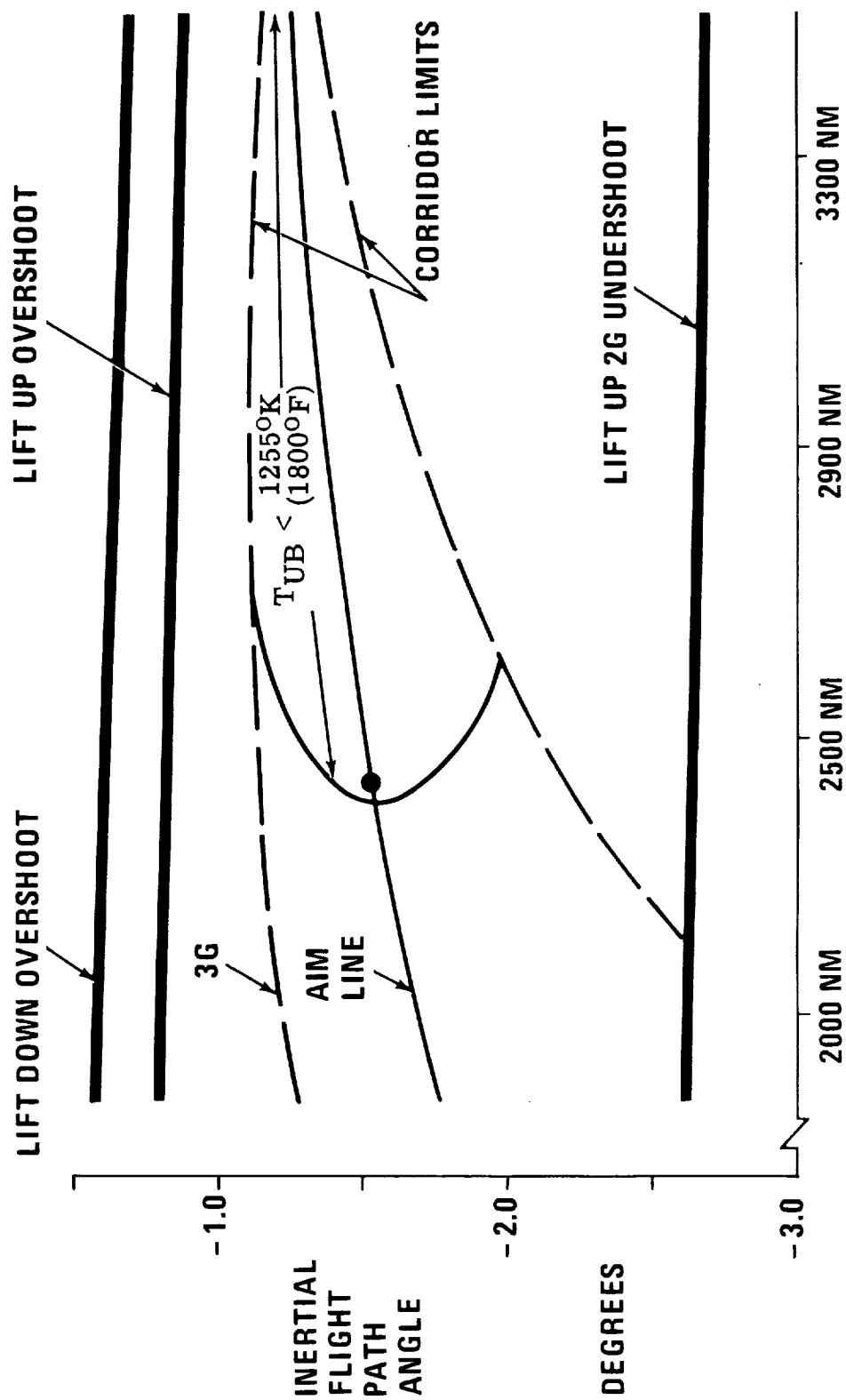
The guided footprint for the low cross range entry mode ($L/D = 0.5$, $W/C_{DA} = 1,436 \text{ N/m}^2$ (30 lb/ft^2)) extends 4259 km (2300 naut. mi.) and 666 km (360 naut. mi.) in the down range and cross range directions, respectively. For targets within this area the maximum G level does not exceed 2.5G while the maximum terminal miss distance is less than 3.7 km (2 naut. mi.).

The height of the flattened reference heat pulse, \dot{Q} , decreases as the target down range location increases. The duration of the heat pulse, however, and the resultant reference total heat (Q) increase as the down range increases.

The maximum radiation equilibrium temperature and total heat (Q_{UB}) at the 30.5m (100 ft.) underbody station are obtained from normal shock and isentropic expansion properties and the assumption that transition to turbulent flow occurs for free stream Reynolds numbers greater than 546,000.

The footprint provides over 1852 km (1000 naut. mi.) of down range target capability within which the maximum underbody temperature is less than 1255°K (1800°F). The underbody total heat remains essentially constant over the down range variation when determined with the above transition criterion. To provide a favorable thermal environment, a 5556 km (3000 naut. mi.) down range target is selected for the performance studies.

RANGE CORRIDOR



TARGET DOWNRANGE LOCATION

RANGE CORRIDOR

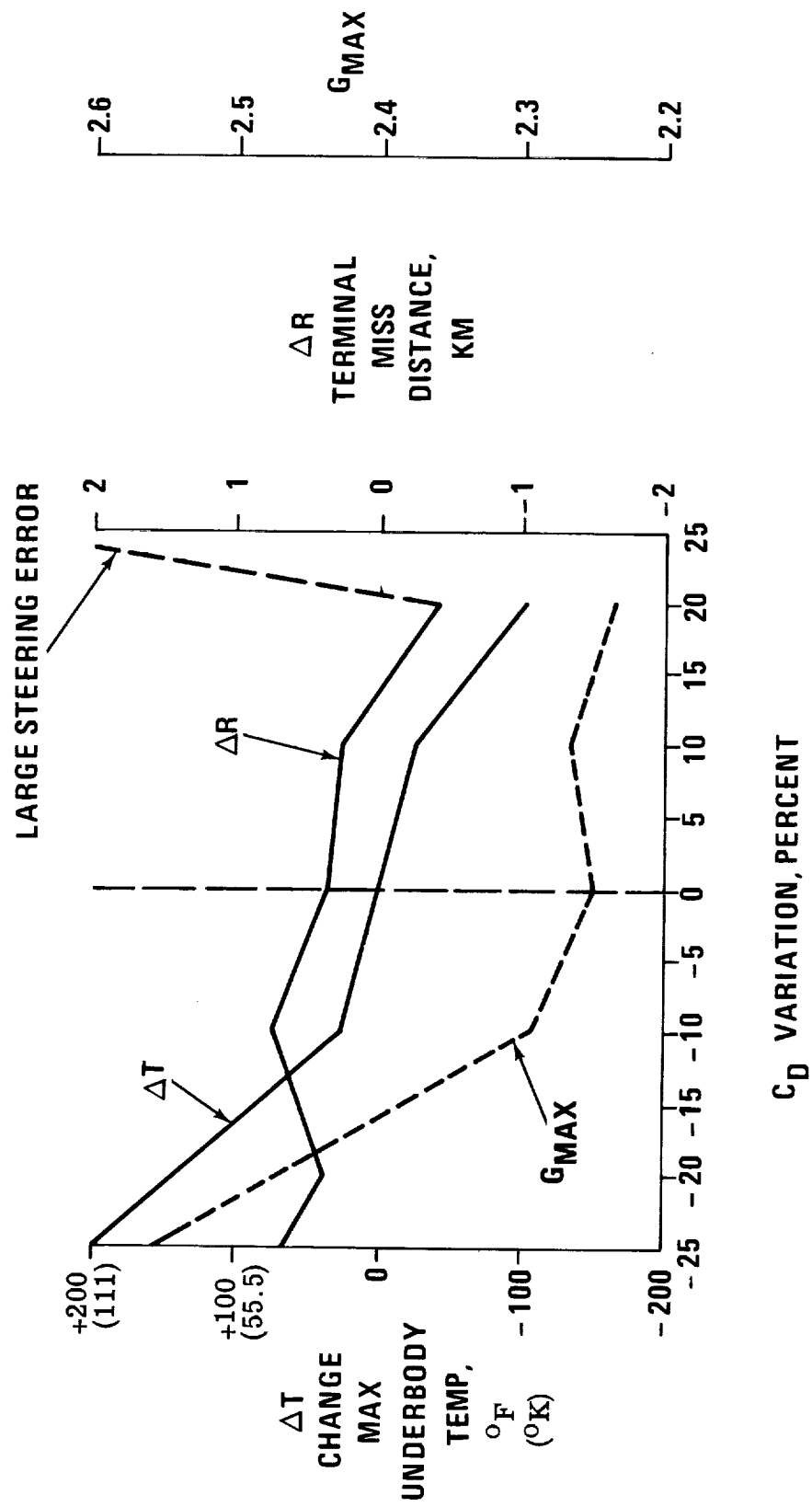
(SLIDE 4)

The flight path angle - range corridor for deorbit from a 500 km (270 naut. mi.) altitude circular orbit decreases from 1.5° at 3978 km to 0.4° at 5957 km. The aim line is selected to provide a stagnation region heat flux for a unit sphere (\dot{Q}) at the first perigee which can be maintained constant during the \dot{Q} phase of the entry. The inertial entry speed, on the aim line, varies between 7910 m/s (25,952 fps) at 3978 km and 7932 m/s (25,995 fps) at 5957 km. The intersection of the aim line with the recommended MSC Shuttle target line is represented by a dot on the slide.

Entry at the shallow flight path angle defining the 3G corridor limit, permits large downrange distances to be traversed prior to the initiation of any significant deceleration. In order to accomplish the velocity reduction within the remaining range to the target, a constant 3G deceleration is commanded immediately. An entry at the steep flight path angle limit results in a significant reduction in velocity during the initial portion of entry. The kinetic energy which remains is insufficient to permit the vehicle to be guided to the specified down range location.

For a metallic Thermal Protection System (TPS), sensitive to heating rate, the entry is planned in the narrow and sensitive end of the corridor where the maximum underbody temperature is less than 1255°K (1800°F). For an external insulation TPS, more sensitive to total heat, the entry is planned in the wide end of the corridor.

AERODYNAMIC UNCERTAINTY



AERODYNAMIC UNCERTAINTY

(SLIDE 5)

The computation of the desired heating flux, \dot{Q} , requires that the down range distance traveled during the constant \dot{Q} phase be predicted. The ballistic parameter, $W/C_D A$, proportional to the ranging capability of the vehicle, is required for this prediction. Errors in the estimate of the aerodynamic coefficient, C_D , and therefore $W/C_D A$, result in \dot{Q} and G penalties.

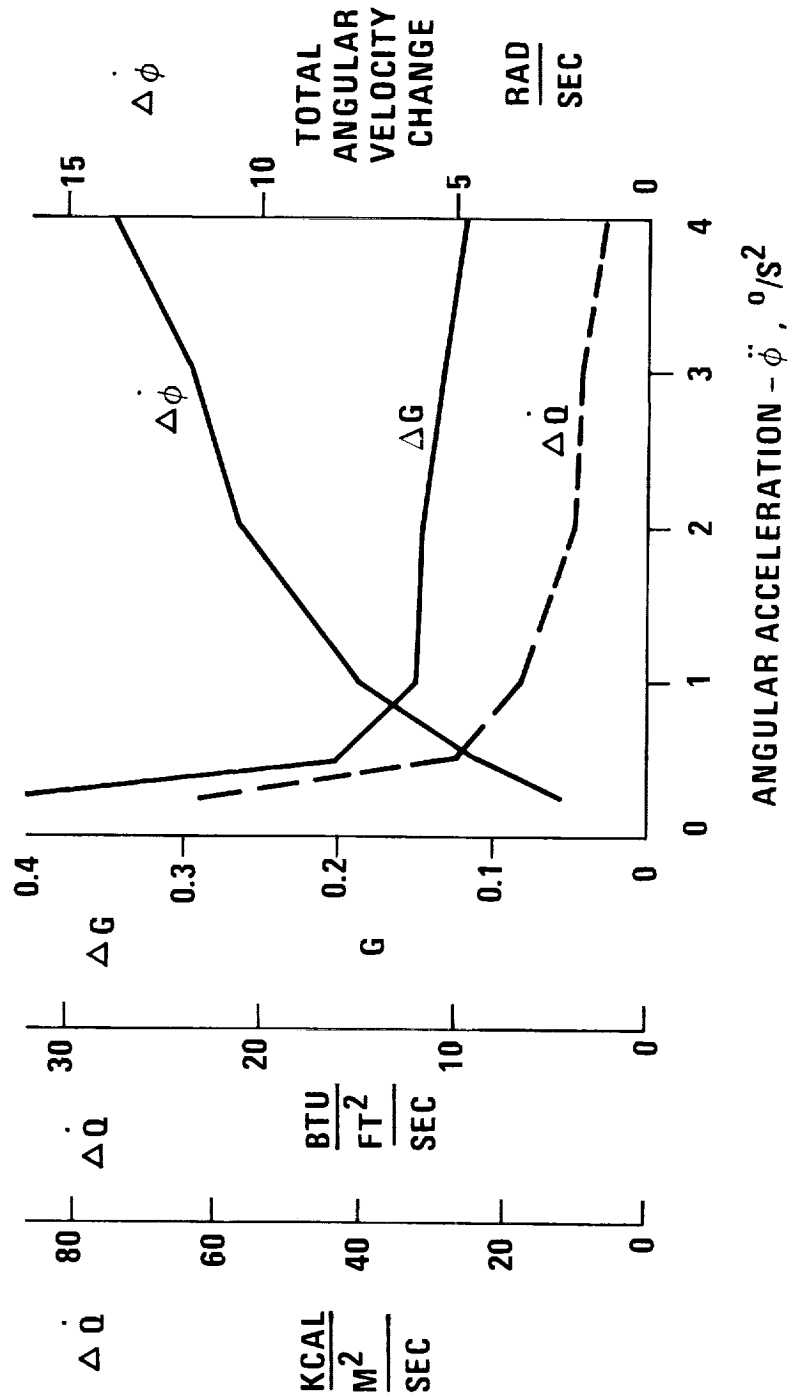
For an actual C_D value which is less than the estimated value, the vehicle's ranging capability is underestimated by the guidance during the \dot{Q} phase. Drag commands are issued which permit the vehicle to approach the target at a velocity higher than in the nominal case. To correct this condition, a higher deceleration level is subsequently requested, resulting in increases in G and temperature. For an actual C_D value 15 percent less than the estimated value, an 44.5°K (80°F) increase in peak underbody temperature occurs.

For $W/C_D A$ estimates which are greater than actual values, the vehicle velocity is reduced too rapidly. Large terminal miss distances occur for actual C_D errors of + 20 percent.

The effect of a variation in atmospheric density is small. A 20 percent decrease in density increases the underbody temperature by 6.7°K (12°F). Variations of up to 10 degrees in the trim angle-of-attack have small effect on target control or environment.

GUIDANCE/CONTROL AUTHORITY REQUIREMENTS

- CONTROL EFFECTOR CAUSES \dot{Q} AND G TO OSCILLATE ABOUT DESIRED VALUE
- PEAK TO PEAK MAGNITUDE $\Delta \dot{Q}$ AND ΔG



Slide 6

GUIDANCE/CONTROL AUTHORITY REQUIREMENTS

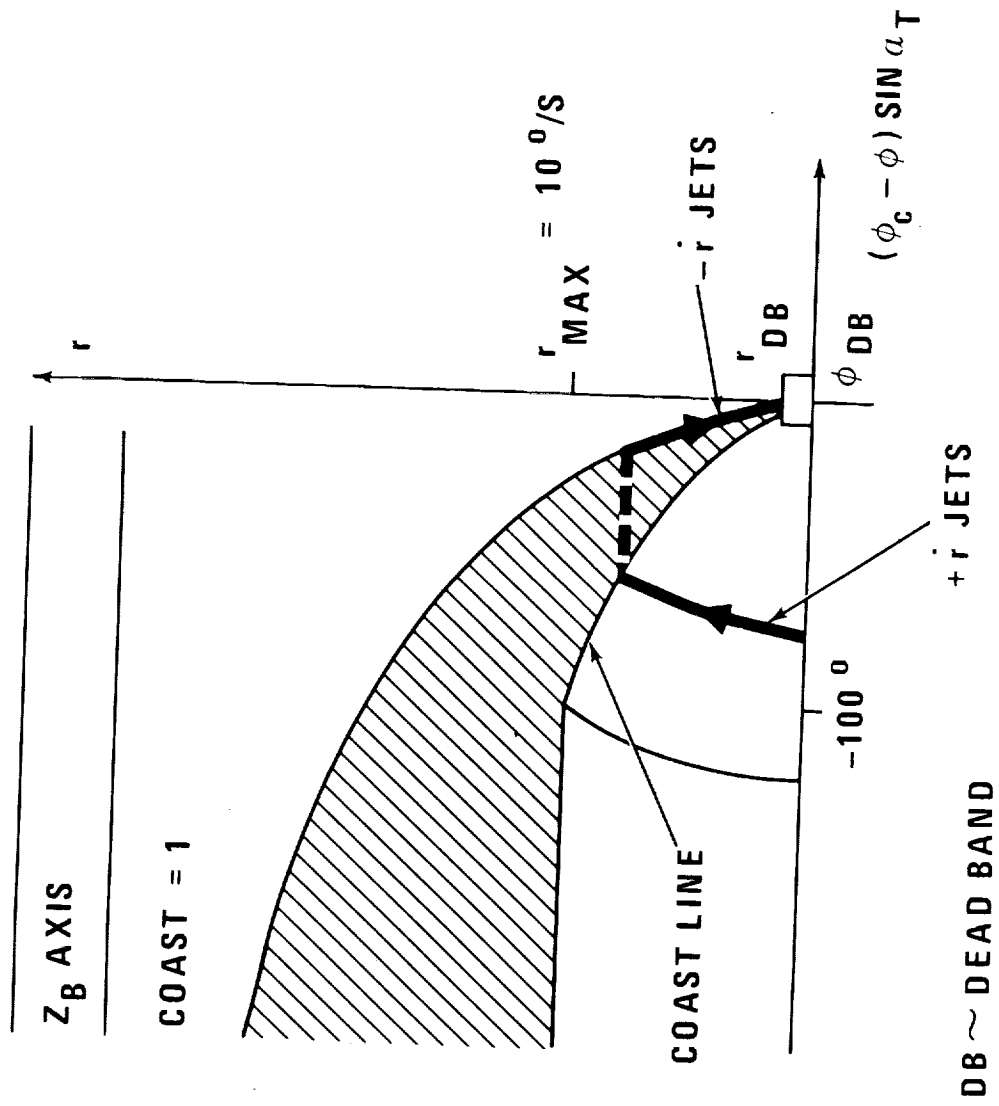
(SLIDE 6)

The introduction of second order dynamics for the bank angle control effector reduces the capability of the guidance to control \dot{Q} and G . The bank angle dynamic model includes a specified maximum angular rate ($\dot{\phi}_{MAX} = 10^\circ/\text{sec}$) and an available angular acceleration $\ddot{\phi}$. The slower lift vector angular response results in \dot{Q} and G profiles which are characterized by oscillations with peak-to-peak magnitudes $\Delta\dot{Q}$ and ΔG .

For an acceleration of $0.25^\circ/\text{sec}^2$, control of \dot{Q} , G and the terminal target is unacceptable. Significant improvement is achieved as $\ddot{\phi}$ increases from 0.25 to $1.0^\circ/\text{sec}^2$. Little improvement in guidance authority is achieved as $\ddot{\phi}$ increases from 2 to $4^\circ/\text{sec}^2$. Selection of an angular acceleration between 1 and $2^\circ/\text{sec}^2$ provides maximum control authority with minimum control effort.

The total angular velocity change accumulated during the entry ($\Delta\dot{\phi}$) is a measure of the control effort expended in response to bank angle command changes. This required effort increases with higher values of angular acceleration $\ddot{\phi}$. For accelerations greater than $2^\circ/\text{sec}^2$, achievement of greater control authority is impractical because of the significant increase in required effort.

Z AXIS ATTITUDE COMMAND AUTOPILOT



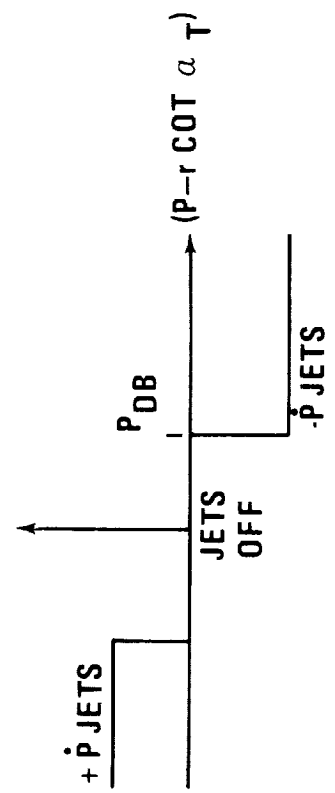
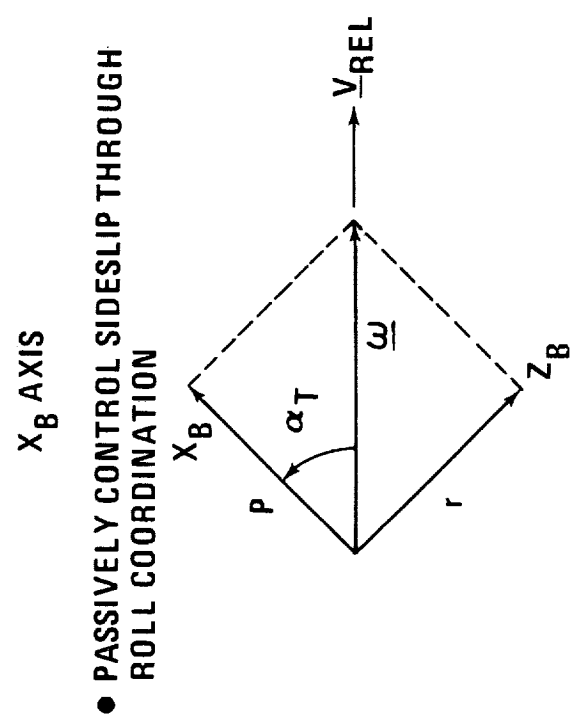
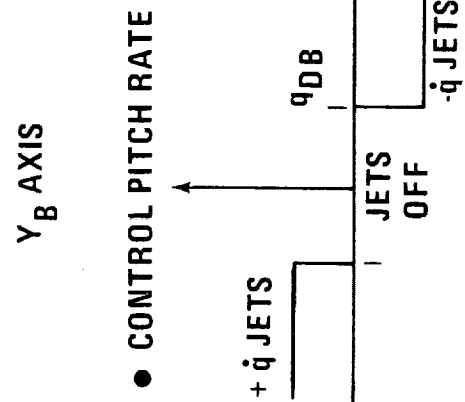
Z AXIS ATTITUDE COMMAND AUTOPILOT
(SLIDE 7)

The control of bank angle is assigned to the Z_B axis (r jets) and is accomplished by computing an attitude error about the Z_B axis from the bank angle error ($\phi_c - \phi$). The yaw dynamic model assumed is that of a simple inertia. This approach makes the phase plane attractive because the motion can be described by straight lines and parabolas (ref. 1).

The control policy utilizes a control line to determine the rate with which an attitude error is reduced. For a given control line the system responds rapidly to large error and slowly to small error. The fundamental advantage in this type of response is that propellant consumption is approximately proportional to error. The overall system response can be reduced by lowering the control line in the phase plane. The coast line is depressed (increasing values of the coast parameter) as far as is consistent with the rate of response required by the guidance for \dot{Q} , G , and target control.

The trajectory shown is initiated with a large negative angle error and zero rate. The $+r$ jets remain on for the time required to intersect the coast line, then are turned off. The vehicle coasts at a rate less than r_{\max} until the terminal parabola is intersected. The $-r$ jets are turned on for the time required to reach the origin. The limit cycle motion will occur within the dead zone described by r_{DB} and ϕ_{DB} .

X_B AND Y_B AXES RATE COMMAND



X_B and Y_B AXES RATE COMMAND

(SLIDE 8)

Within the atmosphere, the aerodynamic forces tend to keep the side slip angle, β , essentially zero and tend to make the angle of attack, α , assume a trim value, α_T . Attitude control, therefore, is required only in bank angle, ϕ . As the vehicle banks about the velocity vector, the Y_B axis should remain normal to the velocity vector. When $\beta = 0$ and $\alpha = \alpha_T$, the condition of banking about the velocity vector, or performing a coordinated bank, requires the angular velocity vector (ω) to lie along the relative velocity vector V_{REL} . Rate control about the X_B and Y_B axes is employed to damp the vehicle dynamics and also to control the coordinated bank maneuver.

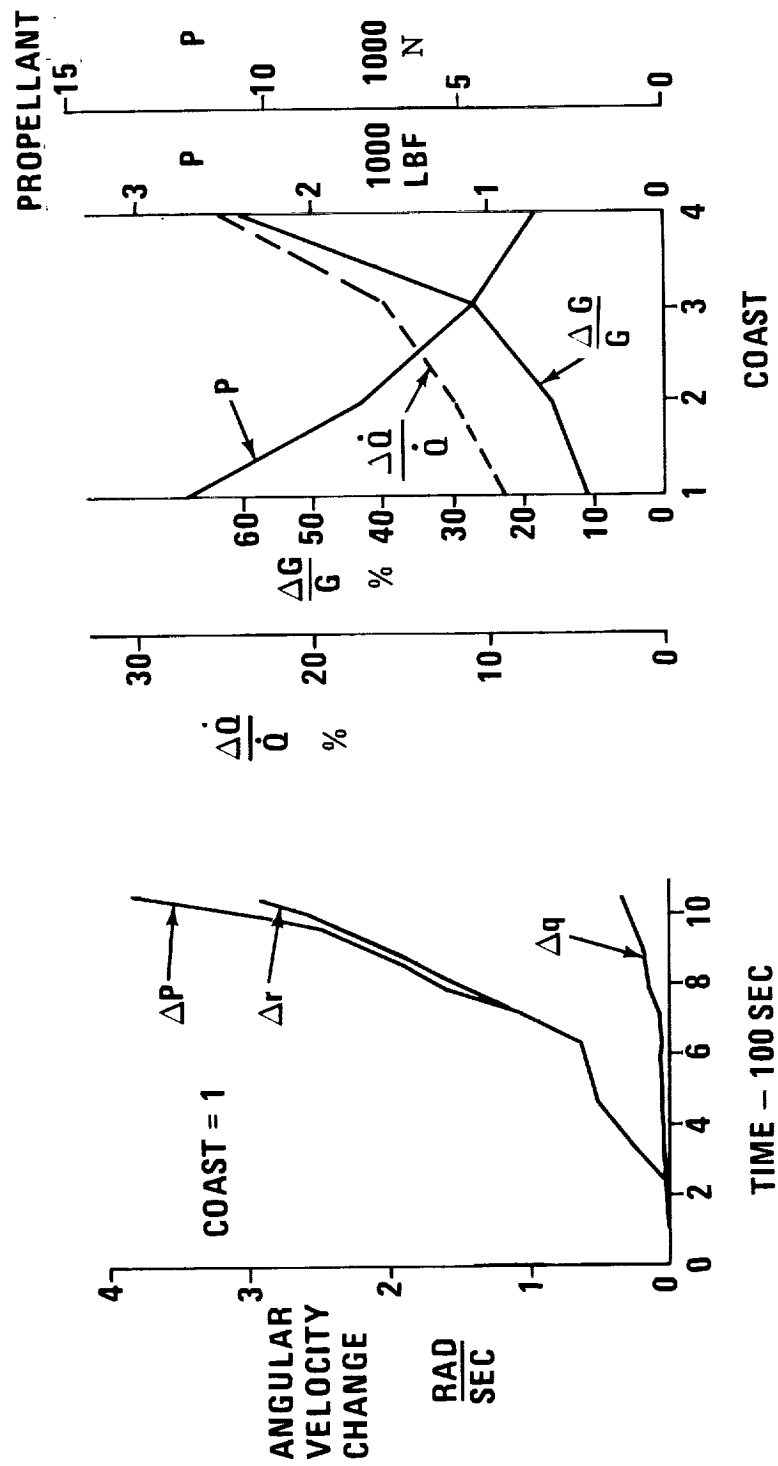
The pitch axis control logic is described by the rate dead band, q_{DB} , centered about $q = 0$ within which q is forced to remain. The roll axis control logic is described by the rate dead band p_{DB} , centered about the coordinated bank angle rate, $p = r \cot \alpha_T$, within which p is forced to remain.

ATTITUDE CONTROL PROPELLANT

VEHICLE: $I_{ZZ}/I_{XX} = 6$, $C\eta_\beta = -0.12 \text{ RAD}^{-1}$, $C\eta_\beta = -0.1 \text{ RAD}^{-1}$

$$\ddot{p} = 4.1^\circ/\text{S}^2, \ddot{q} = 1.1^\circ/\text{S}^2, \ddot{r} = 1.25^\circ/\text{S}^2$$

DEAD BAND: ATTITUDE, 5° ; RATE, $0.2^\circ/\text{S}$



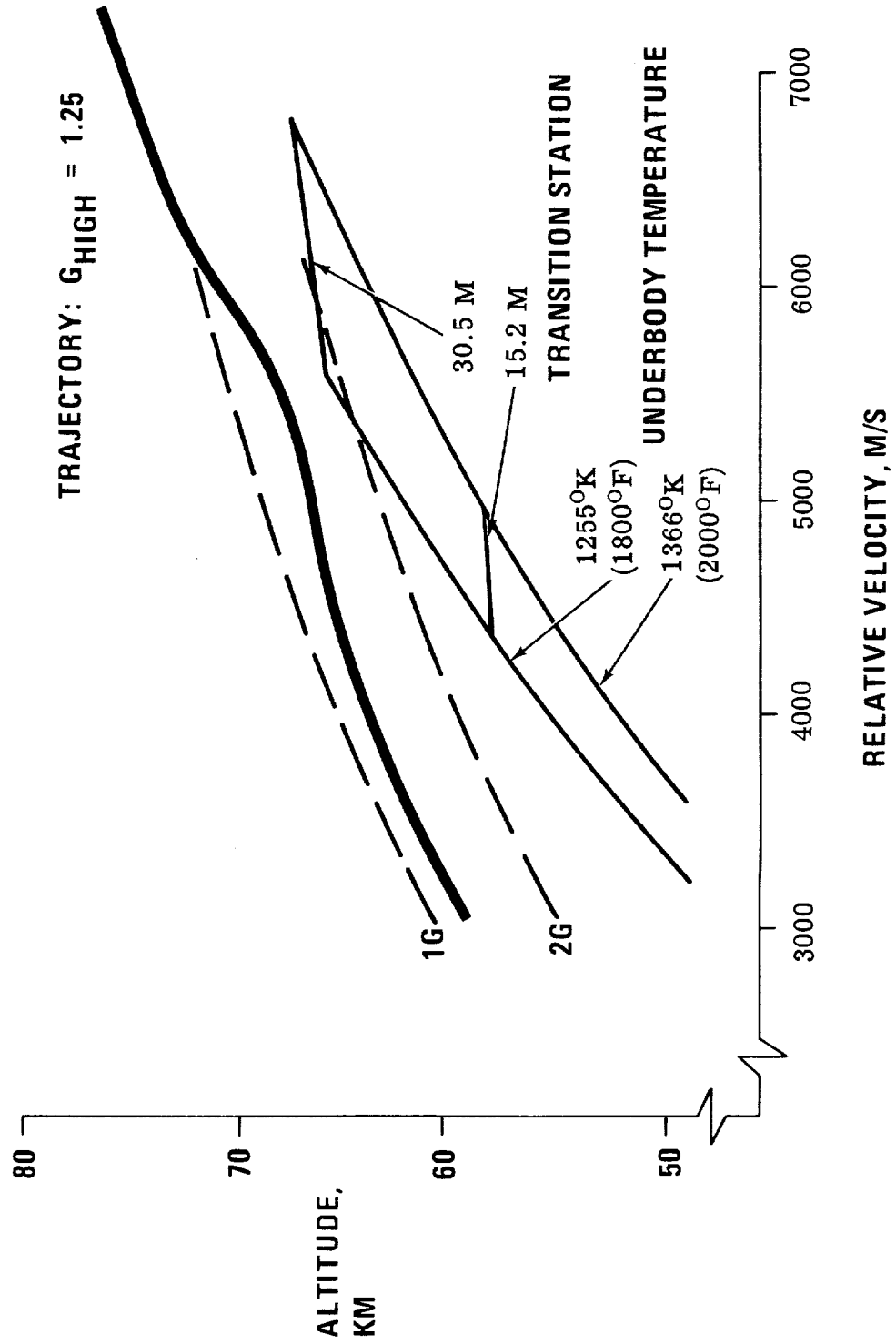
ATTITUDE CONTROL PROPELLANT

(SLIDE 9)

The propellant consumed by the Entry Attitude Control Propulsion System (ACPS) is related to the control system design and the guidance system requirements. The Z_B axis attitude-control phase plane is designed with a 5° attitude deadband and a $0.2^\circ/\text{s}$ angular rate deadband. A $0.2^\circ/\text{s}$ angular rate deadband is also assigned to the X_B and Y_B rate command axes. The propellant consumption associated with a unity value of the phase plane parameter "coast", is 11,787 N (2,650 lb). This value provides maximum guidance authority over \dot{Q} and G . Higher values of the coast parameter, (2,3,4) result in lower propellant consumption and, reduction in trajectory control. The desirable coast value lies between 2 and 3 and requires between 4448 N (1000 lb) and 7784 N (1750 lb) of propellant.

The change in angular velocity is distributed between the X_B (Δp) and Z_B (Δr) axes. There is greater activity about the roll axis due to the smaller moment of inertia and the cross axis coupling. The major portion of the propellant is expended to produce the activity about the yaw axis due to moment of inertia ratio.

MINIMIZE UNDERBODY HEATING



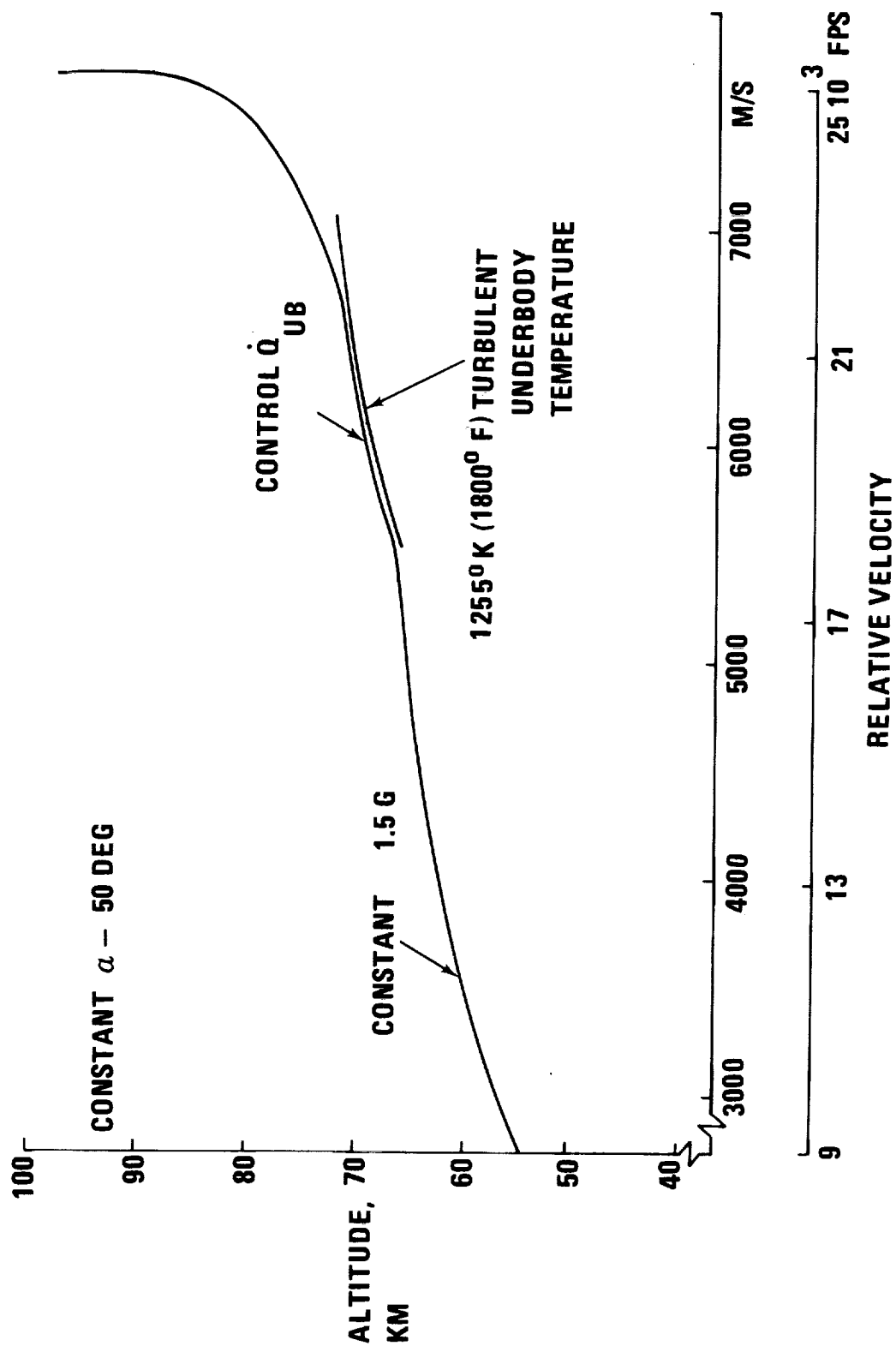
MINIMIZE UNDERBODY HEATING

(SLIDE 10)

The turbulent underbody temperature can be maintained below 1255°K by the proper selection of the guidance parameter, G_{HIGH} . The transition from laminar to turbulent underbody flow, for a given vehicle station, occurs at approximately the same altitude over the range of critical velocities. The guidance objective is to force the trajectory to remain above this altitude without changing the nature of the trajectory control policy.

The selection of $G_{\text{HIGH}} = 1.25$ produces a trajectory which maintains the turbulent flow well aft of the 30.5m vehicle underbody station. For this value of G_{HIGH} , the terminal target and G level control requirements are both satisfied.

CONTROL UNDERBODY HEAT



CONTROL UNDERBODY HEATING

(SLIDE 11)

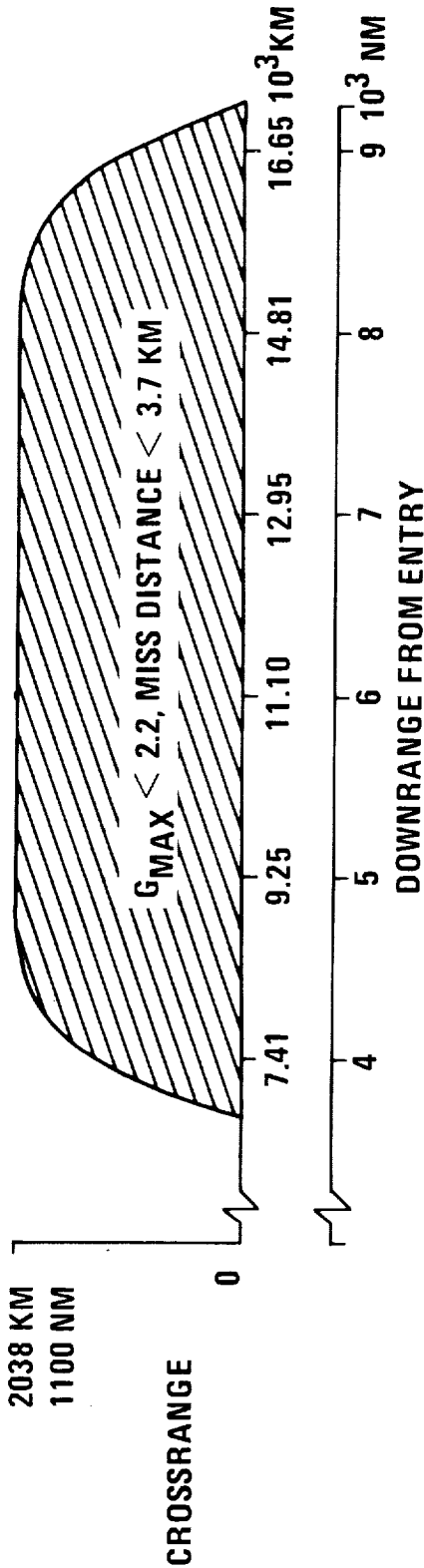
The direct control of turbulent underbody heat rate (\dot{Q}_{UB}) is accomplished by a mathematical model of the underbody heat process. This model enables a specified underbody temperature to be related to the variables employed by the guidance drag controller. The two required variables are drag and the time derivative of drag.

The entry consists of the descent to zero altitude rate followed by the active control of stagnation region heat rate (\dot{Q}). Control of \dot{Q}_{UB} is initiated as the specified underbody temperature value is approached.

The control of \dot{Q}_{UB} is terminated when the range to the target permits a planned transfer to the constant G mode of flight. During the final phase, the guidance requests the constant G value which is consistent with the targeting requirements.

HIGH CROSS RANGE GUIDED FOOTPRINT

- ANGLE OF ATTACK TRANSITION AT FIRST PERIGEE – 50° TO 20°
- AT $\alpha = 20^\circ$: $L/D = 1.8$, $W/C_D A = 14.1 \text{ KN/M}^2$ (294 LB/FT²)
- CONTROL \dot{Q} , G, TARGET



STAGNATION UNIT	\dot{Q}_{MAX}	DOWNRANGE FROM ENTRY						
		5000 NM	6000 NM	7000 NM	8000 NM	9000 NM	10000 NM	11000 NM
SPHERE	KCAL/M ² /S	194	178	175	170	165	160	155
	BTU/FT ² /S	72	66	65	63	61	59	57
	10 ³ KCAL/M ²	276	302	329	359	389	419	449
SPHERE	Q	DOWNRANGE FROM ENTRY						
		5000 NM	6000 NM	7000 NM	8000 NM	9000 NM	10000 NM	11000 NM
SPHERE	Q	102	113	122	132	142	152	162
		102	113	122	132	142	152	162

HIGH CROSS RANGE GUIDED FOOTPRINT

(SLIDE 12)

A guided footprint for the high cross range mode of entry is presented for a vehicle which enters at an angle-of-attack of 50 degrees, executes a transition to 20 degrees at the first perigee, and employs bank angle control during the remaining portion of the entry. The guidance policy discussed initially is employed to control reference heating, applied acceleration, and terminal target control.

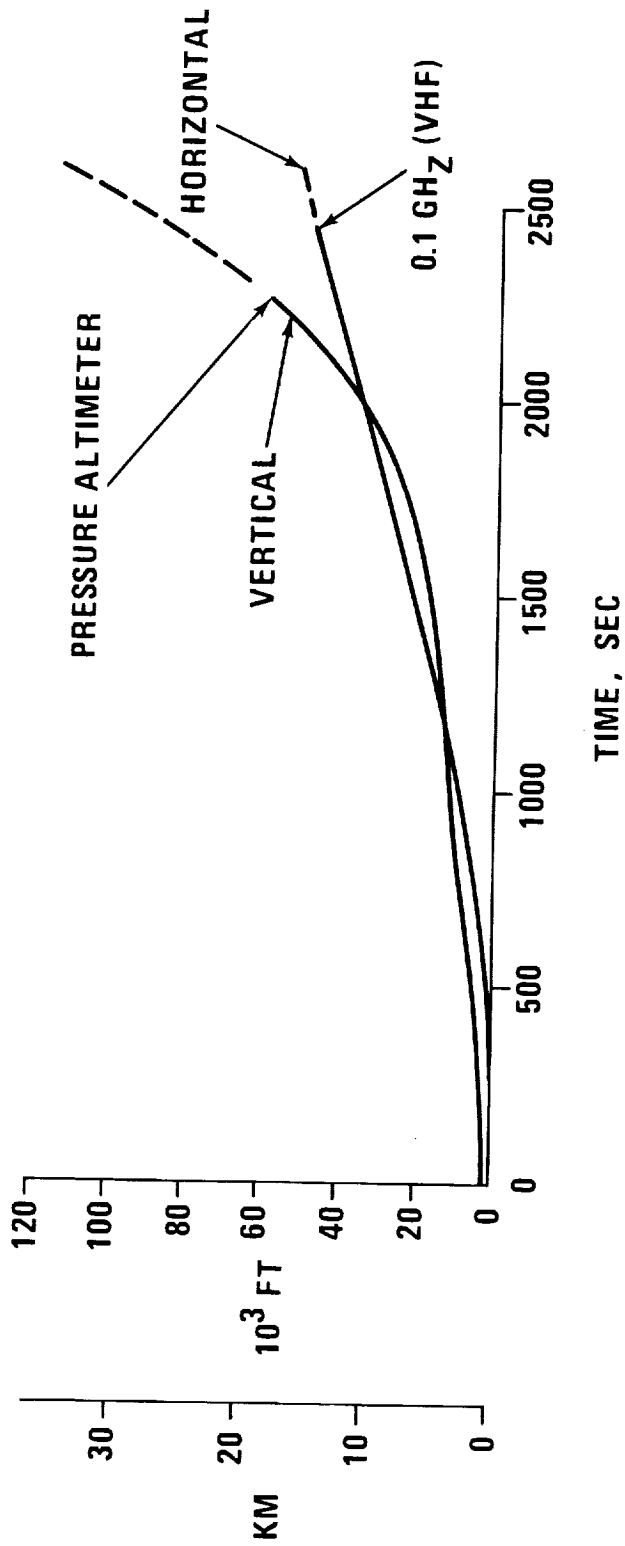
Within the footprint which extends 9260 km (5000 naut. mi.) in the down range direction and 2037 km (1100 naut. mi.) in the cross range direction, the maximum applied acceleration experienced is 2.2G and the maximum miss distance is less than 2.8 km.

For a non-metallic TPS which is sensitive to the total heat, a 25 percent reduction in reference Q can be obtained by flying the second portion of the entry at an angle-of-attack of 27 degrees. A reduction in maximum \dot{Q} also results.

NAVIGATION PERFORMANCE

- TARGET**
 - 12964KM (7000 NM) DOWNRANGE, 2185 KM (1180 NM) CROSSRANGE
- ENTRY**
 - RMS STATE VECTOR ERROR - POSITION 780 M (2550 FT), VELOCITY 0.9 M/S (2.9 FPS)
 - IMU 3 σ MISALIGNMENT - 1 MRAD
- IMU ERROR**
 - 3 σ GYRO BIAS DRIFT RATE - 0.1 DEG/HR
 - 3 σ ACCELEROMETER BIAS - 0.024 CM/SEC

POSITION ERROR (3 σ)



NAVIGATION PERFORMANCE

(SLIDE 13)

The navigation performance of a gimballed Inertial Measurement Unit (IMU) is described by the time history of the 3σ vertical and horizontal position errors. The trajectory target location is 12,964 km (7000 naut. mi.) downrange and 2037 km (1100 naut. mi.) crossrange. The total time of entry is 2600 sec.

A state vector update and IMU alignment is assumed to occur between the de-orbit maneuver and Entry Interface. The RMS position and velocity errors are predominantly in the downrange and altitude directions, respectively.

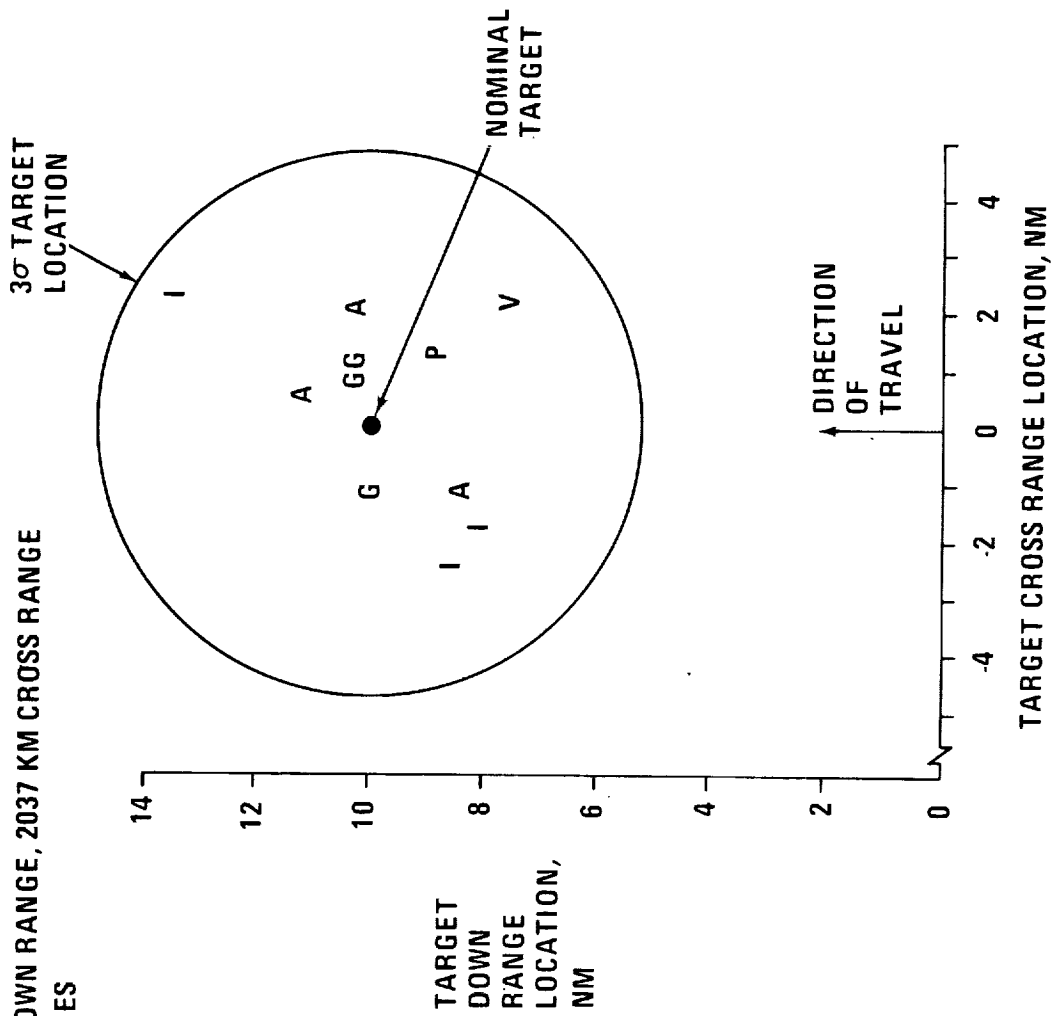
Without external information, the unstable vertical axis experiences a 35.3 km (19 n.mi.) altitude uncertainty toward the end of the entry. Similarly, the horizontal uncertainty increases to a value of 14.8 km (8 n.mi.) at V_{FINAL} . An external measurement of altitude, at approximately 39.6 km altitude, inhibits the growth of the altitude error, and eventually drives the error down to smaller values. The direction and distance to the target can be updated once the VHF blackout boundary is broken and the vehicle is within the operating range and altitude of the terminal sensor. The incorporation of navigation in the horizontal axes, however, is possible only at the lower velocities late in the entry.

GUIDANCE/NAVIGATION INTERACTION

TARGET: 11,112 KM (6000 NM) DOWN RANGE, 2037 KM CROSS RANGE

+3 σ NAVIGATION ERROR SOURCES
INITIALIZE AT ENTRY

POSITION - P
VELOCITY - V
IMU ALIGN - I
GYRO DRIFT - G
ACCEL BIAS - A



GUIDANCE/NAVIGATION INTERACTION

(SLIDE 14)

A series of guided, high cross range trajectories are simulated to determine a typical scatter pattern about the target location due to navigation system errors. Each trajectory is executed with one $+3\sigma$ navigation error source. The entry is performed with IMU information only, without the incorporation of external measurements.

Ideally, the entry phase is terminated at V_{FINAL} with the target 18.52 km (10 naut. mi.) directly in front of the vehicle. The RMS result of the navigated trajectories is to locate the target in an ellipse, centered at the nominal location. The down range and cross range dimension of the ellipse are 8.3 km (4.5 naut. mi.) and 7.9 km (4.3 naut. mi.), respectively.

The divergent altitude error increased to values of 7,620 m (25,000 ft.) on several trajectories. The actual terminal altitude dispersion, which is less than 1,524 m (5,000 ft), is smaller due to the requirement of controlling to a measurable drag value during the critical terminal phase. The drag control technique also makes the control of the thermal environment much less sensitive to the altitude error than would a reference trajectory technique (ref. 2).

The terminal dispersions can be reduced by utilizing external measurements of the relative position to the target during the entry. An on-board minimum variance filter can be used to incorporate the measurements in an optimum manner. The dispersions which result are then required to be absorbed by the spiral glide descent phase of entry.

SUMMARY

DRAG CONTROLLER CAN SHAPE \dot{Q} AND G PROFILES WITHIN :

2 000 BY 180 NAUT. mi. LOW CROSSRANGE MODE FOOTPRINT
5 000 BY 1100 NAUT. mi. HIGH CROSSRANGE MODE FOOTPRINT

AN UNDERBODY HEAT RATE PHASE CAN MAINTAIN T_{UB} BELOW SPECIFIED LIMIT

BANK ANGLE CONTROL AUTHORITY OF $1.5^{\circ}/\text{sec}^2$ IS REQUIRED FOR CONTROL OF
THERMAL ENVIRONMENT

MAX T_{UB} CONSTRAINTS REDUCE RANGE OF ALLOWABLE ENTRY FLIGHT PATH ANGLES

ALTITUDE POSITION ERROR IS 6.1 km (20 000 ft) DURING CRITICAL HEATING AND
20 NAUT. mi. DURING TERMINAL TARGET CONTROL

DRAG CONTROLLER REDUCES SENSITIVITY TO NAVIGATION ERRORS

SUMMARY

The drag control method of entry guidance can be used to shape the reference heating pulse, control the load factor, and steer to a specified target within a 4259 km (2300 naut. mi.) by 666 km (360 naut. mi.) low cross range mode footprint and within a 9260 km (5000 naut. mi.) by 4074 km (2200 naut. mi.) high cross range mode footprint. The control of underbody heating can be introduced to maintain underbody temperature below a specified limit.

Bank angle control authority of $1.5^\circ/\text{sec}^2$ is required for thermal and load factor control. Approximately 6672 N (1500 lb) of attitude control propellant is expended for control in the low cross range mode.

The divergent altitude position error increases to 6,100 m (20,000 ft.) during the critical heating portion and to 37.0 km (20 naut. mi.) during terminal target control. Control of the trajectory to desired drag values, therefore density altitudes, reduces the sensitivity of the trajectory dispersions to navigation errors.

REFERENCES

1. Anon.: Guidance System Operation Plan for Manned CM Earth Orbital and Lunar Missions Using Program COLOSSUS 2c (Commache Rev. 67), Section 3 Digital Autopilots (Rev. 7). R-577, Instrumentation Lab., Massachusetts Inst. Technol., Aug. 1969.
2. Morth, Raymond: Reentry Guidance for Apollo. Vol. I. R-532(Contract NAS 9-4065), Instrumentation Lab., Massachusetts Inst. Technol., Jan. 1966. (Also available as NASA CR-65691.)

ACKNOWLEDGMENT

Contributions to this paper in the following areas were made by:

P. Dunn (Grumman Aerospace)	control system design
F. Wimpfheimer (Grumman Data Systems)	guidance and navigation logic
W. Timlen (Grumman Aerospace)	thermodynamic analysis
R. Domjan (Grumman Aerospace)	navigation performance
J. Kalviste (Northrop Aviation)	footprint analysis
R. Meyer (Grumman Aerospace)	spiral glide descents
H. Watman (Grumman Aerospace)	unpowered landings

II. TERMINAL PHASE ENTRY

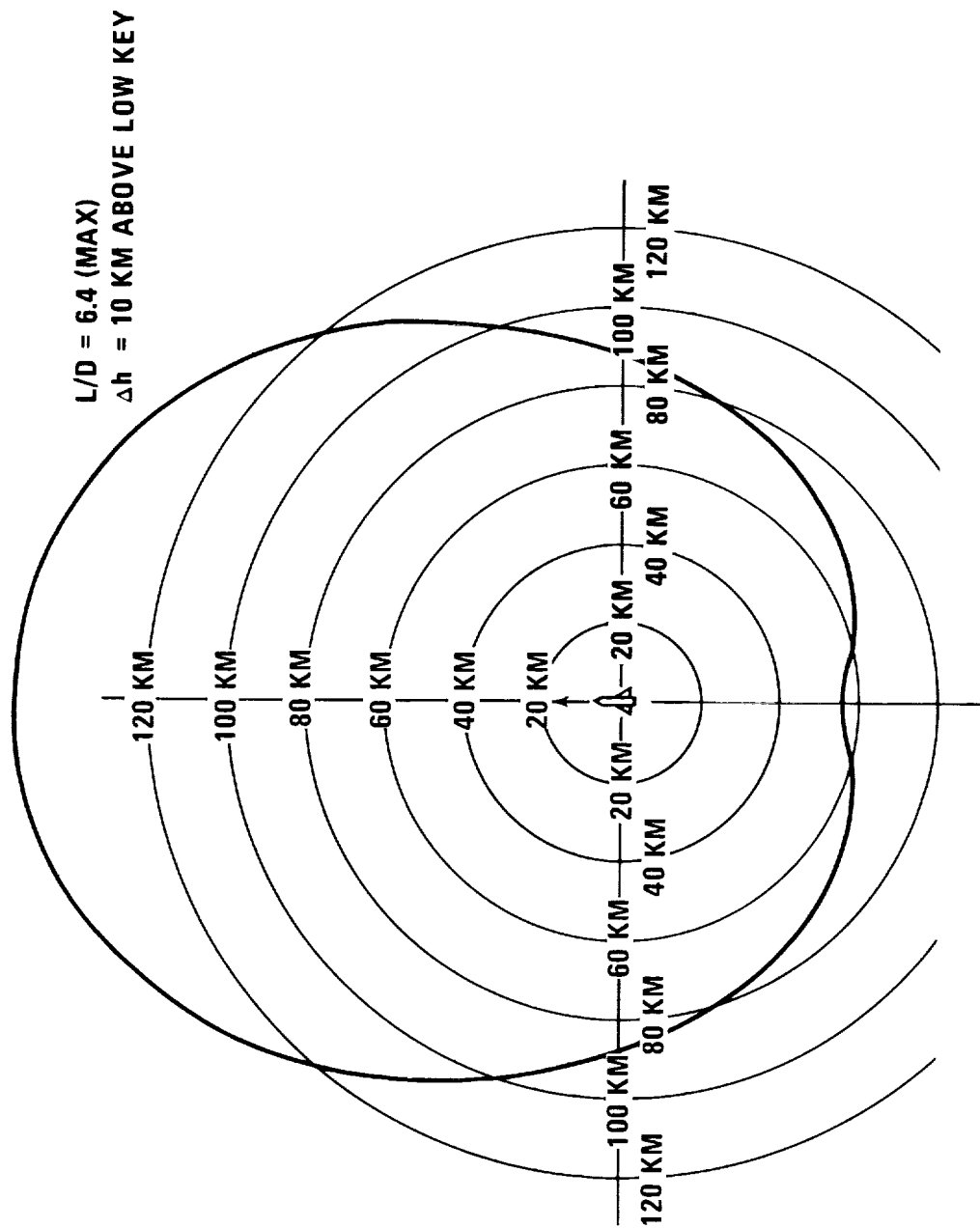
By L. Weiss

INTRODUCTION

After transition to conventional aerodynamic flight, a spiral glide is flown to target the vehicle into the final approach path. Judicious use of energy management techniques permits considerable latitude in gliding the vehicle to a target point with a specified heading angle.

Previous studies indicate that it is desirable to define two points of reference as milestones on the glide path: the high key and the low key. The low key is established a priori as the target point for the descent glide; however, in order to preserve the chronological sequence of events during entry, the discussion of its establishment is held off for the moment.

ORBITER RANGING WITH HEADING CHANGE



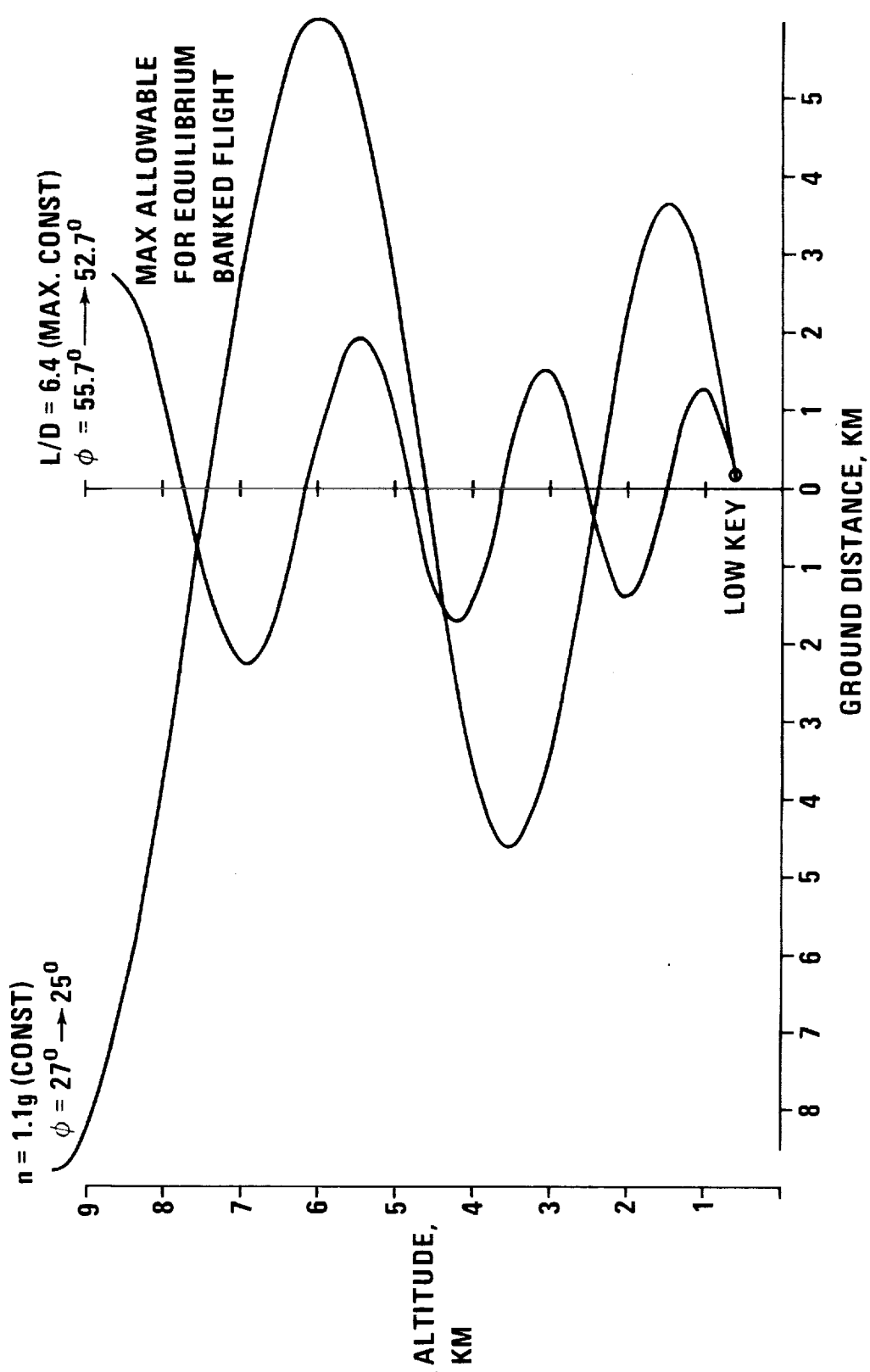
ORBITER RANGING WITH HEADING CHANGE

ENERGY MANAGEMENT WINDOW 10 KM ABOVE THE LOW KEY POINT

(SLIDE 1)

The high key on the glide path is a cardioid-shaped area, or a "window," in the x-y plane which defines the ranging capabilities of the orbiter for all heading angles, the limitation being the maximum lift-to-drag ratio of the vehicle. This energy management window expands with altitude, as the potential energy of the gliding vehicle increases. The window in this example was calculated for an altitude of 10 km above the low key, since at that altitude the vehicle is certain to have made the nosing-down transition to aerodynamic flight. In an actual Mission Operations Manual, the high key would be defined for every altitude, presenting, as it were, a three-dimensional inverted pyramid of expanding cardioids. The low key must be within the ranging capabilities of the orbiter at all times during the descent, ideally in the center of the cardioid.

SPIRAL GLIDE DESCENT TRAJECTORIES TO INITIATION OF FINAL APPROACH (SIDE VIEW)



SPIRAL GLIDE DESCENT TO INITIATION OF FINAL APPROACH (SIDE VIEW)

(SLIDE 2)

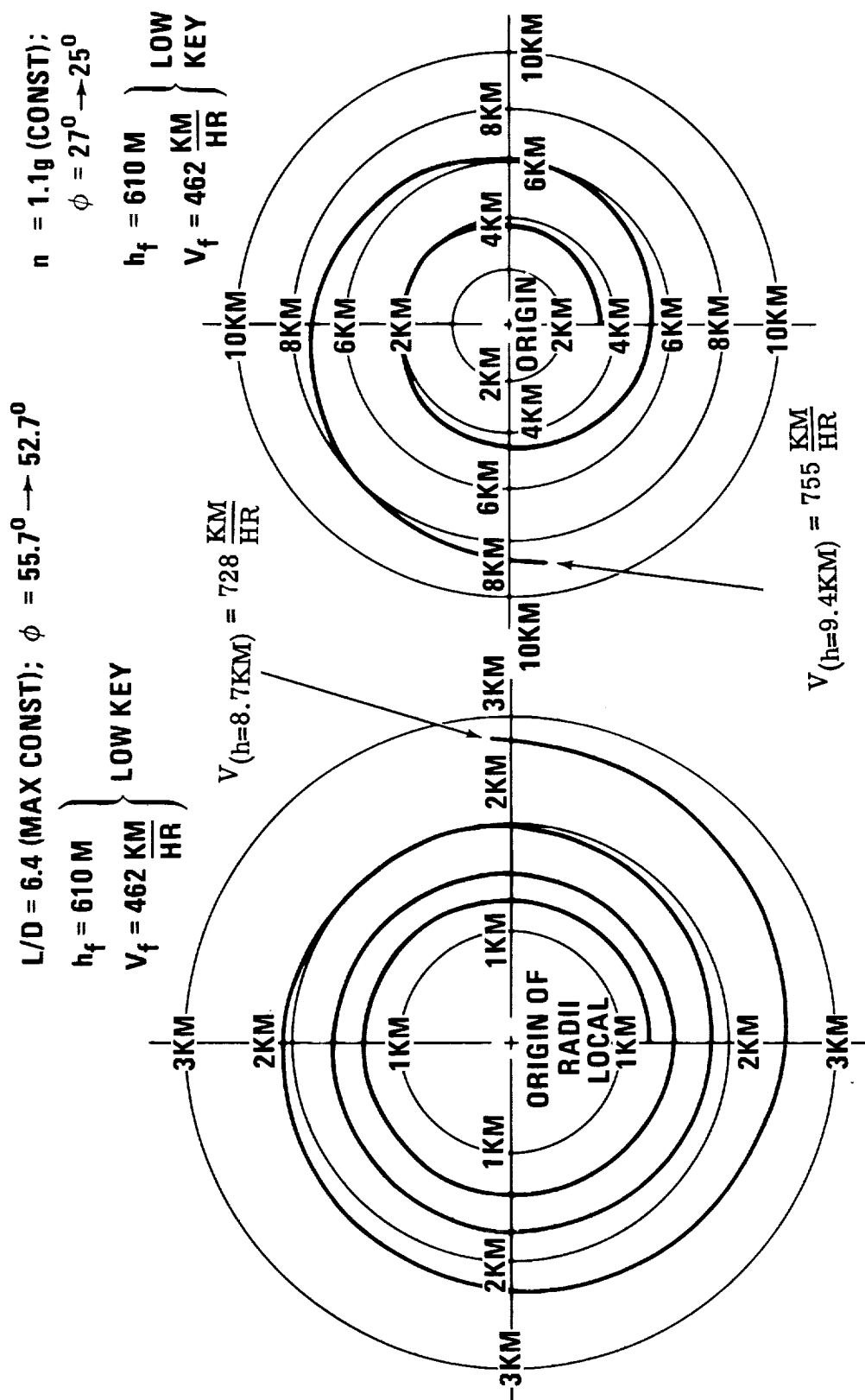
The spiral glides described by the orbiter are conducted at constant equivalent airspeed, bank angle, and load factor, i.e. the craft is very nearly in a state of steady maneuvering flight. The only departure from such steady flight is a very gradual decay in velocity accompanying descent into the more dense lower atmosphere. It is this increase in atmospheric density that causes a decrease in the vehicle's turning radius which results in a descending, inward-spiraling, funnel shaped trajectory. The variation of atmospheric density with altitude is duly accounted for in this analysis, and the resulting descent spirals are judged to be a reasonable representation of pilot landing pattern execution.

The bank angle determines the magnitude of the turning radius: the greater the bank angle the tighter the turns will be. The maximum bank angle (and the narrowest funnel) is that angle which will permit equilibrium turning flight at the maximum lift-to-drag ratio; for this vehicle, with a wing loading of 208 kg/m^2 , the $(L/D)_{\text{max}}$ - bank angle combination for the tightest spiral is 6.4 and 55° . The corresponding trajectory is shown in this figure as the inner spiral.

The wider spiral trajectory shown was constructed for a descent at a constant load factor of 1.1g. Both trajectories were constructed to end at the same nominal low key.

ORBITER GROUND TRACK IN SPIRAL GLIDE DESCENT POLAR VIEW

680



ORBITTER GROUND TRACK IN SPIRAL GLIDE DESCENT (POLAR VIEWS)

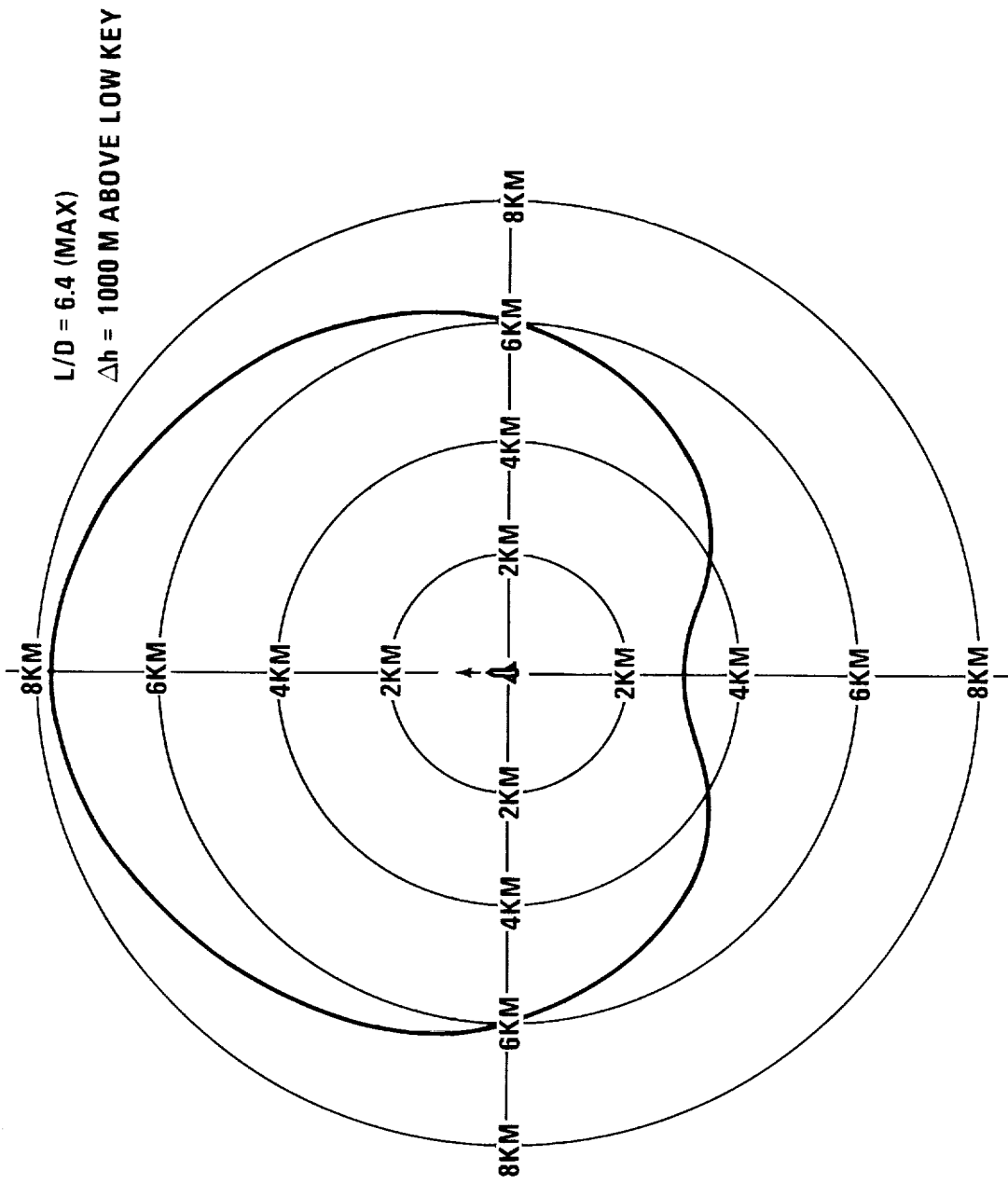
(SLIDE 3)

This plot presents polar views of the same two spiral descents, showing the change in relative heading angle and turning radius as the vehicle slows down.

The relation between heading change and velocity decrement is established by integrating the equation for the rate of turn in steady maneuvering flight, defining from it a quantity termed the "Vehicle Heading Parameter", and plotting it against velocity.

In a constant density atmosphere the ground track would simply be a circle, whose radius is proportional to the square of the velocity times $\cos \gamma$ over $\tan \phi$ ($R = V^2 \cos \gamma / g \tan \phi$). In the real atmosphere the velocity is time dependent and the ground track assumes an inward spiral characteristic. The present analysis shows that the actual ground track may be constructed using the local ground track radius of curvature mentioned before (which is now a function of time) together with a correction angle.

ORBITER RANGING WITH HEADING CHANGE



ORBITER RANGING WITH HEADING CHANGE

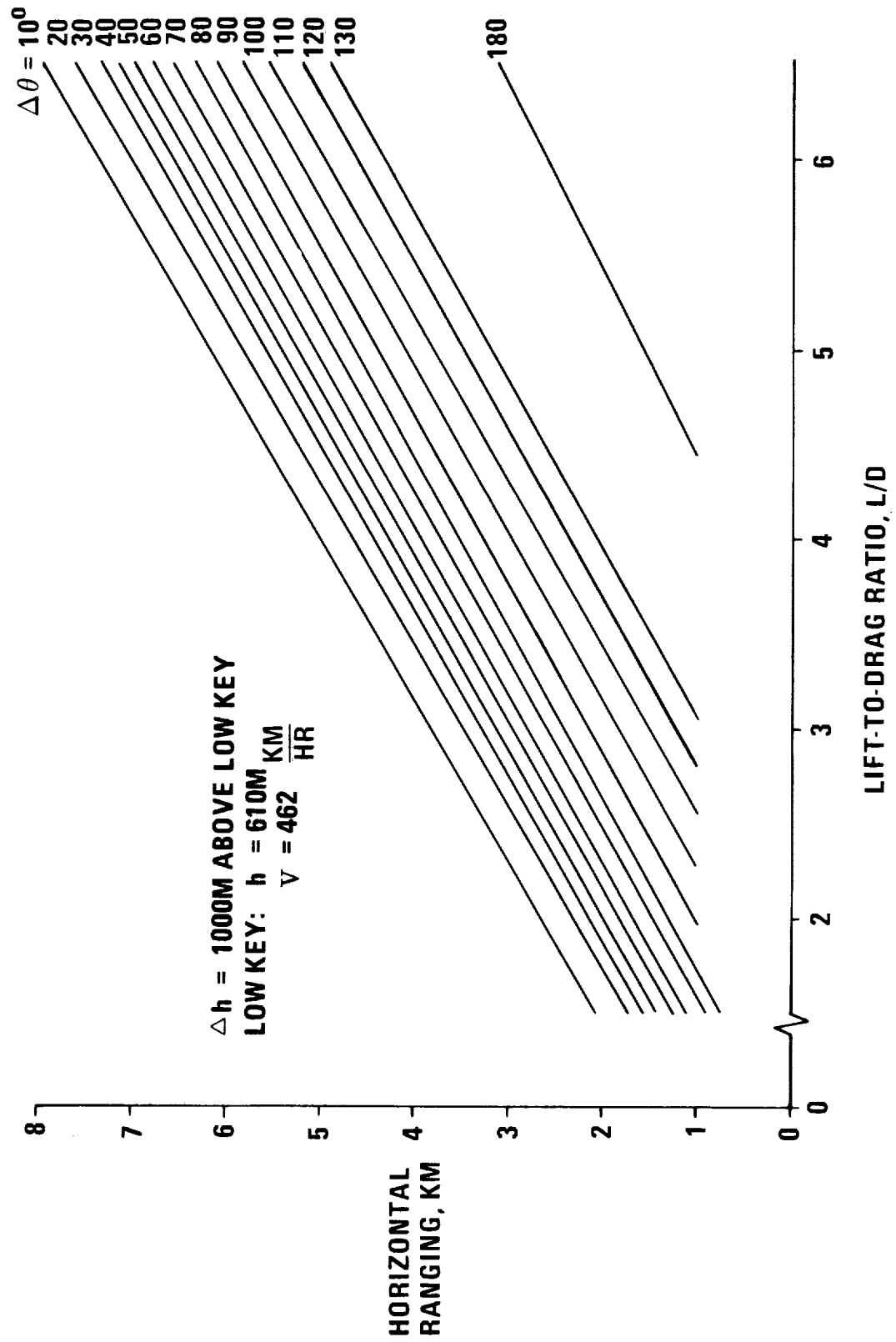
ENERGY MANAGEMENT WINDOW 1 KM ABOVE THE LOW KEY POINT

(SLIDE 4)

The energy management window shown in this figure is only 1 km above the low key. Note the change in scales, and the greatly reduced ranging capabilities of the vehicle at this low altitude, compared with the window shown previously for an altitude of 10 km. above the low key.

With the low key target somewhere inside the window, the pilot must "set up" for the final landing approach and touchdown. In the process, he must simultaneously correct for dispersions in initial altitude, heading and position relative to the runway. It is imperative that vehicle maneuvers required during targeting should be kept at a minimum level. The gliding patterns that suggest themselves in this respect are those constituted of constant bank angle - constant equivalent airspeed legs; this also implies constant load factor and vehicle attitude.

ORBITER RANGING WITH HEADING CHANGE ($\Delta\theta$) AND ALTITUDE LOSS (Δh)



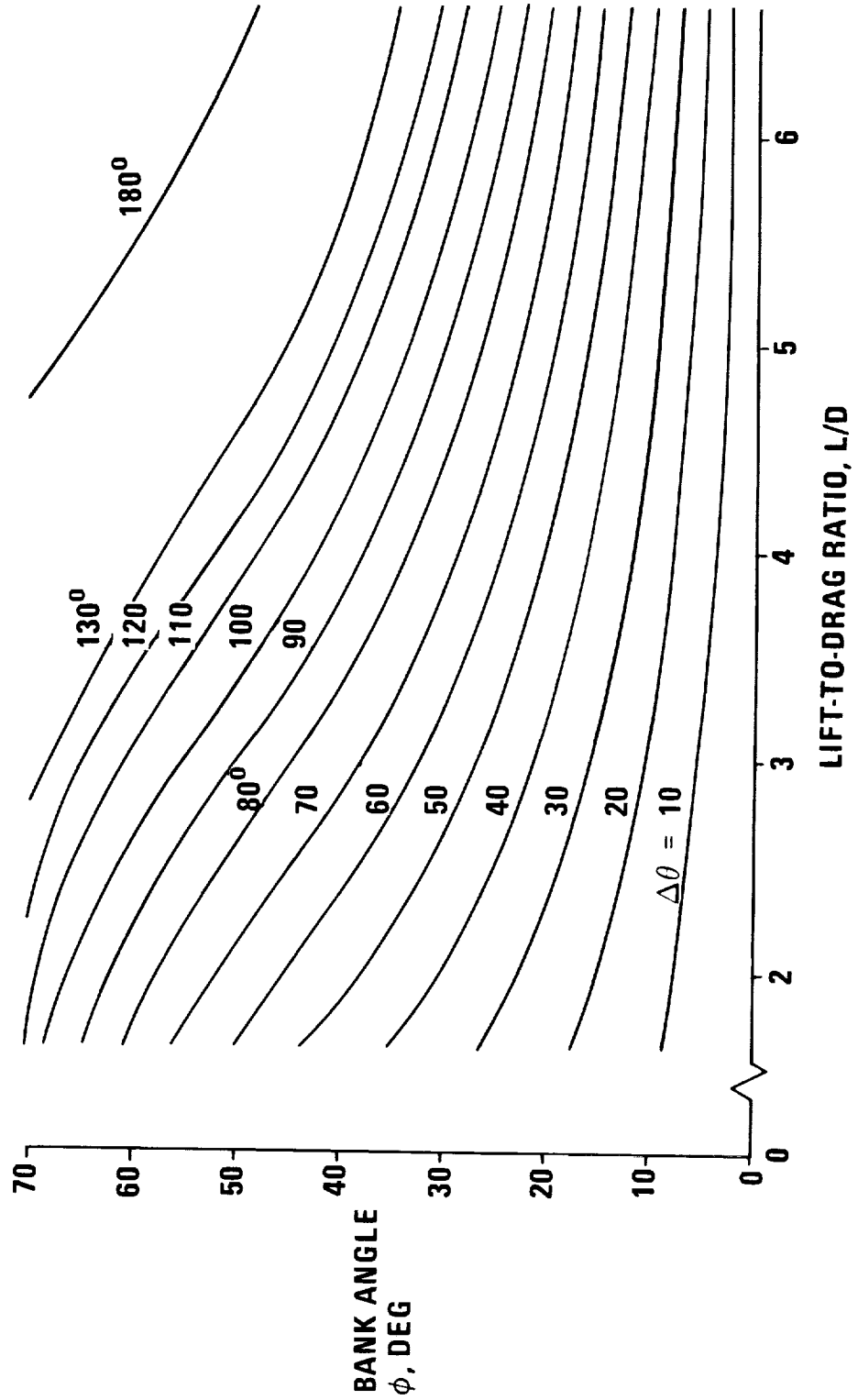
ORBITTER RANGING WITH HEADING CHANGE AND ALTITUDE LOSS

(SLIDE 5)

In the present approximate analysis of constant-load-factor spiral glide descents it was found possible to concisely inter-relate the flight path and ground track time history with vehicle bank angle, lift-to-drag ratio, resultant horizontal displacement, and load factor. Since closed form solutions are obtained, there is no need to revert to a step-by-step integration procedure. It is a simple matter to construct plots such as this for every desired altitude: at a known altitude above the low key (1 km in this example), and at a certain horizontal distance from it requiring a given heading change, one is able to determine the lift-to-drag ratio necessary for the maneuver. The "Horizontal Range to go" scale is entered at the proper value, and extended along the abscissa until it intersects the $\Delta\theta$ line corresponding to the necessary change of heading angle. The resultant L/D , together with the bank angle to be next determined, will target the vehicle to the low key.

ORBITER BANK ANGLES REQUIRED FOR HEADING CHANGE AND ALTITUDE LOSS

$\Delta h = 1000M$ ABOVE LOW KEY
 LOW KEY: $h = 610M$ $\frac{KM}{HR}$
 $V = 462$



ORBITTER BANK ANGLES REQUIRED FOR HEADING CHANGE

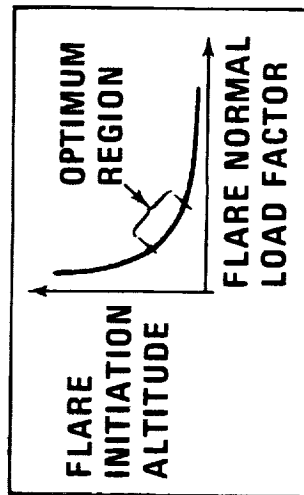
WITH ALTITUDE LOSS

(SLIDE 6)

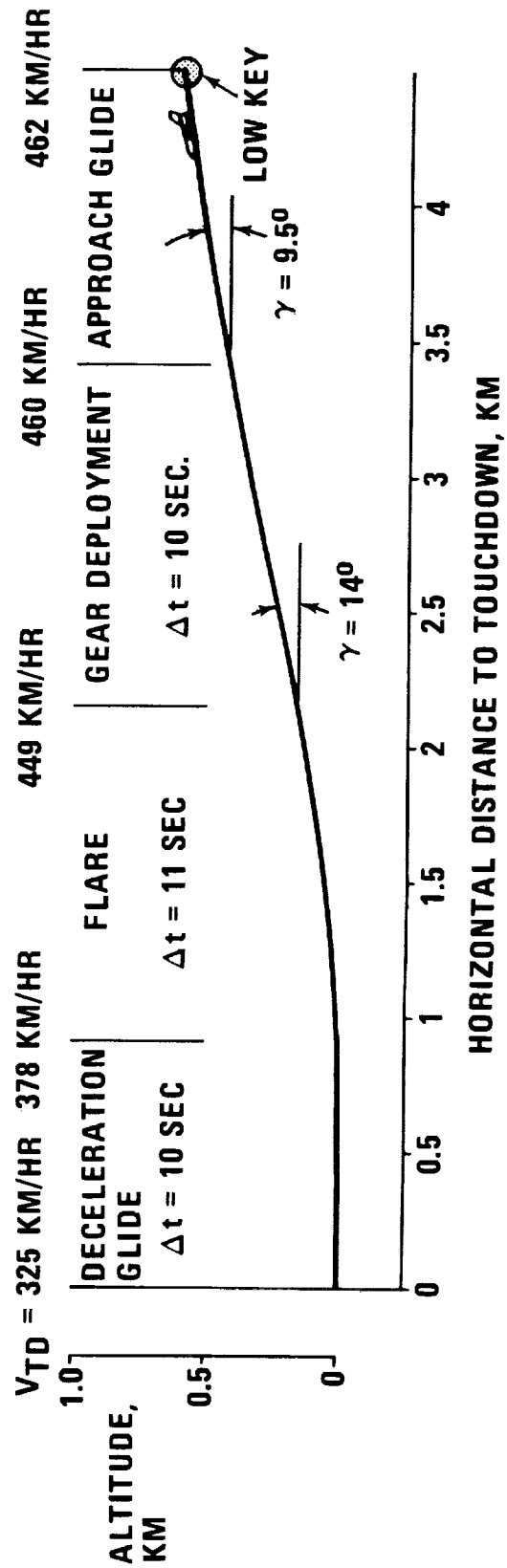
Having determined the lift-to-drag ratio required for targeting, the corresponding bank angle is determined by entering the abscissa of this plot at the known value, and extending a vertical line until the required $\Delta\theta$ line is intersected; the bank angle is then read off the ordinate.

As the vehicle rolls into the bank angle just determined at the lift-to-drag ratio dictated by the target, an equilibrium spiral glide ensues which "funnels" it to the low key point at the necessary heading.

FINAL APPROACH AND LANDING DETERMINATION OF LOW KEY POINT



W/S = 208 KG/M² (43 PSF)



FINAL APPROACH AND LANDING: DETERMINATION OF LOW KEY POINT

(SLIDE 7)

The low key is the threshold of the final approach and landing path. At this point the vehicle must be correctly aligned with the runway at the correct speed and attitude for good landing performance. The final approach and landing path consists of three adjacent flight segments: an equilibrium glide, a flare at constant normal load factor ending at zero altitude and a horizontal deceleration to touchdown. This analysis neglects the time required to change angle-of-attack at the segment interfaces, or to effect any rotation at touchdown.

An important criterion for acceptable dead stick landing characteristics is the "float time," or available deceleration time. A certain minimum float time is required for the pilot to complete any configuration changes and correct any last-minute deviations. In addition, the flare must be flown "hot" to provide stall margin for possible near-end-flare maneuvering.

Since the maximum usable lift coefficient at touchdown is known, it is convenient to construct the maneuver backwards. The vehicle whose landing is shown here has a maximum lift-to-drag ratio of 4.9 with gear down, and the maximum usable lift coefficient is 0.4, corresponding to $(L/D)_{\max}$. Given the vehicle characteristics and touchdown speed, an end-flare velocity is determined by selecting an appropriate deceleration time. Based on pilot experience in glide landings of the X-15, HL-10, and X-24 vehicles, a nominal float time of about 10 seconds was selected as adequate yet not prohibitive in runway distance required before touchdown.

Continuing backwards from the end-flare velocity just determined, a suitable flare initiation altitude-flare load factor combination must be selected to provide roundout close to ground level. In this choice, a compromise is made between the extremes of early high-altitude flare initiation, with diminished accuracy, and late commencement requiring high load factors. A typical trade-off of flare initiation altitude for normal load factor appears in the boxed sketch. Piloting considerations suggest use of an altitude-load factor combination near the knee of the curve. Next, the flare initiation point is determined, that is the matching equilibrium glide $V - \gamma$ condition. For the present vehicle, the gears are assumed to be deployed prior to flare, but this analysis allows such a configuration change at any flight segment interface, assuming it is practically instantaneous. Since the gear deployment time for an orbiter is about 10 seconds, it was deployed in the approach glide, resulting in a low key required altitude of 610 m and velocity of 462 km/hr.

SUMMARY

A performance analysis was conducted in order to define the energy management procedures required to target the orbiter to the landing site in the subsonic phase of unpowered reentry.

The vehicle is assumed to fly a spiral glide descent from sonic transition to final approach. A simple approximate analysis of low-speed, constant-load-factor spiral glide descents is employed; it is based on quasi-steady equilibrium glides flown at constant equivalent airspeeds and bank angles, and it accounts for the variation of atmospheric density. Energy management windows are defined for a delta-wing orbiter with known aerodynamic characteristics; they indicate the targeting capabilities of the unpowered vehicle in terms of altitude, required change in heading angle, ground distance between the vehicle and the target point, and required velocity at target.

The target point and the velocity associated with it are defined by establishing a final approach and landing maneuver for the vehicle, with due consideration given to piloting requirements. The landing path is assumed to be comprised of a constant load factor flare from a steady, wings-level approach glide, followed by an airborne deceleration to touchdown. Flight test results of X-15, HL-10, X-24, and F-104 glide landings are in good agreement with this procedure. An investigation of existing auto-land systems indicates that the Microwave Scanning Beam System can accommodate the higher glide slopes associated with unpowered landings.

The result of this study is an analytical tool that is readily applicable in defining the energy management procedures based on a vehicle's aerodynamic characteristics. Specific trajectories can be constructed for any combination of requirements, such as heading change required, altitude loss, horizontal distance to target, approach and touchdown velocities, or flare load factor.

MINIMUM SHUTTLE THERMAL PROTECTION SYSTEM WEIGHT THROUGH TRAJECTORY SHAPING

By

Henry W. Kipp

David O. Swain

McDonnell Douglas Astronautics Company - East
St. Louis, Missouri

INTRODUCTION

The orbiter entry trajectory shaping philosophy has evolved from pre-phase A studies to the present as the designers became more aware of system interactions. In early studies the orbiter was flown at constant angles of attack and bank angles except immediately following pull-out where bank angle was modulated to avoid skip. Primary attention was focused on the lift-to-drag ratio necessary to satisfy the 2778 kilometer crossrange requirement and determination of entry conditions that would yield a satisfactory pull-out altitude. Consideration of a metallic thermal protection system (TPS) during early Phase B studies resulted in entry trajectories that were bank modulated following pull-out to insure that the orbiter design bottom surface temperature was not exceeded. The angle of attack remained a constant and was selected to yield the L/D required to satisfy performance constraints. This method offers three distinct advantages: 1) allows utilizing the lightest possible metallic TPS on bottom surface, 2) relatively simple entry control, and 3) minimizes the wind tunnel testing program since the hypersonic trajectory is flown at constant angle of attack.

Several studies have indicated that reduction in TPS weight could be achieved by angle of attack modulation. The degree of improvement is a function of the vehicle aerodynamic characteristics, design temperature limits, thermal prediction techniques, and crossrange requirements.

This paper investigates the influence of various types of entry control on TPS requirements for a 2778 kilometer crossrange mission. The types of entry control analyzed are:

- (1) bank angle and angle of attack are held constant;
- (2) modulate bank angle while maintaining a constant angle of attack; and
- (3) modulate bank angle in conjunction with a modulating angle of attack.

Near optimal control profiles have been determined by employing the MDC Steepest Descent computer simulation to solve two entry trajectory problems: (1) maximum crossrange for a fixed angle of attack; and (2) minimum stagnation total heat with a varying bank angle and angle of attack. Each entry trajectory is analyzed to estimate the weight requirements for a metallic and a non-metallic TPS system and to determine the interaction between the type of TPS and the entry trajectory shaping philosophy.

POSSIBLE TRAJECTORY SHAPING OBJECTIVES

(Slide 1)

A number of alternative objectives for trajectory shaping relative to thermal protection system (TPS) design can be formulated. Slide 1 lists four alternative objectives in ascending order of importance.

The first objective has been extensively used in lifting reentry vehicle analysis since such vehicles were first conceived.

The second objective, to minimize TPS weight, is more difficult to accomplish and is not necessarily satisfied by the attainment of the first.

The importance of cost is recognized in objective Statements 3 and 4. Minimization of the TPS impact on total program cost is the legitimate ultimate goal but falls beyond the scope of the present effort because of the dominating influence on cost of factors other than trajectory shaping.

The present study investigates the minimization of TPS weight for both metallic and non-metallic systems on the premise that this will lead to minimization of TPS impact on the total program cost. Specifically, this study concerns itself with minimization of bottom surface TPS weight for a delta orbiter for a 2778 kilometer crossrange entry with a 2 g normal load factor constraint. It is recognized that while a complete study should consider the TPS for nose, leading edge and upper body regions as well as control surfaces, the bottom surface TPS comprises over half the total TPS weight. Furthermore, some of the conclusions resulting from studying bottom TPS apply to other areas as well.

POSSIBLE TRAJECTORY SHAPING OBJECTIVES

1. ATTAINMENT OF SPECIFIED C.R. WITH TEMPERATURE AND LOAD
FACTOR CONSTRAINTS
2. MINIMIZE TPS WEIGHT FOR SPECIFIED C.R. AND LOAD FACTOR
CONSTRAINT
3. MINIMIZE TPS COST FOR SPECIFIED C.R. AND LOAD FACTOR
CONSTRAINT
4. MINIMIZE IMPACT OF TPS ON TOTAL PROGRAM COST FOR SPECIFIED
C.R. AND LOAD FACTOR CONSTRAINT

Slide 1

SYMBOL DIRECTORY

SYMBOL	DEFINITION	UNITS
C_L	Aerodynamic Lift Coefficient	
L/D	Lift-to-Drag Ratio	
H	Altitude	m
H_p	Pull-Out Altitude	m
M	Mach Number	
M_L	Local Mach Number	
N_z	Normal Load Factor	$g's$
\dot{q}	Heating Rate	kW/m^2
Q_T	Total Heat	MJ/m^2
R_c	Crossrange	km
R_d	Down Range	km
Re_t	Reynolds Number at Transition Onset	
Re_T	Reynolds Number at Fully Turbulent Flow	
Re_u	Unit Reynolds Number	m^{-1}
Re_θ	Momentum Thickness Reynolds Number	
S_{REF}	Aerodynamic Reference Area	m^2
t	Time	sec

SYMBOL	DEFINITION	UNITS
V_R	Relative Velocity	m/sec
W/A	TPS Unit Weight	kg/m ²
X/L	Fractional Vehicle Length	
α	Angle of Attack	deg
γ_I	Inertial Flight Path Angle	deg
ϕ_A	Aerodynamic Bank Angle	deg
θ	Duration of the Heating Pulse	sec
θ_p	Vehicle Pitch Angle Relative to Local Horizontal	deg

ENTRY TRAJECTORY GROUND RULES AND THERMAL ENVIRONMENT PREDICTION METHODS

(Slides 2 and 3)

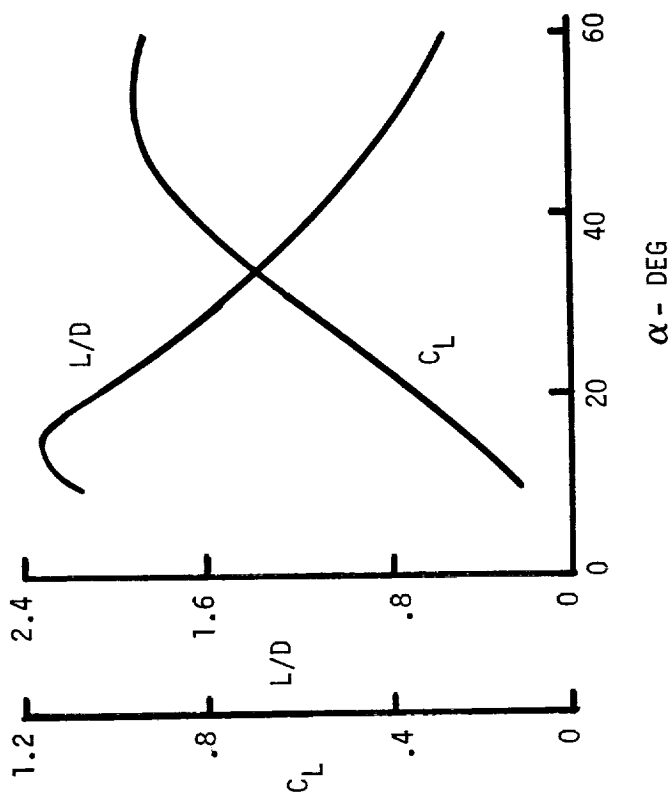
It is emphasized that the purpose of this paper is to explore how to shape entry trajectories in a manner to minimize TPS weight and not to design a TPS system for a specific vehicle or mission. A number of groundrules have been established to facilitate accomplishment of that task. The groundrules can be categorized in the following two areas: 1) entry trajectory and 2) thermal prediction techniques. The groundrules pertinent to entry trajectory and thermal prediction techniques are enumerated in Slides 2 and 3 respectively.

ENTRY TRAJECTORY GROUND RULES

- o 2778 km CROSSRANGE MISSION
- o MAXIMUM NORMAL LOAD FACTOR ≤ 2 g's
- o ENTRY FROM A 500 km CIRCULAR ORBIT, ZERO-DEGREE INCLINATION
- o SPHERICAL ROTATING PLANET
- o AERODYNAMIC CHARACTERISTICS ARE A FUNCTION OF ANGLE OF ATTACK AND ALTITUDE
- o ANGLE OF ATTACK IS CONSTRAINED TO BE GREATER THAN 20 DEGREES
- o ENTRY WEIGHT = 111000 kg

DELTA ORBITER HYPERSONIC TRIM AERODYNAMICS

- o $M = 20$
- o $H = 61000$ m
- o $S_{REF} = 495$ m²



Slide 2

THERMAL ENVIRONMENT PREDICTION METHODS

PARAMETER	METHOD
FLOW FIELD	REAL GAS CONE FLOW
B. L. TRANSITION	
ONSET	$Re_\theta M_L^{-1} Re_u^{-0.2} = f(\alpha)$
EXTENT	$Re_T/Re_t = 2$
ORIGIN OF TURB. B. L.	TRANSITION ONSET
LAMINAR THEORY	ECKERT REFERENCE ENTHALPY
TURBULENT THEORY	REAL GAS SPALDING-CHI WITH VON KARMAN REYNOLDS ANALOGY
CROSS FLOW	BARANOWSKI METHOD (L. C. Baranowski, McDonnell Douglas Astronautics Company - East)

Slide 3

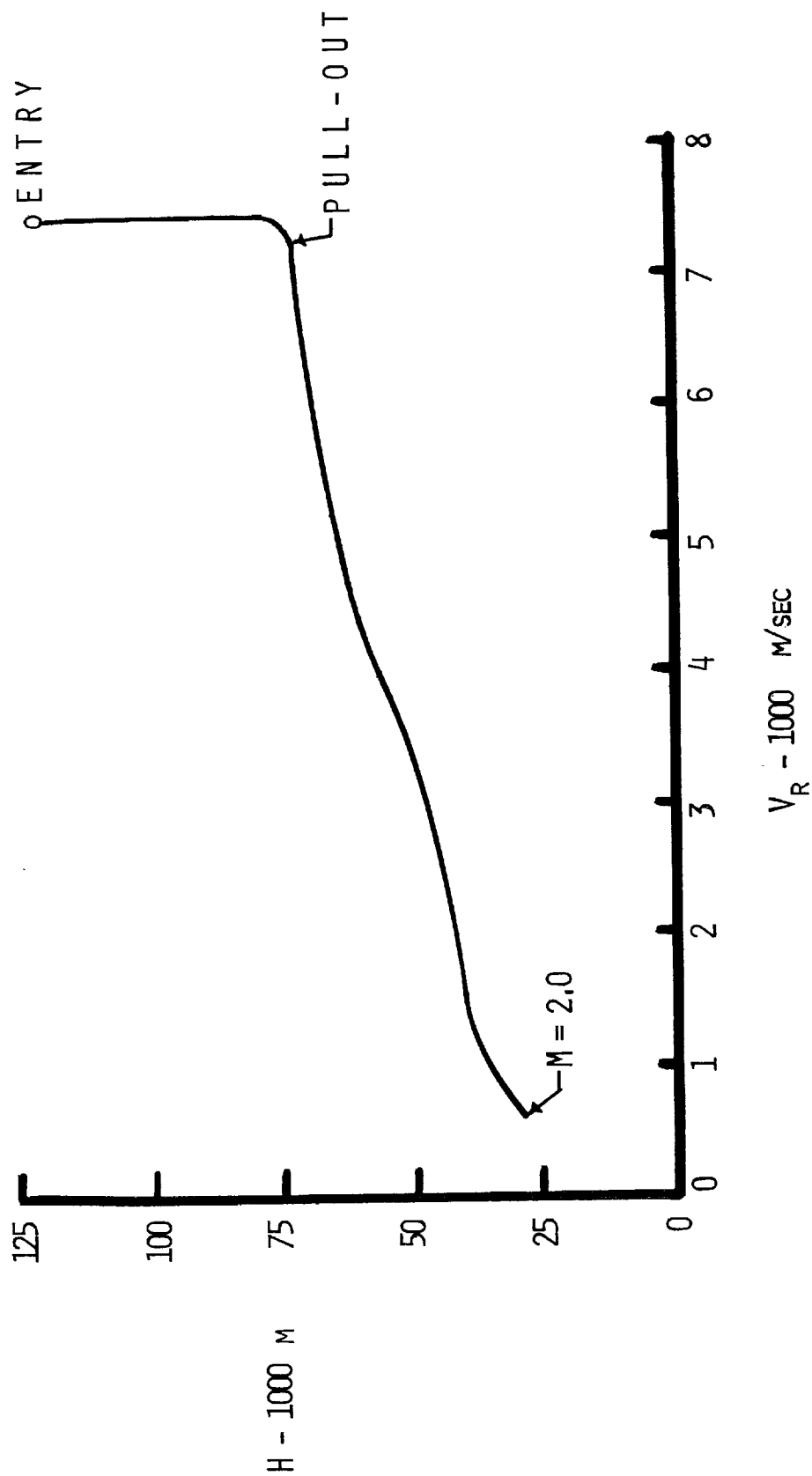
TYPICAL DELTA ORBITER ENTRY TRAJECTORY

(Slide 4)

In the first part of this analysis the entry trajectory is divided into two phases to simplify the trajectory shaping problem and to yield greater insight into what type of entry control will minimize orbiter TPS. The first phase begins at 122000 m altitude and ends at pull-out ($\gamma = 0^\circ$); the second phase starts at pull-out and continues until a Mach number of 2. A typical entry trajectory profile is illustrated in Slide 4.

TYPICAL DELTA ORBITER ENTRY TRAJECTORY

$\alpha = 26^\circ$



Slide 4

EFFECT OF INITIAL BANK ON ENTRY PERFORMANCE

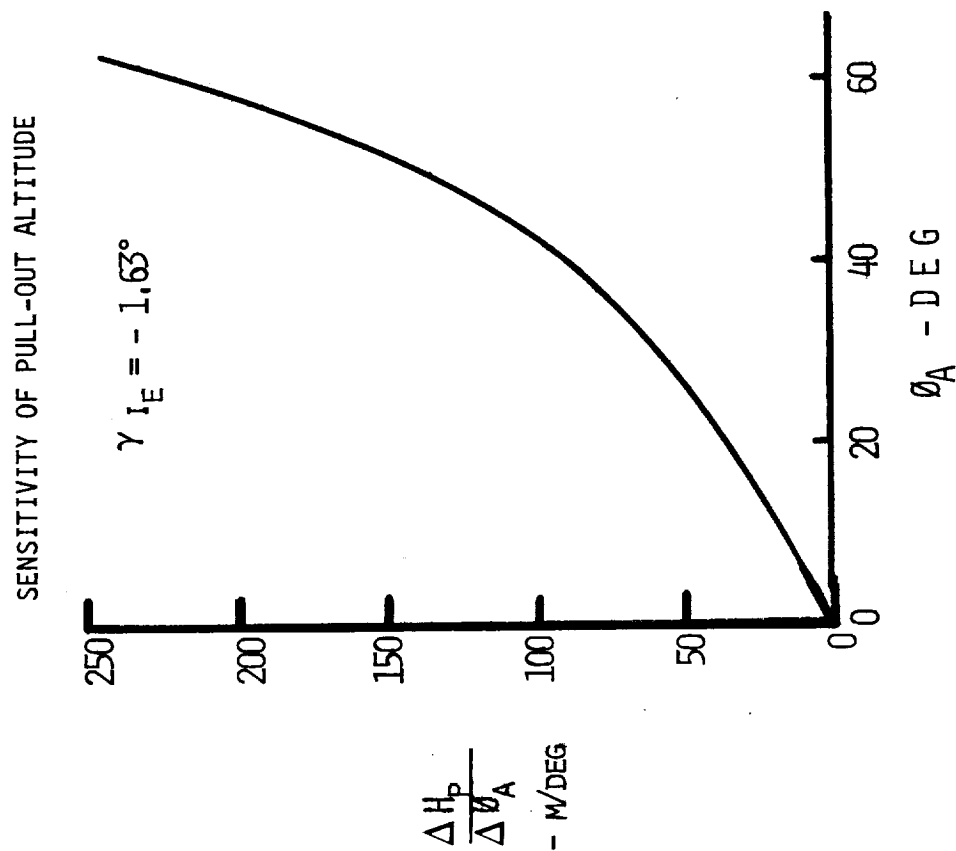
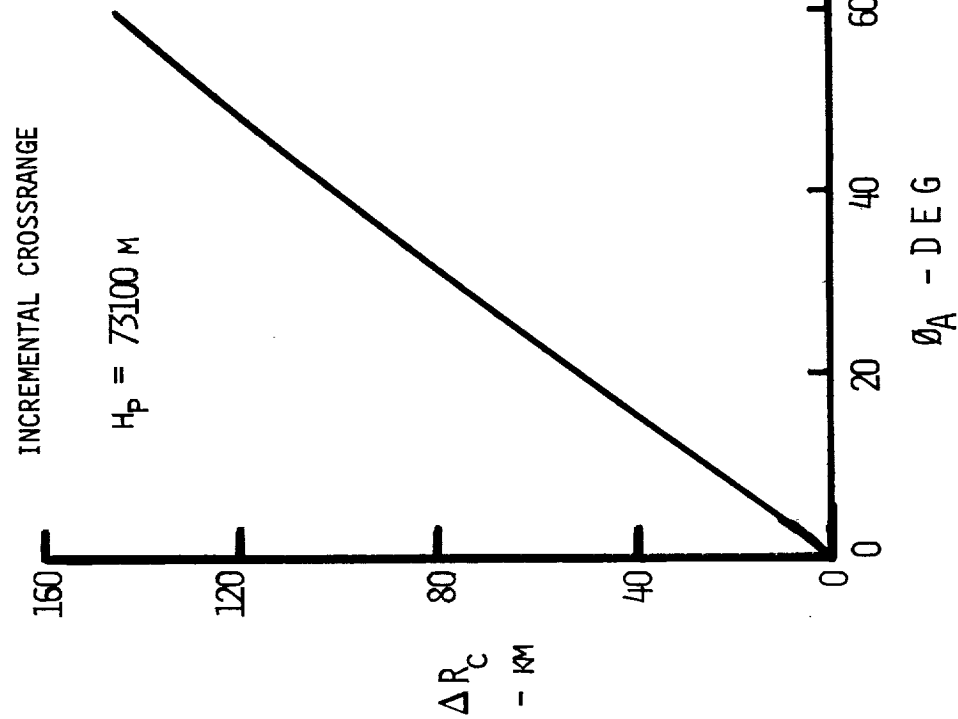
(Slide 5)

The shaping objective during the initial entry phase is to use the available control parameters (entry flight path angle, bank angle, and angle of attack) to increase crossrange without a significant penalty to the thermal protection system. Slide 5 indicates the additional crossrange that can be obtained by banking during the initial entry. It is noted that pull-out altitude is held constant at 73100 m to maintain a constant pull-out temperature. This is accomplished by varying entry flight path angle.

The incremental crossrange increases almost linearly with bank angle. However, as bank angle becomes large, the sensitivity of pull-out altitude to bank angle errors increases exponentially. Therefore, to avoid operation in a region of high sensitivity and yet gain the crossrange benefits, 45 degrees is selected as the baseline initial bank angle. This yields an incremental crossrange of 110 kilometers.

EFFECT OF INITIAL BANK ON ENTRY PERFORMANCE

$\alpha = 26^\circ$



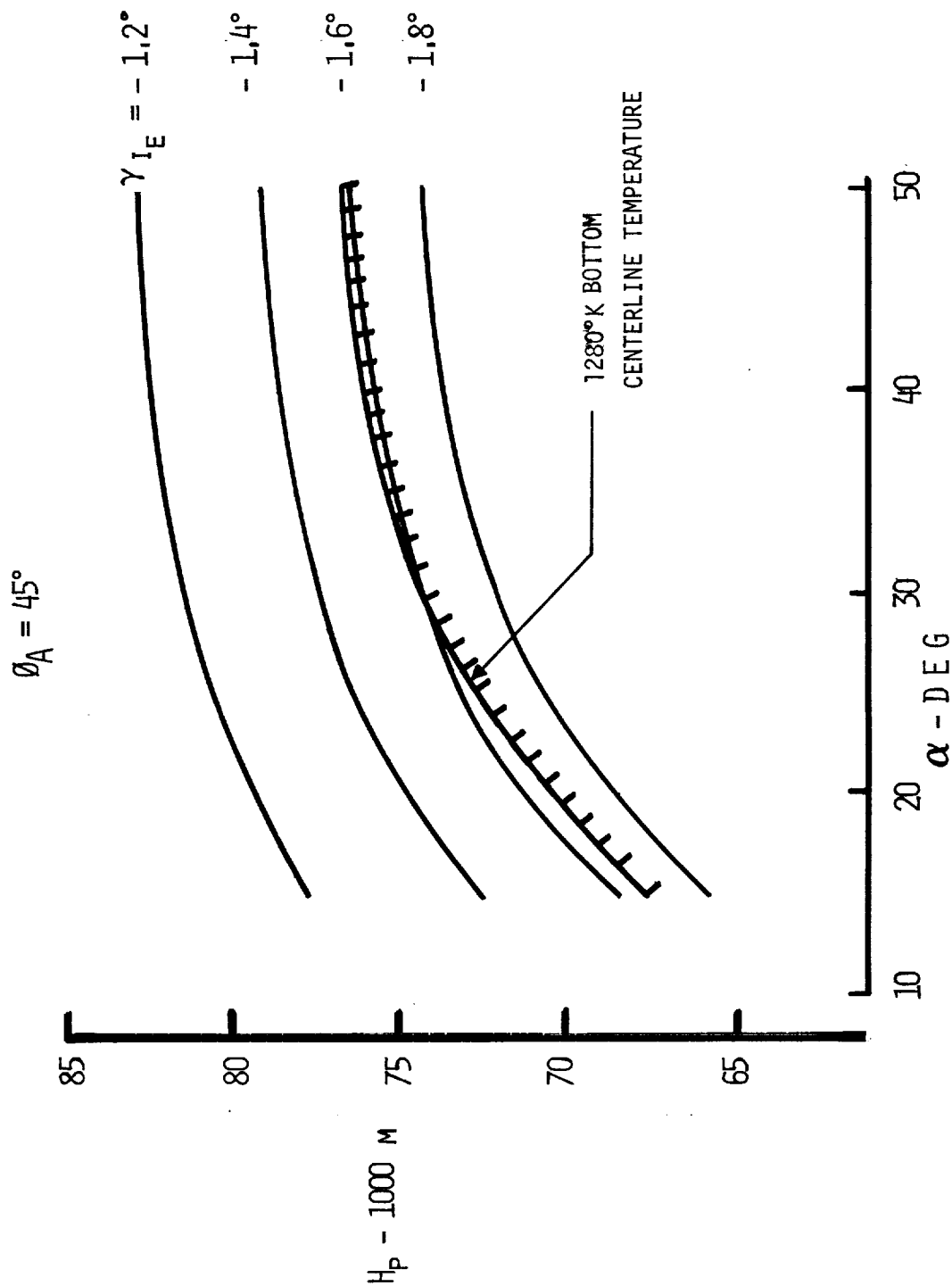
Slide 5

SELECT ENTRY FLIGHT PATH TO CONTROL PULL-OUT

(Slide 6)

Either angle of attack or entry flight path angle may be varied to control the pull-out altitude as shown in Slide 6. However, since the orbiter bottom surface temperature increases with flow deflection angle, little change in pull-out temperature can be realized by increasing pull-out altitude through angle of attack variations. An increase in angle of attack reduces stagnation heating rate significantly. However, stagnation heating rate has no significant influence on the total TPS weight requirements. Furthermore, an increase in angle of attack will result in a crossrange penalty associated with the lower lift-to-drag ratio. The utilization of flight path angle control to achieve a given pull-out altitude will avoid a crossrange penalty while having a significant effect on pull-out temperature and stagnation heating rate. Therefore, the baseline initial entry control mode is to bank 45 degrees and enter at the flight path angle which yields pull-out above the design temperature boundary. The angle of attack employed during Phase I shall be based on considerations of the remaining portion of the entry.

SELECT ENTRY FLIGHT PATH TO CONTROL PULL-OUT



Slide 6

BANK PROFILE TO MAXIMIZE CROSSRANGE

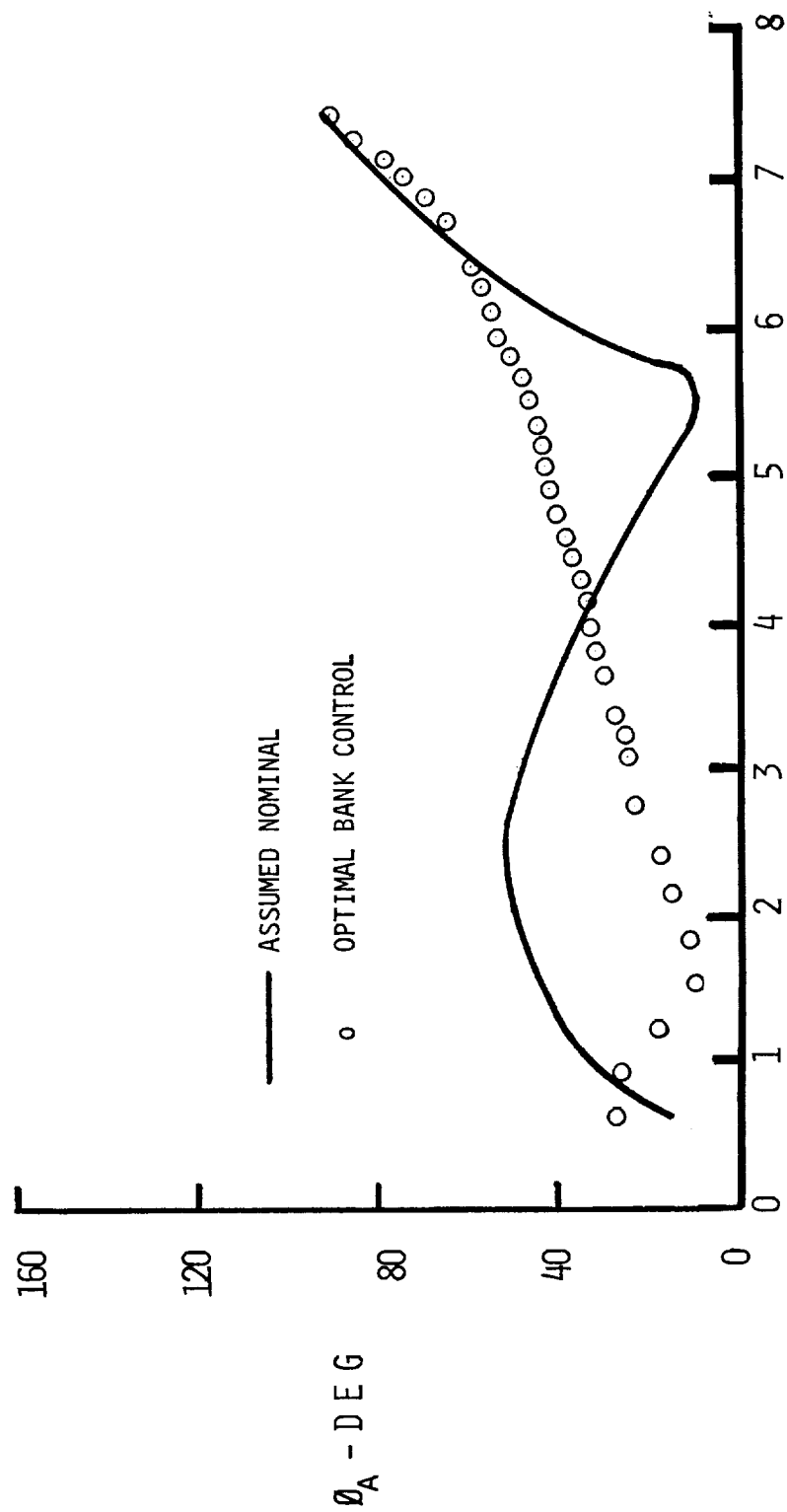
(Slide 7)

The objective during Phase II of the entry is to employ the control parameters (bank angle and angle of attack) to satisfy mission requirements with a minimum weight TPS. Two types of entry are analyzed using the MDC Steepest Descent Optimization Computer Program to determine optimal entry control profiles. The steepest descent optimization procedure involves computing a trajectory based on an assumed control profile. Partial derivatives of the pay-off function (i.e., crossrange) with respect to control parameter (bank angle) are then computed and are used to perturb the control parameter in a direction to improve the pay-off. The largest perturbations occur in the region of greatest sensitivity. This procedure is continued until the pay-off function is in the region of the optimal. A number of inflight constraints may be employed.

For the first type, crossrange is maximized for a fixed angle of attack. The resulting bank angle control profile is compared to the initial nominal in Slide 7. The assumed nominal was selected from a design delta orbiter entry trajectory that was bank modulated to fly constant bottom centerline temperature. The resulting maximum crossrange bank profile is similar to minor circle turn solutions in that the vehicle is banked 90 degrees near orbital speed with a slow rollout as velocity decreases. The slight increase in bank angle when $V_R < 1200$ m/sec is due to the small sensitivity of crossrange to bank angle at low velocities.

BANK PROFILE TO MAXIMIZE CROSSRANGE

$\alpha = 28.5^\circ$



$V_R = 1000 \text{ M/SEC}$

Slide 7

BANK AND PITCH PROFILE TO MINIMIZE TOTAL STAGNATION HEAT

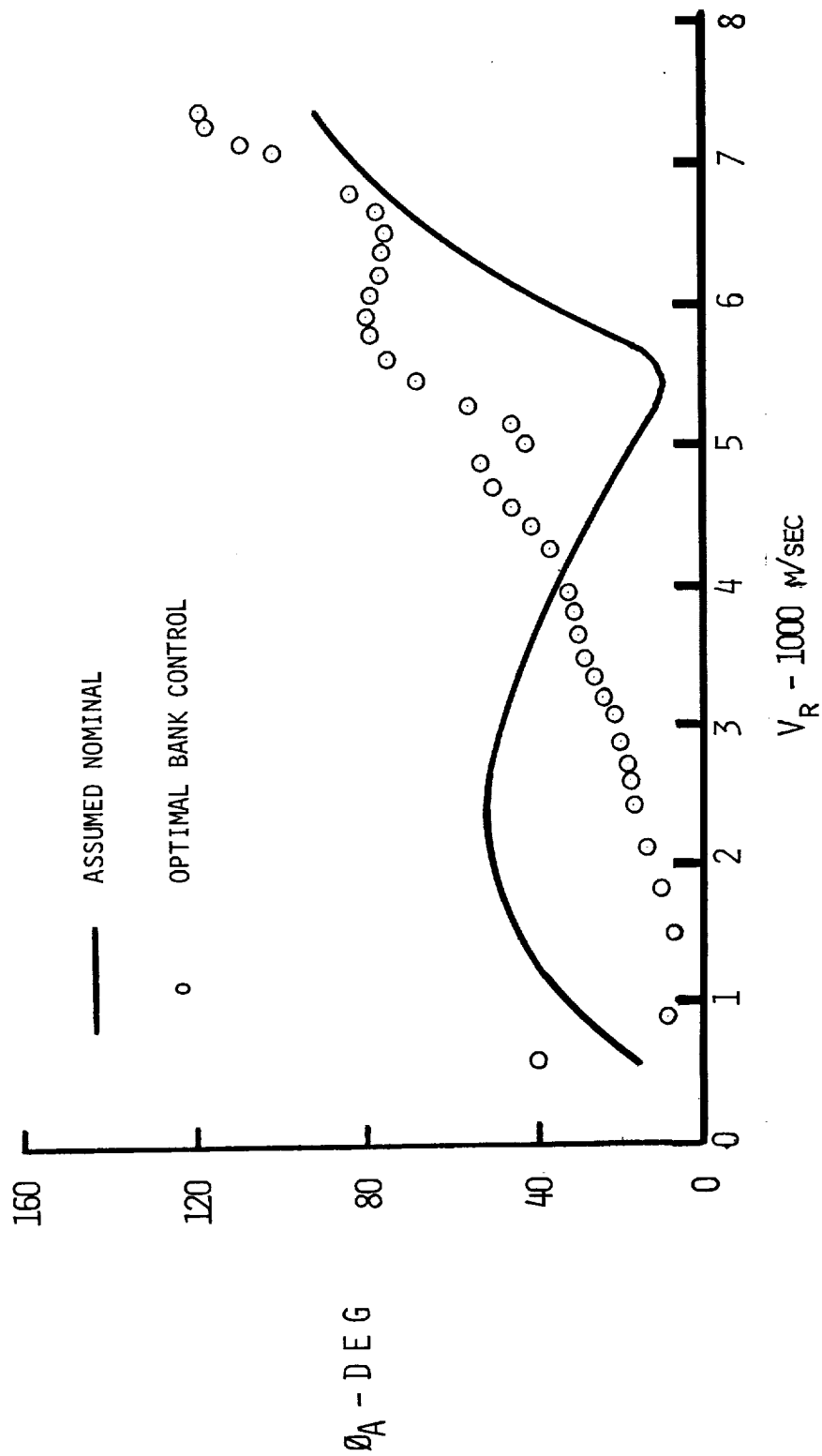
(Slides 8 and 9)

The second problem investigated using the method of steepest descent is to minimize total stagnation heat. The problem was constrained to achieve 2778 km crossrange with a maximum normal load factor of 2.0 g's.

In this case, both bank angle and pitch angle are control parameters. Pitch angle is selected as a control parameter rather than angle of attack to reduce trajectory oscillation and hence expedite problem convergence. The resulting control histories are presented in Slides 8 and 9. Bank angle is similar to that obtained for maximum crossrange except at high velocities ($V_R > 5500$ m/sec). In this region, the vehicle dives rapidly to the load factor constraint. Being at the load factor limit during this high heating phase tends to minimize total stagnation heat because of the rapid deceleration. The same motive is apparent when analyzing pitch angle. High angles and the corresponding high drag are beneficial during the high heating region to reduce time. As the velocity decreases, the vehicle is pitched down to increase L/D necessary to satisfy crossrange requirements. The oscillation in pitch angle is the result of local penetrations of the load factor boundary. Employing this minimum total heat control mode yields 23 percent reduction in total stagnation heat compared to the maximum crossrange case. It is noted that the only constraints imposed are normal load factor and crossrange. Introduction of bottom centerline temperatures as an additional constraint may tend to reduce the amount of improvement that is achievable through angle of attack modulation.

BANK PROFILE TO MINIMIZE TOTAL STAGNATION HEAT

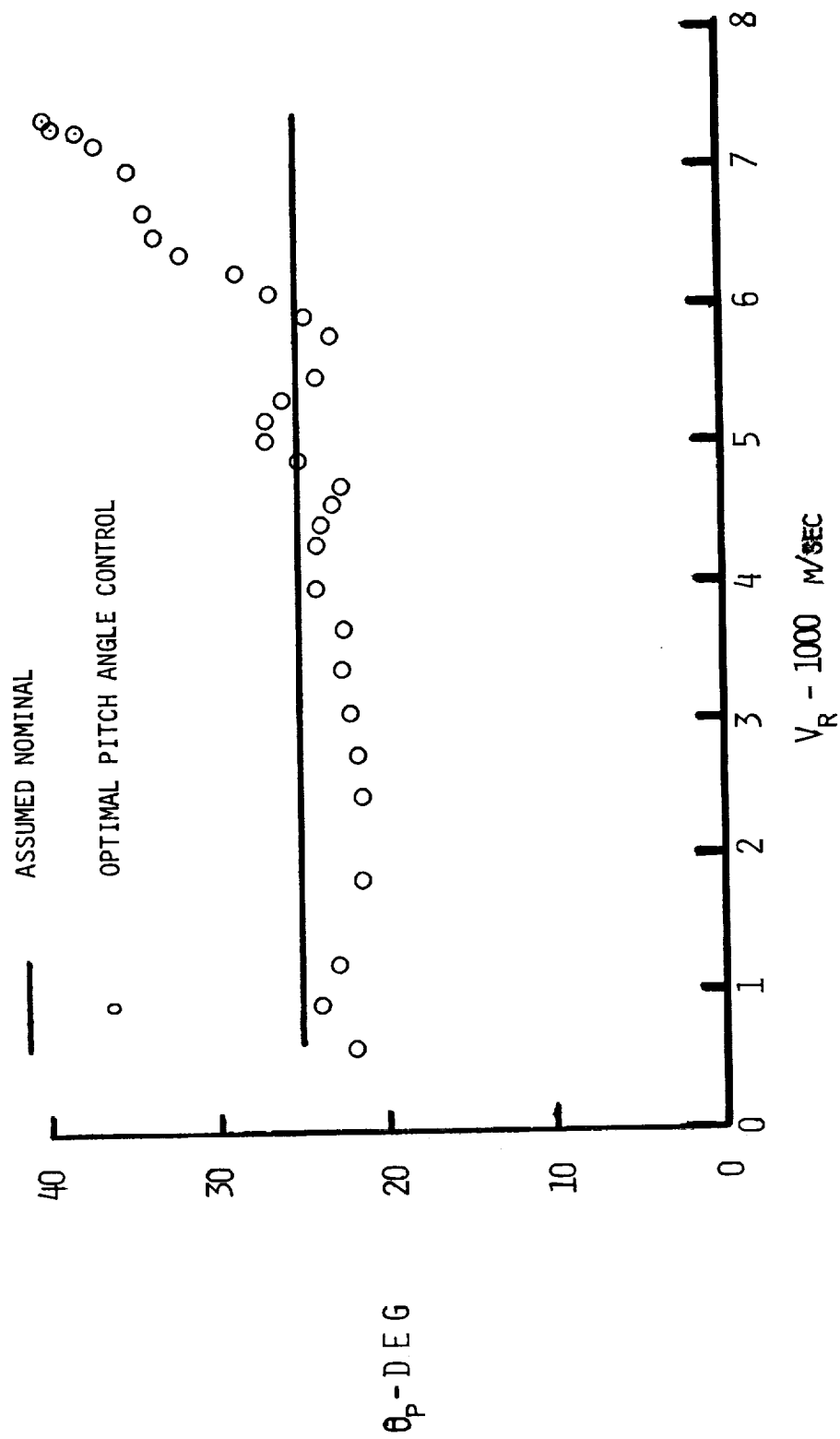
$$R_c = 2778 \text{ KM}$$



Slide 8

PITCH PROFILE TO MINIMIZE TOTAL STAGNATION HEAT

$$R_c = 2778 \text{ km}$$



Slide 9

ENTRY TRAJECTORY AND BOTTOM ϕ TEMPERATURES

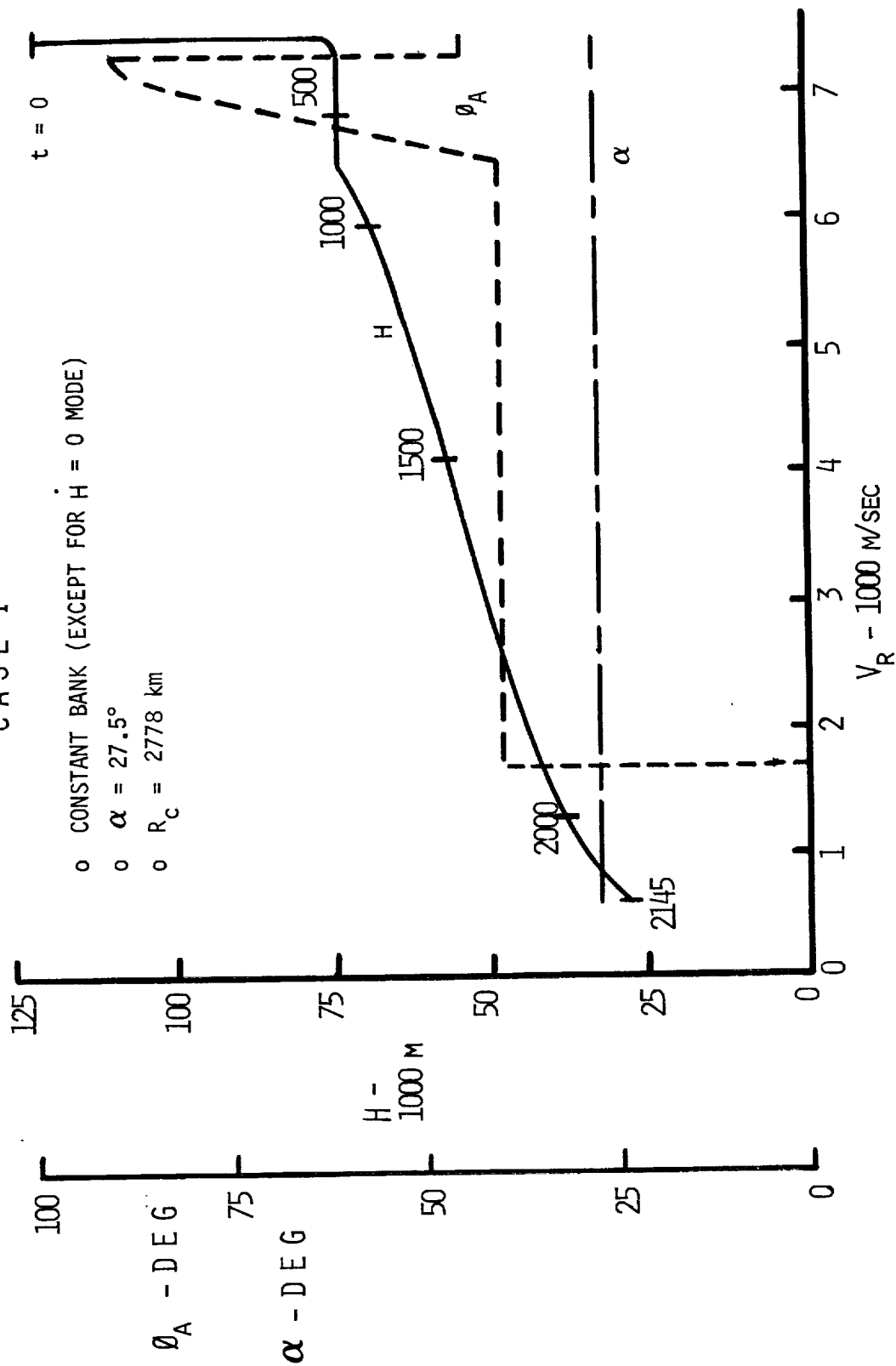
Case I

(Slides 10 and 11)

The selected initial control logic ($\phi_A = 45^\circ$ and the γ_I required to pull-out above the temperature boundary) is now combined with the optimal control profiles derived from the steepest descent solutions to compute a maximum crossrange entry trajectory and a minimum total heat entry trajectory. In addition, three entry trajectories with simpler control profiles are computed for comparison. Since all trajectories are required to obtain a 2778 km crossrange, the lift-to-drag ratio (and consequently the angle of attack) varies as the type of bank modulation is altered.

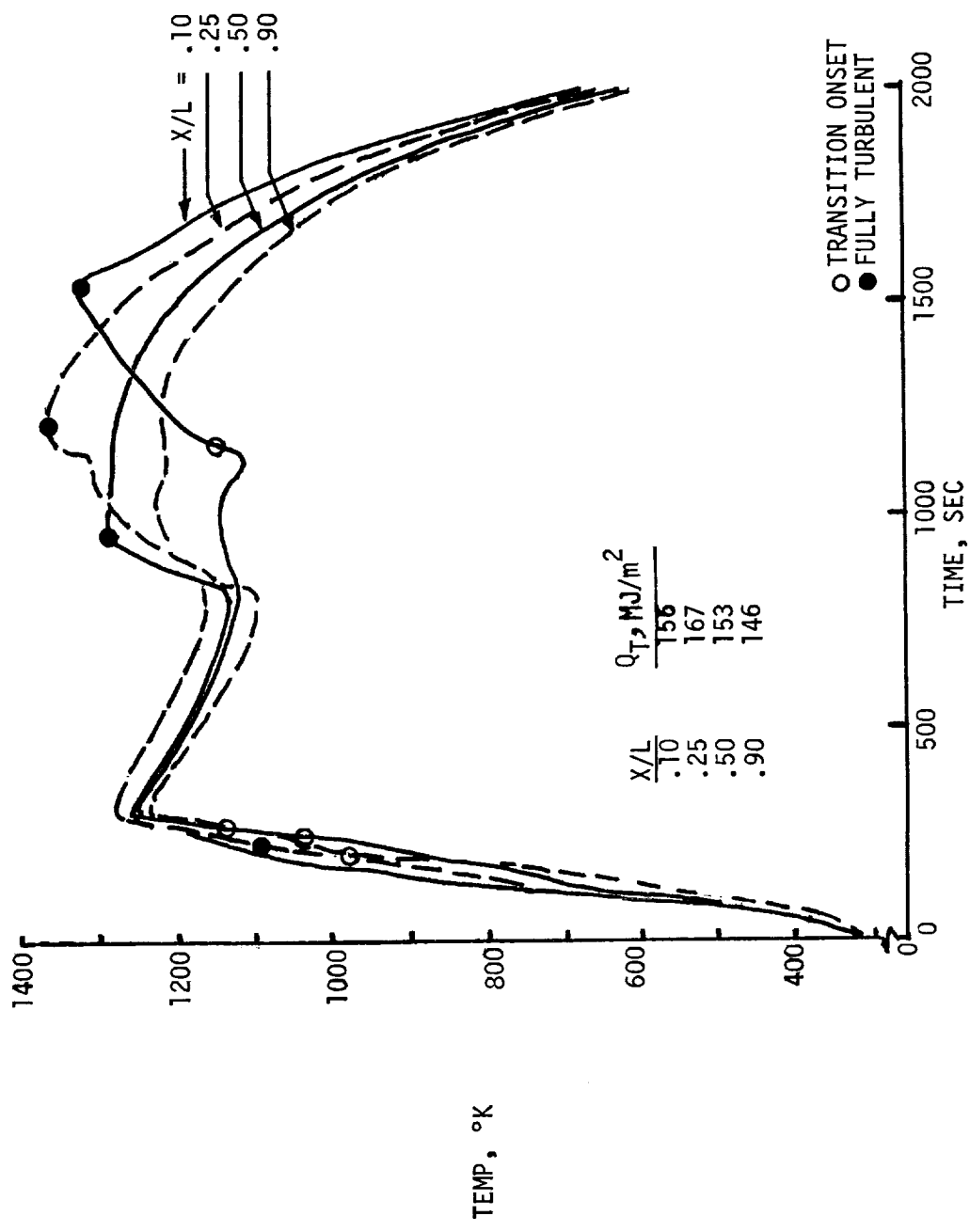
The first and simplest entry control is the constant angle of attack and constant bank angle mode typical of early Phase A studies. The control history and resulting entry trajectory are shown in Slide 10. It is noted that bank is modulated immediately following pull-out to fly constant altitude until the equilibrium glide corresponding to a 40 degree bank angle is achieved. The vehicle is then flown at a 40 degree bank until a 90° heading change is accomplished. The vehicle is then rolled to zero bank. This entry control mode required a 27.5 degree angle of attack to obtain 2778 km crossrange. The corresponding equilibrium temperatures are shown in Slide 11 for longitudinal stations along the bottom centerline. The peak temperature (1367°K) occurs at station $X/L = .25$. The greatest total heat load also occurs for station $X/L = .25$ and is equal to 167 MJ/m².

DELTA ORBITER ENTRY TRAJECTORY CASE I



Slide 10

DELTA ORBITER BOTTOM ζ TEMPERATURES CASE I



Slide 11

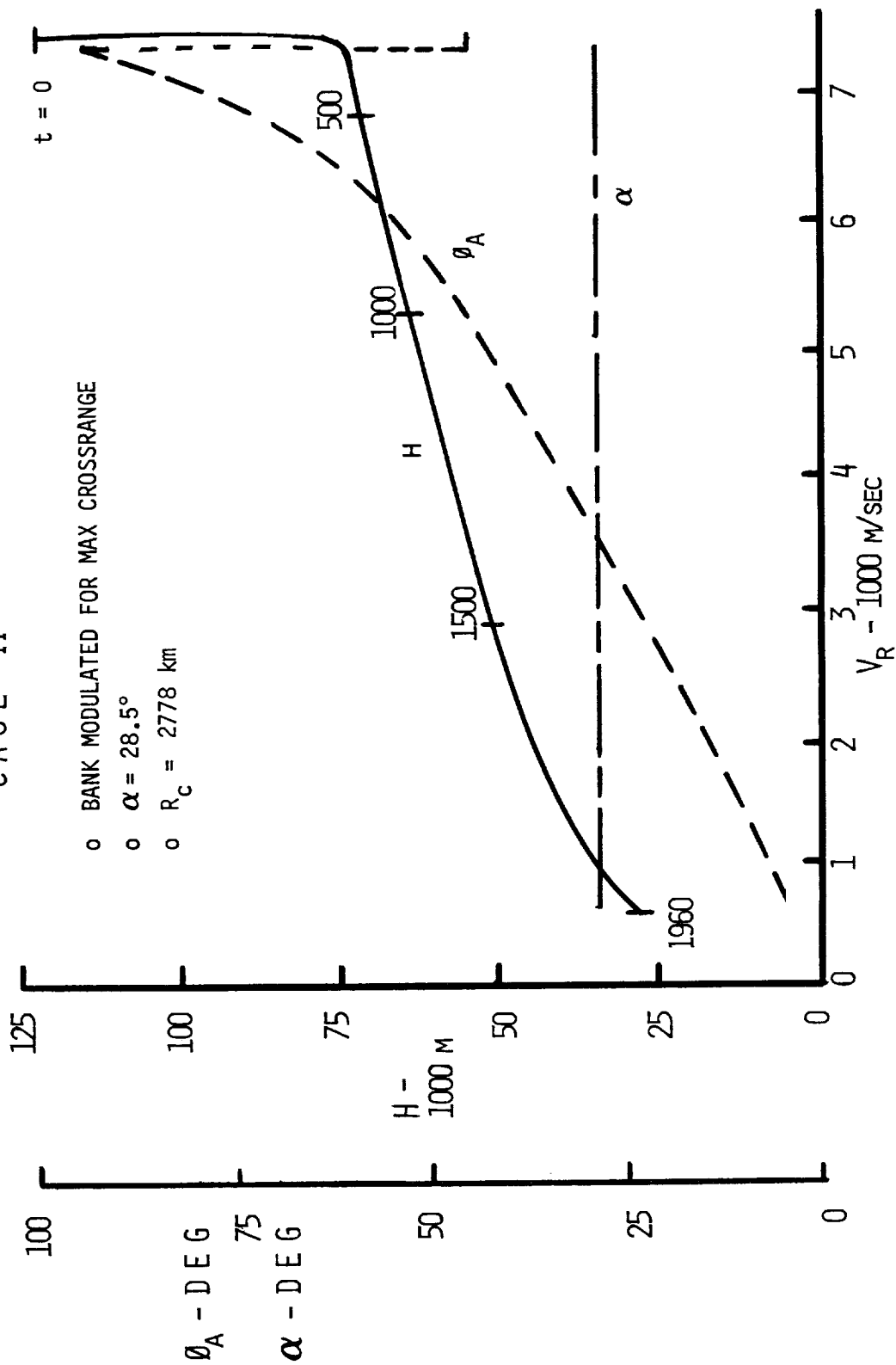
ENTRY TRAJECTORY AND BOTTOM ζ TEMPERATURES

Case II

(Slides 12 and 13)

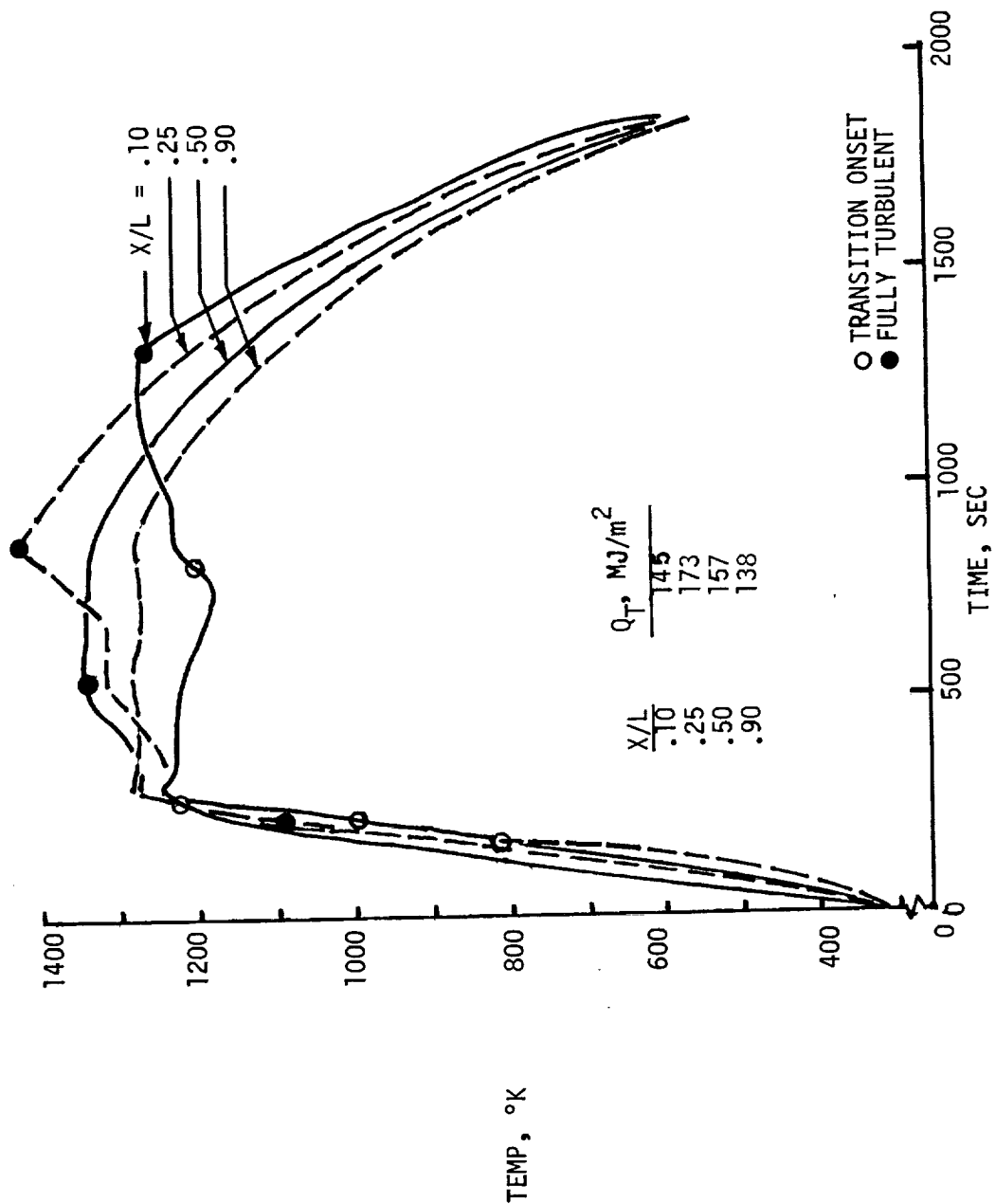
The second type of entry control employed is the maximum crossrange mode for a fixed angle of attack. Because of the more optimum bank control profile than the preceding case, a one degree higher angle of attack (28.5 degrees) will obtain the 2778 km crossrange. Maximum temperature occurs at station $X/L = .25$ and is 1420°K. Since this entry is flown at a lower lift-to-drag ratio than Case I, the total flight time is reduced and consequently the average total heat load is less.

DELTA ORBITER ENTRY TRAJECTORY CASE II



Slide 12

DELTA ORBITER BOTTOM ξ TEMPERATURES CASE II



Slide 13

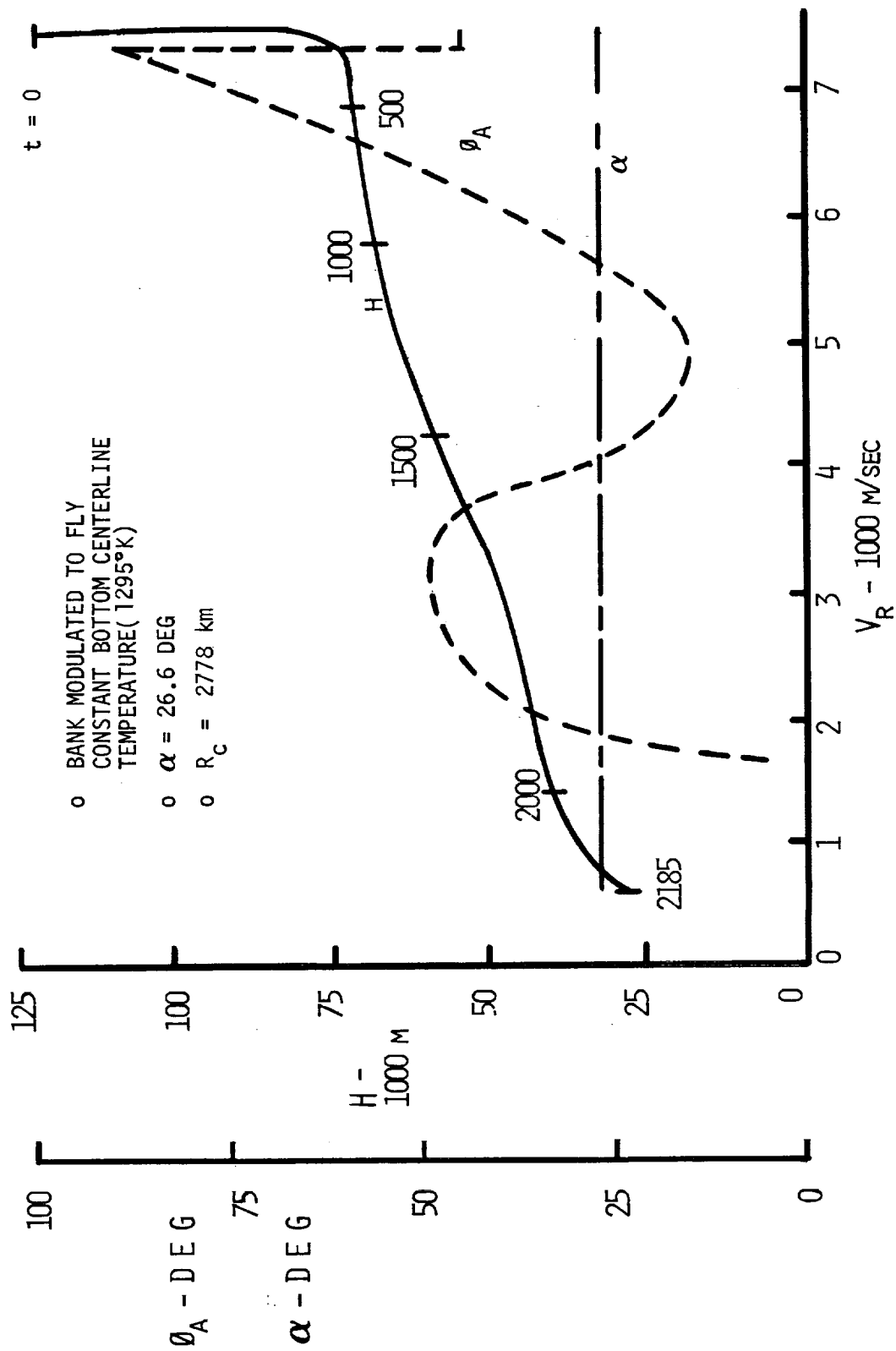
ENTRY TRAJECTORY AND BOTTOM \dot{C} TEMPERATURES

Case III

(Slides 14 and 15)

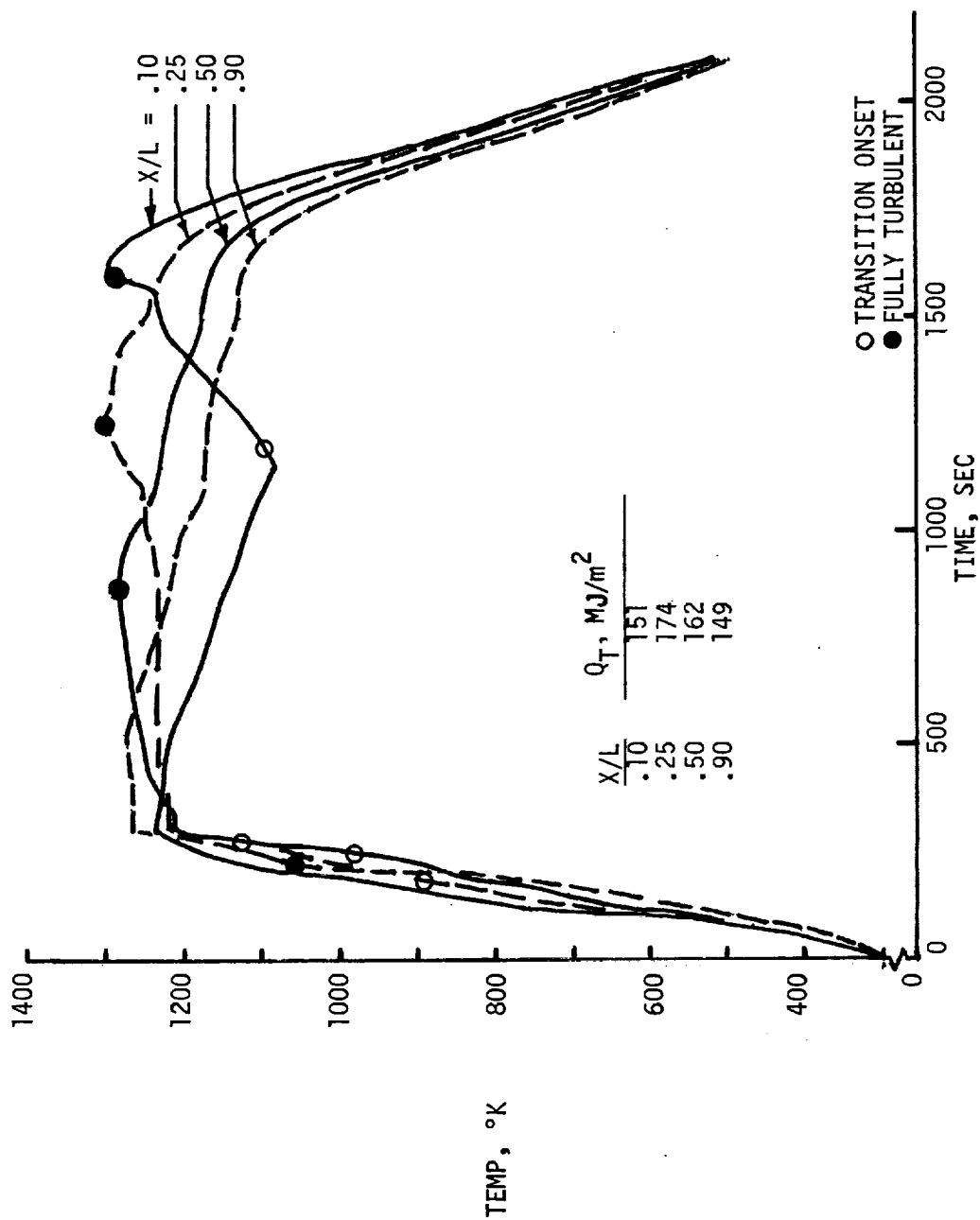
Because of the high temperature encountered for the previous case, Case III is computed to fly a constant bottom centerline temperature by incorporating a fixed angle of attack (26.6°) and by modulating bank angle following pull-out as shown in Slide 14. Constant temperature bank mode is continued until $V_R = 3800$ m/sec. Then the vehicle is bank modulated to fly constant flight path angle until zero bank is achieved. The time to initiate the roll-out is selected to maximize crossrange. The maximum temperature is 1295°K , a significant reduction from Cases I and II. However, the flight time and total heat load at $X/L = .25$ and aft increase as a result of flying a less efficient entry from a crossrange standpoint.

DELTA ORBITER ENTRY TRAJECTORY CASE III



Slide 14

DELTA ORBITER BOTTOM ζ TEMPERATURES CASE III



Slide 15

ENTRY TRAJECTORY AND BOTTOM \dot{C} TEMPERATURES

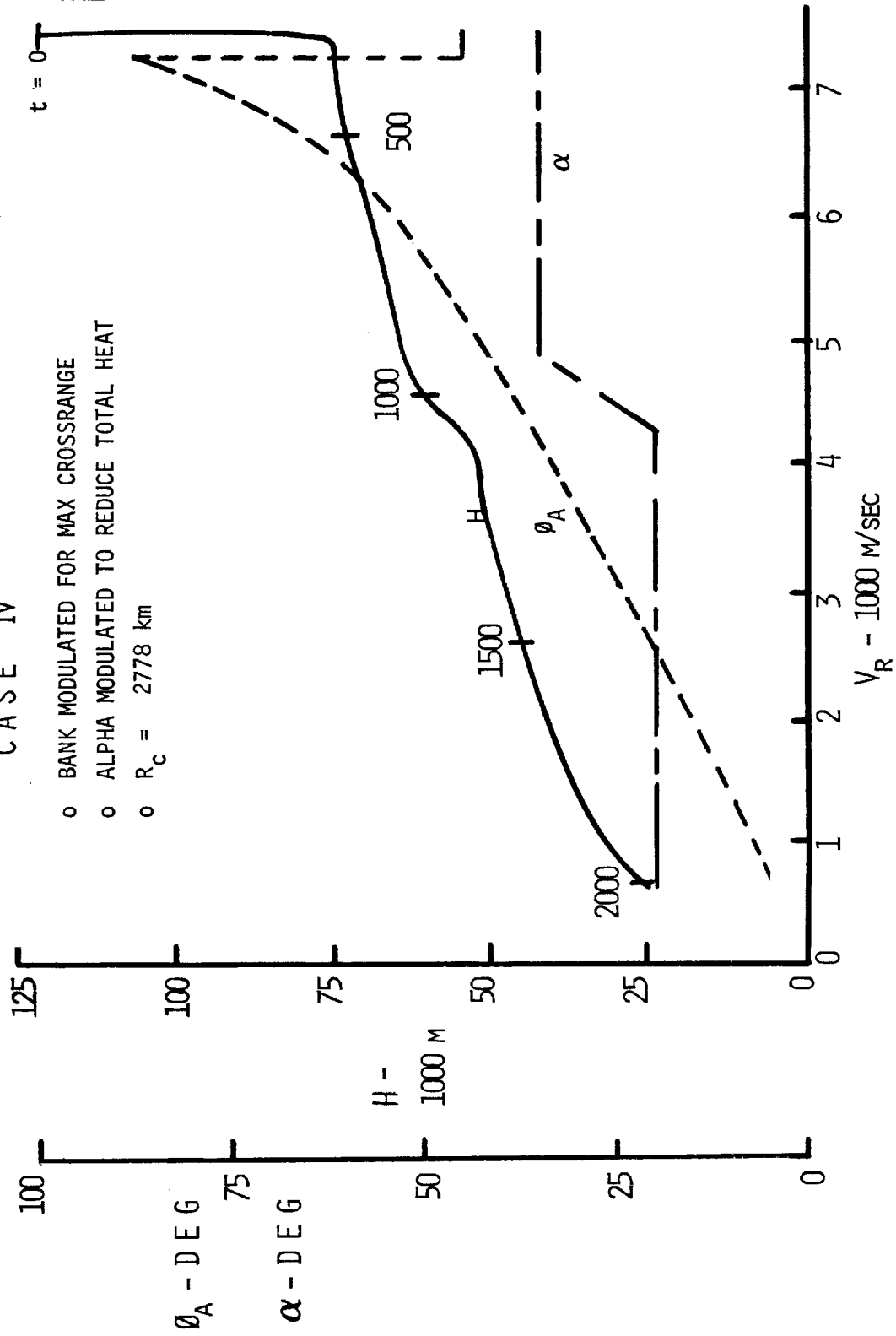
Case IV

(Slides 16 and 17)

Case IV is angle of attack modulated as well as bank angle modulated (Slide 16). Bank angle is controlled to achieve maximum crossrange while angle of attack is varied to reduce total heat. During the high heating region ($V_R > 4900$ m/sec), the angle of attack is maintained at 35 degrees. It is then ramped to 20 degrees when $V_R = 4260$ m/sec. The maximum bottom centerline temperature is 1390°K and again occurs at $X/L = .25$. Compared to the constant angle of attack entries, the average total heat is reduced as a result of flying high angle of attack during the high heating portion of the entry.

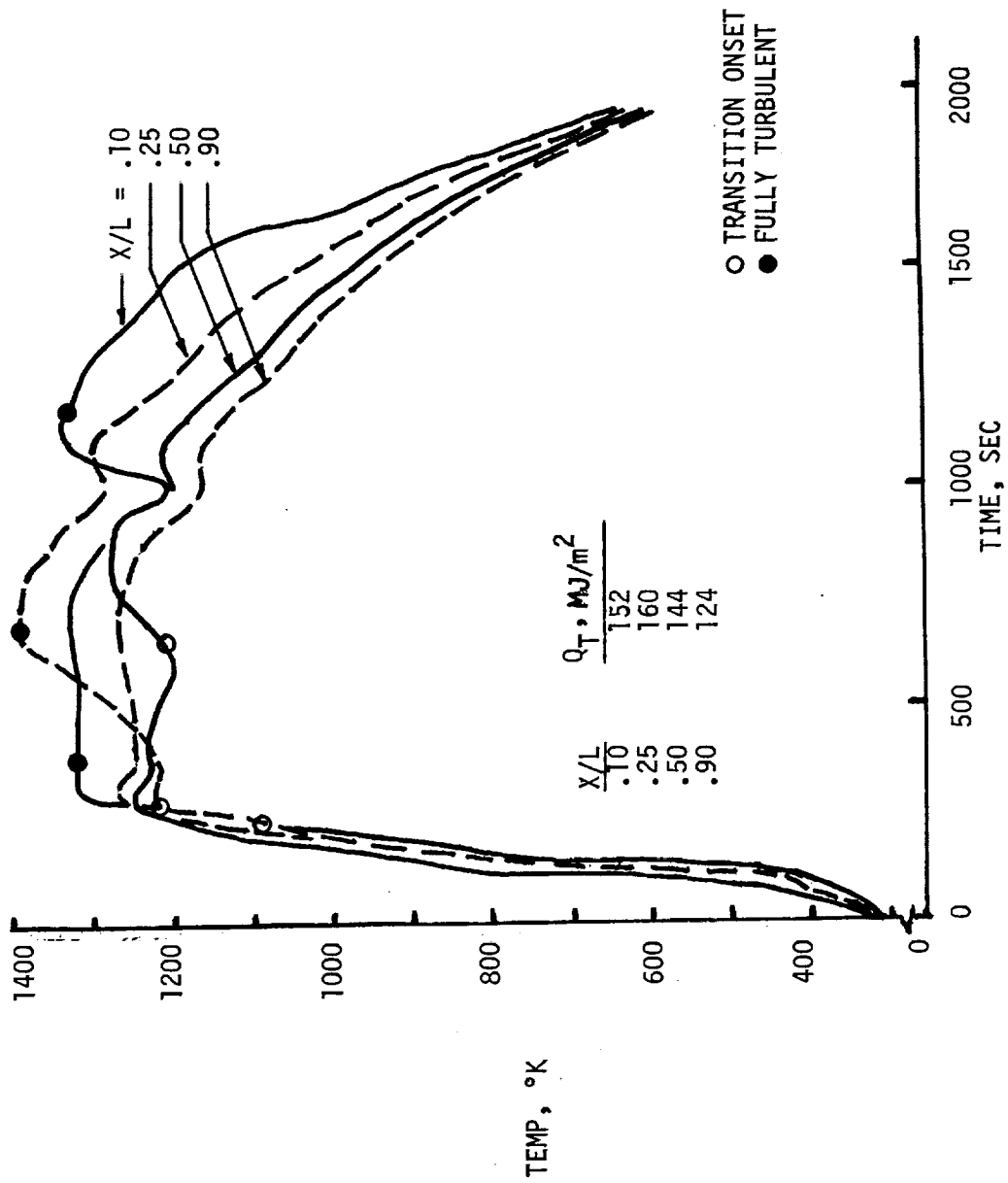
DELTA ORBITER ENTRY TRAJECTORY

CASE IV



Slide 16

DELTA ORBITER BOTTOM ζ TEMPERATURES CASE IV



Slide 17

ENTRY TRAJECTORY AND BOTTOM \bar{C} TEMPERATURES

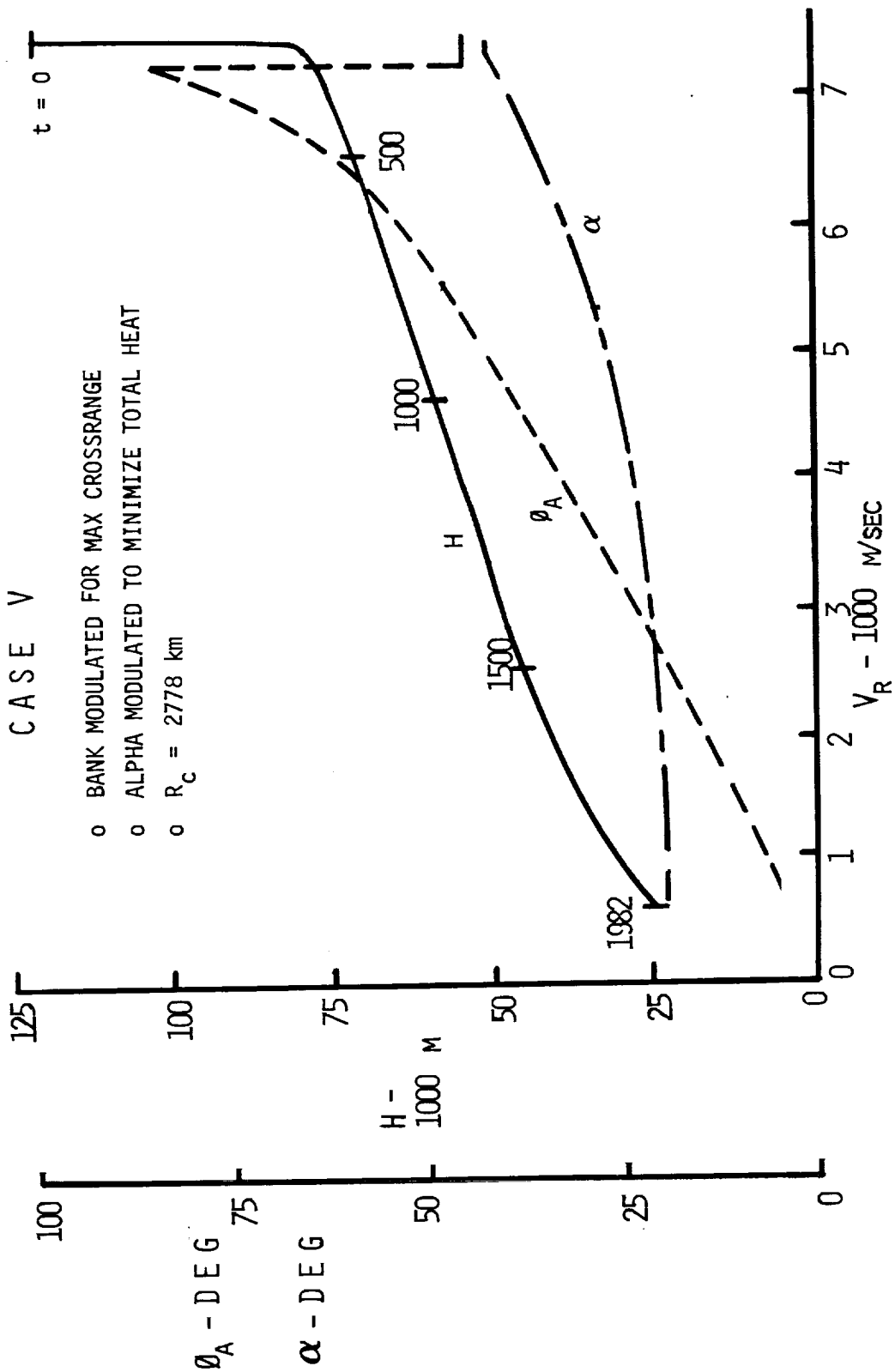
Case V

(Slides 18 and 19)

The minimum total stagnation heating entry control is incorporated in Case V. In this case, Slide 18, the angle of attack is initially 42 degrees. Following pull-out, the angle of attack is slowly reduced as velocity decreases until reaching 20 degrees. As in Cases II and IV, bank angle is modulated to achieve maximum crossrange. This method yields a shorter flight time than Case IV. In addition, there are no abrupt changes in the trajectory as when the angle of attack is ramped.

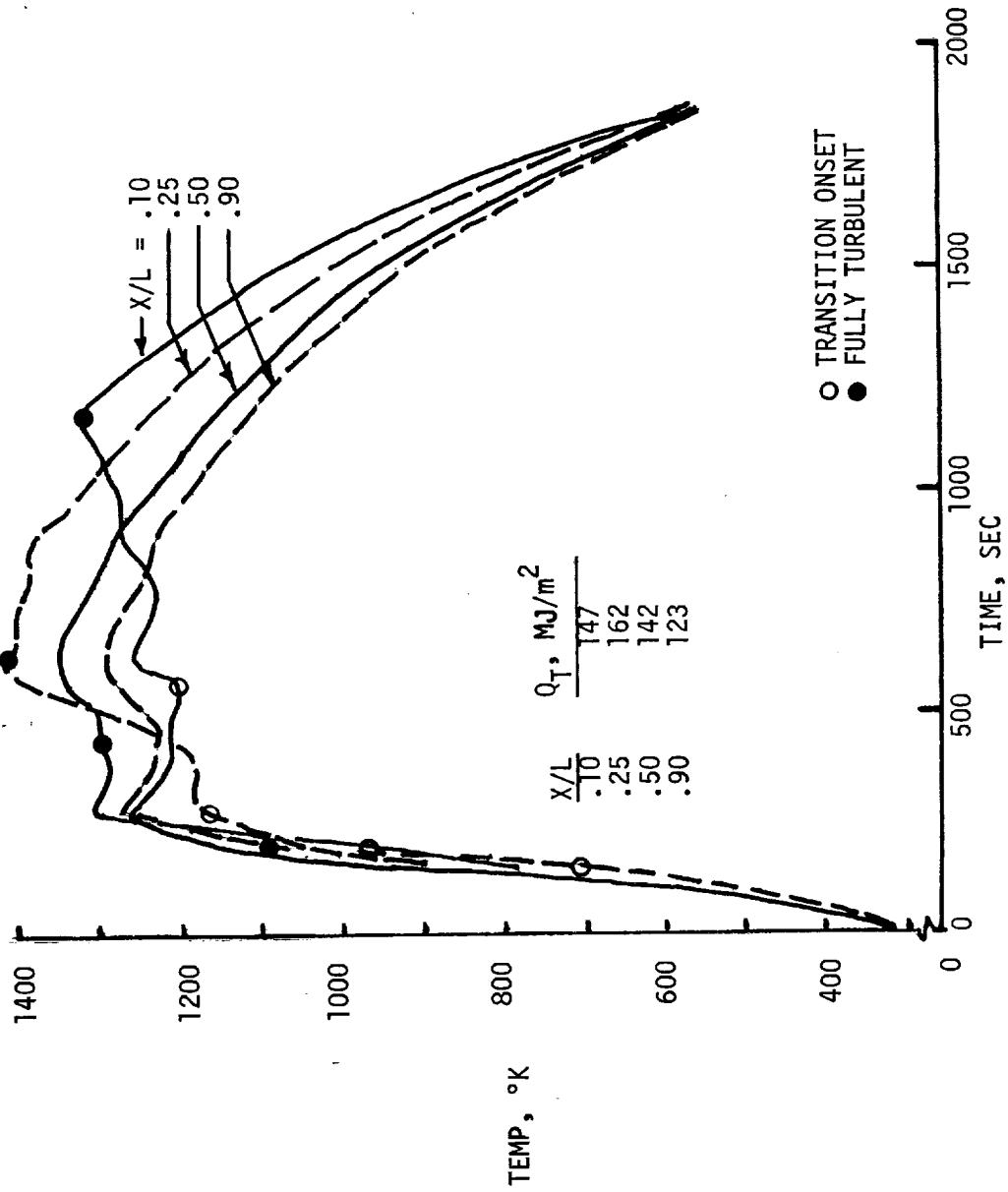
The entry temperatures and total heats are presented in Slide 19. This case encounters a peak temperature of 1410°K as compared to 1390°K for Case IV. However, the shorter flight time does yield a reduction in total heat for all stations except $X/L = .25$.

DELTA ORBITER ENTRY TRAJECTORY CASE V



Slide 18

DELTA ORBITER BOTTOM ζ TEMPERATURES CASE V



Slide 19

TRAJECTORY AND HEATING SUMMARY

(Slides 20 and 21)

A summary of the entry trajectories and corresponding heating data is shown in Slides 20 and 21. The total stagnation heat* and entry time are inversely proportional to the maximum bottom centerline temperature for the constant angle of attack entries. The variation in maximum normal load factor is due to the different bank modulation schemes employed. Cases I and III are banked approximately 40 degrees during the region of peak load factor ($1500 \leq V_R \leq 2500$ m/sec) as opposed to 13 degrees for Case II.

The advantage of angle of attack modulation to reduce total heat is indicated by comparing Cases IV and V to Case II since the same bank modulation scheme is employed. Total stagnation heating is reduced by approximately 14 percent in addition to a slight decrease in the maximum stagnation heating rate; entry time increases slightly. The maximum bottom centerline temperature is decreased by flying higher angles of attack during the peak heating region ($4900 \leq V_R \leq 6000$ m/sec).

There is no apparent correlation between maximum stagnation heating rate and maximum bottom centerline temperature at any body station.

* calculated for a .305 meter radius reference sphere

ENTRY TRAJECTORY SUMMARY

CASE NO.	R_d - km	R_c - km	t - SEC	REFERENCE MAX. \dot{q} - kW/m ²	REFERENCE Q_T - MJ/m ²	MAX. N_z - g's
I	10000	2778	2147	1053	1125	1.37
II	8640	2778	1958	1042	995	1.09
III	10150	2778	2185	1053	1162	1.43
IV	7970	2778	2011	941	870	1.14
V	7850	2778	1982	862	842	1.05

Slide 20

ENTRY HEATING SUMMARY

MAX. TEMPERATURE - °K	CASE NUMBER				
	I	II	III	IV	V
a X/L = .10	1320	1269	1286	1336	1308
= .25	1365	1420	1290	1390	1410
= .50	1280	1347	1274	1263	1342
= .75	1286	1296	1279	1286	1291
= .90	1269	1286	1263	1269	1280
TOTAL HEAT - MJ/m ²					
a X/L = .10	156	145	151	152	147
= .25	167	173	174	160	162
= .50	153	157	162	144	142
= .75	150	144	156	129	128
= .90	146	138	149	124	123

Slide 21

METALLIC SHINGLE UNIT WEIGHTS

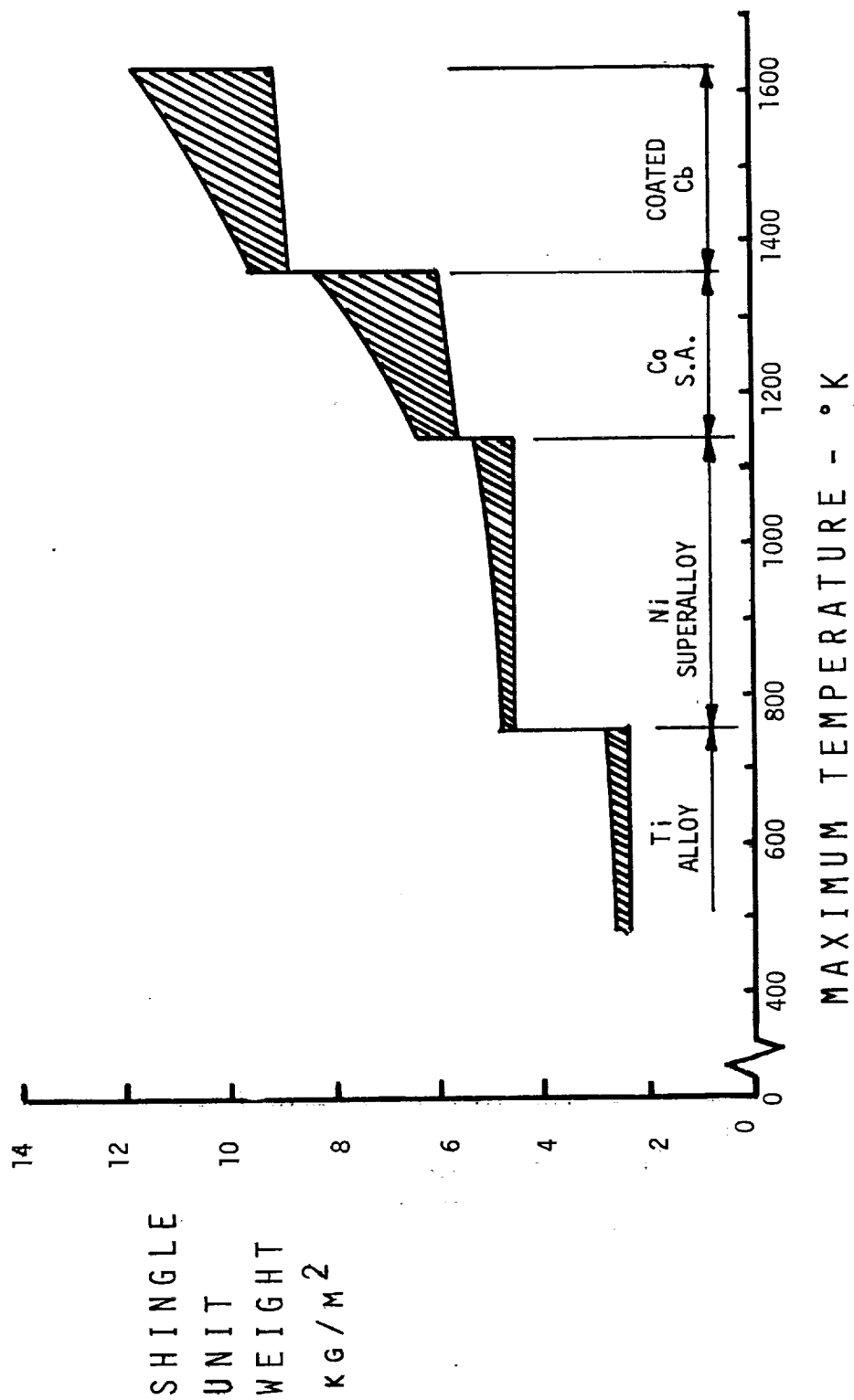
(Slide 22)

The external panel is the heaviest component of a metallic TPS, comprising roughly half the total weight. Slide 22 illustrates unit weights for single faced corrugated panels which are simply supported at 51 cm spans, and sized for critical loading at elevated temperatures. The upper and lower bounds of the shaded areas correspond to applied pressures of 10350 and 3450 newton/meter², respectively.

The slide illustrates the current maximum use temperature for each of the shingle materials. The slide also illustrates the significant weight differential associated with a change in panel material. Aside from its obvious temperature dependency, the unit weight of metallic TPS panels is for all practical purposes invariant with time, neglecting mechanical property degradation.

In the present study, the TPS panel materials were selected by maximum entry temperatures and sized by ascent pressures at room temperature. The bottom surface temperatures were in the range which dictated the use of Cobalt superalloy and coated Columbium. Consistent with the MDC Shuttle design criterion which requires material selection to be based 1.04 x design temperature (°C), coated Columbium alloy was selected for all areas having temperatures in excess of 1320°K.

METALLIC SHINGLE UNIT WEIGHTS



Slide 22

HARDENED COMPACTED FIBERS UNIT WEIGHT

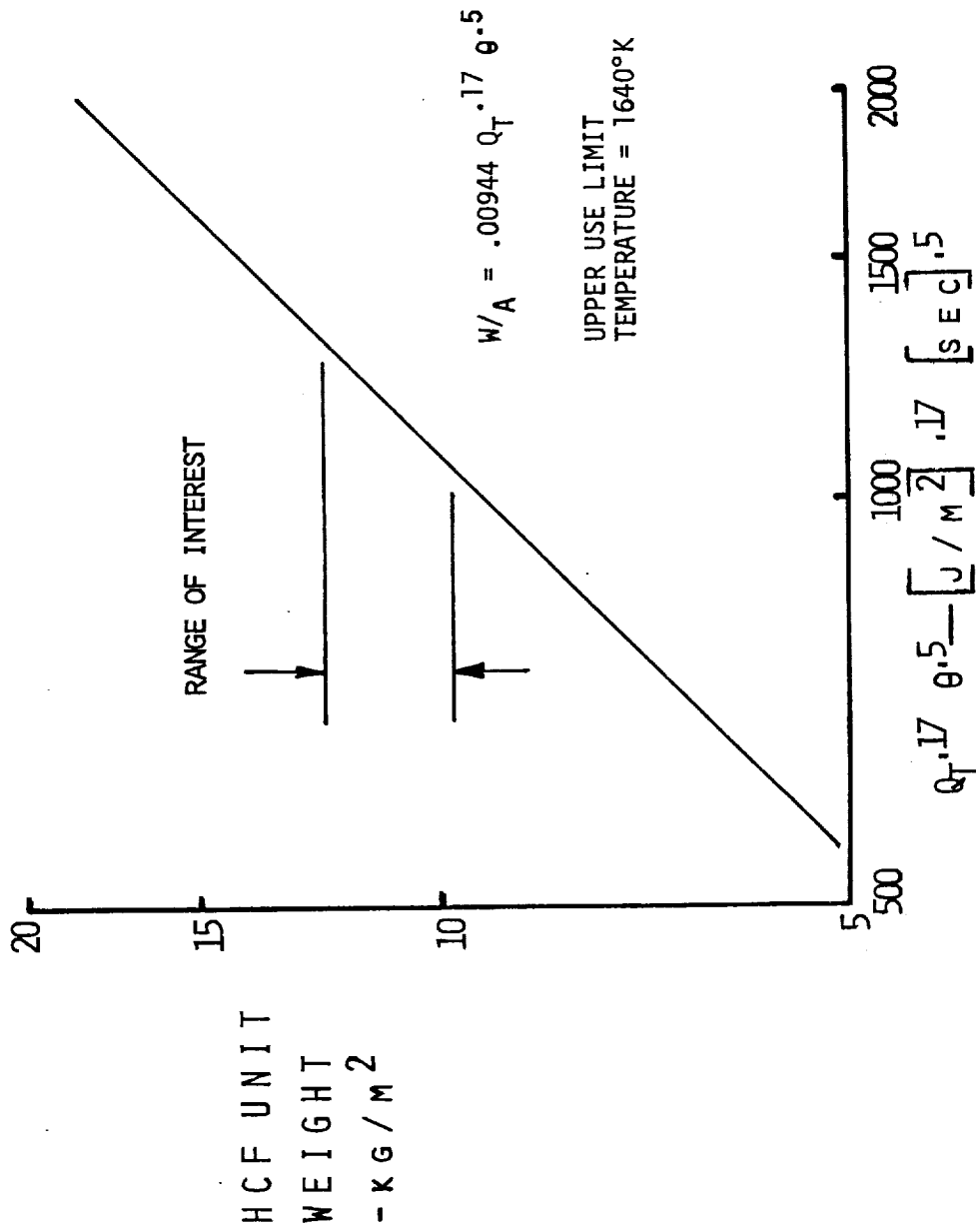
(Slide 23)

The non-metallic TPS typically consists of an approximately 5 cm thick layer of Hardened Compacted Fibers (HCF) surface insulation bonded to a Titanium honeycomb panel. The HCF thickness is sized to limit maximum bondline temperature at 533°K. If the internal structure and subsystems enclosed by the HCF can tolerate this temperature, no additional insulation is required. If not, additional fibrous insulation or low emittance coating is required. The dominant component of the non-metallic TPS weight is the HCF panel itself.

It has been found that the HCF weight required to maintain a specified bondline temperature over a given substructure can be expressed by an empirical relationship such as shown in Slide 23. The equation is used to compute HCF unit weight for the purpose of this paper. (For actual MDC design purposes, the HCF unit weights are computed using finite-difference equations of the appropriate thermal model.) The constants in the equation for unit weight depend upon the HCF physical properties and the heat sink properties of the support structure. This expression closely approximates the weight of the HCF having 240 kg/m³ density required to limit bondline temperatures over a Titanium honeycomb panel to 533°K.

It is seen that the unit weight of surface insulation is dependent upon both total heat input (related to surface temperature level) and the duration of the heat pulse, θ . This is in contrast to metallic TPS panel weight which is insensitive to time. It should be noted that HCF has an upper use temperature limit of 1642°K.

HCF UNIT WEIGHT



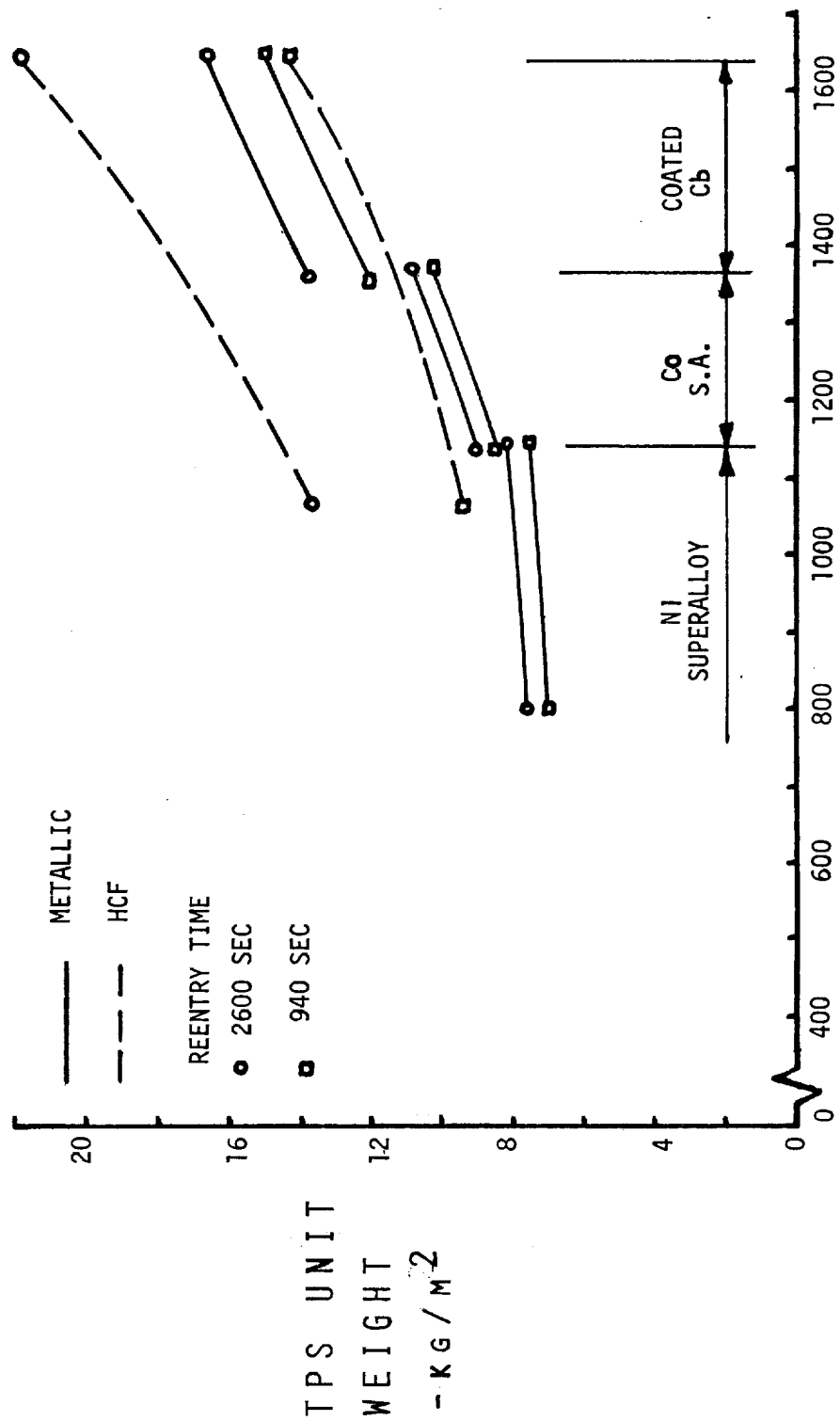
Slide 23

HCF AND METALLIC TPS UNIT WEIGHTS

(Slide 24)

Slide 24 shows complete metallic and non-metallic TPS unit weights for two heating pulse durations. The data in this example show TPS system weights required to protect a Titanium wing structure to a 589°K temperature limit. Critical loads and other design constraints were maintained constant. The slide shows that the unit weights for a complete metallic and non-metallic system both increase with entry time. The metallic system is less sensitive to entry time because the low density fibrous insulation employed in it is more efficient (as an insulator) than the HCF. The slide indicates that which system is the lighter is strongly dependent upon entry time. In addition, the metallic TPS is more sensitive to maximum temperature than the non-metallic for a constant entry time.

HCF AND METALLIC TPS UNIT WEIGHTS WING LOWER SURFACE



MAXIMUM TEMPERATURE - °K

Slide 24

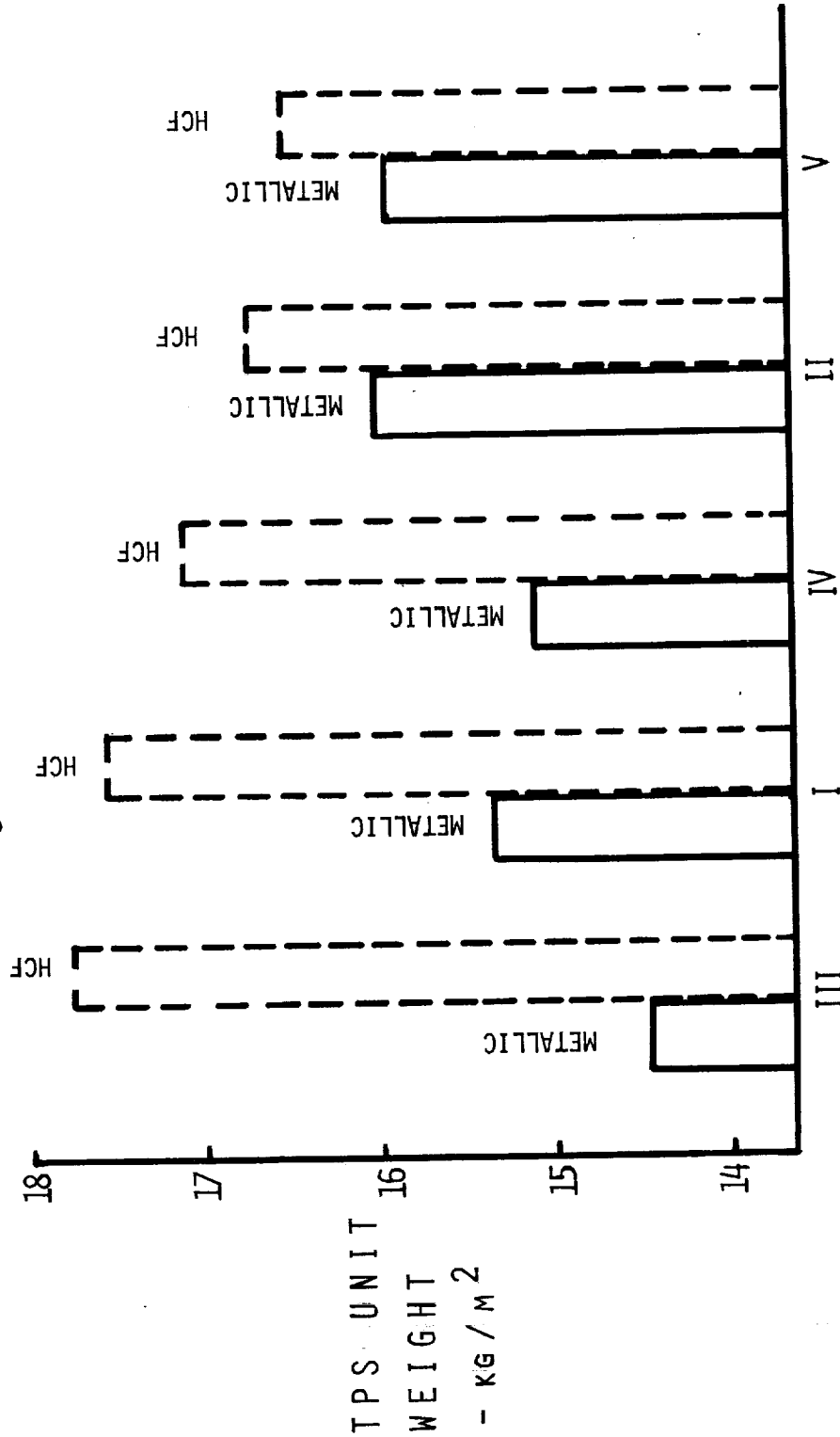
AVERAGE BOTTOM TPS UNIT WEIGHT

(Slide 25)

The impact of trajectory shaping on TPS weight is shown in Slide 25. It becomes apparent that Case III is best from the standpoint of metallic TPS weight while being worst for the non-metallic. This results from a deliberate attempt to minimize entry temperatures, which resulted in the longest flight time. Conversely, Case V which was shaped to minimize reference sphere total heat resulted, as might be anticipated, in the minimum HCF TPS system weight. Because Case V was shaped without regard for a temperature boundary, Columbia was required over a large fraction of the TPS area - with the resulting high average metallic TPS weight. Furthermore, the general tendency is observed that trajectory shaping which reduced HCF unit weight resulted in increased metallic unit weight.

AVERAGE BOTTOM TOTAL TPS UNIT WEIGHT

$$R_c = 2778 \text{ kg}$$



CASE NO.

Slide 25

AVERAGE BOTTOM SURFACE TPS UNIT WEIGHT COMPARISON

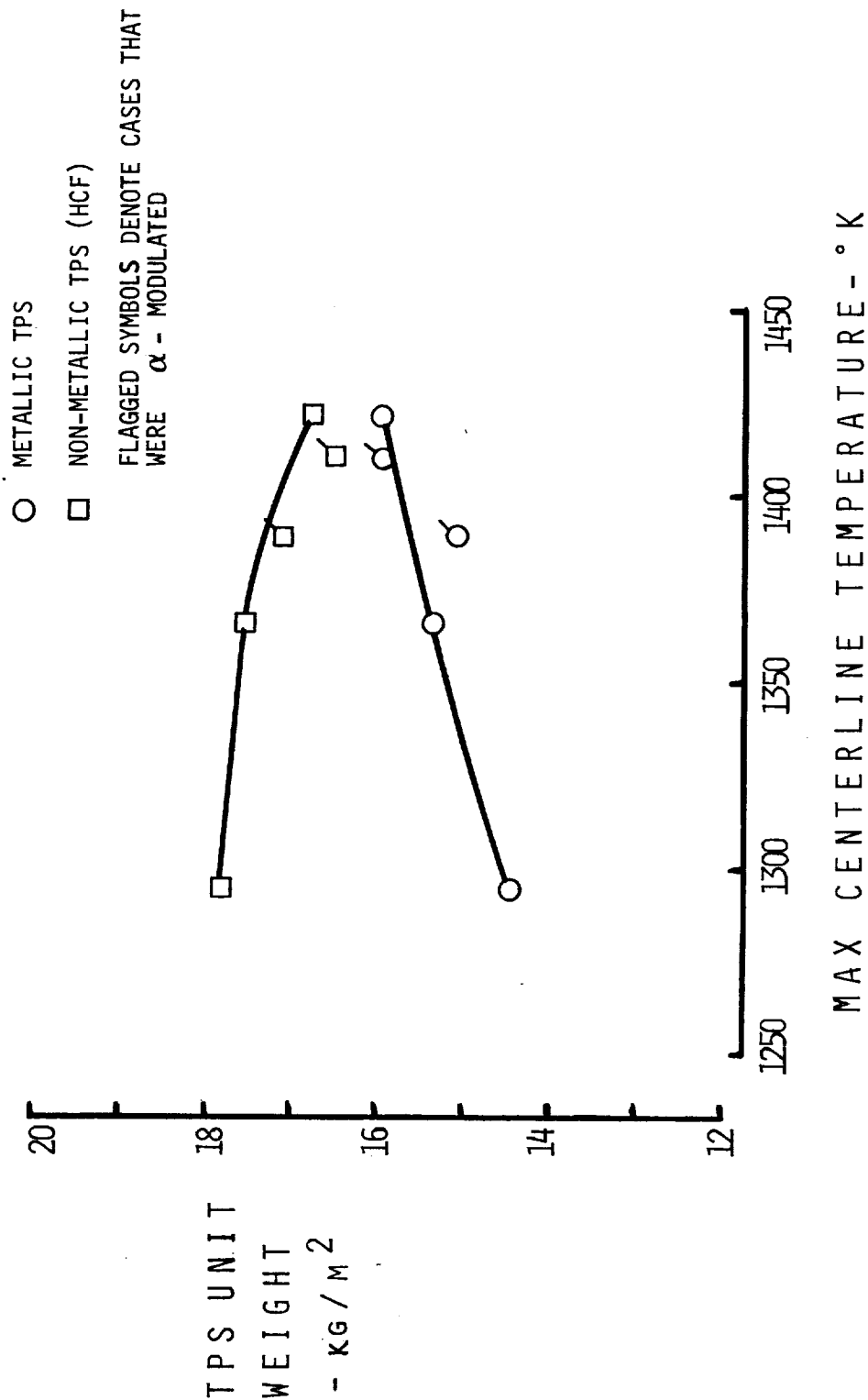
(Slide 26)

Slide 26 compares average TPS unit weights as a function of maximum bottom centerline temperature. The opposite trends of the metallic and non-metallic TPS are clearly indicated, for both constant and modulated angle of attack trajectories. The tendency for HCF TPS to become lighter with increasing maximum centerline temperature is the result of decreasing flight time and total heat load. (As the peak centerline temperature increases, the time required to attain a specified crossrange decreases.) The trend for the HCF system to become lighter as maximum temperature increases will be arrested as the use temperature limit is approached because more dense materials must be substituted for the HCF. Other factors such as airloads will contribute to the arrest.

The recent reduction of the Shuttle crossrange requirement from 2778 km to 2040 km affects the results presented in Slide 26. It is speculated that the non-metallic curve might be lowered by approximately 2 kg/m^2 whereas the metallic TPS curve might be lowered by about $.5 \text{ kg/m}^2$.

AVERAGE BOTTOM TOTAL TPS UNIT WEIGHT COMPARISON

$$R_c = 2778 \text{ kM}$$



Slide 26

CONCLUSIONS

(Slide 27)

The analysis of the entry trajectories presented herein indicates that the type of shaping significantly affects TPS requirements and that a different shaping philosophy should be employed for a metallic system than for a non-metallic system.

The shaping objective for a metallic TPS is to control the vehicle in a manner to minimize peak bottom centerline temperature. This will allow utilization of the lightest possible metallic material on the bottom surface. Particular attention should be focused on keeping stations aft of $X/L = .25$ at a minimal temperature level since approximately 90 percent of the bottom surface area is included in this region for a delta configuration.

For a non-metallic TPS, the shaping objective is to minimize total heat, subject to a constraint not to exceed the non-metallic design temperature. In order to achieve this goal, the entry flight path angle should be selected to yield pull-out near the design temperature limit. Following pull-out, the vehicle is bank/angle of attack modulated to minimize total heat, subject to the following constraints: 1) crossrange; 2) design temperature; and 3) load factors.

The optimal type of bottom surface TPS (from a weight criterion only) is a function of a minimum entry temperature to which the vehicle can be controlled and the design crossrange requirement. As the crossrange requirement is reduced, the unit weight for a non-metallic TPS decreases while the unit weight for a metallic TPS remains relatively constant.

CONCLUSIONS

- MINIMUM WEIGHT TPS (METALLIC OR NON-METALLIC) DEPENDS ON MINIMUM ENTRY TEMPERATURE THAT CAN BE FLOWN AND THE REQUIRED CROSS RANGE.
- ENTRY TRAJECTORY SHAPING IS REQUIRED TO MINIMIZE ORBITER TPS WEIGHT AND THE SAVINGS CAN BE SIGNIFICANT.

Slide 27

